



Fifth Asian School-Conference on
Physics and Technology of
Nanostructured Materials

Vladivostok, Russia, July 30 – August 03, 2020

P R O C E E D I N G S



Vladivostok
Dalnauka Publishing
2020

Fifth Asian School-Conference on Physics and Technology of Nanostructured Materials,
Vladivostok, Russia, July 30 – August 03, 2020: Proceedings. – Vladivostok : Dalnauka
Publishing, 2020. – 199.

ISBN 978-5-8044-1698-1

Copyright © 2020 by Institute of Automation and Control Processes of Far Eastern Branch of Russian Academy of Science. All rights reserved. No part of this publication may be multiple copied, stored in a retrieval system or transmitted in any form or by any means, electronic, mechanical, photocopying, recording or otherwise, without the written permission of the publisher. Single photocopies of single articles may be made for private study or research.

The Proceedings include abstracts of invited talks and contributed papers of the school-conference. The abstracts reflect the new results and scientific achievements in the field of new materials, nanotechnology and surface science. This proceedings volume is intended for scientist, teachers and post-graduate students.

ISBN 978-5-8044-1698-1

© IACP FEB RAS, 2020
© Dalnauka Publishing, 2020

**Fifth Asian School-Conference on
Physics and Technology of Nanostructured Materials**

Organizers

**Institute of Automation and
Control Processes of FEB RAS**



Far Eastern Federal University



The school-conference official website

<http://ntc.dvo.ru/conf/nanomat2020/>

Chair of ASCO-NANOMAT 2020

Professor **Nikolay GALKIN** (Institute of Automation and Control Processes FEB RAS and Far Eastern Federal University, Vladivostok, Russia)

INTERNATIONAL PROGRAMME COMMITTEE

Chair: Corr. Memb. RAS A.A. Saranin
(Vladivostok, Russia)

Vice-chair: Corr. Memb. RAS
A.V. Dvurechenskii (Novosibirsk, Russia)

Prof. E. Arushanov, Academician MAS.
(Chisinau, Moldova)

Prof. R.M. Bayazitov (Kazan', Russia)

Prof. Bakhtizin R.Z. (Ufa, Russia)

Prof. V.E. Borisenko (Minsk, Belarus)

Academician Yu.A. Chaplygin (Moscow, Russia)

Prof. A. Chuvilin (San Sebastian, Spain)

Prof. A.V. Latyshev, Academician RAS
(Novosibirsk, Russia)

Prof. V.G. Dubrovskii (S.-Petersburg, Russia)

Prof. A.V. Dvurechenskii, Corr.-member RAS
(Novosibirsk, Russia)

Prof. A.V. Filimonov (S.-Petersburg, Russia)

Prof. Y. Gao (Hubei, China)

Prof. N.V. Gaponenko (Minsk, Belarus)

Prof. S.A. Gavrilov (Moscow, Russia)

Prof. S.V. Gnedenkov, Corr.-member RAS
(Vladivostok, Russia)

Prof. D.G. Gromov (Moscow, Russia)

Prof. S. Hasegawa (Tokyo, Japan)

Prof. M. Imai (Tsukuba, Japan)

Prof. Y.K. Kim (Seoul, Korea)

Prof. V.V. Khovaylo (Moscow, Russia)

Prof. V.V. Korobtsov (Vladivostok, Russia)

Prof. G.Y. Krasnikov, Academician RAS
(Moscow, Russia)

Prof. D. Migas (Minsk, Belarus)

Prof. M.M. Mikhailov (Tomsk, Russia)

Prof. Y. Miyazaki (Tohoku, Japan)

Prof. A.A. Naberezhnov (S.-Petersburg, Russia)

Prof. S.G. Ovchinnikov (Krasnoyarsk, Russia)

Prof. B. Pecz (Budapest, Hungary)

Prof. V.S. Plotnikov (Vladivostok, Russia)

Prof. O.P. Pchelyakov (Novosibirsk, Russia)

Prof. R.V. Romashko, Corr.-member RAS
(Vladivostok, Russia)

Prof. A. Rogach (Hong-Cong, Peoples R China)

Prof. T.S. Shamirzaev (Novosibirsk, Russia)

Prof. G. Shao (Bolton, UK)

Prof. A.A. Shklyayev (Novosibirsk, Russia)

Prof. S.M. Shivaprasad (Bangalore, India)

Prof. T. Suemasu (Tsukuba, Japan)

Prof. H. Tatsuoka (Hamamatsu, Japan)

Prof. Y. Terai (Kyushu, Japan)

Prof. S.P. Timoshenkov (Moscow, Russia)

Prof. S.B. Vakhrushev (S.-Petersburg, Russia)

Prof. E.A. Vinogradov, Corr. Memb. RAS
(Troitsk, Russia)

Prof. O.B. Vitrik (Vladivostok, Russia)

Prof. H. Udono (Ibaraki, Japan)

Prof. N. Usami (Nagoya, Japan)

Prof. A.V. Zotov, Corr. member RAS
(Vladivostok, Russia)

ORGANIZING COMMITTEE

Chair: Prof. N.G. Galkin (IACP FEB RAS, FEFU)

Vice-chair: PhD., K.N. Galkin (IACP FEB RAS)

Secretary: Ph.D., S.V. Chusovitina (IACP FEB RAS)

Dr. Sci. D.L. Goroshko

(FEFU and IACP FEB RAS)

PhD., E.A. Chusovitin (IACP FEB RAS)

PhD., A.N. Galkina (IACP FEB RAS)

PhD., K.V. Ignatovich (IACP FEB RAS)

PhD., A.A. Kuchmijak (IACP FEB RAS and FEFU)

Dr. Sci., A.V. Ognev (FEFU)

Dr. Sci., A.S. Samardak (FEFU)

Mr., E.Yu. Subbotin (IACP FEB RAS)

PUBLISHING COMMITTEE

Chair: Prof. N.G. Galkin, (Vladivostok, Russia)

Prof. S.A. Gavrilov (Moscow, Russia)

Prof. Y. Gao (Hubei, China)

Prof. S.V. Gnedenkov, Corr. Memb. RAS
(Vladivostok, Russia)

Dr. Sci. D.L. Goroshko (Vladivostok, Russia)

Prof. D.B.Migas (Minsk, Belarus)

Prof. Y. Terai (Kyushu, Japan)

Prof. O.B. Vitrik (Vladivostok, Russia)

Prof. T. Suemasu (Tsukuba, Japan)

Prof. T.S. Shamirzaev (Novosibirsk, Russia)

Prof. Y.K. Kim (Seoul, Korea)

Contents

Invited lectures

PS.01.01i	Chemical synthesis, optical properties, and applications of carbon dots <i>Andrey L. Rogach</i>	17
PS.01.02i	Electrochromic films with plasmonic noble metal nanomaterials <i>Na Li, Jianbo Deng, Jiupeng Zhao, Yao Li</i>	18
PS.01.03i	Gold-decorated titania nanoparticles prepared by laser irradiation in water <i>Sergei A. Kulinich</i>	19
PS.01.04i	Laser ablation for shock generation, synthesis of colloids, and surface nanostructuring of bulk and film targets <i>N.A. Inogamov, A.A. Kuchmizhak, V.V. Zhakhovsky, V.A. Khokhlov, Y.V. Petrov</i>	20
PS.01.05i	Materials for all-dielectric nanophotonics: from silicon to perovskites <i>S.V.Makarov</i>	21
PS.01.06i	High-Q subwavelength dielectric resonators: from microwaves to optics <i>K. Koshelev, S. Kruk, M. Odit, E. Melik-Gaykazyan, J.-H. Choi, S. Gladyshev, K. Ladutenko, H.-G. Park, A. Bogdanov, Yu. Kivshar</i>	22
PS.03.01i	Unusual magnetism and strongly-correlated electrons in quasi-two-dimensional 4f-systems <i>D.V. Vyalikh</i>	23
PS.03.02i	Topological spintronics with (anti)skyrmions and bimerons <i>O.A. Tretiakov</i>	24
PS.03.03i	Magnetization switching in interface engineered W-based nonmagnet/ferromagnet heterostructures <i>Gyu Won Kim, In Ho Cha, Taehyun Kim, Yong Jin Kim, Young Keun Kim</i>	25
PS.03.04i	Electronic structure and magnetic properties of iron silicides <i>S.G. Ovchinnikov, V. Zhandun, N. Zamkova, O. Maximova, S. Lyaschenko, M. Vysotin, I. Sandalov</i>	26
PS.30.02i	Atomic scale tuning of quantum dot nucleation and epitaxial growth of heterostructures for nanophotonic and quantum information processing <i>A.V. Dvurechenskij, Zh.V. Smagina, V.A. Zinovyev, P.L. Novikov, S.A.Rudin, A.F.Zinovieva, A.V. Nenashev</i>	27
PS.30.03i	From first STM to complex analysis systems – 30 years' experience of R&D and production of metrological equipment <i>Victor Bykov, Vyacheslav Polyakov, Andrey V. Bykov, Vladimir Kotov, Stanislav Leesment, Yuri Bobrov</i>	28
PS.30.04i	Spin dynamics in indirect band gap III-As heterostructures <i>T.S. Shamirzaev</i>	32
PS.30.05i	Property modifications of 2D Me ₂ X (Me = Mg, Ca, Sr, Ba and X = Si, Ge, Sn): from 2D to 1D in ternary MeMe'X compounds <i>A.Yu. Alexeev, D. B. Migas, A. B. Filonov, V. E. Borisenko, N. V. Skorodumova</i>	33
PS.31.01i	Rare-earth-free semiconducting silicide solar cells and Mn ₄ N-based spintronic devices for sustainable electronics <i>T. Suemasu</i>	34
PS.31.02i	Development of Mg ₂ Si pn-junction photodiode <i>Haruhiko Udono</i>	35
PS.31.03i	Semiconducting ternary Si clathrates <i>M. Imai</i>	36
PS.31.04i	The role of heterogeneous melting in germanium nanowire growth by the electrochemical liquid-liquid-solid mechanism <i>S.A. Gavrilov</i>	37
PS.31.05i	Sn-nanodot mediated formation of GeSn and Si(Ge)Sn polycrystalline alloys for thermoelectric applications <i>Y. Shimura, J. Utsumi, M. Okado, K. Iwamoto, and H. Tatsuoka</i>	38

I. Physics of nanostructures and interfaces, self-organization processes

I.30.01o	Synthesis of carbon layers on aluminium oxide surfaces <i>M.M. Simunin, E.V. Mikhlina, A.S. Vyatkin, O.E. Bezrukova, I.A. Kharchenko, I.V. Nemtsev, A.S. Voronin, I.A. Tambasov, I.I. Ryzhkov</i>	40
I.30.02o	Atomic and electronic structure of top-down MAWCE silicon nanowires arrays and nanostructures on their basis <i>E.V. Parinova, V. Sivakov, D.A. Koyuda, O.A. Chuvenkova, D.N. Nesterov, A. Schleusener, T. Ming, D. Marchenko, A.K. Pisliaruk, R.G. Chumakov, A.M. Lebedev, D. Smirnov, A. Makarova, S.Yu. Turishchev</i>	41
I.30.03o	Investigation of the porous anodic titanium oxide layers self-organization process during formation by AES and ToF SIMS <i>A.A. Dronov, D.A. Dronova, I.M. Gavrilin, M.S. Kuzmicheva, E.P. Kirilenko, S.A. Gavrilov</i>	42
I.30.04o	Inclusion of the electron-electron interactions in the theory of photoemission by the TDDFT-based theory of the reduced density matrix <i>V.U. Nazarov</i>	43
I.30.05o	Photoemission electron microscopy application for functional nanostructures characterization <i>S.Yu. Turishchev, E.V. Parinova, O.A. Chuvenkova, F. Kronast, D. Marchenko, A.K. Fedotov, V. Sivakov, S.S. Antipov, A.K. Pisliaruk, R. Ovsyannikov, D.A. Koyuda</i>	44
I.30.06o	Theoretical and experimental studies of structural defects in CeO ₂ nanoparticles <i>M.A. Pugachevskii, A.N. Chibisov, A.S. Fedorov</i>	45
I.30.07o	Scanning probe microscopy/spectroscopy of oligonucleotides with a homonucleotide sequence <i>T.I. Sharipov, S. Santer, A. Kopyshv, I.T. Amangulova, R.Z. Bakhtizin</i>	46
I.30.08o	Two-dimensional materials grown on curved crystal substrates <i>Anna A. Makarova, Oleg Vilkov, Kirill Bokai, Dmitry Usachov, Laura Fernandez, Khadiza Ali, Dmitry Smirnov, Clemens Laubschat, Denis Vyalikh, Frederik Schiller, Enrique Ortega</i>	47
I.30.09o	Collective effects in quantum dot Si based nanostructures coupled with the hybrid metal-dielectric metasurfaces for nanophotonic <i>A.V. Dvurechenskii, A.I. Yakimov, V.V. Kirienco, A.A. Bloshkin, A.F. Zinovieva, A.V. Nenashev, V.A. Zinovyev</i>	48
I.30.10o	Soft X-rays synchrotron studies of the multilayered nanopperiodical structures with silicon nanoparticles formation <i>D.A. Koyuda, A.V. Ershov, V.A. Terekhov, E.V. Parinova, D.N. Nesterov, D.E. Spirin, T.V. Kulikova, B.L. Agapov, M.V. Grechkina, E.N. Zinchenko, I.A. Karabanova, U.A. Vainer, S.Yu. Turishchev</i>	49
I.30.11o	Electrical conductivity study of the adsorbate-induced Si(111) surface reconstructions after C ₆₀ adsorption <i>D.A. Tsukanov, M.V. Ryzhkova</i>	50
I.30.12o	Raman spectroscopy and features of magnetic properties of nanostructured carbon materials <i>A.M. Ziatdinov, N.S. Saenko, G.A. Zverev</i>	51
I.30.01p	Investigation of C ₆₀ growth on Si(111) "5×5"-Cu by optical second harmonic generation <i>K.V. Ignatovich</i>	52
I.30.03p	Nanocarbon shell for solid state alumina nanofibers transformations into spinel nanofibers <i>M.M. Simunin, A.S. Voronin, D.Yu Chirkov, S.S. Dobrosmyslov</i>	53
I.30.04p	The approximation of X-ray diffraction profiles of thermally reduced nanostructured graphene oxide <i>N.S. Saenko, D.A. Saritskiy, A.M. Ziatdinov</i>	54
I.30.05p	Scanning tunneling microscopy of Sn adatoms on the Si(111)5×2–Au surface <i>D.A. Olyanich, T.V. Utas, A.N. Mihalyuk, A.V. Zotov, A.A. Saranin</i>	55
I.30.06p	Effect of hydrodynamic conditions on the growth of nanostructured anodic WO _x formed in NH ₄ NO ₃ -based electrolyte <i>Y.V. Nazarkina, V. Benu, V.A. Rusakov, E.M. Eganova</i>	56
I.30.07p	Structural heterogeneity of amorphous-nanocrystalline alloy Fe ₇₇ Cu ₁ Si ₁₆ B ₆ in nanometer range <i>A.V. Ansovich, A.M. Frolov, G.S. Kraynova., V.V. Tkachev, S.V. Dolzhikov, V.S. Plotnikov, E.B. Modin</i>	57

I.30.08p	Highly-efficient photocatalytic degradation of organic compounds via zinc sulfide quantum dots <i>A.A. Sergeev, K.A. Sergeeva</i>	58
I.30.09p	Luminescent sensing via zinc sulfide quantum dots <i>A.A. Sergeev, Leonov A.A., S.S. Voznesenskiy</i>	59
I.30.10p	Initial stages of Bi adsorption on Si(111)5×2-Au <i>T.V. Utas, D.A. Olyanich, A.N. Mihalyuk, L.V. Bondarenko, A.Y. Tupchaya, D.V. Gruznev, A.V. Zotov, A.A. Saranin</i>	60
I.30.11p	Two-dimensional MgTe compound on the Si(111) surface <i>A.Y. Tupchaya, L.V. Bondarenko, Y.E. Vekovshinin, A.N. Mihalyuk, D.V. Gruznev, A.V. Zotov, A.A. Saranin</i>	61
I.30.12p	Comparative study of bismuth structures obtained via pulsed laser ablation in a liquid and in air <i>V.A. Svetlichnyi, E.D. Fakhruddinova, T.S. Nazarova, S.A. Kulinich, O.V. Vodyankina</i>	62
I.30.13p	Cooperation of genetic and metropolis algorithms for finding unconventional thermodynamic behaviour of many-body systems <i>R. Volotovskiy, Y. Shevchenko, A. Perzhu, E. Vasiliev, V. Kapitan, D. Kapitan, A. Rybin, K. Soldatov, A. Makarov, V. Strongin, K. Nefedev</i>	63
I.30.14p	AFM visualization of asphaltenes surface structure <i>T.I. Sharipov, G.F. Gilyazova, R.Z. Bakhtizin</i>	64
I.30.15p	Ab initio calculation of the equilibrium quantum state for hole spin of the B:Si system <i>M.A. Chibisova, A.N. Chibisov, S.I. Malkovsky</i>	65
I.30.16p	Feedback optimized replica-exchange Monte-Carlo algorithm <i>A. Rybin, D. Kapitan, P. Andriushchenko, E. Vasiliev, V. Kapitan</i>	66
I.30.17p	Influence of the surface treatment on the GaAs planar nanowire morphology <i>A.A. Spirina, N.L. Shwartz</i>	67
I.30.18p	Investigation of the plasma treatment process for the regeneration of SERS substrates sensitivity <i>A.I. Savitskiy, S.V. Dubkov, G.S. Eritsyayn, A.M. Tarasov, S.N. Skorik, E.P. Kitsyuk, D.G. Gromov</i>	68
I.30.19p	Calculation of order parameter and critical exponents of the spin glass in the frame of Edwards-Anderson model <i>D. Kapitan, A. Rybin, P. Andriushchenko, E. Vasiliev, V. Kapitan</i>	69
I.30.20p	Modeling of non-collinear magnetic states of the phosphorus qubit in a silicon lattice <i>A.N. Chibisov, M.A. Chibisova</i>	70

II. 4th group material's alloy based on Si, Ge, Sn & Pb: formation, structure and properties and properties

II.31.01o	Structural transformations on the Si(111) surface observed during Sn adsorption, desorption, and electromigration <i>A.S. Petrov, D.I. Rogilo, D.V. Sheglov, A.V. Latyshev</i>	72
II.31.02o	Effect of stoichiometry on aluminum-induced crystallization of a-SiO _x thin films <i>A.O. Zamchiy, E.A. Baranov, I.E. Merkulova, N.A. Lunev</i>	73
II.31.03o	Formation and structure of epitaxial GaSb nanodots in monocrystalline silicon <i>D.L. Goroshko, E.Yu. Subbotin, E.A. Chusovitin, S.V. Chusovitina, S.A. Dotsenko, A.K. Gutakovskii, N.G. Galkin</i>	74
II.31.04o	Etching of the Si(111) surface by a selenium molecular beam <i>S.A. Ponomarev, D.I. Rogilo, A.S. Petrov, L.I. Fedina, D.V. Shcheglov, A.V. Latyshev</i>	75
II.31.01p	Current relaxations in MIS structures based on PbSnTe:In films with low conductivity <i>A.N. Akimov, I.O. Akhundov, V.S. Epov, E.V. Fedosenko, V.A. Golyashov, D.V. Gorshkov, D.V. Ishchenko, A.E. Klimov, E.V. Matyushenko, I.G. Neizvestny, G.Yu. Sidorov, S.P. Suprun, A.S. Tarasov, O.E. Tereshchenko</i>	76
II.31.02p	Magneto-optical properties of Ge nanoparticles in the GeO matrix <i>A.V. Sherepa, V.N. Zabluda, K.N. Astankova, I.A. Azarov, A.E. Sokolov</i>	77
II.31.03p	Indium-based metal induced crystallization of amorphous silicon suboxide thin films <i>A.O. Zamchiy, E.A. Baranov, I.E. Merkulova, N.A. Lunev</i>	78

III. Physics of semiconducting nanostructures and heterostructures, including silicide, germanide and stannide heterostructures: experiment, calculations and technology

III.31.01o	Transport properties of CaSi ₂ and Ca ₂ Si thin films <i>L. Dermenji, K.G. Lisunov, K.N. Galkin, O.V. Kropachev, E.A. Chusovitin, N.G. Galkin, E. Arushanov</i>	80
III.31.02o	Single layer nickel disilicide on Si(111) surface <i>L.V. Bondarenko, A.Y. Tupchaya, A.N. Mihalyuk, D.V. Gruznev, A.V. Zotov, A.A. Saranin</i>	81
III.31.03o	Computer simulation of oxygen vacancy formation in YFeO ₃ perovskite <i>A.A. Gnidenko, P.G. Chigrin, E.A. Kirichenko</i>	82
III.31.04o	Iron disilicide lattice thermal expansion coefficients from first principle calculations <i>M.A. Visotin, I.A. Tarasov, A.S. Fedorov, S.G. Ovchinnikov</i>	83
III.31.05o	Formation of Fe ₂ Si Wetting Coating and Fe Growth on Si(001): AES and EELS Study <i>N.I. Plusnin, A.M. Maslov, V.M. Il'yashenko</i>	84
III.31.06o	Mg ₂ Sn under pressure: first principle evolutionary search results <i>Yu.V. Luniakov</i>	85
III.31.07o	Investigation of the effect of the amount of Au catalyst on the morphology of porous silicon layers obtained by the metal-assisted chemical etching <i>G.O. Silakov, O.V. Volovlikova, K. Bazov</i>	86
III.30.01p	Identification of structure ordering of melt-spun Fe ₇₀ Cr ₁₅ B ₁₅ alloy by the entropy functionals <i>A.M. Frolov, T.A. Pisarenko</i>	87
III.30.02p	Electrochemical properties of electrodes based on anodic titanium oxide nanotubular layers <i>D.A. Dronova, A.S. Gavrilov, A.A. Dronov</i>	88
III.30.03p	Radiation induced defects in hollow particles of zinc oxide <i>A.N. Dudin, V.V. Neshchimenco</i>	89
III.30.04p	Growth and thermoelectric properties of composite thin films based on higher iron and manganese silicides <i>I.A. Tarasov, I.A. Yakovlev, M.N. Volochaev, Z.I. Nazarova, A. Nazarov, A.S. Fedorov, S.N. Varnakov, S.G. Ovchinnikov</i>	90
III.30.05p	Relationship between the photoluminescence spectra and MIR spectroscopy of mesoporous silicon samples during long-term storage: the effect of immersion in LiBr solutions <i>N.G. Galkin, D.T. Yan, K.N. Galkin, S.V. Chusovitina</i>	91
III.30.06p	Electronic structure and morphology at the formation of multilayer heterostructures with embedded nanocrystals CrSi ₂ and β-FeSi ₂ <i>K.N. Galkin, N.G. Galkin, E.Yu. Subbotin</i>	92
III.30.07p	Optical properties and phonon structure of multilayer heterostructures with embedded CrSi ₂ and β-FeSi ₂ nanocrystals <i>N.G. Galkin, K.N. Galkin</i>	93
III.30.08p	Current-voltage characteristics and photoelectric properties of mesa-diodes based on multilayer heterostructures with imbedded CrSi ₂ and β-FeSi ₂ nanocrystals <i>N.G. Galkin, K. N. Galkin, E. A. Chusovitin, D. L. Goroshko</i>	94
III.30.09p	Growth, structure and low temperature magneto transport in Ca ₂ Si films on Si(111) substrate <i>N.G. Galkin, K.N. Galkin, A.V. Tupkalo, S.A. Dotsenko, E.A. Chusovitin</i>	95
III.30.10p	Relationship between the photoluminescence spectra and MIR spectroscopy of mesoporous silicon samples during long-term storage: the effect of immersion in Fe(NO ₃) ₃ solutions <i>N.G. Galkin, K.N. Galkin, D.T. Yan, S.V. Chusovitina</i>	96
III.30.11p	First demonstration of n ⁺ -AZO/p-BaSi ₂ thin film solar cells <i>Y. Yamashita, K. Toko, T. Suemasu</i>	97
III.30.12p	Marked photoresponsivity enhancement of boron-doped BaSi ₂ by atomic H passivation <i>Z. Xu, T. Sato, L. Benincasa, Y. Yamashita, T. Deng, K. Gotoh, K. Toko, N. Usami, A.B. Filonov, D.A. Shohonov, D.B. Migas, T. Suemasu</i>	98
III.30.13p	Structure and optical properties of thick Ca ₂ Si(100) epitaxial films on Si(111) substrate <i>K.N. Galkin, N.G. Galkin, S.A. Dotsenko, E.Y. Subbotin and O.V. Kropachev</i>	99

IV. Formation and properties of ferromagnetic and ferroelectric materials, sensors and spintronics

IV.03.01o	Magnetic circular dichroism and surface plasmon resonance in Ni@C nanoparticles <i>D.A. Petrov, I.V. Beketov, O.S. Ivanova, R.D. Ivantsov, I.S. Edelman, D.K. Baranov, I.A. Nekrasov, and A.A. Bagazeev</i>	101
IV.03.02o	Magnetic properties and FORC-based characterization of electrodeposited Co–W alloy nanowires <i>A.Yu. Samardak, E. Yoo, Y. S. Jeon, S.V. Komogortsev, A.V. Ognev, A.S. Samardak, Y.K. Kim</i>	102
IV.03.03o	Magnetic properties of nanocrystalline (Nd,R)-(Fe,Co)-B (R = Pr, Ho) alloys after melt spinning, severe plastic deformation and heat treatment <i>L.A. Ivanov, T.P. Kaminskaya, I.S. Tereshina, S.V. Dobatkin, G.A. Politova</i>	103
IV.03.04o	Ferroelectric-like structures in antiferroelectric epitaxial films under electric field bias <i>R.G. Burkovsky, G.A. Lityagin, A.F. Vakulenko, A.E. Ganzha, R. Gao, A. Dasgupta, A.V. Filimonov</i>	104
IV.03.05o	Magneto-optics of nanocomposites based on iron chalcogenide nanoparticles <i>R.D. Ivantsov, D.A. Petrov, O.S. Ivanova, I.S. Edelman, S.M. Zarkov, D.A. Velikanov, Chun-Rong Lin</i>	106
IV.03.06o	Novel topological objects in films with easy cone anisotropy <i>A.G. Kolesnikov, M.E. Steblyi, A.V. Davydenko, A.G. Kozlov, A.V. Ognev, A.S. Samardak, In Ho Cha, Yong Jin Kim, Young Keun Kim</i>	106
IV.03.07o	Magnetic and transport properties of trilayered Fe ₃ Si/Ge/Fe ₃ Si hybrid structures synthesized on Si(111) <i>A.S. Tarasov, I.A. Bondarev, M.V. Rautskii, A.V. Lukyanenko, D.A. Smolyakov, T.E. Smolyarova, I.A. Tarasov, I.A. Yakovlev, M.N. Volochaev, S.N. Varnakov, S.G. Ovchinnikov, N.V. Volkov</i>	107
IV.03.08o	Numerical simulation of magnetic skyrmions in ferromagnetic film <i>V. Kapitan, E. Vasiliev, A. Perzhu, D. Kapitan, R. Volotovskiy, A. Rybin, K. Soldatov, A. Makarov, V. Strongin, Y. Shevchenko, K. Nefedev</i>	108
IV.03.09o	Effect of magnetostatic interaction on the blocking temperature of core/shell nanoparticles <i>S.V. Anisimov, L.L. Afremov</i>	109
IV.31.01p	Monte-Carlo simulations of fast remagnetization process in FePt L1 ₀ granular films <i>Y. Shevchenko, R. Volotovskiy, E. Vasiliev, A. Perzhu, D. Kapitan, A. Rybin, K. Soldatov, A. Makarov, V. Strongin, K. Nefedev</i>	110
IV.31.02p	Multiscale magnetic anisotropy in amorphous ferromagnetic ribbon: an example of FeCuNbSiB alloy <i>N.V. Ilin, S.V. Komogortsev, G.S. Kraynova, V.A. Ivanov, A.V. Davydenko, R.S. Iskhakov, V.S. Plotnikov</i>	111
IV.31.03p	Skyrmion-antiskyrmion pairs by Monte-Carlo simulation in two-dimensional antiferromagnetic film <i>V. Kapitan, E. Vasiliev, A. Perzhu, Y. Shevchenko, K. Soldatov, D. Kapitan, R. Volotovskiy, V. Strongin, A. Rybin, A. Makarov</i>	112
IV.31.04p	Structural-magnetic models in search of new magnetic materials <i>L.M. Volkova, D.M. Marinin</i>	113
IV.31.05p	Magnetic and optical properties of the iron oxide nanoparticles obtained via pulsed laser ablation <i>A.V. Kurilova, A.E. Sokolov, V.A. Svetlichnyi, D.A. Velikanov, A.V. Sherepa, M.N. Volochaev, D.A. Goncharova, A.V. Shabalina</i>	114
IV.31.06p	Ferromagnetic oxide coatings on Al, Ti, Zr and Nb <i>V.S. Rudnev, I.V. Lukiyanchuk, M.V. Adigamova</i>	115
IV.31.07p	Features of the surface morphology and magnetic properties of Sm _{0.5} R _{0.5} Fe ₂ (R = Tb, Gd) compounds <i>G.A. Politova, T.P. Kaminskaya, A.Yu. Karpenkov, N.Yu. Pankratov, M.A. Ganin, D.G. Dankin, A.V. Filimonov</i>	116
IV.31.08p	Asymmetric domain wall propagation in epitaxial Pd/Co/Pd(111) trilayers <i>N.I. Sarnavskiy, A.G. Kozlov, A.V. Davydenko</i>	117

IV.31.09p	Dzyaloshinskii-Moriya interaction in [Co(1 nm)/Pd] ₅ superlattices with different thickness of Pd interlayers <i>Ya.S. Drozdovskiy, A.G. Kozlov, A.V. Davydenko</i>	118
IV.31.10p	Structure, crystallization and magnetic properties of new glasses in the MnNbOF ₅ -BaF ₂ -FeF ₃ system <i>L.N. Ignatieva, N.N. Savchenko, Yu.V. Marchenko, V.A. Mashchenko, I.A. Tkachenko</i>	119
IV.31.11p	Optically tunable magnetoimpedance in Fe/Al ₂ O ₃ /p-Si <i>M.V. Rautskii, D.A. Smolyakov, I.A. Bondarev, A.S. Tarasov, A.V. Lukyanenko, I.A. Yakovlev, A.N. Masyugin, M.N. Volochaev, N.N. Kosyrev, N.V. Volkov</i>	120
IV.31.12p	Magnetic properties of Fe ₃ Si synthesized at external magnetic field <i>I.A. Yakovlev, B.A. Belyaev, S.N. Varnakov</i>	121
IV.31.13p	Possibility of using analytical method to calculate magneto-optical parameter from magneto-ellipsometry measurements data <i>O.A. Maximova, S.G. Ovchinnikov</i>	122
IV.31.14p	Current induced manipulation of exchange bias in Pt/Co/NiO structure <i>M.E. Steblyi, A.G. Kolesnikov, M.E. Letushev, M.A. Bazrov, A.S. Samardak, A.V. Ognev, X. Wang, C. Wan, X. Han</i>	123
IV.31.15p	Study of gamma-ray scattering on Fe ₃ O ₄ /SiO ₂ /Au and Ta ₂ O ₅ nanoparticles <i>Yu.M. Borodaenko, K.S. Lukyanenko, Thomas Myeongseok Koo, Min Jun Ko, Yu Jin Kim, A.V. Ognev, A.S. Samardak, L.L. Afremov, Young Keun Kim</i>	124
IV.31.16p	Magnetic properties of Fe ₃ O ₄ /SiO ₂ /Au nanoparticles for enhancement of the radiation therapy effectiveness <i>M.I. Sobirov, L.L. Afremov, Thomas Myeongseok Koo, Min Jun Ko, Yu Jin Kim, A.G. Kolesnikov, A.V. Ognev, A.S. Samardak, Young Keun Kim</i>	125
IV.31.17p	Temperature dependence of the magnetic properties of Fe ₃ O ₄ /Au nanoparticles investigated by means of micromagnetic simulation <i>M.A. Sitnik, L.L. Afremov, Thomas Myeongseok Koo, Min Jun Ko, Yu Jin Kim, A.G. Kolesnikov, A.V. Ognev, A.S. Samardak, Young Keun Kim</i>	126
IV.31.18p	Controller for a VR system based on magnetic field sensors <i>Zh.Zh. Namsaraev, V.N. Kharitonov, P. Savinov, A.S. Samardak, R. Brizitsky, A.V. Ognev</i>	127
IV.31.19p	Development of a mathematical model for describing the motion of a sensor array in a magnetic field <i>V.N. Kharitonov, J.J. Namsaraev, A.S. Samardak, R. Brizitsky, A.V. Ognev</i>	128
IV.31.20p	Concentration phase transition in a two-dimensional ferromagnet <i>A.K. Chepak, L.L. Afremov</i>	129
IV.31.21p	Micromagnetic behavior of Fe/Au barcode nanowires: experiment and simulation <i>V.Yu. Samardak, Y.S. Jeon, E.M. Yoo, A.V. Ognev, A.S. Samardak, Y.K. Kim</i>	130

V. Laser nanofabrication and laser ablation in liquids: fundamentals and applications

V.01.01o	Pulsed laser ablation of silicon nanowires and porous silicon in liquids <i>S.V. Zobotnov, A.V. Skobelkina, F.V. Kashaev, D.E. Presnov, T.P. Kaminskaya, L.A. Golovan, P.K. Kashkarov, D.A. Kurakina, A.V. Khilov, E.A. Sergeeva, P.D. Agrba, M.Yu. Kirillin</i>	132
V.01.02o	Femtosecond pulse structuring of multicore fibers for development of advanced fiber lasers and sensors <i>A.V. Dostovalov, A.A. Wolf, K.A. Bronnikov, M.I. Skvortsov, S.A. Babin</i>	133
V.01.03o	Precise ablation of methylammonium lead iodide perovskite films with femtosecond laser pulses <i>A. Zhizhchenko, S. Starikov, S. Makarov, A. Kuchmizhak</i>	134
V.01.04o	The influence of liquid boiling on nanosecond laser damage threshold of metal immersed into water <i>S.V. Starinskiy, A.A. Rodionov, Yu.G. Shukhov, A.V. Bulgakov</i>	135
V.01.06o	Fabrication of anisotropic structures on amorphous silicon surfaces by femtosecond laser pulses <i>D.V. Shuleiko, M.N. Martyshov, D.V. Orlov, D.E. Presnov, S.V. Zobotnov, A.G. Kazanskii, P.K. Kashkarov</i>	136

V.01.07o	Functionalization of nanostructured Si surfaces for advanced sensing applications <i>A.Yu. Mironenko, A.A. Sergeev, M.V. Tutov, A.A. Kuchmizhak</i>	137
V.01.08o	Ultra-black coating based on micro hollow carbon sphere <i>L. Pan, Y. Hu</i>	138
V.01.09o	Photonic nanojet generation in transmission and reflection mode <i>K.A. Sergeeva, A.A. Sergeev</i>	139
V.01.10o	Beyond diffraction limit: local features of electromagnetic field in plasmon-based nanospectroscopy <i>E. Sheremet, A. Averkiev, S. Shchadenko, V. Kolchuzhin, R.D. Rodriguez</i>	140
V.01.11o	Functional plasmonic materials for targeted surface enhanced Raman spectroscopy: from pollutant detection to tumor discrimination <i>O. Lyutakov, O. Guselnikova, A. Trelin, V. Svorcik</i>	141
V.01.12o	Laser manipulation of microparticles with the help of structured light <i>A.P. Porfirev, A.B. Dubman, S.A. Fomchenkov</i>	142
V.01.13o	Size effect on optical properties of silicon dioxide hollow particles <i>V.I. Iurina, V.V. Neshchimenco, Li Chundong</i>	143
V.01.14o	Microsphere lithography for Fe ₃ Si-Au magnetoplasmonic nanostructures <i>I.A. Tarasov, T.E. Smolyarova, I.A. Yakovlev, I.V. Nemtsev, S.N. Varnakov, S.G. Ovchinnikov</i>	144
V.01.15o	Spectroscopic study of low-temperature dynamics in nanocomposites based on semiconductor colloidal quantum dots <i>K.R. Karimullin, A.I. Arzhanov, A.E. Eskova, K.A. Magaryan, N.V. Surovtsev, A.V. Naumov</i>	145
V.01.16o	Transformation of the nanoporous structure of anodic aluminium oxide and its electroluminescence without electrolysis <i>D.S. Ovechenko, A.P. Boychenko</i>	146
V.01.17o	Obtaining and properties of biomagnetic nanoconjugates based on DNA aptamers and magnetic nanoparticles for magnetodynamic cell therapy <i>A.E. Sokolov, A.V. Kurilova, V.A. Svetlichniy, D.A. Velikanov, A.V. Sherepa, M.N. Volochaev, D.A. Goncharova, A.V. Shabalina</i>	147
V.01.18o	A new efficient luminescent chemosensor of gaseous amines for medicine and food safety <i>A.N. Galkina, A.A. Leonov, R.V. Romashko, JIANG Jyh-Chiang</i>	148
V.31.01p	Laser printing of chiral silicon nanoprotusions by asymmetric donut-shaped femtosecond pulses <i>S.A. Syubaev, A.A. Kuchmizhak, A.P. Porfirev</i>	149
V.31.02p	Photoluminescence and features of the defective structure of nominally pure lithium niobate crystals <i>M. Smirnov, N.V. Sidorov, N.A. Teplyakova, M.N. Palatnikov, A.V. Syuy</i>	150
V.31.03p	Structural features and optical properties of nominally pure crystals of lithium niobate grown from a charge doped with boron <i>N.V. Sidorov, R. Titov, N.A. Teplyakova, M.N. Palatnikov, A.V. Syuy</i>	151
V.31.04p	Control of single crystal silicon wetting by laser ablation and fluoropolymer deposition <i>S.V. Starinskiy, A.I. Safonov, A.A. Rodionov, Yu.G. Shukhov, A.V. Bulgakov</i>	152
V.31.05p	Laser-printed plasmonic metasurfaces for enhancement of second harmonic generation <i>A.B. Cherepakhin, I.I. Shishkin, P.M. Voroshilov, A.A. Kuchmizhak, S.V. Makarov</i>	153
V.31.06p	Synthesis and study of the optical properties of branched organosilicon phosphors <i>M.V. Tutov, A.Yu. Mironenko</i>	154
V.31.07p	Visualization of the optical uniformity of rare-earth doped lithium niobate single crystals <i>O.Y. Pikoul, N.V. Sidorov, N.A. Teplyakova, M.N. Palatnikov</i>	155
V.31.08p	Properties of Bi and BiSb nanodimensional layers in THz frequency range <i>I.L. Tkhorzhevskiy, A.V. Asach, A.S. Tukmakova, E.S. Makarova, N.S. Kablukova, P.S. Demchenko, D.V. Zykov, A.D. Zaitsev, A.V. Novotelnova, M.K. Khodzitsky</i>	156
V.31.09p	Fabrication of laser-induced periodic surface structures for advanced sensing applications <i>Eugeny Mitsai, Alexander Dostovalov, Kirill Bronnikov, Aleksandr Kuchmizhak</i>	157

V.31.10p	Au nanoparticle-decorated TiO ₂ nanospheres produced by laser reshaping in water for sensing applications <i>S.O. Gurbatov, A.A. Kuchmizhak</i>	158
V.31.11p	Investigation of the mechanism of electric conductivity of strontium bismuthate Sr ₆ Bi ₂ O ₁₁ <i>D.S. Shtarev, A.V. Shtareva, A.V. Syuy, V.V. Likhtin</i>	159
V.31.12p	The features of the lateral photovoltaic effect in the Fe ₃ O ₄ /SiO ₂ /n-Si structure depending on silicon substrate orientation <i>T.A. Pisarenko, V.V. Korobtsov, V.V. Balashev, A.A. Dimitriev, S.V. Bondarenko</i>	160
V.31.13p	Generation of laser beams for laser printing of chiral nanoneedles <i>A.P. Porfirev, V.I. Logachev, G.E. Gridin, S.A. Degtyarev, S.N. Khonina</i>	161
V.31.14p	Multifunctional IR sensor platform produced by direct laser patterning <i>D.V. Pavlov, A.A. Kuchmizhak</i>	162
V.31.15p	Improvement of quartz crystal microbalance gas sensors by nanostructured thin films <i>P. Fítl, M. Hruška, D. Tomeček, J. Vlček, J. Otta, J. Fara, M. Vršata, M. Novotný</i>	163
V.31.16p	The influence of temperature on the lateral photovoltaic effect in the Fe ₃ O ₄ /SiO ₂ /n-Si structure <i>T.A. Pisarenko, V.V. Korobtsov, V.V. Balashev, A.A. Dimitriev</i>	164

VI. Nanostructured coverages, nanocomposites, functional hybrid materials: formation, structure and properties

VI.30.01o	Effect of electrolyte temperature on the kinetic of germanium nanowire growth by the electrochemical liquid-liquid-solid mechanism <i>I.M. Gavrilin</i>	166
VI.30.01o	CNT formation at the edge of a Co-Zr-N- (O) alloy film with a low content of catalytic metal for using in VLSI technology <i>G.S. Eritsyan, E.P. Kitsyuk, A.A. Shamanaev, D.G. Gromov</i>	167
VI.30.03o	Study of plasmons and thermoelectric properties of nanoparticles connected by thin conductive bridges <i>A.S. Fedorov, P.O. Krasnov, M. A. Visotin, H. Ågren</i>	168
VI.30.04o	Heat treatment of nanostructured powders obtained by spark erosion of WC-8Co cemented carbide in oil <i>M.I. Dvornik, E.A. Mikhailenko</i>	169
VI.03.05o	Metal and non-metal co-substituted titanium dioxide derivatives: synthesis and electrochemical performance <i>A.A. Sokolov, D.P. Opra, S.V. Gnedenkov, S.L. Sinebryukhov, E.I. Voit, A.Y. Ustinov, V.Y. Mayorov, V.V. Zheleznov</i>	170
VI.03.06o	Enhancement the lithium storage performance of TiO ₂ (B) through zirconium and vanadium doping <i>D.P. Opra, S.V. Gnedenkov, S.L. Sinebryukhov, A.A. Sokolov, A.B. Podgorbunsky, A.Yu. Ustinov, A.I. Neumoin, I.V. Imshinetskiy, K.V. Nadaraia, K.P. Opra, D.V. Mashtalyar</i>	171
VI.03.07o	Composite coatings formed on PEO pretreated MA8 magnesium alloy in aqueous suspension of PTFE <i>E.A. Belov, K.V. Nadaraia, D.V. Mashtalyar, I.M. Imshinetskiy, A.N. Minaev, S.L. Sinebryukhov, S.V. Gnedenkov</i>	172
VI.03.08o	PEO coated porous Mg/HAp implant materials impregnated with bioactive components <i>A.B. Podgorbunsky, S.L. Sinebryukhov, I.M. Imshinetskiy, S.V. Gnedenkov</i>	173
VI.03.09o	Formation of PEO-coatings for implant materials <i>K.V. Nadaraia, A.I. Pleshkova, M.A. Piatkova, I.M. Imshinetskiy, D.V. Mashtalyar, N.G. Plekhova, S.L. Sinebryukhov, S.V. Gnedenkov</i>	174
VI.03.10o	Synthesis of phosphate phases on polysaccharide template <i>V.E. Silant'ev, V.S. Egorkin, L.A. Zemskova, S.L. Sinebryukhov, S.V. Gnedenkov</i>	175
VI.30.01p	Correlation between the properties of PEO-layer and coating formation current density <i>S.N. Suchkov, M.S. Gerasimenko, K.V. Nadaraia, I.M. Imshinetskiy, D. V. Mashtalyar, A.N. Minaev, S.L. Sinebryukhov, S.V. Gnedenkov</i>	176
VI.30.02p	Formation of protective coatings on AMg3 aluminum alloy using fluoropolymer nanopowder <i>V.S. Filonina, K.V. Nadaraia, D.V. Mashtalyar, A.S. Gnedenkov, I.M. Imshinetskiy, I.E. Vyalyiy, V.S. Egorkin, A.N. Minaev, S.L. Sinebryukhov, S.V. Gnedenkov</i>	177

VI.30.03p	Incorporation of TiO ₂ (B) nanoparticles into PEO coatings on MA8 magnesium alloy <i>I.M. Imshinetsky, D.P. Opra, K.V. Nadaraia, V.S. Ivashina, A.A. Sokolov, D.V. Mashtalyar, S.L. Sinebryukhov, S.V. Gnedenkov</i>	178
VI.30.04p	Mesoporous materials based on CeO ₂ and Sn with a core-shell hollow structure for electrochemical energy storage and conversion <i>A.B. Podgorbunsky, D.P. Opra, A.A. Sokolov, A.I. Neumoin, S.L. Sinebryukhov, S.V. Gnedenkov</i>	179
VI.30.06p	Influence of formation conditions on corrosion behavior of PEO-coatings during salt-spray test <i>V.S. Egorkin, I.E. Vyaliy, A.S. Gnedenkov, N.V. Izotov, D.K. Tolkanov, A.K. Runov, A.N. Minaev, S.L. Sinebryukhov, S.V. Gnedenkov</i>	180
VI.30.07p	Morphology and chemical composition of organic coatings formed atop PEO-layers <i>V.S. Egorkin, U.V. Kharchenko, N.V. Izotov, I.E. Vyaliy, A.S. Gnedenkov, D.K. Tolkanov, A.K. Runov, A. N. Minaev, S.L. Sinebryukhov, S.V. Gnedenkov</i>	181
VI.30.08p	Structural heterogeneity of an amorphous nanocrystalline alloy in the nanometer range <i>A.M. Frolov, S.V. Dolzhikov, V.I. Belokon</i>	182
VI.30.09p	The growth of microcrystals on the surface of oxide coatings <i>V.S. Rudnev, K.N. Kilin, I.V. Lukiyanchuk, M.S. Vasilyeva</i>	183
VI.30.10p	Comparison of ordering characteristics of anodicformed nanostructured aluminum and titanium oxides coatings <i>N.B. Kondrikov, P.L. Titov, S.A. Shchegoleva, V.B. Cherepanov, M.S. Vasileva</i>	184
VI.30.11p	Explosive pressing of organic and inorganic compounds <i>G.A. Zverev, L.N. Ignatieva, N.A. Adamenko</i>	185
VI.30.12p	Magnetically active sorption material SiO ₂ – CoFe ₂ O ₄ <i>I.A. Tkachenko, A.E. Panasenko, M.M. Odnokov</i>	186
VI.30.13p	The influence of washing step conditions as-prepared anodic TiO ₂ -NTs structures on their photoactivity <i>T.P. Savchuk, I.M. Gavrilin, A.A. Dronov, S.A. Gavrilov</i>	187
VI.30.14p	Influence of a magnetic field on the scattering of γ -quanta on F ₃ O ₄ /Au particles <i>K.S. Lukyanenko, L.L. Afremov, Y.M. Borodaenko, A.V. Ognev, I.G. Iliushin, V.O. Trukhin</i>	188
VI.30.15p	Photocatalytic reduction of CO ₂ over metal/BaTiO ₃ catalysts <i>A.I. Savitskiy, R.M. Ryazanov, D.G. Gromov, V.I. Shatilo, A.A. Shkal, E.P. Kitsyuk, A. Shtyka, R. Ciesielski, S.V. Dubkov</i>	189
VI.30.16p	Nanocomposite of tin and lead oxides prepared in plasma of pulsed high-voltage discharge process: synthesis and electrochemical characteristics <i>A.I. Neumoin, D.P. Opra, S.V. Gnedenkov, S.L. Sinebryukhov, A.A. Sokolov, V.G. Kuryavyi, V.I. Sergienko</i>	190
VI.30.17p	Composite cryogel for Hg(II) ions recovery <i>I.A. Malakhova, Yu.O. Privar, Yu.A. Azarova, A.Yu. Mironenko, S.Yu. Bratskaya</i>	191
VII. Biomaterials and sensors on their base		
VII.31.01p	Conformational changes in DNA aptamers upon binding to Pb ions <i>R.V. Moryachkov, A.N. Berlina, P.V. Artyushenko, V.N. Zabluda, G.S. Peters, A.E. Sokolov</i>	193
VII.31.02p	The Fe-Si-Au magnetic Janus particles for biomedical applications <i>S.A. Lyaschenko, I.A. Yakovlev, I.A. Tarasov, D.A. Velikanov, Y.L. Mihlin, A.E. Sokolov, S.M. Jarkov, I.V. Nemtcev, M.N. Volochaev, S.N. Varnakov, S.G. Ovchinnikov</i>	194
VII.31.03p	Protein biosensor based on nanowire field effect transistor <i>T.E. Smolyarova, A.V. Lukyanenko, L.V. Shanidze, V.V. Krasitskaya, A.S. Tarasov, N.V. Volkov</i>	195
VII.31.04p	Tomato (cv. Bonsai) plant development under different light spectra <i>O.V. Nakonechnaya, A.S. Kholin, E.P. Subbotin, O.V. Grishchenko, E.V. Burkovskaya, Yu.A. Khrolenko, M.L. Burdukovskii, A.V. Micheeva, I.V. Gafitskaya, I.Yu. Orlovskaya, Yu.N. Kulchin</i>	196
VII.31.05p	Soybean plant growth under different light conditions <i>A.V. Micheeva, O.V. Nakonechnaya, E.P. Subbotin, O.V. Grishchenko, I.V. Gafitskaya, Yu.N. Kulchin</i>	197

VII.31.06p	Increased antibacterial activity by photoactivation of composites based on ZnO nanoparticles <i>D.A. Goncharova, S.A. Kulinich, A.L. Nemoykina, V.A. Svetlichnyi</i>	198
------------	---	-----

Invited lectures

Chemical synthesis, optical properties, and applications of carbon dots

Andrey L. Rogach*

Department of Materials Science and Engineering & Centre for Functional Photonics, City University of Hong Kong, 83 Tat Chee Avenue, Kowloon, Hong Kong S.A.R.

*e-mail: andrey.rogach@cityu.edu.hk

Carbon dots (CDs) – small crystalline or amorphous carbon-based nanoparticles – have attracted much attention as promising fluorescent materials for a wide range of applications, both in the biomedical fields and in optoelectronics [1]. One of their widely accepted advantages is the simplicity of the formation of highly luminescent CDs from a wide variety of organic precursors. At the same time, several recent studies on these chemically synthesized CDs raised questions about the nature of the resulting products. Their strong fluorescence can arise due to the presence of molecular organic fluorophores [2,3], not necessary CDs, as was assumed in the earlier publications. On the other hand, purely carbon dot samples can be synthesized using seeded growth method, yielding CDs of the different sizes, through controlling the amount of seeds introduced into reaction mixture, alongside with the reaction time [4]. This synthetic approach has been demonstrated to be an effective way to tune their optical properties: color-tunable fluorescence of CDs with blue, green, yellow, orange and red emission under UV excitation has been achieved [4,5], with the color depending on size of the π -conjugated domains in the CD graphitic core [6,7]. Very recently, we have extended the family of the light-emitting colloidal carbon nanoparticles towards carbon nanorods with linearly polarized emission [8]. I will also shortly review the emerging applications of CDs in light-emitting devices [5] and as phosphorescent materials for data encryption [4,9].

References

- [1] K. Oyoshi, D. Lenssen, R. Carrius, S. Mantl. *Thin Solid Films* **381** (2001) 194.
- [2] C. J. Reckmeier, J. Schneider, A. S. Susha, A. L. Rogach. *Optics Express* **24** (2016) A313.
- [3] J. Schneider, C. J. Reckmeier, Y. Xiong, M. von Seckendorff, A. S. Susha, P. Kasak, A. L. Rogach. *J. Phys. Chem. C* **121** (2017) 2014.
- [4] Y. Xiong, J. Schneider, E. V. Ushakova, A. L. Rogach. *NanoToday* **23** (2018) 124.
- [5] J. Zhu, X. Bai, X. Chen, H. Shao, Y. Zhai, G. Pan, H. Zhang, E. V. Ushakova, Y. Zhang, H. Song, A. L. Rogach. *Adv. Opt. Mater.* **7** (2019) 1801599.
- [6] Z. Tian, D. Li, X. Zhang, D. Zhou, P. Jing, D. Shen, S. Qu, R. Zboril, A. L. Rogach. *Adv. Opt. Mater.* **5** (2017) 1700416.
- [7] M. Fu, F. Ehrat, Y. Wang, K. Z. Milowska, C. Reckmeier, A. L. Rogach, J. K. Stolarczyk, A. S. Urban, J. Feldmann. *NanoLett.* **15** (2015) 6030.
- [8] N. V. Teplakov, E. V. Kundelev, P. D. Khavlyuk, M. Y. Leonov, W. Zhu, A. V. Baranov, A. V. Fedorov, A. L. Rogach, I. D. Rukhlenko. *ACS Nano* **13**(2019)10737.
- [9] Y. Xiong, X. Zhang, A. F. Richter, Y. Li, A. Döring, P. Kasak, A. Popelka, J. Schneider, S. V. Kershaw, S. J. Yoo, J.-G. Kim, W. Zhang, W. Zheng, E. V. Ushakova, J. Feldmann, A. L. Rogach. *ACS Nano* **13** (2019) 12024.
- [10] X. Bao, E. V. Ushakova, Z. Tian, D. Li, D. Zhou, S. Qu, A. L. Rogach. *Nanoscale* **11** (2019) 14250.

Electrochromic films with plasmonic noble metal nanomaterials

Na Li^{*1}, Jianbo Deng¹, Jiupeng Zhao¹, Yao Li²

¹ MIIT Key Laboratory of Critical Materials Technology for New Energy Conversion and Storage, School of Chemistry and Chemical Engineering, Harbin Institute of Technology, Harbin 150001, P. R. China

² Center for Composite Materials and Structure, Harbin Institute of Technology, Harbin 150001, P. R. China

*e-mail: lina@hit.edu.cn

The unique localized surface plasmon resonance (LSPR) properties of plasmonic noble metal nanomaterials open up exciting opportunities in various applications including optical devices,[1] color filters,[2] sensing,[3] and electro-optical switching.[4] The LSPR properties of these nanoparticles can be generally modulated by altering the size, morphology and composition.[5] The dynamically in response to external stimuli in a reversible manner has been considered as the next revolution in plasmonic materials,[6] which envisions great opportunities in creating novel optical devices, displays and sensors.[7]

Creating dynamic optical switching of plasmonic nanostructures is highly desirable due to their promising applications in many smart optical devices. To date, many efforts have been devoted to achieving this goal. One strategy is to take advantage of plasmonic coupling between adjacent noble metal nanoparticles via controlling their assembly and disassembly, leading to LSPR properties that can be conveniently controlled by various stimuli such as stress, magnetic field, pH and temperature. Another way is to take advantage of the electro-redox chemistry to modify the morphology, chemical composition and fundamental coupling mechanism of plasmonic nanoparticles in a reversible manner.

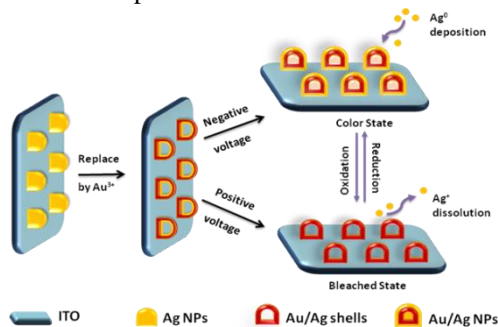


Figure 1. A cartoon illustrating the fabrication of an electrochromic film with hollow Ag/Au alloy nanoparticles and the switching mechanism between the color and bleached states of the film.

Here, we report a novel strategy to fabricate an electrochromic film with hollow Ag/Au alloy nanoparticles, with the color switchable by electro-responsive dissolution and deposition of Ag on these hollow nanoparticles, as illustrated in **Figure 1**.

These hollow Ag/Au alloy nanostructures serve as stable anchor sites for the deposition of Ag such that the self-nucleation events have been eliminated, allowing optimal reversibility of the color switching. The hollow structure further enabled significantly improved transmittance contrast of the electrochromic film between the bleached and color states. With its additional advantages such as convenience to prepare, high sensitivity and tunable optical property in response to electric field, we believe this novel plasmonic electrochromic film offers a unique opportunity in smart optical devices.

Acknowledgements

The authors would like to acknowledge financial support from the National Natural Science Foundation of China (No.51502057, 51572058), Heilongjiang Postdoctoral Science Foundation (LBH-Z14084), National Key Research & Development Program (2016YFB0303903, 2016YFE0201600), the International Science & Technology Cooperation Program of China (2013DFR10630, 2015DFE52770) and Foundation of Equipment Development Department (6220914010901).

References

- [1] F. Qian, S. Gradecak, Y. Li, C. Y. Wen, C. M. Lieber, *Nano Lett.* **5** (2005) 2287.
- [2] T. Xu, Y. K. Wu, X. Luo, L. J. Guo, *Nat. Commun.* **1** (2010) 59.
- [3] K. Saha, S. S. Agasti, C. Kim, X. Li, V. M. Rotello, *Chem. Rev.* **112** (2012) 2739.
- [4] J. Dintinger, S. Klein, T. W. Ebbesen, *Adv. Mater.* **18** (2010) 1267.
- [5] N. Li, Q. Zhang, S. Quinlivan, J. Goebel, Y. Gan, Y. Yin, *Chemphyschem* **13** (2012) 2526.
- [6] Z. Qian, D. S. Ginger, *J. Am. Chem. Soc.* **139** (2017) 5266.
- [7] G. Garcia, R. Buonsanti, E. L. Runnerstrom, R. J. Mendelsberg, A. Llordes, A. Anders, T. J. Richardson, D. J. Milliron, *Nano Lett.* **11** (2011) 4415.

Gold-decorated titania nanoparticles prepared by laser irradiation in water

Sergei A. Kulinich*

Tokai University, Research Institute of Science and Technology, Hiratsuka, Kanagawa 259-1292, Japan

*e-mail: skulinich@tokai-u.jp

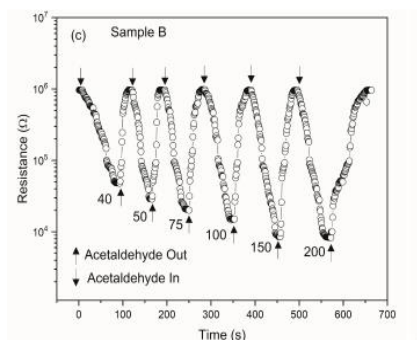
Numerous nanomaterials prepared by means of laser ablation in liquid (or its modification, laser irradiation in liquid) are well-known to be promising for applications in several fields such as electronics, catalysis, biomedicine, optics and optoelectronics, energy related technologies and so on [1,2]. Apart from nano-structures with different morphologies and chemical composition, various hybrid

nanomaterials can also be generated through this approach [1,2]. As representatives of this class, hybrid metal-semiconductor nanostructures based on transition-metal oxide nanoparticles decorated with noble-metal nanoclusters were reported to demonstrate improved sensing, catalytic, and even antibacterial, properties [3-6]. Although more reports emerge on preparing such hybrid nanomaterials using laser approaches [3-6], no systematic information is available yet in this research direction, while thorough control over such nano-structures (their morphology, sizes, chemical composition, etc.) is very important to tune their performance and efficiency.

The present talk will focus on Au@TiO₂ nanomaterials produced through irradiating commercial titania (TiO₂) nano-powder by a Nd:YAG laser in water followed by adding AuCl₄⁻ species. Figure 1 exhibits such Au-decorated titania nanoparticles produced by means of a millisecond pulsed laser (a) and how a gas-sensing device based on this material responded to acetaldehyde at room temperature (b).



(a)



(b)

Figure 1. (a) SEM image of Au@TiO₂ nanoparticles prepared via laser irradiation by millisecond pulsed laser in water and (b) dynamic response curve of sensor device based on such nanoparticles toward acetaldehyde (in ppm) at room temperature.

References

- [1] K. Oyoshi, D. Lenssen, R. Carrius, S. Mantl. *Thin Solid Films* **381** (2001) 194.
- [2] T. Suemasu, T. Fujii, K. Takakura, F. Hasegawa. *Thin Solid Films* **381** (2001) 209.
- [3] R. Bayazitov, R. Batalov, R. Nurutdinov, V. Shustov, P. Gaiduk, I. Dezsi, E. Kotai. *Nucl. Instr. Meth. B* **24** (2005) 224.
- [4] K. Oyoshi, D. Lenssen, R. Carius, S. Mantl. *Thin Solid Films* **381** (2001) 202.
- [5] J. Chrost, J. J. Hinarejos, E. G. Michel, R. Miranda. *Surf. Sci.* **330** (1995) 34.
- [6] S.L. Wu, J. Liu, Y.X. Ye, Z.F. Tian, P.F. Li, Y.Y. Cai, Y. Lin, C.H. Liang. *Appl. Surf. Sci.* **471** (2019) 469.

Laser ablation for shock generation, synthesis of colloids, and surface nanostructuring of bulk and film targets

N.A. Inogamov¹, A.A. Kuchmizhak², V.V. Zhakhovsky¹, V.A. Khokhlov¹, Y.V. Petrov¹

¹ Landau Institute for Theoretical Physics of the RAS, Chernogolovka, Russia

² Institute of Automation and Control Processes FEB RAS, 5 Radio St., Vladivostok, 690041, Russia

*e-mail: nailinogamov@gmail.com

Lasers are used in many applications – we limit ourselves with LSP (laser shock peening), LAL (laser ablation in liquid) and surface structuring. According to these applications this work is divided into three parts. (1) Formation of a shock wave under laser exposure. (2) Synthesis of colloidal solutions of nanoparticles by laser ablation in a liquid. (3) The appearance of surface structures. All listed three topics are substantially related. The movement inside the target (topic 1) is inextricably linked with the movement outside the target (topic 2), i.e. internal motion is connected to a laser plume. A laser plume ejected into a liquid is a source of nanoparticles. Movements inside and near the surface of the target ultimately leave an imprint on this surface (topic 3). These are the structures on the surface.

The exposure scheme is as follows. There are two half-spaces. One of them freely transmits laser radiation (vacuum, glass, water). Another half-space is filled with absorbing material. This is the target. Laser radiation passes through a transparent medium and is absorbed in the target. The specific situation is determined by the type of transparent medium and the pulse duration. The energy of laser pulses for the described applications is fixed. Absorbed fluence is 0.1-10 J/cm² for ultrashort pulses and 1-100 J/cm² for nanosecond actions. We consider effects of non-one-dimensional geometry [1] in the propagation of shock waves in the interests of laser shock peening. One-dimensional evolution of ablation flow is well studied [1-4]. The report discusses how ablation proceeds in a liquid [1,5-9] (for applications connected to LAL) and describes the formation of various surface structures on films and bulk targets that accompanies these processes [10-12] (many applications with structuring).

References

- [1] N.A. Inogamov et al., Picosecond-nanosecond laser flash, formation of powerful elastic waves in crystals, and shock peening. Proc. of the 32nd International Symposium on Shock Waves (ISSW32) (2019).
- [2] Demaske et al., Ablation and spallation of gold films irradiated by ultrashort laser pulses, Phys. Rev. B **82** (2010) 064113.
- [3] Agranat et al., JETP Lett. **91**(9) (2010) 471.
- [4] Zhakhovskii, Inogamov, JETP Lett. **92**(8), 521-526 (2010)
- [5] N.A. Inogamov et al., AIP Conference Proceedings **1979** (2018) 190001.
- [6] N.A. Inogamov et al., Dynamics of Gold Ablation into Water, J. Experim. Theor. Phys. (JETP) **127**(1) (2018) 79.
- [7] Y.V. Petrov et al., Applied Surface Science **492** (2019) 285.
- [8] Y.V. Petrov et al., Contrib. Plasma Phys. **59**(6) (2019) 201800180.
- [9] N.A. Inogamov et al., Opt Quant Electron **52** (2020) 63.
- [10] Wang, Kuchmizhak et al., Phys. Rev. Applied **8**(4) (2017) 044016.

Materials for all-dielectric nanophotonics: from silicon to perovskites

S.V.Makarov*

ITMO University, 49 Kronverkskiy pr., Saint Petersburg 197101, Russia

*e-mail: s.makarov@metalab.ifmo.ru

A driving force for nanophotonics is the discovery of new materials to improve existing concepts or enable new applications. One of the most recent conceptual shift was related to the replacement of metallic nanoparticles by all-dielectric ones (e.g., silicon, GaAs, etc.) bringing a novel opportunities for light manipulation at nanoscale. The next step is to further expanding the range of materials. This report reviews the state-of-the-art in all-dielectric nanophotonics, including recent results on photonic crystals, metasurfaces, and nanoantennas made of organic-inorganic perovskites, as well as their implementation in optoelectronic devices. Finally, we compare efficiencies of light-emitting nanoantennas made of different materials.

Nanophotonics connects optics and nanoscience, and it aims to localize light at the nanoscale in resonant optical modes, allowing us to scale down substantially the size of many optical devices. In order to confine light at the nanoscale, traditional nanophotonics employs metals. Recently, to overcome optical losses and bring novel functionalities, optically resonant dielectric and semiconductor nanostructures were introduced and extensively studied over the last decade [1].

On this way, conventional semiconductors such as silicon or gallium arsenide are employed for such nanostructures due to their high values of the refractive index, excellent nonlinear properties, and well-developed fabrication methods. Various designs with integrated quantum dots or quantum wells were applied to overcome limitations of plasmonics [2]. The next step on the simplification of the developed designs and making them more attractive for large-scale low-cost technological applications is employing a rising star of the modern materials science — halide perovskites [3,4]. Indeed, we show that halide perovskites is a family of materials with outstanding characteristics for creation not only large-scale metasurfaces [5], but also efficient and tunable nanoantennas [6,7], which enables us to demonstrate the smallest ever nonplasmonic nanolaser [8].

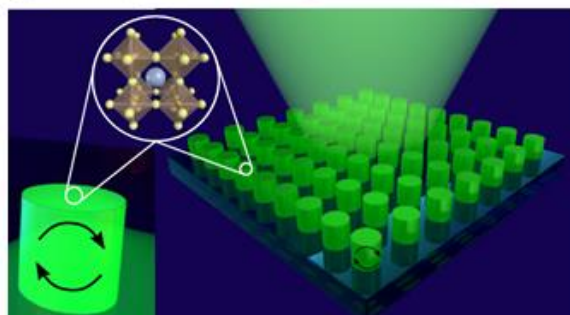
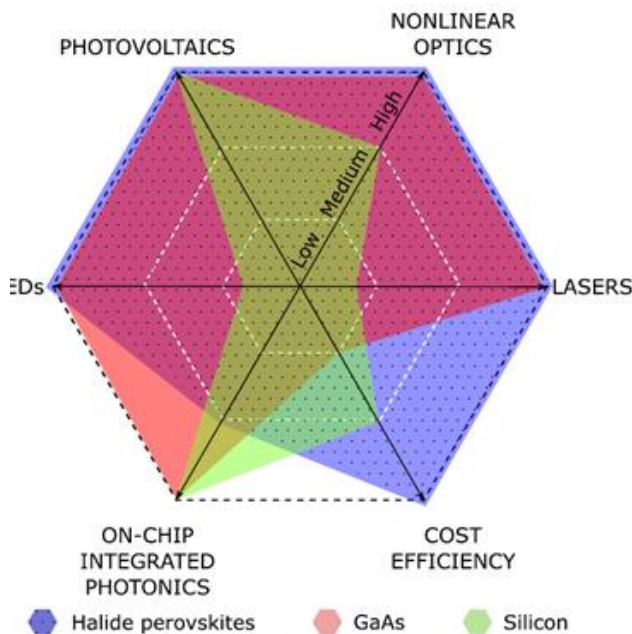


Figure 1. A hexagon scheme shows the comparison of suitability of various materials (Si, GaAs, and halide perovskites) for different applications. 3D figure shows schematic illustration of an array of resonant nanoparticles. Adopted from [4].

Acknowledgements

The work is supported by the Grant of President of Russian Federation (MK-3514.2019.2)

References

- [1] A. Krasnok, S. Makarov, M. Petrov, R. Savelev, P. Belov, and Yu. Kivshar. *Metamaterials X International Society for Optics and Photonics*, **9502** (2015) 950203.
- [2] I. Staude, T. Pertsch, Yu. Kivshar. *ACS Photonics* **6** (2019) 802.
- [3] S. Makarov, A. Furasova, E. Tiguntseva, A. Hemmetter, A. Berestennikov, A. Pushkarev, A. Zakhidov, and Y. Kivshar. *Advanced Optical Materials* **7** (2019) 1800784.
- [4] A. Berestennikov, P. Voroshilov, S. Makarov, Yu. Kivshar. *Applied Physics Reviews* **6** (2019) 031307.
- [5] S. Makarov, V. Milichko, E. Ushakova, M. Omelyanovich, A. Pasaran, R. Haroldson, B. Balachandran, H. Wang, W. Hu, Yu. Kivshar, A. Zakhidov. *ACS Photonics* **4** (2017) 728.
- [6] E. Tiguntseva, G. Zograf, F. Komissarenko, D. Zuev, A. Zakhidov, S. Makarov, Yu. Kivshar. *Nano Letters* **18** (2018) 1185.
- [7] E. Tiguntseva, D. Baranov, A. Pushkarev, B. Munkhbat, F. Komissarenko, M. Franckevičius, A. Zakhidov, T. Shegai, Yu. Kivshar, S. Makarov. *Nano letters* **18** (2018) 5522.
- [8] E. Tiguntseva, K. Koshelev, A. Furasova, V. Mikhailovskii, E. Ushakova, D. Baranov, T. Shegai, A. Zakhidov, Y. Kivshar, S. Makarov. *arXiv:1905.08646* (2019)

High-Q subwavelength dielectric resonators: from microwaves to optics

K. Koshelev^{1,2}, S. Kruk², M. Odit^{1,3}, E. Melik-Gaykazyan², J.-H. Choi⁴, S. Gladyshev¹, K. Ladutenko¹, H.-G. Park⁴, A. Bogdanov¹, Yu. Kivshar^{1,2,*}

¹ Department of Nanophotonics and Metamaterials, ITMO University, St Petersburg 197101, Russia,

² Nonlinear Physics Centre, Australian National University, Canberra ACT 2601, Australia,

³ Electrotechnical University LETI, St Petersburg 197376, Russia,

⁴ Department of Physics, Korea University, Seoul 02841, Republic of Korea,

*e-mail: yshk@internode.on.net

We observed for the first time high-quality modes in subwavelength dielectric resonators. Such modes result from interference of two dissimilar leaky modes, and they are governed by the physics of bound states in the continuum.

High-index dielectric subwavelength structures emerged recently as a new platform for nano-optics and photonics [1]. They benefit from low material losses and provide a simple way to realize magnetic response which enables efficient flat-optics devices reaching and even outperforming the capabilities of bulk components. Yet, the enhancement of near-field effects for individual subwavelength resonators is strongly limited by low quality factor (Q factor) of fundamental Mie resonances governing the optical response. Recently, a novel approach was suggested theoretically to achieve high-quality (high-Q) resonances (also termed supercavity modes) in individual subwavelength resonators [2,3] by approaching genuine nonradiative states – optical bound states in the continuum (BICs) [4]. Supercavity modes attracted a lot of attention in nonlinear nanophotonics [5], however, up to now, they have never been observed. Here, we report on the first experimental observation of the supercavity modes in individual subwavelength dielectric resonators, in the near-infrared range (resonator material permittivity of 11), and then for microwaves (permittivity of 45). We demonstrate efficient excitation of supercavity modes through the near-field and far-field.

First, we observe the supercavity modes in the near-infrared range. We consider cylindrical resonators with height 635 nm made of AlGaAs (permittivity of 11) placed on a silica substrate with an additional highly doped 300 nm ITO layer. This layer provides an additional enhancement of the Q factor due to the interaction between the resonator and the substrate. To engineer the supercavity mode, we vary the resonator diameter between 890 nm and 980 nm to induce strong coupling between a pair of Mie modes [4]. For an efficient excitation, we employ a tightly focused azimuthally polarized vector beam with the wavelength varying from 1500 nm to 1700 nm. The maximal measured Q factor is 190. It is observed for the cylinders with diameter 930 nm, when the supercavity regime is achieved. This value is more than one order of magnitude higher than for conventional dipolar Mie modes.

Next, we study supercavity modes in the microwave range. We consider a cylindrical dielectric resonator consisting of several aligned ceramic disks with radius of 11 mm. The permittivity and loss tangent of the ceramics are of 45 and 10^{-4} , respectively. The aspect ratio of the resonator (R/L) is tuned smoothly by changing the number

of ceramic disks. For excitation of the resonator, we employ a loop antenna placed beneath the resonator concentrically with its axis. We found that the Q factors change drastically with R/L showing sharp maxima. The maximal measured Q factor of 12500 is achieved for the aspect ratio of 0.55. The measured values of the Q factor are limited by absorption in the ceramic disks. The radiative Q factor at the same aspect ratio reaches the value of about 2×10^5 .

We have demonstrated experimentally, for the first time to our knowledge, the existence of high-Q supercavity modes in individual subwavelength dielectric resonators, for both near-infrared and microwave spectral ranges. We have shown that these high-Q resonances can be excited efficiently through a broad spectral range using structured light or near-field sources. For the subwavelength optical resonator made of AlGaAs with permittivity of 11, we have observed the Q factor of about 190, and for the ceramic resonators with permittivity of 45 in microwaves, we have observed the Q factor of 12500. Our study revealed that supercavity modes are formed due to strong interaction of two leaky modes, which interfere destructively resulting in strong suppression of radiative losses. This clearly demonstrates that the supercavity modes are governed by the physics of bound states in the continuum.

Acknowledgements

Experimental studies were supported by the Russian Science Foundation (19-72-10086). Numerical and analytical calculations were supported by the Grant of the President of the Russian Federation (MK-2224.2020.2) and BASIS foundation.

References

- [1] A. I. Kuznetsov et al., *Science* **354** (2016) aag2472.
- [2] M. V. Rybin et al., *Phys. Rev. Lett.* **119** (2017) 243901.
- [3] A. A. Bogdanov et al., *Adv. Photonics* **1** (2019) 016001.
- [4] C. W. Hsu et al., *Nat. Rev. Mater.* **1** (2016) 16048.
- [5] K. Koshelev, A. Bogdanov, Yu. Kivshar, *Science Bulletin* **64** (2019) 836.

Unusual magnetism and strongly-correlated electrons in quasi-two-dimensional 4f-systems

D.V. Vyalikh^{*,1,2}

¹ Donostia International Physics Center, 20080 Donostia/San Sebastián, Basque Country, Spain

² IKERBASQUE, Basque Foundation for Science, 48011 Bilbao, Spain

*e-mail: denis.vyalikh@dipc.org

For a long time, rare-earth (RE) intermetallic materials have attracted considerable interest because of their exotic properties at low temperatures which include complex magnetic phases, valence fluctuations, heavy-fermion properties, Kondo behavior and many others. All of these properties stem from the interplay between almost localized 4f electrons and itinerant states.

In that regard, the class of RE compounds RE_2Si_2 (T is transition metal atoms) of the $ThCr_2Si_2$ type structure attracts considerable attention. Besides their unique bulk properties evolving from a delicate interplay of 4f and spd electrons, these materials serve as toy models for studying exotic physics within the non-centrosymmetric Si-T-Si-RE four layers of the Si-terminated surface. There, the spin-orbit coupling (SOC) can be tuned by choice of suitable transition metal atoms. It gradually increases by exchanging Co (3d) for Rh (4d) and further for Ir (5d). The SOC-based phenomena will be rather weak for Co 3d electrons, while they will be greatly enhanced for Ir 5d orbitals. As a competing ingredient, exchange magnetic interaction may be exploited by inserting elementary 4f magnets like Gd as the RE component. Because the orbital moment of the Gd 4f shell vanishes ($L = 0$), the pure and large spin moment of Gd will be a strong and robust source of magnetic phenomena. A rotation of the 4f moments to a certain angle relative to the surface normal may be achieved by coupling to a crystal electric field (CEF). To make use of notable CEF effects, a non-vanishing orbital moment L is needed, like for instance in Ho or Dy. Then, this option allows to implement an exchange magnetic field with different strength and orientation at the surface, which competes with the Rashba SOC field and creates additional possibilities to manipulate the properties of the 2D electrons within the considered Si-T-Si-RE system. As the next ingredient, the Kondo effect can be introduced by inserting elements with unstable 4f shell as Yb or Ce. This gives the opportunity to explore the interplay of the 2D electrons with 4f moments within a 2D Kondo lattice in the presence of spin-orbit coupling and a non-centrosymmetric environment.

We propose and demonstrate that in general such a Si-T-Si-RE system may serve as a beautiful playground for studying the fundamental properties of 2D electrons. These systems can be nicely used as a veritable construction kit

with spin-orbit, Kondo, crystal-electric field, and exchange magnetic interactions as building blocks. Combining them with one another gives the opportunity to design systems for different scenarios and to study the physics of 2D electron states in the presence of these competing interactions. The most interesting experimental results obtained by our team in the recent past working on these scenarios will be presented.

References

- [1] S. Schulz, I. A. Nechaev, M. Guettler, G. Poelchen, A. Generalov, S. Danzenbacher, A. Chikina, S. Seiro, K. Kliemt, A. Yu. Vyazovskaya, T. K. Kim, P. Dudin, E. V. Chulkov, C. Laubschat, E. E. Krasovskii, C. Geibel, C. Krellner, K. Kummer and D. V. VyalikhK. npj Quantum Materials **4** (2019) 26.
- [2] M. Güttler, A. Generalov, S. I. Fujimori, K. Kummer, A. Chikina, S. Seiro, S. Danzenbacher, Yu. M. Koroteev, E. V. Chulkov, M. Radovic, M. Shi, N. C. Plumb, C. Laubschat, J. W. Allen, C. Krellner, C. Geibel, and D. V. Vyalikh. Nature Comm. **10** (2019) 796.
- [3] A. Generalov, J. Falke, I. A. Nechaev, M. M. Otrokov, M. Güttler, A. Chikina, K. Kliemt, S. Seiro, K. Kummer, S. Danzenbacher, D. Usachov, T. K. Kim, P. Dudin, E. V. Chulkov, C. Laubschat, C. Geibel, C. Krellner, and D. V. Vyalikh. Phys. Rev. B **98** (2018) 115157.
- [4] A. Generalov, M. M. Otrokov, A. Chikina, K. Kliemt, K. Kummer, M. Höppner, M. Güttler, S. Seiro, A. Fedorov, S. Schulz, S. Danzenbacher, E. V. Chulkov, C. Geibel, C. Laubschat, P. Dudin, M. Hoesch, T. Kim, M. Radovic, M. Shi, N. C. Plumb, C. Krellner and D. V. Vyalikh. Nano Letters **17** (2017) 811.
- [5] S. Patil, A. Generalov, M. Güttler, P. Kushwaha, A. Chikina, K. Kummer, T. C. Rödel, A. F. Santander-Syro, N. Caroca-Canales, C. Geibel, S. Danzenbacher, Yu. Kucherenko, C. Laubschat, J. W. Allen and D. V. Vyalikh. Nature Comm. **7** (2016) 11029.
- [6] A. Chikina, M. Höppner, S. Seiro, K. Kummer, S. Danzenbacher, S. Patil, A. Generalov, M. Güttler, Yu. Kucherenko, E. V. Chulkov, Yu. M. Koroteev, K. Kopernik, C. Geibel, M. Shi, M. Radovic, C. Laubschat and D. V. Vyalikh. Nature Comm. **5** (2014) 3171.
- [7] M. Güttler, A. Generalov, M. M. Otrokov, K. Kummer, K. Kliemt, A. Fedorov, A. Chikina, S. Danzenbacher, S. Schulz, E. V. Chulkov, Yu. M. Koroteev, N. Caroca-Canales, M. Shi, M. Radovic, C. Geibel, C. Laubschat, P. Dudin, T. K. Kim, M. Hoesch, C. Krellner and D. V. Vyalikh. Scientific Reports **6** (2016) 24254.

Topological spintronics with (anti)skyrmions and bimerons

O.A. Tretiakov*

School of Physics, University of New South Wales, Sydney 2052, Australia

*e-mail: o.tretiakov@unsw.edu.au

Skyrmions are topologically protected spin textures, which may be used in spintronic devices for information storage and processing. However, skyrmions in ferromagnets have some intrinsic difficulties for their usage in nanodevices, such as the inability to move strictly along electric current due to skyrmion Hall effect [1]. We worked out several routes to solve this problem by using instead of skyrmions novel anisotropic topological objects, such as antiskyrmions [2] and bimerons [3]. Yet as another solution to eliminate the skyrmion Hall effect, topological spin solitons in antiferromagnets are proposed [4,5,6]. It will demonstrate how they can be stabilized [7] and manipulated at finite temperatures [4]. Remarkably, we also show how the Magnus force acting on (anti)skyrmions, and thus in turn skyrmion Hall effect, can be efficiently tuned microscopically via modulation of spin-orbit interaction [8].

References

- [1] K. Litzius, I. Lemesh, B. Kruger, P. Bassirian, L. Caretta, K. Richter, F. Buttner, K. Sato, O.A. Tretiakov, J. Forster, R.M. Reeve, M. Weigand, I. Bykova, H. Stoll, G. Schutz, G.S.D. Beach, and M. Klaui, *Nature Physics* **13** (2017) 170.
- [2] M.N. Potkina, I.S. Lobanov, O.A. Tretiakov *et al.*, arXiv:1906.06383, submitted *Phys. Rev. B* (2019).
- [3] B. Göbel, A. Mook, J. Henk, I. Mertig, and O.A. Tretiakov, *Phys. Rev. B* **99** (2019) 060407(R).
- [4] J. Barker and O.A. Tretiakov, *Phys. Rev. Lett.*, **116** (2016) 147203.
- [5] C.A. Akosa, O.A. Tretiakov, G. Tatara, and A. Manchon, *Phys. Rev. Lett.* **121** (2018) 097204.
- [6] L. Shen, J. Xia, X. Zhang, M. Ezawa, O. A. Tretiakov, X. Liu, G. Zhao, Y. Zhou, *Phys. Rev. Lett.* **124** (2020) 037202.
- [7] P.F. Bessarab, D. Yudin, D. R. Gulevich, P. Wadley, M. Titov, and O.A. Tretiakov, *Phys. Rev. B* **99** (2019) 140411(R).
- [8] C.A. Akosa, H. Li, G. Tatara, and O.A. Tretiakov, *Phys. Rev. Appl.* **12** (2019) 054032.

Magnetization switching in interface engineered W-based nonmagnet/ferromagnet heterostructures

Gyu Won Kim, In Ho Cha, Taehyun Kim, Yong Jin Kim, Young Keun Kim*

Department of Materials Science and Engineering, Korea University, Seoul 02841, Republic of Korea

*e-mail: ykim97@gmail.com

Spin-orbit torque, manifested by accumulated spin-polarized magnetic moments at the nonmagnet (NM) and ferromagnet (FM) interface, is a promising magnetization switching mechanism for spintronic devices such as magnetic random access memory (MRAM). Lately, spin-orbit torque (SOT) driven switching has been discovered in various sets of NM/FM heterostructures such as beta-phase W/CoFeB with MgO capping where an in-plane current injection induces magnetization reversal in a perpendicularly magnetized layer. To fully exploit SOT in practice, materials with a high spin Hall angle, a charge-to-spin conversion efficiency, is very critical. While tremendous efforts have been made in this kind of exploration, materials compatible with semiconductor processing would be more attractive. We introduce the SOT efficiency and switching characteristics of W/CoFeB/MgO thin film junctions where various types of layer structures are inserted in the interface between W and CoFeB. Material screening is conducted using first-principle calculations while subsequent fabrication and verification are confirmed experimentally.

Acknowledgements

This research is supported by the National Research Foundation of Korea (NRF) grant funded by the Ministry of Science and ICT (MSIT) (2015M3D1A1070465).

References

- [1] In Ho Cha, Taehyun Kim, Yong Jin Kim, Gyu Won Kim, and Young Keun Kim. *Journal of Alloys and Compounds* **823** (2020) 153744.
- [2] Changsoo Kim, Byong Sun Chun, Jungbum Yoon, Dongseuk Kim, Yong Jin Kim, In Ho Cha, Gyu Won Kim, Dae Hyun Kim, Kyoung-Woong Moon, Young Keun Kim, Chanyong Hwang, *Advanced Electronic Materials*, 1901004 (2020).

Electronic structure and magnetic properties of iron silicides

S.G. Ovchinnikov*, V. Zhandun, N. Zamkova, O. Maximova, S. Lyaschenko, M. Vysotin, I. Sandalov

Kirensky Institute of Physics, FRC KSC SB RAS, Akademgorodok 50/38, Krasnoyarsk, Russia

*e-mail: sgo@iph.krasn.ru

Spectroscopic ellipsometry in situ measurements on grown single-crystalline Fe₃Si/Si and Fe/SiO₂/Si films are analysed with the ab initio DFT- GGA calculations of the electronic structure and real and imaginary parts of permittivity. Effects of electronic correlations are important for ferromagnetic metal Fe₃Si and are considered within GW approximation. For non magnetic in bulk a-FeSi₂ we present the effect of silicon atoms substitution by the iron atoms and vice versa on the α -FeSi₂ magnetic properties. We find that while the stoichiometric α -FeSi₂ is nonmagnetic, the substitutions generate different magnetic structures depending on the type of local environment of the substitutional Fe atoms. We find that in Fe_{1-x}Si_{2+x} ordered alloys an increase of Si concentration may lead to ferromagnetism.

By means of hybrid ab initio + model approach we show that the lattice distortions in non-magnetic a-FeSi₂ can induce a magnetic state. However, we find that the distortions required for the appearance of magnetism in non-magnetic a-FeSi₂ are too large to be achieved by experimental fabrication of thin films. For this reason we suggest a novel way to introduce magnetism in a-FeSi₂ using “chemical pressure” that is, intercalating the a-FeSi₂ films by light elements. Theoretical study of the distortions

resulting from intercalation reveals that the most efficient intercalants for formation of magnetism and a high spin polarization are lithium, phosphorus and oxygen. Investigation of the dependency of the magnetic moments and spin polarisation on the intercalation atoms concentration shows that the spin polarization remains high even at small concentrations of intercalated atoms, which is extremely important for modern silicate technology.

References

- [1] O.A. Maximova, S.A. Lyaschenko, M.A., Vysotin I.A. Tarasov, I.A. Yakovlev, D.V. Shevtsov, A.S. Fedorov, S.N. Varnakov and S.G. Ovchinnikov, JETP Letters, **110**(3) (2019) 166.
- [2] I. Sandalov, N. Zamkova, V. Zhandun, I. Tarasov, S. Varnakov, I. Yakovlev, L. Solovyov and S. Ovchinnikov, Physical Review B, **92** (2015) 205129.
- [3] V. Zhandun, N. Zamkova, P. Korzhavyi, I. Sandalov, Phys. Chem. Chem. Phys., **21** (2019) 13835.
- [4] N.G. Zamkova, V.S. Zhandun, S.G. Ovchinnikov I.S. Sandalov, Journal of Alloys and Compounds, **695** (2017) 1213.
- [5] V.S. Zhandun, N.G. Zamkova, S.G. Ovchinnikov and I.S. Sandalov, Phys. Rev. B, **95** (2017) 054429.

Atomic scale tuning of quantum dot nucleation and epitaxial growth of heterostructures for nanophotonic and quantum information processing

A.V. Dvurechenskii^{1,2}, Zh.V. Smagina¹, V.A. Zinovyev¹, P.L. Novikov^{1,2}, S.A. Rudin¹,
A.F. Zinovieva¹, A.V. Nenashev^{1,2}

¹ Rzhanov Institute of Semiconductor Physics of SB RAS, 13 pr. Lavrentieva, Novosibirsk 630090, Russia

² Novosibirsk state University, 1 Pirogova St., Novosibirsk, 630090, Russia

*e-mail: corresponding author: dvurech@isp.nsc.ru

CMOS-compatible optoelectronic and nanoelectronic devices if they can be formed in regular and uniform arrays with controlled size, shape, chemical composition, and the properties of their surrounding like choice of matrix material. For realistic integration of QD into Si-technology devices, the QDs have to be site-controlled to ensure their large scale addressability. Besides, ordered QDs provide several more benefits as compared to their randomly nucleated counterparts: a more homogeneous chemical composition and energy spectrum. In this report, we will focus on self-assembled, group-IV, Ge-on-Si epitaxial QDs, formed with dislocation-free growth [1].

The size homogeneity and density of the arrays of quantum dots was found to be tuned with low-energy ion-beam actions during molecular beam epitaxy (MBE). Nucleation of QDs due to a pulsed low-energy (100 eV) beam action of intrinsic ions (Ge⁺) resulted in the increasing of QDs density and improving of homogeneity in QDs sizes.

The linear ordered chains of quantum dots were formed on Si groove patterned Si(001) substrate formed by using combination of nanoimprint lithography and Ge ion irradiation through mask. Ordered structures with grooves and ridges were prepared by the selective etching of regions amorphized by ion irradiation. Laterally ordered chains of Ge nanoislands were grown by MBE of Ge on the prepatterned Si substrates. It was shown that temperature during ion irradiation affects the location of subsequently grown Ge nanoislands at MBE: inside grooves or on ridges. It was shown also, that the location of subsequently grown Ge nanoislands depends upon the sidewall inclination in grooves and grooves shape: in the case of the V-shaped pits, 3D Ge islands nucleate inside the pits. For U-shaped pits the 3D Ge island nucleation takes place around the pit periphery. This effect is attributed to the strain relaxation depending not only on the initial pit shape, but also on its evolution during the Ge wetting layer deposition.

Monte Carlo simulations was shown that in the case of a V-shaped pits with a pointed bottom, the strain relaxation is most effective inside the pit, while for a U-shaped pits with a wide bottom, the most relaxed area migrates during Ge deposition from the pit bottom to its edges, where 3D Ge islands nucleate. The interpretation is consistent with the general approach, considering the strain as a driving

force for the island positioning. In addition, a specific mechanism, associated with a shift of the relaxed area from a pit bottom to its top during Ge deposition, was identified. The mechanism is pronounced in the case of a pit with a wide flat bottom.

The idea to use the built-in elastic strain for controlling the spatial localization of charge carriers, their energy spectrum, overlapping between electron and hole wave functions is fruitful for photoluminescence (PL) enhancement due to strain tuning of electron localization in QD structures. The strain in the Ge-Si system can be enhanced as by increase in the number of QD layers in multilayered structures and by growing the combined structures that represent a combination of large built-in disk-like QDs (nanodisks of 200 ÷ 250 nm size) and ordered groups of smaller QDs grown over strained surface. The presence of nanodisks QDs provides a significant deformation in the surrounding silicon, effectively lowering the level of the conduction band edge and, thereby, forming a wide potential well. Small QDs (around 30 nm), which have a higher Ge content, provide peak deformations, forming narrow and deep potential wells for electrons in silicon. The enhancement of the localization potential for electrons makes possible to observe the PL up to room temperature [2]. Moreover, one could obtain the PL intensity enhancement due to an increase in the overlap integral between electron and hole wave functions. It was found that the strain tuning of site of electron arrangement provides multiple increase of PL intensity from SiGe QDs.

Acknowledgements

This work is funded by RFBR, grant No.18-52- 00014. The authors gratefully acknowledge V. A. Armbrister for the growth of experimental structures.

References

- [1] A. Dvurechenskii, A. Yakimov. Silicon-Based Nanoheterostructures with Quantum Dots. In: *Advances in Semiconductor Nanostructures: Growth, Characterization, Properties and Applications*, Ed. by A. Latyshev, A. Dvurechenskii, A. Aseev. Elsevier, Amsterdam, 2017, p.p. 59 – 99.
- [2] V. Zinovyev, A. Zinovieva, P. Kuchinskaya, Zh. Smagina, V. Armbrister, A. Dvurechenskii, O. Borodavchenko, V. Zhivulko, A. Mudryi, *Appl. Phys. Lett.* **110** (2017) 102101.

From first STM to complex analysis systems – 30 years' experience of R&D and production of metrological equipment

Victor Bykov^{*1,2}, Vyacheslav Polyakov¹, Andrey V. Bykov¹, Vladimir Kotov¹, Stanislav Leesment¹, Yuri Bobrov¹

¹ NT-MDT-Spectral Instruments Companies Group (www.ntmdt-si.com)

² Moscow Institute of Physics and Technology

* e-mail: spm@ntmdt-si.ru

Introduction

In the Soviet Union, the Molecular Electronics program was born in the Ministry of Electronic Industry in the early 70s. It was a powerful program aimed at the creation of microelectronics devices and technologies, the complex functional molecules of which were to become the single functional elements. As the basic technology, the technology of molecular layering of films was considered - the Langmuir-Blodgett technology. Variants of molecular self-assembly technology were also considered.

By the end of the 80s, when monomolecular conductive layers, and e-beam resistes based on LB films, and lyotropic liquid crystal systems were developed. We studied options for creating complex systems based on the technique of layer-by-layer formation of structures, then called LB technology. But no one was able to obtain structures with the expected properties, even electrets, and it became clear that without new methods of analysis, methods of atomic resolution, the further development of this technique is at least unpromising. By that time, spectral methods, X-ray analysis methods, and electron microscopy methods were developed. But this was clearly not enough. At the beginning of the 80s, scanning probe microscopes were invented at the Swiss branch of IBM at the beginning of the tunnel, and then atomic force microscopes, the ability to manipulate individual atoms was demonstrated, methods for studying electrical magnetic properties were proposed, methods of non-contact, semi-contact analysis were proposed (i.e. N. Tapping mode), allowing to study the "soft" film structures, biological materials, even living cells.

We also had separate groups in the USSR (Prof. V.I. Panov's laboratory at the Physics Department of Moscow State University, prof. Khaikin's laboratory in Chernogolovka, prof. V7C7 Edelman in Institute of Physical Problems USSA Academy of Science, prov V.K. Nevolin from Moscow (Zelenograd) Institute of Electronics, prof A.O. Golubok from St. Petersburg Institute of Analytical Instrumentation), in which the development of tunneling microscopes was made, but these were the development of individual devices.

The tasks of creating devices for a wide range of users - this is the task that a group of scientists working in the field of "Molecular Electronics" took up.

First steps of NT-MDT group

The Company's first instruments were scanning tunneling microscopes. They were developed in 1990 (Fig. 1 (a)). Instrument mechanics were developed by the

research group of the Physics Department of Moscow State University, and the processor and software, as well as the instrument as a whole, were developed by the scientific group of MDT Corporation. The STM-10-90-MDT device (Fig. 1 (a) and (b)) provided atomic resolution for HOPG, but had a number of significant drawbacks - a small scanning field, manual supply of the sample up to the range of movement of the piezoelectric bimorph plate (about 50 microns) with the subsequent supply of the sample to the range of the tripod scanner and manual "retraction", which did not allow returning to the previous place of scanning, but he already had such functions as "lithography". As a scanner, a piezoceramic "tripod" was used based on the domestic PZT-19 piezoceramics. The processor of the device was also made on the domestic (USSA) element base, where the analog-to-digital and digital-to-analog converters were made on digital and analog microcircuits and occupied separate boards (in the USSR, there were no ADC and DAC microchips). Using STM-10-90-MDT, the first research work [1,2] was carried out, the results of which were presented at the 1991 conference "10 years of STM" in Interlaken (Switzerland).

The following model was developed together with A.O. Golubok (STM-10-MDT, Fig. 1 c and d), in which a tubular 3-coordinate scanner was used. The inlet and outlet of the sample was carried out by an inertial piezoceramic engine, which was already much more convenient, but the accuracy of returning to the old place was less than the scan range of the scanner. Nevertheless, these devices were already in demand. The first customer of this type of tunneling microscope was the Genova University, Institute of Bioelectronics (Genoa, Italy) and ASSE-Z (Padova, Italy). The device was demonstrated at a number of Russian exhibitions and at the STM-93 exhibition in Beijing. The first scanning probe microscope with the capabilities of both atomic force and tunneling microscopes was developed in 1994 (Fig. 2). As an atomic force microscope, it worked only in the contact mode, but allowed to obtain atomic resolution in tunneling microscopy modes, worked in the lateral and contact AFM modes, provided the ability to visualize atomic lattices both on HOPG, and on mica and layered MoTe semiconductors.

In 1994, we began developing silicon cantilevers in 1995; we already had the first samples.

In 1997, the first multimode microscopes SOLVER-P47 (scanning with a sample, solution 3a) and SOLVER-P47H (Fig. 3b) - scanning with a cantilever (Fig. 3) were developed. These devices successfully worked in all modes known by then, including semi-contact (tapping - mode), in

non-contact modes, including magnetic-power. The creation of devices operating in the tapping mode, in which the degree of impact on the sample is hundreds of times less than in the contact mode, made it possible to understand the essence and limitation of LB technology. By 1998-1999, scanning probe microscopes were created that made it possible to study SOLVER-LS plates with diameters up to 100 mm (Fig. 4)

All these devices worked successfully, were delivered to dozens of institutes in different countries of the world (more than 30 countries), but they were devices belonging to the class of indicator devices — their scanners were not equipped with displacement sensors. The non-linearity of the scanners was compensated by software correction, providing accuracy of not more than 1%, positioning at the desired location, the scan required several adjustments.

In 2003-2006, NT-MDT with 2nd place was included in the 10 small winning companies and received a large

grant from the Ministry of Industry and Science, which made it possible to make a major breakthrough in development and create a powerful line of devices (Fig. 5). Interaction with the Bortnik Foundation allowed us to develop the first devices for the educational sector - nanoeducators, the further development of which allowed us to create real metrological devices for teaching students and schoolchildren.

New SPMs (Fig. 6), as well as combines with spectrometers, had precision scanners with low-noise capacitive sensors, which made it possible to significantly improve their properties, and in the course of further improvement of 2015-2019, develop new scanning modes and introduce artificial intelligence systems SCANTRONICS™ intelligent software module (3) into scanning algorithms, which fundamentally changed the properties of devices.

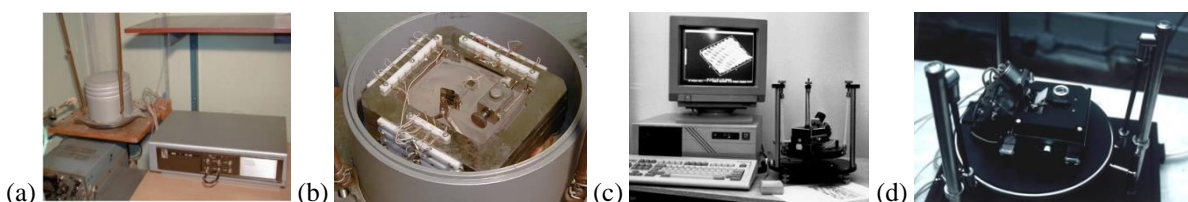


Figure 1. MDT Corporation Tunneling Microscopes - (a), (b) - STM-10-90-MDT, (c), (d) - STM-10-MDT

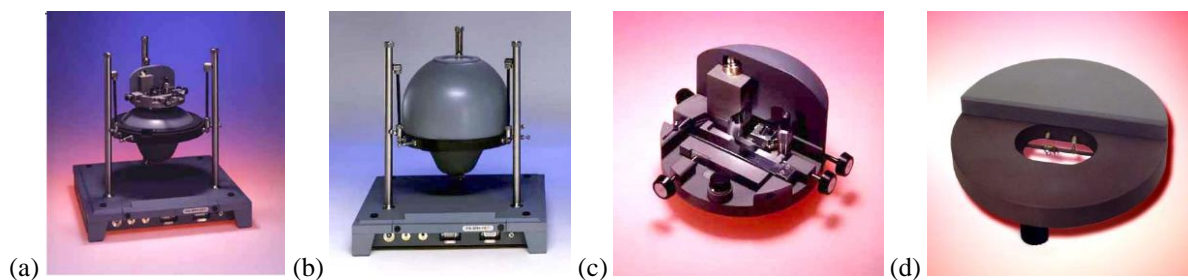


Figure 2. The first SPM of the company Nanotechnology MDT SOLVER-P4 - (a), (b), (c) - "head" of the AFM, (d) - "head" of STM.

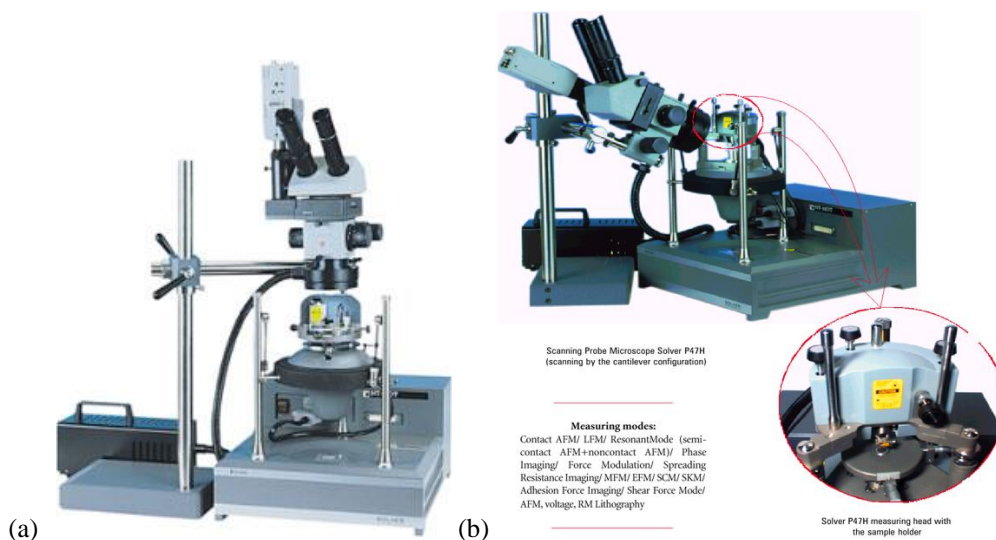


Figure 3. The first multimode SPM of the company Nanotechnology MDT SOLVER-R47 - (a) and SOLVER-R47H.



Figure 4. The first SPM NT-MDT company for the study of "large" plates SOLVER-LS.



Figure 5. Nanotechnological complexes, metrological scanning probe microscopes, nanoeducators and accessories.



Figure 6. Development Instruments NT-MDT Spectrum Instruments 2015-2020. This is the result of our 30 years of work, which, we hope, will never stop in more and more new developments.

Conclusion

For 30 years, the company has grown from a small group of scientists into a powerful group - now it is the NT-MDT Spectrum Instruments group of companies, which has confidently conquered both the Russian and world markets for scanning probe microscopy and spectroscopy - in the world today more than in About 5,000 Russian devices operate in 60 countries.

The development of micro and nanoelectronics gives rise to an increasingly powerful elemental base, which allows implementing a number of operating modes, solving tasks of reducing user requirements by developing methods based on artificial intelligence algorithms, which allows you to quickly and efficiently work on devices with high quality results. This allows you to quickly learn complex analysis methods for

engineers, technologists and even schoolchildren. It is possible to create devices not only for scientists, but also for practical analysts in medicine - quickly and reliably diagnostic complex diseases analyzing individual response of living cells to drugs.

Reference

- [1] Hameroff S.R., Lazarev P.I., Protasenko V.V., Samsonov N.S., Troitsky V.I.// Book of Abstracts, International Conference on Scanning Tunneling Microscopy, 12-16 August, 1991, Interlaken Switzerland, p.31.
- [2] Bykov V.A., Ryabokon V.N., Emelyanov A.V. at al.// Book of Abstracts, International Conference on Scanning Tunneling Microscopy, 12-16 August, 1991, Interlaken Switzerland, p.167. <https://www.ntmdt-si.ru/products/features/intelligent-scant-software>.

Spin dynamics in indirect band gap III-As heterostructures

T.S. Shamirzaev*

Rzhanov Institute of Semiconductor Physics of SB RAS, 13 pr. Lavrentieva, Novosibirsk 630090, Russia

*e-mail: tim@isp.nsc.ru

In bulk semiconductors, relaxation of the spin nonequilibrium polarization for quasi-particles (electrons, holes, or excitons) moving freely over the conduction band (valence band) occurs within hundreds of picoseconds owing to scattering and/or precession of the spin between the scattering events. Theory predicts that in low dimensional heterostructures such as quantum dots (QDs) and thin quantum wells (QWs) the localized character of the quasiparticle wave functions suppresses the most efficient intrinsic mechanisms of spin relaxation related to partial moving (like Elliott-Yafet and Dyakonov-Perel mechanisms) [1]. According to the theoretical estimation, the longitudinal spin relaxation time T_1 of the electrons, holes and excitons in QDs can be as long as milliseconds [1]. They exceed by orders of magnitude typical recombination times of excitons in direct band gap QDs, which are typically about several nanoseconds. The recombination time in low dimensional structures can be controlled by the band gap type, direct or indirect, and the band alignment in heterostructures. They can be increased to hundreds of nanoseconds in direct band gap heterostructures of type II [2]. On the other hand, momentum separation of electrons and holes in type-I indirect band gap heterostructures such as (In,Al)As/AlAs, allows one to increase the exciton lifetime up to hundreds of microseconds [3]. An additional increase in the lifetime is achieved by spatial separation of charge carriers in indirect band-gap heterostructures of type II [4].

Recently we demonstrate that indirect band gap structure in InAs/AlAs QDs with type I band alignment and thin GaAs/AlAs QWs with type II band alignment results in increase of exciton lifetime up to the milliseconds that makes these structures the very interesting objects for study of the spin dynamics of excitations [5,6].

In this report the most interesting features of exciton spin dynamics in ultra-thin GaAs/AlAs QWs and (In,Ga)As/AlAs QDs will be shown. We demonstrate the

possibility to study the spin relaxation mechanisms of the exciton (1) in low and even at zero magnetic fields, in the optical orientation and optical alignments regimes under quasi-resonant excitation; (2) in strong magnetic fields using non resonant excitation, by measuring the dynamics of the magnetic field induced polarization of exciton luminescence [5,7,8,9]. The features of electron-nuclear hyperfine interaction for indirect band gap heterostructures will be also demonstrated.

Acknowledgements

This work was supported by Russian Foundation for Basic Research Grants No. 19-02-00098 and 19-52-12001.

References

- [1] A.V. Khaetskii, Yu.V. Nazarov, Phys. Rev. B **64** (2001) 12316.
- [2] F. Hatami, M. Grundmann, N. N. Ledentsov, F. Heinrichsdorff, R. Heitz, J. Bohrer, D. Bimberg, S.S. Ruvimov, P. Werner, V. M. Ustinov, P. S. Kop'ev, and Zh. I. Alferov. Phys. Rev. B **57** (1998) 4635.
- [3] T.S. Shamirzaev, A.M. Gilinsky, A.K. Kalagin, A.V. Nenashev, K.S. Zhuravlev. Phys. Rev. B **76** (2007) 155309.
- [4] L. P. Fu, F. T. Bacalzo, G. D. Gilliland, R. Chen, K. K. Bajaj, J.Klem, and D.J. Wolford. Phys.Rev. B **52** (1995) 2682.
- [5] J. Rautert, T. S. Shamirzaev, S. V. Nekrasov, D. R. Yakovlev, P. Klenovský, Yu. G. Kusrayev, and M. Bayer. Rev. B **99** (2019) 195411.
- [6] T.S. Shamirzaev, J. Debus, D.R. Yakovlev, M.M. Glazov, E.L. Ivchenko, and M. Bayer. Phys. Rev. B **94** (2016) 045411.
- [7] T. S. Shamirzaev, J. Rautert, D. R. Yakovlev, M. M. Glazov, and M. Bayer. Phys. Rev. B **99** (2019) 155301.
- [8] V. Yu. Ivanov, T. S. Shamirzaev, D. R. Yakovlev, A. K. Gutakovskii, Ł. Owczarczyk, and M. Bayer. Phys. Rev. B **97** (2018) 245306.
- [9] J. Rautert, M. V. Rakhlin, K.G. Belyaev, T.S. Shamirzaev, A. K. Bakarov, A.A. Toropov, I.S. Mukhin, D. R. Yakovlev, and M. Bayer. Phys. Rev. B **100** (2019) 205303.

Property modifications of 2D Me_2X (Me = Mg, Ca, Sr, Ba and X = Si, Ge, Sn): from 2D to 1D in ternary $\text{MeMe}'\text{X}$ compounds

A.Yu. Alexeev¹, D. B. Migas^{*,1,2}, A. B. Filonov¹, V. E. Borisenko^{1,2}, N. V. Skorodumova^{3,4}

¹ Belarusian State University of Informatics and Radioelectronics, P. Browki 6, 220013 Minsk, Belarus

² National Research Nuclear University MEPhI (Moscow Engineering Physics Institute), Kashirskoe Shosse 31, 115409, Moscow, Russia

³ Multiscale Materials Modelling, Department of Materials and Engineering, Royal Institute of Technology (KTH), SE-10044 Stockholm, Sweden

⁴ Department of Physics and Astronomy, Uppsala University, Box 516, SE-75121, Uppsala, Sweden

*e-mail: migas@bsuir.by

The increased interest in the investigation of low-dimensional structures is caused by their unusual properties and possible applications. Recently we have presented the first-principles prove that the formation of two-dimensional (2D) alkaline-earth metal silicides, germanides, and stannides in the phases similar to the phases of 2D transition metal dichalcogenides (so-called T and Td (distorted T) phases [1-3]) is possible. In the T phase of Me_2X (Me = Mg, Ca, Sr, Ba and X = Si, Ge, Sn) one monoatomic layer of X atoms is located between two monoatomic layers of Me atoms so that each X atom is coordinated by the nearest six Me atoms in an octahedral arrangement. The stability of 2D ternary compounds $\text{MeMe}'\text{X}$, in which two different Me atoms form different outer layers (see also Fig. 5 in Ref. 3), has been also predicted [3]. All of the stable 2D Me_2X and 2D $\text{MeMe}'\text{X}$ are found to be semiconductors with the band gaps in the range of 0.1–1.0 eV [3].

In this work we consider the possibility of formation and properties of nanotubes (NTs) formed by rolling up 2D $\text{MeMe}'\text{X}$. In order to roll up a graphene nanoribbon into a NT, the additional mechanical stress must be induced [4]. Despite the dynamical stability of the infinite 2D $\text{MeMe}'\text{X}$ [3], the spontaneous folding of its nanoribbons can occur because of the difference in distances between alkaline-earth metal atoms in 2D $\text{MeMe}'\text{X}$ with respect to the cases of 2D Me_2X and 2D $\text{Me}'_2\text{X}$ [3]. This issue could be enough to provide strain in 2D $\text{MeMe}'\text{X}$ leading to possible the 2D – 1D transformation.

In order to investigate this possibility we have performed the first-principles calculations of zigzag and armchair MgCaSi NTs with the different sizes to reveal changes total energies and band structures with respect to 2D MgCaSi . These calculations have been performed using the projector-augmented wave (PAW) method (VASP code [5]) within the Perdew-Burke-Ernzerhof functionals [6] for the exchange-correlation energy.

After full structural optimization we have found that MgCaSi NTs with Mg atoms forming the inner layer are lower in the total energy with respect to 2D MgCaSi . The zigzag (6,0) and armchair (3,3) MgCaSi NTs are found to be the smallest possible NTs because the sharp increase of total energy occurs for NTs with smaller diameter. The energy gain for the 2D – 1D transformation and the strain relief, caused by distortions in the interatomic Me–Me and Me'–Me' distances in the $\text{MeMe}'\text{X}$ NTs with respect to the parent 2D $\text{MeMe}'\text{X}$, suggest the spontaneous rolling up of

$\text{MeMe}'\text{X}$ nanoribbons. The most stable zigzag (8,0) and armchair (4,4) MgCaSi NTs have diameters of about 11.8 and 10.3 Å, respectively. Diameters are defined by a tube formed by Si atoms.

It has been found that all of investigated MgCaSi NTs are direct-gap semiconductors with the first direct transition in the Γ point, as well as their parent 2D structure. In the limit of large NT diameters, the corresponding band-gap values approach the band-gap value of 2D MgCaSi , which is 0.52 eV. The maximum band-gap values of 0.67 eV for the zigzag (10,0) NT with diameter 14.6 Å and of 0.64 eV for armchair (6,6) NT with diameter 14.0 Å have been found. Preliminary calculations of values of dipole matrix elements of the first direct transition in MgCaSi NTs indicated rather high oscillator strength.

Thus, the theoretical possibility of the 2D – 1D transformation in 2D $\text{MeMe}'\text{X}$ driven by strain relief is presented. All MgCaSi NTs have the Mg outer and Ca inner layers and these NTs are direct band-gap semiconductors. We also discuss a possibility of the similar 2D – 1D transformation in 2D ternary transition metal dichalcogenides.

Acknowledgements

This work has been supported by the Belarusian National Research Programs “Materials science, new materials and technology” and Belarusian Republican Foundation for Fundamental Research (grant No. F20R-003). D.B. Migas and A.B. Borisenko acknowledge the partial financial support of the “Improving of the Competitiveness” Program of the National Research Nuclear University MEPhI–Moscow Engineering Physics Institute.

References

- [1] D. B. Migas, V. O. Bogorodz, A. B. Filonov, V. E. Borisenko, N. V. Skorodumova. *Surf. Sci.* **670** (2018) 51.
- [2] A. Y. Alekseev, A. G. Chernykh, A. B. Filonov, D. B. Migas, and N. V. Skorodumova. *Int. J. Nanosci.* **18** (2019) 1940013.
- [3] A. Y. Alekseev, D. B. Migas, A. B. Filonov, V. E. Borisenko, N. V. Skorodumova. *Japanese Journal of Applied Physics* **59** (2020) SF0801.
- [4] D. Yu, F. Liu. *Nano letters* **7** (2007) 3046.
- [5] G. Kresse, J. Furthmüller. *Comput. Mat. Sci.* **6** (1996) 15.
- [6] J. P. Perdew, K. Burke, M. Ernzerhof. *Phys. Rev. Lett.* **77** (1996) 3865.

Rare-earth-free semiconducting silicide solar cells and Mn₄N-based spintronic devices for sustainable electronics

T. Suemasu*

Institute of Applied Physics, University of Tsukuba, Ibaraki 305-8573, Japan

*e-mail: suemasu@bk.tsukuba.ac.jp

Photovoltaics (PV) systems have been rapidly and globally deployed and exceeded a cumulative installed capacity of 500 GWp in 2018. However, it is necessary to further deploy PV systems to establish a sustainable energy supply. For this purpose, the energy costs per watt-peak must be pursued based on improving the energy conversion efficiency of solar cells and decreasing manufacturing costs. Now, more than 90% of installed solar cells are based on crystalline silicon (c-Si), and a large-scale production system for PV modules based on c-Si solar cells is well established. However, there are two main drawbacks to using c-Si. One thing is that the absorption coefficient is small. Thus the wafer thickness of >100 μ m is necessary, and Si wafers will still account for the majority of the cell's price. Another drawback is the band gap of Si ($E_g=1.1$ eV), which is slightly narrower compared to the ideal one (1.4 eV). Under such circumstances, we have paid special attention to barium disilicide (BaSi₂). It is composed of earth-abundant and non-toxic elements [1,2]. It has attractive features for solar cell applications [3] such as a suitable E_g of 1.3 eV, a large absorption coefficient. Moreover, BaSi₂ has a large minority carrier diffusion length $L \approx 10$ μ m due to its inactive grain boundary. Because of these excellent properties, BaSi₂ is considered a thin-film solar cell material. In previous studies, we have achieved $\eta = 9.9\%$ in p-BaSi₂/n-Si heterojunction solar cells [4]. Furthermore, we have demonstrated the operation of BaSi₂ homojunction solar cells [5]. In the presentation, I talk about what we are now focusing on, that is the improvement of optical properties of BaSi₂ light absorber layers. According to the first-principles calculation by Kumar *et al.* [6], Si vacancies (V_{Si}) are most likely to occur as point defects in BaSi₂. In BaSi₂, Si atoms are bonded covalently. Thus, electron paramagnetic resonance (EPR) is considered one of the most powerful techniques to detect defects which carry a charge and have a spin ($S \neq 0$). Very recently, we succeeded to detect paramagnetic defects in BaSi₂ by EPR for the first time [7]. We also demonstrated that atomic H passivation is beneficial to improve the optical properties of BaSi₂ films from the viewpoints of both experiment and theory [8].

In our future society, low power-consumption electronic devices are of particular importance, too. The development of artificial intelligence and big data requires the development of high-speed and low-power memories and processors. In this context, spintronics possesses compelling advantages over competing technologies: intrinsic nonvolatility, room-temperature operation, and compatibility with the CMOS technology. Spintronics Achilles' heel might be its hazardous dependence on Co, rare-earth elements, and heavy metals (W and Pt). In the presentation, I talk about the magnetic properties of a material made of abundant and cheap elements, and show

that it is a promising candidate for the development of a sustainable spintronics: epitaxial ferrimagnet Mn₄N. Recent experiments have shown that epitaxial Mn₄N thin films exhibit a perpendicular magnetization [9], remarkable magnetic properties within particular millimetric and smooth domain-wall (DW) motion and record DW velocities exceeding 900 m/s at room temperature owing to spin transfer torque [10]. We are now focusing on further enhancing a DW velocity in Mn_{4-x}Ni_xN films by achieving the angular momentum compensation. The DW velocity is considered to diverge at the angular momentum compensation point. Very recently, we found that the magnetic compensation occurs in the range $0.1 < x < 0.25$ by x-ray magnetic circular dichroism [11], and actually achieved the record DW velocity > 1.5 km/s at room temperature.

Acknowledgements

The author acknowledges Dr. K. Toko, and present and past students of the University of Tsukuba. The author also acknowledges Prof. D. B. Migas in Beralus for fruitful discussions and first-principles calculations to pursue the studies on BaSi₂, and Dr. L. Vila, Dr. J. P. Attane, and Dr. S. Gambarelli in France for their collaborations in research on Mn₄N and BaSi₂.

References

- [1] M. Imai and T. Hirano, *Phys. Rev. B* **58**, 11922 (2003).
- [2] D. B. Migas, V. L. Shaposhnikov, and V. E. Borisenko, *Phys. Status Solidi B* **244** (2007) 2611.
- [3] T. Suemasu and N. Usami, *J. Appl. Phys.* **50** (2017) 023001.
- [4] D. Tsukahara, S. Yachi, H. Takeuchi, R. Takabe, W. Du, M. Baba, Y. Li, K. Toko, N. Usami, and T. Suemasu, *Appl. Phys. Lett.* **108** (2016) 152101.
- [5] K. Kodama, Y. Yamashita, K. Toko, and T. Suemasu, *Appl. Phys. Express* **12** (2019) 041005.
- [6] M. Kumar, N. Umezawa, W. Zhou, and M. Imai, *J. Mater. Chem. A* **5** (2017) 25293.
- [7] T. Sato, C. Lombard, Y. Yamashita, Z. Xu, L. Benincasa, K. Toko, S. Gambarelli, and T. Suemasu, *Appl. Phys. Express* **12** (2019) 061005.
- [8] Z. Xu, D. A. Shohonov, A. B. Filonov, K. Gotoh, T. Deng, S. Honda, K. Toko, N. Usami, D. B. Migas, V. E. Borisenko, and T. Suemasu, *Phys. Rev. Mater.* **3** (2019) 065403.
- [9] Y. Yasutomi, K. Ito, T. Sanai, K. Toko, and T. Suemasu, *Jap. J. Appl. Phys.* **115** (2014) 17A935.
- [10] T. Gushi, M.J. Klug, J.P. Garcia, S. Ghosh, J.P. Attane, H. Okuno, O. Fruchart, J. Vogel, T. Suemasu, S. Pizzini, and L. Vila, *Nano Lett.* **19** (2019) 8716.
- [11] T. Komori, T. Gushi, A. Anzai, L. Vila, J.-P. Attane, S. Pizzini, J. Vogel, S. Isogami, K. Toko, and T. Suemasu, *J. Appl. Phys.* **125** (2019) 213902.

Development of Mg₂Si pn-junction photodiode

Haruhiko Uono*

Ibaraki University, 4-12-1 Nakanarusawa, Hitachi, Ibaraki 316-8511, Japan

*e-mail: udono@vc.ibaraki.ac.jp

We have developed a novel short-wavelength-infrared (SWIR) photodiode made from Mg₂Si single crystal. The pn-junction was formed by the thermal diffusion of Ag dopant in n-type Mg₂Si substrate prepared from the melt-grown bulk crystal. The photodiode performed a good photo-response below 2.1 μm at 300K. The photosensitivity of more than 0.1 A/W was achieved between 1.3 and 1.5 μm for the mesh-electrode type pn-junction photodiode

Infrared photodetector is attracting attention as one of the key devices in the fields of machine vision system such as night monitoring, environmental monitoring, process monitoring, food inspection, and also medical imaging [1,2]. Magnesium half silicide (Mg₂Si) is an indirect band-gap semiconductor with the gap energy of about 0.6 eV at room temperature [3,4]. Its gap energy can be decreased as far as 0.3 eV by making alloy compound with Mg₂Sn [5]. Therefore, Mg₂Si and its alloy compounds are expected to be applied for the infrared photodetector with the cut-off wavelength between 2 and 4 μm. Recently, we have developed Mg₂Si pn-junction photodiode of which cutoff wavelength and detectivity are about 2.1 μm and more than 1×10^9 cmHz^{1/2}W⁻¹ at room temperature, respectively [6-13]. In this paper, we report the fabrication of Mg₂Si pn-junction photodiode on the n-type Mg₂Si bulk substrate using a simple thermal diffusion process and also the basic performance of the photodiode.

Bulk single crystal of Mg₂Si was grown from the melt using a pyrolytic graphite coated graphite crucible and high purity Mg (5N) and Si (10N grade) raw materials by the vertical Bridgman method [3,4]. The grown crystal was n-type with typical electron density of in the order of 10^{15} cm⁻³ [4]. The surface of substrate was polished like a mirror by a fumed silica.

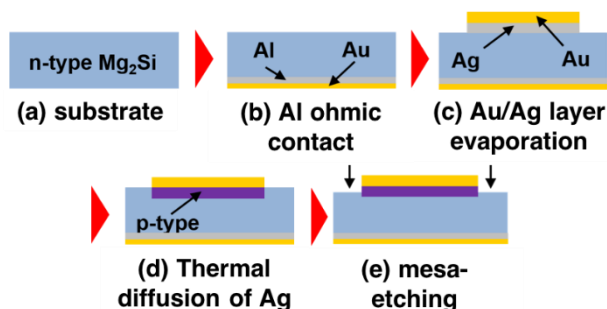


Figure 1. Schematic drawing of the fabrication process for the circle-electrode Mg₂Si pn-junction photodiode.

The Mg₂Si pn-junction photodiode was fabricated by the thermal diffusion of p-type dopant (Ag) into the n-type substrate [6]. Fig. 1 shows the schematic diagram of the fabrication process of the photodiode. A thin Ag-source layer and a following Au-electrode layer were evaporated on the mirror polished Mg₂Si substrate through a circular patterned metal mask using a conventional resistive

evaporation system. Then, the thermal diffusion of Ag-dopant was carried under the conditions of diffusion temperature $T_D = 400$ °C - 450 °C and the diffusion period $t_D = 10$ min in Ar ambient using the gold-imaging furnace (MIRA-3000, ULVAC). After the diffusion process, the surface of the substrate was etched by the fluonitric acid (HF : HNO₃ : H₂O = 1 : 2 : 100) to form mesa-structure. In the fabrication of ring- or mesh-electrode photodiode, the electrode was formed by a conventional lift-off process. The backside ohmic contact was also made by the thermal diffusion of Al [10,11].

The J-V characteristic of the photodiode with the circle-electrode (0.6 mm of diameter) was evaluated between 250 K and 320K. Clear rectifying behavior confirms the formation of a good pn-junction. The reverse bias current decreased with decreasing the temperature due to the decrease of intrinsic carrier density and related diffusion current. We fabricated three types of photodiodes (circle, ring and mesh electrode) and compared their photosensitivity. We found the great improvement of photosensitivity depending on the electrode structure [12,13]. The value of the mesh-electrode photodiode was approximately two order of magnitude higher than that of the circle-electrode one.

We developed Mg₂Si pn-junction photodiode on n-type Mg₂Si substrate for the application of SWIR detector. The photodiodes performed a good photoresponse below the cut-off wavelength of about 2.1 μm. The obtained results indicate that the Mg₂Si is promising material for a novel environment and human friendly SWIR sensor.

References

- [1] D. Feng, et al., Appl. Phys. Lett. **95** (2009) 261105.
- [2] A. Rogalski, Infrared Phys. Technol. **54** (2011) 136.
- [3] D. Tamura, R. Nagai, K. Sugimoto, H. Uono, I. Kikuma, H. Tajima, and I. J. Ohsugi, Thin Solid Films **515** (2007) 8272.
- [4] H. Uono, H. Tajima, M. Uchikoshi, and M. Itakura, Jpn. J. Appl. Phys. **54** (2015) 07JB06.
- [5] W. Scouler., Phys. Rev. **178** (1969) 1353.
- [6] H. Uono, Y. Yamanaka, M. Uchikoshi, and M. Isshiki, J. Phys. Chem. Solids **74** (2013) 311.
- [7] M. Takezaki, Y. Yamanaka, M. Uchikoshi, and H. Uono, Phys. Status Solidi. C **10** (2013) 1812.
- [8] K. Daitoku, M. Takezaki, S. Tanigawa, D. Tsuya and H. Uono, JJAP Conf. Proc. **3** (2015) 011103.
- [9] K. Sekino, M. Midonoya, H. Uono, and Y. Yamada, Phys. Procedia **11** (2011) 171.
- [10] Y. Onizawa, T. Akiyama, N. Hori, F. Esaka and H. Uono, JJAP Conf. Proc. **5** (2017) 011101.
- [11] T. Akiyama, N. Hori, S. Tanigawa, D. Tsuya and H. Uono, JJAP Conf. Proc. **5** (2017) 011102.
- [12] H. Uono, Oyo Butsuri **88** (2019) 797.
- [13] D. Niioka, F. Takahashi, M. Yoshida, D. Tsuya and H. Uono, APAC-Silicide2019, Sun-a-O13.

Semiconducting ternary Si clathrates

M. Imai*

National Institute for Materials Science, Tsukuba, Ibaraki 305-0047, Japan

*e-mail: IMAI.Motoharu@nims.go.jp

The group-14 clathrates have been investigated because of interesting physical properties related to their unique crystal structure. Figure 1 shows the crystal structure of type-I clathrate, whose general chemical formula is A_8X_{46} . X atoms form a cage framework that consists of face-shares X_{20} dodecahedra and X_{24} tetrakaidecahedra, and A atoms are encapsulated in these polyhedra as guest atoms. The clathrates are classified by which kind of polyhedra form the framework. The group-14 clathrates are classified into five types, type-I, type-II, type-III, type-VIII, and type-IX (or type-I'). In the following, we focus on type-I clathrates. In the binary type-I group-14 clathrates, A represents alkaline-metal and alkaline-earth-metal elements, and X represents the group-14 elements such as Si, Ge and Sn. A part of atoms in the framework can be replaced by group-12, 13, and transition-metal atoms, results in ternary group-14 clathrates, $A_8E_xX_{46-x}$.

One of the interesting physical properties of $A_8E_xX_{46-x}$ is thermoelectric properties. The thermoelectric properties of $A_8E_xX_{46-x}$ have been extensively investigated [1] since the discovery of low lattice thermal conductivity in $Sr_8Ga_{16}Ge_{30}$ [2]. This low thermal conductivity is an important factor to achieve a high dimensionless thermoelectric figure of merit, ZT . A ZT value of close to 1 has been reported for the Ge-based clathrate $Ba_8Ga_xGe_{46-x}$ [3], which make $Ba_8Ga_xGe_{46-x}$ a promising thermoelectric material. However, based on elemental abundance in the Earth's crust, Si-based clathrates are preferable to Ge-based clathrates because Si is more abundant than Ge. It is, therefore, necessary to synthesize semiconducting Si clathrates and to change its nature from metallic to semiconducting for tuning the ZT value optimum.

The other is optical properties. Adams *et al.* have indicated by the first principle calculation that a guest-free type-I Si clathrate Si_{46} is a semiconducting material with a band gap (E_g) that is 0.7 eV wider than that of elemental Si with the diamond-type structure [4]. Si-based materials with wider E_g than the diamond-phase Si are attractive for solar cell application since (1) a semiconducting material with E_g of 1.4 eV, which is 0.3 eV wider than that of Si, is ideal for a single junction solar cell, and (2) a Si-based material with E_g that is wider than 1.4 eV can be a candidate top cell material for a tandem Si based solar cell.

Thus, the synthesis of semiconducting Si clathrates was desired in thermoelectric and photovoltaic fields. Although the semiconducting guest-free type-II Si clathrates have been formed, it is difficult to use them in the applications

because the synthesized sample was powder form. In 2011, I succeeded in the synthesis of bulk semiconducting ternary type-I Si clathrates [5].

In this talk, I review the recent progress in the study on semiconducting ternary Si clathrates [6]. I will present synthesis methods, crystal structure, calculated results on the band structure, and physical properties such as optical, transport and thermoelectric properties. Up to now, eight ternary type-I Si clathrates has been reported to be semiconducting. The E_g values of these Si clathrates ranges from 0.64 to 1.4 eV. Their electrical resistivity is relatively high. Their magnitude of Seebeck coefficient is comparable to the other group 14 element clathrates. The thermal conductivity is low as well as the other group 14 element clathrates. As a result, the dimensionless thermoelectric figure of merit of these clathrates are low compared with Ge and Sn clathrates due to their high electrical resistivity.

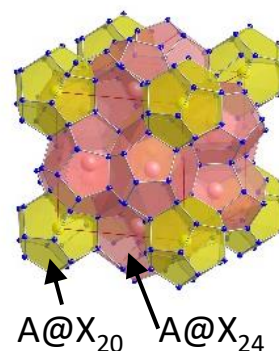


Figure 1. Crystal structure of type-I clathrate A_8X_{46} .

Acknowledgements

This research was partially supported by the ALCA program of the Japan Science and Technology Agency (JST), and KAKENHI of Japan Society for the Promotion of Science (JSPS) (Grant Number JP17H03234, JP22013019).

References

- [1] G.S. Nolas, ed. *The physics and Chemistry of Inorganic Clathrates*. (Springer Netherland, Dordrecht Heidelberg New York London, 2014).
- [2] G.S. Nolas et al., *Appl. Phys. Lett.* **73** (1998) 178.
- [3] E.S. Toberer et al., *Phys. Rev.* **B 77** (2008) 075203.
- [4] G.B. Adams et al., *Phys. Rev.* **B 49** (1994) 8048.
- [5] M. Imai et al., *Dalton Trans.* **40** (2011) 4045.
- [6] M. Imai, *Jpn. J. Appl. Phys.* (accepted).

The role of heterogeneous melting in germanium nanowire growth by the electrochemical liquid-liquid-solid mechanism

S.A. Gavrilov*

National Research University of Electronic Technology – MIET, Bld. 1, Shokin Square, Zelenograd, Moscow, Russia

*e-mail: pcfme@miee.ru

Germanium (Ge) nanowires have a wide range of application due to their electrophysical and optical properties [1]. It was demonstrated that Ge nanostructures may be used in lithium and sodium batteries [2, 3], thermoelectricity [4], photodetectors [5].

The most commonly used technique for the fabrication of semiconducting Ge nanowires is vapor deposition. However this method require substrates that can withstand high process temperatures (300-700°C), greatly limiting the possible choices for electrode support materials. The possibility of germanium nanowires synthesis at a temperatures below 100°C by electrochemical method from germanium (IV) oxide aqueous solutions using the low-melting metals such as Hg, Ga, as germanium crystallization centers was demonstrated in [7]. In this case, the liquid metal particles serve as electrodes for the germanium ions reduction to atomic germanium and as a solvent in which germanium atoms create a crystallization supersaturation. As a result, on the liquid metal-substrate boundary, precipitation of germanium occurs by analogy with the growth of whiskers from the gas phase by the known vapor-liquid-crystal mechanism. Alternative is the use of low-melting metals which can form eutectic composition Ge alloys with higher melting temperatures than Hg and Ga. It should also be considered that the maximum attainable deposition temperature is limited by the electrolyte boiling temperature (for aqueous solutions ~100°C). It is known that the melting temperature decreases with decreasing metal-particle dimensions. It was shown that it is possible to grow germanium structures from aqueous solutions using In particles of sizes not exceeding 100 nm (the melting temperature of bulk In is ~156.6°C) [8]. To analyze the probability of finding the studied particles in the liquid state at a given temperature can be used the dependence of the melting temperature of a spherical particle on its radius was justified [8, 9],

$$T = T_{\infty} \left(\frac{\Delta H(T)}{\Delta H(T_{\infty})} + \frac{3\Delta\delta}{r\Delta H(T_{\infty})} \right) \quad (1)$$

where T_{∞} is the reference melting temperature of the bulk metal, $\Delta\delta = \delta_L - \delta_S$ is the change in the system surface energy during the solid-liquid transition, $\Delta H_m(T_{\infty})$ is the

melting heat at the melting temperature of the bulk material, is the melting heat at the particle melting temperature T .

In this study, based on a comparison of the results of theoretical calculation of the melting temperatures of metal nanoparticles of different diameters and electron microscopy data on the morphology of Ge nanostructures, the crucial role of heterogeneous melting for providing the electrochemical liquid-liquid-solid (ec-LLS) mechanism is shown.

The approach proposed in this study can be used to extend the spectrum of used metal particles and to control the composition and morphology of formed nanowires by ec-LLS mechanism.

Acknowledgements

The reported study was funded by RFBR, project number 18-29-23038 mk.

References

- [1] C. O'Regan, S. Biswas, N. Petkov, J. D. Holmes. *J. Mater. Chem. C* **2** (2014) 14.
- [2] I. M. Gavrilin, V. A. Smolyaninov, A. A. Dronov, S. A. Gavrilov, A. Yu. Trifonov, T. L. Kulova, A. A. Kuz'mina, and A. M. Skundin. *Russian Journal of Electrochemistry* **54** (2018) 1111.
- [3] I. M. Gavrilin, V. A. Smolyaninov, A. A. Dronov, S. A. Gavrilov, A. Yu. Trifonov, T. L. Kulova, A. A. Kuz'mina, and A. M. Skundin. *Mendeleev Communications* **28** (2018) 659.
- [4] J. Kim, J.-H. Bahk, J. Hwang, H. Kim, H. Park, W. Kim. *Phys. Status Solidi RRL* **7** (2013) 767.
- [5] Y. Zhang, S. Yang, Y. Yang, M. Gould, N. Ophir, A. E.-J. Lim, G.-Q. Lo, P. Magill, K. Bergman, T. Baehr-Jones, M. Hochberg. *Optics Express* **22** (2014) 11367.
- [6] K. W. Kolasinski. *Curr. Opin. Solid State Mater. Sci.* **10** (2006) 182.
- [7] E. Fahrenkrug, S. Maldonado. *Accounts of Chemical Research* **48** (2015) 1881.
- [8] I. M. Gavrilin, D. G. Gromov, A. A. Dronov, S. V. Dubkov, R. L. Volkov, A. Yu. Trifonov, N. I. Borgardt, and S. A. Gavrilov. *Semiconductors* **51** (2017) 1067.
- [9] D. G. Gromov, S. A. Gavrilov. *InTech, Rijeka* (2011) 157.

Sn-nanodot mediated formation of GeSn and Si(Ge)Sn polycrystalline alloys for thermoelectric applications

Y. Shimura^{*,1,2,3}, J. Utsumi¹, M. Okado¹, K. Iwamoto², and H. Tatsuoka¹

¹ Graduate School of Integrated Science and Technology, Shizuoka University, 3-5-1 Johoku Naka-ku Hamamatsu 432-8561, Japan

² Faculty of Engineering, Shizuoka University, 3-5-1 Johoku Naka-ku Hamamatsu 432-8561, Japan

³ Research Institute of Electronics, Shizuoka University, 3-5-1 Johoku Naka-ku Hamamatsu 432-8561, Japan

*e-mail: shimura.yohsuke@shizuoka.ac.jp

Attention toward Sn as a component element for new group-IV alloys has been increasing because introduction of Sn into Ge and/or Si crystal drastically expand the controllability in bandgap, lattice constant, electrical/optical properties, etc. For example, Ge, an indirect bandgap material, turns into a direct bandgap material when more than 8 at.% Sn atoms are introduced into substitutional sites of the Ge host crystal [1]. As a result of devoted efforts [2,3] to increase Sn contents limited by solid solubility as 1 at.% under equilibrium condition, a direct bandgap group-IV alloy has been finally realized [4].

Recently, this fascinating alloy has been focused as a promising candidate for a material to be implemented into thermoelectric generators. Thermoelectric devices which can directly convert heat energy into electricity with less environmental impact have been gathering attention widely. The devices are expected to be used for sensors and logic devices on a silicon wafer as a power supply source that does not require battery replacement.

To improve the conversion efficiency of the thermoelectric device, it is crucial to decrease thermal conductivity of the material used in the device. In addition to use polycrystalline material including grain boundaries which can act as phonon scattering site, introduction of heavy Sn atoms into Si or Ge crystal is expected to realize lower thermal conductivity because of additional suppression of phonon propagation due to their mass difference.

It was found that amorphous Sn layer deposited on SiO₂ substrate can be easily transformed into crystalline Sn nanodots by just applying an annealing in vacuum.

Interestingly, Ge deposited on the Sn nanodots penetrates into the nanodots, resulted in the formation of polycrystalline Ge_{1-x}Sn_x having high Sn content [5]. We recently reported that poly-Ge_{1-x}Sn_x binary alloy shows lower thermal conductivity compared to that for poly-Ge [6]. Besides, other material properties, such as Seebeck coefficient, carrier concentration, crystalline structure, phonon dispersion, etc. which contribute the thermoelectric device performance will be discussed. Recent results about the formation of other group-IV alloys, such as Si_{1-x}Sn_x, Si_{1-x-y}Ge_xSn_y, mediated by Sn-nanodots is also planned to be introduced.

Acknowledgements

This work was supported by JSPS KAKENHI Grant Number JP18K13786 from the Japan Society for the Promotion of Science.

References

- [1] Y. Shimura, S. A. Srinivasan, R. Loo, *ECS J. Solid State Sci.* **5** (2016) Q140.
- [2] Y. Shimura, N. Tsutsui, O. Nakatsuka, A. Sakai, S. Zaima, *Thin Solid Films*, **518** (2010) S2.
- [3] Y. Shimura, T. Asano, T. Yamaha, M. Fukuda, W. Takeuchi, O. Nakatsuka, S. Zaima, *Mater. Sci. Semicond. Process.* **70** (2017) 133.
- [4] S. Wirths, R. Geiger, N. von den Driesch, G. Mussler, T. Stoica, S. Mantl, Z. Ikonc, M. Luysberg, S. Chiussi, J. M. Hartmann, H. Sigg, J. Faist, D. Buca, D. Grützmacher, *Nature Photonics* **9** (2015) 88.
- [5] N. Chen, G. Lin, L. Zhang, C. Li, S. Chen, W. Huang, J. Xu, J. Wang, *Jpn. J. Appl. Phys.* **56** (2017) 050301.
- [6] J. Utsumi, T. Ishimaru, Y. Hayakawa, Y. Shimura, *Semicond. Sci. Technol.* **33** (2018) 124004.

**I. Physics of nanostructures and interfaces,
self-organization processes**

Synthesis of carbon layers on aluminium oxide surfaces

M.M. Simunin^{*1,2}, E.V. Mikhlina², A.S. Vyatkin², O.E. Bezrukova¹, I.A. Kharchenko², I.V. Nemtsev³,
A.S. Voronin², I.A. Tambasov², I.I. Ryzhkov^{1,2}

¹ Siberian Federal University, Svobodny 79, 660041 Krasnoyarsk, Russia

² Institute of Computational Modelling SB RAS, Akademgorodok, 50–44, Krasnoyarsk, 660036

³ Federal Research Center KSC SB RAS, Akademgorodok, 50, Krasnoyarsk, 660036

*e-mail: michanel@mail.ru

Carbon nanotubes and graphene are two of the most important forms of nanoscale carbon materials. Both materials can be synthesized by CVD method with the use of various "catalysts". The term "catalyst" is conditional; it refers to a surface, on which graphite islands are formed at a relatively low temperature. Either carbon nanotubes or graphene layers can grow on the surface depending on its shape and physical-chemical properties. As a rule, the materials of such surfaces are the most common metals of auxiliary groups [1], in which the carbon is dissolved after chemical deposition from the gas phase. Then, as a result of supersaturation of carbon solution in metal, the carbon precipitates on the surface in the form of graphite islands, which combine into graphene or nanotubes. However, the ordered carbon structures can be obtained not only by dissolving carbon in metals, but also by using special surfaces, where the surface diffusion of carbon can occur. Aluminum oxide provides an example of such material [2].

There are three types of aluminum oxide used as modeling media. The first one is porous anodic aluminum oxide membrane [3]. The second is a crystal sapphire for electronic applications, while the third one is the material of nanofibrous gamma-alumina with a fiber diameter of about 10 nm [4]. Carbon layers are precipitated by the CVD method from ethanol with argon carrier gas. The reaction is proceeding in a tube furnace after heating to 500-1100 °C at a pressure of 0.1 kPa to atmospheric pressure. As a result of the reaction, we have carbon deposition on the sample.

The membranes of the porous anodic alumina were prepared in the potentiostatic mode in an oxalic or sulfuric acid electrolyte, after which they were annealed at a temperature of 820 °C, and carbon was deposited on them at the same temperature. During deposition, carbon formed a conformal thin film inside the pores. It was shown that the pore diameter in the membrane can be reduced by controlling the carbon deposition time. TEM studies of membranes after carbon deposition showed the absence of soot inside the pores of anodic alumina, which indicates the thermodynamic benefit of carbon deposition on the alumina surface.

Bundles of aluminum oxide nanofibers (Nafen) were placed in the reactor and carbon layers of different thicknesses on the nanofibers were obtained at 900 C and 50 kPa depending on the synthesis time [5] (see Fig. 1). An important feature of the processes was the uniform carbon deposition on the nanofibers without soot inclusions. Four samples were obtained with different synthesis times (60 s, 120 s, 300 s, and 600 s). Thermal analysis, X-ray fluorescent microanalysis, Raman spectroscopy, and electrical resistance measurements of carbon-alumina nanofibers composites showed that increasing of synthesis time not only increases the amount of carbon on alumina

surface, but also the ordering and density of the carbon layers. Nitrogen adsorption data revealed the decrease of total pore volume with increasing the synthesis time.

Finally, we examined the films deposited as a result of ethanol CVD on the sapphire substrates. Deposition was performed at 1100 °C and 50 kPa. At different synthesis times, relatively thick carbon films are obtained. As a result of the ambient conditions, a water adsorbate falls under the carbon film and the film starts to slide over the sapphire with creating a bizarre pattern.

The obtained composite materials could be employed for the preparation of ion-selective membranes with switchable ion transport, electroconductive ceramics, electrochemical sensors, and microelectronic components such as field-effect transistor.

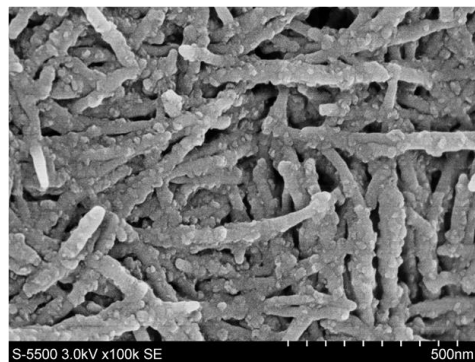


Figure 1. SEM image of Nafen alumina nanofibers after deposition of carbon by CVD.

Acknowledgements

The work is supported by the Russian Foundation for Basic Research Grant № 18-29-19078.

References

- [1] N.M. Mubarak, E.C. Abdullah, et al. *J. of Ind.& Eng. Chem.* **20** (2014) 1186.
- [2] Pang J., Bachmatiuk A., Ibrahim I. et al. *J Mater Sci.* **51** (2016) 640.
- [3] W. Lee. *Chem. Rev.* **114** (2014) 7487.
- [4] Features of Nafen alumina nanofibers, <http://www.anftechnology.com/nafen/>
- [5] V.S. Solodovnichenko, M.M. Simunin, D.V. Lebedev, A.S. Voronin, A.V. Emelianov, Y.L. Mikhlin, V.A. Parfenov, I.I. Ryzhkov. *Thermochimica Acta* **675** (2019) 164.

Atomic and electronic structure of top-down MAWCE silicon nanowires arrays and nanostructures on their basis

E.V. Parinova^{*1}, V. Sivakov², D.A. Koyuda¹, O.A. Chuvenkova¹, D.N. Nesterov¹, A. Schleusener², T. Ming², D. Marchenko³, A.K. Pisliaruk¹, R.G. Chumakov⁴, A.M. Lebedev⁴, D. Smirnov⁵, A. Makarova⁵, S.Yu. Turishchev¹

¹ Voronezh State University, Universitetskaya pl. 1, Voronezh 394018, Russia

² Leibniz Institute of Photonic Technologies, Alber-Einstein Str. 9, Jena 07745, Germany

³ Helmholtz-Zentrum-Berlin, Alber-Einstein Str. 15, Berlin 12489, Germany

⁴ National Research Center "Kurchatov Institute", pl. Akademika Kurchatova 1, Moscow 123182, Russia

⁵ Dresden University of Technology, Zellescher weg 1, Dresden 01062, Germany

*e-mail: parinova@phys.vsu.ru

The unique physico-chemical properties, provided by metal-assisted wet-chemically etched (MAWCE) silicon nanostructures (usually in the form of nanowires arrays, SiNWs) have been attracted considerable attention over the last years. The silicon based approaches are certainly favored due to the material abundance and non-toxicity at a high level of materials control and understanding together with a huge industrial infrastructure to account for low production/processing costs and high production yields.

For that reason, porous silicon nanostructures (nanowires, nanoparticles) have been gained an enormous interest and employed as the semiconductor material toward hydrogen fuel production such as photoelectrochemical water splitting. The band gap of nanostructured silicon can be increased by the shrinking of silicon dimension. Since last few years a growing interest on the formation and application of porous silicon nanostructures as photocatalyst can be recognized from the literature overview. In this study the atomic and electronic structure of free nanopowders formed from SiNWs arrays were investigated.

Additionally the increasing interest in area such as pollution control, detection of hazardous gases and monitoring of combustion processes has lent prominence to gas sensing devices. Solid state gas sensors based on tin oxide thin composite layers have become attractive owing to their manufacturing simplicity and portability. So here SiNWs developed and controlled surface is a highly demanded system. For tin-oxygen films prepared by MOCVD technique, the reports on the presence of the Sn (0) and/or Sn(II) phases are quite conflicting. In present study the growth of tin oxide coverage on the 1D silicon surfaces formed by MAWCE has been investigated.

Obviously, SiNWs and composite nanostructures on their basis and their developed surface could play an important role for possible applications of this modern semiconductor systems. In spite of many research works, only weak study efforts have been paid for investigations of MAWCE silicon nanowires and composites on their basis surface analysis, especially such fundamental properties as atomic and electronic structure.

The arrays of silicon nanowires was fabricated by MAWCE approach. The concentration of Ag ions in the first etching step strongly influences the density and/or distance between neighboring silicon nanostructures, which finally can influence the material penetration to the porous silicon matrix by the further matrix functionalization. Also different silicon substrates used can lead for further free nanoparticles

morphology and composition peculiarities. Thus three groups of structures were studied. First: initial SiNWs with different morphology. Second: free silicon nanopowders formed from different SiNWs samples. Third: SiNWs covered by tin-oxygen composite layer by application of MOCVD technique.

The morphology analysis of nanostructured silicon surfaces and composites was carried out by Carl Zeiss ULTRA 55 scanning electron microscope (SEM). High resolution XANES spectra relative to Si L_{2,3}, Sn M_{4,5} and O K core levels were obtained at the Russian-German Lab end-station (Helmholtz Zentrum Berlin) and NANOPES end-station (NRC "Kurchatov institute") storage rings (BESSY-II and Kurchatov respectively). The same facilities were used for the high-resolution XPS studies. Several BESSY-II undulator beamlines in combination with Focus-PEEM microscope of Russian German LAB were used for the real microspot XANES spectroscopy and chemically selective imaging. Probing depth was considered between 2 and 10 nm depending of the techniques applied. Additionally formed composite structures were pre-characterized by XRD and SEM/EBSD.

The physical chemical state, atomic and electronic structure and composition peculiarities of the MAWCE SiNWs arrays, particles and tin-oxygen system composite layers on their basis were established. We studied not only information from the upper part of the formed SiNWs arrays structures, but also from their deeper bulk part after mechanical removal in situ of the upper part of SiNWs in an inert atmosphere. The transformation of electronic structure in combination with local atomic surrounding character and composition evolution for surface and achievable interfaces of systems under studies allow underlining the effectiveness of SiNWs and composites on their basis as promised material for a range of future technologies and applications.

The part of studies was funded by the Russian Science Foundation (Project 17-72-10287) and partially by the Ministry of Education and Science of Russia, State Tasks for Higher Education Organizations in Science. Russian German Lab provided PEEM microscope facility supported by BMBF grant No 05K12KE1. V.S. is gratefully acknowledges the German Federal Ministry of Education and Research (BMBF) in frame of Baltic Sea Network "NanoPhoto" under Grant No. 01DS14017 and German Research Foundation (DFG) under Grant No. SI1893/18-1 for the financial support.

Investigation of the porous anodic titanium oxide layers self-organization process during formation by AES and ToF SIMS

A.A. Dronov^{*1}, D.A. Dronova¹, I.M. Gavrilin¹, M.S. Kuzmicheva¹, E.P. Kirilenko², S.A. Gavrilov¹

¹ National Research University of Electronic Technology - MIET, Bld. 1, Shokin Square, Zelenograd, Moscow, 124498, Russia

² Institute of Nanotechnology of Microelectronics of the Russian Academy of Sciences (INME RAS), Bld. 32A, Leninsky Prospekt, Moscow, 119991, Russia

*e-mail: Dronov.Alexey@org.miet.ru

Porous anodic titanium oxide (PAOT) layers are currently one of the most promising and actively studied nanostructured materials. Over the past few years, various research groups have published a big number of works devoted to the study of morphology, chemical, electrical and optical properties of the PAOT layers [1-3]. However, until now some anodic TiO₂ morphology evolution aspects during the electrochemical oxidation were not studied well. In particular the formation, evolution and properties of PAOT initial layer from various anodizing process conditions, which is an important factor for design, manufacture and efficiency increasing of PAOT based devices.

As it known electrochemical growth of titania nanotubular layers appears due to several competing processes: the titanium electrochemical oxidation (V_a), electrochemical (V_{ed}) and chemical (V_{cd}) dissolution of titanium oxide [4-9].

One of the most effective ways to investigate such reactions rates in time is to build and analyze current - time dependences. According to [10,11] the typical growth kinetics of PAOT in the potentiostatic mode anodizing three regions can be revealed. The first region is an exponential decreasing of current density, where the current density passes through a minimum value j_A , then increasing to a maximum value j_B in region 2, and after a slight decline stabilized in region 3.

In current investigation 5 “critical” points on these kinetics regions, where the current density transients significantly changes the slope angles were chosen.

A comprehensive analysis was carried out, including a study of the morphology, elemental and chemical composition along the depth of the anodic titanium oxide layer for the subsequent analysis of possible electrochemical and chemical reactions and their rates for each of the stages of the oxide layer formation of anodic oxidation process of titanium substrates in non-aqueous

fluorinated electrolytes to establish possible factors influencing to self-organization mechanisms of the porous layer formation by the means of SEM, AES, and ToF SIMS.

Acknowledgements

This work was supported by RFBR grant № 18-29-23038 mk.

References

- [1] K. Lee, A. Mazare, P. Schmuki, *Chemical Reviews*, **114** (2014) 9385.
- [2] M. Terracciano, V. Galstyan, I. Rea, M. Casalino, L. De Stefano, G. Sbervegleri, *Applied Surface Science*, **419** (2017) 235.
- [3] O. K. Varghese, M. Paulose, and C. A. Grimes, *Nature Nanotechnology*, **4** (2009) 59297.
- [4] A. Valota, D. J. LeClere, P. Skeldon, M. Curioni, T. Hashimoto, S. Berger, J. Kunze, P. Schmuki, G. E. Thompson, *Electrochimica Acta*, **54** (2009) 4321.
- [5] S. Berger, J. Kunze, P. Schmuki, A. T. Valota, D. J. LeClere, P. Skeldon, and G. E. Thompson, *Journal of The Electrochemical Society*, **157** (2010) C18.
- [6] S. Yoriya, M. Paulose, O.K. Varghese, G.K. Mor, C. a Grimes, V. Boule, S. College, V. Pennsylv, *The Journal of Physical Chemistry C*, **111** (2007) 13770.
- [7] A. Belov, I. Gavrilin, S. Gavrilov, A. Dronov, V. Labunov, *Semiconductors*, **47** (2013) 1707.
- [8] A. Valota, M. Curioni, D. J. Leclere, P. Skeldon, P. Falaras, G. E. Thompson, *J. Electrochem. Soc.*, **157** (2010) K243.
- [9] A. Valota, D.J. Leclere, T. Hashimoto, P. Skeldon, G.E. Thompson, S. Berger, J. Kunze, P. Schmuki, *Nanotechnology*, **19** (2008) 355701.
- [10] [J.M. Macak, H. Tsuchiya, A. Ghicov, K. Yasuda, R. Hahn, S. Bauer, P. Schmuki, *Current Opinion in Solid State and Materials Science*, **11** (2007), 3.
- [11] A. Apolinario, C. T. Sousa, J. Ventura, J. D. Costa, D. C. Leitao, J. M. Moreira, J. B. Sousa, L. Andrade, A. M. Mendes, J. P. Araujo, *J. Mater. Chem. A* **2** (2014) 9067.

Inclusion of the electron-electron interactions in the theory of photoemission by the TDDFT-based theory of the reduced density matrix

V.U. Nazarov*

Research Center for Applied Sciences, Academia Sinica, Taipei 11529, Taiwan

*e-mail: nazarov@gate.sinica.edu.tw

We derive the Liouville-type equation of motion for the reduced density matrix ρ_1 , valid to the first order in the electron-electron (e-e) interaction [exact exchange (EXX)] [1]

$$i \frac{\partial \rho_1(\mathbf{r}, \mathbf{r}', t)}{\partial t} = [\hat{h}_s(t), \rho_1(t)] - [v_x(t), \rho_0(t)] + \quad (1)$$

$$\int \rho_0(\mathbf{r}, \mathbf{r}_1, t) \rho_0(\mathbf{r}_1, \mathbf{r}', t) \left[\frac{1}{|\mathbf{r}_1 - \mathbf{r}'|} - \frac{1}{|\mathbf{r}_1 - \mathbf{r}|} \right] d\mathbf{r}_1,$$

where ρ_0 is the noninteracting (Slater-determinant) density matrix, obeying the single-particle equation of motion

$$i \frac{\partial \rho_0(\mathbf{r}, \mathbf{r}', t)}{\partial t} = [\hat{h}_s(t), \rho_0(t)],$$

$\hat{h}_s(t)$ and $v_x(t)$ are the time-dependent Kohn-Sham (KS) [2] and the exchange potentials, respectively.

As a particular application, within the linear response regime, we derive an extension to the Fermi's golden rule for the momentum-resolved stationary photoelectron spectrum, which accounts (to the first order) for the interparticle interaction [1]

$$P_f(\omega) = \sum_{i \in occ} B_{fi}(\omega) \delta[\omega - \epsilon_f + \epsilon_i + \Delta\omega_i], \quad (2)$$

where ϵ_i and ϵ_f are the KS eigenenergies of the initial and final states, respectively, and $\Delta\omega_i$ is the energy shift due to the interparticle interactions

$$\Delta\omega_i = -\langle \phi_i | v_x^{(0)} | \phi_i \rangle - \int \rho_0^{(0)}(\mathbf{r}, \mathbf{r}') \frac{\phi_i^*(\mathbf{r}) \phi_i(\mathbf{r}')}{|\mathbf{r} - \mathbf{r}'|} d\mathbf{r} d\mathbf{r}', \quad (3)$$

Table 1: KS EXX orbital eigenvalues ϵ_i , the energy shifts $\Delta\omega_i$, and the corresponding interaction-corrected IP $-(\epsilon_i + \Delta\omega_i)$ for several spherically symmetric spin neutral atoms, compared to the experimental and the HF values.

atom	$-\epsilon_i$	$-\Delta\omega_i$	$-\epsilon_i - \Delta\omega_i$	$-\epsilon_i^{exp}$	$-\epsilon_i^{HF}$
He(1s)	0.9179	-9.6×10^{-14}	0.9179	0.9036	0.9179
Be(1s)	4.1147	0.6169	4.7316	4.384	4.7327
(2s)	0.3091	-2.7×10^{-6}	0.3091	0.3425	0.3093
Ne(1s)	30.767	1.9951	32.762	31.985	32.772
(2s)	1.7054	0.2187	1.9241	1.781	1.9304
(2p)	0.8478	-5.4×10^{-5}	0.8477	0.7960	0.8504
Mg(1s)	46.267	2.7567	49.024	48.174	49.032
(2s)	3.0927	0.6697	3.7624	3.454	3.7677
(2p)	1.8696	0.4114	2.2811	2.0212	2.2822
(3s)	0.2526	3.2×10^{-5}	0.2526	0.2811	0.2531

In Table I we list the KS EXX eigenvalues ϵ_i , the energy shifts $\Delta\omega_i$, and the total ionization potential (IP) $\epsilon_i + \Delta\omega_i$ according to the present theory. The following observations can be made: (i) For the highest energy levels, the shifts $\Delta\omega_i$ disappear, which is in agreement with the known theorem stating that the highest KS eigenvalue is the

true physical IP (IP-theorem) [3]; (ii) For inner levels, $\Delta\omega_i$ are large and they change the KS eigenvalues in the right direction to the experimental IP. These shifts are, however, too big, making the theoretical IP to overestimate the experimental ones, while the KS values underestimate them. Further terms in the series in the interaction are necessary to improve the agreement with experiment; (iii) Our $\epsilon_i + \Delta\omega_i$ are found very close to the Hartree-Fock (HF) eigenvalues. This has a fundamental reason: The latter give physical IP to the first order in the interaction, which also $\epsilon_i + \Delta\omega_i$ do, but not ϵ_i

Table 2: KS LDA and EXX orbital eigenvalues and the corresponding interaction-corrected IP of the atoms in Table I.

atom	$-\epsilon_i^{LDA}$	$-\epsilon_i^{EXX}$	$-\epsilon_i^{LDA} - \Delta\omega_i^{LDA}$	$-\epsilon_i^{EXX} - \Delta\omega_i^{EXX}$
He(1s)	0.5170	0.9179	0.9354	0.9179
Be(1s)	3.7956	4.1147	4.7547	4.7316
(2s)	0.1736	0.3091	0.3123	0.3091
Ne(1s)	30.229	30.767	32.849	32.762
(2s)	1.2656	1.7054	1.9741	1.9241
(2p)	0.4428	0.8478	0.8958	0.8477
Mg(1s)	45.890	46.267	49.090	49.024
(2s)	2.8454	3.0927	3.7874	3.7624
(2p)	1.6615	1.8696	2.3102	2.2811
(3s)	0.1423	0.2526	0.2542	0.2526

As can be seen from Table II, the use of the local density approximation (LDA) instead of EXX does not change the IP significantly: While the orbital eigenvalues differ largely in the corresponding approximations, adding $\Delta\omega_i$ brings them close together.

We further note that the nonlinear dynamics using Eq. (1) will provide a natural pathway to the quantum-mechanically consistent inclusion of interactions in the theory of photoemission in the *time-domain* (i.e., beyond linear response). Presently this theory is relying on the *ansatz* of the identification of the KS particles with physical electrons [4]. We also anticipate it conceptually feasible to extend the theory to evaluate the *two-electron* density matrix, with an immediate application to the double photoelectron spectroscopy.

References

- [1] V. U. Nazarov, Phys. Rev. Lett. **123** (2019) 095302.
- [2] W. Kohn, L. J. Sham, Phys. Rev. **140** (1965) A1133.
- [3] J. P. Perdew, R. G. Parr, M. Levy, J. L. Balduz, Phys. Rev. Lett. **49** (1982) 1691.
- [4] M. Dauth, S. Kümmel, Phys. Rev. A **93** (2016) 022502.

Photoemission electron microscopy application for functional nanostructures characterization

S.Yu. Turishchev^{*1}, E.V. Parinova¹, O.A. Chuvenkova¹, F. Kronast², D. Marchenko², A.K. Fedotov³, V. Sivakov⁴, S.S. Antipov⁵, A.K. Pisliaruk¹, R. Ovsyannikov², D.A. Koyuda¹

¹ Voronezh State University, Universitetskaya pl. 1, Voronezh 394018, Russia

² Helmholtz-Zentrum-Berlin, Alber-Einstein Str. 15, Berlin 12489, Germany

³ Belarus State University, pr. Nezavisimosti 4, Minsk 220030, Belarus

⁴ Leibniz Institute of Photonic Technologies, Alber-Einstein Str. 9, Jena 07745, Germany

⁵ Immanuel Kant Baltic Federal University, Nevskogo St. 14, Kaliningrad 236016, Russia

*e-mail: tsu@phys.vsu.ru

X-ray and electron spectroscopy and microscopy techniques are known as power tools for modern functional materials fundamental properties deep understanding. These atomic and electronic structure investigations techniques combine high surfaces and interfaces sensitivity with local atomic surrounding specificity. In their turn phase composition and evolution with physical and chemical nature of the objects under study can be revealed by direct experiments analysis. Scientific core advantages mentioned above of the ultrasoft X-rays range spectroscopy measurements are resulted from the wavelengths comparable in general with actual sizes of single or discrete few nanometers morphology elements of structures under study.

Shift to real microscopic scale is really demanded for such experiments allowing to study atomic and electronic structure directly from low-dimensional surface areas making traditional approaches really micro-scale sensitive. PhotoEmission Electron Microscopy (PEEM) technique is one of the best example for this subject area of research combining microscopic imaging possibilities with local atomic structure and chemical state sensitivity at 'one run experiments'.

Several PEEM microscope setups implemented into the Helmholtz Zentrum Berlin synchrotron radiation storage ring BESSY-II facilities (e.g. Russian German Lab) infrastructure made real synchrotron microspot X-ray spectroscopy experiments possible. Extremely bright synchrotron (usually undulator) radiation allowed to move PEEM microscope magnification to real nanoscale. All microscope used were equipped with ultra high vacuum analysis and preparation chambers for pre-experiment characterization/modification possibility. For nearly all experiments (when feasible) regular X-ray absorption near edge structures spectroscopy, X-ray photoelectron

spectroscopy and Scanning Electron Spectroscopy experiments were performed.

Example of PEEM technique applications will be presented characterizing breakthrough experiments that can be conducted to understand microscopic properties of several functional nanostructural materials: metallic Ni or Cu clusters in porous dielectric SiO₂ matrix, wide-gap tin-oxygen composite nanostructures coverage of silicon nanowires and bio-inorganic E-coli cells without and combined with iron-oxide nanoparticles as promised hybrid nanostructures.

The surface (or achievable interfaces) sensitivity at micro-scale plays the crucial role for the deep understanding and searching for the prospective applications of modern nanomaterials and structures on their basis from well-known silicon-based systems to molecule- or cell-based hybrid nature-like objects. The best energy and/or lateral resolution that can be achieved experimentally plays extremely important role in scientifically correct understanding of different kind of structures nature.

The part of studies was funded by the Russian Science Foundation (Project 19-72-20180) and partially by the Ministry of Education and Science of Russia, State Tasks for Higher Education Organizations in Science. Russian German Lab provided PEEM microscope facility supported by BMBF grant No 05K12KE1. V.S. is gratefully acknowledges the German Federal Ministry of Education and Research (BMBF) in frame of Baltic Sea Network "NanoPhoto" under Grant No. 01DS14017 and German Research Foundation (DFG) under Grant No. SI1893/18-1 for the financial support. S.A. funded by the Russian Academic Excellence Project at the Immanuel Kant Baltic Federal University.

Theoretical and experimental studies of structural defects in CeO₂ nanoparticles

M.A. Pugachevskii¹, A.N. Chibisov^{*2}, A.S. Fedorov³

¹ Southwest State University, 94, 50 let Oktyabrya St., Kursk, 305040, Russia

² Computing Center of FEB RAS, 65 Kim Yu Chen St., Khabarovsk, 680000, Russia

³ L.V. Kirensky Institute of Physics of SB RAS, Krasnoyarsk, 660036, Russia

*e-mail: andreichibisov@yandex.ru

Cerium(IV) oxide (CeO₂) is an active rare-earth oxide material [1]; its functional properties in most cases are the result of the presence of a large number of surface structural defects, in particular, oxygen vacancies [2]. Oxygen vacancies on the CeO₂ surface can easily accumulate and release oxygen, and also act as active catalytic centres for the binding of adsorbed substances [3]. The concentration of oxygen vacancies on the oxide surface can be increased either by nanostructuring CeO₂ [4] or by doping [5]. In this work, the atomic and electronic structures and defects of CeO₂ nanoparticles with a size of 1–50 nm, obtained by laser ablation, are experimentally and theoretically investigated. In the experiment, CeO₂ nanoparticles were ablated using an IPG Photonics fibre ytterbium pulsed laser with the High Contrast option and a wavelength of 1.06 μm. The radiation intensity was 10⁹ W/m², the pulse duration was 200 μs and the repetition rate was up to 1 kHz. During laser ablation, CeO₂ nanoparticles were deposited on Si plates located at a distance of 10 mm from the target. Deposition time varied from 1 to 10 min. Subsequently, the obtained layers were dispersed by ultrasonic influence in an aqueous medium. After sedimentation for 24 h, the obtained colloidal solutions of CeO₂ nanoparticles were centrifuged in a Microspin Eppendorf high-speed microcentrifuge to obtain particles of nanosized composition. The concentration of nanoparticles in the colloid was varied by evaporation/dilution of the aqueous phase. The particle size distribution and morphology of the particles were controlled using a SAXSess mc2 small-angle X-ray diffractometer (Austria) with a temperature chamber (–30 to 120 °C). According to the results of experiments, it was found that CeO₂ nanoparticles after laser ablation have a wide size range from 10 nm to values above 500 nm. Subsequent centrifugation at a speed of 12500 rpm and a time of 30 min allows obtaining a colloidal solution with particle sizes from 10 nm to 50 nm (Fig. 1). The semiquantitative analysis of the electron energy-loss spectra (EELS) detected using a transmission electron microscope showed that the ablated CeO₂ nanoparticles were enriched in defects of oxygen vacancies. According to the EELS results, ablated CeO₂ nanoparticles have a substoichiometric composition of 1:1.75. The lowered stoichiometry is indicative of a great number of oxygen vacancies in the ablated nanoparticles.

The calculation of total energies and electronic properties of CeO₂ nanoparticles atomic models was carried out using the VASP package [6] by means of high-performance calculations. Pseudopotentials for cerium and oxygen atoms, in the generalized gradient approximation (GGA), using the projector augmented-wave (PAW) and Coulomb interaction (DFT + U) approaches are taken from

the VASP package. The unit cell of bulk ceria was calculated using 8 × 8 × 8 *k*-points. During calculation of the nanoparticles' characteristics, for the Ce₁₉O₃₂, Ce₄₄O₈₀ and Ce₈₅O₁₆₀ atom models we used a special 1 × 1 × 1 *G*-point with a 400 eV cut-off energy. The equilibrium models were obtained by means of free relaxation of all atoms in the structure. For this purpose, the all-atom models were placed in a cell with a 35 × 35 × 35 Å³ volume. Atomic relaxation was carried out to the interatomic forces' value of about 0.01 eV Å⁻¹. An analysis of the spin density distribution for Ce₁₉O₃₂, Ce₄₄O₈₀ and Ce₈₅O₁₆₀ nanoparticles shows that the Ce atom magnetization in the bulk of the particles is zero, and for atoms on the particle surface it is non-zero. This means that atoms in the Ce⁴⁺ state are located in the particles' interior, and Ce³⁺ atoms are located on the surface of the particles. The obtained results are very important for understanding at the atomic level the process of stabilization of CeO₂ nanoparticles due to the formation of structural defects.

Acknowledgements

This work was funded by RFBR, project number 20-02-00599 A. The research was carried out using the equipment of the Shared Facility Centre 'Data Centre of FEB RAS' (Khabarovsk, Russia) and partly using a cluster at the shared research facilities of HPC computing resources at Lomonosov Moscow State University supported by the project RFMEFI62117X0011. The authors would like to thank the Irkutsk Supercomputer Centre of SB RAS for providing access to HPC-cluster 'Akademik VM Matrosov' (Irkutsk Supercomputer Centre of SB RAS, Irkutsk: ISDCT SB RAS; <http://hpc.icc.ru>, accessed 11.07.2019).

References

- [1] S. Scire, L. Palmisano. Cerium Oxide (CeO₂): Synthesis, Properties and Applications. Elsevier (2019)402p.
- [2] V. Seminko, P. Maksimchuk, I. Bespalova, A. Masalov, O. Viagin, E. Okrushko, N. Kononets, Y. Malyukin. Phys. Status Solidi B **254** (2016) 1.
- [3] Z. Yang, T.K. Woo, M. Baudin, K. Hermansson. J. Chem. Phys. **120** (2004) 7741.
- [4] M.A. Pugachevskii. Tech. Phys. Lett. **43** (2017) 698.
- [5] C. Frayret, A. Villesuzanne, M. Pouchard, F. MauvyJean-Marc, B.-C. Grenier. J. Phys. Chem. C. **114** (2010) 19062.
- [6] G. Kresse, J. Furthmuller. Comput. Mater. Sci. **6** (1996) 15; Phys. Rev. B **54** (1996) 11169; G. Kresse, J. Joubert. *ibid.* **59** (1999) 1758.

Scanning probe microscopy/spectroscopy of oligonucleotides with a homonucleotide sequence

T.I. Sharipov^{*1}, S. Santer², A. Kopyshv², I.T. Amangulova¹, R.Z. Bakhtizin¹

¹ Bashkir State University, 32 Z. Validi St., Ufa, 450076, Russia

² Institute of Physics and Astronomy, University of Potsdam, 24-25 Karl-Liebknecht-Str., Potsdam-Golm, 14476, Germany

*e-mail: sha-t@yandex.ru

The physical properties of DNA molecules, both natural double-stranded and synthesized single-stranded, are currently being actively studied. Thanks to the invention of scanning tunneling (STM) and atomic force microscopes (AFM) it became possible to study various nanoobjects at the molecular and submolecular levels. Obviously, that DNA molecules, and in particular oligonucleotides, are no exception. Synthetic single-stranded DNA with a homonucleotide sequence, that is, consisting of nucleotides of the same type are of particular interest. Such structures assume a special nature of the electron density distribution and charge transfer, so the interest in them is consistently high, what is associated with the prospects of using these molecules in nanoelectronics.

Attempts to measure the electrical resistance of DNA give conflicting results [1-3]. The ambiguity of the results is influenced by the experimental conditions and the type of DNA molecules studied [4], namely length, nucleotide composition, different sequence of nucleotides in the DNA chain, the number of chains in the molecule. The study of the surface topography and immobilization of the DNA molecules by scanning probe microscopy methods is also important in terms of the development of DNA microarrays [5, 6].

We can measure the current-voltage curve of a biomolecule using STM. For this, the molecule is placed between two electrical contacts, one of which is a conducting probe of the microscope, and the other – a fragment of the substrate surface of an electrically conductive material.

We set the task of performing the series of experiments to study the conductivity of oligonucleotides depending on their nucleotide composition. In the report we will present the results of STM/STS studies of oligonucleotides consisting of repeated nucleotide sequences of only one type, for example, cytosine - d(C)_n, where n is the number of such nucleotides.

First, by thermal evaporation of silver on a mica surface in a vacuum, we obtained a silver substrate. Next, the obtained substrate was coated with the studied molecules. Then we carried out STM study of the silver surface with immobilized oligonucleotide molecules by the constant tunneling current mode. In addition to obtaining a number of STM images and identifying oligonucleotides on them, the current-voltage curves of single molecules have been measured. In this case, the current-voltage curve is the dependence of the tunneling current on the applied voltage between the probe and the silver substrate. The current-voltage curves were measured several times at each point, and then the data were averaged. The differential electrical resistance of individual molecules of oligonucleotide d(C)₁₂ and oligonucleotide d(A)₁₂ was estimated.

Acknowledgements

The work was performed with financial support of the grant of the Republic of Bashkortostan for the young scientists for 2019, contract № 29GR and was supported by the Russian Foundation for Basic Research under grant No. 17-42-020616.

References

- [1] H.W. Fink and C. Schonenberger. *Nature* **398**(1999) 407.
- [2] D. Porath, A. Bezryadin, S. De Vries and C. Dekker. *Nature London* **403** (2000) 635.
- [3] T.I. Sharipov, R. R. Garafutdinov, I.T. Amangulova and R.Z. Bakhtizin. *IOP Conf. Series: Materials Science and Engineering* **669** (2019) 012045.
- [4] M. Iijima, T. Kato, S. Nakanishi, H. Watanabe, K. Kimura, K. Suzuki and Y. Maruyama. *Chemistry Letters* **34** (2005) 1084.
- [5] T.I. Sharipov, R.Z. Bakhtizin. *IOP Conf. Series: Materials Science and Engineering* **195** (2017) 012002.
- [6] R.R. Garafutdinov, I.S. Shepelevich, A.V. Chemeris, R.F. Talipov. *Vestnik Bashkirskogo universiteta* **10** (2005) 49.

Two-dimensional materials grown on curved crystal substrates

Anna A. Makarova^{*1}, Oleg Vilkov², Kirill Bokai², Dmitry Usachov², Laura Fernandez³, Khadiza Ali³, Dmitry Smirnov⁴, Clemens Laubschat⁴, Denis Vyalikh^{5,6}, Frederik Schiller³, Enrique Ortega^{3,5,7}

¹Physikalische Chemie, Institut für Chemie und Biochemie, Freie Universität Berlin, Arnimallee 22, Berlin 14195, Germany

²St. Petersburg State University, 7/9 Universitetskaya nab., St. Petersburg 199034, Russia

³CSIC/UPV-EHU-Materials Physics Center, Manuel Lardizabal 5, San Sebastian 20018, Spain

⁴Institut für Festkörper- und Materialphysik, Technische Universität Dresden, Dresden 01062, Germany

⁵Donostia International Physics Centre, San Sebastian 20018, Spain

⁶IKERBASQUE, Basque Foundation for Science, Bilbao 48011, Spain

⁷Departamento Física Aplicada I, Universidad del País Vasco, Manuel Lardizabal 5, San Sebastian 20018, Spain

*e-mail: anna.makarova@fu-berlin.de

Curved crystals are drawing increasing attention due to their unique surface structure: smooth variation of the vicinal angle in a wide range. Multivocality allows systematic studies of various surface and interface phenomena such as catalytic properties, quantum-well states, etc. Moreover, curving crystals is a straightforward approach to explore appropriate templates and tunable substrates for 2D materials. On the one hand, it allows the systematic search and rational determination of an optimal growth substrate. On the other hand, it may result in the interfaces with novel intriguing properties.

As demonstrated repeatedly, the cylindrical geometry is easy to handle and process in standard vacuum setups [1, 2]. Moreover, it is particularly convenient for electron spectroscopies that make use of micron-sized photon beams in synchrotrons, such as Near-Edge X-ray Absorption and X-ray photoemission, since these can be scanned on the curved surface to smoothly probe different vicinal planes.

Recently, we have studied formation of the interface between hexagonal boron nitride monolayer and Ni curved crystal as well as its physicochemical properties [1,2].

As a step forward, we have investigated the structure of another two-dimensional material, nitrogen-doped graphene, grown on a curved crystal. It is well-known that by varying CVD synthesis parameters one can control the amount and bonding configuration of impurities in

nitrogen-doped graphene [3]. This ability is of great importance for the further applications in catalysis, energy storage and conversion, electronic devices, etc. In the case of curved crystal as a growth substrate, atomic steps play a crucial role. They are known to be very chemically active, and seem to be a promising tool to adjust the concentration and local configuration of nitrogen impurities. Here, we report a systematic study of growth conditions, crystalline and electronic structure of nitrogen-doped graphene on the curved nickel with a tunable density of steps separating (111)-oriented terraces.

Acknowledgements

We acknowledge financial support from BMBF (Grant Nr. 05K19KER).

References

- [1] L. Fernandez, A. A. Makarova, C. Laubschat, D. V. Vyalikh, D. Yu. Usachov, J. E. Ortega, F. Schiller. *2D Mater.* **6** (2) (2019) 025013.
- [2] A. A. Makarova, L. Fernandez, D. Yu. Usachov, A. Fedorov, K. A. Bokai, D. A. Smirnov, C. Laubschat, D. V. Vyalikh, F. Schiller, J. E. Ortega. *J. Phys. Chem. C* **123** (2019) 593.
- [3] D. Usachov, O. Vilkov, A. Gruneis, D. Haberer, A. Fedorov, V.K. Adamchuk, A.B. Preobrajenski, P. Dudin, A. Barinov, M. Oehzelt, C. Laubschat, D.V. Vyalikh *Nano Letters*, **11**(12) (2011) 5401.

Collective effects in quantum dot Si based nanostructures coupled with the hybrid metal-dielectric metasurfaces for nanophotonic

A.V.Dvurechenskii^{*1,2}, A.I.Yakimov¹, V.V.Kirienko¹, A.A.Bloshkin^{1,2}, A.F.Zinovieva¹,
A.V.Nenashev^{1,2}, V.A.Zinovyev¹

¹ Rzhanov Institute of Semiconductor Physics of SB RAS, 13 pr. Lavrentiev, Novosibirsk 630090, Russia

² Novosibirsk State University, 1 Piragova St., Novosibirsk 630090, Russia

*e-mail: dvurech@isp.nsc.ru

Semiconductor light-emitters and light sensors compatible with standard Si integration technology (SIT) are of particular interest for overcoming limitations in the quantum efficiency and operating speed of microelectronic devices. Light sources and sensors based on group-IV elements would be SIT-compatible but suffer from the poor optoelectronic properties of bulk Si and Ge. Here it is demonstrated that epitaxially grown Ge quantum dots (QDs) in a Si matrix show extraordinary optical properties in infrared absorption, photoluminescence, and device performance.

An approach to achieve a significant light absorption and emission enhancement caused by resonant interaction of collective surface plasmon modes with optical excitations of QDs heterostructures coupled with regular metal subwavelength gratings on the semiconductor surface was demonstrated to be powerful tool in multiple photocurrent enhancement of mid-IR InAs/(In)GaAs [1] and Ge/Si [2] QDs photodetectors (QDIPs). Besides surface plasmon waves and Rayleigh anomaly are characteristic optical phenomena exhibited by periodic subwavelength grating structures. In this work a hybrid metal-dielectric metasurface is developed to improve the photoresponse of Ge/Si QDIPs. The structure consists of a regular array of silicon pillars protruding through subwavelength holes in a periodically perforated gold film on detector top. The combining synergistically effects of dielectric and plasmonic metal components, the QDIP photoresponse can be significantly improved compared to when all-dielectric and metal gratings work alone. Compared with a bare QDIP, the peak responsivity of the hybrid detector at a wavelength of 4.4 μm was found to be increased by a factor of 15. The enhanced sensitivity is supposed to arise from coupling of the surface plasmon resonance and diffractive effect related to the Rayleigh anomaly.

The hybrid structures containing Ag nanoparticles over SiGe QDs layer were developed using self-organization of metal nanoislands on the surface of a strained semiconductor structure. Enhanced photoluminescence from SiGe QDs coupled with Ag nanoislands was found.

Ag nanoislands grown on the top of the multilayered structures with SiGe QDs support a surface plasmon resonance that can be tuned to the QDs emission wavelength by changing of Ag nanoparticle parameters. Numerical modeling of surface plasmon resonance allows attributing this effect to the increase of the recombination rate due to electromagnetic field enhancement in vicinity of Ag nanoislands.

Numerical simulations of plasmonic near-field enhancement in Si layers covered by gold films perforated with two-dimensional subwavelength hole arrays. The holey gold films with adjusted lattice periodicity were used to convert the incident electromagnetic near-IR radiation into the surface plasmons. The calculations were made in a wide range of hole diameters and allow us to develop a more complete understanding of how the actual electric fields near the plasmon surfaces change with varying the parameters of plasmonic grating. The maximum peak wavelength and local field enhancement are reached at $d/a = 0.5$, where d is the hole diameter and a is the array periodicity. At smaller d/a , the most pronounced electric field enhancement arises due to excitation of a zero-order surface plasmon polariton wave on the Au/Si interface. At larger d/a , the localized plasmon mode confined under the Au regions appears and dominates the near-field intensity spectra. An over 14 times field intensity enhancement was obtained for $d = 200$ nm and $a = 400$ nm. The anticrossing behavior of localized mode with the propagating one was observed suggesting coupling between the modes and formation of a mixed near-field state.

Acknowledgements

This work is funded by Russian Science Foundation, grant No.19-12-00070.

References

- [1] S. Lee, S. Krishna, S. Brueck. *Opt. Express* **17** (2009) 23160.
- [2] A. Yakimov, V. Kirienko, A. Bloshkin, V. Armbrister, A. Dvurechenskii, J-M Hartmann. *Opt. Express* **25** (2017) 25602.

Soft X-rays synchrotron studies of the multilayered nanoperiodical structures with silicon nanoparticles formation

D.A. Koyuda^{*1}, A.V. Ershov², V.A. Terekhov¹, E.V. Parinova¹, D.N. Nesterov¹, D.E. Spirin¹, T.V. Kulikova¹, B.L. Agapov¹, M.V. Grechkina¹, E.N. Zinchenko¹, I.A. Karabanova², U.A. Vainer³, S.Yu. Turishchev¹

¹ Voronezh State University, Universitetskaya pl. 1, Voronezh 394018, Russia

² Lobachevsky State University of Nizhni Novgorod, pr. Gagarina 23, Nizhni Novgorod 603950, Russia

³ Institute for Physics of Microstructures RAS, Akademicheskaya Ul. 7, Nizhni Novgorod 603950, Russia

*e-mail: koyuda@phys.vsu.ru

Silicon nanocrystals formation in dielectric matrix is promising direction for the opto- and nanoelectronics. One of the functional ways for nanocrystals size control and limitation is the formation of the multilayered nanoperiodical structures (MNS) with fixed thicknesses of nanolayers containing silicon nanoparticles located between nanolayers of different materials (e.g. ZrO₂). The redundant silicon in the SiO₂ matrix can be obtained by annealing of the SiO_x films formed from SiO powder. Another way to form silicon nanoparticles can be annealing of amorphous silicon layers.

MNS were formed by SiO_x or a-Si and ZrO₂ or Al₂O₃ or SiO₂ layer by layer deposition on to Si substrates with few nm thickness of each layer type and totally more than 15 nanolayers pairs. The formed structures were annealed at 500–1100 C aimed at photoluminescent Si nanoparticles formation.

a-SiO_x/Al₂O₃, a-SiO_x/SiO₂, a-SiO_x/ZrO₂ and a-Si/ZrO₂ multilayer nanoperiodical structures were studied by means of local atomic surrounding sensitive X-ray absorption near edge structure (XANES) spectroscopy and XPS techniques supported by XRD, AFM and SEM. Room-temperature photoluminescence measurements were compared to the obtained information about composition, atomic and electronic structure of multilayered nanoperiodical structures with possibly formed silicon nanoparticles.

XANES and XPS spectra were recorded at synchrotron radiation center SRC (University of Wisconsin-Madison, Stoughton, USA) and BESSY II (Helmholtz Zentrum Berlin, Germany). Si L_{2,3} and K, O K, Al L_{2,3} and Zr L_{2,3}

core levels excited X-ray absorption fines structures were studied. Different absorption edges photons energies allowed to probe local atomic surrounding specificity at different analysis depths (from 5 to more than 100 nm) while XPS was used to control surface properties of the first layer of MNS.

A noticeable changes of electronic structure and phase composition caused by transformation of the silicon atoms surrounding in investigated a-SiO_x/Al₂O₃, a-SiO_x/SiO₂, a-SiO_x/ZrO₂ and a-Si/ZrO₂ MNS was shown including ones after thermally induced transformation.

a-Si/ZrO₂ structures are partially oxidized at the formation stage. High temperature annealing do not lead to silicon nanocrystals formation in a-Si/ZrO₂ MNS. Silicon nanocluster formation is considered as possible. Moreover the highest temperature anneal of 1100 C leads to multilayers destruction and full silicon oxidation with possible Zr silicide formation. At the same time a-SiO_x/ZrO₂ structures may contain silicon nanocrystals after annealing at 1100 C accompanied with the upper (first from the MNS top) ZrO₂ nanolayer disappearance.

Amorphous silicon interlayer is suggested as possible silicon nanoparticles formation layer but sufficiently less effective if compared with silicon suboxides. Use of SiO₂ interlayer as limiting one in MNS can lead to intermixing of layers boundaries due to close structure and composition. a-SiO_x/Al₂O₃ MNS is suggested as more stable for silicon nanocrystals formation with controlled sizes.

The study was funded by the Ministry of Education and Science of Russia in frameworks of state task for higher education organizations in science.

Electrical conductivity study of the adsorbate-induced Si(111) surface reconstructions after C₆₀ adsorption

D.A. Tsukanov^{*,1,2}, M.V. Ryzhkova¹

¹Institute of Automation and Control Processes FEB RAS, 5 Radio St., Vladivostok 690041, Russia

²Far Eastern Federal University, 8 Sukhanova St., Vladivostok 690950, Russia

*e-mail: tsukanov@iacp.dvo.ru

Last time the study of fullerene interaction with semiconductor surfaces has proven to be a fascinating area of research [1]. In particular, C₆₀ monolayers adsorbed on Si(111) surface demonstrate quite a different properties depending on the fullerene-substrate interaction. This interaction is carried out through a charge transfer between the underlying substrate and fullerenes that is caused by the high electronic affinity of C₆₀ molecules acting as electron acceptors. From this point the surface conductance study of substrate-fullerenes interaction allows to evaluate changes in conductance caused by these charge-transfer effects that are strongly depends on the surface structure and the electronic states of the bare surface. By forming an appropriate adsorbate-induced surface reconstruction it is possible to modify the Si(111) surface properties [2] and in such manner it is possible to modify physical properties of C₆₀ layers. In terms of practical use, such modified underlying surface is expected to alter the transport properties of C₆₀ layers in a directional way. In present study the possibility of controllable tuning of the electronic transport properties of the C₆₀-adsorbed Si(111) surface reconstructions has been studied by four-point probe (FPP) technique, combined with low-energy electron diffraction (LEED) observations.

The experiments were performed in an ultrahigh vacuum chamber with a base pressure of 10⁻¹⁰ Torr, equipped with LEED optics and FPP facility for in situ electrical conductance measurements. The measuring unit of the FPP method incorporated electro-chemically sharpened thick tungsten wires pressed to the surface (in the corners of square with 0.6 mm side) by individual springs. Conductance measurements were carried out at room temperature. Substrates (15×5×0.45 mm³) were cut from a P-doped Si(111) wafers with resistivity of 10–25 Ω·cm. Fullerenes were evaporated from Knudsen cell at a rate of 0.1 ML/min that is was determined by the C₆₀ deposition onto the Si(111)-α√3×√3-Au surface reconstruction and formation of fullerite-like lattice. One monolayer of fullerite C₆₀(111) has concentration of molecules equal to 1.15·10¹⁴ cm⁻² [2].

Due to different interactions between molecules and substrate surface, fullerenes on semiconductors often behave differently than on metallic surface reconstructions. The investigated surfaces, namely, Si(111)√3×√3-Bi, Si(111)6×6-Tl, have opposite transport properties due to the different electronic structures. There are well-defined surface bands for the semiconducting Si(111)β√3×√3-Bi surface [3]. The Si(111)6×6-Tl surface reconstruction has the form of a bilayer with a total thallium coverage of 2.4 ML with metallic electronic structure [4]. If fullerenes are deposited onto the Si(111)6×6-Tl surface, as is shown by electrical measurements, the surface conductivity

decreases. Earlier, this was observed in the case of fullerene deposition onto the Si(111)5×2-Au surface [5]. Its conductivity is higher than that of Si(111)7×7 surface, but during C₆₀ adsorption fullerene molecules, acquiring a part of the electric charge, decrease the number of charge carriers. Such behavior of the conductivity is typical for the fullerenes interacting with metallic films. But in the study of conductance of metallic ultrathin films it must be borne in mind that its properties are highly dependent on the surface defects such, for example, as surface steps, domain walls and so on. Surface conductance of Si(111)6×6-Tl showed a pronounced anisotropy caused by growth of metallic layer which is modulated by substrate steps. During the C₆₀ adsorption surface conductivity along steps demonstrates the decay in conductivity as a function of the fullerenes dose while in perpendicular direction (across the steps) these changes are weak.

In the case of the adsorption of fullerenes on the Si(111)β√3×√3-Bi surface the conductivity is almost unchanged with C₆₀ dose. On this surface C₆₀ molecules form close-packed hexagonal arrays in the layer-by-layer mode with first layer covering about 80% of surface area and then the propagating second layer takes over the surface. Despite the fact that close-packed structure of fullerene layer is typical for most of the metal-covered surfaces; its electronic structure indicated the absence of charge transfer from the substrate to molecules [6]. This is confirmed by the data of surface conductance measurements. Due to the fact that C₆₀ layer on the Si(111)β√3×√3-Bi surface reconstruction has weak interaction with the substrate, this ordered fullerene layer can serve as a platform for the study of alkali metal doping of C₆₀ ultrathin films.

Acknowledgements

The work was supported by the Russian Foundation for Basic Research under Grant 20-02-00497.

References

- [1] P.J. Moriarty. Surf. Sci. Rep. **65**(2010)175.
- [2] A.V. Matetskiy, D.V. Gruznev, A.V. Zotov, A.A. Saranin. Phys. Rev. B **83** (2011) 195421.
- [3] E. Frantzeskakis, S. Pons, M. Grioni. Phys. Rev. B **82** (2010) 085440.
- [4] A.N. Mihalyuk, L.V. Bondarenko, A.Y. Tupchaya, D.V. Gruznev, J.-P. Chou, C.R. Hsing, C.-M. Wei, A.V. Zotov, A.A. Saranin. Surf. Sci. **668** (2018) 17.
- [5] D.A. Tsukanov, M.V. Ryzhkova, E.A. Borisenko, M.V. Ivanchenko. J. Surf. Invest.: X-Ray, Synchrotron Neutron Tech. **10** (2016) 864.
- [6] D.V. Gruznev, L.V. Bondarenko, A.Y. Tupchaya, A.V. Matetskiy, A.V. Zotov, A.A. Saranin. J. Chem. Phys. **143** (2015) 074707.

Raman spectroscopy and features of magnetic properties of nanostructured carbon materials

A.M. Ziatdinov*, N.S. Saenko, G.A. Zverev

Institute of Chemistry of FEB RAS, 159, Prospekt 100-letiya, Vladivostok, 690022, Russia

*e-mail: ziatdinov@ich.dvo.ru

One of the promising areas of modern materials science is carbon nanostructures (nanodiamonds, fullerenes, nanotubes, graphene, nanographene etc.), as well as their various physical and chemical derivatives. Raman spectroscopy is a very powerful tool for studying carbon nanostructures. For every newly discovered carbon nanomaterial and every novel application of a carbon nanostructure, Raman spectroscopy can be used as a characterization tool, either revealing new properties or simply proving the presence of a desired structure or functionalization. In particular, it is widely used to evaluate the lateral sizes of their structural blocks (crystallites). Although the use of Raman spectroscopy for this purpose is a procedure that was introduced many years ago, the protocols developed up to date are still empirical and dominated by large uncertainties. In this report, we consider the advantages and disadvantages of existing approaches to the determination of the lateral sizes of structural blocks (crystallites) of nanostructured carbons from their Raman spectra. The origin of the features of the magnetic properties of some of them is also discussed.

The graphene oxide (GO) flakes have been prepared by oxidation of graphite particles according to the modified Hummers method [1, 2] with subsequent dissolution into water. The reduced graphene oxides (rGO) flakes were obtained in quartz test-tubes, filled with argon, at various annealing temperatures (T_{ann}). Activated carbon fibers were of commercial origin. Raman spectra of all samples have been measured with confocal device Alpha 500 (“Witec”, Germany) with using laser wavelength $\lambda=531.8$ nm. The EPR spectra of GO and rGO have been measured with the X-band EMX-6.1 spectrometer (“Bruker”, Germany). Magnetization of all samples has been measured with MPMS-5S SQUID (“Quantum Design”, USA) magnetometer.

A typical Raman spectrum of rGO is decomposed into three Lorentzians (G, D and D' bands) and two Gaussians (T and D'' bands). In literature the ratio of integrated intensity of D-band (A_D) to the sum of the integrated intensities of G and D' bands ($A_{G+D'} = A_G + A_{D'}$) has been widely used to estimate the in plane correlation length of the aromatic islands, L_a , i.e. the size of graphitic domains. Caňado *et al.* [3] obtained the following formula that gives the value of this parameter for any laser radiation wavelength λ in the visible range:

$$L_a \text{ (nm)} = (2.4 \times 10^{-10}) \times \lambda^4 \times (A_D / A_{G+D'})^{-1}.$$

Ferrari and Basko [4] showed that this relation is valid only at $L_a > 2$ nm. At smaller in plane correlation lengths another formula should be used [4]:

$$L_a^2 \text{ (nm}^2\text{)} = (1.26 \times 10^{11}) \times \lambda^{-4} \times (A_D / A_{G+D'}).$$

Thus, in the general case, to each value of $A_D / A_{G+D'}$ there correspond two different values of L_a and for the right choice between them, additional information about the dimensions of the structural blocks of the material under study is necessary. Maslova *et al.* [5] and Ribeiro-Soares *et al.* [6] suggested considering the bandwidth G (Γ_G) as a source of such information. Ribeiro-Soares *et al.* [6] showed that L_a and Γ_G are related by the expression:

$$L_a = (l_c/2) \times \ln[C / (\Gamma_G - \Gamma_{G(L_a=\infty)})],$$

where l_c - coherence length of optical phonons, is equal to 32 ± 7 nm, Γ_G - the experimental width of G band, $\Gamma_{G(L_a=\infty)}$ - the width of G band in graphene, is equal to 15 ± 3 cm^{-1} , the value of empirical parameter C is equal to 95 ± 20 cm^{-1} . Comparison of the L_a values determined from the Raman spectra and X-ray diffraction data of the investigated nanostructured carbon materials showed that their values found over the bandwidth G are the most reliable. The obtained data on the nanoscale structure of studied materials allow us to explain the unusually high values of the density of electronic states at the Fermi level, which were detected by magnetic methods of investigation in some samples, as a consequence of the presence of specific π -electronic states (topological zero modes) in them, which can be stabilized near the zigzag edges of the carbon network cracks. (near the zigzag edges of nanographenes).

Acknowledgements

We are grateful to Dr. A.V. Gerasimenko (Institute of Chemistry, Far-Eastern Branch of the RAS) for the X-ray diffraction data of nanostructured carbon materials. The work has been financially supported by the Ministry of Science and Higher Education of Russia (State Assignment No. 265-2019-0001).

References

- [1] W.S. Hummers, R.E. Offeman, J. Amer. Chem. Soc. **80** (1958) 1339.
- [2] M. Hirata, T. Gotou, S. Horiuchi, M. Fujiwara, M. Ohba. Carbon **42** (2004) 2929.
- [3] L.G. Cancado, K. Takai, T. Enoki, M. Endo, Y. A. Kim, H. Mizusaki, A. Jorio, L.N. Coelho, M.A. Pimenta. Appl. Phys. Lett. **88** (2006) 163106.
- [4] A.C. Ferrari, D.M. Basko. Nature Nanotech. **8**(2013)235.
- [5] O.A. Maslova, M.R. Ammar, G. Guimbretiere, J.-N. Rouzaud, and P. Simon. Phys. Rev. **86** (2012) 134205.
- [6] J. Ribeiro-Soares, M.E. Oliveros, C. Garin, M.V. David, L.G.P. Martins, C.A. Almeida, E.H. Martins-Ferreira, K. Takai, T. Enoki, R. Magalhaes-Paniago, A. Malachias, A. Jorio, B.S. Archanjo, C.A. Achet, L.G. Cancado. Carbon **95** (2015) 646.

Investigation of C₆₀ growth on Si(111) "5×5"-Cu by optical second harmonic generation

K.V. Ignatovich*

Institute of Automation and Control Processes FEB RAS, 5 Radio St., Vladivostok 690041, Russia

*e-mail: ignat@iacp.dvo.ru

Abstract

Absorption of fullerenes on Si(111)"5×5"-Cu surface was studied by optical second harmonic generation (SHG). It was proposed to determine coverage of ordered submonolayer films with layer-by-layer growth mode by dependence of intensity SHG signal from the adsorbate coverage.

Introduction

The determination of the adsorbate coverage is the open question yet. Even the direct estimation of atoms quantity by scanning tunneling microscopy is not guarantee of truth of measurements. We report on a study of the optical measurements of C₆₀ covered Si(111)"5×5"-Cu surface using SHG method and simple simulative calculations.

Experiment

All the experiments were performed in the Riber LAS-600 UHV chamber. The chamber equipped with low energy electron diffraction (LEED). Si(111) samples (15mm × 5 mm × 0.35 mm in size) were cut from the standard n-type 7 Ω cm Si(111) wafers. Atomically clean Si(111) 7×7 surfaces were prepared in situ by flashing to 1280 °C after the samples were first outgassed at 600 °C for several hours. Cu was deposited from the W filament on Si(111) surface at 450 °C. C₆₀ was deposited from the Ta crucible at a rate of ~0.03 ML/min. The sample was heated by direct current and the temperature was determined by IR pyrometer.

The optical second harmonic generation (SHG) experiments were performed with a Ti:sapphire laser delivering 60 fs pulses with photon energy of ~1.5 eV (810 nm) with a repetition rate of 80 MHz. The beam, which was horizontally polarized on output, was then passed through a half-wave plate producing polarized radiation at any angle. The rotation of half-wave plate and polarizer were done by computer-controlled step-motors.

The SHG signals were detected by a photomultiplier tube connected to a photon counting system.

The laser was obliquely incident at an angle of ~45° and focused to a spot with a diameter less than 2 mm on the sample. The S- and P-polarized components of the SHG signal were selected by a polarizer (Glan-Laser Polarizer). The resultant SHG was separated from the reflected

excitation beam by a combination of color glass filters. All the measurements were done at room temperature. It was measured only anisotropic part of the optical SHG signal due to reduce background noise.

Result and discussion

In this experiments Si(111)"5×5"-Cu was formed by deposition more than 1.5 ML Cu on Si(111) clean surface at 450 °C. LEED show pattern according to 'pseudo-5×5'-Cu surface phase [1]. Fullerenes deposited on Si(111)"5×5"-Cu surface phase at room temperature in range from 0 to 2 ML C₆₀ coverage. It was found that dependence of intensity SHG signal from the C₆₀ coverage has local minimum around 1 ML. The same dependence of SHG intensity from adsorbate coverage with minimum of the anisotropic part of the signal was found for several elements with layer-by-layer growth mode. For example, we found it for Si(111)/In system[2].

It was a problem in previous investigations to explain the correlation the dependence of optical SHG intensity with the processes on the surface during the deposition of adsorbate. The new simple model proposed that SHG intensity correlate with total perimeter of monoatomic height islands and standalone adatoms. Simple simulated dependence of total perimeter of islands from the adsorbate coverage in range from 0 to 1 ML show us similar behavior with local minimum at 1 ML. In this case we can explain decrease of optical SHG signal from C₆₀/Si(111)"5×5"-Cu surface around 1 ML of C₆₀ coverage.

Summary

Growth of C₆₀ on Si(111)"5×5"-Cu surface at RT was investigated by optical SHG and LEED techniques. It was proposed new model of dependence SHG intensity from the total adsorbate coverage.

Acknowledgements

The reported study was funded by RFBR, project number 20-02-00497.

References

- [1] D.A. Olyanich, V.V. Mararov, T.V. Utas, A.V. Zotov, A.A. Saranin. *Surface Science* **642** (2015) 6.
- [2] K.V. Ignatovich, A.V. Zotov, A.A. Saranin. *Solid State Phenomena* **247** (2016) 73.

Nanocarbon shell for solid state alumina nanofibers transformations into spinel nanofibers

M.M. Simunin^{1,2}, A.S. Voronin², D.Yu Chirkov², S.S. Dobrosmyslov^{1,2}.

¹ Siberian Federal University, Svobodny 79, 660041 Krasnoyarsk, Russia

² Krasnoyarsk Scientific Center SB RAS, Akademgorodok, 50, Krasnoyarsk, 660036

*e-mail: michanel@mail.ru

High-temperature transformations in solids associated with phase transitions or chemical reactions are accompanied by particle size enlargement due to sintering. The chain of phase transitions in alumina polymorphs is as follows: γ -Al₂O₃ (Fd3m) → δ - Al₂O₃ (P2₁2₁2₁) → θ -Al₂O₃ (C/2m) → α -Al₂O₃ (R3c) [1,2]. From the point of view of the texture of the material, a significant decrease in the specific surface of the material is observed, due to an increase in its thermodynamic potential, leading, in particular, to sintering of the grains of the nanomaterial [3]. For γ - Al₂O₃, the characteristic values of the specific surface lie in the range of 150–450 m²/g [4], while α - Al₂O₃ is more characteristic for the specific surface, which is in the range of 1-25 m²/g [2, 5].

The concept of a carbon nanoreactor was proposed in [6–8] and is a fairly simple and effective approach to stabilizing the morphology and phase composition. This is due, on the one hand, to a decrease in the surface energy of nanoparticles due to the presence of a nanocarbon shell on their surface, and, on the other hand, the strength of carbon-carbon bonds can compensate for the work done by changing the surface by a nanoparticle during phase transitions. In particular, this can be expressed as excess pressure from the nanocarbon shell during thermal expansion of the nanoparticle or phase transition in its structure.

At present, the question of maintaining the necessary phase and morphology of particles during the removal of the nanocarbon shell remains unexplored. This work is aimed at studying the possibility of preserving the nanofibrous form at temperatures above the temperature of the phase transition of alumina to corundum.

A study of macroscopic morphology of a sample of alumina nanofibers in a nanocarbon shell after high-temperature annealing demonstrates the preservation of the block structure. The TEM image (Fig. 1) demonstrates the fact that the vast majority of the material is in an encapsulated state and is in the form of nanofibers. According to statistical analysis, the diameter of the nanofibers inside the nanocarbon shell is 8.83 ± 1.7 nm. Hollow nanocarbon shells, similar in structure to multi-walled carbon nanotubes, are also observed; apparently, the depletion of the capsules is the reason of recrystallization processes as alumina as nanocarbon shell.

The XRD and TEM methods have shown the possibility of maintaining the 1D morphology of nanofibers with a high aspect ratio at temperatures above the γ , θ - Al₂O₃ → α - Al₂O₃ phase transition. Nanocarbon shell preserves the morphology of the original product, inhibiting sintering and recrystallization processes. It has been shown that after heating the alumina nanofibers coated with carbon to 1400 C, there is no phase transition to corundum and the structural tune of the nanofibers more closely matches γ -Al₂O₃. The indicators of the possibility of obtaining nanofiber spinels, due to the diffusion of components in the nanocarbon shell, were obtained composite fibers MgAl₂O₄.

References

- [1] I. Levin, D. Brandon J. Am. Ceram. Soc., **81** (1998)
- [2] A. C. Vieira Coelho, H. de S. Santos, P. K. Kiyohara, K. N. P. Marcos, P. de S. Santos Surface Materials Research, **10** (2007) 183.
- [3] McHale J. M., Auroux A., Perrotta A. J., Navrotsky A. Science **277** (1997) 788.
- [4] M. Trueba, S. P. Trasatti Eur. J. Inorg. Chem. **2005** (2005) 3393.
- [5] J. Lee, H. Jeon, D. G. Oh, J. Szanyi, J. H. Kwak Applied Catalysis A: General **500** (2015) 58.
- [6] A. M. Volodin, A. F. Bedilo, V. O. Stoyanovskii, V. I. Zaikovskii, R. M. Kenzhin, I.V. Mishakov, A. A. Vedyagin RSC Adv **7** (2017) 54852.
- [7] A. M. Volodin, V.I. Zaikovskii, R. M. Kenzhin, A. F. Bedilo, Ilya V. Mishakov, A. A. Vedyagin Materials Letters **189** (2017) 210.
- [8] Z. Wang, X. Lv, Y. Chen, D. Liu, X. Xu, G. T. R. Palmore, R. H. Nanoscale **7**(2015) 10267.

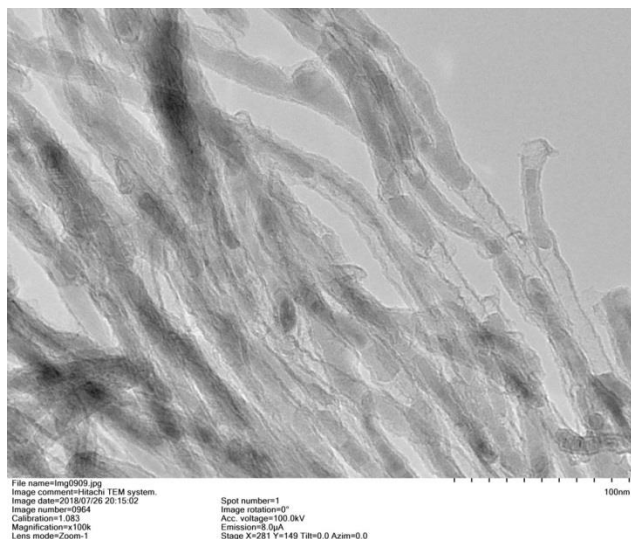


Figure 1. Alumina nanofibers in nanocarbon shell after annealing at 1400 C. TEM.

The approximation of X-ray diffraction profiles of thermally reduced nanostructured graphene oxide

N.S. Saenko*, D.A. Saritskiy, A.M. Ziatdinov

Institute of Chemistry of FEB RAS, 159, Prospekt 100-letiya, Vladivostok, 690022, Russia

*e-mail: saenko@ich.dvo.ru

Graphene oxide (GO) is the common name for a promising class of carbon compounds whose structure can be represented as a honeycomb carbon network with oxygen-containing functional groups attached to the edges and in the inner regions [1]. The structure and properties of GO and its thermally reduced derivatives are sensitive for selection of method for synthesis and reduction, respectively [2]. The aim of the work is to develop a procedure for obtaining the information on dimensions and structure of nanosize blocks (domains) in thermally reduced GO samples by modeling their X-ray diffraction profiles.

The GO used in work has been prepared by the modified Hammers method [3], taking into account our experience in the synthesis of oxygen-containing graphite compounds [4, 5]. The reduction of GO films have been performed by annealing at a fixed temperature (T_{ann}) in an argon atmosphere. The X-ray diffraction patterns of thermally reduced GO films have been recorded on the D8 ADVANCE diffractometer in the Bragg-Brentano setting with a $\text{CuK}\alpha$ source ($\lambda = 0.15417$ nm).

The X-ray diffractograms for films of thermally reduced derivatives of GO were approximated by searching for a linear combination of theoretical profiles of quasi-two-dimensional powders of few-layer nanographenes (nanographites) with a turbostratic layer stacking, which describes the experimental diffractogram of the sample with the lowest R-factor (reliability factor). It was assumed that each such quasi-two-dimensional powder consists of identical particles with a certain orientational distribution. The interatomic distances in the particles of considered hypothetical powders were determined based on empirical dependences. To form their theoretical diffractograms the interference function have been calculated for various systems, whose particle orientation is set by only polar Euler angle β :

$$w(\beta) = \exp(k \cos(2\beta)) \left(\int_0^{\pi} \exp(k \cos(2\beta)) \sin \beta \, d\beta \right)^{-1}, \quad (1)$$

where $w(\beta)$ – the probability density function to find a nanoparticle in the system rotated by angle β , $1/k$ – the parameter (analog to variance in a normal distribution) which is the measure of β -values dispersion near 0° . At $k = 0$, all the nanoparticles in the system are randomly disoriented (three-dimensional powder); the larger the value of k , the higher the probability density to find a particle whose nanographene layers are parallel to the horizontal plane.

The work considers the results of approximation of X-ray diffractograms of GO films reduced at various T_{ann} by the above-described method and the corresponding histogram of the relative contributions of quasi-two-dimensional powders of model nanographites of various sizes. A model have been also proposed to explain the detected changes in the structural parameters of the studied samples from T_{ann} .

Therefore, a new tool for obtaining structural information from X-ray diffractograms of thermally reduced GO films have been proposed and tested in this work.

Acknowledgements

The work has been financially supported by the Ministry of Science and Higher Education of Russia (State Assignment No. 265-2019-0001).

References

- [1] A.M. Dimeev, S. Eigler, Graphene oxide: fundamentals and applications, John Wiley & Sons, Ltd., Chichester, UK, 2017.
- [2] R.K. Singh, R. Kumar, D.P. Singh. RSC Advances **69** (2016) 64993.
- [3] M. Hirata, T. Gotou, S. Horiuchi, M. Fujiwara, M. Ohba. Carbon **42** (2004) 2929.
- [4] A.M. Ziatdinov, Y.V. Zelenskii, A.A. Uminskii, E.G. Ippolitov. Zhurnal Neorganicheskoi Khimii **30** (1985) 1658.
- [5] A.M. Ziatdinov, N.M. Mishchenko, Yu.M. Nikolenko. Synth. Met. **59** (1993) 253.

Scanning tunneling microscopy of Sn adatoms on the Si(111)5×2–Au surface

D.A. Olyanich^{1,*}, T.V. Utas¹, A.N. Mihalyuk¹, A.V. Zotov^{1,2}, A.A. Saranin^{1,2}

¹Institute of Automation and Control Processes FEB RAS, 5 Radio St., Vladivostok 690041, Russia

²Far Eastern Federal University, 10 Ajax Bay, Russky Island Vladivostok, Russia

*e-mail: olyanich@gmail.com

Surface reconstructions on silicon with the metallic property have attracted considerable attention due to the diversity of structural and electronic properties. The Si(111)5×2–Au surface reconstruction in addition to metallic properties has a quasi-one-dimensional metal-chain structure and presents a vivid example of the reconstructions of such type. As was shown in works [1-4], the ideal Si(111)5×2–Au surface adopts 0.7 ML of Au, where 1 ML (monolayer) = $7.8 \times 10^{14} \text{cm}^{-2}$, topmost Si atom density in Si(111)1×1.

The model of Si(111)5×2–Au structure is described by Kwon and Kang [2] and establishes a clear correspondence between STM features and structural elements constituting the intact Si(111)5×2–Au surface. This knowledge yields us a basis for the determination of the Sn adsorption sites on the Si(111)5×2–Au surface using the corresponding STM images. The Si(111)5×2–Au surface might be considered as a promising template for growing quasi-one-dimensional adsorbate nanostructures onto it due to its temperature stability upon to 1173 K [5] and its robustness against overgrowth of various materials [6-7].

In the present work, we study the adsorption of tin (Sn) onto Si(111)5×2–Au surface using the STM and DFT techniques. We perform our experiments with a variable-temperature Omicron VT-STM equipment operated in an ultrahigh vacuum ($\sim 2.0 \times 10^{-10}$ Torr). For sample preparation, the Si(111) substrate (n-type) is degassed at 600 °C for several hours and repeatedly flashed to 1280 °C. Gold and tin are evaporated from an Au-wrapped tungsten filament and a tungsten basket, respectively. To prepare the Si(111)5×2–Au surface gold is deposited on a Si(111)7×7 sample held at about 500 °C. For STM observations, electrochemically etched tungsten tips cleaned by in situ heating are employed.

Adsorption of ~ 0.01 ML of Sn onto Si(111)5×2–Au surface held at RT shows that the majority of Sn adatoms reside in the sites typical for Si adatoms (to be called A site). One part of the rest of the Sn adatoms is located in the hollow sites between Au atoms of the Au row 1 and neighboring Si atoms of the honeycomb Si chain (to be called H₁ site). The other part of the rest of the Sn adatoms occupies the sites adjacent to the Au row 4 (to be called H₂ sites). Annealing of such a surface at 170 °C redistributes Sn atoms to the adsorption sites as pristine Si adatoms (i.e. A sites) filling the originally Si-adatom-free segments. As

was reported [5,8] the same behavior is observed after the deposition of extra Si adatoms on the Si(111)5×2–Au surface. Increasing the Sn coverage up to 0.03 ML followed by annealing at 170 °C leads to the occupation of A positions by Sn adatoms and the formation of the 5×4 superstructure consisting of Sn and pristine Si adatoms on the entire surface. Also, a small part of Sn adatoms begins to occupy the H₂ sites. Starting with Sn coverage of 0.06 ML the one-dimensional stripes begin to be formed along the line running across the hollow site between Au atoms of the Au row 1 and neighboring Si atoms of the honeycomb Si chain. A thorough analysis of the STM images reveals that the Sn adatoms within the one-dimensional stripes occupy H₁ sites. Moreover, along the entire length of the one-dimensional stripes, Sn adatoms in A positions are missing. Increasing the Sn coverage up to 0.3 ML leads to the formation of continuous one-dimensional strips of Sn atoms along the rows of Si(111)5×2–Au. Between the one-dimensional Sn strips, one can observe that both individual Sn atoms are located at a distance of $2a_0$ and $3a_0$ (where $a_0 = 0.384$ nm is the size of the unit cell of the Si(111) surface) in position H₂, and individual Si atoms located in A positions.

Acknowledgments

The work was supported by the RSF Grant No. 19-12-00101. The part of the work devoted to scanning tunneling spectroscopy measurement was supported by the RFBR Grant No. 18-52-52012.

References

- [1] Kautz J, Copel MW, et al. *Phys Rev B Condens Matter*. **89** (2014) 035416.
- [2] Kwon SG, Kang MH. *Physical Review Letters*. **113** (2014) 086101.
- [3] Patterson CH, Banerjee S, McGilp JF. *Phys Rev B Condens Matter*. **94** (2016) 165417.
- [4] Liebhaber M, Halbig B, Bass U, Geurts J, Neufeld S, Sanna S, et al. *Phys Rev B Condens Matter*. **94** (2016) 235304.
- [5] Choi WH, Kang PG, Ryang KD, Yeom HW. *Phys Rev Lett*. **100** (2008) 126801.
- [6] Okuda T, Takeichi Y, He K, Harasawa A, Kakizaki A, Matsuda I. *Phys Rev B Condens Matter*. **80** (2009) 113409.
- [7] Chin AL, Men FK, Liu F. *Phys Rev B Condens Matter*. **82** (2010) 201406.
- [8] Bennewitz R, Crain JN, Kirakosian A, Lin J-L, McChesney JL, Petrovykh DY, et al. *Nanotechnology*. **13** (2002) 499.

Effect of hydrodynamic conditions on the growth of nanostructured anodic WO_x formed in NH₄NO₃-based electrolyte

Y.V. Nazarkina^{*1}, V. Benu¹, V.A. Rusakov¹, E.M. Eganova²

¹ National Research University of Electronic Technology (MIET), Bld. 1, Shokin Square, Zelenograd, Moscow, Russia, 124498

² Establishment of the Russian Academy of Sciences, Institute of Nanotechnology Microelectronics INME of RAS, Leninskiy Prospekt 32A, Moscow, 119991, Russian Federation

*e-mail: engvel@mail.ru

In the past decades, anodic semiconducting metal oxides, such as WO_x, TiO_x, ZnO_x are being widely investigated. The numerous perspective applications of these materials have been presented, e.g., gas and biosensors, photoelectrodes in solar cells, photoelectrochemical water splitting, photodegradation of organic compounds. Among these materials, WO_x is a deserving candidate for such applications due to its relatively narrow band-gap ~2,6 eV, which makes it sensitive to the visible light, and its relative physicochemical stability in aggressive environments. Nanostructured WO_x has a much higher effective surface area that affords to increase the efficiency of WO_x applications.

Anodization is one of the efficient methods for barrier or nanostructured oxides formation. A lot of regimes of nanostructured WO_x synthesis have been discussed, and anodic WO_x with different morphology (nanoholes, nanobowls, nanowires) has been shown [1,2,3]. However, most of the papers evaluate the influence of electrolyte content or anodization current or potential under not well defined hydrodynamic conditions such as magnetic stirring. However, for other oxides, it was shown that hydrodynamic conditions play a crucial role in the kinetics of nanostructured oxide formation and can determine its morphology [4].

In the present study, we investigated the influence of hydrodynamic conditions on the growth of nanostructured anodic WO_x via the Rotating Disk Electrode (RDE) system. The 0.1 M NaNH₄; ethylene glycol: 1% H₂O solution served as the electrolyte for WO_x formation. The three-

electrode system Autolab RDE 81044 was used. The tungsten foils oxidation was performed under different rotation velocities (0 – 1500 rpm).

The morphology of nanostructured WO_x layers was investigated by field-emission scanning electron microscope (FESEM) Helios NanoLab 650. It was found that the morphology could change from almost dense films to the porous films with the pores of around 100 nm in diameter by varying the rotation velocity.

Finally, the photocatalytic degradation of methylene blue (MB) with obtained WO_x photocatalysts. The photoelectrochemical (PEC) properties were studied using a three-electrode system with quartz cell filled with 0.5 M Na₂CO₃.

Acknowledgements

This work was supported by the RFBR grant № 18-29-23038 mk.

References

- [1] N. R. de Tacconi, C. R. Chenthamarakshan, G. Yogeewaran, A. Watcharenwong, R. S. de Zoysa, N. A. Basit, K. Rajeshwar. *J Phys Chem B* **110(50)** (2006) 25347.
- [2] Zhu, T., Chong, M.N., Chan, E.S. *Chem Sus Chem*. **7** (2014) 2974.
- [3] Y.Nazarkina, V. Rusakov, A. Salnikov, A. Dronov, D. Dronova. *Proceedings of 2019 IEEE Conference of Russian Young Researchers in Electrical and Electronic Engineering (EIConRus)* (2019) 1951.
- [4] R.Sánchez-Tovar, K.Lee, J. García-Antón, P. Schmuki. *Electrochem. Commun.* **26** (2013) 1.

Structural heterogeneity of amorphous-nanocrystalline alloy $\text{Fe}_{77}\text{Cu}_1\text{Si}_{16}\text{B}_6$ in nanometer range

A.V. Ansovich*, A.M. Frolov, G.S. Kraynova., V.V. Tkachev, S.V. Dolzhikov, V.S. Plotnikov, E.B. Modin

Far Eastern Federal University, 8 Sukhanova St., Vladivostok, 690950, Russian Federation

*e-mail: nastena_9696@mail.ru

In this article, an alloy of Finemet type $\text{Fe}_{77}\text{Cu}_1\text{Si}_{16}\text{B}_6$ obtained by quenching from a liquid state (spinning method) in the initial state is investigated. The main research methods were scanning and transmission electron microscopy. Representation of electron microscopic images in the form of Fourier spectra made it possible to reveal the nature of the formation of short- and middle-order in amorphous-nanocrystalline alloys according to the principle of self-similar spatial structures. The use of the Lebesgue image comparison technique revealed density differences in the entire alloy volume.

Introduction

Amorphous-nanocrystalline alloys are a new class of materials obtained by rapid quenching from a liquid state. Moreover, in terms of physical and mechanical properties, such two-phase systems are superior to the properties of both nanocrystalline and amorphous materials, thereby creating a noticeable synergistic effect [1]. Amorphous-nanocrystalline materials can be considered natural amorphous-nanocrystalline composites, which have important properties for practical use [2]. Thus, issues related to the study of the structure and properties of such alloys, for example, based on iron, are extremely relevant.

The purpose of this work is to study the nature of the structure and anisotropy of the $\text{Fe}_{77}\text{Cu}_1\text{Si}_{16}\text{B}_6$ alloy obtained by spinning in the nanometer range and at the morphological level.

Objects and research methods

The objects of study were electron microscopic images of a spinning tape $\text{Fe}_{77}\text{Cu}_1\text{Si}_{16}\text{B}_6$ obtained using a TITAN 300 transmission electron microscope (TEM), as well as images of the interfaces of a spinning tape (contact to the quenching disk and free from its influence) obtained using a scanning electron microscope Carl Zeiss Crossbeam 1540XB [3, 4]. For all rapidly quenched alloys, a Fourier spectral analysis was carried out, including the following: integral frequency response (IFR), which allows numerically determining the range of inhomogeneities present in the studied structure and integrated spatial characteristic (ISC), based on which it is possible to judge the isotropy/anisotropy of the studied structure [5 -7].

Showed three ranges of sizes of inhomogeneities of nano – and micrometer were identified: long-wave

($\lambda_3 = 0.2 \text{ nm}$; $\Lambda_3 = 2.8 \text{ }\mu\text{m}$) medium-wave ($\lambda_2 = 0,6 \text{ nm}$; $\Lambda_2 = 7.5 \text{ }\mu\text{m}$), short-wavelength ($\lambda_1 = 1.7 \text{ nm}$; $\Lambda_1 = 19.2 \text{ }\mu\text{m}$). The anisotropy of the periodicities of the nanometer range is determined by short-wave inhomogeneities, $\lambda_1 = 0.2 \text{ nm}$. The formation of mesoscale and long-wavelength structures is accompanied by a decrease in the anisotropy coefficient. It is shown that the integral anisotropy of the morphostructure of the spinning tape is determined by the inhomogeneities of the long-wavelength range. Short-wave periodicities of the free surface are characterized by a lower anisotropy index compared with the contact. The formation of the middle and long-range order of inhomogeneities of the free surface is accompanied by a sharp increase in the anisotropy in their distribution. Received: the formation of medium and long-range order in an amorphous nanocrystalline alloy occurs on the principle of self-similar spatial structures characteristic of modulation-unstable media.

Acknowledgements

The reported study was funded by RFBR, project number 19-32-90182

References

- [1] Glezer, A.M., Shurygina, N.A. Amorphous-nanocrystalline alloys (2017) pp. 1-458.
- [2] Kekalo I.B. Processes of structural relaxation and physical properties of amorphous alloys – M.: Publishing House “MISIS” **1** (2014) 436 and **2** (2016) 834.
- [3] Yudina, L.A., Frolov, A.M., Chukhry, N.I., Yudin, V.V. Izvestiya Akademii Nauk. Ser. Fizicheskaya. **62** (1998) 455. Frolov A.M., Krainova G.S., Dolzhikov S.V. Advanced Materials Research **1025-1026** (2014) 499.
- [5] B.N. Grudin, V.S. Carpenters. Processing and modeling of microscopic images. - Vladivostok: Dalnauka, 2010. -- 350 p.
- [6] Frolov A.M., Ansovich A.V., Tkachev V.V., Kraynova G.S., Dolzhikov S.V. Key Engineering Materials **806** (2019) 124.
- [7] Frolov A.M., Krainova G.S., Dolzhikov S.V. Journal of Surface Investigation. **12** (2018) 370.

Highly-efficient photocatalytic degradation of organic compounds via zinc sulfide quantum dots

A.A. Sergeev*, K.A. Sergeeva

Institute of Automation and Control Processes FEB RAS, 5 Radio St., Vladivostok 690041, Russia

*e-mail: aleksandrsergeev@inbox.ru

Here we report the development of a new physicochemical method to obtain a novel photocatalytic material based on metal sulfide quantum dots in a porous matrix. Such quantum dots may act as an alternative for titanium dioxide-based photocatalysts. The topicality of the research is the necessity of aqueous solutions purification from various toxic organic compounds such as aromatic and cyclic hydrocarbons, dyes, pesticides, etc. At present, the most common way for organic destruction is advanced oxidation processes technique, namely, heterogeneous photocatalysis. The major advantage of such a technique is the simultaneous destruction of an organic molecule by the number of oxidizing agents (hydroxyl radicals, superoxide radicals, hydrogen peroxide and so on) caused by the interaction of photogenerated charge carriers in a quantum dot with water molecules and molecular oxygen.

In its turn, one of the most common parts of industrial water effluents are organic compounds and dyes which can cause, from the one hand, a lot of lethal diseases (like the cancer one [1]) and from the other hand, they block both sunlight penetration and oxygen dissolution, which are essential for aquatic life. In this way, the treating of these pollutants is very important for ecological purposes.

The most effective photocatalytic degradation of organic pollutants occurs when the pollutant molecule is located as close as possible to the photocatalyst surface. Unfortunately, the different pollutant molecules have different physical and chemical properties, namely, the overall charge, so it can be attractive only to photocatalyst of a certain type. Thus, the most efficient pollutant treatment could be achieved when photocatalyst has different reactive sites, attractive for both positive and negative charged molecules.

In this regard, semiconductor quantum dots are the most promising candidates for effective photocatalyst development. First of all, a high volume-to-surface ratio (which is common for nanosized materials) shortens the charge carriers path from the volume to surface making the energy transition in quantum dots very sensitive to surface state. Moreover, the dangling bonds on quantum dots surface act like charge carriers traps, wherein the metal dangling orbitals act as electron traps, while sulfide dangling orbitals act as hole traps [2]. This is very important for the abovementioned possibility of a photocatalyst to be attractive for both positive and negative charged pollutant molecules. Second, a lot of effective photocatalysts (TiO₂, ZnO, etc) demonstrate a photocatalytic performance only under high-energy photon excitation while one of the requirements for photocatalyst is to be active under visible light excitation. To meet this criterion these photocatalysts are doped with other materials [3], combined with plasmonic [4] or photonic [5] structures or form various heterogenic core/shell structures

[6]. In a case of quantum dots, the excitation wavelength range can be easily tuned by varying its size. Nevertheless, the making of quantum dots heterostructures, namely core/shell systems, could be a promising way for further increasing of their photocatalytic properties.

In this work, the physicochemical methods for the formation of a new photocatalyst based on the zinc sulfide quantum dots activated by manganese ions were developed. A simple one-step synthesis of ZnS:Mn quantum dots stabilized in various organic shells (a period of stability of more than six months) in an aqueous solution was carried out. The dependences of the dimensional, structural, optical, and luminescent characteristics of the materials obtained on the synthesis conditions and the type of shell chosen are determined. The efficiency of photocatalytic decomposition of organic pollutants of various nature (cationic and anionic) in the aquatic environment was evaluated. A method for observing the process of photodegradation of a model dye in real-time has been developed. It has been shown that the proposed sulfide quantum dots have high photocatalytic activity and can serve as an alternative to the known titanium dioxide-based photocatalysts.

Moreover, we've synthesized a ZnS/Ag₂S and Ag₂S/ZnS core/shell quantum dots to expand the energy activation range all over the visible region and preserve the high photocatalytic activity obtained for bare ZnS quantum dots. It was found that Ag₂S/ZnS quantum dots heterostructures demonstrate better photocatalytic activity compared to ZnS/Ag₂S, which is primarily because of high-reactive ZnS-sites located on heterostructure surface.

The results will be the basis for the incorporation of sulfide quantum dots into solid porous matrices to form the functional nanostructures for the photocatalytic decomposition of organic compounds.

Acknowledgements

This work was financially supported by the Russian Foundation for Basic Research (project 18-32-00135)

References

- [1] M.A. Rauf, M.A. Meetani, S. Hisaindee. *Desalination* **276** (2011) 13.
- [2] J.Y. Kim, O. Voznyy, D. Zhitomirsky, E.H. Sargent. *Adv. Mat.* **25** (2013) 4986.
- [3] M. Asiltürk, F. Sayllkan, E. Arpaç, J. Photochem and Photobiol. A **203** (2009) 64.
- [4] J. Low, S. Qiu, D. Xu, C. Jiang, B. Cheng. *Appl. Sur. Sci.* **434** (2018) 423.
- [5] V. Likodimos. *Appl. Cat. B* **230** (2018) 269.
- [6] J. Cai, J. Huang, Y. Lai. *J. Mat. Chem. A* **5** (2017) 16412.

Luminescent sensing via zinc sulfide quantum dots

A.A. Sergeev*, Leonov A.A., S.S. Voznesenskiy

Institute of Automation and Control Processes of FEB RAS, 5 Radio St., Vladivostok 690041, Russia

*e-mail: aleksandrsergeev@inbox.ru

Well-proven methods for sensing chemical compounds, such as high-performance liquid chromatography, gas chromatography-mass spectrometry and inductively coupled plasma mass spectrometry, have high sensitivity but require expensive equipment and qualified personnel, which complicates their use in continuous monitoring systems and significantly increases the cost of measurements. Currently, scientific groups around the world are developing new sensor systems that combine the advantages of the "classical" methods for the registration of chemical compounds with low cost and ease of operation. One of the promising ways to create such systems is the use of quantum dots which are nanoscale materials with unique chemical, physical, optical, catalytic and electronic characteristics [1]. Among the variety of developed quantum dots, the metal chalcogenide one is the most promising candidate for sensor system development because their optical and electronic properties can be easily tuned.

In this study, we used zinc sulfide which is a direct-gap semiconductor whose bandgap in the bulk state varies from 3.54 to 3.65 eV [2]. With a decrease in the particle size smaller than the Bohr radius of the exciton (for zinc sulfide of the order of 2.2 nm), the bandgap increases due to the quantum size effect. This means that the excitation of quantum size zinc sulfide by photons with an energy greater than the bandgap will lead to electron transfer from the valence band to the conduction band. Being in the conduction band, the electron can move along the crystal lattice, followed by the transition to the valence band, accompanied by the emission of a photon, or go to the surface of the particle and dissipate into the medium surrounding the particle. When scattered into the environment, the electron can interact in the molecules there, passing to their unoccupied molecular orbitals.

This effect can be used to determine chemical compounds having molecular orbitals allowed for electron transition in the environment surrounding a quantum dot. One such compound is methane which molecular orbitals are formed by the 1s level of hydrogen and 2s and 2p levels of carbon [3]. Altogether, methane has eight molecular orbitals. The four lower orbitals of methane are filled, and they cannot accept electrons, as evidenced by their negative energy. Fifth to eighth methane orbitals, on the contrary, is free and can take on electrons. The energy of the fifth molecular orbital, equal to 1.99 eV, means that an electron with an energy higher than this value can pass to it. The sixth, seventh and eighth orbitals have the same energy equal to 3.9 eV.

Based on these considerations, one can assume that one of the main conditions for the formation of sensor response to methane is to ensure the bandgap of quantum dots of the order of 3.9 eV. As shown by previous studies [4], ZnS quantum dots demonstrate the optical response to the methane presence, but in nature was unclear. Since the

formation of the sensory response may depend on various factors, it is necessary to obtain and study a series of samples with gradually changing characteristics.

It is known that chemical deposition from the colloidal solutions method allows one to quite flexibly vary the optical characteristics of the resulting quantum dots. In this way, the manganese doped ZnS quantum dots were synthesized according to this technique. After synthesis solutions were thermostated at 120 C for 1, 6 and 12 hours to obtain quantum dots with different sizes. Based on the results obtained from the optical absorption and luminescence excitation spectra, as well as X-ray diffraction patterns, the average sizes of the synthesized quantum dots were 1.8, 2.2 and 2.6 nm for quantum dots thermostated at 1, 6 and 12 hours, correspondingly.

From the photoluminescence studies, it was found that increasing thermostatic time gives rise to the Mn-related emission intensity and accompanied by a shift of the maximum of the zinc sulfide band from 2.8 to 3.1 eV. The data obtained confirm the fact that the changes in the spectral characteristics of the luminescence of quantum dots are associated with the process of incorporation of a manganese ion into the crystal lattice of zinc sulfide, which is accompanied by deformations of the latter.

It was found that quantum dots thermostated by 1 hour demonstrate the best sensor response to the presence of methane with a concentration of 100-1000 ppm, which is formed due to the transfer of charge carriers from the conduction band and from quantum dot defects to unoccupied molecular methane orbitals. An increase in thermostated time up to 6 hours leads to a decrease in their sensitivity to methane. The response is indirect and arises due to the passivation of oxygen centers on the surface of a quantum dot, which are centers of nonradiative recombination of charge carriers. Provided that this process is controlled, these quantum dots can be used to record methane in the aquatic environment in the concentration range of 100-1000 ppm. For 12 hours thermostated, a large number of nonradiative charge carrier recombination centers are formed on the surface of the quantum dot, which impede the formation of a reliable sensory response to methane exposure.

Acknowledgements

This work was financially supported by the Russian Foundation for Basic Research (project 18-32-00135)

References

- [1] M.A. Rauf, M.A. Meetani, S. Hisaindee. *Desalination* **276** (2011) 13.
- [2] S. Wageh, Z.S. Ling, X. Xu-Rong. *J. Cryst Growth* **255** (2003) 332.
- [3] U. Gelius. *Electron Spectroscopy*. American Elsevier, New York. (1972), 311.
- [4] A.A. Sergeev, K.A. Sergeeva, A.A. Leonov, I.V. Postnova, S.S. Voznesenskiy. *Semiconductors* **52** (2018) 1846.

Initial stages of Bi adsorption on Si(111)5×2-Au

T.V. Utas^{1,*}, D.A. Olyanich¹, A.N. Mihalyuk^{1,2}, L.V. Bondarenko¹, A.Y. Tupchaya¹, D.V. Gruznev¹,
A.V. Zotov^{1,2}, A.A. Saranin^{1,2}

¹ Institute of Automation and Control Processes of FEB RAS, 5 Radio St., Vladivostok 690041, Russia

² Far Eastern Federal University, Vladivostok 690950, Russia

*e-mail: kasyanova@mail.dvo.ru

The Si(111)5×2-Au surface represents a quasi-one-dimensional surface reconstruction. It consists of Au stripes and honeycomb Si chains. Using scanning tunneling microscopy (STM) and density functional theory (DFT) calculations we have studied initial stages of adsorption of bismuth (Bi) onto the Si(111)5×2-Au. Analysis of the results is based on the recently proposed KK model of the Si(111)5×2-Au surface [1]. An ideal Si(111)5×2-Au surface adopts 0.7 ML of Au, i.e., seven Au atoms per 5×2 unit cell. [1 ML (monolayer) = $7.8 \times 10^{14} \text{ cm}^{-2}$, topmost Si atom density in Si(111)1×1.] As for the real Si(111)5×2-Au surface, its characteristic feature is the presence of Si adatoms occupying a unique adsorption site atop the Au chains. It is impossible to form a Si(111)5×2-Au structure without silicon adatoms. The coverage of Si adatoms is about 0.025 ML. Due to silicon adatoms, which tend to be located at a distance of $4a$ ($a = 3.84 \text{ \AA}$) from each other, a Si(111)5×4-Au structure is formed. A Si-adatom saturation coverage of 0.05 ML can also be obtained by extra Si deposition [2, 3]. It has been shown that Si adatoms affect greatly the electronic properties of the Au chains [4–6]. At the “half-filled” 0.025 ML Si-adatom surface, the bare 5×2-Au segments are metallic, while those occupied by Si adatoms are semiconducting [5]. Increasing Si adatom density to a saturation level of 0.05 ML makes the whole Si(111)5×4-Au surface semiconducting. Thus, by adsorbing submonolayers of other suitable species it might be possible to control the properties of the Si(111)5×2-Au surface. And vice versa, the Si(111)5×2-Au surface might be thought as a promising template for growing quasi-one-dimensional adsorbate nanostructures on it.

Experimental details

Our experiments have been performed with a variable-temperature Omicron VT-STM operating in an ultrahigh vacuum ($\sim 2.0 \times 10^{-10}$ Torr). Atomically-clean Si(111)7×7 surfaces have been prepared in situ by flashing to 1280°C after the samples were first outgassed at 600°C for several hours. Gold has been deposited from an Au-wrapped tungsten filament, bismuth from the Ta-tube. Gold deposition rate has been calibrated using the well-known Au/Si(111)5×2 phase with 0.7 ML of Au [1]. Bismuth

deposition rate has been determined as a result of direct atom count on Si(111)5×2-Au phase at small Bi doses depending on adsorption time.

Results

Using high-resolution images we determined the positions of bismuth atoms on the Si(111)5×2-Au surface. Bi adatoms are located exactly above the gold atoms. Theoretical calculations revealed that bismuth atoms replace gold atoms. Only in this case, we observed a full agreement between the simulated STM images with respect to experimental ones. It is noted that bismuth atoms prefer not to be located between silicon adatoms, the distance between which is $4a$. Thus, bismuth adatoms replace gold atoms only if the distance between neighboring Si atoms is more or equal to $6a$.

With an increase bismuth coverage on the Si(111)5×2-Au surface, when all adsorption positions are occupied, bismuth atoms form identical clusters of three atoms each. The distance between atoms in a cluster is approximately equal to $1.6a \approx 6.14 \text{ \AA}$.

Sequential recording of STM images of the same place showed that single bismuth atoms move between adsorption sites at room temperature, while the clusters are stable.

Acknowledgements

The work was supported by the Russian Science Foundation under Grant 19-12-00101.

References

- [1] S.G.Kwon and M.H.Kang, PRL **113** (2014) 086101
- [2] A. Kirokorian, R. Bennet, F.J. Himpsel, L.W. Bruch, Phys. Rev. B **67** (2003) 205412.
- [3] R. Bennet, J.N. Crain, A. Kirakorian, J.L. Lin, J.L. McChesney, D.Y. Petrovykh, F.J. Himpsel, Nanotech. **13** (2002) 499.
- [4] W.H. Choi, P.G. Kang, K.D. Ryang, H.W. Yeom, Phys. Rev. Lett. **100** (2008) 126801.
- [5] H.S. Yoon, S.J. Park, J.E. Lee, C.N. Whang, I.W. Lyo, Phys. Rev. Lett. **92** (2004) 096801.
- [6] I. Barke, S. Polei, V.V. Oeynhausen, K.H. Meiwes-Broer, Phys. Rev. Lett. **109** (2012) 066801.

Two-dimensional MgTl compound on the Si(111) surface

A.Y. Tupchaya^{*1}, L.V. Bondarenko¹, Y.E. Vekovshinin^{1,2}, A.N. Mihalyuk^{1,2}, D.V. Gruznev¹, A.V. Zotov¹, A.A. Saranin¹

¹ Institute of Automation and Control Processes of FEB RAS, 5 Radio St., Vladivostok 690041, Russia

² School of Natural Sciences, Far Eastern Federal University, 690950 Vladivostok, Russia

*e-mail: tupchaya@iacp.dvo.ru

Two-dimensional (2D) structures on the surface of semiconductors are of great interest to the scientific community due to a large number of unique properties, among which special attention is paid to 2D superconductivity [1], the Rashba-Bychkov effect [2] and the quantum spin Hall effect [3]. Active search for 2D systems that have such interesting properties leads to various ways of modifying already known systems, thus contributing to the emergence of new properties that were not previously observed. For example, it was recently discovered that, despite the fact that graphene is not a superconductor in its pure form, two-layer graphene intercalated with calcium demonstrates a transition to a superconducting state [4]. Thus, modification of 2D compounds by alkali-earth metal atoms may be a promising area of research.

In this paper, magnesium atoms were used as a modifier of the well known Si(111)1×1-Tl surface. The 2D MgTl compound on the Si(111) surface was formed by Mg deposition and as a result, sections of a new structure with a lattice period of $\sqrt{3}\times\sqrt{3}$ appeared on the surface. When the Mg and Tl coverages is subsequently increased, a well-ordered Si(111) $\sqrt{3}\times\sqrt{3}$ -MgTl structure was formed.

Scanning tunneling microscope data have shown that at room temperature (RT), the structure is characterized by the presence of open antiphase domain boundaries that are localized on the surface defects. In addition, this structure looks like as honeycomb array away from defects and as hexagonal array near defects. When this structure was cooled to a temperature of 112K, it was found that the surface is hexagonal and is represented by two domains. This difference in the appearance of the structure at RT and 112K is explained by switching the bright maximum between the two adsorption positions in the $\sqrt{3}\times\sqrt{3}$ unit cell at RT. When cooling, the maxima freeze in the most favorable positions, grouping into domains, forming antiphase domain boundaries.

Based on experimental STM data, an atomic model of this structure was proposed using density functional theory

calculations. According to this model, a 2D MgTl compound is a two-layer structure on the bulk-like-terminated Si(111)1×1 surface. A mixture of Mg and Tl atoms are located in the first layer and the second layer is located above the first and consists only of Tl atoms. It is worth noting that according to the model, the lattice period $\sqrt{3}\times\sqrt{3}$ is set by the lower layer, while the atoms of the upper layer form a lattice close to 1×1 periodicity. This discrepancy leads to two possible positions of the top layer relative to the bottom layer, explaining the domains formation, as well as collective switching.

The electronic properties of the 2D MgTl compound were investigated using angle-resolved ultraviolet photoelectron spectroscopy. The obtained data showed that this compound has metallic surface states, and the theoretical calculations confirmed that these metal states have Rashba-Bychkov type spin splitting. In addition, calculations around highly symmetric M-point show a saddle point feature or Van Hove singularity, which is one of the indirect signs of the presence of superconductivity.

Acknowledgements

The work was supported by the Russian President's Grant MK-1341.2020.2 for young researchers and the Russian Foundation for Basic Research Grant No. 18-52-52012. The calculations were conducted using the equipment of Shared Resource Center "Far Eastern Computing Resource" IACP FEB RAS (<https://cc.dvo.ru>).

References

- [1] M. Yamada, T. Hirahara, S. Hasegawa. *Phys. Rev. Lett.* **110** (2013) 237001.
- [2] K. Yaji, Y. Ohtsubo, S. Hatta, H. Okuyama, K. Miyamoto, T. Okuda, A. Kimura, H. Namatame, M. Taniguchi T. Aruga. *Nat. Commun.* **1** (2010) 17.
- [3] D. Gruznev, S. Ereemeev, L. Bondarenko, A. Tupchaya, A. Yakovlev, A. Mihalyuk, J.-P. Chou, A. Zotov, A. Saranin *Nano Lett.* **18** (2018) 4338.
- [4] S. Ichinokura, K. Sugawara, A. Takayama, T. Takahashi, S. Hasegawa. *ACS Nano* **10** (2016) 2761.

Comparative study of bismuth structures obtained via pulsed laser ablation in a liquid and in air

V.A. Svetlichnyi¹, E.D. Fakhrutdinova¹, T.S. Nazarova¹, S.A. Kulinich², O.V. Vodyankina¹

¹ Tomsk State University, 36 Lenin Ave., Tomsk, 634050, Russia

² Tokai University, 4-1-1 Kitakaname, Hiratsuka-shi Kanagawa, 259-1292, Japan

*e-mail: v_svetlichnyi@bk.ru

Recently, bismuth compounds have attracted great interest due to their unique properties. For example, bismuth oxycarbonate has low toxicity and exhibit antibacterial properties [1], which is attractive for use in the field of medicine. Various modifications of bismuth oxide and bimetallic oxides (silicates, titanates, etc.) have a high refractive index [2] and dielectric permittivity [3], ionic conductivity [4] and photocatalytic activity [5]. This allows using of bismuth compounds as optical coatings and materials for gas sensors. The high interest in bismuth oxides is due to the opportunity to use them as photocatalysts in the visible region of the spectrum.

To date, seven bismuth (III) oxide polymorphs have been identified in the literature, and an additional modification has been postulated recently [6]. Different types of bismuth oxides have various optical, catalytic and other functional properties that determine their field of application. A variety of oxide forms complicates the controlled synthesis of a certain modification of bismuth oxide particles, especially with the necessary size parameters. One of the promising methods for producing nanoparticles (NPs) of reactive metal oxides is the method of pulsed laser ablation (PLA) in a liquid. An important advantage of the PLA method is the ability to obtain “pure” NPs in the absence of additional precursors. Varying the parameters of laser radiation, the target material and the solvent, it is possible to control the size and structure of the materials prepared by PLA. In recent years, the PLA method in gas has also been successfully developed to obtain NPs.

In this work, we used the method of pulsed laser ablation of a bismuth metal target in a liquid and gas for preparation bismuth-containing materials. A comparative study of physical-chemical and photocatalytic properties of the materials obtained was carried out.

Pulsed laser ablation was carried out in distilled water (Bi_{ini} sample) and in atmospheric air (Bi_{air} sample) using a Q-switch Nd:YAG laser (following parameters were used: wavelength 1064 nm, pulse duration 7 ns, frequency 20 Hz, and pulse energy 160 mJ). Metallic Bi (99.9% purity) was used as a target. The dispersion was dried at 60 °C (sample Bi_{ini}).

Sample Bi_{ini} consists of large lamellar particles with an average size of about 500 nm. The NPs obtained by PLA in air have a predominantly spherical shape with a wide size distribution from 3 to 210 nm and the majority of particles

are in the size range of 10-18 nm. Since the particle are quite large, the specific surface area for these materials is low: 1.3 m²/g for Bi_{ini}, and 16.4 m²/g for Bi_{air}.

The crystal structure of the materials and phase transitions after heat treatment (200 and 400 °C) were studied by X-ray diffraction. The Bi_{ini} sample is a mixture of three phases, namely, α -Bi₂O₃ bismuth oxide, Bi(CO₃)O₂ bismuth oxycarbonate and (BiO)₄CO₃(OH)₂ bismuth hydroxycarbonate. The appearance of carbon in the structure can be explained by drying of the colloidal solution in air and a large affinity of bismuth to carbon. After annealing at 200 °C, no phase transitions are observed, the sample retains its structure. However, after annealing at 400 °C, hydroxycarbonate and oxycarbonate of bismuth decompose, and α -Bi₂O₃ forms as the main phase. The Bi_{air} sample is a mixture of metallic bismuth and bismuth oxide β -Bi₂O₃. After annealing at 200 °C, the amount of the metal phase decreases and no other changes in the structure are observed. However, after heat treatment at 400 °C, a phase transition occurs with the formation of the α -Bi₂O₃ structure.

A diffuse reflection spectroscopy study showed that both materials had a quite wide absorption spectrum, including the visible region. It consists of the absorption bands of the Bi(CO₃)O₂, (BiO)₄CO₃(OH)₂ and α -Bi₂O₃ phases for Bi_{ini} and β -Bi₂O₃ and Bi (metallic) for Bi_{air}.

All materials performed good activity in the process of photocatalytic degradation of the Rhodamine B dye in the solution under simulated sunlight.

Acknowledgements

This work was supported by the Russian Science Foundation; Project No. 19-73-30026.

References

- [1] S. Suerbaum, P. Michetti, N. Engl. J. Med. **347** (2003) 1175.
- [2] L. Leontie, M. Caraman, M. Alexe, C. Harnagea, Surf. Sci. **507** (202) 480.
- [3] V. Fruth, M. Popa, D. Berger et al. J. Eur. Ceram. Soc. **25** (2005) 2171.
- [4] P. Shuk, H. D. Wiemhofer, U. Guth et al. Solid State Ionics **89** (1996) 179.
- [5] K. Brezesinski, R. Ostermann, P. Hartmann et al. Chem. Mater. **22** (2010) 3079.
- [6] T. Atou, H. Faqir, M. Kikuchi et al. Mater. Res. Bull. **33** (1998) 289.

Cooperation of genetic and metropolis algorithms for finding unconventional thermodynamic behaviour of many-body systems

R. Volotovskiy^{*1,2}, Y. Shevchenko^{1,2}, A. Perzhu^{1,2}, E. Vasiliev^{1,2}, V. Kapitan^{1,2}, D. Kapitan^{1,2}, A. Rybin^{1,2}, K. Soldatov^{1,2}, A. Makarov^{1,2}, V. Strongin^{1,2}, K. Nefedev^{1,2}

¹ Department of Computer Systems, School of Natural Sciences, Far Eastern Federal University, Vladivostok, 690950, 8 Sukhanova St., Russian Federation

² Institute of Applied Mathematics, Far Eastern Branch, Russian Academy of Science, Vladivostok, 690041, 7 Radio St., Russian Federation

*e-mail: volotovskii.ra@students.dvfu.ru

All magnetic materials have at least two thermodynamic phases — order and disorder, which determine the second-order phase transition. The peak in the temperature behavior of the specific heat, which diverges for infinite systems, is an indirect confirmation of the presence of a phase transition. There is a subgroup of H (2,2) -class magnets (the classification is presented in [1]) where additional temperature phases can exist. For example, frustrated spin-ice lattices, have an additional phase transition, determined by the presence of long-range order [2,3]. Most of modern researches are devoted to lattice structured magnetic materials. We can exploit patterns of lattices to simplify the model and reduce the calculations when dealing with numerical solution. For amorphous magnetic structures, the problem is significantly complicated due to the absence of any lattice regularities.

Is there any exotic configuration of amorphous magnets with additional phases excluding order and disorder? To answer this question, we examined pseudo-random lattices, the spins of which are randomly located on small scales, but the structure pattern repeats on large scales. This allows us to effectively explore amorphous structures using standard approaches and simplifications applied to lattice structures. In this study, we combined the genetic algorithm with the canonical Metropolis algorithm. The Metropolis algorithm was used to calculate the temperature behavior of heat capacity. A genetic algorithm is needed to create random configurations of amorphous structures and their modifications based on heat capacity data. The interaction between the spins is dipole-dipole and is determined as:

$$E_{ij} = \frac{\vec{m}_i \vec{m}_j}{|\vec{r}_{ij}|^3} - 3 \frac{(\vec{m}_i \vec{r}_{ij})(\vec{m}_j \vec{r}_{ij})}{|\vec{r}_{ij}|^5},$$

where \vec{m} – vector of magnetic moment, \vec{r} – radius vector between a pair of spins. In the frame of model we considered a system of Ising-like dipoles, where \vec{m}_i is

replaced by $s_i \vec{m}'_i$, and \vec{m}'_i – is a fixed value, with length $|\vec{m}'_i| = 1$. The value $s_i = \pm 1$ determines the direction of the vector. The initial lattice configuration is determined by randomly filling spins of the square lattice sites. This allows to limit the minimum possible distance between the spins. This defines a small repeating section of the pseudo-random lattice - a pattern. The pattern is then translated along the X and Y axis to achieve the large dimensions of the magnetic system. Large sizes reduce the effect of open borders and the effect of finite size.

We proposed selection, crossing, and mutation schemes, and also proposed a cost-function for the genetic algorithm that encourages configurations with a large number of heat capacity peaks. The function also takes into account the height of each heat capacity peak.

The results of our research show that, after several generations, configurations with one low-temperature peak of heat capacity begin to dominate. The spins of the lattice are concentrated in one zone of the pattern, keeping the magnetic order as much as possible. During the translation of the pattern, sublattices work as a set of weakly interacting subsystems. We did not find exotic phases in the described pseudo-amorphous magnetic structures of dipoles.

Acknowledgements

The results were obtained using the equipment of Shared Resource Center "Far Eastern Computing Resource" IACP FEB RAS (<https://cc.dvo.ru>).

References

- [1] C. A. F. Vaz, J. A. C. Bland and G. Lanhoff, Reports on Progress in Physics **71** (2008) 056501.
- [2] Shevchenko, Y. A., Makarov, A. G., Andriushchenko, P. D., & Nefedev, K. V. Journal of Experimental and Theoretical Physics **124** (2017) 982.
- [3] Chern, G. W., Morrison, M. J., & Nisoli, Physical Review Letters **111** (2013) 177201.

AFM visualization of asphaltenes surface structure

T.I. Sharipov*, G.F. Gilyazova, R.Z. Bakhtizin
Bashkir State University, 32 Z. Validi St., Ufa, 450076, Russia

*e-mail: sha-t@yandex.ru

Many processes of drilling, production, and transportation of oil and oil products are associated with difficulties arising as a result of the unexpected manifestation of the physicochemical properties of oils [1] in different environmental conditions. One of the negative factors in the operation of pipelines and other equipment is the deposition of solid deposits on their internal surfaces: resinous-paraffin components and asphaltenes [2]. All this leads to a decrease in the efficiency of the equipment and damage to materials. Having studied the structure of asphaltene molecules [3], it is possible to apply the obtained knowledge in the future to reduce the negative impact of these deposits.

Asphaltene is a fragile and black solid substance that has a high boiling point. It is difficult to estimate the molecular weight of asphaltene molecules since they are self-associated. At present, their molecular weight ranges from 500-2000 g/mol. Asphaltene passes into a viscous plastic state at temperatures of 200-300 °C, and at higher temperatures, they decompose and produce liquid hydrocarbons, gas and solid coke residue insoluble in ordinary solvents. It is known that asphaltene contains the main amount of salts, ash-forming components, metal-, nitrogen-, oxygen- and sulfur-containing compounds.

The report will present the results of a study of organic molecules, petroleum asphaltene, using an atomic force microscope (AFM). We have used AFM in tapping mode. The AFM images of asphaltene dissolved in toluene and adsorbed in the form of a thin film on the surface of the substrate were obtained. Fresh mica cleavage was used as a substrate. In developing the methodology for preparing asphaltene samples, we were faced with the task of finding the optimal concentration of asphaltene in toluene, in which the supramolecular structure or an individual asphaltene molecule can be identified on the AFM image. Considering the results of other researchers [4], it was decided to use a working solution with a concentration of asphaltene in toluene less than or equal to 0.1 g/l. We deposited small volumes of a working solution of various concentrations on a substrate so that a film was obtained. In addition to varying the concentration of asphaltene in a

toluene solution, we changed some other experimental parameters to obtain the highest quality AFM images.

The method of asphaltene film deposition to a substrate was as follows: the hydrophobic substrate was lowered into a flat vessel with distilled water, and then a drop of asphaltene solution was deposited to the water surface using a dispenser. After the solution forms an asphaltene nanolayer on the water surface without touching the film, the substrate was hooked with tweezers from the edges and lifted upward through the asphaltene film formed on the water. Two cases were experimentally verified: in the first, the substrate was oriented in space vertically, in the second, horizontally. Then, the extracted substrate was dried in air for several hours until completely dried to form a film of asphaltene. After that, the obtained sample was investigated by the AFM method.

The report will discuss AFM images, objects observed on them, their shape, and location on the surface. For a detailed consideration, section profiles on the structures of interest will be made and some geometric parameters will be calculated.

Acknowledgements

The work was supported by the Russian Foundation for Basic Research under grant No. 17-42-020616 and Republic of Kazakhstan under project No. AP05132165.

References

- [1] E.E. Barskaya, Y.M. Ganeeva, T.N. Yusupova, E.S. Romanov. Chemistry of oil and gas, Tomsk, Publ. House of IOA RAS, (2015) 454 (in Russian).
- [2] Edo S. Boek., Thomas F. Headen, Johan T. Padding. J. The Royal Society of Chemistry **144** (2010) 271.
- [3] T.I. Sharipov, R.Z. Bakhtizin, M.Y. Dolomatov, S.A. Shutkova, T.N. Nurakhmetov, Zh.Yu. Salikhodzh, B.R. Badretdinov. Butlerov messages **57** (2019) 99 (in Russian).
- [4] M.Y. Dolomatov, S.A. Shutkova, T.I. Sharipov, R.Z. Bakhtizin, Z.Z. Ishniyazov, T.N. Nurakhmetov, Zh. Yu. Salikhodzh, Bulletin of the Eurasian National University named after L.N. Gumilyov, Series of Physics and Astronomy **126** (2019) 23 (in Russian).

Ab initio calculation of the equilibrium quantum state for hole spin of the B:Si system

M.A. Chibisova*, A.N. Chibisov, S.I. Malkovsky

Computing Center of FEB RAS, 65 Kim Yu Chen St., Khabarovsk, 680000, Russia

*e-mail: omariya2003@yandex.ru

Building a quantum computer has emerged as an important scientific and technological task for modern solid-state nanoelectronics. Quantum computations will allow instant solutions to urgent problems such as designing modern materials with specific desired properties, creating new types of drugs, etc. The hole spins in the valence band of silicon have large internal spin-orbit couplings and are more easily controlled by an electric field [1,2]. Implantation of a boron atom in a bulk silicon lattice creates a local deficit of one electron and forms a hole that is localized in the valence band. Magneto-transport spectroscopy shows that the ground state of the hole splits into four states under the influence of a magnetic field [3]. The two lowest spin states belong to the states of heavy ($m = 3/2$) and light ($m = 1/2$) holes. The two-level system formed by these spin states can be controlled by an electric field and is characterized by a long relaxation time that depends on the magnetic field amplitude [3]. This work presents the results of quantum-mechanical calculations in which the quantum state of the hole spin of the bulk B:Si system are analyzed.

The total energies of the atomic systems were calculated using the Quantum ESPRESSO software package [4]. Perdew-Burke-Ernzerhof (PBE) pseudopotentials for silicon and boron atoms, in the generalized gradient approximation (GGA), were taken from the Quantum ESPRESSO package. Using the Oda-Pasquarello-Car and Gebauer-Baroni techniques, spin-orbit and noncollinear interactions were included [5,6]. The unit cell of bulk silicon was calculated with a special set of $6 \times 6 \times 6$ k-points. A special set of $3 \times 3 \times 3$ k-points with a 476.20 eV cutoff energy for the plane waves was used for calculating the B:Si system, which contained 63 silicon atoms (Si) and one boron atom (B). The equilibrium model was obtained by free relaxation of all atoms in the structure, for which the 64-atom model was placed in a cell with a volume of $10.862 \times 10.862 \times 10.862 \text{ \AA}^3$. Atomic relaxation was carried out to an interatomic force value of $0.026 \text{ eV \AA}^{-1}$.

In this work, we first determined the $|1\rangle$ quantum state of the hole spin in a bulk silicon lattice with an acceptor boron atom. It was shown that the $|1\rangle$ hole spin state, with spin orientation $m_z = -1$, corresponds to the energy state $m = -\frac{3}{2}$ in the band structure. Introducing the impurity B atom into the silicon lattice causes the charge density around the Si-B bond with the nearest silicon atom to increase and reach a maximum at the boron atom. This

causes the electrostatic potential at the locations of the Si and B atoms to increase by 7.33 and 2.16 eV, respectively. The results presented here are very important and promising for the physics of solid-state quantum computers.

Acknowledgements

Computations were performed with the methods and techniques, which were developed under the RFBR scientific project number 18-29-03196. The research is carried out using the equipment of the Shared Facility Centre 'Data Centre of FEB RAS' (Khabarovsk, Russia) [7] and partly using a cluster at the shared research facilities of HPC computing resources at Lomonosov Moscow State University supported by the project RFMEFI62117X0011. The authors would like to thank the Irkutsk Supercomputer Centre of SB RAS for providing access to HPC-cluster 'Akademik VM Matrosov' (Irkutsk Supercomputer Centre of SB RAS, Irkutsk: ISDCT SB RAS; <http://hpc.icc.ru>, accessed 11.07.2019).

References

- [1] J. van der Heijden, T. Kobayashi, M.G. House, J. Salfi, S. Barraud, R. Laviéville, M.Y. Simmons, S. Rogge. *Sci. Adv.* **4** (2018) 9199.
- [2] R. Maurand, X. Jehl, D. Kotekar-Patil, A. Corna, H. Bohuslavskiy, R. Laviéville, L. Hutin, S. Barraud, M. Vinet, M. Sanquer, S. De Franceschi. *Nat. Commun.* **7** (2016) 13575.
- [3] J. Heijden, J. Salfi, J.A. Mol, J. Verduijn, G.C. Tettamanzi, A.R. Hamilton, N. Collaert, S. Rogge. *Nano Lett.* **14** (2014) 1492.
- [4] P. Giannozzi, O. Andreussi, T. Brumme, O. Bunau, M.B. et.al. *J. Phys.: Condens. Matter* **29** (2017) 465901.
- [5] T. Oda, A. Pasquarello, R. Car. *Phys. Rev. Lett.* **80** (1998) 3622.
- [6] R. Gebauer, S. Baroni. *Phys. Rev. B* **61** (2000) R6459.
- [7] A.A. Sorokin, S.V. Makogonov, S.P. Korolev. *Scientific and Technical Information Processing* **44** (2017) 302.

Feedback optimized replica-exchange Monte-Carlo algorithm

A. Rybin^{*,1,2}, D. Kapitan^{1,2}, P. Andriushchenko¹, E. Vasiliev^{1,2}, V. Kapitan^{1,2}

¹ Department of Computer Systems, School of Natural Sciences, Far Eastern Federal University, Vladivostok, 690950, 8 Sukhanova St., Russian Federation

² Institute of Applied Mathematics, Far Eastern Branch, Russian Academy of Science, Vladivostok, 690041, 7 Radio St., Russian Federation

*e-mail: rybin.ae@students.dvfu.ru

Nowadays, there is more and more researches in the field of magnetic data carriers, caused by the rapid growth of data volumes. One of the most popular methods for simulation various spin structures is the Monte Carlo algorithm. However, this method has a drawback: in the phase transition region, the modeling process slows down.

At low temperatures, the value of $\beta = \frac{1}{k_B T}$ is much greater than zero, and therefore from the formula [1], the probability of a spin flip tends to zero. This phenomenon is called the critical slowdown effect.

$$P_{flip} = \min \{1, \exp[-\beta \Delta E]\} \quad (1)$$

Parallel tempering (PT) Monte-Carlo algorithm, also known as replica-exchange Monte-Carlo, was effectively used for a broad spectrum of problems in different areas, such as physics, materials science, logistics, and engineering. PT MC has established itself as a truly effective method in cases of optimization and sampling.

An optimized set of temperature values increases the efficiency of the algorithm due to more frequent visits of temperature extremum by replicas.

Despite that, the method is extremely powerful. Careful setup of parameters is indispensable to ensure optimal execution time.

The speed of the replica roundtrips strongly depends on the simulated statistical ensemble, i.e., the choice of temperature points $\{T_1, T_2, \dots, T_M\}$ in the parallel tempering simulation.

We present an algorithm for systematically increasing the efficiency of parallel tempering Monte Carlo method by optimizing the simulated temperature set in such a way as to maximize the number of cycles between two extreme

temperatures T_1 and T_M for each replica and thereby significantly improve the system equilibrium at all temperatures.

To track the movement of a replica, an up or down label is assigned to the replica when it first visits the lowest or highest temperature. The replica label does not change until the visit to the opposite temperature limit. Replica label i is not originally set, then changes to “down” on the first visit to the highest temperature, remains undiminished until the replica reaches the lowest temperature, and then is set to “up”.

In this work, $n_{up}(T_i)$ and $n_{down}(T_i)$ are defined as the numbers of replicas marked “up” and “down”, respectively, that visit the temperature T_i during the simulation. The percentage of replicas that recently visited the lowest temperature before visiting T_i is shown below. Usually, $f(T_i)$ called a “flow” and defined as

$$f(T_i) = \frac{n_{up}(T_i)}{n_{up}(T_i) + n_{down}(T_i)} \quad (2)$$

In this work, we have demonstrated that by optimizing the set of simulated temperature, we can minimize the replica transit time between the lowest and highest temperatures, which effectively increases the efficiency of the parallel tempering algorithm. In particular, the temperature density in an optimized set of temperatures helps in simulation bottlenecks, such as phase transitions.

Acknowledgements

The research was carried out within the state assignment of FASO of Russia No. 075-00400-19-01.

Influence of the surface treatment on the GaAs planar nanowire morphology

A.A. Spirina^{*,1}, N.L. Shwartz^{1,2},

¹ Rzhanov Institute of Semiconductor Physics of SB RAS, 13 pr. Lavrentieva, Novosibirsk 630090, Russia

² Novosibirsk State Technical University, 20 K. Marx aven., Novosibirsk 630073, Russia

*e-mail: spirina.anna.alex@gmail.com

The interest in planar nanowires based on III-V semiconductors, that is, crystalline wires elongated along the substrate, is associated with the perspectives of their use in devices compatible with standard planar technology. For the manufacture of high-quality devices, arrays of planar nanowires with given sizes and morphology are required. The planar GaAs nanowires are experimentally obtained by chemical vapor deposition (CVD) via the vapor-liquid-solid mechanism, where Au droplets are used as a catalyst [1]. Gold is embedded in the growing crystal and forms an undesirable impurity, which degrades the characteristics of GaAs optoelectronic devices. To avoid additional impurities, GaAs nanowires can be formed through self-catalyzed growth, that is, using gallium catalyst. Self-catalyzed growth requires optimal growth conditions (material deposition rates and temperature) and careful treatment of the substrate surface. Therefore, it is necessary to study in detail the effect of surface passivation properties on the planar nanowire morphology.

This paper presents the simulation results of the self-catalyzed growth of planar GaAs nanowires using the lattice Monte Carlo model [2]. A search of the stable growth conditions of planar nanowires via the vapor-liquid-solid mechanism using gallium droplets as a catalyst is carried out. The influence of substrate orientation on the planar wire morphology is studied. The (111)A, (111)B and (001) orientations of GaAs substrates are considered. It is found that the most stable growth of planar wires is observed on the (111)A substrates. On the (111)B substrates, the nanowire growth breakdowns from planar to vertical growth. On GaAs(100), the growth direction of nanowires may be changed by 90° relative to the initial direction of crystal growth due to turn of the droplet catalysts. It is shown that, at the initial growth stage, a three-dimensional GaAs crystal is formed under the gallium droplet. The shape of this crystal is a half of a truncated octahedron. The 3D crystal surface consists of four {111} planes connected by three {100} planes. The orientation of upper plane of the

3D crystal is determined by the substrate surface orientation. After the formation of a three-dimensional crystal under a droplet, the planar nanowire growth begins due to the seed droplet movement along the substrate through the GaAs crystallization. Preliminary simulation results showed that the gallium droplet size decreases during nanowire growth up to complete droplet consumption. This leads to the nonuniform wire diameter and untimely stop of growth. In addition, the nonuniform wire diameter results in a noticeable radial nanowire growth due to the embedding of gallium and arsenic atoms into the crystal side walls. In order to slow down the consumption of a gallium droplet and to reduce the nanowire radial growth, we studied the effect of the properties of substrate surface passivated layer on the planar nanocrystal morphology. The effective activation energy of molecular arsenic desorption from the mask-film, which corresponds to the stable growth of planar nanowires on the GaAs(111)A surface, is found. The influence of the arsenic diffusion activation energy over the mask-film on the planar nanowire morphology is analyzed. The decrease of arsenic diffusion activation energy relative to the gallium diffusion energy results in reducing of the arsenic inflow to the droplet and the wire side walls. The arsenic diffusion energies, at which the gallium droplet longer preserves its size, are found. At obtained arsenic diffusion energies, the wire radial growth decreases significantly. This leads to planar GaAs nanowire formation with uniform diameter.

Acknowledgements

The work is supported by RFBR (grant 19-31-90023) and the RAS Program.

References

- [1] C. Zhang, X. Miao, P. K. Mohseni, W. Choi, X. Li. *Nano Lett.* **14** (2014) 6836.
- [2] A. N. Karpov, A. V. Zverev, A. G. Nastovjak, S. V. Usenkov, N. L. Shwartz. *Vychisl. Metody Programm.* **15** (2014) 388.

Investigation of the plasma treatment process for the regeneration of SERS substrates sensitivity

A.I. Savitskiy^{*1,2}, S.V. Dubkov^{*1}, G.S. Eritsyayn^{1,2}, A.M. Tarasov¹, S.N. Skorik², E.P. Kitsyuk², D.G. Gromov¹

¹ National Research University of Electronic Technology, Bld. 1, Shokin Square, Zelenograd, Moscow 124498, Russia

² Scientific-Manufacturing Complex "Technological Centre", 1, Bld. 7, Shokin Square, Zelenograd, Moscow 124498, Russia

*e-mail: andr.savitskiy@gmail.com

In the past few decades, plasmon nanostructures have attracted increased attention from the scientific community, which is why over time the list of areas where such structures find their application significantly increases. For example, there are studies that the use of plasmonic nanoparticles can increase the efficiency of photovoltaic converters [1] and photocatalytic structures [2,3]. Today it is known that the use of structures with the effect of plasmon resonance can significantly increase the detection limit of various chemicals. This approach has been successfully used in areas such as pharmacology, materials science, biomedicine, etc. [4].

The main tool for the detection of analytes is Raman spectroscopy. It is worth noting that various SERS (surface-enhanced Raman spectroscopy) substrates are currently used to increase the sensitivity of this method. The SERS active layer is an array of nanostructured plasmon metal, which provides the main increase in the efficiency of such substrates. Silver is a plasmon metal that allows one to achieve the highest amplifications of the Raman signal. However, the chemical activity of nanostructured silver significantly limits the life of the SERS substrates. The rapid oxidation or sulfidization of silver particles leads to a significant decrease in the sensitivity of structures [5]. In this regard, researchers are faced with the task of extending the life of SERS structures. The solution to this problem can be carried out in several directions: 1) increase the inertness of the SERS active layer (by introducing another metal); 2) isolate the SERS-active layer from the analyte (by coating the array of nanoparticles with a thin layer of dielectric); 3) regeneration of the sensitivity of the active layer (carrying out the process of chemical reduction of silver). In this study, the third way was chosen, since the first two lead to a decrease in the overall sensitivity of the SERS substrate due to the partial attenuation of localized surface plasmon resonance caused by a change in the composition of plasmon particles and / or dielectric properties.

In our work, as an SERS active layer, we used arrays of

self-organized silver nanoparticles with an average diameter of 25 nm, which were obtained by vacuum-thermal evaporation of a small weight portion of silver and subsequent annealing of the structure in vacuum at 230 °C. This technique has good reproducibility of the formed arrays and we use it to form planar SERS structures [6]. Thin layer of amorphous carbon (25 nm thick) was used as a detection object. After the formation of the SERS-active layer, the substrate was divided into several samples. The a-C layer was immediately applied to the first sample; for the remaining samples, a-C was applied after some time; the maximum retention time of an array of Ag particles in the atmosphere was ~ 1 month. Immediately after the deposition of a-C on the sample, the signal intensities from the D and G spectral modes of carbon were measured using a LabRAM HR Evolution Raman spectrometer at 514 and 633 nm. At the next stage of the study, experiments were performed to regenerate the sensitivity of SERS substrates of a month ago in the Oxford PlasmaLab System 100.

Acknowledgements

This work was financially supported by the grant of the President of the Russian Federation (project MK-2222.2019.8).

References

- [1] U. Aslam, V. Govind, S. Chavez, S. Linic. *Nature Catalysis* **1** (2018).
- [2] J. Du, H. Du, H. Ge, J. Fan, X. Peng. *Sensors and Actuators B: Chemical*. (2017).
- [3] M. Karmaoui, L. Lajaunie, D.M. Tobaldi, G. Leonardi, C. Benbayer, R. Arenal, J.A. Labrincha, G. Neri, *Applied Catalysis B: Environmental* **218** (2017).
- [4] J.Kneipp. *Theoretical Chemistry Accounts* **125**(2009)
- [5] G.M.Herrera, A.C.Padilla, S.P. Hernandez-Rivera. *Nanomaterials* **3** (2013).
- [6] D.G. Gromov, S.V. Dubkova, A.I. Savitskiy, Yu.P. Shaman, A.A. Polokhin, I.A. Belogorokhovd, A.Yu. Trifonov. *Applied Surface Science* **489** (2019).

Calculation of order parameter and critical exponents of the spin glass in the frame of Edwards-Anderson model

D. Kapitan^{*,1,2}, A. Rybin^{1,2}, P. Andriushchenko², E. Vasiliev^{1,2}, V. Kapitan^{1,2}

¹ Institute of Applied Mathematics, Far Eastern Branch, Russian Academy of Science, Vladivostok, 690041, 7 Radio St., Russian Federation

² Department of Computer Systems, School of Natural Sciences, Far Eastern Federal University, Vladivostok, 690950, 8 Sukhanova St., Russian Federation

*e-mail: kapitan.diu@students.dvfu.ru

Spin glass models have become the main experimental “base” for studying complex disordered systems. In the 1960s, it was discovered that some magnetic alloys have rather anomalous magnetic properties that cannot be described in the framework of the existing theory of phase transitions. Spin glasses are characterized by two main characteristics that strongly distinguish these systems from others: disorder in the position of magnetic atoms in the alloy and the occurrence of strong competition between ferromagnetic and antiferromagnetic interactions.

In this paper, the authors consider the two-dimensional Edwards-Anderson model, with the exchange integral J_{ij} as a random function and the average value of J_{ij} is zero. In such a system, at one-half of the spins the interaction with each other is ferromagnetic, and at the other - antiferromagnetic.

The interaction J_{ij} between the spin pair (ij) changes during the transition from one pair to another. The Hamiltonian is expressed as:

$$H = \sum_{\langle i,j \rangle} J_{ij} S_i S_j - h \sum_{i=1}^N S_i \quad (1)$$

S_i, S_j – spins of the lattice, $\langle i,j \rangle$ denotes the summation over pairs of interacting spins in a system with size N , h is the external magnetic field.

The system was simulated with the replica exchange Monte Carlo algorithm.

For this model, the temperature behavior of the average magnetization modulus $\langle |M| \rangle = 0$. Because of this fact, we calculated an average size of the percolation cluster $\langle \gamma_1 \rangle$, which is defined as the relative size of maximum cluster, which include spins in the ground state to the total number of spins. The average size of the percolation was

chosen as an order parameter.

This order parameter, in contrast to other thermodynamic characteristics, makes it possible to describe the behavior of the system with a change in temperature and makes it possible to calculate critical exponents.

For the presented order parameter, we used the fourth-order Binder cumulant U_L :

$$U_L = 1 - \frac{\langle \gamma_1^4 \rangle_L}{3 * \langle \gamma_1^2 \rangle_L} \quad (2)$$

This expression makes it possible to determine the critical temperature with high accuracy and makes it possible to calculate critical exponents, based on it.

They were determined through the following:

$$\langle \gamma_1^2 \rangle = \left(N^{\frac{1}{2}} \right)^{\frac{2\beta}{\nu}} \left(\frac{T}{T_c} - 1 \right) \left(N^{\frac{1}{2}} \right)^{\frac{1}{\nu}} \quad (3)$$

$$U_L = \left(\frac{T}{T_c} - 1 \right) - \left(N^{\frac{1}{2}} \right)^{\frac{1}{\nu}} \quad (4)$$

In this work, we have demonstrated the temperature dependences of the main thermodynamic quantities of the two-dimensional Edwards-Anderson model for different sizes of the model and with different modeling parameters. The critical exponents were also calculated and compared with the critical exponents for the two-dimensional Ising model and for the two-dimensional lattice in percolation theory.

Acknowledgements

The research was carried out within the state assignment of FASO of Russia No. 075-00400-19-01.

Modeling of non-collinear magnetic states of the phosphorus qubit in a silicon lattice

A.N. Chibisov^{*1}, M.A. Chibisova^{1,2}

¹ Computing Center of FEB RAS, 65 Kim Yu Chen St., Khabarovsk, 680000, Russia

² Pacific National University, 136 Tikhookeanskaya St., Khabarovsk 680035, Russia

*e-mail: andreichibisov@yandex.ru

The ability to control quantum states and implementation of the transferring and transforming processes of quantum information will allow the creation of quantum computers. These machines will make possible instantly solving such important tasks as designing modern materials with desired properties and will also dramatically improve the machine learning operation and artificial intelligence systems. Recently, active interest has been shown in quantum qubits devices based on nuclear spins of phosphorus impurities in a Si crystal [1-3], the technological scheme of which was proposed by Kane in 1998 [4]. The electron-spin states bound to a single phosphorus donor in silicon show long coherence and relaxation times [5].

We believe that the use of the spin-orbit non-collinear coupling method will allow qualitative analysis of the silicon-phosphorus system. To this end, in this work, we study the spin behaviour of phosphorus in bulk silicon.

The calculation of total energies of bulk Si atomic models was carried out using the Quantum ESPRESSO software package [6], by means of high-performance calculations. Perdew-Burke-Ernzerhof (PBE) pseudopotentials for silicon and phosphorus atoms, in the generalized gradient approximation (GGA), are taken from the Quantum ESPRESSO package. Spin-orbit non-collinear coupling is taken into account using the Oda-Pasquarello-Car and Gebauer-Baroni methods [7,8]. The unit cell of bulk silicon was calculated using $6 \times 6 \times 6$ k -points. During calculation of the P:Si system characteristics, for the 64 silicon atom model containing one phosphorus atom we used a special $3 \times 3 \times 3$ k -points set with the 476.2 eV cut-off energy of plane waves. The equilibrium model was obtained by means of free relaxation of all atoms in the structure. For this purpose, the 64-atom model was placed in a cell with a $10.862 \times 10.862 \times 10.862 \text{ \AA}^3$ volume. Atomic relaxation was carried out to the interatomic forces' value of about $0.026 \text{ eV \AA}^{-1}$.

In this work, we studied the quantum qubit behaviour based on an impurity phosphorus atom in a bulk silicon lattice. It was shown that the equilibrium orientation of the P atom spin in the Bloch sphere corresponds to the polar co-ordinates $(\theta; \varphi) = 176^\circ; 102^\circ$ and this orientation is characterized by the $|1\rangle$ quantum state. We calculated the local magnetic field $B(r)$, the local magnetization $m(r)$ and the spin current density $\hat{V} \cdot J^{KS}(r)$ created by the excess electron of the phosphorus atom. The results show that for different spin directions ($|0\rangle$ and $|1\rangle$ - quantum states) there

is a different direction of the spin current densities $\hat{V} \cdot J^{KS}(r)$. We are confident that the obtained results are promising for use in qubit design technology for future quantum computers.

Acknowledgements

This work was supported in accordance with the State assignment for the research work implementation from the Ministry of Education and Science (FEME-2020-0005). The research is carried out using the equipment of the Shared Facility Centre 'Data Centre of FEB RAS' (Khabarovsk, Russia) and partly using a cluster at the shared research facilities of HPC computing resources at Lomonosov Moscow State University supported by the project RFMEFI62117X0011. The authors would like to thank the Irkutsk Supercomputer Centre of SB RAS for providing access to HPC-cluster 'Akademik VM Matrosov' (Irkutsk Supercomputer Centre of SB RAS, Irkutsk: ISDCT SB RAS; <http://hpc.icc.ru>, accessed 11.07.2019).

References

- [1] L. Oberbeck, T. Hallam, N.J. Curson, M.Y. Simmons, R.G. Clark. *Appl. Surf. Sci.* **212–213** (2003) 319.
- [2] M. Fuechsle, J.A. Miwa, S. Mahapatra, H. Ryu, S. Lee, O. Warschkow, L.C.L. Hollenberg, G. Klimeck, M.Y. Simmons. *Nat. Nanotechnol.* **7** (2012) 242.
- [3] M.A. Broome, S.K. Gorman, M.G. House, S.J. Hile, J.G. Keizer, D. Keith, C.D. Hill, T.F. Watson, W.J. Baker, L.C.L. Hollenberg, M.Y. Simmons. *Nat. Commun.* **9** (2018) 980.
- [4] B.E. Kane. *Nature* **393** (1998) 133.
- [5] H. Buch, S. Mahapatra, R. Rahman, A. Morello, M.Y. Simmons. *Nat. Commun.* **4** (2013) 2017.
- [6] P. Giannozzi, O. Andreussi, T. Brumme, O. Bunau, M.B. Nardelli, M. Calandra, R. Car, C. Cavazzoni, D. Ceresoli, M. Cococcioni, N. Colonna, I. Carnimeo, A.D. Corso, S. de Gironcoli, P. Delugas, R.A. Jr DiStasio, A. Ferretti, A. Floris, G. Fratesi, G. Fugallo, R. Gebauer, U. Gerstmann, F. Giustino, T. Gorni, J. Jia, M. Kawamura, H-Y Ko, A. Kokalj, E. Küçükbenli, M. Lazzeri, M. Marsili, N. Marzari, F. Mauri, N.L. Nguyen, H-V Nguyen, A. Otero-de-la-Roza, L. Paulatto, S. Poncè, D. Rocca, R. Sabatini, B. Santra, M. Schlipf, A.P. Seitsonen, A. Smogunov, I. Timrov, T. Thonhauser, P. Umari, N. Vast, X. Wu, S. Baroni. *J. Phys.: Condens. Matter* **29** (2017) 465901.
- [7] T. Oda, A. Pasquarello, R. Car. *Phys. Rev. Lett.* **80** (1998) 3622.
- [8] R. Gebauer, S. Baroni. *Phys. Rev. B* **61** (2000) R6459.

II. 4th group material's alloy based on Si, Ge, Sn & Pb: formation, structure and properties and properties

Structural transformations on the Si(111) surface observed during Sn adsorption, desorption, and electromigration

A.S. Petrov^{*1}, D.I. Rogilo¹, D.V. Sheglov¹, A.V. Latyshev^{1,2}

¹Rzhanov Institute of Semiconductor Physics of SB RAS, 13 pr. Lavrentieva, Novosibirsk 630090, Russia

²Novosibirsk State University, 2 Pirogova St., Novosibirsk 630090, Russia

*e-mail: petrov_alexey13@mail.ru

The structures based on the fourth group IV elements (Si, Ge, Sn) are promising for micro- and photoelectronic applications [1,2]. GeSn solid solutions on the Si(111) surface are of particular interest in comparison with those on the Si(100) due to higher hole mobility [2]. During the growth of GeSn structures, Sn act not only as a part of a solid solution but also as a surfactant [3,4]. Moreover, Sn-induced reconstructions on the Si(111) surface is a prototype system for two-dimensional Mott state [5]. Determining the processes of Sn layers formation on the Si(111) surface at early stages can provide essential fundamental information about Sn adatom behavior on the Si crystal surface for further technology applications.

It was shown by reflection high-energy electron diffraction (RHEED) technique [6] that Sn deposition on clear Si(111)-(7×7) surface induces two main reconstructions depending on substrate temperature: ($\sqrt{3}\times\sqrt{3}$) and ($2\sqrt{3}\times 2\sqrt{3}$) at total Sn coverage from 1/3 to about 1 ML (1 ML = 7.8×10^{14} cm⁻²), further Sn deposition leads to “1×1” structure observation. Si(111) surface morphology and properties with ($\sqrt{3}\times\sqrt{3}$) and ($2\sqrt{3}\times 2\sqrt{3}$) Sn-induced structures were widely investigated by scanning tunneling microscopy at temperatures up to 200°C [7,8]. However, published data lack *in situ* investigations of the morphological and structural transformations during Sn adsorption in 300–700°C temperature range typical for epitaxial growth of Ge films on the Si surface [3,4,9].

In this work, we have studied the processes on clean step-bunched Si(111) surface with wide (up to 10 μm) atomically flat terraces during monolayer Sn deposition at substrate temperatures up to 800°C by *in situ* ultrahigh vacuum reflection electron microscopy (UHV REM). All surface transformations induced by Sn deposition at various temperatures and fluxes were observed *in situ* for the first time, corresponding RHEED patterns were also observed and compared with the published ones. The REM images show the nucleation of ($\sqrt{3}\times\sqrt{3}$) domains when total Sn coverage approaches 1/3 ML. These domains nucleate in the terrace centers and on (7×7) domains boundaries near the steps, expand, and occupy the entire surface at 1/3 ML coverage. When total Sn coverage approaches 1 ML, Sn amorphous phase with atom density more than 7.8×10^{14} cm⁻² nucleates and expands on the terraces. When the whole surface is covered by this Sn amorphous layer, no ($\sqrt{3}\times\sqrt{3}$) reflections are observed in RHEED pattern, which corresponded to a disordered “1×1”-Sn phase. Further Sn deposition to the 1.5–2 ML total amount leads to the formation of 3D Sn islands on the surface (mostly near the step bunches). When Sn deposition stopped at this stage, and at substrate temperature was in 400–800°C

range, 3D islands gradually decrease in size and disappear. Next, as Sn desorbs, “1×1” \Rightarrow ($\sqrt{3}\times\sqrt{3}$) surface structural transition is observed. It should be pointed, that some “1×1” domains remain on the surface at the step edges. The ($\sqrt{3}\times\sqrt{3}$) structure with 1/3 ML Sn coverage is stable at $T = 200\text{--}850^\circ\text{C}$ and disappears after annealing at $T > 900^\circ\text{C}$ only. The ($2\sqrt{3}\times 2\sqrt{3}$) reconstruction appears at $T < 200^\circ\text{C}$ [6–8] and was observed only in surface regions with Sn coverage was higher than 1 ML (“1×1” domains), which corresponds to the ($2\sqrt{3}\times 2\sqrt{3}$) unit cell model consisting of 14 Sn atoms (1.17 ML coverage per unit cell) proposed by Törnevik et al. [7].

In our experiments, the samples were heated resistively by DC or AC passing. It was shown that the electric field strongly affects the formation and disappearance of Sn amorphous layer or, in other words, ($\sqrt{3}\times\sqrt{3}$) \Leftrightarrow “1×1” phase transition. During Sn deposition “1×1” domains expand on the surface in the direction of the electric field at the substrate. Under zero Sn flux, “1×1” domains move in the opposite direction, and, in the regions free from these domains the ($\sqrt{3}\times\sqrt{3}$) structure is observed again, while the total Sn amount on the whole surface has not changed. During these processes, we have found that atomic steps and step bunches serve as barriers for step-up Sn electromigration on the Si(111)-($\sqrt{3}\times\sqrt{3}$)-Sn surface, which is consistent with the idea of the presence of energy barriers at the step edge. Controlled alternation of the electric field on the Si(111) surface allows the creation of self-organized patterns having regions with ($2\sqrt{3}\times 2\sqrt{3}$) and ($\sqrt{3}\times\sqrt{3}$) structures where Sn concentration is enhanced (≥ 1 ML) and reduced ($\sim 1/3$ ML), respectively.

Acknowledgements

This work was performed on the equipment of CKP “Nanostruktury” and was supported by RFBR [19-72-30023].

References

- [1] S. Wirths, D. Buca, S. Mantl, Prog. Cryst. Growth Charact. Mater. **62** (2016) 1.
- [2] T. Maeda, W. Jevasuwan, H. Hattori, N. Uchida, Jpn. J. Appl. Phys. **54** (2015) 04DA07-1.
- [3] A. E. Dolbak, B. Z. Olshanetsky, Cent. Eur. J. Phys. **6** (2008) 634.
- [4] X. W. Lin, Z. Liliental-Weber, J. Washburn, E. R. Weber, J. Vac. Sci. Technol. B **13** (1995) 1805.
- [5] M. Jäger, C. Brand, A. P. Weber, M. Fanciulli, Physical Review B **98** (2018) 165422.
- [6] T. Ichikawa, Surf. Sci. **140** (1984) 37.
- [7] C. Törnevik, et al., Surf. Sci. **314** (1994) 179.
- [8] T. Ichikawa, K. Cho, Jpn. J. Appl. Phys. **42** (2003) 5239.
- [9] A. S. Petrov, D. I. Rogilo, D. V. Sheglov, A. V. Latyshev, J. Cryst. Growth, **531** (2020) 125347.

Effect of stoichiometry on aluminum-induced crystallization of a-SiO_x thin films

A.O. Zamchiy^{*1,2}, E.A. Baranov¹, I.E. Merkulova^{1,2}, N.A. Lunev^{1,2}

¹ Kutateladze Institute of Thermophysics SB RAS, Ac. Lavrentiev Ave. 1, 630090 Novosibirsk, Russia

² Novosibirsk State University, Pirogova Str. 2, 630090 Novosibirsk, Russia

*e-mail: zamchiy@gmail.com

The integration of silicon electronics with low-cost and low-temperature non-silicon substrates (e.g. glass) remains an attractive challenge for modern electronics. Low-temperature silicon thin films deposition leads to formation of amorphous material. Thus, the fabrication of crystalline silicon on glass substrates is carried out as part of a two-stage process including deposition of amorphous silicon (a-Si) followed by crystallization.

Up to present, the most known crystallization techniques for poly-Si thin films fabrication are: solid phase crystallization (SPC) [1], liquid phase crystallization [2] and metal-induced crystallization, MIC) [3] of a-Si. SPC requires higher temperatures (600-650°C) and significantly longer annealing time (tens of hours) to achieve complete crystallization while producing crystalline material with small grain sizes [4]. MIC, specifically aluminum-induced crystallization, is a promising technique allowing to obtain large-grained (>10 μm) poly-Si thin films on glass at lower temperatures (< 577°C) and times (few hours) compared to SPC [5].

In our recent work [6] we demonstrated successful using of a-SiO_x instead of a-Si as the initial silicon-containing layer in AIC process. In the article, it is shown that using a-SiO_x allows one to omit the additional time-consuming step associated with the formation of an Al oxide membrane layer during the fabrication of the initial stack. This, along with the high quality of crystalline silicon obtained, makes it possible to regard a-SiO_x as a promising precursor layer in the AIC process.

A-SiO_x thin films with different stoichiometric coefficient ($x = 0.2 - 1$) were fabricated from the SiH₄-O₂ gas mixture by plasma-enhanced chemical vapor deposition (PECVD) method. The oxygen content in the films was varied by changing the SiH₄ and O₂ gas flow ratio. Borosilicate glass and monocrystalline wafers were used as substrates. The composition and the bonding structure of the films were investigated by energy dispersive X-ray spectroscopy and Fourier transform infrared spectroscopy, respectively. Next, 4-nm-thick SiO₂ layers were formed by PECVD on the top of a-SiO_x film which acted as a membrane layer in the AIC process. Afterwards, Al films with a thickness of about 200 nm were deposited on a-SiO_x layers by the thermal vacuum evaporation method. The a-SiO_x thin film thickness was varied from 270 to 550 nm depending on the stoichiometry of the material. The initial a-SiO_x/Al thickness ratio was adjusted taking into account the a-Si/Al criterion suggested in [7] and the reduced Si atomic density in a-SiO_x material

compared to a-Si [8]. Finally, the substrate/a-SiO_x/SiO₂/Al samples were annealed to high-vacuum (~ 10⁻⁴ Pa) at temperatures of 475 - 550°C for 2 - 70 hours. The crystalline properties of the material were investigated by Raman spectroscopy and X-ray diffraction method. The crystal orientations and the grain sizes of the obtained poly-Si films were investigated by electron backscatter diffraction (EBSD) measurements. The surface morphology of the samples including the continuity of formed poly-Si and crystallized fraction (percentage of the surface covered by poly-Si) was investigated by optical microscopy studies. The realization of the AIC process was confirmed by means of transmission electron microscopy performed in the cross-sectional geometry.

Raman spectroscopy investigations revealed the formation of the crystalline material (the presence of a narrow peak at ~ 519 cm⁻¹). XRD and EBSD analyses revealed formation of poly-Si with (111) crystal orientation. The morphology, composition, and structure of the layers formed in the AIC process depending on the initial a-SiO_x composition were studied.

Acknowledgements

The study was financially supported by the Russian Science Foundation, project # 19-79-10143.

The authors thank Dr. V.A. Volodin for Raman measurements and Dr. E.A. Maximovskiy for EBSD measurements.

References

- [1] S.H. Sedani, O.F. Yasar, M. Karaman, R. Turan. *Thin Solid Films* **694** (2020) 1376392.
- [2] M.Z. Pakhuruddin, J. Huang, S. Kühnappel, J. Dorel, S. Gall, S. Varlamov. *J. Mater. Sci.: Mater. Electron.* **28** (2017) 10391.
- [3] S. Gall in: K. Nakajima, N. Usami (Eds.), *Crystal Growth of Silicon for Solar Cells*, Advances in Materials Research, Springer, Berlin, Heidelberg, 2009, 193.
- [4] S. Gall, C. Becker, E. Conrad, P. Dogan, F. Fenske, B. Gorka, K.Y. Lee, B. Rau, F. Ruske, B. Rech. *Sol. Energy Mater. Sol. Cells* **93** (2009) 1004.
- [5] R. Numata, K. Toko, N. Saitoh, N. Yoshizawa, N. Usami, T. Suemasu. *Cryst. Growth Des.* **13** (2013) 1767.
- [6] A.O. Zamchiy, E.A. Baranov, S.Ya. Khmel, V.A. Volodin, V.I. Vdovin, A.K. Gutakovskii. *Appl. Phys. A* **124** (2018) 646.
- [7] O. Nast and S.R. Wenham. *J. Appl. Phys.* **88** (2000) 124.
- [8] A.O. Zamchiy, E.A. Baranov, I.E. Merkulova, S.Ya. Khmel, E.A. Maximovskiy. *J. Non-Cryst. Solids* **518** (2019) 43.

Formation and structure of epitaxial GaSb nanodots in monocrystalline silicon

D.L. Goroshko¹, E.Yu. Subbotin^{*1}, E.A. Chusovitin¹, S.V. Chusovitina¹, S.A. Dotsenko¹,
A.K. Gutakovskii², N.G. Galkin¹

¹ Institute of Automation and Control Processes of FEB RAS, 5 Radio St., Vladivostok 690041, Russia

² Rzhzanov Institute of Semiconductor Physics of SB RAS, 13 pr. Lavrentieva, Novosibirsk 630090, Russia

*e-mail: jons712@mail.ru

Increasing the efficiency and integration of modern chips require thermal management. Recently, μ -TEG integrated with silicon circuit are widely used for these purposes [1, 2]. High ZT materials [3] is not suitable because they cannot be on-chip integrated seamlessly. There are reports about microstructuring of silicon by photolithography but such generators have low efficiency [1]. Therefore, it is necessary to find the material with required thermoelectric properties and develop the technology of integration silicon with it.

Semiconductor gallium antimonide has a good electric properties but lattice mismatch with silicon is 12 %. Formation GaSb nanodots (ND) embedded in monocrystalline silicon decreases the mismatch strain and increase phonon scattering on Si/GaSb interface. In literature, there are few works about embedding the dots in a silicon, but there is some experience in growth of uncovered islands on a silicon surface by MBE [4]. Due to the special behavior of the atoms at high temperature of MBE different buffer layers or the mixture oversaturated of Sb atoms are used [4]. These approaches are not suitable for silicon multilayer heterostructures growth because excess atoms of Sb or other elements could unintentionally contribute to electric properties. It was demonstrated that using the stoichiometric mixture of Ga-Sb by SPE method GaSb islands with high surface concentration ($2.5 \times 10^{11} \text{ cm}^{-2}$) were formed [5]. By combining SPE and MBE methods, multilayer silicon heterostructures with epitaxial embedded GaSb nanodots have made [6].

Monocrystalline high resistance silicon with orientation (111) were use as substrate. As a surface for growth was chosen mixture of Sb's surface reconstructions (SR) on Si(111): Si(111)-(2 \times 1) and Si(111)-($\sqrt{3} \times \sqrt{3}$)-R30°. GaSb NDs were formed by SPE through deposition of stoichiometric mixture of Ga-Sb 0.3 and 0.5 nm thickness at room temperature and subsequent annealing at 200 and 380 °C. By further silicon deposition at 450 and 609 °C, embedding the dots in silicon matrix was performed. By sequential repetition of such steps, four-layer samples were formed. Each growth stage was controlled with LEED, AES and EELS. After the growth procedures, samples were analyzed with AFM and TEM. Islands parameters and their concentration were calculated by BGA program [7].

Previously, it was demonstrated that such preliminary formed reconstructions prevent decomposition of GaSb nanodots on bare silicon surface at high MBE temperature on embedding stage [5]. In both mixture thickness concentration of GaSb islands is $\sim 2 \times 10^{11} \text{ cm}^{-2}$, average lateral size is 14 nm and height is 1.7 nm. These samples have smooth surface with root mean square 1.09 – 1.7 nm.

Defect density of these structure for both thickness is 10^{11} - 10^{12} cm^{-2} . Greater defectness correspond to greater concentration of islands. Two different characteristic size relations were observed: 2.2×3.6 and 6.2×10.4 nm. Due to bulk pseudomorphism small islands are higher deformed ($-3.84 \div -0.85\%$) than large islands ($-1.12 \div -0.46\%$).

Planes the GaSb (11-1) of large islands are rotated on 8.7° , distance between of these planes is $3.427 \div 3.618 \text{ \AA}$ (for relaxed lattice the parameter is 3.5195 \AA). Rotation of the planes allows decrease internal energy of nanodots if interface area is large. In case of the small interface, the rotation is not observed. For both sizes of crystal the same epitaxial relations GaSb(111)||Si(111) and GaSb[1-10]||Si[1-10] are observed that indicate on epitaxial embedding of GaSb nanodots in silicon [6].

Sample with GaSb nanodots embedded in undoped silicon has Seebeck coefficient $-510 \mu\text{W/K}$ at 420 K, that two times greater than the parameter of silicon. Conductivity of the samples is $11 (\Omega \times \text{cm})^{-1}$. Using of high doped silicon increases conductivity to $56 (\Omega \times \text{cm})^{-1}$ (p-Si) and $154 (\Omega \times \text{cm})^{-1}$ (n-Si). Thermo-EMF these samples is $740 \mu\text{W/K}$ at 470 K and $-670 \mu\text{W/K}$ at $510 \div 580 \text{ K}$, respectively. Power factor of these structure is $3 \text{ mW/m} \times \text{K}^2$ for p-samples and $6.2 \text{ mW/m} \times \text{K}^2$ for n-samples at 450 K [6].

Acknowledgements

The work was performed with support of Russian Found of Fundamental Research (grant № 17-52-52013)

References

- [3] G. Hu, et al., Nature Electronics **2** (2019) 300.
- [4] S. Zhou. Prospects of Thermoelectric Energy Harvesting in 3D ICs //2019 IEEE MTT-S International Wireless Symposium (IWS). – IEEE, 2019. – C. 1-3.
- [5] B. Owens-Baird, Encyclopedia of Inorganic and Bioinorganic Chemistry. 2011. – pp. 1-35.
- [6] R. Machida, et al., Physica Status Solidi (b) **253** (2016) 648.
- [7] D.L. Goroshko, et al. Semiconductor Science and Technology. – 2020 (accepted in print).
- [8] D. L. Goroshko, et al., Japanese Journal of Applied Physics. **59** (2020) SFFB04.
- [9] S.A. Balagan, et al., 2017 Second Russia and Pacific Conference on Computer Technology and Applications (RPC). IEEE, 2017. pp. 19-24.
- [10] D.L. Goroshko, et al., Defect and Diffusion Forum **386** (2018) 102.

Etching of the Si(111) surface by a selenium molecular beam

S.A. Ponomarev^{*1,2}, D.I. Rogilo², A.S. Petrov², L.I. Fedina², D.V. Shcheglov², A.V. Latyshev^{1,2}

¹ Novosibirsk State University, 2 St. Pirogova, Novosibirsk 630090, Russia

² Rzhanov Institute of Semiconductor Physics of SB RAS, 13 pr. Lavrentieva, Novosibirsk 630090, Russia

*e-mail: s.ponomarev1@q.nsu.ru

The study of metal chalcogenide films—their properties and growth methods on various semiconductor substrates—is a rapidly developing area of condensed matter physics [1]. Chalcogen atoms (Se), the adsorption of which is a necessary step of the substrate preparation, strongly interact with the silicon surface and weaken the covalent bonds of the surface atoms Si [2–4]. At elevated temperatures, this interaction of the Si(111) surface with a Se molecular beam leads to the formation and desorption of SiSe₂ molecules [5].

In this work we used *in situ* ultrahigh vacuum reflection electron microscopy (UHV REM) interaction of the selenium molecular beam with the surface of Si(111) were studied at deposition rates of up to 10 BL/s (1 BL=1.56×10¹⁵ cm⁻²) and substrate temperatures in 560–1280 °C range. During the *in situ* experiment, the nucleation of two-dimensional (2D) vacancy islands and the motion of atomic steps in the ascending direction were observed [5]. These processes correspond to the etching of the Si(111) surface by the Se molecular beam. *Ex situ* analysis of surface morphology by the atomic force microscopy (AFM) shows the nucleation of 2D vacancy islands (0.3 nm in depth) on wide terraces and monatomic steps with serpentine shape.

Structural transitions induced by selenium molecular beam on the Si(111) surface were studied by reflection high-energy electron diffraction. Depending on the surface etching rate recorded at 800 °C, the phase transition temperatures of the surface were measured. A phase diagram of the surface structure (“1×1”-Se, 7×7 superstructure, or “1×1” above 830 °C) in 530–1250 °C substrate temperature range and Se deposition rates up to ~ 1 BL/s has been determined. The impurity-induced “1×1”-Se phase corresponds to 0.25 BL Se coverage [3]. We detected a lowering of the “1×1” ↔ 7×7 superstructural transition temperature near 830 °C when the vicinal surface Si(111) is exposed to the Se molecular beam. Nevertheless, under the same conditions, the superstructural transition temperature increases by several degrees in the central regions of large terraces.

The 7×7 ↔ “1×1”-Se superstructural transition temperature was measured as a function of the etching rate. The etching rate was equal to the flux of desorbed SiSe₂ molecules. Based on the fact that the 7×7 ↔ “1×1”-Se transition occurs at the same Se coverage, we have

determined the desorption energy of the SiSe₂ molecules (2.65 eV). This energy agrees with the published value [3]. Below the temperature of this structural transition, the etching rate decreases rapidly, which corresponds to the etching kinetics limited by the formation and desorption of the SiSe₂ molecules.

We have studied the temperature dependence of the Si outflow rate J_{Si}^E . The net silicon outflow flux includes sublimation and etching fluxes J_{subl} and J_{etch} , respectively. The sublimation flux depends on the substrate temperature only. When the temperature is high enough that Si(111) surface is not completely covered by “1×1”-Se structure, the etching rate is constant and is limited by the Se deposition rate. In this temperature range, the silicon outflow rate remains equal to the etching rate until the silicon sublimation flux is negligible. The experimented data are fitted well by this approximation:

$$J_{Si}^E(T) = J_{subl} + J_{etch} = B * \exp\left(-\frac{E_{subl}}{kT}\right) + J_{etch},$$

where k is Boltzmann’s constant, B is a setting parameter, E_{subl} is a Si sublimation energy. This formula has two limiting cases. In the low-temperature limit, J_{subl} is much less than J_{etch} because of high silicon sublimation energy (4.09 eV [6]), which results in $J_{Si}^E(T) \approx J_{etch}$. In the high-temperature limit, J_{subl} is much greater than J_{etch} ; therefore $J_{Si}^E(T) \approx J_{subl}$.

Acknowledgments

This research was performed on the equipment of CKP “Nanostruktury” and was financially supported by the Russian Science Foundation [grant number 18-72-10063].

References

- [1] S Vishwanath, Xinyu Liu, S. Rouvimov, L Basile, Ning Lu, A. Azcatl, K. Magno, J. Mater. Res., **31** (2016) 900.
- [2] B.N. Dev, T. Thundat, W.M. Gibson, J. Vac. Sci. Technol. A **3** (1985) 946.
- [3] A.C. Papageorgopoulos, M. Kamaratos Surface Science **504** (2002) 191.
- [4] S.Q. Wu, Y. Zhou, Q.-H. Wu, C.I. Pakes, Z. Zhu, Chem. Phys. **382** (2011) 41.
- [5] D.I. Rogilo, L.I. Fedina, S.A. Ponomarev, D.V. Shcheglov, A.V. Latyshev, Journal of Crystal Growth **529** (2020) 125273.
- [6] A.B. Pang, K.L. Man, M.S. Altman, T.J. Stasevich, F. Szalma, T.L. Einstein, Phys. Rev. B **77** (2008) 115424.

Current relaxations in MIS structures based on PbSnTe:In films with low conductivity

A.N. Akimov¹, I.O. Akhundov¹, V.S. Epov^{1,*}, E.V. Fedosenko¹, V.A. Golyashov^{1,3}, D.V. Gorshkov¹, D.V. Ishchenko¹, A.E. Klimov^{1,2}, E.V. Matyushenko¹, I.G. Neizvestny^{1,2}, G.Yu. Sidorov¹, S.P. Suprun¹, A.S. Tarasov¹, O.E. Tereshchenko^{1,3}

¹ Rzhanov Institute of Semiconductor Physics of SB RAS, 13 pr. Lavrentieva, Novosibirsk 630090, Russia

² Novosibirsk State Technical University, 20 pr. K. Marx, Novosibirsk 630073, Russia

³ Novosibirsk State University, 1 Pirogova St., Novosibirsk 630090, Russia

*e-mail: epov@isp.nsc.ru

Solid solutions of $\text{Pb}_{1-x}\text{Sn}_x\text{Te}$ are of particular interest because in the composition range with an inverted energy spectrum $x > x_{\text{inv}}$, they exhibit the properties of a topological crystalline insulator (TCI) [1]. At helium temperatures $x_{\text{inv}} \approx 0.35$ [2]. A wide range of homogeneity of PbSnTe is associated with a large concentration of electrically active intrinsic point defects (up to 10^{19} cm^{-3}) and a high conductivity at temperatures up to 4.2 K. Therefore, the surface conductivity due to the Dirac states in the TCI phase is significantly shunted by the bulk even in thin-film PbSnTe samples. Depending on x and temperature, the low-frequency permittivity of PbSnTe can exceed $\varepsilon > (2000-10000)$. Together with high conductivity, this makes it extremely difficult or impossible to study the surface of PbSnTe using MIS structures and the field effect. However, it is known [3] that the addition of indium to PbSnTe of certain compositions at concentrations up to several at. % can reduce the free carrier concentration to the insulating state of PbSnTe:In at $T = 4.2 \text{ K}$. This occurs in the range of $x \approx (0.24-0.3)$ or some higher, i.e., near the range of the TCI compositions. Thus, on the basis of low conductive PbSnTe:In, it is possible to create structures with a surface layer in the TCI phase not shunted by the bulk, and to create MIS structures and study the PbSnTe:In surface using the field effect.

For the first time, the authors have demonstrated the possibility to change, under the action of a gate voltage, the conductivity of PbSnTe:In-based MIS structure channel up to 10^6 times and even more. The experimental MIS structures were fabricated on the basis of single-crystal PbSnTe:In ($x \approx 0.3$) near micron thick films grown by molecular beam epitaxy on (111)BaF₂ substrates. The gate dielectric was made of a 8 μm thick Mylar film and 72–100 nm thick Al₂O₃ layer grown by atomic layer deposition. The source and drain of n^+ -type conductivity were formed by diffusion of indium and separated by an insulating space (channel) near 50 micron wide (or less) and near 0.1 cm long. The electron concentration in the channel was $n_0 < 10^{13} \text{ cm}^{-3}$ at $T < 20 \text{ K}$. At $T = 4.2 \text{ K}$ and zero gate voltage, the source/drain current $I_{\text{sd}} < 10^{-11} \text{ A}$ at the source/drain voltage $U_{\text{sd}} = 0.1 \text{ V}$, i.e. $U_{\text{sd}}/I_{\text{sd}} > 10^{10} \Omega$. The source/drain current-voltage characteristics were nonlinear

and corresponded to the model of currents limited by a space charge. In MIS structures with a Mylar film, the gate voltage U_{gate} was varied in the range $-1250 \text{ V} < U_{\text{gate}} < +1250 \text{ V}$. The dynamics of I_{sd} changes was studied using a linear sweep with $U'_{\text{gate}} = (2.5-250) \text{ V/s}$, and a quick (within submilliseconds) switching from $U_{\text{gate}} = -1250 \text{ V}$ to $U_{\text{gate}} = +1250 \text{ V}$ and vice versa. With a quick application of $U_{\text{gate}} = +1250 \text{ V}$, the channel conductivity linearly depended on U_{sd} with resistance $R \approx 2000 \Omega$. At constant $U_{\text{gate}} = +1250 \text{ V}$, a long-term nonexponential relaxation of I_{sd} was observed with characteristic times $\tau \sim (1-600) \text{ s}$ in the interval of $t \approx (0-400) \text{ s}$ after stopping the U_{gate} sweep. The application of negative U_{gate} up to $U_{\text{gate}} = -1250 \text{ V}$ did not noticeably increase the channel conductivity. The features of current relaxation under illumination at various gate voltages and changes in the relaxation behaviour at higher sample temperature were also studied.

It was found that the relaxation behaviour of both the current without illumination and the photocurrent strongly depended on the conditions at the PbSnTe:In surface in the channel region determined by its treatment using a weak solution of HCl in isopropyl alcohol that removed oxides from the surface, passivation with Al₂O₃, or by exposition to the atmosphere. The authors consider a model where the gate field is shielded both by free electrons injected from the source and by the fixed surface charge due to the recharging of various types of surface traps with various ionization energies and time constants when U_{gate} is applied.

Acknowledgements

This study was supported by the Russian Foundation for Basic Research, project no. 20-02-00324a.

References

- [1] T. Liang, S. Kushwaha, J. Kim, Q. Gibson, J. Lin, N. Kiuoussis, R. J. Cava, N. Phuan Ong. *Science Advances* **3** (2017) 1602510.
- [2] W.W. Anderson. *IEEE Journal of Quantum Electronics* **QE-13** (1977) 532.
- [3] B. A. Volkov, L. I. Ryabova, D. R. Khokhlov. *Physics – Uspekhi* **45** (2002) 819.

Magneto-optical properties of Ge nanoparticles in the GeO matrix

A.V. Sherepa¹, V.N. Zabluda¹, K.N. Astankova², I.A. Azarov², A.E Sokolov¹

¹Kirensky Institute of Physics Akademgorodok 50, bld. 38, Krasnoyarsk, 660036 Russia

²Rzhanov Institute of Semiconductor Physics, Siberian Branch of the Russian Academy of Sciences, 630090 Novosibirsk, Russia

*e-mail: ann12733283@ya.ru

Each year, scientists around the world studying nanoparticles seemingly well-studied substances are discovering their new properties. For example, the magneto-optical properties (magnetic circular dichroism (MCD)) of noble metal nanoparticles are no longer surprising [1], this phenomenon is associated with the presence of surface plasmon resonance in a metal nanoparticles. Recently, our group discovered magnetic circular dichroism in quantum dots of CdTe [2]. This work is a continuation of the study of MCD in semiconductor nanoparticles.

The study of Ge nanoparticles made it possible to use devices based on Ge instead of silicon analogues. In our work, we studied the optical and magneto-optical properties of the sample from Rzhanov Institute of Semiconductor Physics under study consists of 3 pairs of alternating layers of GeO₂ {Ge-HK}/SiO₂ on a substrate (fused silica). The GeO₂ heterolayer {Ge-NK} is a composite material consisting of a GeO₂ dielectric matrix with Ge nanoclusters embedded in it (amorphous or crystalline). The thickness of each GeO₂ {Ge-NK} heterolayer varies wedge-shaped from 10 to 40 nm, and the thickness of each SiO₂ layer is 10 nm. The size of Ge nanocrystals is ~ 2-4 nm.

The MCD spectra of Ge-GeO₂ were measured on a spectropolarimetric setup developed in Kirensky Institute of Physics in the region of 300–1200 nm was measured

using a spectro-polarimetric research facility manufactured at the Kirensky Institute of Physics using an MDR-12 monochromator. In this case, the modulation of the polarization state of the light wave was used: from right to left circular polarization.

In the presence of the MCD effect in the sample under study, the absorption coefficients of light waves polarized along the right and left circles relative to the direction of the magnetic moment of the sample are different, so that the light flux passing through the sample and then incident on the photomultiplier is modulated in intensity. The constant component of the photocurrent of the multiplier was kept at the same level when the light wavelength was changed, and thus the variable signal at the output of the photomultiplier was proportional to the magnitude of the MCD.

The paper will also discuss the nature of the magneto-optical properties of semiconductor and some other plasmon resonance nanoparticles.

References

- [1] A.E. Sokolov, S.G. Ovchinnikov, V.N. Zabluda, A.M. Kal'sin, Ya.V. Zubavichus, JETP Letters **97** (2013) 98.
- [2] A.V. Malakhovskii, A.E. Sokolov, A.S. Tsipotan, S.M. Zharkov, V.N. Zabluda. Physics Letters A **382** (2018) 980.

Indium-based metal induced crystallization of amorphous silicon suboxide thin films

A.O. Zamchiy^{*1,2}, E.A. Baranov¹, I.E. Merkulova^{1,2}, N.A. Lunev^{1,2}

¹ Kutateladze Institute of Thermophysics SB RAS, Ac. Lavrentiev Ave. 1, 630090 Novosibirsk, Russia

² Novosibirsk State University, Pirogova Str. 2, 630090 Novosibirsk, Russia

*e-mail: zamchiy@gmail.com

Polycrystalline silicon (poly-Si) thin films of on foreign inexpensive substrates (e.g., glass) are widely used in the manufacture of large-area semiconductor devices, such as solar cells and thin-film transistors [1]. The most common methods for producing thin poly-Si films low-cost substrates are solid phase crystallization (SPC) [2], liquid phase crystallization [3] and metal-induced crystallization (MIC) [4] of amorphous silicon (a-Si). The MIC method is based on the use of various metals (aluminum, gold, nickel) [5], which induce the crystallization of a-Si during isothermal annealing. In the annealing process, the metal acts as a catalyst for the crystallization process, which reduces the temperature and time of the process.

In the present work, the possibility of obtaining poly-Si by indium-induced crystallization (InIC) of amorphous silicon suboxide (a-SiO_x, 0 < x < 2) [6] is shown for the first time. Indium belongs to the group of metals that do not form silicides with silicon, is compatible with silicon technology, is widely used in electronics and photovoltaics, and also has a low melting point - 157°C. Previously, the fabrication of poly-Si films has been demonstrated by the authors in the aluminum-induced crystallization process of a-SiO_x [7].

400-nm-thick a-SiO_x (x = 0.5) thin films were fabricated from the SiH₄-O₂ gas mixture by plasma-enhanced chemical vapor deposition. Borosilicate glass and quartz were used as substrates. Next, In films with a thickness of about 420 nm were deposited on a-SiO_{0.5} layers by the thermal vacuum evaporation method. Finally, the obtained samples were subjected to high-vacuum furnace annealing (residual vacuum ~ 10⁻⁴ Pa) at temperatures of 550 - 850°C for 5 hours. The crystalline properties of the material were investigated by Raman spectroscopy (RS) using T64000 Horiba Jobin-Yvon spectrometer at λ = 514.5 nm. Optical and scanning electron microscopy (OM and SEM, respectively) methods were used to study the morphology of the initial and annealed samples.

According to OM investigations, three characteristic morphologies of the material formed as a result of annealing at 600°C can be noted. Firstly, there is In-free a-SiO_x film. Secondly, there are In particles on the surface of a-SiO_x film. Regions with the described morphology are also characteristic of the material annealed at 550°C. Thirdly, during annealing at 600°C, dark micron-size areas are formed, which most likely form at the sites of the evaporated during annealing In. The indicated morphology is absent in the samples annealed at the lower temperature.

An increase in the process temperature to 850°C leads to the complete evaporation of In from the surface of the sample. For these annealing conditions, the morphology of two species is distinguishable on the surface of the sample, In-free a-SiO_x film, as well as dark regions, the concentration of which is significantly higher compared to the lower annealing temperatures. A more detailed study of the morphology of dark areas, performed using SEM, shows the formation of micron-sized structures that rise above the surface of the sample and while are in the depressions. RS investigations revealed the polycrystalline nature of the micron-sized structures formed.

As a result of the work, it was shown that the use of In in the annealing process of a SiO_{0.5} thin films allowed to decrease the crystallization temperature to 600°C which was significantly lower than the SPC temperature of the material, 850°C. The high-vacuum InIC of a-SiO_{0.5} led to the formation of free-standing micron-sized polycrystalline silicon particles. Our further studies will be aimed at a more detailed study of the morphology and properties (structural, thermal conductivity, etc.) of the obtained crystalline silicon structures, which seems to be a very attractive task.

Acknowledgements

The study was financially supported by the grant of the President of the Russian Federation, project № MK 638.2019.8 (In evaporation, high-vacuum furnace annealing of the samples) and under state contract with IT SB RAS (synthesis and characterization of a-SiO_x films).

The authors thank Dr. V.A. Volodin for Raman measurements.

References

- [1] D. Song, D. Inns, A. Straub, M.L. Terry, P. Campbell, A.G. Aberle. *Thin Solid Films* **513** (2006) 356.
- [2] R. Numata, K. Toko, N. Usami, T. Suemasu. *Thin Solid Films* **557** (2014) 147.
- [3] J. Haschke, D. Amkreutz, B. Rech. *Jpn. J. Appl. Phys.* **55** (2016) 04EA04.
- [4] S. Gall in: K. Nakajima, N. Usami (Eds.), *Crystal Growth of Silicon for Solar Cells*, Advances in Materials Research, Springer, Berlin, Heidelberg, 2009, 193.
- [5] O. Nast, Ph.D. Thesis, Philipps-Universität Marburg, 2000.
- [6] A.O. Zamchiy, E.A. Baranov, I.E. Merkulova, S.Ya. Khmel, E.A. Maximovskiy. *J. Non-Cryst. Solids* **518** (2019) 43.
- [7] A.O. Zamchiy, E.A. Baranov, E.A. Maximovskiy, V.A. Volodin, V.I. Vdovin, A.K. Gutakovskii, I.V. Korolkov. *Mat. Lett.* **261** (2020) 127086.

III. Physics of semiconducting nanostructures and heterostructures, including silicide, germanide and stannide heterostructures: experiment, calculations and technology

Transport properties of CaSi₂ and Ca₂Si thin films

L. Dermenji¹, K.G. Lisunov¹, K.N. Galkin², O.V. Kropachev², E.A. Chusovitin², N.G. Galkin²,
E. Arushanov^{*1}

¹ Institute of Applied Physics of ASM, Academiei Str. 5, MD-2028, Chisinau, Moldova

² Institute of Automation and Control Processes of FEB RAS, Radio Str. 5, 690041, Vladivostok, Russia

*e-mail: arushanov@hotmail.com

Interest to CaSi₂ and Ca₂Si is connected to their possible incorporation into existing silicon technologies. *Ab initio* calculations of the CaSi₂ band structure suggest that this material is basically a semimetal or gapless semiconductor [1]. Then, it is expected that both electrons and holes contribute to its electronic properties. Optical and transport study of CaSi₂ presume a substantial difference between the electron and hole effective mass [1]. *Ab initio* calculations [2] have been done for semiconductor Ca₂Si ($E_g = 1.02$ eV), but low temperature (LT) transport properties of Ca₂Si films have not been yet studied. Here, we investigate CaSi₂ and Ca₂Si thin (~ 100 nm) films, including the resistivity $\rho(T)$ and the Hall coefficient $R(T)$. Special attention is paid to the samples C306 (Ca₂Si) and C309 (CaSi₂) grown on Mg₂Si/Si(111) and Si(111) substrates, respectively, and exhibiting quite different LT transport.

Namely, the resistivity of C309 is typical of metals, demonstrating a gradual increase of $\rho(T)$ from ~ 1.5×10^{-5} to 8.5×10^{-5} Ω cm between $T \sim 20 - 300$ K. On the other hand, the resistivity of C306 is activated, decreasing from ~ 1.4 to 0.018 Ω cm between $T \sim 20 - 200$ K, typical of open-gap semiconductors [2, 3], and exhibiting a quite weak increase between $T \sim 200 - 300$ K. Both samples demonstrate a substantial dependence of $R(T)$. In particular, the $R(T)$ function in C309 is rather weak between ~ 100 – 300 K, exhibiting, however, a double change of the sign, and a considerable upturn of $R(T)$ up to ~ 3.5×10^{-3} cm³/C on cooling down to 20 K. In C306, $R(T)$ is even more complicated, including a weak increase with decreasing T between 300 – 150 K and the change of the sign near ~ 200 K. A sharp increase of $R(T)$ up to ~ 400 cm³/C at $T \sim 50$ K is changed then to a strong decrease down to ~ 800 cm³/C with decreasing T down to ~ 20 K.

Such behavior of $R(T)$ suggests presence of two groups of carriers, electrons and holes, as has been mentioned above. Therefore, to analyze them we use a conventional two-band model [3], given by the expressions

$$R(T) = (R_1\sigma_1^2 + R_2\sigma_2^2)/(\sigma_1 + \sigma_2)^2 \text{ and } \sigma = \sigma_1 + \sigma_2, \quad (1)$$

for both investigated samples, where $R_j \approx 1/(en_j)$ are the partial Hall coefficients, n_j are the partial concentrations, and $\sigma_j = 1/\rho_j$ are the partial conductivities of the electrons and holes with $j = 1$ and 2, respectively. In addition, for C309 we use the Bloch-Grüneisen type expressions for both presumed electron and hole contributions,

$$\rho_j(T) = \rho_{0j} + B_j (T/T_D)^2 F_2(T_D/T) + A_j (T/T_D)^5 F_5(T_D/T). \quad (2)$$

Here, ρ_{0j} is the remanent resistivity while the second and the third terms in Eq. (2) are addressed to the electron-electron and the electron-phonon scattering, respectively. T_D is the Debye temperature, $F_n(z)$ is the Bloch-Grüneisen function of the index $n = 2$ or 5, $B_j \propto m_j^2/n_j^{3/4}$, $A_j \propto m_j^2/n_j$ [4, 5], and m_j is the effective mass of the particles j . Both dependences of $\rho(T)$ and $R(T)$ for C309 have been fitted with Eq. (1) and (2) simultaneously, exhibiting a reasonable agreement between the experimental and calculated data.

This yields $T_D \approx 530$ K, $n_1 \approx 9.06 \times 10^{19}$ cm⁻³ and $n_2 \approx 2.5 \times 10^{20}$ cm⁻³, where T_D is comparable with that (456 K) found in bulk polycrystalline CaSi₂ [6]. The ratio of $m_2/m_1 \approx 1.73$ and 1.56, obtained with the data of A_j and B_j , respectively, is quite close yielding $m_2/m_1 \approx 1.6 \pm 0.1$.

Interpretation of the semiconducting behavior in C306 is less straightforward, because it is a semiconductor with a gap of 1.02 eV [2], but has complex $R(T)$ dependence at temperatures below 250 K due to formation of defect minibands [7]. It can be suggested an existence of the finite gaps between CB bottom and VB top at least up to $T \sim 100 - 200$ K. Then, the electron-hole transport is governed by the activation of the electrons (holes) into the CB (VB) from the donor (acceptor) minibands with the energy E_1 (E_2). This assumption gives the value of energies $E_1 \approx 2.1$ meV and $E_2 \approx 27$ meV with a reasonable fit of $\rho(T)$ between ~ 20 – 100 K. On the other hand, conventional expressions of n_j in this case (see e.g. [3]) permit a good fit of the whole dependence of $R(T)$. This leads to the strong (on the 2 orders of the magnitude) and quite strong (on the 8 orders of the magnitude) decrease of n_1 and n_2 , respectively, when T is decreased from 300 to 20 K. Although such behavior of n_j in semiconductors is not surprising, one cannot exclude some influence of the hopping conduction contribution below ~ 30 K. If, however, such contribution is negligible, then we can deduce the product of $m_1 \times m_2 \approx 0.24$ (m_j - free el. mass). To conclude, LT transport properties of Ca₂Si and CaSi₂ thin films were investigated and interpreted assuming two groups of charge carriers, electrons and holes. The effective mass parameters were estimated, suggesting that holes in CaSi₂ are on ~ 60 % heavier than electrons. Both conclusions support the results of Refs. [1,7].

Acknowledgements

The part of the work on the growth and test structure preparation was performed with financial support from the RFBR grant (No. 19-02-00123_a).

References

- [1] N. G. Galkin *et al.*, J. Alloys Comps **770** (2019) 710.
- [2] S. Lebegue, *et al.*, Phys. Rev. B **72** (2005) 085103.
- [3] B. I. Shklovskii, A. L. Efros, Electronic Properties of Doped Semiconductors (Springer, Berlin, 1984).
- [4] D. Svizhovich, Theor. Math. Phys. **166** (2011) 44.
- [5] A. A. Abrikosov, Fundamentals of the Theory of Metals (Moscow, Nauka, 1987) (in Russian).
- [6] M. Affronte *et al.*, J. Alloys & Comp. **274** (1998) 68.
- [7] K.N. Galkin *et al.*, Abstracts of the APAC-Silicide 2019, 2019, Miyazaki, Japan, p-O2.

Single layer nickel disilicide on Si(111) surface

L.V. Bondarenko^{*,1}, A.Y. Tupchaya¹, A.N. Mihalyuk^{1,2}, D.V. Gruznev¹, A.V. Zotov¹, A.A. Saranin¹

¹ Institute of Automation and Control Processes of FEB RAS, 5 Radio St., Vladivostok 690041, Russia

² School of Natural Sciences, Far Eastern Federal University, 690950 Vladivostok, Russia

*e-mail: bondarenko@dvo.ru

Among transition metal silicides, NiSi₂ has exceptional fluorite structure (along only with CoSi₂) with remarkably close lattice matching to crystal silicon, such that it displays perfect epitaxial growth on Si surfaces with an atomically abrupt interface [1, 2]. More importantly, nickel disilicide is a ‘good’ metal and known to be metallic down to 1 K [3]. In 1983, Tung et al [1] showed that NiSi₂ layers can be grown epitaxially on Si(111) and Si(100) surfaces, which has generated considerable interest in the subject due to its importance for semiconductor microelectronics. In subsequent years the formation process of epitaxial NiSi₂ layers on silicon surface has been studied and it was shown that thick NiSi₂ films can be controllably formed in two possible orientations [2]: type-A (Si lattice planes continue through the interface) and type-B (180° rotated). However, it was also shown that single or double monolayer NiSi₂ cannot be formed [4 – 7]. Its formation remains a desirable task because single monolayers of various materials (e.g. graphene, silicene, bismuthene, plumbene, etc) have recently become fascinating and promising objects in modern condensed-matter physics and nanotechnology. However, growing a monolayer of non-layered material is still challenging.

In the present study, single layer NiSi₂ on Si(111) was grown for the first time, using Tl [2], Pb or In monolayers for stabilization. The structural and electronic properties of the Me/NiSi₂/Si(111) (Me = Tl, Pb, In) systems were characterized using a set of experimental techniques, including low-energy electron diffraction, scanning tunneling microscopy, angle-resolved photoelectron spectroscopy, and also first-principles density-functional-theory calculations. Type-B single layer NiSi₂ was formed by Ni adsorption onto Si(111)1×1-Tl, Si(111)1×1-Pb or Si(111)2×2-In surfaces. Nickel atoms were found to intercalate the stabilizing metal layers and to reside in the interstitial sites inside the first silicon bilayer of

bulk-like-terminated Si(111)1×1 surface. In the case of Si(111)1×1-Tl surface thallium initial positions remain almost unchanged after Ni intercalation. From the other hand in cases of Si(111)1×1-Pb and Si(111)2×2-In surfaces single layer NiSi₂ formation resulted in Pb and In layers reconstruction to 7×7-R21.8° and 1×1 periodicities respectively. Nickel d electrons were found to dominate electronic structure providing strong metallisity in all three cases.

Acknowledgements

The work was supported by the Council on grants of the President of the Russian Federation Grant No. MK-343.2019.2 and the Russian Foundation for Basic Research Grant No. 20-02-00510. The calculations were conducted using the equipment of Shared Resource Center “Far Eastern Computing Resource” IACP FEB RAS (<https://cc.dvo.ru>).

References

- [1] R. T. Tung, J. M. Gibson, and J. M. Poate. *Phys. Rev. Lett.* **50** (1983) 429.
- [2] H. von Känel. *Mater. Sci. Rep.* **8** (1992) 193.
- [3] J. C. Hensel, R. T. Tung, J. M. Poate, and F. C. Unterwald. *Appl. Phys. Lett.* **44** (1984) 913.
- [4] M. Henzler, C. Adamski, and K. Rönner. *Journal of Vacuum Science & Technology A* **5** (1987) 2127.
- [5] M. Yoshimura, S. Shinabe and T. Yao. *Surf. Sci.* **357** (1996) 917.
- [6] Y. Hoshino, T. Nishimura, Y. Taki, Y. Asami, K. Sumitomo and Y. Kido. *Surf. Sci.* **511** (2002) 112.
- [7] J. Falta, M. Horn and M. Henzler. *Appl. Surf. Sci.* **41** (1990) 230.
- [8] L.V. Bondarenko, A.Y. Tupchaya, A.N. Mihalyuk, S.V. Eremeev, A.V. Matetskiy, N.V. Denisov, Y. E. Vekovshinin, A.V. Slyshkin, D.V. Gruznev, A.V. Zotov, A.A. Saranin. *2D Materials.* **7** (2020) 025009.

Computer simulation of oxygen vacancy formation in YFeO₃ perovskite

A.A. Gnidenko*, P.G. Chigrin, E.A. Kirichenko

Institute of Material Science of Khabarovsk Scientific Centre of Far Eastern branch of Russian Academy of Sciences, 153 Tihookeanskaya St., Khabarovsk 680042, Russia

*e-mail: agnidenko@mail.ru

Complex oxides with perovskite structure (ABO₃) have a lot of specific physical and chemical properties, which makes them objects of intense experimental and theoretical researches. The high catalytic activity of perovskites allows the use of these compounds as promising catalysts for soot combustion, thereby reducing the emission of diesel gases into the atmosphere. A lot of perovskite characteristics are sensitive to stoichiometry and structural changes within ABO₃[1]. It had been shown that perovskite activity can be explained by a high value of the absolute oxygen non-stoichiometry ABO_{3-δ}, which can reach δ = 0.25 [2]. In the present work, quantum-mechanical calculation methods were used to study formation of oxygen vacancy in yttrium orthoferrite YFeO₃.

The calculations were performed by using the density functional theory combined with the pseudopotential method implemented in the Quantum Espresso software package [3]. The exchange-correlation functional was chosen in generalized gradient approximation form of PBE (Perdew-Burke-Ernzerhof). Sets of k-points were specified by the Monkhorst-Pack procedure. The cutoff energy of the plane wave basis was 60 Rydberg. The pseudopotentials for yttrium, iron, and oxygen were selected from the Quantum Espresso library. We have used the ultrasoft Vanderbilt pseudopotentials generated by A. Dal Corso [4]. Pseudopotentials were tested for a correct description of the Y and Fe crystal lattice properties (lattice constants and bulk modulus), as well as O₂ molecule properties (bond length, dissociation energy). Test calculations showed that the equilibrium configuration for YFeO₃ corresponds to the G-type antiferromagnetic state. The presence of strongly localized Fe-3d states requires using of the Hubbard correction (DFT + U).

To simulate oxygen vacancies, two YFeO₃ structures were considered. In one case, the oxygen atom was removed from a primitive 20-atom cell, in the other case, from a structure consisting of 4 unit cells. In the YFeO_{3-δ} non-stoichiometry representation, for the first case we get δ = 0.25, and for the second – δ = 0.0625, respectively. In addition, we had taken into account two types of oxygen arrangement in the YFeO₃ crystal lattice, leading to the two types of oxygen vacancy. The formation energies were calculated to characterize the vacancies. In the simplest approximation, taking the chemical potential of oxygen as a half of the O₂ molecule energy, the formation energy is determined as follows:

$$E_{form} = E_{vac} - E_{ideal} + \frac{1}{2}E_{O_2} \quad (1)$$

where E_{ideal} is the energy of the ideal YFeO₃ cell, E_{vac} is the energy of the cell with a vacancy, E_{O₂} is the energy of an isolated O₂ molecule. The calculated values are shown in table I.

Table I. Formation energies for the two types of oxygen vacancies

Configuration	E _{form} , eV	Difference, eV
YFeO _{3-δ} (δ = 0.0625) – O _I	3.13	
YFeO _{3-δ} (δ = 0.0625) – O _{II}	3.42	0.29
YFeO _{3-δ} (δ = 0.25) – O _I	3.69	
YFeO _{3-δ} (δ = 0.25) – O _{II}	3.79	0.10

In both cases, the same type of vacancy is energetically more favorable (O_I type), the smallest value of the formation energy (3.13 eV) corresponds to a lower concentration of oxygen vacancies. The obtained value is in good agreement with the value (3.19 eV) from the perovskite database presented by Emery and Wolverton [5]. In the case of high oxygen non-stoichiometry (δ = 0.25) the difference in the formation energies of two different vacancy types is lower. It reduces from 0.3 eV to 0.1 eV. Thus, the formation of a large number of oxygen vacancies in the YFeO₃ crystal lattice makes both types of vacancies almost equally probable.

We also examined changes in the electronic structure of YFeO₃ during the vacancy formation. The use of the Hubbard correction (DFT+U, U_{eff} = 4 eV) allowed us to obtain the energy gap (HOMO-LUMO gap) of 2.31 eV, which is close to the experimental one. In the case of high oxygen non-stoichiometry (δ = 0.25), the changes affect almost all levels, including yttrium states. In the gap above the valence band maximum, there are levels which correspond in general to the O-2p states, and, partially, to the Fe-3d states. At δ = 0.0625, the form of the density of states is preserved, but vacancy levels are also formed in the gap.

Acknowledgements

This research was supported in through computational resources provided by the Shared Services Center “Data Center of FEB RAS” (Khabarovsk) [6]

References

- [1] M. Pena, J.L.G. Fierro. Chem. Rev. **101** (2001) 1981.
- [2] M.R. Pai, B.N. Wani, B. Sreedhar, S. Singh, M. Gupta. J. Mol. Catal. A Chem. **246** (2006) 128.
- [3] P. Giannozzi, S. Baroni, N. Bonini, M. Calandra, et al. J. Phys.: Condens. Matter. **21** (2009) 395502.
- [4] A. Dal Corso. Comput. Mater. Sci. **95** (2014) 337.
- [5] A. Emery, C. Wolverton. Sci Data. **4** (2017) 170153.
- [6] Shared Facility Center "Data Center of FEB RAS" (Khabarovsk), <http://lits.ccfefbras.ru>.

Iron disilicide lattice thermal expansion coefficients from first principle calculations

M.A. Visotin^{*,1,2}, I.A. Tarasov¹, A.S. Fedorov^{1,2}, S.G. Ovchinnikov^{1,2}

¹Kirensky Institute of Physics, Federal Research Center KSC SB RAS, Krasnoyarsk, 660036 Russia

²Siberian Federal University, 79 Svobodny pr., Krasnoyarsk, 660041 Russia

*e-mail: visotin.maxim@gmail.com

The ongoing search for new functional materials includes looking for ecologically safe, yet highly efficient, technologies and compounds. From this point of view, iron silicides attract much attention due to Earth's core abundance of Fe and Si, compatibility with current silicon-based technology and a variety of possible industrial application in different fields. Besides ferromagnetic silicides, which have great prospects in spintronics, metallic α -FeSi₂ with possible spin polarization, and semiconducting β -FeSi₂ phases are a promising candidate for several industrial applications. They can be utilized as active material in photonic crystals [1], for photovoltaics [2], thermoelectrics [3] and finally in light emitting diodes for optical fiber data transfer [4]. However, synthesis of high-quality epitaxial thin films or nanostructures of α -, and β -FeSi₂ faces many difficulties due to high lattice mismatches with the substrates, which in turn may change drastically with the temperature. While the reports on lattice thermal expansion are scarce or contain some contradictory results [5,6], herein we present theoretical calculations of the thermal expansion coefficients.

The lattice dynamics properties were calculated in the framework of the density functional theory (DFT) implemented in VASP 5.4.1 software package [7,8] within the plane wave basis and using the projector augmented wave (PAW) formalism [9]. For accurate description of the second derivatives of the total energy that contribute to the dynamical matrix and therefore to all phonon-related quantities, the cutoff energy of the plane-wave basis E_{cutoff} was set to 750 eV. Also, the sampling of the first Brillouin zone in the reciprocal space was made using the Monkhorst-Pack scheme meshes [10] with resolution of not lower than $0.017 \ 2\pi/\text{\AA}$. The convergence criterion for electronic degrees of freedom minimisation was set to 10^{-7} eV. None of considered phases showed magnetic behaviour at the DFT ground state calculations, and thus all further calculations were non-spin-polarised.

The calculated properties of the lattice dynamics is known to be very sensitive to the choice of the exchange-correlation functional [11]. We used the generalised gradient approximation (GGA) in the PBEsol formulation [12] because it correctly reproduces silicon lattice constant, while other popular functionals (LDA, PW91, PBE and rPBE) give errors of the order of 0.03 \AA . In addition to this, we have also compared the results for thermal expansion coefficients for PBE [13] and PBEsol against the experimental data [14]. The PBE functional systematically overestimates the expansion coefficient by 14 % in the ranges $T = 300 - 900$ K, while PBEsol gives an average error of 3.8 %.

The calculations of phonon spectra and corresponding thermodynamic potentials were carried out using the

PHONOPY code [15] and its quasi-harmonic approximation extension, phonopy-gha [16].

The calculated linear lattice thermal expansion coefficients were fitted to linear temperature dependence in the range of $T = 300-600$ K. The values for lattice parameters a and c of α -FeSi₂ are:

$$a: 7.16 \times 10^{-9} T + 7.45 \times 10^{-6}$$

$$c: 4.51 \times 10^{-9} T + 4.69 \times 10^{-6}$$

The coefficients for lattice parameters a , b and c of β -FeSi₂ are:

$$a: 6.18 \times 10^{-9} T + 6.91 \times 10^{-6}$$

$$b: 4.53 \times 10^{-9} T + 5.07 \times 10^{-6}$$

$$c: 7.16 \times 10^{-9} T + 5.65 \times 10^{-6}$$

The obtained values show that the iron disilicides have larger expansion coefficients than pure silicon (2.35×10^{-6} at 300 K), which sheds light on the origin of structural defects of FeSi₂ films obtained during high-temperature synthesis on Si substrates. It also worth noting the absence of high anisotropy in β -FeSi₂ thermal expansion questioned earlier [5,6].

Acknowledgements

This work was supported by the Russian Science Foundation, project no. 16-13-00060II. The authors want to thank the Joint Supercomputer Center for providing access to computational resources.

References

- [1] H. Tokushige, T. Endo, K. Hiidome, K. Saiki, S. Kitamura, T. Katsuyama, et al. *Jpn. J. Appl. Phys.* **54** (2015) 07JB03.
- [2] Y. Gao, H.W. Liu, Y. Lin, G. Shao. *Thin Solid Films.* **519** (2011) 8490.
- [3] M. Mohebbali, Y. Liu, L. Tayebi, J.S. Krasinski, D. Vashaee. *Renew. Energy* **74** (2015) 940.
- [4] D. Leong, M. Harry, K.J. Reeson, K.P. Homewood. *Nature* **387** (1997) 686.
- [5] M. Imai, Y. Isoda, H. Udono. *Intermetallics* **67** (2015) 75.
- [6] K. Maex, M. van Rossum (Eds.), *Properties of Metal Silicides*, INSPEC, London (1995).
- [7] G. Kresse, J. Furthmüller. *Phys. Rev. B.* **54** (1996) 11169.
- [8] G. Kresse, J. Hafner. *Phys. Rev. B.* **47** (1993) 558.
- [9] P.E. Blöchl. *Phys. Rev. B.* **50** (1994) 17953.
- [10] H.J. Monkhorst, J.D. Pack. *Phys. Rev. B.* **13** (1976) 5188.
- [11] A. Jain, A.J.H. McGaughey. *Com. Mat. Sci.* **110** (2015) 115.
- [12] J.P. Perdew et al. *Phys. Rev. Lett.* **100** (2008) 136406.
- [13] J.P. Perdew, K. Burke, M. Ernzerhof. *Phys. Rev. Lett.* **77** (1996) 3865.
- [14] H. Ibach. *Phys. Status Solidi* **31** (1969) 625.
- [15] A. Togo, I. Tanaka. *Scr. Mater.* **108** (2015) 1.
- [16] A. Togo, L. Chaput, I. Tanaka, G. Hug. *Phys. Rev. B* **81** (2010) 1.

Formation of Fe₂Si Wetting Coating and Fe Growth on Si(001): AES and EELS Study

N.I. Plusnin^{*1,3}, A.M. Maslov^{1,2}, V.M. Il'yashenko¹

¹ Institute of Automation and Control Processes of FEB RAS, 5 Radio St., Vladivostok 690041, Russia

² Far Eastern Federal University, 8 Sukhanova St., Vladivostok 690950, Russia

³ St. Petersburg State University, 7–9 Universitetskaya nab. St., St. Petersburg 199034, Russia

*e-mail: plusnin@iacp.dvo.ru

Introduction

Recently, interest in ultrathin layers of ferromagnetic metals on silicon for silicon spintronics has increased significantly [1]. Moreover, the tunnel spin injector Fe/Si(001) can be very effective as predicted by theoretical calculations: it can achieve 100% polarization at low reverse voltage [2]. Therefore, the study of the growth of Fe nanofilms on Si(001) seems important especially due to the fact that the surface (001) in silicon microelectronics is the most technologically important.

Results and discussion

Fe films on Si(001) were prepared in an ultrahigh-vacuum (UHV) chamber, which was equipped with a two-sample manipulator, a tape evaporative source of iron, as well as AES (EELS) and LEED analyzers from Riber. Fe was deposited from Fe film on Ta-ribbon onto Si(001) substrate (n-type, $\rho = 4.5 \text{ Ohm cm}$, $d = 420 \text{ }\mu\text{m}$), which maintained at room temperature. During growth, it was carried out annealing (annealing temperature, in parentheses) under a thickness of Fe: $d = 1 \text{ ML}$ (500–600 °C); $d = 3 \text{ ML}$ (250 °C) and $d = 10 \text{ ML}$ (250 °C).

For analysis of data of AES we used the energy position and intensity of: (1) MVV peak of Fe (E_1); (2) the energy difference ($E_4 - E_2$) between main $L_{23}VV$ Auger peak of Si (E_4) and its plasmon satellite (E_2); (3) the doublet Auger peak (E_3), which correspond to transition through the sp or pd valence band of Si or Fe-Si silicide, respectively, and (4) main $L_{23}VV$ Auger peak of Si (E_4), which correspond to transition through the pp or pd valence band of Si or Fe-Si silicide, respectively.

Dependence of these characteristics in the AES spectra on the thickness show a change with increasing thickness of (1) the composition; (2) the electron density and (3) states in valence electron bond. The electron density in the boundary bonds depends on the atomic density of the layers adjacent to the interface. Consequently, electron density of interface layers change shows a change in their atomic density.

We showed that the difference $E_4 - E_2$, at 2, 4 and 10 ML corresponds to the formation of: (1) a certain non-bulk phase of Fe with a reduced electron density, which borders the non-bulk phase of Si with an increased electron density, (2) of the bulk silicide Fe₃Si and (3) of the bulk phase of Fe. Also we calculate the density change in the

boundary layer of the substrate and showed an increase in the density of this layer by about 6%.

As for the behavior of the difference $E_4 - E_3$ and E_3 peak amplitude on the thickness, we showed this behavior (peak E_3 remains unchanged in amplitude regardless of an increase in the thickness of the Fe film) can be explained by formation of segregated Si at a thickness of 4 - 10 ML.

For analysis of data of EELS we used the energy position and intensity of (1) ΔE_1 loss peak (7.5 - 8.0 eV) belonging to interband transitions and peaks of (2) surface (ΔE_2) and (3) bulk plasmon (ΔE_3), respectively.

This analysis showed that increase in the energy ΔE_1 to 8.0 eV, after 3 ML, also corresponds to the transition to the bulk Fe-Si phase. But the change in the loss energies ΔE_2 and ΔE_3 is explained by the state of the surface on which segregated Si is located.

As for the amplitude of EELS peaks, which rapidly decreased with increasing thickness to 3 ML, this is due to transition from Si(001) and coherent two-dimensional Fe phases to the bulk amorphous Fe₃Si and Fe. At the same time, the stabilization of this amplitude in the range of 4–10 ML is associated with the formation of a layer of segregated Si on the surface.

The nanophase nature of the 3 ML film was confirmed by the ΔE_3 bulk plasmon loss peak width reaches a maximum at a thickness of 3 ML.

The model for the growth of Fe on Si(001) has been formulated. At 0 - 1 ml, iron is chemically adsorbed in the form of coherent atomic structures. Then, at 1-2 ml, the stretched wetting two-dimensional coating of Fe grows, which causes the transition of the near-boundary silicon into a high-pressure phase. About 3 ml, an agglomeration occurs, and the wetting coating acquires a nanophase structure with a new layer of nanostructured Si. Annealing causes the formation of a wetting coating of the composition Fe₂Si. At 4 ml, the following mixing of Fe and Fe₂Si go to a stable Fe₃Si phase and an excess of Si is released on the surface of Fe₃Si. After that, at 4-10 ml, Fe islands with Si dissolved in it are nucleated and grow, and a transition from Fe₃Si to Fe occurs. As the thickness of Fe increases, the solubility of Si in Fe decreases and Si segregates on the surface of Fe.

References

- [1] R. Jansen, Nature Materials, **11**(5) (2012) 400.
- [2] P. Mavropoulos, Physical Review B **78** (2008) 5.

Mg₂Sn under pressure: first principle evolutionary search results

Yu.V. Luniakov*

Institute of Automation and Control Processes of FEB RAS, 5 Radio St., Vladivostok 690041, Russia

e-mail: luniakov@iacp.dvo.ru

Magnesium stannide Mg₂Sn is one of the few intensively studied semiconductors along with the similar compounds Mg₂Si and Mg₂Ge, attracting much attention in the last few years. Its relatively high melting point T=1030°K [1] and high electrical conductivity make Mg₂Sn very useful for high thermoelectric material applications in the temperature range from 500 to 800 K [2, 3] for the automotive products and manufacturing processes. Similar to many alkali-metal oxides and sulphides, magnesium stannide Mg₂Sn adopts the following phase transition: anti-fluorite (Fm3m) → anti-cotunnite (Pnma) → Ni₂In-type (P6₃/mmc) [4, 5]. The present study is devoted to extensive evolutionary search for the optimal Mg₂Sn structures in the pressure range from 0 to 200 GPa using the USPEX code [6, 7] in conjunction with ab-initio structure relaxations as implemented in the DFT code VASP [8]. The one-electron wave functions were expanded using a plane-wave basis with a kinetic energy cutoff of E_{cut}=350 eV. Exchange and correlation potentials are treated in the generalized gradient approximation (GGA) of the Perdew Burke Ernzerhof (PBE) form [9]. The present DFT evolutionary search was undertaken for Mg₂Sn stannide with 8 Mg and 4 Si atoms per unit cell at pressures of 0 ≤ P ≤ 200 GPa with pressure steps ΔP ≤ 5 GPa. The local optimizations were carried out until the total energy converged to 10⁻⁶ eV per formula unit and the total force converged to 10⁻² eV/Å.

Table I. The best structure obtained during evolutionary search at every given pressure P.

P (GPa)	Structure	P (GPa)	Structure	P (GPa)	Structure
1	164, 194	65	2, 65	135	11
3	2, 11	70	12, 65	140	11
5	2	75	12	145	2, 164
10	2, 15	80	2, 62	150	2, 11
15	2	85	6, 11	155	2, 164
20	1, 12	90	2, 11	160	2, 164
25	2, 12	95	156, 194	165	11, 164
30	1, 11	100	12	170	2, 164
35	2, 14	105	11, 62	175	12, 164
40	164, 194	110	10, 194	180	11, 164
45	11	115	2, 11	185	2, 164
50	2	120	2, 11	190	2, 164
55	2, 62	125	2, 11	195	11
60	2, 164	130	2, 11	200	11

Table I summarizes space symmetries of the most energetically favourable structures at a number of given pressures identified by the FINDSYM utility [10]. As the results of this identification depend on atomic displacement tolerances, there are more than one number on the Structure columns. In order to investigate which structure is better for every P, a series of high precision calculations with the E_{cut}=500 eV and a doubled grid of k-points was undertaken for each identified structure shown in Table 1. At pressures P < 2.4 GPa the best structure appeared to be simple cubic Fm3m, that converts to the orthorhombic Pnma structure in agreement with other data [4, 5]. At pressures P > 5.9 GPa the orthorhombic Pnma structure is lost in enthalpy to the hexagonal P6₃/mmc one as being expected. At pressures P > 4 GPa another structure monoclinic C2/m, that was predicted for the silicide Mg₂Si [11], appeared to have the lower enthalpy for stannide Mg₂Sn also. Moreover, there is an orthorhombic structure Pmmm (space group 47), that has the lowest enthalpy at any pressure under consideration.

Acknowledgements

The calculations were carried out using the equipment of the Shared Resource Center “Far Eastern Computing Resource” IACP FEB RAS (<https://cc.dvo.ru>). The work was supported by the Program of Fundamental Researches of Far Eastern Branch of the Russian Academy of Sciences (Grant No 18-3-022) and by the state budget of the IACP FEB RAS (theme No. 0262-2019-0002)

References

- [1] A.A. Nayeb-Hashemi, J.B. Clark. Bulletin of Alloy Phase Diagram. **5** (1984) 466.
- [2] A.M. Iida, T. Nakamura, K. Fujimoto, Y. Yamaguchi, R. Tamura, T. Iida, and K. Nishio. MRS Advances **1** (2016) 3971.
- [3] M. Akasaka, T. Lida, A. Matsumoto, K. Yamanaka, Y. Takanashi, T. Imai, N. Hamada. J. Appl. Phys. **104** (2008) 13703.
- [4] M. Guezlane, H. Baaziz, Z. Charifi, A. Belgacem-Bouzida, Y. Djaballah. J. Sci: Adv. Mat. Dev. **2** (2017) 105.
- [5] F. Yu, J.-X. Sun, T.-H. Chen. Physica B: Cond. Matt. **406** (2011) 1789.
- [6] A.R. Oganov and C.W. Glass. J. Chem. Phys. **124** (2006) 244704.
- [7] A.O. Lyakhov, A.R. Oganov, H.T. Stokes, and Q. Zhu. Comp. Phys. Commun. **184** (2013) 1172.
- [8] G. Kresse and J. Furthmuller, Phys. Rev. B **54** (1996) 11169.
- [9] J.P. Perdew, K. Burke, M. Ernzerhof, Phys. Rev.Lett. **77**, (1996) 3865.
- [10] H.T. Stokes, D.M. Hatch. J. Appl. Cryst. **38** (2005) 237.
- [11] T.D. Huan, V.N. Tuoc, N.B. Le, N.V. Minh, L.M. Woods, Phys. Rev. B **93** (2016) 094109.

Investigation of the effect of the amount of Au catalyst on the morphology of porous silicon layers obtained by the metal-assisted chemical etching

G.O. Silakov*, O.V. Volovlikova, K. Bazov

National Research University MIET, Id. 1, Shokin Square, Zelenograd, Moscow, 124498, Russia

*e-mail: mr.komrad-13@ya.ru

In recent years, nanostructured semiconductors with a Schottky barrier are finding more extensive application [1, 2]. Such structures are usually a matrix of a porous semiconductor (usually silicon) with nanoparticles of noble metals deposited inside [3]. This is primarily due to the prospect of their usage in direct methanol (ethanol) fuel cells [4]. It was shown in early work [5] that in the process of ethanol electrooxidation on the structure of porous silicon – noble metal nanoparticles (Por-Si/NM), various gases, such as oxygen, hydrogen, and CO, are released. Special attention is given to the generation of electron carriers that occurs in the process of ethanol electrooxidation.

Usually, Por-Si/NM structures are formed by using a two steps method. In the first step, the porous silicon matrix must be formed. This is done by the electrochemical method. In the second step, nanoparticles of noble metals must be deposited inside pores. However, this method of forming Por-Si/NM structures requires an external current source. As a result of this, the problem of a stable current supply to the formed surface of the porous layer arises. In addition, the area of formation of the porous layer is limited by the geometric dimensions of the electrochemical cells which are used. Also, in this method, the possibilities of group processing of wafers are limited [3].

The alternative of the two-step method – is metal-assisted chemical etching (MACE). In this method, noble metal nanoparticles firstly deposited in the semiconductor substrate. Then, this substrate must be etched in the solution containing HF and oxidizer, such as H₂O₂, KMnO₄, etc. So, in MACE, noble metal nanoparticles remained in the bottom and walls of the pores.

Usually, pure Pd, Pt, or Pt-Rh alloys are used as the metal catalyst in direct methanol (ethanol) fuel cells [4]. But, those metals are expensive. In addition, when using Pt or Pt-Rh, a phenomenon known as catalyst poisoning is observed [6]. Catalyst poisoning is also observed in the case of Au; however, with the Au catalyst, large currents are observed during electrooxidation.

The electrooxidation properties of the Por-Si/NM structure obtained in the MACE process depend primarily on morphology. Morphology, in turn, depends on the metal catalyst, the duration, and temperature of the etching.

So, the goal of this work is to study the effect of Au catalyst on the morphology of the layers obtained in the MACE process.

Materials and methods

Por-Si/NM structures were formed by the one-step method. Boron doped silicon wafer (100) with resistance 0,01 Ohm/□ was used as a substrate. Firstly, wafers were cleaned by solution H₂O₂(30%): NH₄OH(aq.): H₂O (1/1/3

in volume). Au nanoparticles were deposited from an aqueous solution of the HNO₃:HCl: Au (1/1/4 in volume) by the 10-420 sec. Then, porous silicon was formed in standard solution – HF (40%): H₂O₂(30%): H₂O (25/10/4 in volume). The duration of the formation was 60 min.

Discussion

Table I shows the SEM image analysis of Au nanoparticles (or worm-like structures) deposited on the Si surface and formed Por-Si/NM structures.

Table I. The results of the analysis of SEM images.

Time of Au deposition, s	Type (particles or worm-like and predominant size (width), nm)	The area occupied by Au particles, %	Porosity, %	Predominant pore size, mkm.
10	Particles, 8	25	-	-
30	Particles, 10	32	-	-
60	Worm-like, 18	37	25	3
180	Worm like, 25	50	42	5
300	Worm-like, 26	57	68	20
420	Worm-like, 28	58	68	10

In addition, as established from SEM images, after Au deposition with 180 s duration, various structures begin to form. Thus, the formation of whiskers and two layers of porous silicon were detected. In addition, a long Au deposition duration (more than 300 s) leads to a decrease in the prevailing pore diameter. This may be due to the difficult access of the etchant solution to the surface Si.

Acknowledgments

This investigation was supported by the Russian Science Foundation (project No. 19-79-00205).

References

- [1] L. Wali, A. Alwan, A. Dheyab, D. Hashim. *Optik* **179** (2019) 708.
- [2] Z. Huang, N. Geyer, P. Werner, J. De Boor, U. Gösele. *Advanced Mater.* **23** (2011) 285.
- [3] S. Polisski. Abstract of PhD thesis. (2010).
- [4] E. A. Kozlova, V. N. Parmon. *Advances in chemistry* **86** (2017) 870 (in Russian).
- [5] O. Volovlikova et al. *Micromachines* **10** (2019) 872.
- [6] Z. Kang et al. *J. Am. Chem. Soc.* **129** (2007) 12090.

Identification of structure ordering of melt-spun Fe₇₀Cr₁₅B₁₅ alloy by the entropy functionals

A.M. Frolov^{*1}, T.A. Pisarenko^{1,2}

¹ Far Eastern Federal University, 8 Sukhanova St., Vladivostok 690950, Russia

² Institute of Automation and Control Processes of FEB RAS, 5 Radio St., Vladivostok 690041, Russia

*e-mail: froloff5@yandex.ru

In this work, new techniques for the analysis of complex images were advanced using entropy functionals to characterize structurally complex images of a surface microrelief of the melt-spun Fe₇₀Cr₁₅B₁₅ ribbons obtained at different linear velocity of a quenching roller.

Alloys of composition Fe₇₀Cr₁₅B₁₅ obtained by the melt-spinning technique under Ar atmosphere with single Cu roller at a linear velocity of 20, 30 and 45 m/s have been manufactured at the Bardin Central Research Institute of Ferrous Metallurgy (Moscow). We have examined the microstructure of the ribbons by scanning electron microscope Carl Zeiss Cross Beam 1540XB and by optic microscope Observer D1m. The XRD patterns for each of the samples were parallelly recorded by the diffractometer Bruker D8 ADVANCE. Details of fast statistical analysis of complex image based on the fast Fourier transform (FFT) were described in works Ref. [1]. Theory of entropy functionals was described in the work Ref. [2], and the fracton/fractal technique was represented in the work Ref. [3].

The microimages of the contact surface of the amorphous Fe₇₀Cr₁₅B₁₅ ribbons obtained in the chosen range of cooling roller velocities were selected for the test analysis, since according to the data of XRD these alloys are X-ray amorphous. The Vajda entropy was calculated on the basis of mode distributions by

$$H\{P[I(\lambda_i)]\} = H[P(\lambda_i)] = \sum_{i=1}^N P(\lambda_i) [1 - P(\lambda_i)], \quad (1)$$

then the entropic index of a structuring was determined by

$$\eta[P(k)] = 1 - H[P(k)]/H_{max}. \quad (2)$$

Very small value of the entropic index of structuring for the melt-spun Fe₇₀Cr₁₅B₁₅ alloy obtained at 30 m/s indicates almost maximum disordering of a spectral function for the microrelief of contact ribbon surface. Whereas for spinning conditions at 20 and 45 m/s the entropic index of structuring of a contact surface indicates the increase of the structure ordering up to 5-10%. Thus, according the entropic index of structuring for the melt-spun Fe₇₀Cr₁₅B₁₅ alloy obtained at 30 m/s is more disordered (almost complete randomization) among selected spinning conditions.

Moreover, XRD patterns for all the as-quenched Fe₇₀Cr₁₅B₁₅ alloys show a halo-pattern typical of amorphous alloys. However, in XRD patterns for the Fe₇₀Cr₁₅B₁₅ ribbons obtained at 20 and 45 m/s the diffuse peaks have residual crystalline sharpening, indicating the formation of smaller crystalline precipitates. While XRD pattern for the Fe₇₀Cr₁₅B₁₅ ribbon obtained at 30 m/s shows the broad smooth hump, without any crystal remainder indicating the formation of completely amorphous

structure. Thus, the better glass-forming ability is achieved, when $\eta \rightarrow 0$.

Based on the results, according to the spinning velocity and the entropic index of structuring, the Fe₇₀Cr₁₅B₁₅ alloys obtained at 20, 30 and 45 m/s can be ranged as amorphous (heterogeneous or microcrystalline), vitreous (homogeneous) and nanocrystalline, respectively.

The spectra of fracton dimension define the nature of the structure ordering of the morphology of melt-spun alloy. It was discovered the Fe₇₀Cr₁₅B₁₅ ribbons obtained at 20 m/s have identical spectra of fracton dimension on the contact surface and on the free surface. This result determines the topological uniformity of heat transfer. The spectrum of fracton dimension at 30 m/s is significantly differed by the curve form and by the dimension value on the opposite surfaces. At the free surface of this ribbon the large-scale and small-scale defects have a scaling ordering and a fractal ordering, respectively [3]. The structure ordering on the free surface of the Fe₇₀Cr₁₅B₁₅ ribbons obtained at 45 m/s also changes, but the dimension value is comparable with the dimension of the contact surface, therefore, a heat transfer is topologically agree. Thus, the glass-forming ability of melt-quenched alloy may be identified by the spectrum of fracton dimension having fractal ordering, when the fracton dimension tends to a constant value.

Converting the fracton dimension to the fractal dimension was carried by $D_f = (5-\gamma)/2$ Ref. [3]. The fractal dimension is greater than 2 for the contact surface and the free surface of the Fe₇₀Cr₁₅B₁₅ ribbons obtained at 20 and 45 m/s demonstrates that the main contribution to dimension makes the distribution of ordered spatial inhomogeneities, whereas the fractal dimension on the free surface of the Fe₇₀Cr₁₅B₁₅ ribbon obtained at 30 m/s is less 2, that may be explained by a competition of a randomized hierarchical system of mesodeflects with a system of ordered inhomogeneities. As a result, the concurrence leads to the appearance an order from a chaos.

Using the techniques based on the entropy functionals it was determined that the spinning condition at 30 m/s is optimal for a vitrification of the Fe₇₀Cr₁₅B₁₅ alloy. Better glass-forming ability in the melt-spinning process is identified by a scale of the order-disorder based on minimum of the entropic index of structuring and/or by the fractally ordered spectrum of fracton dimension.

References

- [1] B.N. Grudin, V.S. Plotnikov, Processing and simulating of microscopic images, Dal'nauka, Vladivostok, 2010.
- [2] N.I. Chukhrii, V.V. Yudin, A.M. Frolov, L.A. Yudina., J. Surf. Investig-X-Ray Synchro. **15** (2000) 653.
- [3] T.A. Pisarenko, A.M. Frolov, G.S. Kraynova, Solid State Phenom. **215** (2014) 190.

Electrochemical properties of electrodes based on anodic titanium oxide nanotubular layers

D.A. Dronova*, A.S. Gavrilov, A.A. Dronov

National Research University of Electronic Technology, Zelenograd 124498, Russia

*e-mail: demetpatakai@gmail.com

The growing energy crisis and environmental problems caused by the depletion of fossil fuels, decisively contribute to the development of renewable energy sources and energy storage devices [1,2]. At present, renewable energy devices, especially advanced lithium-ion current sources, are widely used in portable electronic devices, including cell phones, laptops, and handheld devices [3,4]. However, the limited lithium resources and uneven distribution on the ground are the inevitable problems that will prevent the development of lithium-ion current sources for large-scale applications [5,6].

Ionic chemical current sources such as Al-ion and Na-ion have emerged as a potential alternative to lithium-ion current sources, the advantages of which are abundant supplies of aluminum and sodium, low costs and safety. The search and study of suitable electrode materials are one of the main tasks in the development of such ionic current sources.

One such electrode material may be titanium dioxide (TiO₂). Titanium dioxide is considered one of the most promising materials due to stable anode structure, a large reserve of resources and environmental friendliness [7]. However, pure TiO₂, known as n-type semiconductor, usually exhibits low electronic and ionic conductivity [8,9].

One way of improving the properties of titanium oxide is nano-sized particles that can reduce the ion diffusion path and improve the kinetics of diffusion of ions. Another promising TiO₂ nanomaterial morphology form as an electrode are vertically oriented arrays of anode nanotubes of titanium oxide, which has a large effective surface area due to its "three-dimensional architecture."

Thus, the development and optimization of the geometry, chemical and phase composition of the formed electrodes based on anodic nanotubular titanium oxide layers (TiO₂ NTs) and selection of optimal electrolyte

compositions for the developed electrodes have the great scientific and practical interest.

In this work, a change in the electrochemical properties of an electrode based on an anode nanotube layer of titanium oxide depending on the heat treatment and the composition of the electrolyte were demonstrated.

The TiO₂ NTs layers were obtained by the two-stage method of anodic oxidation in a fluorine-containing electrolyte and then annealed at different temperatures and atmospheres. The results show changes in cyclic voltammetry and electrochemical impedance of the samples while maintaining the intact structure of the array of nanotubes.

Acknowledgements

This work was supported by RFBR grant № 19-33-90287.

References

- [11] C. P. Grey, J. M. Tarascon. *Nat. Mater.* **16** (2017) 45.
- [12] X. Xiang, K. Zhang, J. Chen. *Adv. Mater.* **27** (2015) 5343.
- [13] J.-Y. Hwang, S.-T. Myung, Y.-K. Sun. *Chem. Soc. Rev.* **46** (2017) 3529.
- [14] J. Chen, F. Cheng. *Acc. Chem. Res.* **42** (2009) 713.
- [15] K. Zhang, Y. Hu, L. Wang, M. J. Monteiro, Z. Jia. *ACS Appl. Mater. Interfaces.* **9** (2017) 34900.
- [16] B. Luo, Y. Hu, X. Zhu, T. Qiu, L. Zhi, M. Xiao, H. Zhang, M. Zou, A. Cao, L. Wang. *J. Mater. Chem.* **6** (2018) 1462.
- [17] C. Chen, Y. Yang, S. Ding, Z. Wei, X. Tang, P. Li, T. Wang, G. Cao, M. Zhang. *Energy Storage Mater.* **13** (2018) 215.
- [18] M. Wagemaker, G.J. Kearley, A.A. van Well, H. Mutka, F.M. Mulder. *J. Am. Chem. Soc.* **125** (2003) 840.
- [19] M. Xie, X. Sun; C. Zhou, A.S Cavanagh, H. Sun, T. Hu, G. Wang, J. Lian, S.M. George. *J. Electrochem. Soc.* **162** (2015) A974.

Radiation induced defects in hollow particles of zinc oxide

A.N. Dudin*, V.V. Neshchimenko

Amur State University, 21 Ignatievskoe highway, Bagoveshchensk 675027, Russia

*e-mail: andrew.n.dudin@gmail.com

Radiation stability of ZnO hollow particles under 100 keV proton exposure have been investigated. The experimental data were compared with the calculated ones obtained by modeling in the GEANT4 software package. Hollow particles have better radiation stability compared with bulk microparticles cause by low defects accumulation in the hollow particles, which was confirmed by simulation in GEANT4.

Experimental

Hollow ZnO particles were obtained hydrothermally from a solution containing 2.5 mol of $Zn(CH_3COO)_2 \cdot 2H_2O$, 1 mol of deionized water and 7.5 mol of NH_4HCO_3 , which was poured into an autoclave with a Teflon glass and heated to 180° C with a holding time of 15 hours. After synthesis, the powders were washed with alcohol, dried at 60° C in air and heat treated at a temperature of 650° C. The surface morphology was analyzed on a Helios NanoLab 660 SEM. The specific surface area measured by the BET method on an AutoSorb 6 ISA device amounted to 32 to 57 m²/g for hollow particles.

Irradiation was carried out by protons with an energy of 100 keV, a fluence of $5 \times 10^{15} \text{ cm}^{-2}$, a flux density of $1 \times 10^{12} \text{ cm}^{-2} \text{ s}^{-1}$, in a vacuum of $5 \times 10^{-5} \text{ Pa}$. The simulation was carried out in the GEANT4 software package, where similar values were set.

The concentration of the absorption centers was calculated based on the Smakula-Dexter formula [1]:

$$N = A \frac{n}{(n^2 + 2)^2} K_m \Delta E f^{-1} \quad (1)$$

where n is the refractive index ZnO, K_m is the maximum absorption coefficient (cm^{-1}), ΔE is the half-width of the band (eV), f is the oscillator strength (taken as a unit), the numerical coefficient A is taken to be 0.96×10^{17} .

The Frenkel defect concentration calculated in GEANT4 was determined using the modified Kinchin-Pease formula [2]:

$$N_{fr} = \frac{0.8 E_{dis}(\varepsilon)}{2 E_d} \quad (2)$$

where E_d is the threshold bias energy, $E_{dis}(\varepsilon)$ is the dissipated energy in nuclear collisions.

Results and discussion

During synthesis by the hydrothermal method, hollow ZnO particles of a spherical shape from 500 to 2000 nm in size are formed, some of which are bonded to each other. The yield of spherical particles is about 90%.

X-ray diffraction analysis showed that during the synthesis of hollow ZnO particles, peaks related to the wurtzite structure (P63mc) are recorded, and there are no amorphous phases. Changes in the constant lattices are associated with various tensile stresses caused by packing defects and leading to inelastic deformation of the lattice.

From the diffuse reflectance spectra obtained on a

Perkin Elmer Lambda 950, it follows [3] that the reflectance in the UV and visible regions reaches 90%. The reflectivity of bulk particle powders is higher than that of hollow powders [3], in the wavelength region from the edge of the main absorption to the near infrared region. The lower reflection coefficient of hollow particles is due to the high concentration of intrinsic defects in the crystal lattice of nanostructured particles.

From the spectra of induced absorption after irradiation with protons with an energy of 100 keV, a fluence of $5 \times 10^{15} \text{ cm}^{-2}$ of hollow particle powders, that the action of ionizing radiation creates color centers whose bands form a continuous absorption spectrum in the UV and visible regions. ZnO powders are characterized by absorption bands with high intensities in the range from 2 to 3.2 eV, in the near IR region, the band intensities are insignificant.

An analysis of the spectra of proton-irradiated zinc oxide powders with micron grains, taking into account the known values of the energy of absorption bands of intrinsic defects capable of absorbing in these ranges, implies that the main contribution to the absorption is made by interstitial zinc ions Zn_i' associated with $V_{Zn}''-Zn_i'$ pair, oxygen vacancies V_{O}'' , zinc vacancies V_{Zn}' and V_{Zn}'' .

Summary

The increased radiation stability to protons exposure of hollow particles compared to bulk particles is probably due to the fact that in these particles the main mechanism for the formation of radiation defects is surface in nature. Such structures are characterized by large ionization losses and a high ability to relax radiation defects in a thin layer of the sphere.

The results of the performed studies showed that the reflectivity of hollow ZnO particles in the entire spectral region from 200 to 2500 nm is less than that of bulk micron-sized particles [3]. The reason for this decrease is the large specific surface of the hollow particles, which leads to a high concentration of unsaturated bonds and surface defects. The analysis of experimental and calculated data demonstrates the correspondence of the concentration of the formed defects in order of magnitude. For hollow particles, the experimental concentration is $17.7 \times 10^{16} \text{ cm}^{-3}$ and $17.1 \times 10^{16} \text{ cm}^{-3}$ is the calculated concentration.

References

- [1] D.L. Dexter, Phys. Rev. B **101** (1956) 48.
- [2] C. Leroy, P. Rancoita, Principles of Radiation Interaction in Matter and Detection, fourth ed., World scientific publishing, New Jersey, 2016.
- [3] V.V. Neshchimenko, Li Chundong, M.M. Mikhailov, J. Surface Investigation. X-ray, Synchrotron and Neutron Techniques **1** (2019) 60.

Growth and thermoelectric properties of composite thin films based on higher iron and manganese silicides

I.A. Tarasov^{1,1}, I.A. Yakovlev¹, M.N.Volochaev¹, Z.I. Nazarova², A. Nazarov², A.S.Fedorov^{1,2}, S.N. Varnakov¹, S.G. Ovchinnikov^{1,2}.

¹ Kirensky Institute of Physics, Federal Research Center KSC SB RAS, Krasnoyarsk, 660036 Russia

² Siberian Federal University, 660041, Krasnoyarsk, Russia

*e-mail: tia@iph.krasn.ru

The main properties of new thermoelectrics, in addition to high quality, should be low cost, availability, environmental friendliness, mechanical and chemical strength. In fact, silicon is the fourth element among the most widely distributed elements of the earth's crust. Silicon and the main components of the best thermoelectrics based on silicides are cheap, do not contain rare or toxic elements, and are also environmentally friendly. Moreover, they represent various mechanisms of electronic transport, so among them there are new groups to be found. The most interesting in this regard are the higher manganese silicide (HMS) $\text{MnSi}_{1.75}$ [1], iron silicide $\beta\text{-FeSi}_2$ and magnesium silicide Mg_2Si .

This work aims to study the structural, optical and thermoelectric properties and processes of the formation of thin composite films based on semiconducting iron $\beta\text{-FeSi}_2$, manganese $\text{MnSi}_{1.75}$ silicides. Semiconducting silicides in the composite system are the main fraction; in addition, the system may contain non-stoichiometric silicon oxide separating the crystallites of the semiconducting phases, as well as some fractions of the metal phases of silicides and pure metals. These composite systems are poorly explored, which is associated with the difficulties of studying the structural properties of such systems due to the low symmetry of semiconducting iron and manganese silicides, the low dimensionality of crystallites obtained, and the interchangeability of manganese, iron in crystal structures of the silicides.

Thin films of substituted higher manganese silicide with thickness modulation of iron content $\beta\text{-(Fe}_{[1-x]}\text{Mn}_{[x]}\text{Si}_{[2-y]})$ with metal phase inclusions and composite films $\beta\text{(Fe}_{[1-x]}\text{Mn}_{[x]}\text{Si}_{[2-y]})$ together with $\text{(Mn}_{[1-y]}\text{Fe}_{[y]}\text{Si}_{1.75})$ were obtained using thermal evaporation under ultrahigh vacuum on substrates of amorphous silicon oxide SiO_2 , including coated with an Al_2O_3 layer. Before growing, the substrate was chemically cleaned, then the substrate was annealed under ultrahigh vacuum at a temperature of 650°C . Next, the samples were cooled to 500°C to begin the procedure of sample synthesis. Manganese, iron, and silicon were simultaneously evaporated from a Knudsen effusion cells onto the substrate surface at a speed of about 1.25, 1.5, and 5 nm / min, respectively. The base pressure in the chamber was 6.5×10^{-8} Pa. A thin film of silicide was grown layer-by-layer, where the chemical composition of the odd and even layer, in accordance with the deposition order, was different. The first layer in pair corresponds to the composition of manganese silicide enriched in iron, and the second - a mixture of pure manganese with silicon. As a result, three samples of the $[(\text{Mn}_{1-x}\text{Fe}_x)\text{Si}_{1.75} / \text{MnSi}_{1.75}]_n$ series were obtained, where the parameter n was 5, 10, 14 with a obtained thin film thickness of about 70 nm. The atomic Mn / Fe ratio in the resultant thin film varied in the

obtained series of samples in a wide range from 1 to 5. The atomic Mn / Fe ratio in the range from 1.04 to 1.18 relates to composite samples $[\beta\text{-FeSi}_2 / \text{MnSi}_{1.75}]_5$. Thus, the designation of the sample used below in the text consists of n number of deposited pairs of layers and the Mn / Fe ratio (sample n - Mn / Fe), i.e. sample 5 - 1.04. After the deposition of each sample was completed, a diffraction image of reflection high energy electron diffraction (RHEED) was recorded. As a result of the analysis of the evolution of the RHEED patterns during the formation of thin composite films it was shown that changes in the crystal lattice parameter of the resultant silicide show periodic and modulating behavior, decreasing to increasing unit cell volume (Figure 1) for the deposited layers of $\text{MnSi}_{1.75}$ silicide, with and without substitution of manganese atoms for iron atoms, respectively, up to a thickness of the deposited layer of 3.5 nm.

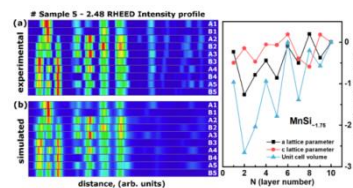


Figure 1. Experimental (a) and calculated (b) RHEED intensity profiles measured after deposition of each layer of the sample 5 - 2.48; (c) the relative change in the lattice parameter of the unit cell of higher manganese silicide $\text{MnSi}_{1.75}$ during the synthesis of each layer.

In summary, studies of thermoelectric properties of multilayer structures $[(\text{Mn}_x\text{Fe}_y)\text{Si}_{1.75} / \beta\text{-FeSi}_{2 \pm z}]_n$ showed a wide variation in their properties due to morphological and structural characteristics. The obtained values are comparable and exceed those available in the literature for single phase samples of thin films of manganese and iron silicide [2]. The most interesting result is the possibility of changing the temperature range of existence of high values of the power factor, i.e. from room temperature to 700-800 K typical for semiconducting iron and manganese silicides.

Acknowledgements

This work was supported by the Russian Science Foundation, project no. 16-13-00060-II.

References

- [1] I.A. Tarasov, et al., J.Mater. Sci. **53** (2018) 7571.
- [2] S.N. Girard, et al., Chem. Mater. **26** (2014) 5097.

Relationship between the photoluminescence spectra and MIR spectroscopy of mesoporous silicon samples during long-term storage: the effect of immersion in LiBr solutions

N.G. Galkin¹, D.T. Yan^{*2}, K.N. Galkin¹, S.V. Chusovitina¹

¹ Institute of Automation and Control Processes of FEB RAS, 5 Radio str., 690041, Vladivostok, Russia

² Far Eastern State Transport University, 47 Serysheva Str., 680021, Khabarovsk, Russia

*e-mail: dmitry_yan@mail.ru

Porous silicon (por-Si) continues to attract the attention of researchers in recent years [1,2], although the focus of work has changed. The problem of electroluminescence in por-Si-based diodes attracts very little attention [3], since it has not been possible to solve the problem of low resistance and contact stability to por-Si so far. Currently, the main emphasis is on the possibility of using por-Si as an antireflection coating for solar panels [4]. The second problem is the change in the properties of por-Si during long-term storage in atmospheric conditions due to oxidation, which affects the stability of future sensor devices. One of the possibilities for preserving por-Si layers is their processing in salt solutions, for example, lithium bromide (LiBr) [5, 6]. Studies have shown that for mesoporous Si (m/por-Si), in contrast to nanoporous Si [7], photoluminescence (PL) intensity increases with storage time, but a detailed analysis of the effect of immersion in LiBr solution on the intensity has not been carried out.

In this work, we studied the effect of the storage duration of m/por-Si layers treated by immersion with various durations (5, 10, and 20 minutes) in an aqueous LiBr solution with the previously established optimal concentration [6], and etalon por-Si sample on the PL intensity and changes in the intensity of absorption peaks in the MIR spectrum on various silicon-hydrogen, silicon-oxygen and silicon-hydroxyl groups. Samples were anodized under the following conditions: current density of 10 mA/cm² and duration of 5 minutes in a solution of HF : CH₃OH = 2 : 1. This ensured the formation of a m/por-Si layer with a porosity of about 55% and a thickness of 4 μm [6]. After anodizing, each sample was divided into 4 parts, one of which was an etalon por-Si, and the other three were working samples. After immersion in a LiBr water solution, the all samples were dried in a stream of dry nitrogen at room temperature. The equipment and methods for measuring the PL and MIR spectra are described in [6]. The PL spectra and transmission spectra were recorded at T = 20 °C for 171-200 days. The intervals between measurements up to 53 days were small: 2-7 days. Then they increased to 15-30 days, since the changes in the spectra reached saturation.

It was found that in the comparison sample and samples treated by immersion for 5, 10, and 20 minutes in an aqueous LiBr solution with an S/3 concentration (S is the limiting solubility of LiBr in water at 20 °C), a different behavior of the dependence of the PL intensity maximum on storage time is observed. The main difference was found in the period up to 74 days, which is expressed with a higher PL intensity for samples processed in LiBr. After 120 days of storage, the curves for the etalon por-Si sample and the sample with 5 minutes of immersion coincide and reach

saturation. However, with increasing immersion time, the intensity of PL saturation decreases. Throughout the entire storage period, the position of the PL peak remains unchanged (690±10 nm), which indicates the absence of a contribution from the quantum confinement effect in m/por-Si.

Registration of optical transmission spectra and analysis of the dependence of the main peaks of Si-H, Si-H₂, Si-O-Si, Si-OH, O₃-SiH on the storage duration for the etalon por-Si and working m/por-Si samples showed a similar character. In the initial storage period (0 days), the peak of the Si-O-Si rocking bond (470 cm⁻¹) is absent in the etalon por-Si sample, but appears in the working m/por-Si sample with an immersion time of 20 minutes, which indicates the formation of Si-O-Li bonds, as in [6]. With an increase in the storage time from 5 to 171 days, a Si-O-Si peak (470 cm⁻¹) appears and grows in the etalon por-Si sample and more intensively in working m/por-Si samples, which proves the conservation of the contribution of Si-O-Li bonds at all storage periods. The intensities of the Si-H and Si-H₂ peaks almost exponentially decrease due to hydrogen desorption. In this case, the Si – OH bond intensity (3400 cm⁻¹) increases linearly, while the Si – O – Si bond (1105 cm⁻¹) and O₃ – SiH bonds (880 and 2250 cm⁻¹) increase polynomially, saturating dangling bonds without hydrogen. This indicates the chemisorption of the OH⁻ ion group, the incorporation of oxygen into silicon, and the change in the configuration of bonds. The nature of the increase in the PL intensities and Si-O-Si and O₃-SiH bonds in the MIR spectra upon long-term storage for the por-Si reference and working m/por-Si samples indicates the main contribution of nonstoichiometric Si oxides with interstitial oxygen to the radiative recombination and PL signal. The role of adsorbed Li is to form a passive diffusion barrier, with an increase in the thickness of which the PL intensity decreases. It has been established that Si – O – Li bonds do not affect the PL intensity of m/por-Si subjected to immersion in an aqueous LiBr solution.

References

- [1] D.W. Cooke, *et.al.* J. Appl. Phys. **96** (2004) 197.
- [2] W.J. Aziz, *et.al.*, Optik **122** (2011) 1462.
- [3] J. Linnros, *et.al.*, Appl. Phys. Lett. **69** (1996) 833.
- [4] R.S. Dubey, D.K. Gautam, Superlattices and Microstr. **50** (2011) 269.
- [5] W. Dimassi, *et.al.*, J. Luminescence **131** (2011) 829.
- [6] N.G. Galkin, *et.al.*, Def. & Diff. Forum **386** (2018) 75.
- [7] A.S. Lenshin, *et.al.*, Mat. Sci. Semic. Proces. **30** (2015) 25.

Electronic structure and morphology at the formation of multilayer heterostructures with embedded nanocrystals CrSi₂ and β-FeSi₂

K.N. Galkin*, N.G. Galkin, E.Yu. Subbotin

Institute of Automation and Control Processes of FEB RAS, 5 Radio str., 690041, Vladivostok, Russia

*e-mail: galkinkn@iacp.dvo.ru

Semiconductor materials based on quasi-zero-dimensional semiconductor layers embedded in silicon with smaller band gap exhibit new optical and photoelectric properties. Such materials can be used to create new silicon-based photo generating devices. It is known that not only silicon heterojunctions with narrow-gap semiconductors [1], but also nanocrystals (NCs) of narrow-gap semiconductors embedded in the i-layer of a p-i-n diode, can be used to expand the spectral sensitivity range of silicon diodes to 1.6 microns or more [2]. A new approach to expanding the spectral sensitivity region of Si diodes was tested for incorporation of two types of β-FeSi₂ and CrSi₂ NCs [3]. It was found that the region of the photoresponse of structures expanded to 0.7 eV, but no morphological studies were carried out, and the electronic structure was not determined depending on the number of embedded layers.

In this work, we carried out a comprehensive study of the electronic structure and morphology of silicon with embedded layers of β-FeSi₂ and CrSi₂ NCs. All samples were grown on Si(111) substrates in the VARIAN UHV chamber. The electronic structure of a clean surface and a surface with islands and embedded nanocrystals was monitored by the AES and EELS methods ($E_p = 150$ eV). The NC embedding scheme was as follows. Multilayers of CrSi₂ NCs were the first to be embedded, and then two layers of β-FeSi₂ NCs were embedded. This was done in order to ensure first the absorption of light with a higher photon energy (0.8 - 1.1 eV) in the upper layer with embedded β-FeSi₂ nanocrystals, and then to ensure the absorption of low-energy photons (0.35-0.8 eV) in the underlying layer with CrSi₂ NCs. To study morphology, multilayer heterostructures (MLH) with embedded nanocrystals were formed. The first MLH included 6 layers of embedded CrSi₂ NCs, and the second MLH consisted of 4 embedded layers of CrSi₂ nanocrystals and two layers of embedded β-FeSi₂ NCs. After unloading the samples with embedded NCs layers, their topography was studied using a Solver P47 atomic force microscope (AFM) in a semi-contact mode.

After annealing the silicon substrate at $T = 1160$ °C, a silicon peak with a fine structure characteristic of the atomically clean silicon surface (Si (111) 7x7) was formed in the AES spectrum. In this case, the surface (10.0 eV, 14.2 eV) and bulk (17.0 eV) silicon plasmons were observed in the EELS spectrum. After deposition of 0.3 nm Cr at $T = 550$ °C and annealing at 600 °C, intense Cr peak appeared on the AES spectrum, which is characteristic of CrSi₂ islands. According to AFM data, the island density was

$(4-5) \cdot 10^{10}$ cm⁻², and their sizes vary from 15 nm to 30 nm. Such a layer of islands was overgrown with a Si layer according to a two-step procedure. The first 10 nm of Si was deposited at $T = 600$ °C, and the second 30 nm of Si was deposited at $T = 750$ °C. According to AFM data, the regime ensured a lower yield of CrSi₂ NCs and maintained the epitaxial quality of Si top layer. To increase the number of layers of embedded CrSi₂ NCs, the deposition of Cr and Si was repeated up to 4 times.

Islands of iron disilicide (β-FeSi₂) have always been formed on top of the embedded CrSi₂ NCs by the solid phase epitaxy method. For this, 0.3 nm Fe was deposited at room temperature, followed by annealing for 20 minutes at $T = 630$ °C. The formation of β-FeSi₂ islands was controlled by the appearance of intense Fe AES peak and a small change in the shape of the surface plasmon peak in the EELS spectrum. After unloading, according to the AFM data, islands with sizes of 20–40 nm and a density of $(1-2) \cdot 10^{10}$ cm⁻² were observed. In the case of deposition of Si cap layer, a two-stage Si deposition procedure was performed, similar to the case of embedding of CrSi₂ NCs.

According to the proven technique, two six-layer samples were formed, consisting of 6 embedded layers of CrSi₂ NCs, and also of 4 embedded layers of CrSi₂ NCs and 2 layers of β-FeSi₂ NCs, covered by Si epitaxial layers. According to the AES and EELS data, the surface of the first sample contained pure epitaxial silicon with atomic steps and a certain density of small pins up to $3 \cdot 10^9$ cm⁻² in which faceted nanocrystals were sometimes faceted. The root mean square roughness of the first sample was 0.37 nm. According to the AES and EELS data, silicon was also located on the surface of the second sample, and the root mean square roughness for it was 0.92 nm. Its increase is associated with the observed high density (up to $2 \cdot 10^{10}$ cm⁻²) of two-dimensional islands of silicon (with a height of up to 1 monolayer), which do not have time to integrate into the epitaxial silicon layer.

Acknowledgements

The work performed with partial financial support of RFBR grant No 19-02-000123_a.

References

- [1] D.Z. Chen, *Thin Solid Films* **537** (2013) 1.
- [2] A.V. Shevlyagin, D.L. Goroshko, E.A. Chusovitin, N.G. Galkin, *Applied Physics Letters* **109** (2016) 171101.
- [3] D.L. Goroshko, E.A. Chusovitin, A.V. Shevlyagin, M.V. Bozhenko, R.I. Batalov, R.M. Bayazitov, and N.G. Galkin, *Physica Status Solidi C* **10** (2013) 1844.

Optical properties and phonon structure of multilayer heterostructures with embedded CrSi₂ and β-FeSi₂ nanocrystals

N.G. Galkin, K.N. Galkin*

Institute of Automation and Control Processes of FEB RAS, 5 Radio str., 690041, Vladivostok, Russia

*e-mail: galkinkn@iacp.dvo.ru

Semiconductor silicides are of undoubted interest for silicon technology, as materials containing silicon and possessing new optical properties. Most studies were devoted to the growth of epitaxial films on silicon, the study of their structure, optical and electrical properties [1]. Among them, transition metal silicides are among the most studied [2,3]. To study the optical properties of films of semiconductor silicides with a gap smaller than that of silicon, a thickness of several hundred nanometers is needed to ensure a noticeable change in absorption in the region close to the absorption edge in the silicide. This allows us to calculate the optical constants of the films and determine correctly their band gap. Recently, interest has appeared in silicon with embedded nanocrystals (NCs) of semiconductor silicides [4]. But their total number, despite the high density of NCs, is insignificant for determining the optical characteristics in the region of the absorption edge. However, in the energy range of slightly larger absorption edges in silicon (1.2-2.5 eV) and an insignificant depth (50-100 nm) of narrow-gap semiconductor silicide NCs, it becomes possible to register a reflection signal from embedded nanocrystals or an interference signal from a thin layer with modified optical constants. Thus, we can state the fact of embedding of NCs into a Si lattice prior to transmission electron microscopy with TED [5] and EDS [6] data. Another possibility of identifying embedded narrow-gap nanocrystals in a Si matrix is the registration of Raman spectra. However, the occurrence depth in this case is limited by the probing depth in silicon for the incident exciting radiation, which is no more than 20 nm. Thus, using Raman spectroscopy, it is possible to register a signal from an embedded silicide nanocrystal if it is capped with silicon with a thickness of less than 20 nm or, conversely, enters the surface region of the sample.

In this paper, we studied the optical properties of grown multilayer heterostructures by optical spectroscopy (OS) and Raman spectroscopy. To study the OS spectra, six-layer samples with one (CrSi₂) and two types of nanocrystals (CrSi₂ + β-FeSi₂) were selected, which is associated with the need to increase the absorption on nanocrystals. A reference p-i-n sample was also studied, in which the deposition of chromium (iron), process shutdown and annealing were simulated, as for working samples. To identify the Raman peaks from the embedded nanocrystals, Raman spectra of the grown multilayer samples were recorded, as well as from the samples with uncovered CrSi₂ nanocrystals (0.5 Cr) and one Si capped layer of CrSi₂ nanocrystals and over it one uncoated NC layer (β-FeSi₂). The OS spectra were recorded at room temperature on

Hitachi U-3010 spectrophotometers with an integrating sphere and a Bruker Vertex 80v Fourier spectrophotometer. Raman spectra emitted by light with a wavelength of 488 nm were also recorded at room temperature with a LabRam HR 800 spectrophotometer. Raman spectra were recorded on samples with embedded nanocrystals of chromium and iron disilicides in the macro mode with a long accumulation time to increase the intensity of weak signals.

The transmission and reflection spectra of multilayer structures with embedded nanocrystals revealed interference maxima, as well as weak reflection peaks from the embedded nanocrystals CrSi₂ at 2.0 eV and β-FeSi₂ at 1.75 eV. The interference is explained by a change in the effective refractive index in a thin Si i-layer (250 nm) with embedded nanocrystals and the formation of a reflection signal from the interface of silicon/NCs modified silicon. In the reference p-i-n sample with emulation of deposition of chromium and iron atoms, interference features were absent, since refractive index did not change. The shifts in the energy of interference maxima in samples with 6 layers of CrSi₂ nanocrystals and 4 layers of CrSi₂ nanocrystals and 2 layers of β-FeSi₂ nanocrystals are explained by an increase in the effective refractive index in the sample with β-FeSi₂ nanocrystals due to the higher refractive index in β-FeSi₂ compared to CrSi₂. According to Raman scattering data, a weak peak at 415 cm⁻¹ was found in six-layer samples with β-FeSi₂ nanocrystals, which corresponds to one of the β-FeSi₂ Raman peaks [7], which is associated with a partial exit to the surface region of β-FeSi₂ nanocrystals oriented perpendicular to surface coating layer.

Acknowledgements

The work performed with partial financial support of RFBR grant No 19-02-000123_a.

References

- [1] Semiconducting silicides, ed. V.E. Borisenko (Springer, Berlin, 2000).
- [2] H. Lange, *Thin Solid Films*, **381** (2001) 171.
- [3] T. Suemasu, *J. Luminescence* **80** (1999) 473.
- [4] N.G. Galkin, *Thin Solid Films* **515** (2007) 8179.
- [5] A.V. Shevlyagin, *et. al.*, *Scientific Reports*, **10** (2015) 14795.
- [6] N.G. Galkin, K. N. Galkin, A.V. Tupkalo, Z. Fogarassy, B. Pécz, *J. Alloys and Compounds* **813** (2020) 152101.
- [7] Y. Maeda, H. Udono, Y. Terai, *Thin Solid Films* **461** (2004) 165.

Current-voltage characteristics and photoelectric properties of mesa-diodes based on multilayer heterostructures with imbedded CrSi_2 and $\beta\text{-FeSi}_2$ nanocrystals

N.G. Galkin, K. N. Galkin^{*}, E. A. Chusovitin, D. L. Goroshko

Institute of Automation and Control Processes of FEB RAS, 5 Radio str., 690041, Vladivostok, Russia

^{*}e-mail: galkinkn@iacp.dvo.ru

The growth of semiconductor silicides in the form of epitaxial films on silicon is complicated by the different lattice symmetries of the silicides of most metals, the difference in lattice constants, and the difference in temperature expansion coefficients with Si one [1]. This complicates the creation of epitaxial films of silicides of high crystalline quality due to the formation of a dislocation network [2, 3] and even peeling from the silicon substrate [4]. However, the transition to the growth of quasi-zero-dimensional nanocrystals (NCs) in silicon matrix removes these limitations by introducing stresses in nanocrystals and silicon instead of dislocations [5]. For film solar cells, the principle of the formation of cascade diode structures consisting of few p-n junctions from semiconductors with different band gaps is known, which ensures the expansion of spectral photosensitivity. This approach can also be used to create a cascade element using embedded layers of nanocrystals with different widths of the band gaps. In this case, the semiconductor silicide NCs with a larger band gap should be used as the upper layer.

In this work, we carried out a comprehensive study of the current – voltage and photoelectric properties of diode structures with embedded multilayers of $\beta\text{-FeSi}_2$ NCs (upper) and CrSi_2 NCs (lower). In the UHV chamber of the VARIAN installation on p-type silicon substrates (Si (111) KEF- (0.1-0.5)), $\text{p}^+\text{-i-n}$ diode structures with 6 layers of NCs embedded in Si i-layers are grown. Ohmic contacts are made to the reverse side of the substrate and the upper covering layer of the $\text{p}^+\text{-type}$ of conductivity. As a reference, a sample of a $\text{p}^+\text{-i-n}$ diode structure was grown with emulation of the Cr and Fe deposition and the repetition of all deposition processes, interruption of deposition, and step-by-step annealing in accordance with the formation of working diode structures with embedded NCs. Three families of 4 mesa diodes of 4 pieces were created by chemical etching on top of round Al contacts in each working sample to study their transport and photoelectric properties.

When studying the dark current-voltage characteristics (CVC) of two working and one reference diodes, it was found that good rectification is observed. The difference between the maximum forward and reverse current of the diode is 5-6 orders of magnitude. In the CVC mode of measuring under integrated illumination by a tungsten lamp, a photocurrent was detected in all diodes. The maximum photocurrent ($1 \cdot 10^{-5}$ A) was observed for a diode with 6 embedded layers of CrSi_2 NCs and a reference diode, and the open circuit voltage in them was 0.38 V and 0.29 V, respectively. The minimum photocurrent value ($(4-5) \cdot 10^{-7}$ A) was found for a diode with 4 layers of CrSi_2 NCs

and 2 layers of $\beta\text{-FeSi}_2$ NCs, which is associated with a high density of defect levels that capture carriers generated by light.

Studies of the dark capacitance-voltage characteristics of the working and reference diodes in the frequency range from 1 kHz to 1 MHz and reverse biases have shown that the reference diode has the maximum capacitance at all frequencies. The decrease in capacitance in the working diodes is associated with a decrease in the concentration of free carriers due to their capture at defect levels or in embedded NCs. It was found that linear sections are observed only for the $1/C^2$ dependences, which made it possible to evaluate the created diodes as sharp. The extrapolation of this dependence to a value of $1/C^2 = 0$ in the region of direct biases approximately gave the contact potential difference $\Phi_k = 0.95$ V for two working and reference diodes, which is independent of the incorporation of CrSi_2 and $\beta\text{-FeSi}_2$ NCs.

When studying the spectral photoresponse of the working diodes in the current mode at room temperature, a low-energy peak at 0.75 eV was detected, this is associated with recharging when illuminating the acceptor states of defects in the Si band gap associated with NCs.

At $T = 90$ K, an absorption band was detected in the working diodes associated with carrier generation in the embedded NCs of semiconductor CrSi_2 and $\beta\text{-FeSi}_2$. The extrapolation of the square root dependence of the photoresponse in the photocurrent mode at a temperature of liquid nitrogen to the region of zero photoresponse yielded the value $E_g = 0.50$ eV for diodes with 6 layers of CrSi_2 NCs, and the value $E_g = 0.70$ eV for 4 diodes with 4 layers of CrSi_2 and 2 layers of $\beta\text{-FeSi}_2$ NCs. Changes in the values of E_g are associated with both the stresses in the NCs and the averaging over two types of NCs with different band gaps.

Acknowledgements

The work performed with partial financial support of RFBR grant No 19-02-000123_a.

References

- [1] Semiconducting silicides, ed. V.E. Borisenko (Springer, Berlin, 2000).
- [2] Y. Ugajin, M. Takauji, T. Suemasu, *Thin Solid Films* **508** (2006)376.
- [3] T Suemasu, *Journal of Physics: Conference Series* **596** (2015) 012005.
- [4] N.G. Galkin, *Journal of Physics: Conf. Ser.*, **1236** (2019) 1003.
- [5] N.G. Galkin, *Thin Solid Films* **515** (2007) 8179.

Growth, structure and low temperature magneto transport in Ca₂Si films on Si(111) substrate

N.G. Galkin, K.N. Galkin, A.V. Tupkalo*, S.A. Dotsenko, E.A. Chusovitin

Institute of Automation and Control Processes of FEB RAS, 5 Radio str., 690041, Vladivostok, Russia

*e-mail: andrey.tupkalo@gmail.com

Silicides of alkaline earth metals (Ca, Mg) are promising for the creation of both photoelectric diode structures and thermoelectric converters. There are 6 silicides in the Ca – Si system, two of which Ca₂Si [1] and Ca₃Si₄ [2] are semiconductors, and the rest are metals and semimetals. The main attention is paid to the growth and study of the properties of Ca₂Si semiconductor, which can be grown in the form of thin films on various substrates, including Si(111) through a Mg₂Si sacrificial layer in the form of bulk [3] and very thin films [4]. Thick enough films with the composition of Ca₂Si on a Si(111) substrate were not previously grown, and their magnetoresistive properties were not studied.

Samples with Ca₂Si films on Si(111) silicon substrate with thicknesses from 80 nm to 100 nm were grown in an ultrahigh vacuum chamber (UHV) of the OMICRON Compact setup with a base vacuum of 1×10^{-10} Torr with LEED, AES and EELS facilities. To study the transport properties of structures like "Hall cross" with contact pads were etched on the substrate. The magneto-resistive effect was measured with direct current and a constant magnetic field in the temperature range 10–300 K using a "TeslatronTM-CF" installation.

The work tested the growth of thin films with a Ca₂Si structure on silicon with a preformed two-dimensional Mg₂Si(111)1x7 layer as a sacrificial template, which was transformed into a two-dimensional Ca₂Si layer during Ca reactive deposition. It was established that at a substrate temperature of 250 °C, the Mg₂Si layer is destroyed, but some Mg atoms remain in the near-surface region. At a temperature of 300 °C, Mg atoms completely desorb from the surface, and the Ca₂Si layer formed according to the AES and EELS data does not give a LEED picture in both cases, which indicates a small domain size. In the process of molecular beam epitaxy (MBE) at a temperature of 250 °C, an epitaxial Ca₂Si(100)1x1 film with a two-domain orientation grows over a Ca₂Si template to a thickness of 80-100 nm: Ca₂Si(100)||Si(111), Ca₂Si[010]||Si[1 $\bar{1}$ 0] и Ca₂Si[001]||Si[11 $\bar{2}$]. When the substrate temperature is increased to 300 °C and the film thickness is 100 nm, the reflections in the LEED pattern broaden, which corresponds to a decrease in the size of Ca₂Si domains. All grown films on AFM data consist of fused and elongated rectangular crystals with sizes: width 30-80 nm and length 80-250 nm, which were located on the surface at different angles. The minimal sizes of nanocrystals were possessed by grown samples, which corresponded to their minimum root mean square roughness (σ_{rms} =3.0 - 3.2 nm. An increase in the MBE growth temperature to 300 °C led to a slight decrease in roughness due to the intensification of diffusion transfer processes.

Low-temperature measurements of the magnetoresistive effect were carried out after unloading the

samples and manufacturing test structures. A sample with a Ca₂Si structure grown at a temperature of 250 °C showed high instability of the contacts at temperatures below 150 K. This led to the fact that the dependences of the magnetoresistive effect in the form of $\Delta\rho/\rho$ curves on the magnetic field (B) were recorded starting from T = 200 K. For temperatures of 250 K and 300 K, the dependences were parabolic, which was confirmed by the linearity of the characteristics of $\Delta\rho/\rho(B^2)$ with one slope in the entire range of magnetic fields. This indicates only one type of carrier in the Ca₂Si film at given temperatures and corresponds to the semiconductor type of conductivity [5]. At 200 K, the $\Delta\rho/\rho(B)$ dependence strongly deviated from the parabolic one, which indicates the possible contribution of carriers with a different sign.

In the Ca₂Si film formed at T = 300 °C, the measurements of the magnetoresistive effect were stable, starting at a temperature of 1.5 K. However, at T = 1.5 K the $\Delta\rho/\rho(B)$ values were negative, which corresponds to the existence of weak electronic localization in the film [6]. At a temperature of 50 K, the $\Delta\rho/\rho$ values became positive, but did not depend on the magnitude and direction of the magnetic field. At temperatures of 100–250 K and magnetic fields up to 0.5 T, the $\Delta\rho/\rho$ values remained negative, but at high magnetic fields the $\Delta\rho/\rho(B)$ dependence approached parabolic. Only at T = 300 K did the $\Delta\rho/\rho(B)$ dependence become parabolic for all magnetic fields. This was confirmed by quasi-linearity at T = 100–250 K and linearity at T = 300 K. The more complex character of the $\Delta\rho/\rho(B)$ dependence on temperature indicates a competition between the contributions of carriers with different signs at these temperatures, which correlates with the data of LT Hall measurements and confirms the presence of two types of carriers in the Ca₂Si film grown at T = 300 °C.

The presence in Ca₂Si films of two types of carriers to be specified according to transmission electron microscopy for the existence of embedded Mg atoms and a triple silicide (Ca_{2-x}Mg_xSi).

Acknowledgements

The work performed with financial support of RFBR grants No 19-02-000123_a.

References

- [1] S. Lebegue, *et.al.*, Phys. Rev. B **72** (2005) 085103.
- [2] D.B. Migas, *et.al.*, J. Phys.: Cond. Mat. **19** (2007) 346207.
- [3] H. Tatsuoka, *et.al.*, Thin Solid Films **461** (2004) 57.
- [4] S.A. Dotsenko, *et.al.*, Physics Procedia **11** (2011) 95.
- [5] Y. P. Yu and M. Cardona, Fundamentals of Semiconductors, 4 edition, 2000.
- [6] B. M. Askerov, Electron Transport Phenomena in Semiconductors, 5th edn. (Singapore: World Scientific, 1994. P. 416).

Relationship between the photoluminescence spectra and MIR spectroscopy of mesoporous silicon samples during long-term storage: the effect of immersion in $\text{Fe}(\text{NO}_3)_3$ solutions

N.G. Galkin¹, K.N. Galkin^{*1}, D.T. Yan², S.V. Chusovitina¹

¹ Institute of Automation and Control Processes of FEB RAS, 5 Radio str., 690041, Vladivostok, Russia

² Far Eastern State Transport University, 47 Serysheva Str., 680021, Khabarovsk, Russia

*e-mail: galkinkn@iacp.dvo.ru

The renewed interest of researchers in porous silicon (por-Si) in recent years is associated both with the problem of resistance to oxidation of por-Si during long-term storage under atmospheric conditions [1, 2], and with the development of various microresonators, photonic crystals, biosensors and nanocomposites [3-7]. To stabilize the photoluminescence (PL) intensity of a por-Si, its surface structure must be modified, for example, by incorporating iron ions from an aqueous solution of iron nitrate ($\text{Fe}(\text{NO}_3)_3$) into the pores and replacing Si-H bonds with Si-Fe bonds [8, 9]. In [10], the optimal concentration of $\text{Fe}(\text{NO}_3)_3$ in an aqueous solution was determined, which ensured the preservation and enhancement of the luminescent properties of por-Si after their immersion. However, no correlation was established between the PL and MIR spectra for mesoporous silicon (m/por-Si).

In this paper, we study the relationship between the parameters of the PL spectra (intensity, position of the PL peak) and the main peaks in the MIR optical spectra responsible for the formation of various bonds of silicon with atoms and ions on the surface and in the near-surface region. The objects of the study were m/por-Si layers treated by immersion with various durations (5, 10, and 20 minutes) in an aqueous solution of $\text{Fe}(\text{NO}_3)_3$ with the previously established optimal concentration [10] and a reference por-Si sample. The modes of anodizing the samples, washing and drying, their thickness, sizes and porosity, as well as registration methods, were consistent with the data of [10]. The sample was divided into 4 parts before measurements, one of which was a reference sample, and the other three were working samples. The PL spectra and transmission spectra were recorded at $T = 20^\circ\text{C}$ with small intervals for 200 days.

It was found that in the reference sample and samples treated by immersing for 5 - 20 minutes in an aqueous solution of $\text{Fe}(\text{NO}_3)_3$ with a concentration of 0.5 M, the same type of the PL intensity maximum dependences on storage time is observed. After 150 days of storage, the curves for the reference and working samples saturate at different levels of intensity. The maximum PL intensity is observed for a sample with 10 minutes of immersion, and the minimum for a sample after 5 minutes of immersion. For the reference and the sample, with an immersion time of 20 minutes, a slight "blue" shift of the PL peak maximum by 20–25 nm is observed, which corresponds to the manifestation of active por-Si oxidation, a decrease in the size of nanocrystals (NCs), and an increase in the effective band gap in NCs. In the case of a working sample (20 min), this corresponds to a decrease in protection

against oxidation due to the formation of iron islands on the NCs surface. On the contrary, for 5 and 10 minute's immersions, such shifts were not noticed and indicate the formation of a continuous layer of iron atoms, which protects the PC from deep oxidation.

Registration of the MIR transmission spectra of the reference and working samples showed that the peaks of Si-H and Si-H₂ decrease rapidly, and the peaks of Si-O-Si, Si-OH, O₃-Si-H increase with the storage time. In the initial storage period (0-10 days), the peak of the rocking bond Si-O-Si (470 cm⁻¹) is absent in all samples. It appears only after 14 days of storage for all samples, which corresponds to the beginning of the oxidation stage of m/por-Si, which is most pronounced appears after 53 days of storage in accordance with the PL peak shift. The m/por-Si treatment in an aqueous solution of $\text{Fe}(\text{NO}_3)_3$ somewhat delays oxidation according to the Si-O-Si peak (1170 cm⁻¹). The intensities of the Si-H and Si-H₂ peaks almost exponentially decrease due to H₂ desorption. The dangling bonds are saturated with hydroxyl and oxygen ions: the Si-OH (3400 cm⁻¹) bond intensity increases linearly, and the Si-O-Si (1105 cm⁻¹) and O₃-SiH bond intensities (880 and 2250 cm⁻¹) grow polynomially, which confirms the change in the configuration of the bonds. In this case, the optimal behavior according to the PL data is shown by a sample with 10 minutes of immersion, which retains a higher density of Si-H and Si-H₂ bonds. Iron ions do not enter into a chemical bond with silicon and oxygen; therefore, the role of adsorbed Fe lies in the formation of a passive diffusion barrier, with an increase in the thickness of which the PL intensity decreases.

The nature of the increase in the PL intensities and S-O-Si and O₃-SiH bonds in the MIR spectra during long-term storage for the working sample (10 minutes of immersion) indicates the main contribution of nonstoichiometric Si oxides with interstitial oxygen to the PL signal. The 5 and 20 min immersions are not optimal.

References

- [1] A.S. Lenshin, *et.al.*, Techn. Phys. **59** (2014)224.
- [2] A.S. Lenshin, *et.al.*, Mat. Sci. Sem. Proc. **30** (2015) 25.
- [3] S.K. Lazaruk, *et.al.*, Semiconductors **39** (2007) 136.
- [4] D.N. Goryachev, *et.al.*, Semiconductors **44** (2010) 1588.
- [5] O.A. Aktsipetrov, *et.al.*, Physica Solid State **47** (2005) 156.
- [6] E.V. Astrova, *et.al.*, Semiconductors **38** (2004) 1084.
- [7] F.M. Liu, *et.al.*, Thin Solid Films **471** (2005) 257.
- [8] X.J. Li, *et.al.*, Appl. Phys. Lett. **74** (1999) 389.
- [9] D. Zhu, *et.al.*, Appl. Surf. Sci. **191** (2002) 218.
- [10] N.G. Galkin, *et.al.*, Optics and Spectrosc. **125** (2018) 199.

First demonstration of n⁺-AZO/p-BaSi₂ thin film solar cells

Y. Yamashita*, K. Toko, T. Suemasu

Institute of Applied Physics, University of Tsukuba, Tennodai 1-1-1, Tsukuba-shi, Ibaraki, Japan

*e-mail: bk201311068@s.bk.tsukuba.ac.jp

Barium disilicide (BaSi₂) shows great promise as a new material for thin film solar cells [1]. It has a suitable bandgap of 1.3 eV, a large optical absorption coefficient (α) of $3 \times 10^4 \text{ cm}^{-1}$ for a photon energy of 1.5 eV [2], and a large minority-carrier diffusion length of about 10 μm [3]. Furthermore, it is composed of only earth abundant elements and highly stable. Therefore, BaSi₂ can be used for future terawatt-class power generation. We succeeded to increase the minority carrier lifetime from 0.1 to 10 μs by covering BaSi₂ with an amorphous Si (a-Si) passivation layer [4]. And we have achieved the operation of BaSi₂-pn homojunction solar cell [5,6]. In this structure, an open-circuit voltage (V_{OC}) beyond 0.8 V and a conversion efficiency (η) beyond 25% are expected [7]. However, very recently, 3D optical simulations showed that the parasitic absorption in the n⁺-BaSi₂ electron transfer layer (ETL) is too large because of large α [8]. To reduce such absorption, the material of ETL must be wide-gap-semiconductor, which transfers sun-light into a BaSi₂ absorber layer efficiently. According to optical simulation, the photocurrent increased from 18.0 to 30.2 mA/cm^2 by changing ETL from n⁺-BaSi₂ to Al-doped ZnO (AZO). However, no such device has been reported in operation. In this study, we aimed to demonstrate the operation of n⁺-AZO/p-BaSi₂ heterojunction solar cells.

We fabricated a 520-nm-thick BaSi₂ layer by molecular beam epitaxy (MBE). After thermal cleaning at 900 °C, we prepared a 5-nm-thick BaSi₂ template layer by reactive deposition epitaxy on a Czochralski-p⁺-Si (111) substrate ($\rho < 0.01 \text{ }\Omega\text{cm}$), followed by co-deposition of Ba and Si, and B to form a 20-nm-thick B-doped p⁺-BaSi₂ emitter with $p \sim 10^{19} \text{ cm}^{-3}$, and 500-nm-thick B-doped BaSi₂ absorber layer with $p \sim 10^{17} \text{ cm}^{-3}$ by MBE. After the MBE growth, the BaSi₂ films were passivated by plasma enhanced H atoms [9]. Finally, a 3-nm-thick a-Si layer was deposited *in situ* on the surface for surface passivation. 300-nm-thick AZO and 50-nm-thick ZnO electrodes with a diameter of 1 mm were sputtered on the surface, and Al electrodes on the back side. Furthermore, 100-nm-thick Ga₂O₃ was also sputtered instead of ZnO, in order to reduce the conduction band offset (CBO). The evaluation was carried out by the current density versus voltage (J - V) characteristics under standard AM 1.5 illumination and photoresponse properties were measured. The band alignments were simulated by automat for simulation of heterostructures (AFORS-HET).

J - V characteristics under AM1.5 illumination of n⁺-AZO/p-BaSi₂ showed the rectifying property. It showed $\eta = 0.04\%$, a short circuit current density (J_{SC}) of 3.7 mA/cm^2 , and an V_{OC} of 50 mV. The internal quantum efficiency (IQE) exceeded 30% at $\lambda = 600 \text{ nm}$. This efficiency is almost the same value as that obtained for BaSi₂-pn homojunction solar cells. Therefore, we can state that we succeeded the demonstration of n⁺-AZO/p-BaSi₂ heterojunction solar cells for the first time.

However, the values of IQE were much smaller than simulation results, and leakage current was too large. Maybe various factors are involved in this, but among them, the interface defect at the heterojunction should be considered. The electron affinity (EA) of BaSi₂ and ZnO are 3.2 and 4.1 eV, respectively. So, it indicates a cliff conformation with a negative CBO between ZnO and BaSi₂ of 0.9 eV. The cliff conformation acts as a barrier against the flow of injection electrons under the forward bias condition, accumulates the electrons at the ZnO/BaSi₂ interface and increases the probability of interfacial recombination.

In order to reduce such CBO, we investigated a Ga₂O₃ buffer layer as a next step. EA of Ga₂O₃ is between the values of ZnO and BaSi₂, and Ga₂O₃ shows n-type conductivity natively. In this work, we formed n⁺-AZO/n-Ga₂O₃/p-BaSi₂ heterojunction solar cells. The J - V characteristics were dramatically improved and the reverse saturation current density (J_0) was reduced from 5.3×10^0 to $4.2 \times 10^{-3} \text{ mA/cm}^2$. However, due to the high series resistance (R_s) of Ga₂O₃, the R_s increased from 340 to 6170 Ω and the η was not achieved. In the future, the high η will be achieved by decreasing the thickness of Ga₂O₃.

Acknowledgements

This work was financially supported by JSPS KAKENHI Grant Numbers 17K18865 and 18H03767 and JST MIRAI. One of the author (Y. Y.) was financially supported by a Grant-in-Aid for JSPS Fellows (19J21372).

References

- [1] T. Suemasu, N. Usami. J. Phys. D: Appl. Phys. **50** (2017) 023001.
- [2] K. Toh, T. Saito, T. Suemasu. Jpn. J. Appl. Phys. **50** (2011) 068001.
- [3] M. Baba, K. Toh, K. Toko, N. Saito, N. Yoshizawa, K. Jiptner, T. Sakiguchi, K. O. Hara, N. Usami, T. Suemasu. J. Cryst. Growth **348** (2012) 75.
- [4] R. Takabe, K. O. Hara, M. Baba, W. Du, N. Shimada, K. Toko, N. Usami, T. Suemasu. J. Appl. Phys. **115** (2014) 193510.
- [5] K. Kodama, R. Takabe, T. Deng, K. Toko, T. Suemasu. Jpn. J. Appl. Phys. **57** (2018) 050310.
- [6] K. Kodama, Y. Yamashita, K. Toko, T. Suemasu. Appl. Phys. Express **12** (2019) 041005.
- [7] T. Suemasu. Jpn. J. Appl. Phys. **54** (2015) 07JA01.
- [8] Y. Yamashita, T. Sato, K. Toko, T. Suemasu. JSAP Spring meeting, 11p-W834-7 (2020).
- [9] Z. Xu, D. A. Shohonov, A. B. Filonov, K. Gotoh, T. Deng, S. Honda, K. Toko, N. Usami, D. B. Migas, V. E. Borisenko, T. Suemasu. Phys. Rev. Materials **3** (2019) 065403.

Marked photoresponsivity enhancement of boron-doped BaSi₂ by atomic H passivation

Z. Xu^{*1}, T. Sato¹, L. Benincasa¹, Y. Yamashita¹, T. Deng¹, K. Gotoh², K. Toko¹, N. Usami², A.B. Filonov³, D.A. Shohonov⁴, D.B. Migas³, T. Suemasu¹

¹ Institute of Applied Physics, University of Tsukuba, Tsukuba, Ibaraki 305-8673, Japan

² Graduate School of Engineering, Nagoya University, Nagoya 464-8603, Japan

³ Department of Micro- and Nanoelectronics, Belarusian State University of Informatics and Radioelectronics, P. Brovki 6, 220013 Minsk, Belarus

⁴ Institute of Applied Physics, National Academy of Sciences of Belarus, Akademicheskaya 16, 220072 Minsk, Belarus

*e-mail: xudaodao0812@hotmail.com

Semiconducting BaSi₂ has many advantages for solar cell applications, such as a suitable band gap of 1.3 eV, a large absorption coefficient of $3 \times 10^4 \text{ cm}^{-1}$ at 1.5 eV, and a large minority-carrier diffusion length of ca. 10 μm [1]. According to the first-principle calculation which was performed by Dr. Kumar [2], the Si vacancies are most likely to occur as point defects in BaSi₂ in both Si-rich and Si-poor growth condition that lead to the degradation of the optical properties of BaSi₂. In our previous research [3], we passivated these point defects by atomic H using the plasma generator. The photoresponsivity of undoped BaSi₂ is enhanced markedly by irradiation of H atoms onto BaSi₂ thin films for 15 min thanks to the improvement of minority carrier lifetime. The basic solar cell structure is a *pn* junction. Thus, the next important step is the passivation of impurity-doped p- or n-BaSi₂ thin films. In this study, we investigate the effect of atomic H passivation on the optical properties of B-doped p-BaSi₂.

First, Ba, Si, and B atoms were co-deposited at 600 °C on the low-resistivity (ρ) Czochralski (Cz) n⁺-Si(111) substrate ($\rho = 0.01 \Omega\text{cm}$) to form approximately 500 nm-thick B-doped BaSi₂ for photoresponsivity measurement. The crucible temperature of B (T_B) was set at 1100 °C, wherein, the hole concentration (p) was $7 \times 10^{16} \text{ cm}^{-3}$ respectively at room temperature. Hereafter, we refer to these as “lightly B-doped” sample. Second, we supplied the atomic H by using the plasma generator with various H supply duration (t_H). Here, the power of plasma generator and vacuum level was kept at 10 W and 10^{-3} Pa respectively. Finally, 3 nm-thick amorphous Si (a-Si) layer was formed to prevent oxidation. For photoresponsivity measurement, 80 nm-thick indium-tin-oxide (ITO) electrodes and 150 nm-thick Al were sputtered on the front and back side of samples. This measurement was performed at room temperature. To fully understand the influence of B doping and H passivation on properties of BaSi₂, the first-principle calculation of total energy projector-augmented wave method (VASP code) has been used to calculate density of states (DOS) of H passivated B-doped BaSi₂. We used a $2 \times 3 \times 2$ enlarged unit cell to avoid strong defect-defect interactions. For the exchange and correlation potentials, the generalized gradient approximation of Perdew-Burke-Ernzerhof has been implemented. The energy cutoff of 400 eV and a $5 \times 5 \times 5$ mesh of Monkhorst-pack points for the Brillouin zone integration were sufficient to ensure the total energy convergence.

The photoresponsivity of all samples started to increase at the wavelength of 1000 nm which corresponded to the

band gap of BaSi₂. The smallest photoresponsivity was obtained for the lightly B-doped BaSi₂ without H passivation. The atomic H supply improved the photoresponsivity of samples remarkably, where photoresponsivity reached a maximum value of $\sim 4 \text{ A/W}$ at the wavelength of 800 nm of the lightly B-doped BaSi₂ with t_H of 5 min. This value is almost twice the highest value previously reported for H-passivated undoped BaSi₂ films. The photoresponsivity of lightly B-doped BaSi₂ with t_H of 15 min, exhibited further degradation, signifying that both the bulk and surface regions acquired defects. In the bulk region, the superabundant H atoms generated additional defects, the same phenomenon has already observed in crystalline Si [4]. Next, we studied the effect that B doping with and without H incorporation had on the properties of BaSi₂. The B atoms sit in both substitutional site and interstitial site which exist simultaneously. When a B atom is a substitutional impurity, degenerated p-type semiconducting properties occur. An H atom is directly bonded to B atom, the Fermi level shifts to the band gap; indicating semiconducting properties that are no longer degenerated with no states in the band gap. In the case of B atom acting as an interstitial impurity, we have found that the localized states exist in the band gap and the Fermi level is in the middle of these localized states. However, an H atom is connected to B atom, the Fermi level shifts above the localized states, meaning that these localized states are inactive due to occupied by electrons.

Our investigation clearly shows that the photoresponsivity of lightly B-doped BaSi₂ can be significantly improved by the H passivation. These results are in perfect agreement with the first-principle calculation. The lightly B-doped BaSi₂ passivated by atomic H has a great potential to be an absorber layer in BaSi₂ homojunction solar cells in the future.

References

- [1] T. Suemasu, N. Usami J. Phys. D: Appl. Phys. **50** (2017) 023001.
- [2] M. Kumar, N. Umezawa, W. Zhou, and M. Imai, J. Mater. Chem. A **5** (2017) 25293.
- [3] Z. Xu, D. A. Shohonov, A. B. Filonov, K. Gotoh, et al., Phys. Rev. Mater. **3** (2019) 065403.
- [4] D. Chen, P. G. Hamer, M. Kim, T. H. Fung, et al., Sol. Energy Mater. Sol. C. **185** (2018) 174.

Structure and optical properties of thick $\text{Ca}_2\text{Si}(100)$ epitaxial films on $\text{Si}(111)$ substrate

K.N. Galkin, N.G. Galkin, S.A. Dotsenko, E.Y. Subbotin and O.V. Kropachev

Institute of Automation and Control Processes of FEB RAS, 5 Radio str., 690041, Vladivostok, Russia

*e-mail: galkinkn@iacp.dvo.ru

Alkaline earth metals such as magnesium (Mg) and calcium (Ca) are inexpensive due to their wide distribution in the earth's crust, and their compounds with silicon - semiconductor silicides are interesting for creating thermoelectric converters [1]. According to theoretical calculations [2–4], semiconductors include calcium semisilicide (Ca_2Si) with a band gap of 0.3–0.36 eV [2,3] to 1.02 eV [4]. The greatest difficulties for the growth of Ca_2Si on silicon substrates are poorly controlled diffusion of Ca into the silicon substrate, the presence of a large amount of silicides in the Si-Ca system, and their close heats of formation [5]. In this regard, to date, experimental studies of thick epitaxial Ca_2Si films are lacking due to the lack of a method for growing such films on a silicon substrate. For the formation of bulk Ca_2Si layers (100–300 μm), the method of Ca diffusion through a sacrificial Mg_2Si layer on a Si substrate in low vacuum was proposed and optically tested, but without determining the band gap [6]. As a result of this approach, large-pore Ca_2Si layers with poor adhesion to the Si substrate were formed. We tested this approach in ultrahigh vacuum (UHV) conditions using reactive Ca deposition on a preformed thin (2.0 nm) sacrificial Mg_2Si layer on a Si (111) substrate to form a Ca_2Si film [7]. An ultrathin Ca_2Si layer (2.0–7.0 nm) was grown in this way on a Si(111) substrate under UHV conditions.

In this work, for the first time, thick epitaxial $\text{Ca}_2\text{Si}(100)$ films on a Si(111) substrate were grown by molecular beam epitaxy (MBE) at low temperatures with a preformed $\text{Mg}_2\text{Si}(111)$ sacrificial layer, and their atomic and electronic structures, crystal structure, and optical properties were studied.

The growth of Ca_2Si films was carried out in the UHV chamber of the OMICRON Compact unit with a basic vacuum of $1 \cdot 10^{-10}$ Torr. The UHV chamber was equipped with sublimation sources of Si and Knudsen cell for Ca and Mg deposition, LEED, AES and EELS analyzers and quartz thickness sensor. Rectangular FZ Si(111) strips (4.6x12 mm^2) of the n-type conductivity with a resistivity of 1000 $\Omega \cdot \text{cm}$ were used as both substrates and/or sublimation sources of silicon. The deposition rates for Ca according to a quartz thickness sensor were 0.1 nm/min for Mg substitution and 2.5 nm/min for MBE growth and for Si it was 0.5 nm/min in all growth experiments. Three samples with Ca_2Si films were grown atop $\text{Ca}_2\text{Si}/\text{Mg}_2\text{Si}$ template with thicknesses of about 100 nm (2 samples) and 400 nm (1 sample) by MBE method at the substrate temperatures 250 °C and 300 °C. The optical spectra of the grown samples were measured on a Hitachi U-3010 spectrophotometer in the energy range 1.0–6.5 eV and on a Bruker Vertex 80v Fourier transform spectrophotometer in the infrared wavelength range (1–25 microns). Raman spectra emitted by light with a wavelength of 488 nm were

recorded at room temperature with a LabRam HR 800 spectrophotometer. The structure and phase composition of the grown samples were determined by X-ray diffraction (XRD) on a DRON-7 diffractometer using $\text{CuK}\alpha$ radiation ($\lambda = 1.54 \text{ \AA}$).

Thick epitaxial $\text{Ca}_2\text{Si}(100)$ films were first grown on Si(111) substrates by forming a sacrificial $\text{Mg}_2\text{Si}(111)$ template and converting it into the Ca_2Si template. It was found that a temperature of 250 °C is sufficient to transfer it into the Ca_2Si template with sufficient uniformity. During Ca and Si co-deposition at 250°C, epitaxial $\text{Ca}_2\text{Si}(100)$ domains with two orientations are formed in a thin (100 nm) film, and increasing the substrate temperature to 300°C leads to a deterioration in the Ca_2Si crystalline quality due to a partial violation of its continuity and grain growth of the CaSi phase from Si substrate. An increase in the film thickness to 400 nm at 250°C led to the appearance, in addition to the $\text{Ca}_2\text{Si}(100)$ epitaxial phase, of the second $\text{Ca}_2\text{Si}(010)$ epitaxial phase with both contributing to the LEED pattern. The calculations of the optical functions from the transmittance and reflectance spectra in the framework of the two-layer model showed the presence of a first direct interband transition with an energy of $E_{1d} = 1.095 \pm 0.015$ eV for all grown Ca_2Si films, but the nature of the fundamental transition is not yet precisely established due to strong defect absorption at 0.5–1.0 eV. The presence of CaSi phase in thin Ca_2Si epitaxial films (by XRD data) leads to the appearance of absorption on free carriers at photon energies below 0.5 eV. In the far infrared absorption spectra of Ca_2Si epitaxial films, 6 peaks were found (94.5, 163.7, 172.9, 197.8, 235.9, and 245.3 cm^{-1}), which are also in good agreement with the theoretical calculations [8]. For these peaks, absorption coefficients were determined by which it will be possible to quickly and accurately (10% - 14%) determine the thickness of Ca_2Si films grown on Si substrates. According to Raman spectroscopy, 8 peaks (108.7, 116.8, 132.8, 144.1, 188.3, 204.6, 241.2 and 252.7 cm^{-1}) were first established and identified in Ca_2Si epitaxial films, which are in good agreement with the theoretical calculations [8].

The study was financially supported by RFBR (grant No 20-52-00001-Bel_a).

References

- [1] V.K. Zaitsev, et.al., in: D.M. Rowe (Ed.), Thermoelectrics Handbook Macro to Nano, 2006.
- [2] D. B. Migas, et.al., Physical Review B **67** (2003) 205203.
- [3] J. Hu, et.al., Int. J. Mod. Phys. B **24** (2010) 4639.
- [4] S. Lebegue, et.al., Phys. Rev. B **72** (2005) 085103.
- [5] P. Manfrinetti, et.al., Intermetallics **8** (2000) 223.
- [6] H. Matsui, et.al. J. Crys. Growth **237–239** (2002) 2121.
- [7] S.A. Dotsenko, et.al. Physics Procedia **11** (2011) 95.
- [8] J.-I Tani and H. Kido, Comput. Mat. Sci. **97** (2015) 36.

IV. Formation and properties of ferromagnetic and ferroelectric materials, sensors and spintronics

Magnetic circular dichroism and surface plasmon resonance in Ni@C nanoparticles

D.A. Petrov^{*1}, I.V. Beketov^{2,3}, O.S. Ivanova¹, R.D. Ivantsov¹, I.S. Edelman¹, D.K. Baranov², I.A. Nekrasov³, and A.A. Bagazeev³

¹Kirensky Institute of Physics, Federal Research Center KSC SB RAS, Krasnoyarsk, 660036, Russia

²Ural Federal University, 19 Mira street, Ekaterinburg, 620002, Russia

³Institute of Electrophysics UB RAS, 106 Amundsen St., Ekaterinburg, 660016, Russia

*e-mail: petrov@iph.krasn.ru

Synthesis and study of nanostructured materials is a priority task for several sections of modern science. This area of research is developing at an ever-increasing rate because of its importance for understanding the properties of matter on a nano-scale, on the one hand, and the need for new functional materials for a wide variety of areas of human activity. Nano-electronics, nano-photonics, communications, energy, biotechnology, medicine - this is not a complete list of applications of nano-materials. In this connection, nickel nanoparticles (NPs) are of great interest since surface plasmon resonance can be excited in them [1]. The use of a carbon shell protects metal NPs from oxidation and various damage and also facilitates the creation of samples in which interaction between particles is excluded. The present work is devoted to the synthesis of the core-shell Ni@C NPs by the electric explosion of the wire (EEW) and their magneto-optical study. Magnetic circular dichroism (MCD) was chosen for this study as one of the most informative magneto-optical effects. MCD spectral dependencies make it possible to evaluate the efficiency of the plasmon excitations in dependence on the NPs characteristics.

The synthesis of nickel NPs was carried out in the EEW installation described in detail in [2]. To create carbon shells on the surface of the particles during NPs synthesis, gaseous butane was continuously fed into the apparatus, where it was mixed with the working gas of the installation immediately before entering the explosion chamber. The amount of added butane determines the thickness of the C-shell.

The energy introduced into the wire was determined by the oscillograms of the current pulse passing through the wire segment during EEW. The specific surface area of the produced NPs was determined by low temperature nitrogen adsorption using Micromeritics TriStar 3000 analyzer. The BET data were used to estimate the NPs average size and carbon shell thickness. Several characteristics of samples are collected in Table 1.

X-ray phase analysis (XRD) and transmission electron microscopy (TEM) were used for the fabricated NPs characterization. To carry out the magneto-optical measurements, NPs were embedded to transparent silicon-based matrix. Magnetic circular dichroism (MCD) was measured in the normal geometry as the difference between the photomultiplier voltages for two opposite directions of an applied magnetic field in the spectral range 1.2–3.6 eV in a magnetic field up to 12 kOe in the temperature range 95–300 K. The MCD dependencies on an external magnetic field were measured at the light wave energy 3.25 eV.

Table 1. Parameters of several Ni@C powder samples and MCD values in the spectral maxima at 1.52 and 3.3 eV measured for NPs in silicon matrices.

Sample	Specific surface area, (m ² /g)	Average NPs size (nm)	Carbon shell thickness, (nm)	MCD value, 10 ⁻⁴	
				1.5 eV	3.3 eV
1	8.8	82	4.3	-1.5	7.9
2	8.1	88	3.98	-1.7	8.2
3	9.36	79	5.46	-2.1	11.7
4	13.2	57	4.48	-2.7	15.5

XRD patterns confirm the NPs good crystallinity, the average NPs size determined with XRD and electron microscope image corresponds to the BET data. The spherical NPs shape and narrow carbon shell are seen well in the electron microscope image.

Two wide maxima of the opposite signs are the dominant features in the MCD spectrum for all samples: negative maximum is centered at 1.5 eV and positive – at 3.3 eV. Distribution of the maxima intensities change from sample to sample, at that the highest intensity is observed for the smallest NPs size. The high energy maximum corresponds to the surface plasmon resonance (SPR) energy observed in the absorption spectrum of Ni NPs fabricated in the SiO₂ substrate with the Ni negative-ions implantation [1]. In contrast to the diamagnetic shape of the MCD spectrum in the region of SPR observed in noble metals, for example, in gold [3], in our case, the MCD has a paramagnetic line shape. This is not surprising since nickel is a ferromagnetic metal. Thus, it is reasonable to attribute the positive maximum in the MCD spectrum to the SPR excitation in NPs. The negative maximum origin is not clear now. However, this maximum can be useful for the applications, since the energy of its gravity center corresponds to the radiation energy of a semiconductor diode laser (880 nm).

Acknowledgements

The reported study was funded by the Russian Science Foundation, Project №20-62-47031.

References

- [1] H. Amekura, Y. Takeda, and N. Kishimoto. Nucl. Instr. Meth. B **222** (2004) 96.
- [2] Yu.A. Kotov. Nanotechnologies in Russia, **4** (2009) 415.
- [3] A. Sokolov, S. Ovchinnikov, V. Zabluda, A. Kalsin, Y. Zubavichus. JETP Letters, **97** (2013) 98.

Magnetic properties and FORC-based characterization of electrodeposited Co–W alloy nanowires

A.Yu. Samardak^{*1}, E. Yoo², Y. S. Jeon², S.V. Komogortsev³, A.V. Ognev¹, A.S. Samardak¹, Y.K. Kim²

¹ Far Eastern Federal University, 8 Sukhanova St., Vladivostok 690950, Russia

² Department of Materials Science and Engineering, Korea University, Seoul 02841, Republic of Korea

³ Institute of Physics, SB Russian Academy of Sciences, Krasnoyarsk 660036, Russia

*e-mail: lsamardak@gmail.com

Cobalt (Co)-tungsten (W) alloys have attracted much interest of researchers because of their outstanding mechanical, tribological, anti-corrosion properties and their high wear resistance and potentially can be used in many industries [1-2]. Nanowires (NWs) with high aspect ratio are promising candidates as elements of computer logic, magnetic memory and sensors [3]. In this study, we have characterized magnetic properties of NWs according to W content variations using the first order reversal curve (FORC)-diagram method and micromagnetic simulations.

Nanowires with different composition were electrodeposited in porous alumina template with a nominal pore diameter of 200 nm and pore length of 4 μm under constant current density. The citrate electrolyte contained cobalt sulfate heptahydrate (CoSO₄·7H₂O), sodium tungstate dihydrate (Na₂WO₄·2H₂O), sodium citrate tribasic dihydrate (C₆H₇Na₃O₈), boric acid (H₃BO₃), citric acid (C₆H₈O₇). Bath temperature was maintained at 30 °C. The concentration and applied current density were adjusted to control the concentration of Co-W alloy NWs. Finally, 8 samples with different atomic percentage of W within range from 0 to 25.8 at. % were obtained.

Surface morphology and crystal structure of CoW NWs was inspected by field-emission scanning electron microscope and high-resolution transmission electron microscopy. Microstructural modifications depending on the tungsten content was studied by selected area electron diffraction. The composition of NWs was determined by inductively coupled plasma with mass spectrometer.

Magnetic properties of NWs were investigated by vibrating sample magnetometer (LakeShore VSM 7410). To determine the non-trivial magnetic behavior of magnetic nanowires arrays the First Order Reversal Curves (FORC) method have been used [4]. The FORC-diagram method represents measurements of a number of minor hysteresis loops, beginning at various starting fields H_r and going to positive saturation with a fixed step. A FORC-distribution is formed by hysterons with individual values of H_r and H and can be calculated with a second order

mixed derivative of magnetization M in respect to applied field H :

$$\rho(H_R, H) = -\frac{1}{2} \frac{\partial[M(H_R, H) - M(H_R)]}{\partial H_R \partial H} \quad (1)$$

This method does not show the information about reversible processes that makes it perfect for studying the irreversible mechanisms of magnetization, such as individual Barkhausen jumps. Resulting datasets were processed with FORCinel and doFORC software to provide the complete image of FORC-distribution.

To deeply investigate the magnetic structure of NWs, micromagnetic simulations were performed with help of MuMax³ software package. An effective model, which represents a magnetic CoW nanowire as a set of discs located one on top of another with diameter equal to the diameter of the nanowire and with the thickness equal to the alloy grain size, was developed. Each disc had the same constant of magnetic anisotropy, but random orientation of crystallites in the disc's plane. This model allowed us to achieve the good agreement between the simulated and experimental data.

As a result, an evolution of magnetic properties based on structural and morphologic properties of Co-W alloy nanowires was described, values of interaction fields and coercive force were determined, mechanisms of magnetization and domain structure were studied using simulations.

Acknowledgements

This work has been supported by the Russian Ministry of Science and Higher Education under the state task (0657-2020-0013) and by RFBR (grant 19-02-00530).

References

- [1] U. Admon, M. P. Dariel, J. Appl. Phys. **59** (1986) 2002
- [2] N. Tsyntsaru, H. Cesiulis, A. Budreika, X. Ye, R. Juskenas, J. -P. Celis. Surf. Coat. Technol. **206** (2012) 4262.
- [3] S. Tottori et al. Adv. Mater. **24** (2012) 811.
- [4] C. R. Pike, C. A. Ross, R. T. Scalettar, G. Zimanyi, Phys. L. Rev. B **71** (2005) 134407.

Magnetic properties of nanocrystalline (Nd,R)-(Fe,Co)-B (R = Pr, Ho) alloys after melt spinning, severe plastic deformation and heat treatment

L.A. Ivanov¹, T.P. Kaminskaya¹, I.S. Tereshina^{*1}, S.V. Dobatkin², G.A. Politova²

¹ Lomonosov Moscow State University, Faculty of Physics, Leninskie Gory, Moscow 119991, Russia

² Baikov Institute of Metallurgy and Material Science RAS, Leninskii pr. 49, Moscow 119991, Russia

*e-mail: irina_tereshina@mail.ru

Modern hard magnetic materials are multicomponent systems with hysteresis properties provided by a careful choice of chemical composition of alloy and methods of its treatment [1]. The studies of relation between microstructure and magnetic characteristics are in focus for both known and new alloys. The rapidly growing field of nano-technologies offers novel ways for creating nano-materials. In present time the following methods exist: powder metallurgy, melt spinning (MS), mechanical alloying, severe plastic deformation (SPD) and others. SPD has a number of useful properties such as production of non-porous dense materials free of contamination. In the present work we study the effect of multistage treatment (including SPD) on the microstructure and magnetic properties of (Nd,R)₂(Fe,Co)₁₄B (R = Pr and Ho) alloys.

Initial bulk samples of different composition [2-4] Nd₂Fe₁₄B, (Nd,Pr)₂Fe₁₄B and (Nd,Ho)₂(Fe,Co)₁₄B were prepared in an induction or arc furnaces followed by remelting in quartz ampoules and injection through the bottom orifice onto the surface of a quenching wheel (centrifugal melt-spinning method). The obtained ribbon-shaped flakes were about 10 mm long, 2-5 mm wide and 0.3 mm thick. Further SPD treatment was performed in Bridgman anvils by torsion under high hydrostatic pressure of 4 GPa at room temperature with the achieved true strain of ~6 (5 revolutions). The samples after SPD were about 5 mm in diameter and 0.3 mm thick. The direction of pressure application was perpendicular to the flakes plane. Samples were also annealed (heat treatment (HT)) at various temperatures and different duration in vacuum.

The phase composition of samples was analyzed with the X-ray diffraction technique at room temperature. Surface morphology and chemical composition of the samples were studied using scanning electron microscopy (SEM) and atomic-force microscopy (ASM). The magnetic measurements were performed with an SQUID magnetometer and a PPMS installation (Quantum Design, USA) in the temperature range 4.2 – 550 K. The measurements were carried out for separate ribbons with magnetic field oriented along the longest edge. For comparison, bulk samples were also measured providing similar $M(H)$ results.

A highly anisotropic tetragonal Nd₂Fe₁₄B-type phase prevails in all compounds after MS procedure. Additional phases of the RFe₂-type and rare-earth oxides are also detected. The analysis of X-ray patterns did not reveal a presence of the α -Fe phase. The volume of amorphous phase did not exceed 5%. Average grain size for the main phase is 80-100 nm. It is worthwhile to mention that high coercivity is usually obtained for the samples with grains smaller than ~80 nm [5]. Nd₂Fe₁₄B, (Nd,Pr)₂Fe₁₄B and

(Nd,Ho)₂(Fe,Co)₁₄B alloys have a strong uniaxial anisotropy only at room temperature. Compounds exhibit a spin-reorientation transition with the spontaneous magnetic moment deviating from the c-axis as the temperature is lowered (for example, below 73 K for Nd₁Pr₁Fe₁₄B). We measured the magnetic hysteresis loops at 4.2, 150 and 300 K. The alloys have a high coercivity $iH_C = 20-22$ kOe at room temperature. However, the negative kink of magnetization occurring in low demagnetizing field on the descending part of the loop deteriorates the magnetic energy product of the samples. Evidently, this characteristic behavior is related to structural non-uniformities of the material, such as coarse grains of Nd₂Fe₁₄B-type phase and amorphous soft magnetic phases.

The structure, phase and chemical composition of melt-spun alloys after SPD was also investigated by X-ray analysis, SEM and ASM. X-ray analysis gave a confirmation of a considerable increase of the amorphous phase volume (about 65 vol%). A cross-sectional SEM and ASM images of a fracture of the sample show that SPD favors the formation of a more uniform structure, but large volume of amorphous phase prevents the formation of high-coercive state. To crystallize the amorphous phase into the 2-14-1 phase, the samples were further annealed. Heat treatment regime consisting of an annealing at 750°C for 15 minutes was found as optimal. This allowed us to increase coercivity of samples ($iH_C = 23-25$ kOe at 300 K). A SEM and ASM images of MS+SPD+HT sample seen that the quantity of highly anisotropic crystalline Nd₂Fe₁₄B-type phase prevails in MS+SPD+HT sample with average grain size of 70-80 nm for the main phase.

Summarizing, the described results provide a strategy to multistage treatment of (Nd,R)-(Fe,Co)-B alloys in view of their potential use as permanent magnets with improved magnetic characteristics.

Acknowledgements

This work is performed with financial support of the grant of Russian Science Foundation (project № 18-13-00135). Politova G. thanks RFBR, pr. No. 18-03-00798_a.

References

- [1] J.F. Herbst. Rev. Mod. Phys. **63** (1991) 819.
- [2] I.S. Tereshina, I.A. Pelevin, E.A. Tereshina et.al. J. Alloys. Compd. **681** (2016) 555.
- [3] G.A. Politova, I.S. Tereshina, T.P. Kaminskaya et.al. Russian Metallurgy (Metally) **9** (2018) 859.
- [4] D.S. Neznakhin, et.al. DDF **386** (2018) 125.
G.C. Hadjipanayis. J. Magn. Magn. Mater. **200** (1999) 373.

Ferrielectric-like structures in antiferroelectric epitaxial films under electric field bias

R.G. Burkovsky^{*1}, G.A. Lityagin¹, A.F. Vakulenko¹, A.E. Ganzha¹, R. Gao², A. Dasgupta²,
A.V. Filimonov¹

¹ Peter the Great Saint-Petersburg Polytechnic University, 29 Politekhnikeskaya, 195251, St.-Petersburg, Russia

² Department of Materials Science and Engineering, University of California, Berkeley, California 94720, United States

*e-mail: roman.burkovsky@gmail.com

Antiferroelectric (AFE) materials are important for a number of applications, including their present large-scale use in creating highly-piezoelectric solid solutions [1] and prospective applications in future energy storage [2], non-volatile memory technologies [3] and electrocaloric devices [4]. In the scientific aspect, AFEs give difficult questions on their theoretical description.

In the form of epitaxial films, AFEs offer additional challenges such as not-yet-explained smearing of originally very sharp (in crystals) double hysteresis (polarization -- electric field, P - E) loops [5], as well as smearing of temperature-driven phase transitions [6]. The understanding of these effects in AFE films is much behind the one for ferroelectric (FE) films, where the role of effective internal bias field due to the asymmetry of the interfaces has been rather rigorously identified as the origin of smearing in many cases [7]. For AFEs this explanation does not apply, since the homogeneous electric field is not a conjugate field for the inhomogeneous AFE order parameter. The missing explanation limits the practical uses of AFE films that demand fine control over switching processes.

We report on the direct characterization of the structural changes in AFE films on approaching the critical field by using *in-situ* x-ray diffraction. Instead of the anticipated expansion of the volume, occupied by the near-interface FE phase [5], an unusual ferrielectric structure is formed in relatively large amount. Due to its non-zero net polarization, it is expected to play the dominant role in producing nonlinearity at low fields in the smeared P - E double-hysteresis loops. The analysis of energetics of this structure indicates that its formation is driven by a competition of three trends -- towards short-period modulations in defect-influenced sub-volumes in the film, towards maximizing the polarization due to the interaction with the field, and towards being commensurate with the surrounding lattice still having the prototype AFE structure.

Epitaxial thin film PbZrO_3 samples were grown using pulsed laser deposition technique at UC Berkeley. The field has been applied using Cr-Au top electrodes. The bottom electrode was from SrRuO_3 , which was the buffer layer between PbZrO_3 film and SrTiO_3 substrate. The *in-situ* x-ray characterization was done using SuperNova single crystal diffractometer.

An unusual new structure grows in volume continuously on the increase of electric field, implying the presence of two-phase state with moving boundary. We manage reproducing this structure within the model adapted from the analysis of magnetic modulated structures, widely known as Anisotropic Next Nearest Neighbor Ising Model [8].

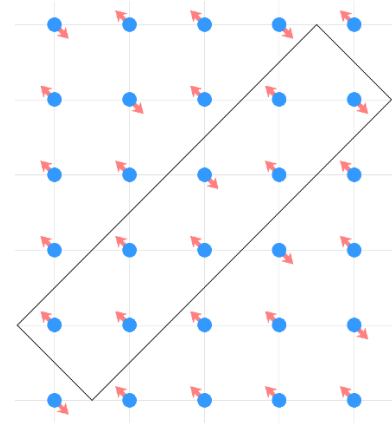


Figure 1. Schematic representation of the field-induced ferrielectric phase unit cell. Arrows show displacements of Pb ions.

Acknowledgements

The work has been supported by RFBR (Project 20-32-70215).

References

- [1] G. H. Haertling, *Journal of the American Ceramic Society* **82** (1999) 797.
- [2] B. Xu, J. Iniguez, and L. Bellaiche, *Nature Communications* **8** (2017).
- [3] X. Wei, A. Tagantsev, A. Kvasov, K. Roleder, C. Jia, and N. Setter, *Nature communications* **5** (2014) 3031.
- [4] M. Guo, M. Wu, W. Gao, B. Sun, and X. Lou, *Journal of Materials Chemistry C* **7** (2019) 617.
- [5] A. R. Chaudhuri, M. Arredondo, A. Hahnel, A. Morelli, M. Becker, M. Alexe, and I. Vrejoiu, *Phys. Rev. B* **84** (2011) 054112.
- [6] G. Lityagin, D. Andronikova, I. A. Bronwald, M. Kniazeva, M. Jankowski, F. Carla, R. Gao, A. Dasgupta, A. Filimonov, and R. Burkovsky, *Ferroelectrics* **533** (2018) 26.
- [7] A. Bratkovsky and A. Levanyuk, *Physical review letters* **94** (2005) 107601.
- [8] P. Bak and J. Von Boehm, *Physical Review B* **21** (1980) 5297.

Magneto-optics of nanocomposites based on iron chalcogenide nanoparticles

R.D. Ivantsov^{*1}, D.A. Petrov¹, O.S. Ivanova^{1,2}, I.S. Edelman¹, S.M. Zarkov^{1,2}, D.A. Velikanov¹, Chun-Rong Lin³

¹ Kirensky Institute of Physics, Federal Research Center KSC SB RAS, Krasnoyarsk, 660036, Russia

² Siberian Federal University, Krasnoyarsk, 660041, Russia

³ National Pingtung University, Pingtung City, Pingtung County, 90003, Taiwan

*e-mail: ird@iph.krasn.ru

Iron sulphide Fe_xS_y and selenide Fe_xSe_y nanoparticles (NPs) attract many attentions several last decades owing, in particular, to wide range of their applications [1]. The properties of these compounds depend strongly on the technological conditions and can be changed noticeable at the transition from the bulk to the nano-metric samples. The present work is devoted to synthesis of the Fe_xS_y and Fe_xSe_y nanoparticles with the polyol mediated process using different regimes of the heat treatment and to study of their structure, magnetic and magneto-optical properties.

The nanoparticles were synthesized by the polyol mediated process. It is a one-pot method involving the reaction of stable precursors and solvent: iron (II) acetate ($\text{Fe}(\text{COOCH}_3)_2$) was used as the cation source, thiourea (NH_2CSNH_2) – as the sulfur source in the case of sulphides and selenium–oleylamin complex in the case of selenides, diethylene glycol (DEG) – as solvent, and polyvinylpyrrolidone powder (PVP) – as a capping agent. The mixture of precursors was loaded into a three-neck round-bottom flask equipped with a magnetic stirrer and an inlet of argon gas and then heated with stirring to refluxing temperature between 180 °C and 320 °C for 2-5 hrs. After cooling to room temperature, a black colloid suspension containing PVP-coated nanocrystals were formed. The x and y values and, consequently, the particles phase composition depended on the heating temperature. The nanocrystals were separated from the suspension with a magnetic field.

X-ray powder diffraction (XRD), high-resolution transmission electron microscope (HRTEM) and selected-area electron diffraction (SAED) were used to determine the structure of the nanoparticles. Magnetization dependences on an external magnetic field and temperature were studied with the vibrating sample magnetometer at 80 – 300 K in the magnetic field up to 0.1 T.

To carry out the magneto-optical measurements, NPs were embedded to transparent matrix. Magnetic circular dichroism (MCD) was measured in the normal geometry as it was described in [2]. As seen from Table 1 built on the basis of the XRD and SAED data, the sulphide NPs phase composition depended strongly on the heat treatment temperature. HRTEM images show the sulphide NPs to be irregular near-rectangular or hexagon plates with dimensions of about 50 nm.

Magnetization curves of sulphide NPs with hysteresis loops indicate their ferromagnetic behavior. The gradual saturation magnetization (M_s) decrease from NPs 240 to NPs 310 allows concluding that the FeS phase gives no significant contribution to the measured M_s value. MCD spectra are due to the Fe_3S_4 phase also. It was shown that the low energy maximum in the MCD spectrum can be

associated with the one-ion $^5\text{T}_2(^5\text{D}) \rightarrow ^5\text{E}(^5\text{D})$ transition in the Fe^{2+} ions while higher energy maxima can be due the interband electron transitions.

Table I. Temperatures of the Fe_xS_y samples heat treatment, phase concentrations and space group.

T (°C)	Phase	Phase content (%)	Space group
240	Fe_3S_4	100	Fd-3m
250	Fe_3S_4	100	Fd-3m
260	Fe_3S_4	54(4)	Fd-3m
	FeS	46(4)	P63/mmc
280	Fe_3S_4	40(5)	Fd-3m
	FeS	60(5)	P63/mmc
300	Fe_3S_4	22(5)	Fd-3m
	FeS	78(5)	P63/mmc
310	FeS	100	P63/mmc

In the case of the selenide NPs, the picture is more complicated: for all regimes coexistence of several phases was observed. It was difficult to single out any preferable phase. The general features of the selenide MCD spectra are a broad positive peak centered at about 1.65 eV and a negative peak at about 2.75 eV. These spectra are similar in shape to the MCD spectra for the polycrystalline α -FeSe thin film presented in Ref. [3]. So, supposing is possible that α -FeSe phase is the main magnetic phase in the selenide NPs investigated.

Acknowledgements

The reported study was funded by Russian Foundation for Basic Research, Government of Krasnoyarsk Territory, Krasnoyarsk Regional Fund of Science, to the research project: № 19-42-240005, by Joint Research Project of Russian Foundation for Basic Research № 19-52-52002 and Ministry of Science and Technology, Taiwan MOST № 108-2923-M-153-001-MY3 and № 106-2112-M-153-001-MY3.

References

- [1] A.B. Seabra, P. Haddad, N. Duran, IET Nanobio-Technology **7** (2013) 90.
- [2] C-R Lin, Y-T Tseng, S.G. Ovchinnikov, et al., Materials Research Express **1** (2014) 025033.
- [3] D.Z. Shen *et al.*, Applied Physics Letters **88** (2006) 012505.

Novel topological objects in films with easy cone anisotropy

A.G. Kolesnikov^{*,1}, M.E. Stebliy¹, A.V. Davydenko¹, A.G. Kozlov¹, A.V. Ognev¹, A.S. Samardak^{1,2}, In Ho Cha³, Yong Jin Kim³, Young Keun Kim³

¹ School of Natural Sciences, Far Eastern Federal University, 8 Sukhanova St., Vladivostok 690950, Russia

² National Research South Ural State University, Chelyabinsk, Russia

³ Department of Materials Science and Engineering, Korea University, Seoul 02841, Republic of Korea

*e-mail: alexanderkolesnickov@yandex.ru

Spin configurations with topological stability promise as a bit carriers for a new type of magnetic memories [1-3]. Well known topological states as meron [4], vortex [5] and skyrmion [3,6] have already widely described theoretically and studied on experiment. These states are characterized by a fixed value of the topological charge (N_{sk}):

$$N_{sk} = \frac{1}{4\pi} \iint \vec{m} \cdot \left(\frac{\partial \vec{m}}{\partial x} \times \frac{\partial \vec{m}}{\partial y} \right) dx dy \quad (1)$$

where \vec{m} - unit vector of the local of magnetization [7] (for meron and vortex $N_{sk}=\pm 0.5$, for skyrmion $N_{sk}=\pm 1$). Here we show observation novel particle-like spin textures with non-half-quantized topological charge. Easy cone anisotropy (ECA) obtained experimentally in films Cu(2.1)/Pd(12.6)/Pt(2)/CoFeSiB(1.5)/Ru(3)/Ta(5) (thickness in nm) promotes to stabilize non-trivial objects. Micromagnetic structure of this objects was investigated by simulation using Mumax³ [8].

Perpendicular magnetic anisotropy (PMA) with Dzyaloshinskii-Moriya interaction (DMI) [9,10] are usually used for skyrmion stabilization in ferromagnetic films. Since the value of N_{sk} depends on the rotation angle of the magnetization in domain wall, we proposed to modulate the rotation angle by using easy cone anisotropy. ECA occurs in films with strong second-order anisotropy constant (K_2), the origin of high K_2 is surface contribution. In our films surface anisotropy was variates by surface roughness of buffer layer. Easy cone anisotropy type in the films was established from measurements of the magnetization reversal process by VSM. The tilting angle of the easy axis of magnetization (45°) was experimentally determined from the polar diagram $M_r/M_s=f(\theta)$ with angle θ to the film plane.

Bases on experimentally measured magnetic parameters was performed micromagnetic simulations. Detailed study revealed nucleation of meron-like state with $N_{sk}=0.89$ during out-of-plane magnetization process. After relaxation in a zero field a meron-like spin configuration has a mixed Bloch-Neel type domain wall structure. Meron-like states have topological charge $N < 1$ because magnetization rotates less than 180 degrees from the center to periphery. Moreover, we found that ECA allows stabilize

different chirality of topological states (left-handed and right-handed) in comparison with DMI. Since the tilting angle of the magnetization depends on the values of perpendicular magnetic anisotropy constants (formula 2) it possible to modulate the winding angle inside the domain wall.

$$\theta_{EAM} = \arcsin \sqrt{\frac{-K_{1,eff}}{2K_2}} \quad (2)$$

K_1 u K_2 – the first and second order anisotropy constants. We performed micromagnetic simulations of the film with variable θ_{EAM} and found that topological charge of meron-like states could be precisely control in range from 0.5 to 1.0. Also, the changing of anisotropy allows to control diameter of the core in these states.

Acknowledgements

This research was supported by the Russian Ministry of Science and Higher Education under the state task (0657-2020-0013), by the Russian Foundation for Basic Research (grant 19-02-00530) and Scholarship of the President of the Russian Federation for young scientists and graduate students (SP-350.2019.1).

References

- [1] S.S.P. Parkin, M. Hayashi, L. Thomas Science **320** (2008) 5873.
- [2] N.S. Kiselev, A.N. Bogdanov, R. Schäfer, U.K.J. Röbber, Phys. D: Appl. Phys. **44** (2011) 392001.
- [3] A. Fert, V. Cros, J. Sampaio. Nature Nanotech. **8** (2013) 152.
- [4] S. Wintz, C. Bunce, A. Neudert, M. Körner, T. Strache, M. Buhl, A. Erbe, S. Gemming, J. Raabe, C. Quitmann, J. Fassbender, Phys. Rev. Lett. **110** (2013) 177201.
- [5] R.P. Cowburn, D.K. Koltsov, A.O. Adeyeye, M.E. Welland Phys. Rev. Lett. **83** (1999) 5.
- [6] T. Skyrme, Nuclear Physics **31** (1962) 556.
- [7] S. Heinze, K. von Bergmann, M. Menzel, J. Brede, A. Kubetzka, R. Wiesendanger, G. Bihlmayer, S. Blügel, Nat. Phys. **7** (2011) 713.
- [8] A. Vansteenkiste, J. Leliaert, et al. AIP Advances **4** (2014) 107133.
- [9] I.E. Dzyaloshinskii, Sov. Phys. JETP **5** (1957) 1259.
- [10] T. Moriya, Phys. Rev. **120** (1960) 91.

Magnetic and transport properties of trilayered $\text{Fe}_3\text{Si}/\text{Ge}/\text{Fe}_3\text{Si}$ hybrid structures synthesized on Si(111)

A.S. Tarasov^{*,1}, I.A. Bondarev^{1,2}, M.V. Rautskii¹, A.V. Lukyanenko¹, D.A. Smolyakov¹,
T.E. Smolyarova^{1,2}, I.A. Tarasov¹, I.A. Yakovlev¹, M.N. Volochaev¹, S.N. Varnakov¹,
S.G. Ovchinnikov^{1,2}, N.V. Volkov¹

¹ Kirensky Institute of Physics, Federal Research Center KSC SB RAS, Krasnoyarsk 660036, Russia

² Institute of Engineering Physics and Radio Electronics, Siberian Federal University, Krasnoyarsk 660041, Russia

*e-mail: taras@iph.krasn.ru

At present, more and more spintronics devices are already close to be manufactured by the semiconductor industry, including MRAM based on STT and even SOT effects [1,2]. Typically, such devices are built on vertical MTJ [3]. While semiconductor spintronics usually works in planar geometry. Vertically stacked ferromagnetic metal (FM)/ semiconductor (SC)/ FM trilayer structures can combine both methods and therefore can be prospective for both vertical- and planar-type SC-based spintronic device applications. Large scientific interest is paid to FM Heusler alloys with high spin polarization, like Fe_3Si , Co_2FeSi , Fe_2MnSi , Co_2FeAl , since they have cubic crystal structures and can be epitaxially grown on various semiconducting substrates [4]. In this work the epitaxial $\text{Fe}_3\text{Si}/\text{Ge}/\text{Fe}_3\text{Si}$ structure was synthesized. Structural, magnetic and transport properties were studied. Also using lithography process two simplest devices based on $\text{Fe}_3\text{Si}/\text{Ge}/\text{Fe}_3\text{Si}$ structure was fabricated.

The multilayer $\text{Fe}_3\text{Si}/\text{Ge}/\text{Fe}_3\text{Si}$ structure on Si(111)7×7 was obtained using the modernized ultrahigh-vacuum molecular beam epitaxy unit “Angara”. Epitaxial film growth was controlled in situ by reflection high-energy electron diffraction (RHEED). In addition, the structural properties of the films were investigated by transmission and scanning electron microscopy (TEM and SEM). Transport properties measurements of trilayered structure and prepared devices were performed at cryogenic probe station Lakeshore EMPX-HF 2 and home built facility equipped with a helium cryostat, an electromagnet and KEITHLEY-2634 source meter in the temperature range from 4.2 K to 300 K. Ferromagnetic resonance (FMR) spectra were measured using Bruker Elexsys E580 spectrometer operating at the X-band (9.7 GHz).

Iron silicide layers were obtained by simultaneous thermal evaporation in a ratio of Fe:Si = 3:1. The Fe_3Si deposition rate was about 0.33 nm/min, and Ge – 0.54 nm/min. The thickness of the first layer of iron silicide was $d_1 = 62$ nm, of the layer of germanium – $d_2 = 39$ nm, and of the second layer of Fe_3Si – $d_3 = 20$ nm. The base vacuum in the process chamber was 1.3×10^{-8} Pa. Before synthesis, the Si (111) silicon substrate was subjected to chemical treatment in air followed by thermal annealing in ultrahigh vacuum at 900 °C. Annealing was performed until additional reflections from the reconstructed Si (111) 7 × 7 surface appeared on the RHEED pattern. After that, the temperature of the substrate was reduced to $T = 230$ °C, and was maintained for 60 minutes before sputtering. After deposition of the first layer of iron silicide Fe_3Si on Si(111)7×7 reflections in the form of vertically elongated strands appear on the diffraction pattern, forming an

ordered network. Such diffraction pattern geometry corresponds to an island single crystal structure, and its formation proceeded epitaxially. The analysis shows the formation of Fe_3Si silicide, the orientation ratio of the silicide film is - Fe_3Si (111) [1-21] || Si (111) [11-2]. Then the germanium was deposited at the same temperature. Dot-shaped reflections are present on the RHEED pattern, which corresponds to an island monocrystalline structure. From here we can conclude that the germanium layer on the surface of single-crystal Fe_3Si at $T = 230$ °C is also formed epitaxially. When the upper layer of silicide is sputtered onto a single-crystal $\text{Ge}/\text{Fe}_3\text{Si}/\text{Si}(111)7 \times 7$ structure at a temperature of 230 °C, reflections in the form of points forming a rectangular network are also present in the diffraction pattern. Analysis of the pattern confirms the formation of Fe_3Si silicide. Using the RHEED pattern analysis, we determined the orientation ratios of each layer of the three-layer structure of $\text{Fe}_3\text{Si}/\text{Ge}/\text{Fe}_3\text{Si}$ on Si(111): $\text{Fe}_3\text{Si}(111)[1-21] \parallel \text{Si}(111)[11-2]$; $\text{Ge}(111)[1-21] \parallel \text{Fe}_3\text{Si}(111)[1-21]$; $\text{Fe}_3\text{Si}(-211)[01-1] \parallel \text{Ge}(111)[0-11]$. In support of this, the angular dependences of FMR spectra have a periodic shape, which is due to the magnetic crystalline anisotropy of the films. The maxima of the resonance field correspond to the crystalline directions of the Fe_3Si [111] film.

To study the magnetotransport properties, 1) three samples were prepared: a three-layer structure with electrical contacts on the upper film; 2) a planar device with a gap in the upper film; 3) a vertical device with contacts on the upper and lower Fe_3Si films. The structure and the devices demonstrate magnetoresistive effects, which are most likely related to spin-dependent electron transport and caused by spin injection in Ge and spin detection in Fe_3Si .

Acknowledgements

The work was partially supported by the Ministry of Education and Science, Fundamental research program of the Presidium of the RAS no. 32 «Nanostructures: physics, chemistry, biology, basics of technologies».

References

- [1] S. Bhatti, R. Sbiaa, A. Hirohata, H. Ohno, S. Fukami, S.N. Piramanayagam. *Materials Today* **209**(9) (2017) 530.
- [2] Y. Kim, X. Fong, K.W. Kwon, M.C Chen, K. Roy. *IEEE Transactions on Electron Devices* **62**(2) (2015) 561.
- [3] D.C. Ralph, M.D. Stiles. *J. Magn. Magn. Mater.* **320**(7) (2008) 1190.
- [4] S. Yamada, S. Honda, J. Hirayama, M. Kawano, K. Santo, K. Tanikawa, T. Kanashima, H. Itoh, & K. Hamaya. *Physical Review B* **94**(9) (2016) 094435.

Numerical simulation of magnetic skyrmions in ferromagnetic film

V. Kapitan^{*1,2}, E. Vasiliev^{1,2}, A. Perzhu^{1,2}, D. Kapitan^{1,2}, R. Volotovskiy^{1,2}, A. Rybin^{1,2}, K. Soldatov^{1,2}, A. Makarov^{1,2}, V. Strongin^{1,2}, Y. Shevchenko^{1,2}, K. Nefedev^{1,2}

¹ Department of Computer Systems, School of Natural Sciences, Far Eastern Federal University, Vladivostok, 690950, 8 Sukhanova St., Russian Federation

² Institute of Applied Mathematics, Far Eastern Branch, Russian Academy of Science, Vladivostok, 690041, 7 Radio St., Russian Federation

*e-mail: kapitan.vyu@dvfu.ru

Crystals with a certain symmetry and magnetic films are of particular interest from the practical point of view. Due to the formation in these systems of stable spiral formations - magnetic skyrmions. Individual skyrmions can be stabilized using the Dzyaloshinskii–Moriya (DM) interaction. Recent demonstrations of control of individual nanoscale skyrmions - including their creation, detection, manipulation, and annihilation - have raised expectations for their use in future spintronic devices.

In the simulation of spin systems, the Metropolis algorithm, one of the numerical Monte Carlo methods, has proven itself well. It allows to successfully study the critical properties of systems with complex Hamiltonians in a wide range of temperatures and other external parameters.

The relevance of studying of spin systems with DM interaction using computer simulation lies in the possibility of studying phase transitions, critical phenomena, and thermodynamic and magnetic properties of such systems. Understanding these properties is important because of the development of data storage devices that use magnetic spin systems to store information.

In this work, we developed a model and a software for simulation of magnetic skyrmions taking into account the DM interaction. The influence of the DM interaction on the spin system in frame of the Heisenberg model was analysed. We used the next Hamiltonian in our research:

$$H = H_J + H_{DMI} + B + A \quad (1)$$

$$H_J = -J \sum_r \mathbf{S}_r \cdot (\mathbf{S}_{r+\hat{x}} + \mathbf{S}_{r+\hat{y}} + \mathbf{S}_{r+\hat{z}}), \quad (2)$$

$$H_{DMI} = -D \sum_r \mathbf{S}_r \times \mathbf{S}_{r+\hat{x}} \cdot \hat{x} + \mathbf{S}_r \times \mathbf{S}_{r+\hat{y}} \cdot \hat{y} + \mathbf{S}_r \times \mathbf{S}_{r+\hat{z}} \cdot \hat{z} \quad (3)$$

$$B = -B_z \sum_r S_r \quad (4)$$

$$A = A_z \sum_r S_r^2 \quad (5)$$

The ferromagnetic-exchange interaction (the first term), the Dzyaloshinskii-Moriya interaction (the second term), the Zeeman coupling (the third term), magnetic anisotropy (the fourth term) are considered.

We studied skyrmions of various types, determined the values of the external and internal simulation parameters, which are necessary for the creation and stabilization of skyrmions in magnetic two-dimensional ferromagnetic films. We have demonstrated switching between different stable skyrmionics states depends on various external and internal parameters, e.g. a value of DMI or external magnetic field. We have proposed a method for creating and controlling the motion of magnetic skyrmions in 2D films.

Acknowledgements

The research was carried out within the state assignment of FASO of Russia No. 075-00400-19-01.

Effect of magnetostatic interaction on the blocking temperature of core/shell nanoparticles

S.V. Anisimov*, L.L. Afremov

Far Eastern Federal University, 8 Sukhanova St., Vladivostok 690950, Russia

*e-mail: anisimovsv25@gmail.com

This paper presents a theoretical study of the effect of the magnetostatic interaction on the blocking temperature of core/shell nanoparticles. It was shown that the blocking temperature of nanoparticles increases with an increase in the magnetostatic interaction between them, and the influence of the interaction exerted is more pronounced for larger nanoparticles.

In this work, we use the core/shell model of a nanoparticle, which was described in detail in our earlier articles [1, 2]. According to [1, 2], nanoparticles can be in one of four magnetic states that differ in the mutual orientation of the magnetic moments of both phases (core and shell): ($\uparrow\uparrow$), ($\uparrow\downarrow$), ($\downarrow\downarrow$) and ($\downarrow\uparrow$). The magnetic states of the studied nanoparticles are determined using the matrix of the frequency of transitions from one state to another:

$$\tilde{W}_{ik} = \begin{cases} -\sum_{j \neq i}^4 W_{ij} - W_{4i}, & i = k, \\ W_{ki} - W_{4i}, & i \neq k, \end{cases}, \quad \mathbf{V} = \begin{pmatrix} W_{41} \\ W_{42} \\ W_{43} \end{pmatrix}$$

where $W_{ik} = f_0 \exp(-E_{ik}/k_B T)$ are matrix elements of the matrix of probabilities of transition from the i -th equilibrium state to the k -th, f_0 is frequency factor, $E_{ik} = E_{ik}^{(max)} - E_i^{(min)}$ is the height of the potential barrier, and $E_{ik}^{(max)}$ is the smallest of the maximum energies that correspond to the transition of the magnetic moment from the i -th equilibrium state with energy $E_i^{(min)}$ to k -th state.

Using the transition matrix, it is possible to determine the relaxation time τ_k of the core/shell nanoparticle through the eigenvalues w_k of the transition matrix W_{ik}

$$\text{Det} |W_{ik} - w_k \delta_{ik}| = 0, \quad (1)$$

which are the inverse times of the transition from one state to another $|w_k| = 1/\tau_k$.

Using the maximum transition time $\tau = \tau_{k \max}$, it is possible to exclude all transitions to the equilibrium state with shorter relaxation times, since all such transitions will be completed.

$$\tau(T_b(a)) = \tau_{k \max}(T_b(a), a, h) = t_{exp}. \quad (2)$$

This relation is used to estimate the blocking temperature of particles of size a located in the interaction field h . In this case, all nanoparticles with relaxation times equal to or greater than the measurement time t_{exp} are “blocked”.

However, in real systems, particles are distributed over the sizes a and the fields of the magnetostatic interaction h . In this case, the ratio averaged over a and h takes the following form:

$$\int \tau_{k \max}(T_b, a, h) f(a) da W(h) dh = t_{exp}, \quad (3)$$

where $f(a) da$ and $W(h) dh$ are the distribution functions over the sizes and fields of interaction [1], respectively.

The calculation of the dependence of the blocking temperature T_b on the concentration (magnetic interaction)

showed that an increase in the concentration of core/shell nanoparticles leads to an increase in T_b , which is confirmed by a number of experimental [3, 4] and theoretical works [5, 6]. An increase in the blocking temperature occurs due to an increase in the degree of randomization of the magnetic moments of nanoparticles. The effect of magnetostatic interaction on the blocking temperature is more significant for larger particles. So, for example, at a high concentration of nanoparticles ($c = 0,5$), T_b of interacting particles with a size of $a = 40$ nm increased by 19% compared with the T_b value of non-interacting nanoparticles. For particles $a = 10$ nm in size, the increase in the blocking temperature of interacting nanoparticles compared to T_b of non-interacting nanoparticles was only 4%. This feature of the behavior of the blocking temperature is due to the increased interaction of the magnetic moments of the particles ($m \sim a^3$).

Acknowledgements

This work was financially supported by the state task of the Ministry of Science and Higher Education (Russia) # 3.7383.2017/8.9.

References

- [1] L. Afremov, S. Anisimov, I. Iliushin. Journal of Magnetism and Magnetic Materials, **447** (2018) 88.
- [2] S. Anisimov, L. Afremov, A. Petrov. Journal of Magnetism and Magnetic Materials, **500** (2020) 166366.
- [3] D.A. Balaev, S.V. Semenov, A.A. Dubrovskiy, S.S. Yakushkin, V.L. Kirillov, O.N. Martyanov. Journal of Magnetism and Magnetic Materials, **440** (2017) 199.
- [4] K. Nadeem, H. Krenn, T. Traussnig, R. Wurschum, D.V. Szabo, I. Letofsky-Papst. Journal of Magnetism and Magnetic Materials, **323** (2011) 1998.
- [5] T. N. Lan, T. H. Hai. Computational Materials Science, **49** (2010) S287.
- [6] V. Russier. Journal of Magnetism and Magnetic Materials, **409** (2016) 50.

Monte-Carlo simulations of fast remagnetization process in FePt L1₀ granular films

Y. Shevchenko^{*1,2}, R. Volotovskiy^{1,2}, E. Vasiliev^{1,2}, A. Perzhu^{1,2}, D. Kapitan^{1,2}, A. Rybin^{1,2},
K. Soldatov^{1,2}, A. Makarov^{1,2}, V. Strongin^{1,2}, K. Nefedev^{1,2}

¹ School of Natural Sciences, FEFU, Vladivostok, Sukhanova 8, 690091, Russia

² Institute of Applied Mathematics, FEB RAS, Vladivostok, Radio 7, 690041, Russia

*e-mail: shevchenko.ya@dvfu.ru

In paper [1] authors showed the possibility of remagnetization of FePt L1₀ granular films by ultrashort femtosecond laser pulses. The magnetization direction is dependent on polarization helicity of laser beam. This happens due to inverse Faraday effect. The physics of this phenomenon and exact effect of laser pulse to magnetization is not fully theoretically described.

Moreover, in detailed experimental review of the material after the experiment it was showed that the magnetisation is non-uniform and consists of uniformly magnetized clusters with diameter 10-100nm.

In our work we treat the inverse Faraday effect as external directed magnetic field B_{opt} and simulate the remagnetization process in frames of probabilistic approach with using Metropolis method. We showed the dependence of cluster size on time of laser impulse, its

strength. We proposed and checked the cluster-size-based order parameter:

$$D = \frac{\sum_{\langle i,j \rangle} \delta(s_i s_j + 1)}{(N^2 + N)/2},$$

where s_i defines the direction of granule along z-axis (+1 if up -1 if down), N is total number of granules and summation runs over all interacting pairs $\langle i, j \rangle$ of granules.

Acknowledgements

The results were obtained using the equipment of Shared Resource Center "Far Eastern Computing Resource" IACP FEB RAS (<https://cc.dvo.ru>).

References

- [1] R. John et al. Sci. Rep. **7** (2017) 4114.

Multiscale magnetic anisotropy in amorphous ferromagnetic ribbon: an example of FeCuNbSiB alloy

N.V. Ilin^{*1}, S.V. Komogortsev^{2,3}, G.S. Kraynova¹, V.A. Ivanov¹, A.V. Davydenko¹, R.S. Iskhakov^{2,3}, V.S. Plotnikov¹

¹ Far Eastern Federal University, Vladivostok 690090, Russia

² Kirensky Institute of Physics, Federal Research Center KSC SB RAS, 660036 Krasnoyarsk, Russia

³ Siberian State Aerospace University, 660049 Krasnoyarsk, Russia

*e-mail: ilina@dvfu.ru

A complete understanding of the magnetic response of an amorphous alloy requires comprehensive studies of magnetic anisotropy at various scales. In this paper such a study is carried out for the soft magnetic amorphous FeCuNbSiB ribbons in as-quenched state, the ribbon compositions are shown in Table I.

Table I. Composition of ribbons.

Fe (at. %)	Cu (at. %)	Nb (at. %)	Si (at. %)	B (at. %)
70	1	3	13	13
71.5	1	5	16.5	6
73	1.5	3	16.5	6
74	1	3	16	6
74.3	0.2	3	16.5	6
74.5	1	3	13.5	8
75	1	3	13.5	7.5
77	1	0	16	6
77	1	3	13	6
77	1	3	14	5
77.5	0.5	3	8.5	10.5

The rapidly quenched FeCuNbSiB ribbons fabricated by the spinning technology are amorphous alloys in which a certain amount of the crystalline phase can form, depending on the elemental composition, production conditions, and external influence (temperature treatment) [1,2]. These alloys have a number of advantages: excellent magnetic properties, high strength and corrosion resistance. Amorphous FeCuNbSiB alloy is known as precursor for the soft magnetic nanocrystalline alloy prepared by the thermal treatment of it, that have had found application in magnetic cores for high-frequency transformers, sensors for weak magnetic fields and deformations, magnetic screens [2]. In a ferromagnetic amorphous alloy, any structural defect generates a non-uniform magnetization, which can be described using local magnetic anisotropy, characterized by direction of its easy axis, the magnetic anisotropy constant, and the scale within which the local easy axis is uniform. Ultimately these features determine the magnetic response of the alloy and, therefore, its applied potential.

The structure of the ribbons was controlled by x-ray diffraction (Bruker D8 Advance) and transmission electron microscopy (FEI TITAN 300). The domain structure was studied using a magneto-optical Kerr microscope Evico Magnetics GmbH; magnetic hysteresis and Curie temperature of the alloys was measured using a vibromagnetometer (heating rate 10 K/min).

Despite the fact that the magnetic anisotropy induced by the rolling of the ribbon is not observed in hysteresis loops, a fingerprint-like stress pattern in the domain structure of the ribbon disappears in different fields when they are oriented along and across the rolling axis [3]. The fingerprint-like domains and planar domains of amorphous FeCuNbSiB alloys are shown to be elongated along some directions, indicating the existence of an effective easy axis near the ribbon surface [3].

A correlation between the local magnetic anisotropy constant and the value of the nanoscale within which the local easy axis is ordered was found [4]. The correlation of these parameters is established and can be described using the Eq. 1:

$$K_{local} = K_V + \frac{\alpha}{R_c^2} \quad (1)$$

A similar dependence with an exponent equal to one was previously observed for nanoparticles, nanogranules, and nanocrystalline substances [5]. The formation of an internal surface separating regions with an ordered local easy axis as the cause of this correlation is discussed.

Acknowledgements

The reported study was funded by RFBR, project number 19-32-90182

References

- [1] N. V. Ilin, A.K. Tcesarskaia, V. V. Tkachev, V.A. Ivanov, A.M. Frolov, S. V. Dolzhikov, G.S. Kraynova, V.S. Plotnikov, Bull. Russ. Acad. Sci. Phys. **81** (2017) 387.
- [2] M.A. Willard, M. Daniil, in: K.H.J. Buschow (Ed.), Handb. Magn. Mater., North Holland, 2013: pp. 173–342.
- [3] R. Schäfer, J. Magn. Mater. **215–216** (2000) 652.
- [4] S.V. Komogortsev, R.S. Iskhakov, J. Magn. Mater. **440** (2017) 213.
- [5] E.A. Denisova, S.V. Komogortsev, R.S. Iskhakov, L.A. Chekanova, A.D. Balaev, Y.E. Kalinin, A.V. Sitnikov, J. Magn. Mater. **440** (2017) 221.

Skyrmion-antiskyrmion pairs by Monte-Carlo simulation in two-dimensional antiferromagnetic film

V. Kapitan^{*1,2}, E. Vasiliev^{1,2}, A. Perzhu^{1,2}, Y. Shevchenko^{1,2}, K. Soldatov^{1,2}, D. Kapitan^{1,2},
R. Volotovskiy^{1,2}, V. Strongin^{1,2}, A. Rybin^{1,2}, A. Makarov^{1,2}

¹ Department of Computer Systems, School of Natural Sciences, Far Eastern Federal University, Vladivostok, 690950, 8 Sukhanova St., Russian Federation

² Institute of Applied Mathematics, Far Eastern Branch, Russian Academy of Science, Vladivostok, 690041, 7 Radio St., Russian Federation

*e-mail: kapitan.vyu@dvfu.ru

Antiferromagnets are inherently promising for active elements as they have net zero magnetization, making them robust to external magnetic fields. These qualities combined with the rich physics of their spin dynamics have inspired new theoretical investigations and experimental techniques, including fundamental studies of spin-orbit interaction, new electrical and optical methods of controlling antiferromagnetic order, and the creation of hybrid structures with novel switching characteristics and to energize the field of antiferromagnetic spintronics, which aims to understand and control the dynamics of antiferromagnetic moments or spin transport for use in new-concept solid-state devices.

In this work, we developed an antiferromagnetic model and a software for simulation of magnetic skyrmions taking into account the DM interaction in frame of classical Heisenberg model. The Hamiltonian was:

$$H = H_J + H_{DMI} + B + A \quad (1)$$

$$H_J = J \sum_r S_r \cdot (S_{r+\hat{x}} + S_{r+\hat{y}} + S_{r+\hat{z}}), \quad (2)$$

$$H_{DMI} = -D \sum_r S_r \times S_{r+\hat{x}} \cdot \hat{x} + S_r \times S_{r+\hat{y}} \cdot \hat{y} + S_{r+\hat{z}} \cdot \hat{z} \quad (3)$$

$$B = -B_z \sum_r S_r \quad (4)$$

$$A = A_z \sum_r S_r^2 \quad (5)$$

The antiferromagnetic-exchange interaction (the first term), the Dzyaloshinskii-Moriya interaction (the second term), the Zeeman coupling (the third term) and magnetic anisotropy (the fourth term) are considered.

In this work, we demonstrate that a skyrmion-antiskyrmion pairs can be nucleated in antiferromagnets, based on Monte-Carlo simulations in frame of Heisenberg model with Dzyaloshinskii-Moriya (DM) interaction.

In our work, we plan to develop a method for controllable generation of skyrmions and antiskyrmions in 2D antiferromagnet films. To study methods for stabilizing skyrmions in antiferromagnets.

Acknowledgements

The research was carried out within the state assignment of FASO of Russia No. 075-00400-19-01.

Structural-magnetic models in search of new magnetic materials

L.M. Volkova*, D.M. Marinin

Institute of Chemistry, Far Eastern Branch, Russian Academy of Sciences, 690022 Vladivostok, Russia

e-mail: volkova@ich.dvo.ru

To search for new magnetic materials, we suggest to use a traditional crystal chemistry sequence composition → structure → property → function in a reverse order. In this case, first, we choose a functional material – a prototype for prediction, and, thereafter, the structural-magnetic model of this compound is calculated based on the crystal chemistry method we developed [1, 2]. Such a structural-magnetic model is based on crystal chemistry parameters (crystal structure and ions sign and strength). This model is characterized with (1) sign and strength of magnetic couplings; (2) dimensions of the magnetic structure, which not always coincide with those of the crystal structure; (3) presence of magnetic frustrations on specific geometric configurations; and (4) possibility of reorientation of magnetic moments (transition of the antiferromagnetic – ferromagnetic type) at shifts of intermediate ions localized in critical positions.

The structural-magnetic models enable one to reveal main correlation relationships between the compounds structures and magnetic properties and to determine, on their basis, the crystal chemistry criteria for targeted search of new functional magnetics in the Inorganic Crystal Structure Data (ICSD) database.

Below are presented the examples of our method application:

- We have built structural-magnetic models of well-known multiferroics TbMn_2O_5 , BiMn_2O_5 [3], and BiFeO_3 [4], formulated the crystal chemistry criteria for the search of multiferroics, and revealed four potential ones in the ICSD database: $\text{Pb}_2\text{Cu}(\text{OH})_4\text{Cl}_2$, $\text{Pb}_5\text{Cr}_3\text{F}_{19}$, $\text{Mn}(\text{SeO}_3)\cdot\text{H}_2\text{O}$, and $\text{BiPbSr}_2\text{MnO}_6$ [5].

- We have determined the crystal chemistry criteria of the formation of chiral magnetic soliton lattice in $\text{Cr}_{1/3}\text{NbS}_2$ and six isostructural compounds: $\text{Cr}_{1/3}\text{TaS}_2$, $\text{V}_{1/3}\text{TaS}_2$, $\text{V}_{1/3}\text{NbS}_2$, $\text{Ti}_{1/3}\text{NbS}_2$, $\text{Cr}_{1/3}\text{NbSe}_2$, and $\text{Cr}_{1/3}\text{TaSe}_2$ [6]. We have demonstrated the possibility of emergence of chiral magnetic solitons in hexagonal metal formates $[\text{NH}_4][\text{M}(\text{HCOO})_3]$, with $\text{M}^{2+} = \text{Mn}, \text{Fe}, \text{Co}, \text{Ni}$, and $\text{KCo}(\text{HCOO})_3$, in which these criteria are valid [7].

The search for potential materials characterized with realization of quantum spin liquids (QSL) comprises an

important task in the physics of condensed matter. At the present stage of study, the frustration of magnetic interactions is considered as the main parameter, which must characterize possible candidates for QSL.

- We have determined the structural-magnetic models of frustration of volcanic minerals of Kamchatka based on copper oxocentric tetrahedra (OCu_4). We have also identified quasi-one-dimensional frustrated antiferromagnets piypite ($\text{K}_4\text{Cu}_4\text{O}_2(\text{SO}_4)_4\text{MeCl}$), klyuchevskite ($\text{K}_3\text{Cu}_3(\text{Fe}_{0.82}\text{Al}_{0.18})\text{O}_2(\text{SO}_4)_4$) [8], and kamchatkite ($\text{KCu}_3\text{OCl}(\text{SO}_4)_2$) [9] and quasi-two-dimensional frustrated AFM averievite ($\text{Cu}_5\text{O}_2(\text{VO}_4)_2(\text{Cu}^+\text{Cl})$), ilinskite ($\text{NaCu}_5\text{O}_2(\text{SeO}_3)_2\text{Cl}_3$), and avdoninite ($\text{K}_2\text{Cu}_5\text{Cl}_8(\text{OH})_4\cdot 2\text{H}_2\text{O}$) built from layers of corner-sharing Cu_4 tetrahedra located on the kagome [10].

- We have built the structural-magnetic model of herbertsmithite ($\text{ZnCu}_3(\text{OH})_6\text{Cl}_2$) – the most well-known spin liquid – and performed, on its basis, the search and study of potential spin liquids in the ICSD database.

Acknowledgements

The work was partially supported by the Program of Basic Research ‘Far East’ (Far-Eastern Branch of the Russian Academy of Sciences), project no. 18–3–048.

References

- [1] L. M. Volkova, S. A. Polyshchuk J. Supercond. **18** (2005) 583.
- [2] L. M. Volkova. J. Struct. Chem. **50** (2009) S49.
- [3] L. M. Volkova, D. V. Marinin. J. Phys.: Condens. Matter. **21** (2009) 015903.
- [4] L. M. Volkova, D. V. Marinin. J. Supercond. **24** (2011) 2161.
- [5] L.M. Volkova, D. V. Marinin. J. Supercond. **24** (2011) 1839.
- [6] L. M Volkova, D. V. Marinin. J. Appl. Phys. **116** (2014) 133901.
- [7] L. M. Volkova, D. V. Marinin. J Supercond. **29** (2016) 2931.
- [8] L. M. Volkova, D. V. Marinin. J Supercond. **30** (2017) 959.
- [9] L. M. Volkova, D. V. Marinin. Phys Chem Minerals **45** (2018) 655.
- [10] L.M. Volkova, D. V. Marinin. J. Phys.: Condens. Matter **30** (2018) 425801.

Magnetic and optical properties of the iron oxide nanoparticles obtained via pulsed laser ablation

A.V. Kurilova¹, A.E. Sokolov^{1,2}, V.A. Svetlichnyi³, D.A. Velikanov², A.V. Sherepa², M.N. Volochaev², D.A. Goncharova³, A.V. Shabalina³

¹ Siberian Federal University, 79 Svobodny Prospect, 660041 Krasnoyarsk, Russia

² Kirensky Institute of Physics, Federal Research Center KSC SB RAS, Akademgorodok 50, bld. 38, Krasnoyarsk 660036, Russia

³ Siberian Physical-Technical Institute of Tomsk State University, Novosobornaya sq., 1, Tomsk 634050, Russia

*e-mail: list.ru-00@inbox.ru

Today, there is a question about the need to modernize technologies in various fields of life and production. One solution to this problem is to use and introduce new types of magnetic nanoparticles into some of them.

Small sizes of particles and their compounds and the possibility of varying their shape are often useful when exposed to an electromagnetic field, especially, if the particles in one way or another react to its change (heating, change of magnetization orientation, etc.) But depending on the modification of ion compounds, the synthesis method, and coatings, the nanoparticles can have chemical, optical, and magneto-optical properties are different from each other.

Tomsk State University provided samples of iron nanoparticles obtained by laser ablation in air at different temperatures to the Institute of Physics named after L.V. Kirensky SB RAS.

Synthesis of the materials

NPs were obtained using the focused radiation of an Nd:YAG laser LS-2131M-20 (LOTIS TII, Belarus). The PLA was carried out at the wavelength of 1064 nm. The pulse duration was 7 ns and the repetition frequency was maintained at 20 Hz. In this work, the total energy of the laser pulse from the nanosecond laser (150 mJ) was used. Changing the focusing allows one to change the pulse density of the radiation power (energy) on the target surface. In this case, a power density of 400 MW/cm² was chosen.

The obtained sample was annealed in a muffle furnace SNOL 6.7/1300 (Lithuania) in the temperature range of 100–600 °C. The heating rate was 10 °C/min, and the holding time at a given temperature was 4 h. Next, the initial sample was marked as Fe_{initial}. The Fe_T was used to mark the samples after annealing, where T is the annealing temperature.[1]

Nanoparticle's morphology were studied with a Hitachi TM 5500 transmission electron microscope equipped with an EDS attachment.

Magneto-optical spectra were received at room

temperature in range 350-620 nm with an apparatus for spectrometric studies developed at the IPH SB RAS based on the MDR-2 monochromator. Field up to 15 kOe, spectral resolution was 1 nm.

The average particle size obtained at room temperature is 20 nm. Particle size of Fe₆₀₀ (average) is 65 nm. This shows that with an increase in the firing temperature, the particles begin to unite into groups/ ensembles.

The spectra of all samples have several common features and a rather complex structure, which is due to interband electronic transitions in the iron ion. A comparative analysis of the graphs of MCD makes it clear that the "FeAir initial" sample has magneto-optical properties corresponding to magnetite (Fe₃O₄), the "FeAir 600°C" sample rather exhibits characteristics close to hematite (α-Fe₂O₃). The sample "Fe Air 300°C" is superposition of this states. It is also noticeable that the transition to maghemite (γ-Fe₂O₃) is not observed.

Conclusion

A number of magnetic NPs with varying characteristics were obtained as a result of synthesis via nanosecond PLA of the iron target in air and the subsequent annealing treatment. The powder initially obtained by PLA contains spherical NPs of iron oxide with the magnetite (Fe₃O₄). Annealing led to the enlargement of the particles and to transition to hematite(α-Fe₂O₃) with increasing firing temperature.

Acknowledgements

The reported study was funded by Russian Foundation for Basic Research, Government of Krasnoyarsk Territory, Krasnoyarsk Region Science and Technology Support Fund to the research project No.17-42-240080

References

- [1] V.A. Svetlichnyi, A.V. Shabalina, I.N. Lapin, D.A. Goncharova, D.A. Velikanov, A.E. Sokolov. J. Sci. Commun. **163** (2000) 51.

Ferromagnetic oxide coatings on Al, Ti, Zr and Nb

V.S. Rudnev¹, I.V. Lukiyanchuk^{1,2}, M.V. Adigamova¹

¹ Institute of Chemistry of FEB RAS, 159 Pr. 100-letiya, Vladivostok 690022, Russia

² Far Eastern Federal University, 8 Sukhanova St., Vladivostok 690950, Russia

*e-mail: lukiyanchukl@ich.dvo.ru

Fe-, Co-containing ferromagnetic oxide coatings on different valve metals have been formed by Plasma electrolytic oxidation (PEO) technique under the same conditions. It has been established that the value of the coercive force decreases in the series Zr > Nb > Ti > Al, and the value of the saturation magnetization of the ferromagnetic component decreases in the series Al > Zr > Nb > Ti. Differences in the ferromagnetic properties of Al-samples and Ti-, Zr- and Nb-samples correlate with differences in the elemental composition of the pores of the coatings.

PEO is the formation of oxide coatings on valve metals in electrolytes under electric spark and / or microarc electric discharges. During PEO, electrolyte components can be introduced into a growing coating. To impart ferromagnetic properties to PEO layers, the iron triad metals, including disperse particles, oxides and complex salts can be added to electrolyte formula before PEO treatment [1-3]. Our approach is related with using the electrolytes with colloidal hydroxides of these metals [4].

Fe-, Co-containing PEO coatings have been formed galvanostatically at an effective current density of 0.1 A/cm² for 10 min in PBWFeCo electrolyte-sol, containing (mol/L): 0.066 Na₃PO₄ + 0.034 Na₂B₄O₇ + 0.006 Na₂WO₄ + 0.02 Fe₂(C₂O₄)₃ + 0.04 Co(CH₃COO)₂.

Table I gives the elemental compositions and magnetic characteristics of PEO-coated samples. As can be seen from the data obtained, the use of electrolytes-sols with dispersed particles of iron and cobalt hydroxides allows obtaining the coatings with a ferromagnetic component on all the studied paramagnetic valve metals (Al, Zr, Nb, Ti).

Table I. Calculated values of the coercive force H_c , magnetic susceptibility μ of the samples and saturation magnetization M_s of the ferromagnetic component at 300 K and element composition of the coatings (as to X-ray spectrum analysis)

Metal	Element composition, (at. %)	H_c , (Oe)	$\mu \times 10^6$	M_s , (emu/g)
Al	2.1 Fe, 2.4 Co, 0.2 W, 0.6 P, 27.8 Al, 73.2 O	113	0.9	3.2×10^{-2}
Ti	4.1 Fe, 4.2 Co, 1.1 W, 7.1 P, 2.4 Na, 7.5 Ti, 73.6 O	144	3.02	3.8×10^{-3}
Nb	3.8 Fe, 3.0 Co, 1.6 W, 6.3 P, 1.4 Na, 7.7 Nb, 72.6 O	308	1.39	6.5×10^{-3}
Zr	5.4 Fe, 3.6 Co, 1.4 W, 5.2 P, 1.2 Na, 10.5 Zr, 73.2 O	364	1.26	7.3×10^{-3}

As to the values of the coercive force H_c at room temperature (Table I), the samples with ferromagnetic PEO coatings are arranged in a row: Zr > Nb > Ti > Al. At the same time, the series Al > Zr > Nb > Ti is obtained from

the values of the saturation magnetization of the ferromagnetic component of the samples. M_s for aluminum samples is 5-10 times higher than that for Ti-, Zr- and Nb-samples. This may be because the total concentration of iron and cobalt in the pores of the coatings is higher for Al-sample than for other studied samples (Table II).

Table II. Elemental composition of the pores (at. %)

Metal	O	Na	P	Fe	Co	W	M
Al	12.1	-	-	25.6	45.6	-	22.1 Al
Ti	35.7	2.9	10.2	12.8	12.9	1.3	24.2 Ti
Zr	48.3	1.0	0.8	7.5	5.6	6.4	30.4 Zr
Nb	50.3	0.4	5.0	10.5	9.4	11.0	13.4 Nb

Elevated concentration of iron triad metals and a lack of oxygen for the formation of their stoichiometric oxides may indicate the presence of reduced and even metallic iron and cobalt in the pores of the coatings. The presence of reduced iron in PEO coatings on aluminum and titanium was previously shown by XRD and XPS methods [5, 6].

As to the fraction of iron in the total atomic concentration of iron and cobalt $[Fe]/([Fe] + [Co])$, the series Zr (0.57) > Nb (0.53) > Ti (0.5) > Al (0.36) is obtained for the pores of the coatings on Zr, Nb, Ti and Al, respectively. This series of decreasing iron fractions correlates with a series of decreasing coercive forces of the samples.

Acknowledgements

The work was carried out within the Institute of Chemistry FEBRAS State Order (project no. 265-2019-0001).

References

- [1] F.Y. Jin, H.H. Tong, J. Li, L.R. Shen, P.K. Chu. Surf. Coat. Technol. **201** (2006) 292.
- [2] A. Jagminas, R. Ragalevicius, K. Mazeika, J. Reklaitis, V. Jasulaitiene, A. Selskis, D. Baltrunas. J. Solid State Electrochem. **14** (2010) 271.
- [3] A.B. Rogov, O.P. Terleeva, I.V. Mironov, A.I. Slonova. Appl. Surf. Sci. **258** (2012) 2761.
- [4] V.S. Rudnev, V.P. Morozova, I.V. Lukiyanchuk, M.V. Adigamova, et al., Russ. J. Phys. Chem. A. **87** (2013) 1052.
- [5] V.S. Rudnev, M.V. Adigamova, I.V. Lukiyanchuk, A.Yu. Ustinov, I.A. Tkachenko, P.V. Kharitonov, A.M. Frolov, V.P. Morozova. Prot. Met. Phys. Chem. Surf. **48** (2012) 543.
- [6] V.S. Rudnev, V.P. Morozova, I.V. Lukiyanchuk, et al., Prot. Met. Phys. Chem. Surf. **49** (2013) 309.

Features of the surface morphology and magnetic properties of $\text{Sm}_{0.5}\text{R}_{0.5}\text{Fe}_2$ (R = Tb, Gd) compounds

G.A. Politova^{*,1,2}, T.P. Kaminskaya³, A.Yu. Karpenkov⁴, N.Yu. Pankratov³, M.A. Ganin¹,
D.G. Dankin⁵, A.V. Filimonov²

¹ Baikov Institute of Metallurgy and Materials Science, Russian Academy of Sciences, Moscow 119334, Russia

² Peter the Great St. Petersburg Polytechnic University, St. Petersburg 195251, Russia

³ Lomonosov Moscow State University, Moscow 119991, Russia

⁴ Tver State University, Tver 170002, Russia

⁵ National University of Science and Technologi MISiS, Moscow, Russia

*e-mail: gpolitova@gmail.com

A comprehensive study of the structure and phase composition, magnetostrictive and magnetic properties of the compounds $(\text{Sm}_{0.5}\text{R}_{0.5})\text{Fe}_2$ (R = Gd, Tb) was performed. Using atomic force and magnetic force microscopy, the surface topology at the micro and nanoscale has been established, and information on the magnetic domain structure at room temperature has been obtained. The effect of partial replacement of samarium with gadolinium and terbium on the surface microstructure and domain structure, the temperature of phase transitions, the magnitude of magnetostrictive deformations and magnetization is studied.

The high magnetostrictive Laves phases of the RFe_2 type are of great interest from both the applied and fundamental points of view. SmFe_2 and TbFe_2 compounds have the highest saturation magnetostriction values at room temperature ($-1.5 \cdot 10^{-3}$ and $+1.7 \cdot 10^{-3}$, respectively), while they are opposite in sign. GdFe_2 at room temperature shows an insignificant positive value of magnetostriction. When samarium is partially replaced with terbium, with a terbium content of 0.4–0.5 at./f.u., the sign of magnetostriction changes [1]. In addition, when replacing the light rare-earth ion Sm^{3+} with heavy Tb^{3+} and Gd^{3+} , a composition with magnetic compensation of magnetization can be obtained. The contents of Tb^{3+} and Gd^{3+} in this case, according to calculations, are also close to 0.5 at./f.u.

The aim of this work was a comprehensive study of the structural, magnetic, and magnetostrictive characteristics of $\text{Sm}_{0.5}\text{Gd}_{0.5}\text{Fe}_2$ and $\text{Sm}_{0.5}\text{Tb}_{0.5}\text{Fe}_2$ compounds and their comparison with similar SmFe_2 characteristics obtained by us earlier [2,3].

As the initial components, metals of a high degree of purity were used: (99.99%). $\text{Sm}_{0.5}\text{Gd}_{0.5}\text{Fe}_2$ alloy was obtained by high-frequency induction melting in an atmosphere of highly pure argon, while $\text{Sm}_{0.5}\text{Tb}_{0.5}\text{Fe}_2$ was obtained by the arc melting method. In order to equalize the composition of the obtained alloys, homogenizing annealing was performed. As shown by x-ray studies, the content of the main phase with the MgCu_2 structure in the compound with gadolinium reaches 97%, while in the compound with Tb - 88%. No significant distortions of the cubic crystal structure at room temperature were detected, the unit cell parameters are 0.7397 and 0.7375 nm, respectively (decreased compared to SmFe_2).

The morphology of the surface of the alloys was studied by atomic force microscopy (AFM) using a SMENA-A scanning probe microscope (Solver, NT – MDT Zelenograd, Russia) in the semi-contact mode at room temperature. The obtained AFM images of the surfaces of

the chips were processed by the software for visualization and analysis of Nova_873. Studies of the domain structure of the samples were performed on polished thin sections by magnetic force microscopy (MFM) using a two-pass technique. Unlike SmFe_2 [3], the studied alloys have a nonuniform and inhomogeneous surface microstructure with large (diameter 5–7 μm , height up to 500 μm) agglomerates in the form of a radially-cellular crystallization front of small particles (50–70 nm). Regions of the cell-like surface, similar to SmFe_2 , but with large sizes (from 1.2 to 1.4 μm), are unevenly distributed between the agglomerates. The domain structure of the samples is irregular; strip domains with a strip width of 10–20 μm of a cellular shape are observed.

The magnetization of the alloys was measured using induction and vibration magnetometers in the temperature range of 80 - 800 K in magnetic fields up to 1.8 T. Studies have shown that the Curie temperatures of $\text{Sm}_{0.5}\text{Gd}_{0.5}\text{Fe}_2$ and $\text{Sm}_{0.5}\text{Tb}_{0.5}\text{Fe}_2$ compounds have close values (~ 645 K), lower than the initial SmFe_2 . The magnetization of compounds at room temperature decreased by about 3 times, i.e., partial compensation of magnetization is observed.

Magnetostriction was measured by a strain gage method in magnetic fields up to 1.2 T along the direction of the magnetic field (longitudinal magnetostriction) and perpendicular to it (transverse magnetostriction) in the temperature range from 80 to 360 K. The significant decrease in the anisotropic (difference between longitudinal and transverse magnetostriction) magnetostrictions was established. The peak in the temperature region of the spin reorientation expands significantly, compared with the initial SmFe_2 composition, and shifts to the region of low temperatures

Acknowledgements

This work was supported by the Russian Foundation for Basic Research under Project 18-03-00798_a.

References

- [1] A.S. Ilyushin, E.V. Solodov, Z.S. Umkhayeva. *Journal Perspektivnye materialy* **11** (2013) 42.
- [2] G.A. Politova, A.Yu. Karpenkov, T.P. Kaminskaya, M.A. Ganin, R. Kumar, A.V. Filimonov. *St. Petersburg Polytech. State Univ. J. Phys.Math.* **2** (2019) 28.
- [3] T.P. Kaminskaya, G.A. Politova, A.Yu. Karpenkov, M.A. Ganin *IEEE Magn. Lett.* **10** (2019) 7109705.

Asymmetric domain wall propagation in epitaxial Pd/Co/Pd(111) trilayers

N.I. Sarnavskiy, A.G. Kozlov, A.V. Davydenko*

¹ Far Eastern Federal University, 8 Sukhanova St., Vladivostok 690950, Russia

*e-mail: avdavydenko@gmail.com

Effects related with strong spin-orbit interaction attract much attention in magnetism. One of such effects is Dzyaloshinskii-Moriya interaction (DMI). Interface DMI reveals in the thin film systems consisting of adjacent heavy metal and ferromagnetic layers. It was considered that solely DMI is responsible for asymmetric growth of the domains in combination of lateral and perpendicular magnetic fields [1]. A method of DMI evaluation based on the measurements of the velocities of domain walls was proposed [1, 2]. However, recently it was shown that there is another spin-orbit effect which may lead to asymmetrical domain walls propagation, so-called chiral damping effect [2]. Since these effects act together, it is challenge to divide the contributions from them to the domain wall motion. In the present paper the Pd/Co/Pd (111) system with strong chiral damping effect was investigated. In spite of symmetric composition of the system, Co layers are asymmetrically strained. Asymmetry of the strains may be origin of non-zero DMI and chiral damping in this system. The aim of the paper was investigation of the DMI and chiral damping effect as functions of the thickness of bottom Pd layer. We found a strong increase of the chiral damping effect with increasing of the thickness of Pd bottom layer which is related with increasing roughness of Pd/Co/Pd trilayers.

Pd(1–10 nm)/Co(1 nm)/Pd(3 nm) trilayers were epitaxially grown on Si(111) substrates with Cu(2 nm) buffer layers. Dependencies of the lattice parameters of the layers on the thickness of the layers were determined by means of reflection high energy electron diffraction. Lattice parameter of Pd bottom layer depended on the Pd thickness and increased from 0.383 nm to the value of bulk Pd lattice parameter, 0.389 nm, if the thickness of Pd bottom layer increased from 1 to 3 nm. Hence Co layers grown on thicker Pd layers were more strained than Co layers deposited on thinner Pd layers. However, asymmetry of the strains, the relative difference between the lattice parameters of the Co bottom and top interface layers, weakly depended on the Pd bottom layer thickness. Distribution of the strains in the Co layers was constant if the thickness of Pd underlayer was larger than 3 nm.

Contrary the roughness of the Pd bottom layer was almost the same in the Pd thickness interval from 1 to 3 nm and strongly increased with increase of Pd thickness larger than 3 nm [3]. We used this fact to analyse the influence of different strains and roughness on the magnetic properties of the samples. We found an increase of energy of perpendicular magnetic anisotropy with increase of the thickness of Pd underlayer. We relate this fact with increase of magnetoelastic anisotropy in the bottom Pd thickness interval from 1 to 3 nm and increase of magnetostatic contribution due to increase of Co roughness in the bottom Pd thickness interval from 3 to 10 nm.

DMI was measured by method proposed by Je et al. [1]. The method is based on the measurement of the velocities of the domain walls in combination of lateral and perpendicular magnetic fields. Existence of DMI may be considered as occurrence of chiral magnetic field inside domain walls. This DMI-field set the specific chirality of the domain walls (left-handed or right-handed). DMI-field is summarized with lateral external magnetic field in one domain wall and is subtracted from external magnetic field in opposite domain wall. Therefore one, for example left, domain wall propagates faster than right domain wall in the perpendicular magnetic field and domain grows asymmetrically. DMI-field and DMI energy may be evaluated by minimum of the velocity in the $V(H_x)$ curve, where V is the velocity of domain wall, H_x is lateral magnetic field.

We found that $V(H_x)$ curves were similar in the Pd(1–3 nm)/Co(1 nm)/Pd(3 nm) samples. In spite of increasing strains in the Co layers with increase of Pd underlayer thickness asymmetry of the strains remained the same and DMI was constant. However, $V(H_x)$ curves of the samples with thicker Pd underlayers ($d_{Pd} = 3–10$ nm) changed. Minima of the $V(H_x)$ curves shifted to the larger H_x fields which indicated increase of DMI energy. Moreover, $V(H_x)$ curves became asymmetric relative to the DMI field, which is the sign of strong chiral damping effect. In these samples a position of the minima in $V(H_x)$ curves depended on the magnitude of perpendicular magnetic field. It prevented us from exact determination of DMI-field in the samples with thick Pd underlayers. The strength of chiral damping effect was evaluated by the measurement of the ratio of the velocities of fast and slow domain walls V_F / V_S in lateral magnetic fields of 40 mT. The largest value of the ratio V_F / V_S was equal to 700 and observed in the Pd(10 nm)/Co(1 nm)/Pd(3 nm) sample. We relate increase of chiral damping effect in the samples with thick Pd underlayers with increase of the roughness of the samples.

Acknowledgements

The reported study was funded by RFBR under the research project 18-32-20057.

References

- [1] S.G. Je, D.H. Kim, S.C. Yoo, B.C. Min, K.J. Lee, and S.B. Choe. *Phys. Rev. B* **88** (2013) 214401.
- [2] A. Hrabec, N.A. Porter, et al., *Phys. Rev. B* **90** (2014) 020402.
- [3] E. Jue, C.K. Safeer, M. Drouard, A. Lopez, P. Balint, L. Buda-Prejbeanu, O. Boulle, S. Auffret, A. Schuhl, A. Manchon, I.M. Miron, G. Gaudin. *Nat. Mat.* **15** (2016) 272.
- [4] A.V. Davydenko, A.G. Kozlov, A.V. Ognev, M.E. Steblyi, L.A. Chebotkevich. *Appl. Surf. Sci.* **384** (2016) 406.

Dzyaloshinskii-Moriya interaction in [Co(1 nm)/Pd]₅ superlattices with different thickness of Pd interlayers

Ya.S. Drozdovskiy, A.G. Kozlov, A.V. Davydenko*

Far Eastern Federal University, 8 Sukhanova St., Vladivostok 690950, Russia

*e-mail: avdavydenko@gmail.com

Dzyaloshinskii-Moriya interaction (DMI) is the antisymmetric exchange interaction which favors chiral structures like skyrmions, homochiral Neel domain walls, spin spirals in thin magnetic films with perpendicular magnetic anisotropy. These magnetic structures are very interesting since they may be used in new types of magnetic memories and logic devices. DMI of interfacial type may be stabilized in thin ferromagnetic (FM) films enclosed between heavy metal (HM) layers with strong spin-orbit coupling. An appropriate choice of materials of HM layers leads to amplification of the net DMI in the structure. A possible way of increasing the stability of skyrmions is using superlattices consisting of HM1/FM/HM2 structures repeating N times. In these structures dipolar interlayer coupling facilitates skyrmions formation. Precise measurement of the DMI energy is needed for magnetic devices construction. A method of determination of effective DMI energy by periodicity of labyrinth domains was proposed [1]. We tested this method on [Pd(0.5 – 4 nm)/Co(1 nm)]₅ superlattices with different thickness of Pd interlayers and obtained effective DMI energies in investigated system.

Superlattices [Pd(0.5 – 4 nm)/Co(1 nm)]₅ were epitaxially grown on Si(111) substrates with Cu(2 nm) buffer layers. Dependencies of the lattice parameters of the layers on the thickness of the layers were determined by means of reflection high energy electron diffraction. Lattice parameter on the top of the Pd interlayers depended on the Pd thickness and increased from 0.385 nm to the value of bulk Pd lattice parameter, 0.389 nm, if the thickness of the Pd interlayers increased from 0.5 to 4 nm. Hence Co layers grown on thicker Pd layers were more strained than Co layers deposited on thinner Pd layers. We suppose that asymmetry of the strains, the relative difference between the lattice parameters of the Co bottom and top interface layers, is origin of existence of DMI in this symmetric system.

Magnetic anisotropy was calculated by magnetic hysteresis loops analysis. All the samples demonstrated perpendicular magnetic anisotropy. The energy of effective perpendicular magnetic anisotropy increased from 0.14 to 0.64 MJ/m³ with increasing of the Pd interlayers thickness due to increasing of the magnetoelastic magnetic anisotropy.

The energy of effective DMI was evaluated by comparison of periodicities of demagnetized domain structures and magnetic structures obtained by micromagnetic simulations. Magnetic parameters used in the simulations were following: the saturation magnetization, $M_s = 1.544$ MA/m³, exchange constant, $A = 25$ pJ/m. Micromagnetic simulations were carried out using MuMax3 software. Periods of labyrinth structures obtained by micromagnetic simulations were compared

with the values calculated by means of analytical model [2]. We found good correlation of the results.

The superlattices were demagnetized by alternating in-plane (IP) and out-of-plane (OP) magnetic fields with a decaying amplitude. The magnetic structures in demagnetized state were measured by a magnetic force microscopy. Periodicities of labyrinth structures depended on the direction of the demagnetizing magnetic field. IP demagnetized structures had lower periodicity than OP ones. We used both of them and hence obtained two types of effective DMI energies: IP and OP DMI energies, if one compares simulated magnetic structures with experimental IP and OP demagnetized structures, respectively.

Both IP and OP effective DMI energies increased with an increase of Pd interlayers thickness in a similar way. Rapid increase of DMI energies was observed when the thickness of Pd interlayers was 1.5 nm. This observation may be explained by two processes. The first one is a formation of Pd/Co interfaces with a good quality. Several atomic layers is needed to cover all Co atoms. The second process is an increase of asymmetry of the strains between the bottom Pd/Co and top Co/Pd interfaces with increasing of Pd interlayers thickness. We believe that asymmetry of the strains between the bottom and top interfaces is the origin of strong DMI in this system. Therefore, relationship between DMI energy and the thickness of Pd interlayers become reasonable. These results correlate well with the literature data [3].

Despite IP effective DMI energies are basically used in the papers concerning the method of measurement of DMI energies by domain periodicity analysis [4], we suppose that OP DMI energies are more reasonable. At first, they are smaller by magnitude than IP DMI energies. In the [Pd(4 nm)/Co(1 nm)]₅ superlattices IP and OP DMI energies are 3 and 2 mJ/m², respectively. Since the investigated system is symmetric by composition large DMI energies raise doubts. Secondly, micromagnetic simulations demonstrate isotropic labyrinth structures as OP demagnetized experimentally obtained ones.

Acknowledgements

The reported study was funded by RFBR under the research project 18-32-20057.

References

- [1] S. Woo, et.al. Nat. Mat. **15** (2016) 501.
- [2] I. Lemesh, G.S.D. Beach. Phys. Rev. B **98** (2018) 104402.
- [3] S. Tacchi, et.al. Phys. Rev. Lett. **118** (2017) 147201.
- [4] P. Agrawal, F. Buttner, I. Lemesh, S. Schlotter, G.S.D. Beach. Phys. Rev. B **100** (2019) 104430.

Structure, crystallization and magnetic properties of new glasses in the MnNbOF₅-BaF₂-FeF₃ system

L.N. Ignatieva, N.N. Savchenko, Yu.V. Marchenko*, V.A. Mashchenko, I.A. Tkachenko
Institute of Chemistry of FEB RAS, 159 100-letya Vladivostoka Prosp., Vladivostok, 690022, Russia

*e-mail: gor_dvo@mail.ru

Among the representatives of optically active oxyfluoride materials, systems based on niobium oxyfluoride occupy a prominent place [1]. The idea of introducing fluoride components, such as BiF₃, InF₃, REE fluorides, into these glasses resulted in fabrication of the new systems with specific crystallization properties, since these systems appeared to be a suitable base for creation of glass ceramics. Earlier [2, 3] compositions of the glasses based on MnNbOF₅ containing BiF₃, InF₃, and REE fluorides with specific transport and luminescence properties were revealed by us. Taking into account the revealed features of the structure and crystallization, optical and electrophysical properties of oxyfluoroniobate glasses containing fluoride components (BiF₃, InF₃), it was of interest to consider the option of fabricating similar systems with iron trifluoride. For this purpose, new glasses were fabricated in the system of MnNbOF₅-BaF₂-FeF₃, and results of their study are described in the present work.

Glasses in the system of MnNbOF₅-BaF₂-FeF₃ have been fabricated for the first time. The specially synthesized compound of MnNbOF₅·4H₂O was used to fabricate the glasses. The glasses structure, thermal characteristics, crystallization and magnetic properties have been investigated using the IR and Raman spectroscopy, DSC, XRD and SQUID magnetometry.

Table 1. Thermal characteristics of MnNbOF₅-BaF₂-FeF₃ glasses and crystalline phases under heating at 500 °C

Composition of the batch mixture	t _g	Δt	S, K	Crystalline Phases (500 °C)
20MnNbOF ₅ -50BaF ₂ -30FeF ₃	327	58	0.28	Amorph. BaMnO ₄ , BaFeF ₅ , FeO(OH)
20MnNbOF ₅ -40BaF ₂ -40FeF ₃	342	64	1.61	Amorph. BaFeF ₅ , BaFeF ₄
30MnNbOF ₅ -40BaF ₂ -30FeF ₃	323	85	1.58	Amorph. Ba ₂ FeF ₆ , Ba ₃ Fe ₂ O ₆ , BaMnO ₆ ;
30MnNbOF ₅ -50BaF ₂ -20FeF ₃	316	81	1.31	Amorph. BaFeF ₅ , BaNbOF ₅ ;
30MnNbOF ₅ -60BaF ₂ -10FeF ₃				Amorph. BaFeF ₅
40MnNbOF ₅ -40BaF ₂ -20FeF ₃				Amorph. BaMnO ₄ , Ba ₃ Fe ₂ O ₆

As can be seen from the table changes in the glass transition temperature (t_g) regarding the synthesized compositions were generally insignificant and located

within the range 335–316 °C. The region is characteristic of oxyfluorobiobates. The thermal stability interval (Δt) of the glasses substantially depends on the ratio of the components, showing a tendency to increase with an increase of the MnNbOF₅ component in the glass composition. At devitrification of most of the glasses, the BaFeF₅ phase was found in the crystallization products. For all the investigated compositions, even after the emergence of crystalline phases in the glass, the sample as a whole remained amorphous, which suggests the possibility of fabricating transparent glass-crystal composites in the glasses of the MnNbOF₅-BaF₂-FeF₃ system by the thermal treatment.

Based on analysis of IR and Raman spectra we showed that glasses in the MnNbOF₅-BaF₂-FeF₃ system are built of NbO_nF_n polyhedra linked by oxygen bridges, and the introduction of the fluoride component (FeF₃) into the system leads to the formation of glass-like FeF_n polyhedra. FeF_n groups are not built into oxyfluoroniobate chains, but are presumably linked to the oxyfluoroniobate polyhedron via axial or basal fluorine and the iron-containing polyhedra are interconnected by bridges of Fe-F-Fe. So glass network consists of two subsystems: the network formed by oxyfluoroniobate polyhedra linked by oxygen bridges and the subsystem which is formed by iron trifluoride. Crystallization could be initiated in one of the subsystems, while the second subsystem remained amorphous.

The emergence of some specific magnetic properties was expected. For this purpose, magnetic characteristics of a number of the samples were investigated. From analysis of the temperature and field dependencies of the magnetization for the samples of some compositions concluded the paramagnetic behavior of the system but upon the thermal treatment, a transition to a magnetically ordered state has been observed in some samples

Acknowledgements

The present work was supported by the Russian Foundation for Basic Research (project no. 18-03-00034).

References

- [1] J-L. Adam, J. Fluorine Chem. **107** (2001) 265.
- [2] L.N. Ignat'eva, N.N. Savchenko, S.A. Polishchuk, Yu.V. Marchenko et al Russ. J. Inorg. Chem. **59** (2014) 831.
- [3] L.N. Ignatieva, N.N. Savchenko, Yu.V. Marchenko. J. Fluorine Chem, **213** (2018) 37.

Optically tunable magnetoimpedance in Fe/Al₂O₃/p-Si

M.V. Rautskii¹, D.A. Smolyakov¹, I.A. Bondarev^{*,1,2}, A.S. Tarasov¹, A.V. Lukyanenko^{1,2},
I.A. Yakovlev¹, A.N. Masyugin³, M.N. Volochaev¹, N.N. Kosyrev¹, N.V. Volkov¹

¹ Kirensky Institute of Physics, Siberian Branch, Russian Academy of Sciences, Krasnoyarsk 660036, Russia

² Siberian State University of Science and Technology, Krasnoyarsk 660014, Russia

³ Reshetnev Siberian State University of Science and Technology, Krasnoyarsk, 662850

*e-mail: bia@iph.krasn.ru

Studies of magnetic transport in multilayered MIS structures have revealed the potential for integrating MIS based devices into modern electronics and significantly expanding its capabilities. This is achieved by the interaction of electronic and magnetic subsystems, which can be illustrated by the giant magnetoimpedance (GMI) effect, spin injection, etc. In addition, the optical irradiation can affect electronic transport. Previously we established the optically induced giant DC magnetoresistance effect in Fe/SiO₂/p-Si structure [1]. The current work is devoted to the study of AC magnetoimpedance (MI) in Fe/Al₂O₃/p-Si structure under optical irradiation.

The sample was prepared on single-crystal boron-doped p-Si substrate. The substrate surface was precleaned by the Shiraki method (chemical etching and long-term annealing of 400-600°C) [2]. The 50nm-thick Al₂O₃ layer was formed by atomic layer deposition (ALD) using a trimethylaluminum precursor (TMA), deionized water, and a nitrogen carrier gas of 99,9999 purity at a growth temperature of 250°C on a PICOSUN R-200 facility. To obtain the thickness of ≈ 50 nm, 50 ALD cycles were performed (0,95 nm per cycle). Fe film with thicknesses of 15 nm was deposited by thermal evaporation under ultrahigh vacuum conditions at a sputtering rate of 0,25 nm/min. The base pressure in the Angara chamber [3] was $8,6 \times 10^{-6}$ Pa. The fabricated structure was characterized by cross-sectional transmission electron microscopy (TEM). The magnetic properties were examined by the magneto-optical Kerr effect (MOKE) on a NanoMOKE 2 setup. The impedance measurements were performed by a two-probe method. Ohmic contacts were formed on the metallic film using silver epoxy and at the bottom of the Si substrate by indium alloying.

We studied temperature dependences of the impedance at various conditions by changing frequency, magnetic field, bias voltage and optical irradiation power. The dependences have a pronounced peak at helium temperatures, which is explained by the recharging process

of the interface states that are localized at the Al₂O₃/p-Si interface [4]. Magnetic field slightly shifts the peak (by ≈ 1 K) and does not significantly affect the impedance in the absence of optical irradiation (the MI value $\approx 1.5\%$). However, when the optical radiation of wavelength $\lambda = 665$ nm and power $P = 1$ mW is applied, the GMI effect is observed, the MI value reaches $\approx 300\%$ at $T=10$ K and decreases with the increasing of temperature. It is also established that applying of bias voltage can affect the shape of the R(T) peak, and shift the MI(T) peak from 10 K towards higher temperatures.

In this work we demonstrated the possibility to control the magnetoimpedance in Fe/Al₂O₃/p-Si structure, using bias voltage and optical irradiation. We believe that obtained results can serve as a basis for the manufacture of magneto-optical sensors and spintronic devices.

Acknowledgements

The work was partially supported by the Ministry of Education and Science, Fundamental research program of the Presidium of the RAS no. 32 «Nanostructures: physics, chemistry, biology, basics of technologies». The reported study was funded by Russian Foundation for Basic Research, Government of Krasnoyarsk Territory, Krasnoyarsk Region Science and Technology Support Fund by project № 18-42-243022.

References

- [1] Volkov, N. V., Tarasov, A. S., Eremin, E. V., Baron, F. A., Varnakov, S. N., & Ovchinnikov, S. G. *J Appl Phys.* **114** (2013) 093903.
- [2] T. Morikawa, Y. Nishibe, H. Yamadera, Y. Nonomura, M. Takeuchi, Y. Taga. *IEEE Trans. Magn.* **33** (1997) 4367.
- [3] S.N. Varnakov, A.A. Lepeshev, S.G. Ovchinnikov, A.S. Parshin, M.M. Korshunov, P. Nevorol. *Instrum. Exp. Tech.* **47** (2004) 839.
- [4] Smolyakov D.A., Tarasov A.S., Yakovlev I.A., Masyugin A.N., Volochaev M.N., Bondarev I.A., Kosyrev N.N., Volkov N.V. *Thin Solid Films.* **671** (2019) 18.

Magnetic properties of Fe₃Si synthesized at external magnetic field

I.A. Yakovlev*, B.A. Belyaev, S.N. Varnakov

Kirensky Institute of Physics, Federal Research Center KSC SB RAS, Akademgorodok 50, bld. 38, Krasnoyarsk 660036, Russia

*e-mail: via@iph.krasn.ru

High sensitive weak magnetic fields sensors are widely used in science and technology: in the search and exploration of minerals, in near-field magnetic communication systems, in magnetic location systems and navigation-measuring systems, medicine etc. Improving the characteristics of these devices will allow more accurately determine the measured parameters. Ferromagnetic thin films based on Fe-Si have wide prospects in this area, since they have better magnetic properties than the materials currently used such as permolium [1].

In our work we studied the magnetic anisotropy of Fe₃Si films obtained on five types of substrates. Si(001), (111) with and without a SiO₂ oxide layer, as well as amorphous quartz substrates were used. Samples were synthesized at an external magnetic field equals 290 and 480 Oe and without one.

The experiment was carried out with ultrahigh vacuum molecular-beam epitaxy (MBE) "Angara" set-up [2], equipped with a system of reflection high-energy electron diffraction (RHEED). The base pressure in the growth chamber was about 6.5×10^{-8} Pa. The Si(111)7×7 and Si(100)2×1 substrates were prepared by special treatment [2]; SiO₂/Si(111), SiO₂/Si(100) and amorphous quartz were cleaned with almost same treatment but heated only up to 450 °C. The component materials were evaporated from Knudsen effusion cells.

The Fe₃Si films were prepared by molecular-beam epitaxy technique with simultaneous deposition of Si and Fe with Fe:Si=3:1 atoms rates on substrates at room temperature. The structures were deposited at 290, 480 Oe magnetic field and without one. The thickness of the films was about 50 nm. The structure formation was monitored *in situ* by RHEED. The magnetic properties of the films were investigated with a scanning spectrometer of ferromagnetic resonance at 1.2 - 3.3 GHz pump frequency range [3]. In the film plane an angular dependence of the resonance field $H_R(\varphi)$ at 5 or 10° step was measured. To investigate the magnetic anisotropy for films from the angular dependence of FMR field phenomenological model

calculation [4] was used.

RHEED investigation shows polycrystalline almost amorphous structure of Fe₃Si films on Si covered SiO₂ and amorphous quartz, as well as epitaxial monocrystalline silicide on Si(111)7×7 and Si(100)2×1.

Magnetic anisotropy for silicide deposited on SiO₂/Si(111), SiO₂/Si(100) increases on external magnetic field according to FMR measurements and an uniaxial magnetic anisotropy for Fe₃Si/SiO₂/Si(100) equals 9.17 and 14.85 Oe at 290 and 480 Oe corresponding. But it does not dependent on substrate plane and equals 14.60 Oe for Fe₃Si/SiO₂/Si(111) at 480 Oe. Magnetic properties for silicide on quartz have a similar character and uniaxial magnetic anisotropy is 3.43 Oe at 290 Oe and 12.68 Oe at 480 Oe.

The external magnetic field attached during Fe₃Si deposition on Si(111)7×7 and Si(100)2×1 has almost no effect on magnetic anisotropy.

It is found that uniaxial magnetic anisotropy for polycrystalline (almost amorphous) Fe₃Si increases with external magnetic field almost 3.5 times for amorphous quartz substrate.

Acknowledgements

The work was supported by the President Program of the RF SP- 375.2019.3 and Krasnoyarsk Regional Fund of Science according to the participation in the event/internship: Fifth Asian School-Conference on Physics and Technology of Nanostructured Materials (ASCO-NANOMAT 2020).

References

- [1] A. N. Babitskii, B. A. Belyaev, G. V. Skomorokhov et al. *Technical Physics Letters* **41** (2015) 324.
- [2] I.A. Yakovlev, S.N. Varnakov, B.A. Belyaev et al. *JETP letters* **99** (2014) 527.
- [3] B.A. Belyaev, A.V. Izotov, A.A. Leksikov. *IEEE Sens. J.* **5** (2005) 260.
- [4] B.A. Belyaev, A.V. Izotov *JETP Letters* **103** (2016) 41.

Possibility of using analytical method to calculate magneto-optical parameter from magneto-ellipsometry measurements data

O.A. Maximova^{*,1,2}, S.G. Ovchinnikov^{1,2}

¹ Kirensky Institute of Physics, Akademgorodok 50, bld. 38, Krasnoyarsk 660036, Russia

² Siberian Federal University, 79 Svobodny pr., Krasnoyarsk 660041, Russia

*e-mail: maximo.a@mail.ru

Magneto-ellipsometry combines ellipsometry and magneto-optical Kerr effect measurements. The main difficulty usually is in data processing as a number of parameters should be extracted from measured ellipsometric angles ψ_0 , Δ_0 , $\delta\psi$ and $\delta\Delta$.

However, the introduction of small parameters can facilitate this process when if we consider the situation when the contribution from magnetism is small. Below we provide expressions necessary for finding the dependences of the real and imaginary parts of the magneto-optical parameter $Q=Q_1-iQ_2$ on $\delta\psi$ and $\delta\Delta$ [1].

The basic ellipsometry equation is

$$tg(\psi_0 + \delta\psi) e^{i(\Delta_0 + \delta\Delta)} = \frac{R_{p0} + R_{p1}}{R_{S0}} \quad (1)$$

where 0 is a subindex for measurements without external magnetic field, 1 – for applying external magnetic field.

From the basic ellipsometry equation written for a nonmagnetic state in terms of real (') and imaginary (") parts we get

$$tg\psi_0 = \frac{\sqrt{(R'_{p0}R'_{S0} + R''_{p0}R''_{S0})^2 + (R''_{S0}R'_{p0} - R'_{p0}R''_{S0})^2}}{(R'_{S0})^2 + (R''_{S0})^2} \quad (2)$$

$$\Delta_0 = arctg \frac{R''_{S0}R'_{p0} - R'_{S0}R''_{p0}}{R'_{p0}R'_{S0} + R''_{p0}R''_{S0}} \quad (3)$$

Then, in the case of applying a magnetic field:

$$R_p = R_{p0} + R_{p1} = R'_{p0} - iR''_{p0} + R'_{p1} - iR''_{p1} \quad (4)$$

and taking into account the above expressions (2, 3) for the nonmagnetic case, we have

$$\delta\Delta = arctg \frac{R''_{S0}(R'_{p0} + R'_{p1}) - R'_{S0}(R''_{p0} + R''_{p1})}{R'_{S0}(R'_{p0} + R'_{p1}) + R''_{S0}(R''_{p0} + R''_{p1})} - arctg \frac{R''_{S0}R'_{p0} - R'_{S0}R''_{p0}}{R'_{p0}R'_{S0} + R''_{p0}R''_{S0}} \quad (5)$$

$$\delta\psi = arctg \left(tg(\psi_0) \sqrt{1 + \frac{\chi}{\gamma}} \right) - \psi_0 \quad (6)$$

where

$$\frac{\chi}{\gamma} = \frac{((R'_{S0})^2 + (R''_{S0})^2)(R'_{p1}{}^2 + R''_{p1}{}^2 + 2(R'_{p0}R'_{p1} + R''_{p0}R''_{p1}))}{(R'_{p0}R'_{S0} + R''_{p0}R''_{S0})^2 + (R''_{S0}R'_{p0} - R'_{S0}R''_{p0})^2} \quad (7)$$

We expand the obtained expressions for $\delta\psi$ и $\delta\Delta$ in small parameters in the Maclaurin series and restrict ourselves to the first order of smallness because a hysteresis loop $\delta\psi(H)$ is observed in the experiment [2], i.e. the effect

is proportional to the first degree of the magneto-optical parameter.

$$\alpha = \frac{R'_{p1}}{R'_{p0}}; \quad \beta = \frac{R''_{p1}}{R''_{p0}} \quad (8)$$

Thus, we have

$$\delta\psi \approx \frac{tg\psi_0}{1 + tg^2\psi_0} \frac{\alpha(R'_{p0})^2 + \beta(R''_{p0})^2}{(R'_{p0})^2 + (R''_{p0})^2} \quad (9)$$

$$\delta\Delta \approx \frac{(\alpha - \beta)R'_{p0}R''_{p0}}{(R'_{p0})^2 + (R''_{p0})^2} \quad (10)$$

The contribution made by the magnetic field to the reflection coefficients is denoted by R'_{p1} and R''_{p1} R, and in expressions (5-7) small parameters α and β are responsible for magnetism. Therefore, it is necessary to express α and β from (5-7) in terms of $\delta\psi$ and $\delta\Delta$ measured in the experiment

$$\alpha \approx \frac{\delta\psi(1 + tg^2\psi_0)}{tg\psi_0} + \frac{R''_{p0}}{R'_{p0}} \delta\Delta \quad (11)$$

$$\beta \approx \frac{\delta\psi(1 + tg^2\psi_0)}{tg\psi_0} - \frac{R'_{p0}}{R''_{p0}} \delta\Delta \quad (12)$$

Then we need to obtain the expressions for R''_{p1} and R'_{p1} , which will lead to the desired Q_1 and Q_2 . So after that, it is necessary just to set the complex refractive index of the external medium N_0 , the angle of incidence of light on the sample φ , the data of spectral ellipsometry (ψ_0 and Δ_0) and magneto-ellipsometry ($\delta\psi$ and $\delta\Delta$). As a result, we get the analytically calculated real and imaginary parts of magneto-optical parameter Q from the data of ellipsometric and magneto-ellipsometric measurements. The expressions above can be used for thick ferromagnetic films or samples that are typically fit by the model of a semi-infinite medium.

Acknowledgements

This study was supported by the Research Grant No. 075-15-2019-1886 from the Government of the Russian Federation.

References

- [1] O. Maximova, N. Kosyrev, I. Yakovlev, et al. *JMMM* **440** (2017) 153.
- [2] S. Lyaschenko, I.Tarasov, S. Varnakov, et al. *ZHTF* **83** (2013) 139.

Current induced manipulation of exchange bias in Pt/Co/NiO structure

M.E. Stebliy^{*1}, A.G. Kolesnikov¹, M.E. Letushev¹, M.A. Bazrov¹, A.S. Samardak¹, A.V. Ognev¹, X. Wang², C. Wan², X. Han²

¹ Far Eastern Federal University, 8 Sukhanova St., Vladivostok 690950, Russia

² Beijing National Laboratory for Condensed Matter Physics, Chinese Academy of Sciences, Beijing 100190, China

*e-mail: steblii.me@dvfu.ru

Fabrication and investigation of antiferromagnetic materials (AFM) in combination with ferromagnets (FM) and heavy metals (HM) is a promising direction in the development of spintronics. The exchange bias field (B_{eb}) enables the inversion symmetry breaking of magnetic properties, which makes possible to switch magnetization direction of a FM layer using the current induced spin-orbit torque (SOT) effect [1]. On the other hand, a AFM layer itself can be an object of switching [2-3], and its spin ordering can change the magnitude and direction of the B_{eb} field.

In this work the method of changing the magnitude and direction of the exchange bias field in the Pt(5)/Co(0.5)/NiO(15 nm) structure was investigated. Polycrystalline films were prepared by magnetron sputtering at room temperature on substrates of naturally oxidized silicon SiO_2 . Using optical photolithography and ion-plasma etching methods, Hall bars with a current guide width of 10 μm were fabricated. While films sputtering, we used a sample holder allowing to set the permanent magnets for generating the in-plane (60 mT) or perpendicular-to-plane (120 mT) magnetic fields. The parameters of the NiO layer were selected in such a way that the antiferromagnetic ordering was realized by partitioning into layers with a multidirectional orientation of the magnetization. In this case, as a result of the exchange interaction at the FM/AFM interface, the effect of exchange bias arises, which makes the magnetization reversal process of the FM layer asymmetric. This asymmetry can be numerically estimated by the effective field - B_{eb} .

The contact of Pt and Co makes it possible to use the SOT effect for current induced magnetization reversal in the FM layer. Propagation of current leads to the generation of the pure spin current in the Pt layer, as a result of the spin Hall effect, which is injected into the Co layer. The current transmission is also accompanied by heating of the structure, up to 200°C. As a result of the current propagation, in addition to the magnetization orientation switching, a change in the magnitude and orientation of the B_{eb} field occurs in the range of ± 10 mT. Our study showed that the magnitude of this field does not depend on the direction and magnitude of external magnetic fields, nor on the duration and amplitude of the current pulse. The

decisive role is played by the magnetic configuration in the FM layer and by temperature. To confirm this fact, the experiment was repeated with heating by an external source. Thus, it was found that the spin current does not affect the spin ordering in the AFM layer, and the observed effect is associated with annealing in the field of the FM layer.

Our investigation of the magnetization reversal process at the micromagnetic level using a magneto-optical Kerr microscope made it possible to conclude that the current-induced change in the orientation of the B_{eb} field leads to a change in the magnetization reversal mechanism. If the exchange bias field has a value of +10 mT, then the transition from the +M state to -M proceeds gradually, over a wide range of fields; the reverse transition is spasmodic. In the first case, the domains nucleate at the edges and gradually grow towards the center, and in the second, the domains that originate at the edges begin to grow uniformly across the Hall bar area.

As a result, it was shown that the properties of the AFM layer can be controlled independently of the SOT magnetization switching mechanism. It was also demonstrated that using an inhomogeneous magnetic configuration in the FM layer, it is possible to create regions with different B_{eb} field orientations, which can be used to control the origin of domains during magnetization reversal.

Acknowledgements

This work is supported in part by the Russian Ministry of Science and Higher Education under the state task (0657-2020-0013), the Grant Council of the President of the Russian Federation (Grant No. MK-2281.2019.2), by the Russian Foundation for Basic Research (Grants No. 18-32-00867 and 18-52-53038).

References

- [1] Seyed Armin Razavi, Di Wu, L. Wang. *Phys. Rev. App.* **7** (2017) 024023.
- [2] Z.P. Zhou, X.H. Liu, K.Y. Wang, *Appl. Phys. Lett.* **116** (2020) 062403.
- [3] X. H. Liu, K. W. Edmonds, Z. P. Zhou, K. Y. Wang. *Phys. Rev. App.* **13** (2020) 014059.

Study of gamma-ray scattering on Fe₃O₄/SiO₂/Au and Ta₂O₅ nanoparticles

Yu.M. Borodaenko^{*1}, K.S. Lukyanenko¹, Thomas Myeongseok Koo², Min Jun Ko², Yu Jin Kim³,
A.V. Ognev¹, A.S. Samardak¹, L.L. Afremov¹, Young Keun Kim²

¹ Far Eastern Federal University, 8 Sukhanova St., Vladivostok 690950, Russia

² Department of Materials Science & Engineering, Korea University, Seoul 02841, Republic of Korea

³ Institute for High Technology Materials and Devices, Korea University, Seoul 02841, Republic of Korea

*e-mail: borodaenko.iu@students.dvfu.ru

Inasmuch as the treatment of aggressive radioresistant tumors is extremely difficult with the established methods of cancer treatment being almost ineffective in the delivery of local tumor control.

Radiotherapy is a common form of cancer treatment with over 50% of cancer patients receiving some form of radiotherapy as part of their cancer management plan. Nanoparticles have played a key role in the enhancement of the radiation therapy.

Scientific research on magnetic nanoparticles is intense, inasmuch as a particle that can be manipulated and accumulated in desired regions via magnetically guided delivery. This allows for better targeting nanoparticles within the tumor tissues allowing for more localized and consolidated damage.

This strategy is using for targeted drug delivery or for the delivery of magnetic particles to cancer tumors [1,2] for the purpose of the subsequent hyperthermia, to enhance the effect of radiation therapy due to scattering radiation by injected particles [3].

The main objective of this research is to explore the energy spectrum of photons when passing through layers of magnetic Fe₃O₄/SiO₂/Au nanoparticles and nonmagnetic Ta₂O₅ nanoparticles.

It was assumed that presence of tantalum or gold in the particles, will allow a more percentage of gamma quanta to be reflected, which makes possible to increase the effectiveness of radiation therapy.

The relevance of the tantalum oxide and gold for use in cancer research based on radiopaque and low toxicity to healthy human's cells. Tantalum as well as gold being a high-Z material and very inert to tissue interactions is ideal

for photosensitization reactions.

In an *in vitro* experiment, we used a gamma spectrometer with a semiconductor detector GEM-15P4 and two sources of gamma radiation ⁶⁰Co with a total activity of ~2·10⁵ Bq. The measured spectra were processed by the methods of mathematical statistics and smoothing.

In the spectra, we analyzed the energy regions of the peaks of the total absorption of ⁶⁰Co radiation, the annihilation peak of 511 keV (the 511-keV region, which is associated with the formation of electron-positron pairs [4]; electron and positron are absorbed in the irradiated tissues, with the positron annihilating, giving rise to two secondary photons, each with an energy of 511 keV), and the low energy region of 20-200 keV (low-energy quanta will promote apoptosis of the infected cells) [5].

Acknowledgements

This work has been supported by the Russian Ministry of Science and Higher Education under the state task (0657-2020-0013).

References

- [1] F. Alexis., E. Pridgen., R. Langer, O. C. Farokhzad. Drug delivery. Springer Berlin Heidelberg **197** (2010) 55.
- [2] S. K. Murthy. International journal of nanomedicine **2** (2007) 129.
- [3] K. S. Lukyanenko, V. I. Apanasevich, L. L. Afremov, , V. N. Kustov et al. Defect and Diffusion Forum **386** (2018) 156.
- [4] U. Gneveckow, A. Jordan, R. Scholz et al. Biomed. Tech **50** (2005) 92.
- [5] V.V. Temchenko, K. S. Lukyanenko, V. N. Kustov et al. Solid State Phenomena **265** (2017) 428.

Magnetic properties of Fe₃O₄/SiO₂/Au nanoparticles for enhancement of the radiation therapy effectiveness

M.I. Sobirov^{*,1}, L.L. Afremov¹, Thomas Myeongseok Koo², Min Jun Ko², Yu Jin Kim³, A.G. Kolesnikov¹, A.V. Ognev¹, A.S. Samardak¹, Young Keun Kim²

¹ Far Eastern Federal University, 8 Sukhanova St., Vladivostok 690950, Russia

² Department of Materials Science & Engineering, Korea University, Seoul 02841, Republic of Korea

³ Institute for High Technology Materials and Devices, Korea University, Seoul 02841, Republic of Korea

*e-mail: sobirov.mi@students.dvfu.ru

Particles of iron oxides magnetite (Fe₃O₄) are a promising material for using as magnetic storage media, contrast enhancers for magnetic resonance imaging, agent for magnetic hyperthermia therapy of tumors and targeted drug delivery [1–4]. One of the most relevant areas of application of nanoparticles based on iron oxides, for example, coated with gold, is oncology [1]. Interest in gold-coated particles in the treatment of cancer is related to the radiopacity, biocompatibility and non-toxicity of these particles in relation to healthy cells. In addition, the presence of a magnetic moment in the “core/shell/satellites” nanoparticles such as Fe₃O₄/SiO₂/Au allows them to be concentrated in the tumor area using an inhomogeneous magnetic field, which leads to an increase in the radiation dose and enhancement of the efficiency of the technology for destroying malignant cells.

In this paper, we conducted a study of the magnetic properties of Fe₃O₄/SiO₂ particles with and without Au nanoparticle satellites. Nanoparticles were synthesized by the polyol process. For Au nanoparticles satellites two cases were studied: satellites were formed by Au nanoparticles with low density (sample 1) and high density (sample 2).

The magnetic hysteresis loop and the hysteresis characteristics of the Fe₃O₄ and Fe₃O₄/Au nanoparticle system were determined by the Lake Shore VSM 7400 magnetometer.

Table I. The coercive force (H_c) and remanent magnetization (M_r/M_s) for nanoparticles Fe₃O₄/SiO₂ and Fe₃O₄/SiO₂/Au

Sample	Composition	H_c , Oe	M_r/M_s
1	Fe ₃ O ₄ /SiO ₂ /Au	12.0	0.01
2	Fe ₃ O ₄ /SiO ₂ /Au	2.9	0.01
3	Fe ₃ O ₄ /SiO ₂	7.7	0.003

The coercive force H_c and the ratio of the residual magnetic moment to the magnetic moment of saturation M_r/M_s were determined from the hysteresis loops. The experimental results are shown in Table I.

The presented values of the hysteresis characteristics turned out to be significantly lower than magnetite ($H_c \sim 100$ Oe, $M_r/M_s \sim 0.2 \div 0.5$).

From the experimental data it is visible that the surface density of Au nanoparticles leads to the significant change of the coercive force. The main reason is the possible agglomeration of Fe₃O₄/SiO₂/Au nanoparticles, which level depends on the ability to form nanoparticle clusters. This fact defines the magnetostatic interaction between nanoparticles and magnetization reversal mechanism.

The experimental results for temperature dependence of the magnetic properties were obtained. The blocking temperature was calculated. As further expected, these results can help to increase the efficiency of radiation therapy.

Acknowledgements

This work has been supported by the Russian Ministry of Science and Higher Education under the state task (0657-2020-0013).

References

- [1] Sinibaldi, Edoardo, et al., Journal of Nanotechnology in Engineering and Medicine **1** (2010) 021008.
- [2] Pankhurst, Q. A., et al., Journal of Physics D: Applied Physics **42** (2009) 224001.
- [3] Laurent, Sophie, et al., Advances in colloid and interface science **166** (2011) 8.
- [4] Alexis, Frank, et al. "Nanoparticle technologies for cancer therapy." Drug delivery. Springer Berlin Heidelberg, 2010. 55-86.

Temperature dependence of the magnetic properties of $\text{Fe}_3\text{O}_4/\text{Au}$ nanoparticles investigated by means of micromagnetic simulation

M.A. Sitnik¹, L.L. Afremov¹, Thomas Myeongseok Koo², Min Jun Ko², Yu Jin Kim³,
A.G. Kolesnikov¹, A.V. Ognev¹, A.S. Samardak¹, Young Keun Kim²

¹ Far Eastern Federal University, 8 Sukhanova St., Vladivostok 690950, Russia

² Department of Materials Science & Engineering, Korea University, Seoul 02841, Republic of Korea

³ Institute for High Technology Materials and Devices, Korea University, Seoul 02841, Republic of Korea

*e-mail: sitnik.ma@students.dvfu.ru

The magnetic properties of nanoparticles are determined by many factors, including the chemical composition, type of crystal lattice, particle size and shape, and the interaction of particles with neighbors. By changing the size, shape, composition and structure of nanoparticles, it is possible, within certain limits, to control the magnetic characteristics of materials based on them. Among the magnetic materials that have found wide technological application, various ferromagnets like Fe_3O_4 , Co, Fe, Ni should be noted.

The spontaneous magnetization of ferromagnets is due to the interaction between neighboring atoms, which tends to order their spins (magnetic moments) in one preferred direction. The thermal vibrations of atoms tend to disrupt the spin ordering. Therefore, the ferromagnetic properties in a substance are preserved only up to a certain temperature. If a ferromagnet is heated, its magnetization ability decreases saturation magnetization, residual induction, coercive force and other magnetic characteristics decrease. Above a certain temperature, which is called the Curie temperature (T_c), spontaneous magnetization disappears, the material becomes paramagnetic [1].

In the abstract, we present the results of modeling the magnetic properties of core-shell $\text{Fe}_3\text{O}_4/\text{SiO}_2$ nanoparticles without and with the satellite made of Au nanoparticles. Particular attention is paid to the temperature dependence of the magnetic property's behavior of nanoparticles.

For the model, we used data for the structure and morphology of particles obtained by scanning electron and transmission microscopy. Nanoparticles were synthesized by the polyol process [2]. The diameter of the Fe_3O_4 core is 220 nm, and the SiO_2 shell has the thickness of 16 nm. We found that the satellite is formed by Au nanoparticles with the diameter of about 15 nm. We will demonstrate an effect

of the Au nanoparticles density on the magnetic properties of the core-shell-satellite magnetite nanoparticles.

The behavior of the magnetic properties of materials can be predicted using micromagnetic simulation with a thermally dependent parameter. Modeling the magnetic characteristics was carried out in two software packages: OOMMF [3] and MuMax³ [4]. We investigated the behavior of the ground state of magnetization on the size of magnetite nanoparticles.

We showed that with the increasing size the single-domain structure transforms to the magnetic vortex state. This magnetic structure has the lower total energy with closed magnetic flux.

A further goal of the study is micromagnetic simulation of the temperature dependence of the magnetic properties of Fe_3O_4 nanoparticles, and then the effect of Au satellite on the magnetic properties of Fe_3O_4 depending on the size and temperature.

The results can be used for optimization of parameters of nanoparticles for anticancer therapy.

Acknowledgements

This work has been supported by the Russian Ministry of Science and Higher Education under the state task (0657-2020-0013).

References

- [1] Purcell, "Electricity and Magnetism, 3rd Edition," p. 546
- [2] J. Cha, J. S. Lee, S. J. Yoon, Y. K. Kim, and J.-K. Lee, RSC Adv. **3** (2013) 3631.
- [3] M.J. Donahue, D.G. Porter, OOMMF User's Guide Nat. Inst. Stand. Technol., Gaithersburg, MD, Tech. Rep. NISTIR 6376, 1999.
- [4] Vansteenkiste, A. et al., AIP Adv. **4** (2014) 107133.

Controller for a VR system based on magnetic field sensors

Zh.Zh. Namsaraev^{*1}, V.N. Kharitonov¹, P. Savinov^{1,2}, A.S. Samardak², R. Brizitsky³, A.V. Ognev^{1,2}

¹National Technology Initiative Center of Neurotechnology, Virtual and Augmented Reality Technologies, FEFU, Vladivostok, Russia

²Laboratory of thin film technologies, FEFU, Vladivostok, Russia

³Department of Informatics, Mathematical and Computer Modeling, FEFU, Vladivostok, Russia

*e-mail: namsaraev.zhzh@students.dvfu.ru

This work is devoted to the hardware part of a device being developed and its interaction with a computer (game engine). Parallel reading and processing of data from six sensors was implemented, each of which contains an accelerometer, gyroscope, and magnetometer. The processed data is transmitted to the user's computer via the TCP protocol. The Unity game engine is installed on a computer where a VR environment is created that the user must interact with using the device being developed.

Currently, the device is a microcontroller with sensors connected to it via the SPI bus. The microcontroller itself is connected to a Raspberry Pi microcomputer. Sensors register accelerometer readings (acceleration vector in the sensor coordinate system), gyroscope readings (angular velocities in the sensor coordinate system), and magnetometer readings (projections of the magnetic field induction vector in the sensor coordinate system). The microcontroller reads these readings and transmits them via the COM port to the Raspberry Pi microcomputer. The microcomputer uses 2 threads/cores to work with the microcontroller [1]. The first thread reads data from the COM port, and the second thread processes this data and sends it over TCP to a specific port for further transmission to the user's computer in the Unity game engine. Unity also uses two threads, the first thread works with the engine interface [2] (visual component and calculations for rendering frames) and its speed depends directly on the number of frames per second, and the second thread reads the processed data from the specified port over the TCP Protocol and prepares it for the first thread that uses it in the game environment.

Data processing on the microcomputer is performed as follows:

1. Calibration;
2. Filtration [3];
3. Apply the Madgwick's filter to obtain the quaternion [4];
4. Application of an algorithm for calculating coordinates in a magnetic field.

Parallelism is necessary for the device to work correctly. The raspberry Pi microcomputer reads data from sensors at a speed of 5-7 milliseconds and processes 3-5 milliseconds. Sequential reading and processing accumulates data that was not read in time, resulting in a

delay between the time when the data was applied in the unit and the time when the data was read by the microcomputer.

In Unity, parallelism is necessary, because the standard "Update" method that runs in a loop depends on the frame rate: one update execution is one frame. The standard "FixedUpdate" method, which does not depend on the frame rate, is strictly dependent on the static "deltaTime" parameter. Because the time for reading and processing data is unstable, using this method also results in delays.

The end device should only be a microcontroller with sensors, without using the Raspberry Pi. The microcontroller must not only read data from sensors, but also process them, as well as output data about orientation and position in the magnetic field for use in a virtual environment. Currently, the Raspberry Pi is used for developing and testing algorithms, since it is easier to do this on the Raspberry Pi than to reprogram the microcontroller.

At the moment, there are no delays, except for the time spent reading and processing a single data packet. Each of the six game objects corresponding to the six sensors is updated at least 20 times per second, which is minimally convenient for a human eye.

The increase in this frequency of updates is planned due to the use of multithreading when reading data from sensors.

Acknowledgments

This work is supported by the National Technology Initiative Center of Neurotechnology, Virtual and Augmented Reality Technologies of the FEFU (Grant No. 1/1251/2018 16.10.2018) and the Russian Foundation for Basic Research (grant № 19-02-00530).

References

- [1] Multiprocessing. Python – <https://docs.python.org/2/library/multiprocessing.html>
- [2] Threading. C# – <https://docs.microsoft.com/ru-ru/dotnet/api/system.threading.thread?view=netcore-3.1>
- [3] Low-pass filter – <https://www.w3.org/TR/motion-sensors/#low-pass-filters>
- [4] S.O.H. Madgwick, An efficient orientation filter for inertial and inertial/magnetic sensor arrays, **2010** (2010) 1.

Development of a mathematical model for describing the motion of a sensor array in a magnetic field

V.N. Kharitonov¹, J.J. Namsaraev¹, A.S. Samardak², R. Brizitsky³, A.V. Ognev^{1,2}

¹National Technology Initiative Center of Neurotechnology, Virtual and Augmented Reality Technologies, FEFU, Vladivostok, Russia

²Laboratory of thin film technologies, FEFU, Vladivostok, Russia

³Department of Informatics, Mathematical and Computer Modeling, FEFU, Vladivostok, Russia

*e-mail: kharitonov.vn@dvfu.ru

In this paper, a mathematical model about the motion of the sensor in a magnetic field induced by one or several dipoles is developed. We used sensor data for calculations of three projections of the acceleration vector and magnetic field in the sensor coordinate system, as well as the sensor rotation angles in a fixed coordinate system. The position of the sensor in a fixed coordinate system is calculated at real-time (coordinates of its center and tilt angles to the axes of the fixed coordinate system). The movement of the sensor is visualized.

For this model the various methods for finding the orientation of the sensor in space were independently verified. They would be assembled into a software package using complex Madgwick-type filters [2]. On the other hand, the evaluation of the effectiveness of each method will allow build the faster algorithms based on one of the methods that are most suitable for a particular situation. At first, the coordinates of the sensor center are located just with the three projections of acceleration in the case when the sensor does not deviate from its position, i.e. the projections of the acceleration vector in the sensor system coincided with its projections in a fixed coordinate system in which it was required to find its position. The corresponding algorithm was developed and implemented, and the errors and possibility of using this method were estimated.

Next, the plane motion of the sensor in the magnetic field of the dipole was simulated. The dipole was located at the beginning of the fixed coordinate system, while the magnetic moment vector was directed strictly along the Y-axis of the fixed system. With the help of the well-known formulas for the induction of a magnetic field induced by a dipole at a point in space with a radius vector r [1], the inverse problem of finding the coordinates of the sensor center from the magnetic field measured by it was

solved analytically. Also, the magnetic field was used to check the readings of the gyro sensor. A comparative analysis of the “kinematic” and “magnetic” methods of the sensor trajectory recovery was conducted. Finally, in the field of one dipole, the Madgwick filter was tested, specifying the corners of the gyroscope on a set of indicators. The constructed model is generalized to the case of several dipoles.

The developed algorithm for determining spatial position and orientation was tested using the inverse kinematics FABRIK method [3], which is used to solve the problem of manipulating segments of the manipulator or for tracking human movements.

The algorithm developed in the course of working on a mathematical model can be used in various kinds of activity where high accuracy in determining position and orientation is important, including medicine. For example, carrying out remote operations using high-precision manipulators, tracking the dynamics of patient movements that are at the stage of medical rehabilitation.

Acknowledgements

This work is supported by the National Technology Initiative Center of Neurotechnology, Virtual and Augmented Reality Technologies of the FEFU (Grant No. 1/1251/2018 16.10.2018) and the Russian Foundation for Basic Research (grant № 19-02-00530).

References

- [1] Hui-Min Shen, ICIRA 2017: Intelligent Robotics and Applications (2017)428.
- [2] S.O.H. Madgwick, An efficient orientation filter for inertial and inertial/magnetic sensor arrays, **2010** (2010) 1.
- [3] Andreas Aristidou, Joan Lasenby. FABRIK: A fast, iterative solver for the Inverse Kinematics problem

Concentration phase transition in a two-dimensional ferromagnet

A.K. Chepak^{*1,2}, L.L. Afremov²

¹ Institute of Chemistry of FEB RAS, Avenue of the 100th anniversary of Vladivostok 159, Vladivostok 690022, Russia

² Far Eastern Federal University, 8 Sukhanova St., Vladivostok 690950, Russia

*e-mail: chepak.ak@mail.ru

It is known that the concentration of magnetic atoms significantly affects the various characteristics of magnetic materials. Among these characteristics are spontaneous magnetization, magnetic susceptibility, thermal capacity, critical temperature of the phase transition, as well as the behavior of the above characteristics near the critical point [1–4]. Despite the importance of studying the characteristics of critical phenomena in diluted magnetics, the concentration phase transition is considered much less frequently than the temperature transition. In the best case, the effect of dilution on the temperature phase transition is studied [3,4], but the direct problem of the concentration phase transition is ignored or mathematically solved within the framework of percolation theory as a formal problem of the geometric phase transition [5, 6].

In this paper, we consider the influence of nonmagnetic atoms on the critical characteristics of the concentration phase transition of a «ferromagnetic - paramagnetic» in a two-dimensional magnetic.

The problem was solved by computer modeling Monte Carlo using the Wolf cluster algorithm [7]. Calculations were carried out within the Ising model, in the approach of the nearest neighbors. You have selected an initial, ordered state. In the phase transition region, the concentration of magnetic atoms changed in steps of 0.001, averaging was carried out in 10^6 Monte Carlo stages and 10^4 different lattice configurations.

The critical characteristics were calculated using three order parameters: magnetic M_{ma} (1), cluster M_{cl} (2) and percolation M_{pe} (3). The order parameters were determined as the average magnetization of the system, the average magnetization of a random cluster and the magnetization of a percolation cluster, referred to saturation magnetization.

$$M_{ma} = [\langle \sum_i^N s_i \rangle] / N, \quad (1)$$

$$M_{cl} = [\langle \sum_i^{N_{cl}} s_i \rangle] / N, \quad (2)$$

$$M_{pe} = \langle \sum_i^{N_{pe}} s_i \rangle / N. \quad (3)$$

Here $s_i = \pm 1$ – is the spin of the magnetic node; N , N_{cl} , N_{pe} – number of atoms in the lattice, in a randomly selected cluster and percolation cluster; the brackets $\langle \rangle$, $[\]$ denote averaging over Monte Carlo steps and averaging over all possible configurations, respectively. The magnetic susceptibility was calculated using the known relation (4), where $K = J/k_B T$.

$$\chi = NK[\langle M^2 \rangle - \langle M \rangle^2]. \quad (4)$$

The calculation results were generalized by universal values - critical indicators. Critical indicators of the concentration phase transition "ferromagnetic - paramagnetic" in a two-dimensional magnetic are presented in Table I.

Table I. Calculated critical indices based on various order parameters (OP)

Critical index	Magnetic OP, M_{ma}	Cluster OP, M_{cl}	Percolation OP, M_{pe}	Critical index [2,6]
β	0.152	0.080	0.108	0.139, 0.125
γ	1.751	1.948	2.030	2.41, 1.75
ν	0.963	1.039	1.030	1, 1.33
d	2.055	2.109	2.247	2
d_f	1.897	2.032	2.142	1.896

Table I indicates that the magnetic order parameter gives the most reliable values of the critical indices. This fact is determined by the fact that the dimensional index d coincides with the dimension of the flat lattice. In this case, the fractal dimension d_f of the structures formed during the phase transition indicates that the resulting system, consisting of magnetic clusters, behaves like a two-dimensional magnetic. Thus, it should be assumed that individual clusters can retain magnetic properties, and the absence of interaction between such clusters makes ferromagnetic ordering impossible, which leads to a phase transition. Moreover, this situation does not exclude the existence of spin glass at a concentration below critical, which is of interest for future studies.

Acknowledgements

This work is supported by Russian Foundation of Basic Research (Grant no. 18-33-20159).

References

- [1] L.L. Afremov, V.I. Belokon, O.I. Dyachenko, A.A. Petrov (2016)110.
- [2] K. Binder, D.V. Heerman (1995)144.
- [3] V.V. Prudnikov A.N. Vakilov. JETP Letters **15** (1992) 709.
- [4] R. Folk, Yu. Golovach, T. Yavorsky. UFN **2** (2003) 175.
- [5] M.A. Bureev, V.N. Udodov. RAS: Department of Mathematical Sciences (2012) 72.
- [6] D.I. Iudin, E.V. Kuposov (2012) 200.
- [7] L.A. Bulavin, N.V. Vygornitsky, N.I. Lechovka (2011) 352.

Micromagnetic behavior of Fe/Au barcode nanowires: experiment and simulation

V.Yu. Samardak^{*1}, Y.S. Jeon², E.M. Yoo², A.V. Ognev¹, A.S. Samardak¹, Y.K. Kim²

¹ School of Natural Sciences, Far Eastern Federal University, Vladivostok, Russia

² Department of Materials Science and Engineering, Korea University, Seoul 02841, Republic of Korea

*e-mail: vadimsamardak@gmail.com

Growing interest in recent years in nanomaterials with magnetic ordering is due to significant prospects for their practical applications. The development of nanotechnology involves the development and production of new nanostructured systems with a unique set of functional properties used to implement instruments and devices. Among a wide range of barcode nanostructures, nanowires of type “ferromagnet / non-magnetic metal”, named barcode nanowires (BNWs) attract the attention of researchers because of their unique physical properties. These nanowires can consist of many alternating layers that can be identified by an electron microscope, which is why they are called a “barcode” of nanowires.

In this work, we studied the “barcode” nanowires consisting of the sequence of magnetic (Fe) and non-magnetic (Au) nanosized segments. Considerable attention is paid to a review of the achievements and prospects of synthesis, the properties and applications of metal “barcode” nanowires, the dependence of their magnetic, optical and mechanical properties on the material, composition, shape and microstructure. The aim of this work is to study the effect of structural composition on the magnetic characteristics of both arrays and individual Fe/Au BNWs [1, 2].

To study magnetization reversal using conventional induction magnetometry, the First Order Reversal Curve (FORC) method was used [3]. The FORC-diagram method involves measuring a series (several tens) of minor hysteresis curves, called FORC-curves. The measurement step size is small enough to produce a highly detailed FORC diagram. The FORC diagrams in our study were used to obtain not only qualitative information, but quantitative one about the distribution of the coercive force and magnetostatic interaction fields. Based on the results of studies and micromagnetic modeling of the magnetic characteristics of Fe/Au BNWs, data were obtained on the behavior of the saturation fields and the interaction, the reduced remanent magnetization M_r/M_s , as well as the coercive force measured in two different ways - using the FORC-diagram method and from magnetic hysteresis loops.

Values of the coercive force defined from the main hysteresis loop and from the FORC diagram for some samples are very different. This effect can be explained as a consequence of the fact that the coercive force extracted from the FORC diagram reflects the coercive force of individual nanostructures, while the information obtained from magnetic hysteresis loops is integral and characterizes the collective magnetic behavior of the entire array of nanowires. Therefore, the difference between the coercive forces can be due to the magnetostatic interaction of Fe segments of nanowires. We have done a series of micromagnetic simulations that fit the experimental data and show that the application of an external magnetic field along the long axis of the nanowires helps to generate non-trivial spin configurations – vortices or even skyrmions - in each Fe segment along the entire length of the nanowires. The type of spin configuration is defined by the cylindrical shape of Fe segments and the magnetostatic interaction between neighboring magnetic segments separated by Au spacers.

Our results broaden the understanding of shape- and magnetostatic interaction-dependent formation of topological magnetic quasi-particles in complex systems such as BNWs, which can be used to create innovative storage and information processing systems, as well as for biomedical applications.

Acknowledgements

This work has been supported by the Russian Ministry of Science and Higher Education under the state task (0657-2020-0013) and by RFBR (grant 19-02-00530).

References

- [1] J. H. Lee, J. H. Wu, H. L. Liu, J. U. Cho, M. K. Cho, B. H. An, J. H. Min, S. J. Noh, and Y. K. Kim, *Angew. Chem. Int. Edit.* **46** (2007) 3663.
- [2] Y. S. Jeon, H. M. Shin, Y. J. Kim, D. Y. Nam, B. C. Park, E. Yoo, H.-R. Kim, Y. K. Kim, *ACS Appl. Mater. Interfaces* **11** (2019) 23901.
- [3] M. Vazquez, *Magnetic nano- and microwires: design, synthesis, properties and applications*, 1st Edition ed., Elsevier, Boston, MA, 2015.

V. Laser nanofabrication and laser ablation in liquids: fundamentals and applications

Pulsed laser ablation of silicon nanowires and porous silicon in liquids

S.V. Zobotnov^{*1}, A.V. Skobelkina¹, F.V. Kashaev¹, D.E. Presnov¹, T.P. Kaminskaya¹,
L.A. Golovan¹, P.K. Kashkarov¹, D.A. Kurakina², A.V. Khilov², E.A. Sergeeva^{1,2}, P.D. Agrba^{1,3},
M.Yu. Kirillin²

¹ Lomonosov Moscow State University, Faculty of Physics, 1/2 Leninskie Gory, Moscow 119991, Russia

² Institute of Applied Physics RAS, 46 Uljanov St., Nizhny Novgorod 603950, Russia

³ Lobachevsky State University of Nizhny Novgorod, 23 Gagarin Ave., Nizhny Novgorod 603950, Russia

*e-mail: zobotnov@physics.msu.ru

Nowadays pulsed laser ablation of solid-state targets in different liquids and gases is a powerful tool to produce a variety of nanoparticles with desirable size, physical and chemical properties [1]. Silicon nanoparticles (Si-NPs) produced by this technique have potential in different biomedical applications [2, 3] due to high biocompatibility and biodegradability of this material [4].

In this work we present a novel two-stage technique of Si-NPs fabrication. At the first stage silicon nanowires (Si-NWs) arrays or porous silicon (por-Si) films are fabricated by the metal-assisted chemical etching [5] or electrochemical etching [3] technique, respectively. At the second stage the Si-NPs are produced by pulsed laser ablation of these targets in liquids (PLAL). The ablation was performed in distilled water, ethanol and liquid nitrogen under picosecond (1064 nm, 34 ps, 10Hz) and femtosecond (1250 nm, 125 fs, 10 Hz) laser irradiation.

Measurement of ablation thresholds for Si-NWs and por-Si samples in liquids revealed that they are several times less in comparison to the corresponding values for the crystalline silicon (Table I).

Table I. Picosecond laser ablation thresholds of SiNWs, por-Si and crystalline Si in water and ethanol.

Sample	Ablation threshold in water, J/cm ²	Ablation threshold in ethanol, J/cm ²
Si-NWs	0.32±0.01	0.10±0.02
por-Si	0.66±0.04	0.57±0.04
Si	1.26±0.11	1.18±0.09

The lower values are explained by a lower thermal conductivity of the porous matrix in contrast to bulk material and partial destruction of Si–Si bonds in the crystal lattice during chemical etching. As a result, in the process of subsequent laser irradiation of the Si-NW arrays or por-Si layers, the yield of ablation products and, respectively, the efficiency of agglomeration of the latter in the Si-NPs is several times higher in comparison to the case of using crystalline silicon [3].

Scanning electron and atomic-force microscopy techniques revealed polydisperse size distributions of the formed Si-NPs. The average size varies from 16 to 120 nm depending on the used buffer liquid and duration of laser pulses. Such sizes are substantially smaller than ones for Si-NPs prepared by traditional mechanical grinding of Si-NWs, por-Si and crystalline silicon, thus facilitating more effective administration of the Si-NPs into biological tissues. Therefore, PLAL technique has an additional advantage for biomedical applications.

Raman spectroscopy analysis of the Si-NPs fabricated via PLAL showed that the volume fraction of crystalline Si in them is higher than 87% for all types of the studied samples. The remainder is amorphous Si. This indicates that the optical properties of the Si-NPs are close to those for silicon nanocrystals with similar sizes.

Photoluminescence studies revealed a high fluorescence of all Si-NPs fabricated in ethanol and liquid nitrogen with fluorescence peaks in the range 600 – 900 nm for excitation wavelength of 532 nm. The initial Si-NWs arrays and por-Si films exhibit similar fluorescence. However, the lifetime for this process changes significantly before and after ablation at the microsecond scale. Fluorescence emission for the Si-NPs produced in water was not detected. We assume that the observed fluorescence efficiency depends on numerous defects in the studied nanocrystalline structures.

Spectrophotometry measurements of the ablated Si-NPs suspensions revealed that scattering coefficient reaches value ~ 1 mm⁻¹ in the spectral range of 400 – 1000 nm indicating their potential as contrast agents in biomedical imaging. Optical coherence tomography imaging of the suspensions drops administered on agar gel surfaces confirmed this by providing the contrast of up to 30 dB.

Thus, PLAL of Si-NWs arrays and por-Si layers provide high yield fabrication of Si-NPs with relatively small size and high level of crystallinity, that are promising as fluorescence markers and scattering contrast agents in bioimaging.

Acknowledgements

This work was supported by the Russian Science Foundation (project № 19-12-00192).

References

- [1] D. Zhang, B. Gökce, S. Barcikowski. *Chem. Rev.* **117** (2017) 3990.
- [2] M. B. Gongalsky, L. A. Osminkina, A. Pereira, A. A. Manankov, A. A. Fedorenko, A. N. Vasiliev, V. V. Solovyev, A. A. Kudryavtsev, M. Sentis, A. V. Kabashin, V. Yu. Timoshenko. *Sci. Rep.* **6** (2016) 24732.
- [3] S. V. Zobotnov, D. A. Kurakina, F. V. Kashaev, A. V. Skobelkina, et al. *Quantum Electron.* **50** (2020) 69.
- [4] O. I. Ksenofontova, A. V. Vasin, V. V. Egorov, A. V. Bobyl', F. Yu. Soldatenkov, E. I. Terukov, V. P. Ulin, N. V. Ulin, O. I. Kiselev. *Tech. Phys.* **59** (2014) 66.
- [5] S. V. Zobotnov, M. M. Kholodov, V. A. Georgobiani, D. E. Presnov, L. A. Golovan, P. K. Kashkarov. *Las. Phys. Lett.* **13** (2016) 035902.

Femtosecond pulse structuring of multicore fibers for development of advanced fiber lasers and sensors

A.V. Dostovalov^{*,1,2}, A.A. Wolf^{1,2}, K.A. Bronnikov^{1,2}, M.I. Skvortsov^{1,2}, S.A. Babin^{1,2}

¹ Institute of Automation and Electrometry of the SB RAS, 1 Acad. Koptuyug Ave., Novosibirsk, 630090, Russia

² Novosibirsk State University, 1 Pirogov St., Novosibirsk, 630090, Russia

*e-mail: corresponding_autor_dostovalov@iae.nsk.su

Fiber lasers and sensing systems are the applications where the use of multicore optical fibers is actively studied [1]. In the first case, MCFs can be used for a coherent spatial division multiplexing to increase the effective area of the mode field in order to reduce the influence of nonlinear effects, while keeping the total radiation power constant [2]. In the second case, fiber-optic sensors based on a MCF for 3D shape sensing [3], as well as multi-parameter sensors, can be created. In both cases, the key element of laser and sensor systems based on a MCF is the fiber Bragg grating (FBG) – a periodic modulation of the refractive index in the core of the fiber, which reflects light at a specific resonant wavelength [4]. For this reason, development of methods for the selective inscription of FBGs in a MCF is relevant. The traditional method of FBG inscription using an UV radiation interference scheme has several disadvantages associated with the need to remove protective coating before inscription and use photosensitive materials.

The technology of femtosecond laser modification of the refractive index in non-photosensitive materials with a localization of the modification region of less than 1 μm offers new opportunities for FBG inscription [5]. That is why this technology allows point-by-point FBG inscription in selected MCF cores with precise localization in both longitudinal and transverse directions.

Using this technology, elements of an erbium-doped fiber laser were created based on homogeneous and chirped FBGs inscribed in a MCF for smooth tuning of the central wavelength. In the first configuration, output coupling (OC) FBG array was inscribed in a central core, and an array of highly reflective (HR) FBG in side cores (one per core) with different resonant wavelengths corresponding to the OC FBGs. The wavelength tuning by 17 nm due to the compression/extension of the MCF region with a FBG pair at the selected wavelength is demonstrated. By combining the corresponding pairs of FBGs with other wavelengths, it is possible to obtain tuning in a larger spectral range. In the second configuration, chirped FBG with a wide reflection spectrum of 30 nm was inscribed in the central core, while FBGs with narrow spectrum were inscribed in side cores. The tuning scheme was similar to the first configuration. In this case, tuning by more than 30 nm was achieved.

Moreover, this FBG inscription technology allows creation of fiber-optic sensors to reconstruct the 3D shape of an object. In this case, FBG arrays were inscribed in the MCF in several sections along the fiber. In each individual section, FBGs are located in the central and various side cores. By measuring the wavelength shift of each of the FBGs, the magnitude and direction of the bending-induced strain can be determined. In addition, by subtracting the wavelength shift of the central core from the corresponding values of the side cores, it is possible to carry out measurements at various temperatures, so the sensor is athermal in this case. The results of reconstructing various 2- and 3-dimensional curves were obtained using the proposed shape sensor with a reconstruction error of less than 2% for a total length of ~ 10 cm. Experiments were also carried out to reconstruct different shapes based on the analysis of reflectograms obtained using a high resolution OFDR reflectometer OBR 4600 (Luna Inc.). In this case, the reconstruction error of the curves was less than 1% over a total length of 45 cm.

Acknowledgements

Results of fiber sensors development was obtained under support of Russian Science Foundation (project number 18-72-00139), results of fiber laser development was obtained under support of RFBR (project number 20-32-70132).

References

- [1] J. P. Moore and M. D. Rogge, *Optics Express*, **20** (2012) 2967.
- [2] M. I. Skvortsov, S. R. Abdullina, A. A. Wolf, A. V. Dostovalov, A. A. Vlasov, I. A. Lobach, S. Wabnitz, and S. A. Babin, *Opt. Lett.* **44** (2019) 295.
- [3] M. Amanzadeh, S. M. Aminossadati, M. S. Kizil, and A. D. Rakić, *Meas. J. Int. Meas. Confed.* **128** (2018) 119.
- [4] R. Kashyap, *Fiber Bragg Gratings* (Academic Press, 1999).
- [5] A. V. Dostovalov, A. A. Wolf, A. V. Parygin, V. E. Zyubin, and S. A. Babin, *Opt. Express* **24** (2016) 16232.

Precise ablation of methylammonium lead iodide perovskite films with femtosecond laser pulses

A. Zhizhchenko^{*,1,2}, S. Starikov³, S. Makarov⁴, A. Kuchmizhak

¹ Institute of Automation and Control Processes of FEB RAS, 5 Radio St., Vladivostok, 690041, Russia

² Far Eastern Federal University, 8 Sukhanova St., Vladivostok, 690950, Russia

³ Joint Institute for High Temperatures of RAS, 13 Bd.2, Izhorskaya St., Moscow, 125412, Russia

⁴ ITMO University, 49 Kronverksky Pr., St. Petersburg, 197101, Russia

*e-mail: zhizhchenko@iacp.dvo.ru

Metal-halide hybrid perovskites (MAPbX₃, where X = [I, Br, Cl] and MA=CH₃NH₃) represent a promising class of materials for advanced optoelectronic applications. Particularly, both perovskite solar cells and light-emitting devices based on such materials exceeded 20% efficiency level, the value that keeps growing rapidly [1]. Very recently, the progress achieved on perovskite nanophotonics brought novel approaches to this field [2]. The refractive index ($n > 2$) of lead halide perovskite is large enough to support the Mie resonances in a single nanoparticle [3], which can thus enhance local electromagnetic field and provide various spectral changes in scattering and absorption of incident light [4]. At the same time, large-scale and low-cost methods for fabrication of nano- and microstructures from halide perovskite films would enable neutral- and multi-colored semitransparency for building-integrated photovoltaics [5], tandem solar cells [6], light-emitting devices [7], and lasers [8]. In this regard, development of high-throughput methods for perovskite patterning and processing without irreversible reduction of luminescent and charge-carriers transport properties of the material is still challenging.

Individual perovskite-based nano- and microstructures can be fabricated through inexpensive approaches such as chemical vapor deposition or chemical synthesis. Yet, these methods do not permit such individual structures to be placed at desired locations on the substrate unless the latter is preliminary treated by additional multi-step lithography. In turn, lithography-based techniques used for perovskites nanostructuring are still far from large-scale processing performance, which is crucial for industrial applications. Common fabrication approaches, such as e-beam lithography, also have limited applicability for perovskite processing as liquid-based post-processing steps are harmful for the material quality in many cases [2]. Standard direct laser processing was mainly implemented for rough scribing of perovskite-based solar cells with a typical feature size on the order of tens of micrometers [9]. On the other hand, ultrafast material removal from a perovskite film via femtosecond (fs) pulsed laser ablation could potentially combine a technological simplicity and scalability of the fabrication process with the flexibility of producing various separated and properly arranged microstructures, while preserving properties of the pristine

material and providing precision high enough to create compact microlasers [10]. However, in order to push advanced laser technology toward more precise non-destructive patterning at nanoscale lateral and vertical resolution, one has to develop novel approaches and carry out more systematic studies providing better understanding how tightly focused ultrashort laser pulses of high intensities interact with metal-halide perovskites.

Here, we demonstrate novel approach for 3D micropatterning of perovskite films via direct femtosecond laser projection lithography. Whereas majority of previous works used laser processing only for rough cutting/scribing of perovskite materials at microscale level, here by using advanced laser beam engineering and delicate multi-pulse processing we showed capability of flexible non-destructive 3D processing of perovskites at sub-diffraction resolution down to 250 nm. Additionally, for the first time in literature, we provide valuable theoretical insight into ablation mechanism of halide-perovskite material with ultrashort laser radiation. The elaborated optimized laser processing regime allowed to control 3D surface morphology preserving optoelectronic properties of the irradiated perovskite material, thus opening pathway for high-performing inexpensive and large-scale fabrication of nanostructures and surface textures suitable for advanced light-emitting, surface coloring and information encryption applications.

Acknowledgements

This work was supported by the Russian Foundation for Basic Research (grant no. 20-32-70056).

References

- [1] M. Lu, et al., *Advanced Functional Materials* **19**02008 (2019).
- [2] X. Yang, J. Wu, T. Liu, and R. Zhu, *Small Methods* **2** (2018) 1800110.
- [3] E. Tiguntseva, et al., *Nano Letters* **18** (2018) 1185.
- [4] S. V. Makarov, et al., *Nano Letters* **17** (2017) 3047.
- [5] W. Zhang, et al., *Nano Letters* **15** (2015) 1698.
- [6] K. Deng and L. Li, *Small Methods* (2019) 1900150.
- [7] Q. Zhang, M. et al., *Nature Communications* **10** (2019) 727.
- [8] S. Chen, et al., *ACS Nano* **10** (2016) 3959.
- [9] C. Zhou, et al., *ACS applied materials & interfaces* **11** (2019) 26017.
- [10] A. Zhizhchenko, et al., *ACS Nano* **13** (2019) 4140.

The influence of liquid boiling on nanosecond laser damage threshold of metal immersed into water

S.V. Starinskiy^{*,1,2}, A.A. Rodionov^{1,2}, Yu.G. Shukhov¹, A.V. Bulgakov^{1,3}

¹ S.S. Kutateladze Institute of Thermophysics SB RAS, 1 Lavrentyev Ave, 630090 Novosibirsk, Russia

² Novosibirsk State University, Pirogova Str. 2, 630090 Novosibirsk, Russia

³ HiLASE Centre, Institute of Physics, Czech Academy of Sciences, Za Radnicí 828, 25241 Dolní Břežany, Czech Republic

*e-mail: starikhbz@mail.ru

Pulsed laser ablation in a liquid is a flexible method for the synthesis of colloidal solutions and precise surface nanostructuring. In particular it was shown recently that laser synthesis of colloidal solutions is not inferior traditional chemical synthesis in cost-effectiveness [1]. Although PLAL is simple in realization and does not require expensive equipment like vacuum chambers, the PLAL process itself is still poorly understood in spite of recent extensive studies and optimization of the method

The presence of liquid makes the process much more complicated as compared to conventional laser ablation in vacuum or an ambient gas. Apart. Firstly, the liquid medium can participate in the removal of material from the irradiated surface, and secondly, many traditional research methods (mass spectrometry, spectroscopy, etc.) are limitedly applicable. As a result of a the mechanisms of laser ablation in liquid are poorly understood. Moreover, many experimental results are controversial. In particular, data on the ratio of damage threshold fluence of materials in air and in water differ in different paper. The most common point of view is the damage thresholds in a liquid are higher than in air [2,3], which is associated either with heat removal into the liquid or with the action of high-pressure water vapor on the target surface. On the other hand, in a number of studies, a decrease in damage thresholds in a liquid is explained by an increase in the light absorption of the material in a liquid, as well as by surface modification under the influence of a shock wave [4].

We systematically measure the damage thresholds of tin, silver, gold, and their alloys in distilled water and in air under nanosecond IR laser irradiation. It was found that the damage thresholds of refractory metals in a liquid is ~ 1.5 times higher than in air [5]. At the same time, the damage thresholds of tin in a liquid is several percent lower than in air [6]. To analyze the obtained results, a numerical simulation was carried out based on the solution of the non-stationary heat conduction equation taking into account heat removal to the liquid, as well as its homogeneous boiling near the target surface.

Good agreement was reached between the experimental values of damage threshold and the calculated values of laser fluence at which materials reach their melting points in air. The calculated value of damage threshold of refractory metals immersed into liquid were significantly lower than the experimental ones despite of taking into account heat removal from the target and increasing the melting temperature under the influence of water vapor pressure. However, we obtained the good agreement between experimental and calculation result for tin. The observed decrease in the threshold for refused metal in comparison with the case of irradiation in air was explained

by the decrease in the reflection coefficient of immersed in the optical denser medium.

We underline the main difference between tin and noble metals (gold, silver and their alloys) in respect of the ns-PLAL process. The melting temperature of noble metals is higher 1000 K those higher than a water vaporization temperature (~ 600 K) obtained in calculation of ns laser heating of the metal targets immersed in water. So, the refractory metal melting follows after water vaporization which occurs at an early heating stage. Formation liquid-vapor interface near the target surface leads to scattering of a fraction of the incident laser pulse. This assumption are confirmed by a comparison of results probe-beam measurements and calculation data of boiling moment. This results in higher metal damage thresholds than the corresponding values in air. In contrast, the Sn melting temperature is well below 600 K so the laser-induced tin melting occurs before water vapor nucleation and thus before the scattering process starts and leads to energy losses. As a result, the tin damage thresholds in water and air (and in vacuum) are identical. On the other hand, this indicates that, since the water-explosive vaporization under tin ns-PLA usually also occurs early target heating stages, the laser light scattering processes also take place in this case. According to calculation, the energy losses due to the scattering effects can reach up to 30% of the total pulse energy that has to be taken into account when analyzing the PLAL process even for low-melt targets.

Acknowledgements

This work was carried out under state contract with IT SB RAS (AAAA-A17-117022850025-1).

References

- [1] K. Oyoshi, D. Lenssen, R. Carrius, S. Mantl. *Thin Solid Films* **381** (2001) 194.
- [2] Jendrzey S., Gökce B., Epple M., Barcikowski S., *ChemPhysChem*. **18** (2017) 1012.
- [3] Perez D., Béland L., Deryng D., Lewis L., Meunier M., *Phys. Rev. B* **77** (2008) 014108.
- [4] Stafe M., Negutu C., Ducariu A.N., *Rom. Reports Phys.* **64** (2012) 155.
- [5] Kim D., Oh B., Lee H., *Appl. Surf. Sci.* **222** (2004) 138.
- [6] Starinskiy S.V., Shukhov Y. G., Bulgakov A.V., *Appl. Surf. Sci.* **396** (2017) 1765.
- [7] Starinskiy S.V, Rodionov A.A., Shukhov Y.G., Maximovskiy E.A., Bulgakov A.V., *Appl. Phys. A* **125** (2019) 1.

Fabrication of anisotropic structures on amorphous silicon surfaces by femtosecond laser pulses

D.V. Shuleiko^{*1}, M.N. Martyshov¹, D.V. Orlov¹, D.E. Presnov^{1,2,3}, S.V. Zobotnov^{1,4}, A.G. Kazanskii¹, P.K. Kashkarov^{1,4}

¹ Lomonosov Moscow State University, Faculty of Physics, 1/2 Leninskie Gory, Moscow, 119991, Russia

² Lomonosov Moscow State University, Skobeltsyn Institute of Nuclear Physics, 1/2 Leninskie Gory, Moscow, 119991, Russia

³ Quantum Technology Centre, Faculty of Physics, Lomonosov Moscow State University, 1/35 Leninskie Gory, Moscow, 119991, Russia

⁴ National Research Centre «Kurchatov Institute», 1 Akademika Kurchatova sq., Moscow, 123182, Russia

*e-mail: shuleiko.dmitriy@physics.msu.ru

Irradiation of amorphous hydrogenated silicon (a-Si:H) by femtosecond laser pulses provides uniform nanocrystallization of near surface layer [1] and allows to fabricate laser-induced periodic surface structures (LIPSS). The latter effect can be explained by excitation of surface plasmon-polaritons under high-power laser radiation [2]. Such anisotropic one-dimensional gratings on a-Si:H film surface demonstrate birefringence and dichroism, and can be used in polarization-sensitive optoelectronic devices [3]. Also, LIPSS formation by femtosecond laser pulses is perspective for thin-film photovoltaics, as such periodic gratings on the surface of a-Si:H heterojunction solar cells can improve their efficiency due to grating-induced interference effects [4].

However, to show the possibility of a-Si:H LIPSS practical application it is necessary to theoretically describe formation of such gratings depending on irradiation conditions, and investigate influence of structural anisotropy on the modified film electrical and photoelectrical properties.

In this work a-Si:H films were irradiated by femtosecond laser pulses ($\lambda = 1250$ nm, $\tau = 125$ fs, $f = 10$ Hz) in raster mode. Laser spot diameter varied from 150 to 300 μm and laser fluence – from 0.15 to 0.5 J/cm^2 during irradiation. Scanning speed V was changing from 2 to 60 $\mu\text{m}/\text{s}$. 4 samples were produced in total (Table I).

Table I. Sample modification parameters and LIPSS periods.

Sample	Fluence, J/cm^2	Scanning speed, $\mu\text{m}/\text{s}$	Laser spot diameter, μm	LIPSS period, μm
1	0.15	60	300	1.19±0.02
2		3		1.21±0.02
3	0.5	50	150	0.88±0.03
4		2		1.12±0.02

Various LIPSS types with periods close to laser wavelength were revealed by scanning electron microscopy on the irradiated a-Si:H surfaces. When scanning speed V was from 50 to 60 $\mu\text{m}/\text{s}$, LIPSS with ridges orientation orthogonal to laser polarization were formed (samples 1 and 3). These LIPSS periods were from 0.88 to 1.19 μm and decreased with increasing of the laser fluence (Table 1). Irradiation at lower scanning speed V from 2 to 3 $\mu\text{m}/\text{s}$ resulted into formation of LIPSS with ridges oriented along the laser polarization (samples 2 and 4). The period of these

LIPSS varied in range 1.12–1.21 μm and also decreased for higher laser fluence (Table I).

Formation of such structures is caused by nonequilibrium carriers photoexcitation and subsequent surface plasmon-polaritons generation [2].

The observed change of structure orientation with decreasing of laser beam scanning speed can be explained by the feedback between the optical properties of irradiated surface and the mode of plasmon-polaritons excited. According to theoretical modeling using so-called «efficacy factor» [5], LIPSS change their direction depending on the sign of instant (during laser irradiation) dielectric permittivity real part $\text{Re } \varepsilon$ of a-Si:H film. Namely, LIPSS ridges direction varies from orthogonal to parallel relatively to laser polarization, when the $\text{Re } \varepsilon$ sign changes from negative to positive in the near-surface region of the film.

Dark conductivity of modified films increased by 3 orders of magnitude according to electrical measurements, due to formation of nanocrystalline silicon phase after femtosecond laser treatment. According to Raman spectra, nanocrystalline phase volume fraction was from 17 to 45% depending on modification conditions. Also, dark conductivity and charge carriers mobility demonstrated artificial anisotropy in the irradiated a-Si:H films. Observed anisotropy can be explained both by LIPSS depolarizing effect and non-uniform film crystallization within raster lines and LIPSS.

Acknowledgements

The work was supported by a Joint Grant of the Moscow Government and the Russian Foundation for Basic Research (project 19-32-70026).

References

- [1] L. Hong, X.C. Wang, H.Y. Zheng, L. He, H. Wang, H. Y. Yu, Rusli. *J. Phys. D: Appl. Phys.* **46** (2013) 195109.
- [2] D.V. Shuleiko, F.V. Potemkin, I.A. Romanov, I.N. Parhomenko, A.V. Pavlikov, D.E. Presnov, S.V. Zobotnov, A.G. Kazanskii, P.K. Kashkarov. *Laser Phys. Lett.* **15** (2018) 056001.
- [3] R. Drevinskas, M. Beresna, M. Gecevičius, M. Khenkin, A.G. Kazanskii, I. Matulaitiene, G. Niaura, O.I. Konkov, E.I. Terukov, Y.P. Svirko, P.G. Kazansky. *Appl. Phys. Lett.* **106** (2015) 171106.
- [4] H. Bencherif, L. Dehimi, F. Pezzimenti, F.G. Della Corte. *Optik* **182** (2019) 682.
- [5] J.E. Sipe, J.F. Young, J. S. Preston, H.M. van Driel. *Phys. Rev. B* **27** (1983) 1141.

Functionalization of nanostructured Si surfaces for advanced sensing applications

A.Yu. Mironenko^{*1}, A.A. Sergeev², M.V. Tutov^{1,3}, A.A. Kuchmizhak^{2,3}

¹ Institute of Chemistry of FEB RAS, 159 Pr. 100-let Vladivostoka, Vladivostok 690022, Russia

² Institute of Automation and Control Processes of FEB RAS, 5 Radio St., Vladivostok 690041, Russia

³ Far Eastern Federal University, 8 Sukhanova St., Vladivostok 690950, Russia

*e-mail: almironenko@gmail.com

The design and fabrication of chemical sensors with high sensitivity and selectivity have attracted considerable attention for several decades due to their great role in such fields like environmental monitoring, medical diagnosis or forensic analysis [1-5]. Detection of nitroaromatic compounds (NACs) is of particular interest since they, on the one hand, are the primary constituents of many explosives and, on the other hand, are highly toxic pollutants, which can cause many chronic diseases [6-7]. Therefore, fast, reliable and selective detection of NACs is an applied relevant task for the social, workplace and environmental safety [8-11].

Currently, a wide range of instrumental techniques on the basis of various transduction methods (absorption, fluorescence, conductivity, etc.) are being employed to detect NACs [12-15]. Among others, popularity of the fluorescence (FL) quenching based detection has grown rapidly due to its high sensitivity, fast response combined with easy handling and readout. The chemical principle of this method is based on analytes ability to form stable pi-complexes with polycyclic aromatic molecules. The planar structure and the presence of electron-withdrawing nitro groups in the aromatic ring make NACs capable of accepting electrons during donor-acceptor interactions with electron donors. The detection principle is based on FL quenching of chemosensor (donor molecule) upon complete or partial electron or energy transfer after the contact with a nitroaromatic analyte (acceptor molecule). Typically, NACs vapor detectors consist of a substrate-supported sensitive material, either a polymer or a low molecular weight fluorophore impregnated into a polymer matrix, and the general strategy aimed at boosting their performance revolves around the search for more efficient sensitive materials.

This work presents a fluorescent chemosensor for highly sensitive and selective detection of nitroaromatic vapors (detection limit ~ ppt). The developed sensor is a nanotextured silicon substrate (optical resonator that

enhances the luminescent response) with covalently bound carbazole functional groups (sensor phosphor), which demonstrates excellent sensory characteristics - reversibility, short response and regeneration times, which makes the developed chemosensor a promising candidate for creating effective sensory systems for public and environmental safety applications.

Acknowledgements

This work is supported by Russian Foundation of Basic Research (Grant no. 18-33-20159).

References

- [1] J. Lopez-Gejo, A. Arranz, A. Navarro, C. Palacio, E. Munoz, G. Orellana. *J. Am. Chem. Soc.* **132** (2010) 1746.
- [2] J. Homola. *Chem. Rev.* **108** (2008) 462.
- [3] L. Ding, Y. Fang. *Chem. Soc. Rev.* **39** (2010) 4258.
- [4] A. Mironenko, A. Sergeev, S. Voznesenskiy, D. Marinin, S. Bratskaya. *Carbohydr. Polym.* **93** (2013) 769.
- [5] A. Mironenko, A. Sergeev, A. Nazirov, E. Modin, S. Voznesenskiy, S. Bratskaya. *Sens. Actuat. B* **225** (2016) 348.
- [6] G. Sathiyar, P. Sakthivel. *RSC Adv.* **6** (2016) 106705.
- [7] M. Hussain, A. Nafady, S. Sirajuddin, S. Hussain Sherazi, M. Shah, A. Alsalmeh, M. Kalhor, S. Mahesar, S. Siddiqui. *RSC Adv.* **6** (2016) 82882.
- [8] V. Mothika, A. Raupke, K. Brinkmann, T. Riedl, G. Brunklaus, U. Scherf. *ACS Appl. Nano Mat.* **1**(2018)6483.
- [9] B. Xu, X. Wu, H. Li, H. Tong, L. Wang. *Macromol.* **44** (2011) 5089.
- [10] S. Kumar, N. Venkatramiah, S. Patil. *J. Phys. Chem. C* **117** (2013) 7236.
- [11] K. Ponnuel, G. Banupriya, V. Padmini. *Sens. Actuat. B* **234** (2016) 34.
- [12] G. Zyryanov, D. Kopchuk, I. Kovalev, E. Nosova, V. Rusinov, O. Chupakhin. *Russ. Chem. Rev.* **83** (2014) 783.
- [13] X. Sun, Y. Wang, Y. Lei. *Chem. Soc. Rev.* **44** (2015) 8019.
- [14] F. Akhgari, H. Fattahi, Y. Oskoei. *Sens. Actuat. B* **221** (2015) 867.
- [15] R. Glenn, M. Dantus. *J. Phys. Chem. Lett.* **7** (2016) 117.

Ultra-black coating based on micro hollow carbon sphere

L. Pan*, Y. Hu

MIT Key Laboratory of Critical Materials Technology for New Energy Conversion and Storage, School of Chemistry and Chemical Engineering, Harbin Institute of Technology, Harbin, 150001, China

*e-mail: panlei@hit.edu.cn

“Ultra-black” surfaces with extremely low reflectance in a broad wavelength range are expected in high performance optical instruments. Traditional black coatings consisting of carbon and binders hardly achieve reflectivity lower than 2% for their relatively high density and flat surface.[1, 2] In recent years, extremely low reflectivity has been reported in low density carbon materials such like aligned carbon nanotube array (1×10^{-7}) [3] or carbon aerogels (<0.24%)[4, 5]. However, low mechanical property is highly possibly resulted from fragile subwavelength structure, restricting the application of these coatings. Furthermore, complicated equipment and processes such like chemical vapor deposition[3] or supercritical drying[5] are needed to fabricate these coatings, which are not suitable for large area surface too.

Herein, an ultra-black coating (reflectivity < 2%) employing hollow carbon spheres (HCSs) is proposed. HCSs can bring non-open sub-wavelength pores into the coating without breaking the continuity of the film and decreasing mechanical property. The sub-wavelength pores can reduce overall density of the coating, leading to a low equivalent refractive index and then a low reflectivity subsequently. Besides, HCS can work as matting agent, helping to form large nodules and pits which increase absorption too.

The HCSs are synthesized through a four-step process: synthesizing SiO₂ nanospheres, coating SiO₂ nanospheres with RF resin, carbonizing RF resin by calcination and removing SiO₂ cores.[6] The HCSs are mixed with fluororesin as binder and are sprayed on substrates. A solar

absorptance as high as 98.3% is achieved after the optimization of the binder ratio. The existence of the sub-wavelength pores is confirmed by TEM and SEM for both HCSs and coatings. The molecules of the binder do not enter the hollow portion of the HCS. The key effect of the pores on the high solar absorptance is demonstrated by comparison between coatings contained HCSs and solid carbon spheres. Moreover, the agglomerated HSC particles form a micro-scale light-trapping structure, which further improves the solar absorptance. The adhesion of the ultra-black coating is tested and is good enough for real application.

Acknowledgements

This work was supported by Shanghai Astronautic Science and Technology Fund (SAST2017-065).

References

- [1] S. Azoubel, R. Cohen, S. Magdassi. *Surface and Coatings Technology*. **21** (2015) 262.
- [2] R. Bera, S. Magdassi, D. Mandler, et al. *Energ. Convers. Manage.* **287** (2016) 120.
- [3] NT. Panagiotopoulos, EK. Diamanti, LE. Koutsokeras, M. Baikousi, E. Kordatos, TE. Matikas, et al. *ACS nano*. **10475** (2012) 6.
- [4] Z. Yang, L. Ci, J. Bur, S. Lin, P. Ajayan. *Nano Letters*. **446** (2008) 8.
- [5] W. Sun, A. Du, Y. Feng, J. Shen, S. Huang, J. Tang, et al. *ACS Nano*. **9123** (2016) 10.
- [6] N. Li, Q. Zhang, J. Liu, J. Joo, A. Lee, Y. Gan, et al. *Chem. Commun.* **5135** (2013).

Photonic nanojet generation in transmission and reflection mode

K.A. Sergeeva*, A.A. Sergeev

Institute of Automation and Control Processes of FEB RAS, 5 Radio St., Vladivostok 690041, Russia

*e-mail: kspetrovyh@mail.ru

This work is related to the investigation of the interaction of optical radiation with dielectric particles, leading to the spatial field localization on the shadow surface of a structure. This phenomenon is characterized by a high intensity, a considerable length (up to several wavelengths) and a small half-width (several tenths of wavelengths), and is called the "photonic nanojet" [1]. Despite a rather detailed theoretical description of the process and conditions of photonic nanojet formation in various media, as well as the prospect application of this effect in optics and photonics, studying practical methods for photonic jet application is currently limited within the areas of science associated with amplification of Raman signal and superresolution optical microscopy [2].

At the same time, the possibilities of using the photonic nanojet effect to enhance the luminescence have been studied to a much lesser extent and mainly theoretically. The single experimental works connected with the use of photonic jets for multiphoton excitation of luminescence and fluorescence microscopy are known. Here, we expand the field of practical application of photonic nanojets for local excitation of a sensitive layer of luminescent sensors of chemical compounds in liquid and gas media.

In general, the sensor system under discussion is a film of a matrix material (polymer or sol-gel) several micrometers thick doped with a chemosensitive receptor which luminescence parameters change upon contact with the analyte. Sensor response studies of such systems, including those conducted by the project leader, indicate that the detection limit of the analyte directly depends on the ability to register the sensor response from a single chemosensitive receptor. This fact is confirmed by an increasing number of publications devoted to the development of sensor systems based on the plasmon resonance effect [3]. However, the exciting radiation is localized only in the immediate vicinity of the plasmon structure, limiting the thickness of the sensitive layer and, correspondingly, the specific number of molecules of the chemosensitive receptor.

Overcoming this problem is associated with the formation of a preconcentrator that provides for the "targeted delivery" of the analyte molecule to the chemosensitive receptor, significantly complicating the design of the sensor. In turn, the localization of the exciting radiation to the photonic nanojet makes it possible to extend the localization region by several wavelengths and increase its intensity, leading to an enhancement of the luminescence of the chemosensitive receptor.

To create such structures, it is necessary to conduct complex studies of the conditions for the appearance of photonic nanojets, which ensure the highest efficiency of luminescence excitation throughout the thickness of the sensitive layer. The task is complicated by the fact that during sensor response measurements, primarily in the

water environment, significant changes in the refractive index of the sensitive layer can occur, affecting the length, half-width, and intensity of the photonic nanojet. Current theoretical descriptions of photonic nanojets formed by various microstructures do not take this fact into account, which causes difficulties for the practical application of the calculation result. In this connection, we numerically simulate the appearance process of a photonic nanojet under the conditions of a changing refraction index of the environment in order to determine the optical and geometric parameters that provide an optimal correlation between its half-width, length, and intensity. Based on the simulation results we develop a technique for creation the microstructures that are suitable for the formation of a photonic nanojet in a real experiment in transmission and reflection modes. Direct observations of the photonic nanojets were conducted by means of the fluorescence microscope experimental setup. The main advantage of the setup is the image of the working region is constructed and the luminescence spectrum is recorded in both the "transmission" and "reflection" modes.

The sensor response under the excitation of a sensitive layer by the PNJ generated by microstructures of various types in aqueous and gaseous media was studied. It was shown that the PNJ excitation in transmission mode extend the analyte detection limit from 2 to 0.5 μM when registering metal ions in the aquatic environment and from 0.5 to 0.05 ppm when registering gaseous ammonia in the air. The observed enhancement of the detection limit is associated both with large PNJ length (16λ) and a sufficiently long region of high-intensity ($\approx 5\lambda$) ensuring high excitation efficiency throughout the sensitive layer volume. In turn, the PNJ excitation in reflection mode leads to an increase in the value of the sensor response in its linear region ($\approx 10\text{-}50 \mu\text{M}$ for gold ions and 1-30 ppm for ammonia), but does not affect significantly the detection limit due to the relatively low intensity and short length (10λ) of the PNJ.

Acknowledgements

This work was financially supported by the Russian Science Foundation (project 18-72-00095).

References

- [1] Y.F. Lu, L. Zhang, W.D. Song, Y.W. Zheng, B.S. Luk'yanchuk. *JETP Lett.* **72** (2000) 457.
- [2] Z. Wang, W. Guo, L. Li, B. Luk'yanchuk, A. Khan, Z. Liu, Z. Chen, M. Hong. *Nat. Commun.* **2** (2011) 218.
- [3] J. Zhu, L.L. Goddard. *Opt. Exp.* **24** (2016) 30444.
- [4] A.A. Sergeev, K.A. Sergeeva, A.A. Leonov, I.V. Postnova, S.S. Voznesenskiy. *Semiconductors* **52** (2018) 1846.

Beyond diffraction limit: local features of electromagnetic field in plasmon-based nanospectroscopy

E. Sheremet^{*1}, A. Averkiev¹, S. Shchadenko¹, V. Kolchuzhin², R.D. Rodriguez¹

¹ Tomsk Polytechnic University, Lenin ave. 30, Tomsk 634034, Russia

² Qorvo Munich GmbH, Konrad-Zuse-Platz 1, 81829 München, Germany

*e-mail: esheremet@tpu.ru

Raman spectroscopy became nanoscale with the development of tip-enhanced Raman spectroscopy (TERS). This approach uses a plasmonic nanoantenna mounted on a scanning probe microscopy tip. Due to the plasmon resonance it locally enhances electromagnetic field creating a nanoscale light source. By scanning a tip across a sample under the laser illumination and analyzing inelastically scattered light, it is possible to obtain spectral maps with the spatial resolution of this optical technique below 50 nm, well beyond the diffraction limit [1].

The TERS spectra provide information about the chemical composition just like Raman spectroscopy. However, it is well-known that the polarization of the local electric field is changed around a plasmonic antenna leading to the scrambling of the selection rules [2,3]. To be able to extract key information about the molecular and crystalline structure and orientation, the Raman tensor needs to be completed with the tip-amplification tensor T as proposed by Ossikovsky *et al.* [4,5].

In this work we consider a dipole over a substrate where the image dipole p_{im} can be described using the following expression

$$p_{im} = \pm Kp$$
$$K = \frac{\epsilon_s - \epsilon_m}{\epsilon_s + \epsilon_m}$$

where ϵ_s is the dielectric function of the substrate and ϵ_m is the dielectric function of the medium surrounding the dipole. Here two models are created using a simple image dipole model and three-dimensional finite element method model of a 10 nm sphere above the surface in COMSOL Multiphysics. By studying the three field components (E_x , E_y , E_z) and their distribution as a function of the substrate dielectric function and the sphere-substrate distance, the dependence of the dipole-substrate coupling and its effect on the tip-amplification tensor is described.

The resulting tip-amplification tensor

- has off-diagonal components that result in the change of the spectral shape when the selection rules are applied;
- in specific cases for the X polarization of the electric field and strong dipole-substrate coupling (negative dielectric function of the substrate and small dipole-

substrate distance), the off-diagonal components can be comparable or even exceed the diagonal ones.

Knowing the tip-amplification tensor would allow to extract the Raman tensor and distinguish depolarization from the other effects such as the break of the selection rules due to the large electric field gradient or chemical effects [6-9].

Acknowledgements

The research was supported by RFBR project №18-42-700014.

References

- [1] Sheremet, E., Rodriguez, R. D., Agapov, A. L., Sokolov, A. P., Hietschold, M., & Zahn, D. R. T. Carbon, **96** (2016) 588.
- [2] D. Mehtani et al., J. Raman Spectrosc., **36** (2005) 1068.
- [3] P. G. Gucciardi and J. C. Valmalette, Appl. Phys. Lett. **97** (2010) 1.
- [4] R. Ossikovski, Q. Nguyen, and G. Picardi, Phys. Rev. B **75** (2007) 1.
- [5] R. Ossikovski, G. Picardi, G. Ndong, and M. Chaigneau, Comptes Rendus Phys. **13** (2012) 837.
- [6] E. C. Le Ru and P. G. (Pablo G. Etchegoin, Principles of surface-enhanced Raman spectroscopy : and related plasmonic effects. Elsevier, 2009.
- [7] D. Mehtani et al., J. Opt. A Pure Appl. Opt. **8** (2006) S183.
- [8] J. Zuloaga and P. Nordlander, Nano Lett. **11** (2011) 1280.
- [9] J. Vogt, C. Huck, F. Neubrech, A. Toma, D. Gerbert, and A. Pucci, Phys. Chem. Chem. Phys. **17** (2015) 21169.

Functional plasmonic materials for targeted surface enhanced Raman spectroscopy: from pollutant detection to tumor discrimination

O. Lyutakov*, O. Guselnikova, A. Trelin, V. Svorcik

University of Chemistry and Technology, Prague, Technicka 5, 166 28, Czech Republic

*e-mail: lyutakoo@vscht.cz

Actually, surface enhanced Raman spectroscopy (SERS) represents one of the more sensitive and reliable methods for various compounds detection [1]. The main advantages of SERS are based on the light energy concentration near the plasmon-active surface, where the typically weak Raman response of targeted molecules can be enhanced by many orders of magnitude [2]. In fact, the SERS allows reaching the absolute detection limit – discriminating single molecule [3]. However, the real utilization of SERS is significantly restricted by the fact that most of the relevant molecules should be detected in complex media, where the Raman bands from various chemical groups interfered and produce “unreadable” spectral pattern.

To overcome this drawback our group propose the surface functionalization of plasmonic materials with various organic moieties, able to selectively entrap the targeted molecules from complex medium [4]. We started from the optimization and construction of SERS substrate, favoured by a homogeneous distribution of plasmon evanescent wave [5]. Unlike the common approaches (based on localized plasmon excitation) we utilized the periodical plasmonic substrate, where the so-called surface plasmon-polariton wave is excited, providing the homogeneous distribution of SERS intensity across the full “active” area [6,7]. In the next step, we introduced the plasmonic surface functionalization with the aim to increase the surface affinity to targeted molecules and restrict the potential surface sorption of undesired compounds. Next, we demonstrated the advantages of our approaches in the various relevant fields of sensorics: detection and recognition of environmental contaminants, drugs, tumour markers, forbidden compounds etc [8-11].

Especially interesting is the recently proposed by us enantioselective detection. It should be noted that common routes, used for enantiomers discrimination are complicated by time and equipment demands [12]. Our functional SERS substrate allows to performed chiral detection with high accuracy and limit of detection

never demonstrated before. In this case, we used two based principles: a combination of chiral plasmonic structures and enantio-selective entrapping of the targeted analyte [13, 14].

Finally, we also recently introduced the utilization of functional plasmonic material for SERS in the combination with deep machine learning. The proposed approach allows complicated SERS spectra, with high (closed to absolute) degree of accuracy and reliability and us to evaluate interfering. Such method is especially useful for analysis of (bio) samples, including the different bacterial strains normal, tumour or tumour-associated cells and large biomolecules [15, 16].

Acknowledgements

This work was supported by GACR, under the project number 20-19353S.

References

- [1] Zong, Ch, et al. *Chem. Rev.* **118** (2018) 4946.
- [2] Ding, S-Y., et al. *Chem. Soc. Rev.* **46** (2017) 4042.
- [3] Zrimsek, A. B., et al. *Chem. Rev.* **117** (2017) 7583.
- [4] Guselnikova, O. et al. *ChemNanoMat* **3** (2017) 135.
- [5] Kalachyova, Y. et al. *J. Phys. Chem. C* **119** (2015) 9506.
- [6] Kalachyova, Y., et al. *J. Phys. Chem. C* **120** (2016) 10569.
- [7] Kalachyova, Y. et al. *Phys. Chem. Chem. Phys.* **19** (2017) 14761.
- [8] Guselnikova, O., et al. *Sens. Act. B: Chem.* **253** (2017) 830.
- [9] Guselnikova, Olga, et al. *Sens. Act. B: Chem.* **262** (2018) 180.
- [10] Guselnikova, Olga, et al. *Sens. Act. B: Chemical* **265** (2018) 182.
- [11] Guselnikova, O., et al. *Anal. Chim. Acta* **1068** (2019) 70.
- [12] Ilisz, I., et al. *J. Pharmac. Biomed. Anal.* **47** (2008) 1.
- [13] Kalachyova, Y., et al. *ACS Appl. Mater. Interfac.* **11** (2018) 1555.
- [14] Guselnikova, O, et al. *ACS Sens.* **4** (2019) 1032.
- [15] Guselnikova, O., et al. *Biosens. Bioelectron.* **145** (2019) 111718.
- [16] Erzina, M., et al. *Sens. Act. B: Chem.* **308** (2020) 127660.

Laser manipulation of microparticles with the help of structured light

A.P. Porfirev^{*1,2}, A.B. Dubman², S.A. Fomchenkov^{1,2}

¹Image Processing Systems Institute—Branch of the Federal Scientific Research Centre “Crystallography and Photonics” of the Russian Academy of Sciences, 151 Molodogvardeyskaya St., Samara 443001, Russia

²Samara National Research University, 34 Moskovskoye Shosse, Samara 443086, Russia

*e-mail: porfirev.alexey@gmail.com

The optical tweezer is a unique non-contact technique for manipulation of nano- and micro-objects in different media [1–3]. The optical trapping and guiding of different types of microscopic objects is possible due to the actions of different forces: the gradient force from a single strongly focused laser beam in the case of transparent particles suspended in liquids [2] and the photophoretic (PP) forces in the case of light-absorbing particles in gaseous media [4, 5]. PP forces arise when the surface of a particle in a gaseous medium is nonuniformly heated by an incident light beam and can lead to the movement of the particle away from the light source (the phenomenon of positive photophoresis) or toward the light source (the phenomenon of negative photophoresis).

Despite the fact that a single focused Gaussian beam can be used as an optical tweezer for various particles in various media [2, 3], the use of so-called structured laser beams with different profiles of amplitude, phase, and even polarization state distribution [6] provides much greater opportunities for advanced laser manipulation. Here, we demonstrate using structured laser beams for realization of trapping and manipulation of different particles – transparent polystyrene microparticles in water and light-absorbing agglomeration of carbon nanoparticles in air. Different types of manipulations - laser trapping of a set of particles, laser guiding of the trapped particles and their controllable rotation are presented.

The most popular example of the structured laser beam that can be used for laser manipulation is the so-called optical bottle beams – intensity minima bounded in three dimensions by regions of higher intensity [7] is the most convenient way for three-dimensional stable trapping of different particles both in liquid [8] and gaseous media [9]. The specially designed diffractive optical elements (DOEs) and different elements can be used for the generation of such laser beams.

The structured laser beams can be used for optical rotation of the trapped particles too. There are two main types of optical rotation: the rotation around the axis of the optically trapped object and the orbital rotation around the optical axis of the laser beam used for trapping. In the case of transparent micro-objects in liquid media, these two types of rotation are easily realized by the transfer of either spin angular momentum (SAM) or orbital angular momentum (OAM) from the illuminating laser beam to the trapped object [10, 11]. However, such laser rotation techniques are not universal; for example, for airborne light-absorbing particles, the magnitude of the so-called photophoretic forces can exceed the radiation pressure by several orders [5], so SAM and OAM transfer effects become neglectable in comparison with the thermal effects

arising from the anisotropic heating of the surface of the trapped particles. We propose to use linear optical bottle beams generated with the help of a combination of a circular aperture and a rotating cylindrical lens for the realization of controllable orbital rotation of light-absorbing agglomerations of carbon nanoparticles. Previously, we have used an optical light sheet trap generated by a cylindrical lens for the realization of an “optical mill”, a tool for the massive transfer of light-absorbing particles in air [12]. The modification of the light sheet trap allowed us to generate an elongated optical BB that can be used for trapping and holding the trapped particle inside the dark area during the rotation of the generated beam.

The considered examples demonstrate only a small part of possibilities in the field of laser trapping with the help of structured laser beams. The structured laser beams have a great potential in high-performance laser trapping of nano- and microparticles and can be used for realization of different all-optical tools for massive transfer and analysis of such particles, including bacteria, fungal spores, plant pollen and small fragments of plants and fungi that are potential carriers of various human or plant diseases [13].

Acknowledgements

This work was financially supported by Russian Science Foundation (Grant no. 19-72-00018).

References

- [1] A. Ashkin. *Phys. Rev. Lett.* **24** (1970) 156.
- [2] A. Ashkin, J.M. Dziedzic, J.E. Bjorkholm, S. Chu. *Opt. Lett.* **11** (1986) 288.
- [3] Z. Zhang, D. Cannan, J. Liu, P. Zhang, D.N. Christodoulides, Z. Chen. *Opt. Express* **20** (2012) 16212.
- [4] F. Ehrenhaft. *Ann. Phys.* **56** (1918) 81.
- [5] V.G. Shvedov, A.S. Desyatnikov, A.V. Rode, W. Krolikowski, Y.S. Kivshar. *Opt. Express* **17** (2009) 5743.
- [6] H. Rubinsztein-Dunlop, A. Forbes, M.V. Berry, M.R. Dennis, D.L. Andrews, M. Mansuripur, C. Denz, C. Alpmann, P. Banzer, T. Bauer, E. Karimi. *J. Opt.* **19** (2016) 013001.
- [7] J. Arlt, M.J. and Padgett. *Opt. Lett.* **25** (2000) 191.
- [8] A.P. Porfirev, R.V. Skidanov. *Computer Optics* **36** (2012) 211.
- [9] C. Wang, Y.-L. Pan, S.C. Hill, B. Redding. *J. Quant. Spectrosc. Radiat. Trans.* **153** (2015) 4.
- [10] E.J. Friese, T.A. Nieminen, N.R. Heckenberg, H. Rubinsztein-Dunlop. *Nature* **394** (1998) 348.
- [11] N.B. Simpson, K. Dholakia, L. Allen, M.J. Padgett. *Opt. Lett.* **22** (1997) 52.
- [12] A. Porfirev. *Appl. Phys. Lett.* **115** (2019) 201103.
- [13] U. Poschl. *Angew. Chem.* **44** (2005) 7520.

Size effect on optical properties of silicon dioxide hollow particles

V.I. Iurina¹, V.V. Neshchimenko¹, Li Chundong²

¹ Amur State University, 21 Ignatievskoe highway, Blagoveshchensk 675027, Russia

² Harbin Institute of Technology, 92 West Dazhi St., Nan Gang District, Harbin 150000, China

*e-mail: viktoriay-09@mail.ru

The optical properties of silicon dioxide hollow particles with different size were investigated in UV/visible/near-IR region, as well as X-ray photoelectron spectra were analyzed. It was established that hollow particle reflectance lower than bulk microparticles. Absorbance in the red and near infrared spectral ranges increases with decreasing size of hollow particles, but in the UV-region conversely. This is due to different absorption centers.

Experimental

Synthesis of SiO₂ hollow particles was carried out using a template method. Polystyrene balls (PS) were used as a template. A similar method was used to obtain hollow spheres of silicon dioxide. Tetraethylorthosilicate (TEOS (C₂H₅O)₄Si) was applied to the surface of the templates. It forms a layer around the polystyrene in the form of dioxide, and C₂H₅ binds to the external environment. Then the polystyrene template is dissolved with ammonia and annealed.

Results

The silicon dioxide hollow particles with different sizes were obtained: nano-, submicro-, micro-, submacrospheres. Based on the obtained X-ray spectra, it was found that all of silicon dioxide spheres of various sizes and nano-, microparticles have an amorphous structure, which is determined by a diffuse peak near 21 degrees. BET analysis showed that an increase in mean particle size, specific surface area decreases. The largest specific surface area of nanoparticles is 244.2 ± 20.1 m²/g.

In the diffuse reflectance spectra of SiO₂ hollow nano-, submicro, micro-, submacrospheres in the region up to 500 nm, as well as for micro- and nanoparticles, two characteristic “dips” are recorded - a decrease in the reflectance to 70-80 %, and for submicroparticles, a decrease up to 45 % is registered.

In the region above 500 nm, the reflectance of hollow particles gradually decreases and in the near infrared region is 30-45 %, depending on the type of particles. For micropowders and submicropowders, it is equal to 80-85 % in the entire interval. Absorption bands characteristic of chemisorbed on the surface of gas powders (CO, CO₂ and OH groups) are also recorded in this spectral region.

In the absorption spectra of hollow particles are observed identical absorption bands at 5.75, 4.9, 4.1-4.2 eV and bands of chemisorbed gases at 0.86, 0.76, 0.64 and 0.55 eV. The characteristic absorption band for silicon dioxide, 5.75 eV, may be due to the absorption of the E'_γ center, the band at 4.9 eV due to defects on non-bridging oxygen atoms (≡Si-O•), the nature of the band at 4.1 eV is not known.

XPS analysis is a good tool for detecting defects associated with bridging oxygen (Si-O-Si), non-bridging oxygen (-O-Si), and free oxygen (O₂-) [1]. The binding energies of SiO₂ and SiO have values near 103.3 and 101.9 eV. When choosing a half-height at half-width equal to 1.5 eV near the values for pure silicon equal to 99.7 eV [2]. It should be noted that the silicon suboxide components, described here as SiO, are not well defined, but correspond to the superposition of various suboxide states of Si₂O₃. From the obtained decompositions, it was found that for hollow particles the absence of bridging oxygen prevails, while for particles of the nano-sized range including nanospheres, stoichiometry corresponds to the SiO₂ compound.

The XPS line O1s is characterized by three peaks with centers at 530.52, 532.22, and 528.06 eV [3, 4]. The shift of the O1s binding energy of nano- and hollow particles from microparticles indicates a change in the type of oxygen bond, which is associated with the formation of Si³⁺.

Summary

The optical properties of silicon dioxide hollow particles with different size were investigated in UV/visible/near-IR region. It was established that hollow particle reflectance lower than bulk microparticles. Absorbance in the red and near infrared spectral ranges increases with decreasing size of hollow particles, but in the UV-region conversely. This is due to different absorption centers: absorption in UV region cause by the E'_γ center and on non-bridging oxygen atoms; absorption in NIR region cause by chemisorbed gases CO, CO₂, and OH-groups.

References

- [1] M. Morra, E. Occhiello, R. Marola, F. Garbassi, P. Humphrey, D. Johnson. *J. Colloid. Interf. Sci.* **137**(1990) 11.
- [2] A. Thøgersen, J.H. Selj, & E.S. Marstein. *Journal of The Electrochemical Society* **159** (2012) D276.
- [3] R. Zhang, *J. Physica B: Condensed Matter* **553** (2019) 23.
- [4] L. Khriachtchev, T. Nikitin, C.J. Oton, R. Velagapudi, J. Sainio, J. Lahtinen, S. Novikov. *J. Applied physics* **104** (2008) 104316.

Microsphere lithography for Fe₃Si-Au magnetoplasmonic nanostructures

I.A. Tarasov^{*1}, T.E. Smolyarova^{2,3}, I.A. Yakovlev¹, I.V. Nemtsev³, S.N. Varnakov¹,
S.G. Ovchinnikov^{1,2}

¹ Kirensky Institute of Physics, Federal Research Center KSC SB RAS, Krasnoyarsk, Russia

² Siberian Federal University, Krasnoyarsk, Russia

³ Federal Research Center KSC SB RAS, Krasnoyarsk, Russia

*e-mail: tia@iph.krasn.ru

Magnetoplasmonic nanostructures combine ferromagnetic and plasmonic materials to exploit field enhancement in order to create active optical devices, which are tunable by an external magnetic field [1,2]. One of the approaches to utilize this fruitful combination of the ferromagnetic and plasmonic nanostructure is to alter the polarization state of light through magneto-optical (MO) Kerr effect. Presence of plasmonic excitation, localized surface plasmons and propagating surface plasmon polaritons, may drastically enhance polar or transversal Kerr effect.

Nowadays, hybrid noble metal/ferromagnetic metal nanostructures being investigated are FM-Au bi- and trilayers (FM – Co, Fe, Ni, YiG), and patterned thin films with a dot and antidot structures. The further investigations spread on other plasmonic materials as Ag, Cu or Al.

In this work, we aim to examine the MO activity of ferromagnetic iron silicide thin films coupled with gold layers. The patterned dot and antidot nanostructures are also under investigation (Fig. 1).

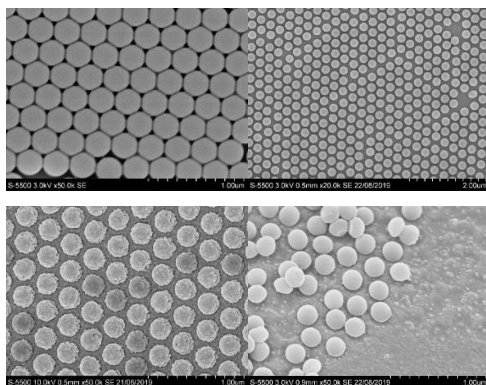


Figure 1. Scanning electron microscopy image of polystyrene nanospheres used for preparation of dot and antidote Fe₃Si-Au nanostructures (a) 320 nm and (b) 272 nm in diameter, (c) covered with gold layer, (d) on Fe₃Si surface treated in HNO₃ acid.

The utilization of Fe₃Si instead of pure ferromagnetic metals gives us an opportunity to alter intrinsic optical and MO properties of ferromagnetic metal through the chemical composition and chemical order [3].

The optical and magneto-optical properties of highly textured hybrid nanostructures of four types with different layer thicknesses were studied: I - Fe₃Si, II - Fe₃Si / Au, III - Au / Fe₃Si / Au, IV - Au / Fe₃Si. Some samples were used to create a monolayer of polystyrene microspheres on their surface with the help of microsphere lithography.

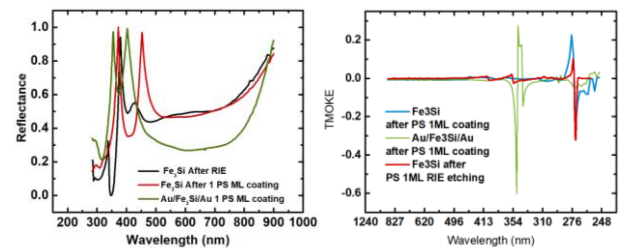


Figure 2. (a) Measured spectral reflectivity and (b) transversal Kerr effect spectra for the heterostructure samples with the nanosphere monolayer on the surface.

A positive result was achieved using a weakly concentrated solution of ethyl alcohol and a surfactant (1: 200), with an aqueous suspension of microspheres 300 nm in size. On structures with a surface modified by a monolayer of polystyrene nanospheres, a significant increase in the magneto-optical response was shown. The maximum position of the magneto-optical effect can vary in the wavelength range from 270 to 413 nm for samples with an initial nominal size of 320 nm by changing their size to 276 nm (Fig. 2).

As a result of the studies, a wide variability of changes in the magneto-optical properties of nanostructures based on thin epitaxial films of ferromagnetic iron silicide by modifying the surface through the creating of a monolayer of polystyrene microspheres, changing their size, and also applying a plasmon metal to their surface was demonstrated.

Acknowledgements

The work is carried out with the assistance of Krasnoyarsk Regional Center of Research Equipment of Federal Research Center «Krasnoyarsk Science Center SB RAS» and Russian Foundation for Basic Research, Government of Krasnoyarsk Territory, Krasnoyarsk Regional Fund of Science to the research project № 18-42-243013.

References

- [1] D. Bossini, V.I. Belotelov, A.K. Zvezdin, A.N. Kalish and A.V. Kimel, ACS Photonics **3** (2016) 1385.
- [2] G. Armáles, A. Cebollada, A. Garcia-Martin and M.U. González, Adv. Opt. Mater. **1** (2013) 10.
- [3] I. Tarasov, Z. Popov, M. Visotin, I. Yakovlev and S. Varnakov, EPJ Web Conf. **185** (2018) 03014.

Spectroscopic study of low-temperature dynamics in nanocomposites based on semiconductor colloidal quantum dots

K.R. Karimullin^{*1,2}, A.I. Arzhanov^{1,2}, A.E. Eskova², K.A. Magaryan², N.V. Surovtsev³,
A.V. Naumov^{1,2}

¹ Institute for Spectroscopy RAS, 5 Fizicheskaya St., Troitsk, Moscow 108840, Russia

² Moscow State Pedagogical University, 29/7 Malaya Pirogovskaya St., Moscow 119435, Russia

³ Institute of Automation and Electrometry SB RAS, 1 Akademika Koptyuga ave., Novosibirsk 630090, Russia

*e-mail: kamil@isan.troitsk.ru

Nanocomposites doped with semiconductor quantum dots (QDs) are of great interest in modern physics and material science as effective LEDs, gain media for laser generation, elements for photovoltaic devices and nanoelectronics. Developing of new QD-based materials requires the fundamental study of dynamical processes in QDs and their interaction with a solid matrix, in particular, electron-phonon interaction. One of the most effective methods for studying the dynamic properties of solid state composites with QDs is photon echo spectroscopy [1, 2], however, standard luminescent techniques, supplemented by temperature measurements, can also be useful for such studies [3, 4].

In this paper, we studied polymers and frozen glasses doped with double-coated colloidal CdSe/CdS/ZnS QDs. QDs were spread on glass plate and embedded in polyisobutylene (PIB), polymethylmethacrylate (PMMA), frozen toluene, porous polyethylene terephthalate (PETP) and polypropylene (PP).

The exciton luminescence spectra of the samples were measured at different temperatures in the range from 4.5 to 300 K, and the temperature dependencies of the spectra maximum, i.e. of the exciton energy, and the spectral width were plotted. The temperature dependence of the exciton energy was approximated using the model developed in [5], obtaining the following parameters: $E_g(0)$ – the bandgap at zero temperature, the Huang–Rhys factor and the average energy of local optical (LO) phonons associated with relaxation of electronic excitation E_{LO} .

The obtained values of the band gap $E_g(0)$ are the same for all samples. Other parameters for different samples are different. Close values of the Huang-Rhys factor were obtained for polymer (PIB, PMMA, PETP) composites, which indicates similar parameters of the electron-phonon interaction. The S value is different for the sample, which is a thin layer of QDs on a glass substrate, and for porous polypropylene. A significant difference in the value can be caused in one case by the interaction of QDs with a glass substrate, and in the other, with the peculiarities of QDs incorporation into the pores of the polymer matrix. E_{LO} values for polymer composites differ from each other, which may indicate a noticeable effect of the interaction of the emitting quantum dot core not only with QD local phonons, but also with phonons of the matrix. In this case, the influence of the phonons of the matrix is small, which, together with close values of the strength of the electron-phonon interaction, leads to a slight change in the E_{LO} value.

Finally, the value of factor S, which is very different from the rest of the samples, was obtained for a frozen solution of QDs in toluene. Differences in the parameters of the electron-phonon interaction lead to a noticeable change in the effective frequency of the local phonon, which indicates a strong influence of the matrix dynamics on the spectral and luminescent properties of QDs. The last conclusion is supported by the behavior of the temperature dependence for frozen toluene near the glass transition temperature. The nature of the temperature dependence changes radically, i.e. the anomalous dynamics of the matrix under phase transition conditions begins to play the main role.

Table I. Photophysical Parameters of Nanocomposites

Matrix	$E_g(0)$, (eV)	S	E_{LO} , (meV)	E_{LO} , (cm^{-1})
QDs on glass	$2.09 \pm$ 0.02	1.67 ± 0.02	$21.4 \pm$ 0.5	172.6
PIB	$2.10 \pm$ 0.02	1.31 ± 0.02	$21.1 \pm$ 0.5	170.2
PMMA	$2.10 \pm$ 0.02	1.37 ± 0.02	$20.2 \pm$ 0.6	162.9
PP	$2.09 \pm$ 0.02	1.55 ± 0.04	$17.5 \pm$ 0.1	141.1
PETP	$2.09 \pm$ 0.02	1.66 ± 0.04	$23.5 \pm$ 0.1	189.5
Toluene	$2.07 \pm$ 0.02	2.66 ± 0.10	$22.8 \pm$ 0.7	183.9

The average E_{LO} values of QDs on glass and in PIB were also obtained by Raman spectroscopy at room temperature as high as 25 meV (206 cm^{-1}), that is almost the same as obtained from photoluminescence study. Additional information about relaxation processes in QDs has been obtained by the photon echo technique and luminescence kinetics studies.

Acknowledgements

This work was supported by the Russian Foundation for Basic Research (project # 18-02-01121).

References

- [1] K.R. Karimullin *et al.*, J. Phys. Conf. Ser. **859**(2017) 012010.
- [2] A.I. Arzhanov *et al.*, Bull. Leb. Phys. Inst. **45** (2018) 91.
- [3] K.R. Karimullin *et al.*, Laser Phys. **29** (2019) 124009.
- [4] K.A. Magaryan, K.R. Karimullin, I.A. Vasil'eva, A.V. Naumov. Opt. Spectrosc. **126** (2019) 41.
- [5] K.P. O'Donnell, X. Chen. Appl. Phys. Lett. **58** (1991) 2924.

Transformation of the nanoporous structure of anodic aluminium oxide and its electroluminescence without electrolysis

D.S. Ovechenko, A.P. Boychenko*

Kuban State University, Russia, 149 Stavropolskaya St., Krasnodar 350040, Russia

*e-mail: bojchenco@yandex.ru

The nanoporous oxide of this metal (Al_2O_3) formed by the electrolysis of aluminum (Al) is currently the subject of a comprehensive study, which is associated with the possibility of creating various multifunctional products and systems of nano-, micro- and optoelectronics on its basis [1–4]. Since 1962, the possibility of electrolysis of the formation of an oxide film in chemically pure water was demonstrated by the authors on the example of Si n- and p-types [5], and in 2019 under the same anodizing conditions on the example of Ti, W, In, Ga, Nb, Al, Ta, including Si, we detected their electrogenerated luminescence (EL) [6, 7]. Further studies on the anodic Al_2O_3 formed in distilled water (DW) showed that in nonelectrolysis electrolytes, such as ketones and related compounds containing a carbonyl group (CNG) [8], a transformation of the nanoporous oxide structure is possible, accompanied by a very bright EL with stationary luminosity (I_c) [9]. The highest oxidized Al anode was found in acetylacetone (Acac) and methylpyrrolidone (Mp) compared with the simplest representative of ketones, acetone (Ac) [9]. However, the relationship of such a conversion with the brightness characteristics of the EL is not fully understood. The present work is devoted to its clarification.

For 5 μm thick formed in DW Al_2O_3 , I_c EL was recorded in the above compounds, and geometric inhomogeneities of its structure were estimated from 10000-fold SEM images of the oxide film [9, 10], determining the coefficient (K) of the electric field gain (E_{max}) relative to its average value (E) by the formula [9]: $E_{\text{max}} = K \cdot E$. The table presents the results of the assessment of the values averaged over three replicates of measurements K , E и E_{max} (the error did not exceed 15%) at an external voltage of 1.2 kV with values of the dielectric constant (ϵ) of ketones and DW.

From the data in the table, a clearly traced regularity is clearly visible: with increasing field strength E_{max} increases I_c . At constant voltage and other external factors, the growth of is determined not only by the morphological features of the structure of the oxide film, but also the electrical properties of the liquid dielectric, in particular, its dielectric constant permeability.

The revealed regularity sheds light on the reason for the lack of high brightness of Al_2O_3 EL in Ac in comparison with DW and other CNG-containing compounds. As can be seen from the table, in this ketone the smallest values are K , E and E_{max} , which indicates the absence of conversion of the nanoporous structure of the oxide film,

therefore, only the electrical characteristics of the liquid dielectric have a decisive influence on the generation of EL.

Table. Averaged results of measurements of stationary EL and estimates of the electric field strength on inhomogeneities of the nanoporous structure of Al_2O_3 in DW and ketones

Dielectric	DW	Ac	Mp	Acac
ϵ	78.2	20.7	34.9	25.7
K	5.4	5.2	6.6	9.8
E , 10^5 V/m	5.5	4.4	5.0	4.7
E_{max} , 10^6 V/m	3.0	2.3	3.3	4.6
I_c , 10^{-5} lm/m ²	12	2.6	19.1	88

Thus, with the constant external voltage, thermodynamic parameters, and the absence of electrolysis, the brightness characteristics of the EL of the anodic Al_2O_3 of constant thickness are influenced by its structural organization and the electrophysical characteristics of the nonelectrolysis electrolyte surrounding the oxide film.

Acknowledgments

The reported study was funded by RFBR, project number 19-32-90112.

References

- [1] S. Lazarouk, S. Katsouba, A. Leshok, A. Demianovich, V. Stanovski, S. Voitech, V. Vysotski, V. Ponomar. *Microelectron. Eng.* **50** (2000) 321.
- [2] S. Katsouba, P. Jaguiro, S. Lazarouk, A. Smirnov. *Physica E.* **41** (2009) 931.
- [3] G.D. Sulka, K. Hnida. *Nanotechnology.* 23(2012)075303.
- [4] W. Lee, S. J. Park. *Chemical reviews.* **114** (2014) 7487.
- [5] L.A. Dubrovsky, V.G. Melnik, L.L. Odynets. *Journal of Physical Chemistry.* **36** (1962) 2199.
- [6] D.S. Ovechenko, A.P. Boychenko. *Technical Physics Letters.* **45** (2019) 503.
- [7] D.S. Ovechenko, A.P. Boychenko. *Ecological bulletin of research centers of the Black sea economic cooperation.* **16** (2019) 59.
- [8] M.I. Eidelberg. *Optics and spectroscopy.* **16**(1964)97.
- [9] D.S. Ovechenko, A.P. Boychenko. *Optics and spectroscopy.* **128** (2020) 256.
- [10] S.K. Lazaruk, P.S. Katsuba, A.A. Leshok, V.B. Vysotsky. *J. Technical Physics.* **85** (2015) 86.

Obtaining and properties of biomagnetic nanoconjugates based on DNA aptamers and magnetic nanoparticles for magnetodynamic cell therapy

A.E. Sokolov^{*1,2}, A.V. Kurilova¹, V.A. Svetlichniy³, D.A. Velikanov², A.V. Sherepa²,
M.N. Volochaev², D.A. Goncharova³, A.V. Shabalina³

¹ Siberian Federal University, 79 Svobodny Prospect, 660041 Krasnoyarsk, **Russia**

² Kirensky Institute of Physics, Federal Research Center KSC SB RAS, Akademgorodok 50, bld. 38, Krasnoyarsk 660036, Russia

³ Siberian Physical-Technical Institute of Tomsk State University, Novosobornaya sq., 1, Tomsk 634050, Russia

*e-mail: alexey@iph.krasn.ru

Recently, in the field of molecular cell surgery of malignant tumors is increasingly common term theranostics, it combined diagnosis and therapy. For these purposes it is widely used bionanoconjugates consisting of magnetic nanoparticles and DNA- aptamers. For the development of targeted drugs a vital role plays research of properties used bionanoconjugates.

A review of study of magnetic, optical and magneto-optical properties of some kinds bionanoconjugates consisting of different shapes metals nanoparticles immobilized DNA-aptamers for Ehrlich ascites carcinoma cell is given.

The magnetic core bionanoconjugates provides required magnetic properties for the provision of physical exposure to a low frequency alternating magnetic field. Magnetomechanical cell disruption using nano and micro-sized structures is a promising biomedical technology using for noninvasive elimination of diseased cells. It applies alternating magnetic field for ferromagnetic microdiscs making them oscillate and causing cell membrane disruption with following cell death by apoptosis [1,2]. It is shown that it is possible to replace microdiscs with spherical nanoparticles decorated with gold.

One of such nanoparticles is the Fe and Ni nanoparticles decorated with Au studied in this work. Nanoparticles were obtained by pulsed laser ablation of a bulk gold target in a solution of 3-d electroplating nanoparticles produced by Advanced Powder Technologies LLC with an average particle size of 50-110 nm (TU 1791-003-36280340-2008).

The morphology of the obtained nanoparticles was studied using a Hitachi TM 5500 transmission electron microscope. The images show that the samples are coated with gold particles with an average size of 16–18 nm (for a

Fe-Au sample, an average Fe size of about 70 nm), 7–8 nm (for Ni -Au, the average size of Ni is about 65-75 nm).

Measurements of the magnetization of the samples were carried out at room temperature using a vibration magnetometer, developed at the IP SB RAS. The presence of a hysteresis loop indicates that the samples are ferrimagnetic.

The absorption spectra of nanoparticles in the range of 200–750 nm were recorded on a SKD-2 MUF dichrograph, with a spectral resolution of 3 nm. In the spectra obtained, peaks characteristic of Fe and Ni nanoparticles are observed, the absorption peak characteristic of Au nanoparticles is absent in the 520 nm region.

Small sizes of particles and their compounds and the possibility of varying their shape are often useful when exposed to an electromagnetic field, especially, if the particles in one way or another react to its change (heating, change of magnetization orientation, etc.) But depending on the modification of ion compounds, the synthesis method, and coatings, the nanoparticles can have chemical, optical, and magneto-optical properties are different from each other.

Nanoparticle's morphology were studied with a Hitachi TM 5500 transmission electron microscope equipped with an EDS attachment.

The relationship of shape, size, magnetic properties of bionanoconjugates and the possibility of their use in theranostics is discussed.

References

- [1] Zamay Tatiana, Kolovskaya Olga S., Sokolov Alexey E., et.al, *Nucleic Acid Therapeutics* **27** (2017) 105.
- [2] P.D. Kim, S.S. Zamay, A.E. Sokolov, et.al, *Doklady Biochemistry and Biophysics* **466** (2016) 66.

A new efficient luminescent chemosensor of gaseous amines for medicine and food safety

A.N. Galkina^{*1}, A.A. Leonov¹, R.V. Romashko^{1,3}, JIANG Jyh-Chiang²

¹ Institute of Automation and Control Processes of FEB RAS, 5 Radio St., Vladivostok 690041, Russia

² National Taiwan University of Science and Technology, Taipei 10607, Taiwan

³ Far Eastern Federal University, 8 Sukhanova St., Vladivostok 690950, Russia

*e-mail: galkina@iacp.dvo.ru

The development of sensitive and selective gas sensor systems for detecting chemical and biological agents is a priority of many research groups of scientists since they involve issues of safety of industrial objects. In this field of research, a special televised pay sensor systems based on carbon nanotubes. The analysis of the works in this direction has shown that the functionalization of nanotubes has become a classic approach in creating sensor materials based on carbon nanotubes and hybrid systems polymer/carbon nanotubes become effective and selective materials for gas sensing with a wide range of detected gases [1]. The most promising in our opinion is the functionalization of carbon nanotubes photochromic polymeric materials with thermal stability [2, 3]. This approach to functionalization allows obtaining optically active and thermally stable material, which expands its range of application and functions of the sensor based on it.

It is known that the decomposition of protein compounds of meat, fish and other marine animals in the environment is highlighted in the breakdown products of volatile amines. So check the concentration of free amines in the product can serve as a marker of their quality and freshness. Previous our studies have shown [4] that the interaction of a complex material based on functionalized single-walled carbon nanotubes (poly-SWCNTs) with gaseous amines leads to a change in the optical characteristics in the UV and visible wavelength range, which makes it applicable and compatible with continuous monitoring of biological processes and events [5]. This paper presents the latest advances in luminescent chemosensors for medicine and food safety. The contents consist of the optical and sensory characteristics of a complex material based on functionally single-wall carbon nanotubes, using the poly-SWCNTs system as a sensitive marker of the quality of protein products during storage under different conditions. In addition, some latest field deployment case studies and data analysis are introduced.

Studies of the sensor response of films of poly-SWCNTs to determine the freshness of the protein products (fish, crab meat) in the store, with standard conditions (+20C), as well as the conditions of refrigeration (+4C) and freezer storage (-24C). The test systems under study showed a good correlation of the luminescent response with the storage time and storage conditions and can be used to study the quality and suitability of food protein products during their storage. So for samples freezer storage (-24C), which implies preservation of quality products for a long time, did not observe changes in the spectrum of the luminescence of poly-SWCNTs. The correlation between the quality of the test object and touch response: there is no breakdown of proteins, no free amines in the environment,

not recorded changes in the intensity of the private band of the luminescence of poly-SWCNTs. Processes of refrigeration temperatures (+4C) slow down the speed of the decay products of protein origin but are not the optimum way to store them. Therefore, a slow increase of intensity in his own band luminescence poly-SWCNTs, as touch responsiveness on the presence of free amines in the test system corresponds to the slow decay of the protein products. Moreover, these test systems have allowed identifying another marker of the "freshness" of the product, namely, a slowly growing, additional maximum luminescence at wavelengths $\lambda=550-552$ nm, due to the peroxidation process of the lipids and phospholipids that are also present in protein foods. The results of the last block of experiments perfectly correlated with the real picture of the spoilage of food protein products. In terms of storage at +20C meat fish and seafood spoils in less than a day. This block of the experiment, we recorded a rapid increase of the intensity maximum of the private band of the luminescence of poly-SWCNTs ($\lambda=432$ nm) as a sensory response to the rapid increase in the concentration of free amines, as well as a sharp increase in the intensity of luminescence in blue-green region of the spectrum characteristic of an intensive process of lipid peroxidation.

Thus, this dynamic process is applicable to study the process of spoilage of protein foods and can be a marker of their quality and freshness. It was possible to single out one more marker of freshness, "blue-green glow", caused by the process of peroxidation of lipids and phospholipids, which are also present in protein products, that is very relevant because allows you to track the beginning of the process of spoiling meat and fish with other negative markers. In addition, the materials have application prospects in such areas as medicine and food safety.

Acknowledgments

Financial support from FEB RAS grant № 17-MST-007

References

- [1] H. Choi, J. Lee, Ki-Y. Dong. *Macromolecular Research* **20** (2012) 143.
- [2] F. Untem, E. Botelho. *J. Nanosci. Nanotechnol.* **14** (2014) 5145.
- [3] Chih-Chiao Yang, Yung-Chih Lin. *Polymer* **55** (2014) 2044.
- [4] A.N. Galkina, A.A. Sergeev. *Defect and Diffusion Forum* **386** (2018) 244.
- [5] T. Han, Jacky W. Y. *Chem. Commun.* **49** (2013) 4848.

Laser printing of chiral silicon nanoprotusions by asymmetric donut-shaped femtosecond pulses

S.A. Syubaev^{*1,2}, A.A. Kuchmizhak^{1,2}, A.P. Porfirev³

¹Institute of Automation and Control Processes of FEB RAS, 5 Radio St., Vladivostok 690041, Russia

²Far Eastern Federal University, 8 Sukhanova St., Vladivostok 690950, Russia

³Samara National Research University, Moskovskoe shosse, 34, Samara 443086, Russia

*e-mail: [corresponding author trilar@bk.ru](mailto:corresponding_author_trilar@bk.ru)

To date, the concept of “structured” light was directly associated with optical vortex (OV) beams carrying orbital angular (OAM) and spin angular momenta (SAM). Owing to specific character of OV interaction with matter, such beams are widely employed for pulsed laser processing of various materials to form chiral nanostructures [1].

Laser pulses with nanosecond duration were mainly explored for formation of chiral nanostructures, while much shorter femtosecond (fs) radiation was believed to be not capable of producing helical morphology as one can expect in the case of explanation of this phenomenon by either OAM transfer formalism [2] or helical surface tension gradient [3]. Noteworthy, Rahimian *et al.* recently demonstrated chiral-shaped Si nanocones using fs donut-shaped OV pulses [4], although authors did not highlight the helical shape of their structure evident from the presented electron microscopy images.

Here, we provide clear explanation unraveling formation of recently reported chiral Si nanostructures as a consequence of uneven helical flow of laser-melted Si material caused by asymmetry of initial intensity and temperature pattern on laser-irradiated Si surface. Specifically, breaking circular symmetry of the irradiating donut-shaped fs-pulse beam was demonstrated to switch the geometry of formed surface nanoprotusions from regular to chiral, while the chirality of the obtained Si nanostructures was found to promote with a degree of asymmetry of the laser beam.

The experiments on chiral Si nanostructures formation were started from conversion of Gaussian-shaped laser pulse, generated by Yb:KGW-based fs laser system, to the donut-shaped laser beam. To do this, the as-generated laser beam was passed through commercial polarization converter (S-waveplate). This element was mounted on a precise 2D motorized translation stage to provide calibrated radial displacement with respect to the center of the laser beam. Such gradual displacement resulted in tailoring symmetry of the generated focal-plane spot intensity distribution. Then, donut-shaped laser pulses were focused onto polished bulk crystalline (100) silicon by microscope objective (Mitutoyo, numerical aperture = 0.14). Every structure was produced under single laser shot.

In our previous demonstrations of chiral nanostructures formation via nanosecond laser ablation we used common noble-metal (Au, Ag) films of variable thickness covering silica glass substrates [3]. Fs “structured” pulse ablation of such metal films, however, doesn’t lead to the formation of chiral structures owing to much stronger acoustic effects initiated by fs-pulse irradiation and resulted in thermo-mechanical spallation of the transiently molten surface layer. In a sharp contrast, single-pulse fs-laser irradiation of

bulk Si target creates a pool of molten material. The surface tension gradient laterally pulls the molten Si towards colder areas, resulting in material accumulation in the area which corresponds to the center of the donut-shaped beam with zero intensity as well as to the periphery of the molten pool producing a circular rim of resolidified material.

This indicates that the “dark” spot at the center of the generated donut-shaped beam governs the formation of the Si nanoprotusion there. To get more insight into formation of this protrusion, we gradually break the ideal circular symmetry of the irradiating donut-shaped fs-pulse. More specifically, the stepwise radial displacement of the S-waveplate center with respect to the center of the Gaussian-shaped laser beam produced corresponding lateral shift of the “dark” spot as well as redistribution of the intensity between beam shoulders. Remarkably, the Si nanoprotusions formed via fs-laser ablation with asymmetric beams acquire chiral shape, while the chirality of the obtained Si nanostructures was found to promote with a degree of asymmetry of the laser beam. Chirality of laser-induced nanoprotusions increases as relative position of the formed protrusion is becoming more distant from the donut center, which correlates with the shift of the “dark” spot with S-waveplate displacement.

Here, we showed formation of chiral nanoprotusions upon direct laser ablation of bulk crystalline silicon wafer with single fs pulses having asymmetric donut-shaped intensity profile. Breaking circular symmetry of the irradiating donut-shaped fs-pulse beam was demonstrated to switch the geometry of formed surface nanoprotusions from regular to chiral, while the chirality of the obtained Si nanostructures was found to promote with a degree of asymmetry of the laser beam. The obtained experimental results explain the formation of previously reported chiral Si nanostructures in terms of uneven helical flow of laser-melted Si material caused by asymmetry of initial intensity and temperature pattern on laser-irradiated Si surface.

Acknowledgements

Authors acknowledge support from Russian Foundation for Basic Research (20-32-70056).

References

- [1] T. Omatsu, K. Miyamoto, et.al. *Adv. Opt. Mater.* **7** (2019) 1801672.
- [2] K. Toyoda, et.al. *Nano Lett.* **12** (2012) 3645.
- [3] S. Syubaev, A. Zhizhchenko, O. Vitrik, et.al. *Appl. Surf. Sci.* **470** (2019) 526.
- [4] M. Rahimian, F. Bouchard, et.al. *APL Photonics* **2** (2017) 086104.

Photoluminescence and features of the defective structure of nominally pure lithium niobate crystals

M. Smirnov¹, N.V. Sidorov¹, N.A. Teplyakova¹, M.N. Palatnikov¹, A.V. Syuy^{*,2}

¹ Tananaev Institute of Chemistry and Technology of the Federal Research Centre "Kola Science Centre of the Russian Academy of Sciences», 26a Akademgorodok, Apatity 184209, Russia

² Far Eastern State Transport University, 47 Seryshev St., Khabarovsk 680021, Russia

*e-mail: alsyuy271@gmail.com

This paper presents the results of comparative studies of photoluminescence in a nominally pure congruent crystal ($\text{LiNbO}_{3\text{cong}}$), as well as in crystals whose composition is close to stoichiometric, obtained by two technologies: from a melt with 58.60 mol. % Li_2O ($\text{LiNbO}_{3\text{stoich}}$) and HTTSSG (High temperature technology top speed solution growth) from congruent melt with the addition of flux 6 wt. % K_2O ($\text{LiNbO}_{3\text{stoich}}$ (6 wt. % K_2O)) [1, 2].

In the photoluminescence spectra of $\text{LiNbO}_{3\text{stoich}}$, $\text{LiNbO}_{3\text{stoich}}$ (6 wt. % K_2O) and $\text{LiNbO}_{3\text{cong}}$ crystals obtained from the sample volume, a halo is observed in the range from 380.0 to 650.0 nm, as well as a general increase in the luminescence intensity in the long-wavelength region (> 700.0 nm). The halo is complex and contains a broad band with a main maximum at 527.0 nm ($\text{LiNbO}_{3\text{stoich}}$), 613.0 nm ($\text{LiNbO}_{3\text{cong}}$) and 612.0 nm $\text{LiNbO}_{3\text{stoich}}$ (6 wt. % K_2O) and several incidental maxima. Table 1 shows the quantitative characteristics of the photoluminescence spectra of the studied LiNbO_3 single crystals. Luminescence centers in the form of Nb_{Li} defects in LiNbO_3 crystals correspond to the maxima of the luminescence bands at 510.0–520.0 nm [3]. The intensity of luminescence bands with maxima at 510.0–527.0 nm increases in the series of $\text{LiNbO}_{3\text{stoich}}$, $\text{LiNbO}_{3\text{stoich}}$ (6 wt. % K_2O), and $\text{LiNbO}_{3\text{cong}}$ crystals, which indicates a sequential increase in the number of point defects in Nb_{Li} in this series of crystals. However, the calculation of the number of Nb_{Li} defects showed their minimum content in the $\text{LiNbO}_{3\text{stoich}}$ (6 wt. % K_2O) crystal.

The maximum luminescence intensity at 611.0–613.0 nm is associated with the presence of a complex defect in the form of a bipolaron $\text{Nb}_{\text{Nb}}^{4+}\text{-Nb}_{\text{Li}}^{4+}$. One of the theoretically calculated values of the optical transitions for the bipolaron ($\text{Nb}_{\text{Nb}}^{4+}\text{-Nb}_{\text{Li}}^{4+}$) is 2.0 eV (620.0 nm) [4]. If we assume that the radiation intensity of an individual luminescence center in the first approximation depends only on the concentration of a particular type of defect, then the number of luminescence centers of this and other defects increases as the ratio Li/Nb decreases. However, this result is not consistent with the calculated Li/Nb ratio in the studied crystals. Therefore, it can be assumed that the transfer of absorbed energy between the centers of luminescence is observed in the crystals under study, which causes differences with the experimental data obtained by studying the IR spectra and the fundamental absorption edge.

In addition, the optical and electrical properties of lithium niobate crystals are strongly affected by the presence of OH groups in the structure, which occupy oxygen ion sites. The calculation results show that the concentration of OH groups in the $\text{LiNbO}_{3\text{cong}}$ crystal is

maximum, and the number of OH groups in the $\text{LiNbO}_{3\text{stoich}}$ crystal (6 wt. % K_2O) is intermediate between their number in $\text{LiNbO}_{3\text{cong}}$ and $\text{LiNbO}_{3\text{stoich}}$ crystals.

Studies of the photoluminescence spectra of $\text{LiNbO}_{3\text{cong}}$, $\text{LiNbO}_{3\text{stoich}}$ (6 wt. % K_2O) and $\text{LiNbO}_{3\text{stoich}}$ crystals obtained upon excitation by the 325.0 nm line from the crystal volume show that photoluminescence is not unambiguously dependent on stoichiometry and crystal production technology. In the $\text{LiNbO}_{3\text{cong}}$ crystal, the dominant luminescence centers are the centers in the form of Nb_{Li} defects, which are the deepest electron traps. In $\text{LiNbO}_{3\text{stoich}}$ crystals (6 wt. % K_2O) and $\text{LiNbO}_{3\text{stoich}}$, point defects of Nb_{Li} are practically absent, but the luminescence of the corresponding luminescence centers is quite intense. According to the calculations, an increased content of OH groups is observed in the structure of these crystals. This fact allows us to make the assumption that the contribution to luminescence can be made not only by the main types of luminescence centers in the form of point defects (when the main and impurity cations are not in their positions), but by the luminescence centers in the form of complex defects with the participation of hydrogen atoms.

Acknowledgements

Work supported by RFBR № 18-03-00231.

References

- [1] K. Lengyel, A. Peter, L. Kovacs, G. Corradi, L. Palfavi, J. Hebling, M. Unferdorben, G. Dravecz, I. Hajdara, Zs. Szaller, K. Polgar, *Appl. Phys. Rev.* **2** (2015) 040601.
- [2] R.N. Balasanyan, E.S. Vartanyan, V.T. Gabrielyan, L.M. Kazaryan, A method of growing lithium niobate crystals. Auth. certificate №845506 from 0.6.03.81 r. Priority from 233.03.79. Open Publishing Formula 27.02.2000. (In Russian)
- [3] M.N. Palatnikov, N. V. Sidorov, Some fundamental points of technology of lithium niobate and lithium tantalite single crystals, In: *Oxide electronics and functional properties of transition metal oxides*, NOVA Science Publishers, USA, 2014, pp. 31-168.
- [4] M.H.J. Emond, M. Wiegel, G. Blasse, R. Feigelson, *Mat. Res. Bull.* **28** (1993) 1025.
- [5] I.Sh. Akhmadullin, V. A. Golenishchev-Kutuzov, S. A. Migachev, *Phys. Sol. St.* **40** (1998) 1012.

Structural features and optical properties of nominally pure crystals of lithium niobate grown from a charge doped with boron

N.V. Sidorov¹, R. Titov¹, N.A. Teplyakova¹, M.N. Palatnikov¹, A.V. Syuy^{*,2}

¹ Tananaev Institute of Chemistry and Technology of the Federal Research Centre "Kola Science Centre of the Russian Academy of Sciences», 26a Akademgorodok, Apatity 184209, Russia

² Far Eastern State Transport University, 47 Seryshev St., Khabarovsk 680021, Russia

*e-mail: alsyuy271@gmail.com

At present, LiNbO₃ crystals that are near stoichiometric composition are grown in air in two main ways: from a N₂O₅-Li₂O melt with 58.60 mol. % Li₂O (LiNbO₃stoich) and from a congruent melt with ~ 6 wt. % alkaline solvent (flux) K₂O (HTTSG method - High temperature top speed solution growth) - LiNbO₃: (6 wt. % K₂O). The method of growing from a melt with 58.60 mol. % Li₂O is currently practically not used in industry due to the high heterogeneity of the composition and refractive index of the grown crystal along the growth axis. The HTTSSG method allows single crystals of a high degree of compositional homogeneity to be obtained from a congruent melt. However, this method of obtaining stoichiometric single crystals is much more complicated.

In recent years, we have been developing a method for growing LiNbO₃ crystals close to the stoichiometric composition from a congruent melt using boron compounds. In this work, we studied the nominally pure LiNbO₃ crystals obtained by us with different Li/Nb ratios, grown from a congruent melt doped with boron, using a charge of different genesis. The research results were compared with the results obtained for LiNbO₃stoich and LiNbO₃cong crystals.

The boron element does not enter the structure of the lithium niobate crystal, since the LiNbO₃ phase does not have a solubility region of boron in the solid state. But boron compounds can be used as a flux. The only crystallizing phase from the boron-containing melt is LiNbO₃. At the same time, during crystallization of LiNbO₃, an increase in the concentration of boron in the melt will occur, leading to an increase in the viscosity of the melt and a decrease in the crystallization temperature. A calculation based on the Curie temperature of the Li/Nb ratio and the concentration of Nb_{Li} defects in the studied LiNbO₃ crystals shows that with an increase in the boron concentration in the charge, an increase in the Li/Nb ratio in the grown crystals is observed with a simultaneous decrease in the number of Nb_{Li} defects. It can be assumed that boron-containing polyanions in the melt form stable covalent bonds with niobium-containing polyanions, thereby binding an excess of niobium.

The stoichiometric approximation of the LiNbO₃:B³⁺ crystal structure is confirmed by Raman data, which indicate an increase in the alternation order of the main, doping cations and vacancies along the polar axis, as well as the data of IR absorption spectra in the region of valence vibrations of OH groups, Table I. Compared with a congruent crystal, the widths of the components of the absorption band of the IR spectrum of LiNbO₃stoich and LiNbO₃:B³⁺ crystals (0.12 and 0.18 wt. %) are narrower,

Table. I, which indicates a greater ordering of the proton sublattice in a stoichiometric crystal and crystals grown from a melt containing boron, in comparison with a congruent crystal.

Table I. Quantitative characteristics (frequency ν , cm⁻¹, width S , cm⁻¹, intensity I , arb. units) of Raman spectra in the scattering geometry $Y(ZX) \bar{Y}E(TO)$ in the region of cation vibrations in oxygen octahedra and in IR absorption spectra in the region of stretching vibrations of OH groups in LiNbO₃stoich, LiNbO₃cong, LiNbO₃:B³⁺ crystals (0.12 and 0.18 wt. %)

LiNbO ₃ stoich		LiNbO ₃ cong		LiNbO ₃ :B (0.12 wt. %)		LiNbO ₃ :B (0.18 wt. %)					
The parameters of the lines in the Raman spectra											
ν	S	ν	S	ν	S	ν	S				
152	7	152	12	152	9	152	10				
240	9	240	11	240	10	240	11				
268	10	268	14	270	13	270	13				
324	10	324	13	324	14	323	16				
Line parameters in IR absorption spectra											
ν	I	S	ν	I	S	ν	I	S			
3	0.1	4	3	0.1	1	3	0.10	1	3	0.14	1
4	4	.	4	2	6	4	0	6.	4	2	2.
6		2	7		.	6		2	6		5
5		8	0		4	6			7		
3	0.1	5	3	0.4	2	3	0.13	2	3	0.11	1
4	1	.	4	9	4	4	0	0.	4	9	9.
8		3	8		.	8		1	8		9
0		7	3		8	1			0		
3	0.0	8	3	0.3	2	3	0.10	2	3	0.28	2
4	7	.	4	3	7	4	4	2.	4	8	7.
8		1	8		.	8		6	8		2
8		8	6		1	5			5		

It was shown that by structuring the congruent melt with a nonmetallic element by boron, the number of point defects in the Nb_{Li} cationic sublattice can be effectively controlled in a nominally pure LiNbO₃ crystal, thereby controlling the Li/Nb ratio and bringing the crystal structure closer to a stoichiometric structure with a constant refractive index along the growth axis. In addition, it was shown that boron compounds reduce the content of uncontrolled metallic impurities in the crystal, including multiply charged transition metal impurities, which significantly affect the photorefractive effect.

Acknowledgements

Work supported by RFBR № 19-33-90025.

Control of single crystal silicon wetting by laser ablation and fluoropolymer deposition

S.V. Starinskiy^{*1,2}, A.I. Safonov^{1,2}, A.A. Rodionov^{1,2}, Yu.G. Shukhov¹, A.V. Bulgakov^{1,3}

¹ S.S. Kutateladze Institute of Thermophysics SB RAS, 1 Lavrentyev Ave, 630090 Novosibirsk, Russia

² Novosibirsk State University, Pirogova Str. 2, 630090 Novosibirsk, Russia

³ HiLASE Centre, Institute of Physics, Czech Academy of Sciences, Za Radnicí 828, 25241 Dolní Břežany, Czech Republic

*e-mail: starikhbz@mail.ru

The extreme wettability (superhydrophobicity and superhydrophilicity) of surface is very promising phenomena for different application [1–3]. Much attention is paid to biphilic materials combined such wettability properties on small spatial scales. It is very important to find the flexible method to local obtain the stable superhydrophobic and superhydrophilic patterns. In present work we propose three-stage approach for local variation of the wetting properties of silicon in a wide range of parameters. The first stage is gentle laser treatment of silicon surface [4]. It was found that the self-organized microstructure on single crystal silicon may be obtained by multipulse nanosecond IR irradiation in very narrow range of condition: laser fluence 3-5 J/cm², number of pulses 25-75. In this case the morphology of central part of laser spot is mesh of orthogonal cracks (the step is 40-50 mkm) and the microhillocks form on its cross. Formation of cracks weakly depended on laser treatment conditions and surrounding. However, the microhillocks forms only in oxygen content background with pressure around the atmospheric. It was analyzed the dependence of silicon ablated mass on background pressure. It was found that at pressures above 60 Pa the mass of the irradiated target remains unchanged. The increase of oxygen partial pressure lead to formation lager hillocks. The processing of some area at founded regimes for microhillock formation lead to contact angle transition of silicon from 55° to 0°. It is found that such bright properties are not achieved when the surface is treated by a green laser or in a inert background.

The second stage is deposition of fluoropolymer films on silicon surface by hot wire chemical deposition. The deposition parameters (temperature of wire and substrate, pressure of gas and so on) determine the film morphology and structure [5] on which the resistance of the coating and its hydrophobicity strongly depend. As a rule, the developed morphology of fluoropolymer provides the hydrophobic properties up to superhydrophobicity however the increase of contact angle lead to loss of durability. The most durable coating has a smooth and continuum morphology. It was found that gradual deposition of fluoropolymer on single crystal silicon in condition providing high stability of coating lead to gradual change of the contact angle from 55° to 120°. The finished contact angle closed to value for bulk fluoropolymer are achieved at 35 nm of coating thickness. We suggest that this saturation effect is due to the limitation of the action of the van der Waals forces between the water molecules and the substrate. Preliminary laser processing of silicon to achieve the superhydrophilicity of surface allowed us to expand the range of water contact angles for our samples to ~ 0° - 170°.

A plateau is reached with a twice longer deposition time of a fluoropolymer of ~ 300 s. This is due to the thinning of the film deposited on a rough surface (roughness $r = 1.96$) for the sample after laser treatment. Scanning electron microscopy of the surface showed that the selected deposition modes are characterized by identity of fluoropolymer and treated silicon morphology at the nano- and microscale both. It was found that the expansion of contact angles range are in a good agreement with the Wenzel theory [6], taking into account that the thickness of the fluoropolymer coating decreases in proportion to the roughness of the material for a given deposition time.

The third step is local laser removal of the fluoropolymer from the obtaining samples which have the superhydrophilic sublayer with superhydrophobic coating. This allows us to give to material the properties of contrasting wettability with a sharp spatial transition from superhydrophobicity to superhydrophilicity. The conditions for laser ablation of a fluoropolymer without influence on the superhydrophilic characteristics of the sublayer were found. The possibility of suggested three-stage approach demonstrated by design of superhydrophobic samples with local high adhesive force for reliable fixation of water droplet with spherical form.

Acknowledgements

The work was supported by the Russian Science Foundation (grant number 18-79-10119 control the wettability properties) and by the grant of president of the Russian Federation (project MK 2404.2019.8, analysis of silicon laser ablation products).

References

- [1] Z. Xue, Y. Cao, N. Liu, L. Feng, L. Jiang, J. Mater. Chem. A. **2** (2014)2445
- [2] J.L. Liu, X.Q. Feng, G. Wang, S.W. Yu, J. Phys. Condens. Matter. **19** (2007) 356002.
- [3] F. Su, K. Yao, ACS Appl. Mater. Interfaces. **6** (2014)8762
- [4] S. V. Starinskiy, A. V. Bulgakov, E.Y. Gatapova, Y.G. Shukhov, V.S. Sulyaeva, N.I. Timoshenko, A.I. Safonov, J. Phys. D. **51** (2018) 255307
- [5] A.I. Safonov, V.S. Sulyaeva, E.Y. Gatapova, S. V. Starinskiy, N.I. Timoshenko, O.A. Kabov, Thin Solid Films. **653** (2018) 165.
- [6] Drelich, A. Marmur, Surf. Innov. **2** (2014) 211.

Laser-printed plasmonic metasurfaces for enhancement of second harmonic generation

A.B. Cherepakhin^{*1}, I.I. Shishkin¹, P.M. Voroshilov¹, A.A. Kuchmizhak^{2,3}, S.V. Makarov¹

¹Information Technologies, Mechanics and Optics University, 49 Kronverksky Pr., St. Petersburg, 197101, Russia

²Institute of Automation and Control Processes of FEB RAS, 5 Radio St., Vladivostok 690041, Russia

³Far Eastern Federal University, 8 Sukhanova St., Vladivostok 690950, Russia

*e-mail: artem.cherepakhin@metallab.ifmo.ru

One of the fundamental parts of nanophotonics is the problem of localizing light in sub-wavelength volumes. Conventional methods for solving this problem are to use the unique properties of surface plasmon polaritons (SPPs). A wide range of plasmonic applications was found for many materials and objects that can support such excitations [1,2]. In addition to the capabilities of detecting, modulating and directing light, the substantial boost in field intensity by extreme light concentration can lead to facilitation of non-linear effects such as second harmonic (SH) generation. SH intensity at metal interfaces can be enhanced by more than an order of magnitude through coupling of the pump light to SPPs. Random and ordered nanostructures made of plasmon-active materials were shown to provide reliable way for SPP excitation thus giving rise to SHG effect [3,4].

However, mentioned periodically arranged nanostructures are typically fabricated using expensive and time-consuming lithography-based techniques limiting their applicability for realistic devices. Here, we present a novel plasmonic platform representing periodically arranged Au nanobumps produced by cheap and high-performing direct laser printing. Arrangement of such unique nanostructures supports lattice-type plasmon resonances tailored by either array period p or nanobump diameter d . By optimizing both parameters we achieved at least 35-fold more enhanced SH yield being compared to smooth Au film.

We used the following procedure to fabricate Au nanobump arrays. First, using electron beam evaporation 100-nm thick Au film was deposited on pre-cleaned smooth glass substrate. Then using direct laser printing method [5] fabricated films were irradiated with the second harmonic ($\lambda = 515$ nm) femtosecond (≈ 200 fs) pulses generated by a solid state laser system. Lens with numerical aperture (NA) 0.42, 20x was used for focusing of laser pulses in air. To achieve a high-speed patterning the samples were arranged on PC-controlled micropositioning platform and scanned by a laser beam at 200 kHz pulse repetition rate. The morphology of the produced nanostructures was characterized by high-resolution scanning electron microscopy.

We used a Yb:YVO₄ pulsed (150 fs) laser with center wavelength at 1049 nm to pump SH yield. A lens with NA=0.33 was used to focus the laser pulses onto the Au nanobump array under normal incidence. The reflected beam was collected through the same lens and after being

passed through two filters to reduce intensity of the pump radiation was analyzed with Horiba LabRAM HR spectrometer.

Results show strong dependents of SHG yield versus main geometric parameter: nanobump period p and diameter d . More specifically, the strongest SH yield was observed at $d=600$ nm and $p=800$ nm providing 35 times more enhanced signal being compared to the smooth Au film, when the pump wavelength is close to the main lattice-type resonance of the nanobump array. Such enhancement correlates also with our theoretical simulation carried out in COMSOL multiphysics software. Dispersion diagram calculated for optimal geometry of nanobump array shows presence of characteristic zone-folded modes close to the SH wavelength. These modes are expected to facilitate SH yield via efficient outcoupling of the generated radiation by plasmonic grating. We also measured the pump-power dependence of the SHG signal giving a slope of 1.87 on log-log plot, that correlates well with expected value of 2 from SH signal.

To summarize, we have observed substantial enhancement of SH yield by laser-printed plasmonic bump array. We found a strong dependence of the magnitude of the SHG to the geometric parameters of the nanobumps. The enhanced SH yield is attributed to the coupling between localized SPPs eigenmodes and zone-folded modes, which was confirmed by electromagnetic simulations of dispersion curves in COMSOL multiphysics software. The proposed plasmonic platform holds for realization of novel nanophotonic devices for efficient control over nonlinear optical response.

Acknowledgements

This work was supported by the Russian Science Foundation (Grant No. 16-12-10165).

References

- [1] Boriskina, S. V.; Ghasemi, H.; Chen, G. *Mater. Today* **16** (2013) 375.
- [2] Schuller, J. A.; Barnard, E. S.; Cai, W.; Jun, Y. C.; White, J. S.; Brongersma, M. L. *Nat. Mater.* **9** (2010) 193
- [3] Lesuffleur, A., Kumar, L. & Gordon, R. *Appl. Phys. Lett.* **88** (2006) 261104.
- [4] Xu, T., Jiao, X., Zhang, G.P. & Blair, S. *Opt. Express* **15** (2007) 13894.
- [5] Pavlov, D., Syubaev, S., Kuchmizhak, A., Gurbatov, S., Vitrik, O., Modin, E. & Lapine, M. *Applied Surface Science*, **469** (2019) 514.

Synthesis and study of the optical properties of branched organosilicon phosphors

M.V. Tutov^{*1,2}, A.Yu. Mironenko².

¹ Far Eastern Federal University, 8 Sukhanova St., Vladivostok 690950, Russia

² Institute of Chemistry of FEB RAS, 159, prosp. 100-letiya Vladivostoka, Vladivostok 690022, Russia

*e-mail: thunderbird87@mail.ru

The development of optical chemical sensors for the determination of metal cations in aqueous media is a dynamically developing area of modern chemistry. At the same time, more and more attention is paid to the synthesis, the study of physicochemical properties and the use of compounds of the dendrimeric structure, due to the unique properties that such compounds possess. Of particular interest are the photochemical and photophysical properties of dendrimers [1].

In this work, synthesis methods were developed, a number of new photoactive compounds of the dendrimer structure containing 2, 4, 6, 8, 12, 16 and 24 chromophore functional groups were obtained and characterized by physicochemical methods (fig. 1).

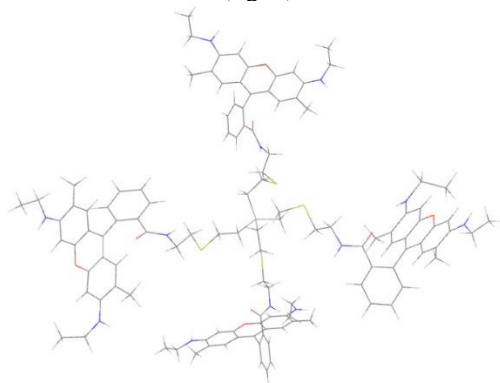


Figure 1. Optimized structure of dendrimer with 4 chromophore functional groups.

It was shown that the interaction of cysteamine hydrochloride with vinyl-functionalized organosilicon compounds, including dendrimer nature, proceeds with practically quantitative yields even in the case of an equimolar ratio of vinyl and thiol groups, which will allow avoiding difficulties at the stage of isolating the target products. It was also shown that the interaction of the obtained cysteamine-functionalized compounds with rhodamine 6G in high yields is possible only in dimethyl sulfoxide in the form of free amines.

It was shown that in this series, there is a strong electronic interaction of peripheral chromophore groups, which determines the change in the optical properties of compounds with an increase in their functionalization.

A nonlinear dependence of the maximum value of the molar absorption coefficient (with excess of hydrochloric acid) on the degree of functionalization of the molecule was established, which indicates the presence of an intramolecular interaction between chromophores (fig. 2).

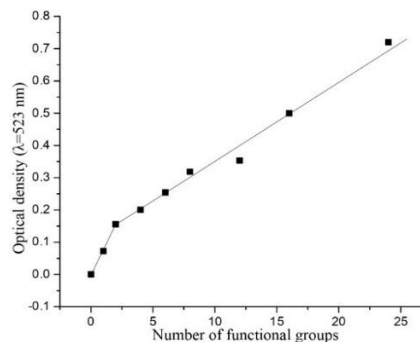


Figure 2. Dependence of absorption on the number of chromophore groups in a molecule.

It was shown that the fluorescence intensity of all compounds, starting from the 4 functionalized derivatives, is approximately at the same level, despite the fact that the amount of light that they absorb differs significantly. The obtained results also indicate the appearance of a new nonradiative relaxation process in the system of chromophores (fig. 3).

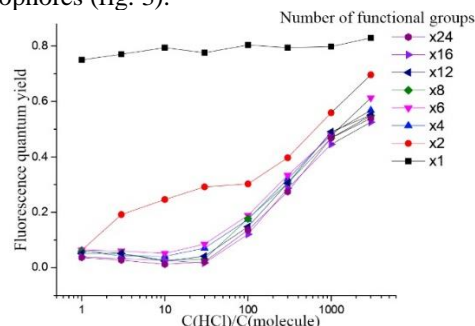


Figure 3. Quantum yield of fluorescence at various degrees of protonation.

The performed quantum mechanical calculations for a molecule with four functional groups confirm effective energy absorption and rapid transfer to the acceptor group.

Acknowledgements

Financial support from Russian Foundation for Basic Research is gratefully acknowledged. The work on the synthesis was performed as a part of the project No. 18-33-00459, the studies of optical and sensing properties were performed as a part of the project No. 18-33-20159.

References

- [1] M.V. Tutov, A.A. Sergeev, P.A. Zadorozhny, S.Yu. Bratskaya, A.Yu. Mironenko. *Sensors and Actuators B: Chemical* **273** (2018) 916.

Visualization of the optical uniformity of rare-earth doped lithium niobate single crystals

O.Y. Pikoul^{*1}, N.V. Sidorov², N.A. Teplyakova², M.N. Palatnikov²

¹ Far Eastern State Transport University, 47 Seryshev str., Khabarovsk 680021, Russia

² Institute of Chemistry and Technology of Rare Elements and Mineral Raw Materials of RUS, 26a Akademgorodok, Apatity 184209, Russia

*e-mail: pikoul2008@gmail.com

Ferroelectric single crystal of lithium niobate is one of the most important and sought-after photorefractive nonlinear optical materials. Lithium niobate is a phase of variable composition with a wide homogeneity region of the phase diagram that effectively allows altering physical characteristics of the crystal by doping and stoichiometry changing [1].

The observation method in converging (or diverging) polarized radiation (the conoscopic method) allows us to study the optical properties of anisotropic crystals, which manifest themselves differently depending on their orientation with respect to the direction of observation and the polarization of the radiation. The radiation is passed through a polarizer, a $\lambda/4$ plate at its various positions, which allows you to change and control the polarization of the radiation, and through the studied crystalline plate. Then changes in the radiation intensity are studied using an analyzer and various optical compensators. Such changes are used to judge the main optical characteristics of anisotropic crystals: birefringence, the number of optical axes and their orientation, rotation of the plane of polarization, dichroism, as well as optical anomalies and crystal defects [1-5].

The advantages acquired by the conoscopic method in connection with the advent of lasers were manifested primarily in the ability to observe on the large screen and explore the conoscopic patterns of significant aperture, high contrast and resolution, as well as mathematically process them. Laser conoscopy has acquired particular information for the investigation of subtle structural distortions, both intrinsic and induced by laser radiation in photorefractive nonlinear optical crystals. It has become possible to use laser conoscopy to study the fine features of the structure, the effect of photorefractive, nonlinear optical effects in combination with other research methods: Raman scattering, photoinduced (photorefractive) light scattering, electron spectroscopy, etc., significantly supplementing the data of these methods [4].

The high sensitivity of conoscopic patterns to structural defects and optical anomalies of the material makes the conoscopy method promising for monitoring the optical quality of crystals in industrial synthesis [4]. When illuminating the lithium niobate crystal plate placed between the polarizer and the analyzer with a conical radiation beam, an interference (conoscopic) pattern is observed. For visual observation of defects in the grown crystals was applied to the experimental setup [3], in which the single crystalline sample was mounted between crossed polarizer and analyzer on the movable XY stand, allowing you to scan the laser beam perpendicular to the optical axis the entire plane of the input face and get a lot conoscopic

patterns, corresponding to different portions of the cross section of the investigated sample. Diffuser placed close to the input face of the sample.

In the absence of internal defects conoscopic pattern of a single crystal of lithium niobate at each point of the input face is a system of concentric black and light rings-isochrome centered on the axis of the system with black "Maltese cross", consisting of two branches-isogyres. At constant radius of each ring-isochrome conoscopic pattern and lack of enlightenment in the center of the black "Maltese cross" make a conclusion about the optical homogeneity of the crystal at a given point of the input face in the direction of scanning and the absence of anomalous birefringence. The lithium niobate crystal under ideal conditions, is uniaxial, but under the influence of stresses that occur during alloying and thermal history of obtaining a single crystal in a plane perpendicular to its optical axis, can be acquired abnormal does not, which is evident when viewed in converging polarized radiation in the form of distortion isochrome and divergence isogyres by the angle $2V$, which characterizes the deformation of the optical indicatrix.

The "non-photorefractive" impurities (optical damage resistant) include cations (Mg^{2+} , Zn^{2+} , B^{3+} , In^{3+} , Ta^{5+} , etc.) that do not change their charge in the crystal under the influence of light, on the other hand, such doping leads to a high structural heterogeneity of the crystal. The effect of the alloying element on the properties of lithium niobate single crystals is often spasmodic. This type of concentration dependence of the properties is called the "concentration threshold". Moreover, in the general case, in doped lithium niobate crystals there can be several concentration thresholds, in the region of which the characteristics of the melt and crystals grown from it can experience anomalous behavior. The threshold values for divalent ions Mg^{2+} and Zn^{2+} are, respectively, 5.5 and 7.5 mol. %.

The results of a study of the optical homogeneity of crystals by laser conoscopy showed the presence of two types of conoscopic patterns - characteristic of a uniaxial crystal, as well as conoscopic patterns with signs of anomalous optical biaxiality.

Acknowledgements

Work supported by RFBR № 19-33-90025.

References

- [1] N. Sidorov *et al.*, *Optik* **126** (2015) 1081.
- [2] M. Geday, A. Glazer. *J. Appl. Cryst.* **35** (2002) 185.
- [3] L. Dumitrascu, *et al.* *J. Appl. Cryst.* **42** (2009) 878.
- [4] O. Pikoul. *J. Appl. Cryst.* **43** (2010) 949.
- [5] O. Pikoul. *Optik* **161** (2018) 146.

Properties of Bi and BiSb nanodimensional layers in THz frequency range

I.L. Tkhorzhevskiy^{*,1}, A.V.Asach¹, A.S. Tukmakova¹, E.S. Makarova¹, N.S. Kablukova^{1,2},
P.S. Demchenko¹, D.V. Zykov¹, A.D. Zaitsev¹, A.V. Novotelnova¹, M.K. Khodzitsky¹

¹ ITMO University, Kronverkskiy str. 49, Saint-Petersburg 197101, Russia

² State University of Industrial Technologies and Design, Bolshaya Morskaya str. 18, Saint-Petersburg 191186, Russia

*e-mail: tkhorzhevskiy.ivan.i@gmail.com

Research of optical and galvanomagnetic properties of Bi and BiSb thin films has been carried out. Influence of film thickness, antimony content and a substrate material on these properties is studied.

Due to their unusual properties, bismuth-type semimetals are used in various fields, and they are promising for application in THz photonics systems such as single-pixel detection for contactless diagnostics[1-3] as well as for security systems [4,5] The research interest in bismuth is also due to its thermoelectric properties.

The photoelectric and electrophysical properties of structures based on nanoscale bismuth layers and bismuth layers with different antimony contents on dielectric substrates are considered. Transparent mica and polyimide were used as the dielectric substrate.

Effective optical and galvanomagnetic properties of bismuth thin films were obtained in the thickness range from 10 to 150 nm.

The studies were performed by the method of THz time-domain spectroscopy in the frequency range of 0.2-1.0 THz.

The dynamical conductivity of thin-film alloys non-linearly depends on the antimony concentration and is determined by their band structure. The increase of conductivity is observed for more thick films and in case of mica substrate and is associated with lower scattering rates. With increasing of THz signal frequency, the real part of sheet conductivity tends to decrease, while the imaginary one has some peak value (in accordance with Drude model). The variation of antimony concentration allows to tune the mentioned spectra.

It is shown that thin-film structures based on semimetallic bismuth and a solid solution of bismuth and antimony are promising for use in THz conversion optics. Based on them, broadband devices (for example, masking media) can be built. They can be used as hyperbolic metamaterials.

Acknowledgments

This research was funded by Russian Science Foundation, grant number 19-72-10141.

References

- [1] K.I. Zaytsev, K.G. Kudrin, S.A. Koroleva, I. N. Fokina, S.I. Volodarskaya, E.V. Novitskaya, S.O. Yurchenko, Phys. Conf. Ser. **486** (2014) 012014.
- [2] X. Yang, X. Zhao, K. Yang, Y. Liu, Y. Liu, W. Fu, Y. Luo, Trends Biotechnol. **34**(10) (2016) 810.
- [3] Hyunyong Choi, Joo-Hiuk Son Terahertz Imaging and Tomography Techniques. In Terahertz Biomedical Science and Technology; Joo-Hiuk Son; CRC Press; Boca Raton, USA 2014 p 47.
- [4] H. Hoshina, Y. Sasaki, A. Hayashi, C. Otani, K. Kawase, Appl. Spectrosc. **63**(1) (2009) 81.
- [5] J. F. Federici, B. Schulkin, F. Huang, D. Gary, R. Barat, F. Oliveira, D. Zimdars, Semicond. Sci. Tech. **20**(7) (2005) 266.

Fabrication of laser-induced periodic surface structures for advanced sensing applications

Eugeny Mitsai^{*1}, Alexander Dostovalov^{2,3}, Kirill Bronnikov^{2,3}, Aleksandr Kuchmizhak^{1,4}

¹ Institute of Automation and Control Processes of FEB RAS, 5 Radio St., Vladivostok 690041, Russia

² Institute of Automation and Electrometry of the SB RAS, 1 Acad. Koptuyug Ave., 630090 Novosibirsk, Russia

³ Novosibirsk State University, 2 Pirogova St., 630090 Novosibirsk, Russia

⁴ Far Eastern Federal University, 8 Sukhanova St., Vladivostok 690950, Russia

*e-mail: mitsai@dvo.ru

Nowadays silicon micro- and nanostructures find many applications in various fields of science and industry. A promising direction is the fabrication of silicon laser-induced periodic surface structures (LIPSS, ripples), which are a universal phenomenon that provides a simple way of surface functionalization and finds many applications such as structural color, wetting, cell growth, tribology and Surface Enhanced Raman Scattering [1]. In this paper, we describe the fabrication of silicon ripples.

Amorphous Si (a-Si) films of variable thicknesses (180 to 370 nm) were deposited onto a borosilicate glass substrate by magnetron sputtering and used as a sample for direct laser nanotexturing. LIPSS were fabricated by “Pharos” femtosecond laser pulses at constant pulse repetition rate of 0.2 MHz. The output Gaussian-shaped laser beam laser was first converted to astigmatic Gaussian beam using a cylindrical concave lens and then was focused onto the sample surface via a convex lens yielding in elliptical focal spot. Laser processing of the sample surface was performed at variable pulse energies (between 1.15-1.65 mJ) and scanning speeds (between 1 to 100 mm/s) at single pass regime, where the electric-field polarization vector was oriented parallel to the scan direction [2].

Surface morphology of the laser-processed areas was carefully characterized using scanning electron microscopy (Ultra 55+, Carl Zeiss). We show that depending on the thickness of the initial a-Si film, the pulse power of the femtosecond laser and scanning speed, the resulting surface morphology can be tuned and some characteristic configurations can be distinguished. For a more detailed study of the structures in the resulting morphologies, focused ion beam cutting was performed with “Raith ionLiNE” system after deposition of a 200-nm metal layer. Typical cross-sectional cuts show the distribution of the silicon phase and subwavelength structural features.

The optical properties of the fabricated surfaces were characterized using a Fourier-Transform Infrared spectrometer (Vertex-80v, Bruker) coupled to an infrared microscope (Hyperion 1000, Bruker). The obtained reflectance spectra demonstrate strong anti-reflection performance (1-7%) in the visible spectral range.

We study the distribution of amorphous and crystalline silicon on fabricated surfaces using spectrally resolved Raman mapping. Raman experiment was performed by means of Raman microscope (Alpha500, WiTec) equipped with a 532-nm CW laser source focused onto the sample surface with a dry microscope objective with numerical aperture of 0.95. Raman signal was collected by the same objective and analyzed with grating-type spectrometer equipped with CCD-camera. Mapping of crystalline silicon (c-Si, 521 cm⁻¹) Raman peak performed from 2 μm² area

indicates its presence along the laser pass lines, hidden in subsurface inclusions. This band was absent in the Raman spectra of the as-deposited a-Si films. Averaged Raman spectra measured from the elevation areas of various samples indicate small amount of c-Si, which can be attributed to the overlapping of the probing laser beam with the neighboring sub-surface c-Si features in between.

The obtained experimental results regarding variation of quasi-regular surface relief allow us to suggest the following physical picture underlying formation of diverse surface morphologies. At slow scanning speeds, the formation of the surface elevation appears to be driven by thermal-induced oxidation of the near-surface Si atoms by oxygen molecules from surrounding air [3]. The most intense oxidation proceeds at the surface areas with highest temperature, which coincide with the maxima of the periodic intensity pattern originated from interference of the incident and scattered fields. In the bulk of the film situated far from the surface contacting with air, the amorphous Si can recrystallize forming c-Si features.

At elevated scanning speeds, along with disordering of the near-wavelength LIPSS one can also observe formation of subwavelength ripples oriented perpendicularly to the polarization direction. Formation of such structures appears to be governed by a standing wave interference pattern having periodicity of produced by laser-excited SPPs in the laser-induced dense electron-hole plasma layer near the air-silicon interface [4].

In conclusion, we have shown fabrication of laser-induced periodic surface structures on amorphous silicon film with multiple femtosecond pulses. This technology allows manufacturing arrays up to mm² scale with different surface morphologies. The optical properties of the fabricated surfaces and the distribution of amorphous and crystalline silicon were measured.

Acknowledgements

Authors acknowledge support from Russian Foundation for Basic Research (20-32-70056).

References

- [1] J. Bonse, S. Höhm, S. V. Kirner, A. Rosenfeld, J. Krüger. *IEEE J. Sel. Top. Quantum Electron.* **23** (2016) 3.
- [2] A. V. Dostovalov, K. A. Okotrub, et.al. *Las. Phys. Lett.* **16** (2019) 026003.
- [3] B. Öktem, I. Pavlov, S. Ilday, et.al., *Nat. Photonics*, **7** (2013) 897.
- [4] M. Straub, M. Afshar, D. Feili, H. Seidel, K. König, *Opt. Lett.* **37** (2012) 190.

Au nanoparticle-decorated TiO₂ nanospheres produced by laser reshaping in water for sensing applications

S.O. Gurbatov^{*,1,2}, A.A. Kuchmizhak^{1,2}

¹Institute of Automation and Control Processes of FEB RAS, 5 Radio St., Vladivostok 690041, Russia

²Far Eastern Federal University, 8 Sukhanova St., Vladivostok 690950, Russia

*e-mail: gurbatov_slava@mail.ru

The resonant metallic nanoparticles are proven to be efficient systems for the electromagnetic field control at nanoscale, owing to the ability to localize and enhance the optical field via excitation of strong plasmon resonances [1]. In turn, high index dielectric nanoparticles with low dissipative losses in the visible range, possessing magnetic and electric Mie-type resonances, offer a great opportunity for light control via designing of scattering properties [2,3]. Recently, the combination of these two paradigms in the form of metal-dielectric (hybrid) nanostructures (nanoantennas and metasurfaces) has allowed utilizing the advantages of both plasmonics and all-dielectric nanophotonics [4]. The hybrid nanostructures are prospective for beam steering, optical switching, high-harmonics generation, directional emission, engineering of local density of states, ultrahigh optical absorption, room-temperature laser emission, and enhancement of photophysical effects.

However, the significant difference in characteristic sizes between the plasmonic and dielectric nanoparticles that resonate in the visible wavelength range makes the production of such hybrid nanostructures through the modern lithography methods quite hard and time-consuming. In present work we demonstrate the synthesis of spherical titania (TiO₂) nanoparticles decorated with Au nanoclusters via nanosecond pulse irradiating of commercially available TiO₂ nanopowders dispersed in an aqueous solution of chloroauric acid (HAuCl₄).

To do that, raw commercial TiO₂ powder of high purity (99.99%, Wako Chemicals) with average size of 120 nm and random shape was first dispersed in deionized water by ultrasonic vibration at a mass concentration of 0.001%. The suspension (7.5 ml) was then transferred into a quartz cuvette and 10⁻³M aqueous solution of HAuCl₄ (0.25 ml, 0.5 ml, 0.75 ml for different cases) was added. After that, 2-hour irradiation with a lens-focused laser beam of 532 nm from a pulsed ND:YAG laser (20 Hz, 8 ns, Quantel Ultra 50) was performed. The suspension was consistently stirred with a magnetic stir bar. The laser energy was 25mJ, which was monitored with a FieldMaxII-TOP laser energy meter (Coherent). After LAL, the products dispersed in the liquid were collected, washed, and dialyzed carefully with deionized water to remove the remaining HAuCl₄ residues.

Such irradiation led to the formation of spherical TiO₂ nanoparticles decorated with Au nanoclusters. The average

TiO₂ particle size increased to 220 nm, and spherical particles with a diameter of up to 1 μm appeared due to agglomeration of the initial nanostructures during irradiation and their remelting into a single spherical particle. The average size and amount of gold nanoclusters on the surface of titania particle rise with increasing HAuCl₄ concentration.

Generation of such hybrid nanostructures was appear to be results from laser-induced remelting of the initial nanoparticles, stimulated by gold nanoclusters reduced on their surface, that enhances absorption of visible laser radiation by titania. Irradiation of the initial TiO₂ nanoparticles without HAuCl₄ by laser pulses of the same energy did not lead to their reshaping into spheres, which is apparently due to the low absorption of visible radiation by titanium dioxide. The morphology and chemical composition of the obtained hybrid nanomaterials were studied in detail via electron microscopy, Raman spectroscopy and energy dispersive x-ray spectroscopy. The average size and number of gold nanoclusters reduced on the surface of synthesized spherical TiO₂ nanoparticles was shown to be tunable by varying the initial nanoparticles / HAuCl₄ concentration ratio. The results obtained indicate synthesized functional nanomaterials as extremely promising for numerous applications of modern optics, optoelectronics and nanophotonics, e.g., for realization on their basis of chemo- and biosensing platforms, as well as of new-generation solar cells [5,6].

Acknowledgements

The reported study was funded by Russian Foundation for Basic Research (grant No. 20-32-70056)

References

- [1] Z. Fang, X. Zhu. *Adv. Mater.* **25** (2013) 3840.
- [2] P. Moitra, B. Slovick, W. Li, I. Kravchenko, D. Briggs, S. Krishnamurthy, J. Valentine. *ACS Photonics.* **2** (2015) 692.
- [3] Y. Fu, A. Kuznetsov, A. Miroschnichenko, Y. Yu, B. Lukyanchuk. *Nat. Commun.* **4** (2013) 1527.
- [4] R. Jiang, B. Li, C. Fang, J. Wang. *Adva. Mater.* **26** (2014) 52745309.
- [5] D. Zhang, B. Gökce, S. Barcikowski. *Chemical Reviews* **117** (2017) 3990.
- [6] N. Mintcheva, P. Srinivasan, J. B. Rayappan, A. A. Kuchmizhak, S. O. Gurbatov, S. A. Kulinich. *Applied Surface Science* **507** (2019) 145169.

Investigation of the mechanism of electric conductivity of strontium bismuthate $\text{Sr}_6\text{Bi}_2\text{O}_{11}$

D.S. Shtarev^{*1}, A.V. Shtareva^{1,2}, A.V. Syuy², V.V. Likhtin³

¹ Yu. A. Kosygin Institute of Tectonics and Geophysics, FEB RAS, 65 Kim U Chen St., Khabarovsk, 680000, Russia

² Far Eastern State Transport University, 47 Seryshev St., Khabarovsk, 680021, Russia

³ Komsomolsk-na-Amure State University, 27 Lenin St., Komsomolsk-na-Amure, 681013, Russia

*e-mail: shtarev@mail.ru

The paper presents data on the temperature dependence of the conductivity of strontium bismuthate $\text{Sr}_6\text{Bi}_2\text{O}_{11}$. It is shown that the temperature dependence of conductivity cannot be described in the framework of existing models. An assumption was made about the existence of a phase transition in strontium bismuthate $\text{Sr}_6\text{Bi}_2\text{O}_{11}$ in the region of 400 K, at which a change in the conductivity mechanism is observed.

Alkaline earth metal bismuthates are promising photoactive materials. There is an assumption [1, 2] that they can form a new class of photoactive materials. They can be used in water and air purification systems from organic pollutants, for the production of hydrogen through the photocatalytic decomposition of water or the recovery of carbon dioxide to produce solar fuel. Bismuthates of alkaline earth metals, as typical perovskite-like materials, have a high tolerance to defects in the anionic sublattice. In order to understand the prospects of using alkaline earth metal bismuthates for the direct conversion of solar energy into electrical energy, it is necessary to determine the mechanism of their conductivity.

The strontium bismuthate $\text{Sr}_6\text{Bi}_2\text{O}_{11}$ was chosen as the object of study in this work: it is known [3] that it has high photocatalytic activity and, at the same time, is characterized by a large number of defects in the anion sublattice.

The synthesis of strontium bismuthate was carried out by solid-phase synthesis in accordance with the procedure described in [3]. To study the electrophysical properties of strontium bismuthate $\text{Sr}_6\text{Bi}_2\text{O}_{11}$, the method of electrochemical impedance spectroscopy (EIS) was used. For this, a NOVOCONTROL BDS dielectric spectrometer was used.

During the study of the electrophysical properties of strontium bismuthate $\text{Sr}_6\text{Bi}_2\text{O}_{11}$ by electrochemical impedance spectroscopy, data were obtained on the frequency and temperature dependences of the active and reactive resistances (Z' and Z'' , respectively). This allowed the construction of a Nyquist plot for each of the temperatures in the range from 0 °C to 400 °C.

A typical Nyquist plot for a semiconductor material consists of two semicircles of different diameters. The first semicircle emerging from the vicinity of the zero point characterizes the investigated semiconductor material itself. The second semicircle characterizes the contact of the semiconductor material with the electrodes. Therefore, we are interested in the first semicircle for the subsequent analysis.

Interpolating the experimental data with a semicircle, we can find the point of its intersection with the line $Z''=0$. This point characterizes the true resistance of a material to

direct current (Z_{DC}). Knowing this value and the geometric dimensions of the test sample, it is possible to determine its specific conductivity σ .

There are several basic models to describe the hopping conductivity in semiconductor materials: the model of thermal delocalization of carriers; nearest-neighbor hopping and variable-range hopping models. For the strontium bismuthate under study, the most suitable model is the variable-range hopping model, in which the temperature dependence of conductivity obeys the Efros-Shklovsky law:

$$\sigma = \sigma_0 \exp\left(-\sqrt{\frac{T_{ES}}{T}}\right), \quad (1)$$

where T_{ES} – characteristic temperature.

From obtained experimental data it can be seen, that this model is not in good agreement with experimental data. This problem is solved if we assume that at a temperature of 398 K, a phase transition is observed with a change in the characteristic temperature.

It is known [5] that the characteristic temperature T_{ES} is related to the radius of localization of the charge carrier (ξ) by the following relation:

$$T_{ES} = \frac{6.2e^2}{k_B k \xi}, \quad (2)$$

where e – electron charge, k_B is the Boltzmann constant, k is the relative permittivity.

The relative dielectric permittivity of the studied strontium bismuthate is unknown. However, if the characteristic temperature in the region of less than 398 K is designated as T_{ES}^1 , and in the region of more than 398 K as T_{ES}^2 , then it is easy to show that:

$$T_{ES}^1/T_{ES}^2 = \xi^2/\xi^1.$$

If we substitute the numerical values of the characteristic temperatures, we get that $\xi^2 = 0.198\xi^1$.

Thus, at a temperature of 398 K in strontium bismuthate $\text{Sr}_6\text{Bi}_2\text{O}_{11}$, the radius of the localization of the charge carrier decreases by about 5 times.

Acknowledgements

The research was carried out at the expense of a grant from the Russian Science Foundation (project No. 19-73-10013).

References

- [1] D.S. Shtarev, et. al. *ChemCatChem* **11** (2019) 3534.
- [2] D.S. Shtarev, et. al. *ChemCatChem* (2020) DOI: 10.1002/cctc.201902236.
- [3] D.S. Shtarev, et. al. *Catalysis Today* **340** (2020) 70.
- [4] M. Portilla. *Journal Solid State Chemistry* **105** (1993) 371.
- [5] D.N. Tsiganokov, A.L. Efros. *Phys. Rev. Lett.* **88** (2002) 176602.

The features of the lateral photovoltaic effect in the $\text{Fe}_3\text{O}_4/\text{SiO}_2/\text{n-Si}$ structure depending on silicon substrate orientation

T.A. Pisarenko^{*1,2}, V.V. Korobtsov^{1,2}, V.V. Balashev^{1,2}, A.A. Dimitriev^{1,2}, S.V. Bondarenko^{1,2}

¹ Institute of Automation and Control Processes of FEB RAS, 5 Radio St., Vladivostok 690041, Russia

² Far Eastern Federal University, 8 Sukhanova St., Vladivostok 690950, Russia

*e-mail: tata_dvo@iacp.dvo.ru

It is known [1, 2] that at nonuniform illumination of the metal-oxide-semiconductor (MOS) structure, in addition to the conventional transverse photovoltage between the interface layer and the substrate, the lateral photovoltage (LPV) is generated along the interface layer, so-called lateral photovoltaic effect (LPE). In a number of papers [3-12], it has been shown that LPE parameters for the MOS structures depend on the material of the metal film [3], its thickness [3-12], and the doping level of a silicon substrate [9, 10].

In continuation of these studies, in this report, we present the results of investigations of the influence of the silicon substrate orientation on the LPE in the $\text{Fe}_3\text{O}_4/\text{SiO}_2/\text{n-Si}$ structure.

Samples were fabricated on n-type single-crystal Si(001) and Si(111) substrates having the same resistivity of 7.5 $\Omega\cdot\text{cm}$. The magnetite films of ~40 nm thickness were formed by reactive deposition of iron in oxygen atmosphere onto the chemically oxidized silicon substrates. The magnetite film thickness was chosen based on the dependence of LPE sensitivity on film thickness in the $\text{Fe}_3\text{O}_4/\text{SiO}_2/\text{n-Si}$ (001) structure as near-optimal [12]. Details of the preparation and the characterization of magnetite film are described in Ref. [13]. Aluminum electrodes for LPV measurements were formed on the Fe_3O_4 film surface by thermal vacuum deposition through a metal mask with a distance between contacts of 2 mm. The LPE in the $\text{Fe}_3\text{O}_4/\text{SiO}_2/\text{n-Si}$ structures was studied at room temperature using He-Ne laser (633 nm, 0.3 mW and laser spot diameter of 50 μm) and Keithley 2000 multimeter. The response time of the structures at pulsed illumination was observed by combining optical bench, a chopper and a digital oscilloscope (AKIP-4115) of 150 MHz.

The result of experiments has shown that the LPV varies linearly with the position of the laser spot for both orientations of the silicon substrate. The LPE sensitivity, defined as $\kappa = dLPV(x)/dx$, in the $\text{Fe}_3\text{O}_4/\text{SiO}_2/\text{Si}$ (001) structure is equal to 112 mV/mm, which is ~2 times greater than that in the $\text{Fe}_3\text{O}_4/\text{SiO}_2/\text{Si}$ (111) structure. Simultaneously, the nonlinearity, defined as $\delta = 2\sigma/F$ (where σ is the standard deviation from the linear approximation, F is the maximum value of the LPV), in the $\text{Fe}_3\text{O}_4/\text{SiO}_2/\text{Si}$ (001) structure is 4.7%, which is ~2 times lower than that in the $\text{Fe}_3\text{O}_4/\text{SiO}_2/\text{Si}$ (111) structure.

Effect of the substrate orientation on the LPE was also detected in experiments at pulse illumination of the $\text{Fe}_3\text{O}_4/\text{SiO}_2/\text{n-Si}$ structure. So, the shape of the LPV response for the $\text{Fe}_3\text{O}_4/\text{SiO}_2/\text{Si}$ (001) structure is characterized by a peak at the rising edge of LPV signal,

whereas for the $\text{Fe}_3\text{O}_4/\text{SiO}_2/\text{Si}$ (111) structure the shape of the LPV response close to a rectangular. With respect to the time characteristics, the rise time (from 10 to 90% of the peak photovoltage) in the $\text{Fe}_3\text{O}_4/\text{SiO}_2/\text{Si}$ (001) structure is equal to 8.3 μs , which is ~3 times faster than that in the $\text{Fe}_3\text{O}_4/\text{SiO}_2/\text{Si}$ (111) structure, while the fall time (from 90 to 10% of the peak photovoltage) in the $\text{Fe}_3\text{O}_4/\text{SiO}_2/\text{Si}$ (001) structure is equal to 25 μs , which is ~2 times faster than that in the $\text{Fe}_3\text{O}_4/\text{SiO}_2/\text{Si}$ (111) structure.

Observed features of the LPE in the $\text{Fe}_3\text{O}_4/\text{SiO}_2/\text{n-Si}$ structure depending on the silicon substrate orientation were analyzed using the existing LPE theory [1-3], taking into account differences in the density of surface states at the $\text{SiO}_2/\text{n-Si}$ interface [14]. According to the carried out analysis, it is supposed that a higher LPE sensitivity and a faster photoresponse in the $\text{Fe}_3\text{O}_4/\text{SiO}_2/\text{Si}$ (001) structure, compared with the $\text{Fe}_3\text{O}_4/\text{SiO}_2/\text{Si}$ (111) structure, are caused by a lower density of surface states at the SiO_2/Si (001) interface than that at the SiO_2/Si (111) interface.

Thus, obtained results suggest that the density of surface states at the $\text{SiO}_2/\text{n-Si}$ interface may serve as an additional parameter to control the LPE in MOS structures.

References

- [1] G. Lucovsky. J. Appl. Phys. **31** (1960) 1088.
- [2] T. Shikama, H. Niu, M. Takai. Jap. J. Appl. Phys. **33**(10) (1984) 1314.
- [3] C. Yu, H. Wang. Sensors. **10** (2010) 10155.
- [4] H. Wang *et al.* New J. Phys. **10** (2008) 093006.
- [5] L. Chi, P. Zhu, H. Wang, X. Huang, X. Li. J. Opt. **13** (2011) 015601.
- [6] S. Liu, X. Xie, H. Wang. Opt. Express. **22**(10) (2014) 11627.
- [7] X. Huang *et al.* IEEE Electron Device Lett. **37** (2016) 1018.
- [8] S.Q. Xiao, H. Wang, Z.C. Zhao, Y.Z. Gu, Y.X. Xia, Z.H. Wang. Opt. Express. **16**(6) (2008) 3798.
- [9] W. M. Liu, Y. Zhang, G. Ni. Opt. Express. **20**(6) (2012) 6225.
- [10] Y. Zhang, Y. Zhang, T. Yao, C. Hu, Y. Sui, X. Wang. Opt. Express. **26**(26) (2018) 34214.
- [11] X. Wang, B. Song, M. Huo, Y. Song, Z. Lv, Y. Zhang, Y. Wang, Y. Song, J. Wen, Y. Sui, J. Tang. RSC Adv. **5** (2015) 65048.
- [12] T.A. Pisarenko *et al.* Phys. Solid State. **60** (2018) 1316.
- [13] V.V. Balashev, V.A. Vikulov, T.A. Pisarenko, V.V. Korobtso. Phys. Solid State. **57**(12) (2015) 2532.
- [14] B.E. Deal *et al.* Soc.: Solid State Science. **114**(3) (1967)266

Generation of laser beams for laser printing of chiral nanoneedles

A.P. Porfirev^{*1,2}, V.I. Logachev², G.E. Gridin², S.A. Degtyarev^{1,2}, S.N. Khonina^{1,2}

¹ Image Processing Systems Institute—Branch of the Federal Scientific Research Centre “Crystallography and Photonics” of the Russian Academy of Sciences, 151 Molodogvardeyskaya St., Samara 443001, Russia

² Samara National Research University, 34 Moskovskoye Shosse, Samara 443086, Russia

*e-mail: porfirev.alexey@gmail.com

We investigate nonlinear spiral phase plates (SPPs), diffractive optical elements with transmission functions defined as $\exp(im\varphi^n)$, where m is the topological charge of the nonlinear SPP and n is an arbitrary number. The intensity distributions generated by these elements have a spiral shape with an intensity gradient. The phase distribution of the generated light fields is also spiral shaped. Such spiral-shaped light beams can be used for realization of laser fabrication of chiral nano- and microelements for 2D and 3D metasurfaces.

Nowadays, spiral phase plate (SPP), an optical element with a height that varies linearly with the azimuthal angle [1, 2] is often used for the generation of optical vortex (OV) beams. Such beams are widely used not only for optical manipulation [3, 4] and optical communication [5] but also for laser material processing [6]. Recently, it was shown that OV beams allow one to fabricate unique chiral nanoneedles in thin metal films with the help of pulsed laser radiation [7-9]. Toyoda et al explained this possibility by the orbital angular momentum (OAM) transfer from the illuminating OV beam to transient melts [7]. However, in 2017 the formation of twisted metal nanoneedles on silver and gold films under their irradiation by zero-OAM laser beams, having various spiral-shaped lateral intensity distributions was demonstrated [10]. The experimental results indicated the corresponding temperature-gradient induced chiral thermocapillary mass transfer of the molten material as an alternative fabrication mechanism, inducing the chiral relief on the noble-metal films. Moreover, the chirality of the laser-printed nanoneedles was found to be efficiently tailored via optimization of the corresponding intensity pattern of the zero-OAM spiral-shaped beam, while the increase of the topological charge (TC) of the OV beam was shown to weakly affect the nanoneedle geometry [11]. In order to generate such spiral-shaped intensity distribution with controllable dimensions, an unconventional SPP with a spiral phase distribution which does not change linearly with an increase in the azimuthal angle (as in the case of a conventional SPP) but has a nonlinear dependence described as $2\pi m(\varphi/2\pi)^n$ [12] can be used. The vortex beams formed in this case had a spiral shape with a gradient of intensity and phase. The unique structure of such vortex beams determines the energy flow directed in spirals, which can be useful also in the laser manipulation of nano- and micro-scale objects. Here, we numerically investigate the properties of a nonlinear SPP with a transmission function in the form of $\exp(im\varphi^n)$ from the point of view of using them to control the spiral shape of both the intensity and the phase distribution.

In contrast to the conventional SPP, the transmission function of a nonlinear SPP is described as follows

$$T(r, \varphi) = \text{circ}(r/R)\exp(im\varphi^n), \quad (1)$$

where n is an arbitrary natural number. As seen from the near-field distributions, the generated intensity distributions are similar to those obtained in the case of fractional optical vortices [13]. The increase in power value n in the case of a fixed TC leads to the increase of the lateral size of the generated intensity distribution. When the power value n is fixed, the increase in TC leads to the increase in lateral size of the generated spiral intensity distribution. The phase difference at the ends of the generated light spiral corresponds to the structure of the initial nonlinear SPP.

Acknowledgements

This work was financially supported by Russian Foundation for Basic Research (RFBR) (Grant no. 20-37-70025) and by RF Ministry of Science and Higher Education (007-GZ/Ch3363/26).

References

- [1] S.N. Khonina, V.V. Kotlyar, M.V. Shinkaryev, V.A. Soifer, G.V. Uspleniev. *J. Mod. Opt.* **39** (1992) 1147.
- [2] M.W. Beijersbergen, R.C. Coerwinkel, M. Kristensen, J.P. Woerdman. *Opt. Commun.* **112** (1994) 321.
- [3] N.B. Simpson, K. Dholakia, L. Allen, M.J. Padgett. *Opt. Lett.* **22** (1997) 52.
- [4] V.V. Kotlyar, A.A. Kovalev, A.P. Porfirev. *Computer Optics* **42** (2018) 550.
- [5] N. Bozinovic, Y. Yue, Y. Ren, M. Tur, P. Kristensen, H. Huang, A.E. Willner, S. Ramachandran. *Science* **340** (2013) 1545.
- [6] K. Anoop, R. Fittipaldi, A. Rubano, X. Wang, D. Paparo, A. Vecchione, L. Marrucci, R. Bruzzese, S. Amoroso. *J. Appl. Phys.* **116** (2014) 113102.
- [7] K. Toyoda, K. Miyamoto, N. Aoki, R. Morita, T. Omatsu. *Nano Lett.* **12** (2012) 3645.
- [8] T. Omatsu, K. Miyamoto, K. Toyoda, R. Morita, Y. Arita, K. Dholakia. *Adv. Opt. Mater.* **7** (2019) 1801672.
- [9] S. Syubaev, A. Zhizhchenko, A. Kuchmizhak, A. Porfirev, E. Pustovalov, O. Vitrik, Y. Kulchin, S. Khonina, S. Kudryashov. *Opt. Express* **25** (2017) 10214.
- [10] S. Syubaev, A. Porfirev, A. Zhizhchenko, O. Vitrik, S. Kudryashov, S. Fomchenkov, S. Khonina, A. Kuchmizhak. *Opt. Lett.* **42** (2017) 5022.
- [11] S. Syubaev, A. Zhizhchenko, O. Vitrik, A. Porfirev, S. Fomchenkov, S. Khonina, S. Kudryashov, A. Kuchmizhak. *Appl. Surf. Sci.* **470** (2019) 526.
- [12] P. Li, S. Liu, T. Peng, G. Xie, X. Gan, J. Zhao. *Opt. Express* **22** (2014) 7598.
- [13] J. Strohaber, Y. Boran, M. Sayrac, L. Johnson, F. Zhu, A.A. Kolomenskii, H.A. Schuessler. *J. Opt.* **19** (2017) 015607.

Multifunctional IR sensor platform produced by direct laser patterning

D.V. Pavlov^{*,1,2}, A.A. Kuchmizhak^{1,2}

¹Institute of Automation and Control Processes of FEB RAS, FEB RAS, 5 Radio St., Vladivostok 690041, Russia

²Far Eastern Federal University, 8 Sukhanova St., Vladivostok 690950, Russia

*e-mail: pavlov_dim@mail.ru

Fast identification of various analytes (such as explosive or toxic substances, bacteria, viruses or cancer cells) at trace concentrations is an important task for personalized medicine, security, microbiology etc. Surface-enhanced infrared absorption (SEIRA) based sensors are among promising routes towards non-invasive detection of analytes [1,2]. Here, we demonstrate a novel IR sensor platform fabricated by low-cost and high-performance direct femtosecond (fs) laser patterning of thin films of plasmon-active materials. The proposed sensor is based on arrays of nanostructures, either nanovoids or coaxial holes, and supports tunable lattice-type plasmon resonance in the near- and middle IR spectral range.

Ordered arrays of nanovoids or coaxial-shaped microholes were produced on a surface of 50-nm-thickness Au films deposited on the surface of SiO₂ or IR-transparent MgF₂ substrates, respectively [3]. Samples were placed on a high-precision positioning system and scanned by tightly focused 220-fs 515-nm pulses generated by a laser system at repetition rate of 200 kHz. To imprint coaxial-shaped microholes, the as-generated Gaussian laser beam was converted to donut-shaped beam via s-waveplate. The fabricated sensor elements were characterized by scanning electron microscopy (SEM) and Fourier-transform infrared (FTIR) spectroscopy. It has been found that ordered arrays of nanovoids containing millions of identical elements exhibit pronounced first-order lattice plasmonic resonance (FLPR) in the near-IR reflection spectrum. It is noteworthy that FLPR shows a redshift in the spectral range from 1 to 2.5 μm with an increase in the array period or nanovoid size. At the same time, a vortex phase plate was used to convert a Gaussian laser beam into a donut-shape beam to fabricate arrays of coaxial microholes. The imprinted arrays of coaxial microholes demonstrate pronounced dip in reflection associated with lattice-type plasmon resonance, which spectral position can be tailored within the range of 6-12 μm via array period and geometric shape of coaxial holes.

Finally, we evaluated the performance of the nanovoid sensor in some applications. First, by measuring the refractive index (RI) of a thick layer of H₂O, isopropanol, or a mixture thereof, a sensitivity of 1600 nm per refractive index unit was obtained at a figure-of-merit of 12. Such competitive characteristics are good enough to detect the changes of the refractive index of the bulk dielectric

superstrate as small as 10⁻⁵. Second, we tested the performance of the nanovoid array with respect to a deposition of nm-thick Al₂O₃ layers. The data obtained in the experiment reveal a 2-nm spectral shift per 1-nm layer thickness, which would allow for the detection of sub-nm capping layers with conventional spectrometers. Thirdly, to test the ability of the sensor to detect gaseous media, we placed the sensor in a gas chamber filled with ethanol-saturated air concentration of 7.8 vol.% (or 160 mg / L). In the experiment, obtained spectral shift of the FLPR by ≈ 7 nm via the corresponding change of the local RI of the surroundings. Thus, the detection limit achieved in this work was around 20 mg / L (4.3 × 10⁻⁴ mol / L) [4].

In conclusion, we present a novel IR sensor platform based on arrays of nanovoids or coaxial microholes that support pronounced plasmon resonance in the near- and middle- IR ranges, respectively. We demonstrate the high sensitivity of the nanovoid array plasmonic sensors for measuring the refractive index of the analyte, as well as for gas detection and determining the thickness of thin deposited films. Note that coaxial microholes arrays have outstanding potential for further study due to the ability to support strong tunable plasmon resonance in the mid-IR region of the spectrum. Thus, the remarkable sensory performance of the proposed plasmonic IR sensor platform fabricated by an inexpensive and high-performance direct laser printing method makes it a promising tool for various applications in medicine, chemistry, microbiology, photonics, etc.

Acknowledgements

The authors acknowledge partial support from Russian Foundation for Basic Research (grant No. 19-32-90115).

References

- [1] F. Neubrech, C. Huck, K. Weber, A. Pucci, H. Giessen. *Chem. Rev.* **117** (2017) 5110.
- [2] F. Neubrech, A. Pucci, T.W. Cornelius, S. Karim, A. García-Etxarri, J. Aizpurua. *Phys. Rev. Lett.* **101** (2008) 157403.
- [3] D. Pavlov, S. Syubaev, A. Kuchmizhak, S. Gurbatov, O. Vitrik, E. Modin, S. Kudryashov, X. Wang, S. Juodkazis, M. Lapine. *Appl. Surf. Sci.* **469** (2019) 514.
- [4] D.V. Pavlov, A.Y. Zhizhchenko, M. Honda, M. Yamanaka, O.B. Vitrik, S.A. Kulinich, S. Juodkazis, S.I. Kudryashov, A.A. Kuchmizhak. **9** (2019) 1348.

Improvement of quartz crystal microbalance gas sensors by nanostructured thin films

P. Fitl¹, M. Hruška¹, D. Tomeček¹, J. Vlček¹, J. Otta¹, J. Fara¹, M. Vršata¹, M. Novotný²

¹ University of Chemistry and Technology Prague, Dept. of Physics and Measurements, Technická 3, Prague, 16628, Czech Republic

² Institute of Physics of the Czech Academy of Sciences, Na Slovance 1999/2, Prague 8, 182 21, Czech Republic

*e-mail: fitlp@vscht.cz

Focused Laser beam is a widely used for deposition, localized annealing and patterning of various materials (eg. metals, oxides, organic substances). Our work is focused on possibilities of usage of continuous wave (CW) lasers for local deposition and patterning of black metal [1] and organic semiconductors [2,3] on the QCM sensor substrates. Our method is based on laser direct write to sensing layer on the active electrode and laser induced forward transfer of sensing material to sensing substrates. For our test we used QCM substrates based on circular (d=8.65 mm) quartz AT cuts with chrome + gold electrode with base working frequency at 10.880 MHz. As the sensing layer we used black gold, black palladium, Zinc Phthalocyanine. The direct write/ deposition apparatus includes micro CNC machine (minimal step adjustable to 300 nm) equipped with the semiconductor laser ($\lambda = 405$ nm, power of 50 mW, spot size 6 microns) in CW mode and focusing optics.

Deposition process was held in an inert gas (Argon, Nitrogen) at atmospheric pressure. Morphology and microstructure of modified and deposited layers were studied by optical, electron microscopy and AFM. Chemical composition of deposited Phthalocyanine was studied by FTIR and compared with the source substances.

It was proved that chemical structure of all chosen substances is not affected by this deposition technique. Employing our technique we are able to achieve precise and reproducible laser transfer of organic semiconductors to the target sensor substrate with lateral resolution of 14 microns. Our sensors were tested for detection of NO_x, VOCs and the results shown significant improvement of sensitivity caused by enhanced surface morphology.

Acknowledgements

This work was supported by Czech Science Foundation (GACR), Project No. 18-09347S and also by Ministry of Education, Youth and Sports within the projects LTC17058 and by COST Action CA15107 MultiComp.

References

- [1] M. Novotny, P. Fitl, A.K. Sytchkova, J. Bulir, J. Lancok, P. Pokorny, D. Najdek, J. Bocan. *Central European Journal of Physics* **7** (2009) 327.
- [2] D. Tomecek, M. Hruska, P. Fitl, J. Vlcek, E. Maresova, S. Havlova, L. Patrone, M. Vrnata *ACS Sensors* **3** (2018) 2558.
- [3] P. Fitl, M. Vrnata, D. Kopecky, J. Vlcek, J. Skodova, J. Bulir, M. Novotny, P. Pokorny, *Applied Surface Science* **302** (2014) 37.

The influence of temperature on the lateral photovoltaic effect in the Fe₃O₄/SiO₂/n-Si structure

T.A. Pisarenko^{*1,2}, V.V. Korobtsov^{1,2}, V.V. Balashev^{1,2}, A.A. Dimitriev^{1,2}

¹ Institute of Automation and Control Processes of FEB RAS, 5 Radio St., Vladivostok 690041, Russia

² Far Eastern Federal University, 8 Sukhanova St., Vladivostok 690950, Russia

*e-mail: tata_dvo@iacp.dvo.ru

The lateral photovoltaic effect (LPE) was firstly discovered in experiments at nonuniform illumination of a *pn*-junction [1, 2], this effect was later found in hybrid systems such as metal-semiconductor [3-7] and metal-oxide-semiconductor (MOS) [7-13]. Recently, in order to increase the LPE sensitivity, the LPE in MOS structures with different materials of a top thin film is actively investigated [7-13]. Based on the theoretical calculations, authors [7] concluded that the use of metals with high work function and high resistivity in MOS structure leads to an LPE increase. Thus, the Fe₃O₄/SiO₂/Si structure is of interest, since magnetite (Fe₃O₄) satisfies these conditions [14, 15]. Really, in Ref. [16, 17] it was shown that at room temperature the LPE sensitivity in the Fe₃O₄/SiO₂/n-Si structure is higher than in the structures with the other top thin-films [7-13]. On the other hand, the magnetite resistivity exhibits a strong dependence on temperature [15], and in this connection it is interesting to study the influence of temperature on the LPE in the Fe₃O₄/SiO₂/n-Si structure.

Here we report on the results of a study of the lateral photovoltaic effect in the Fe₃O₄/SiO₂/n-Si(001) structure at temperatures of 300 and 122 K.

Lateral photovoltaic effect in the structure was investigated using He-Ne laser (633 nm, 0.3 mW and laser spot diameter of 50 μm) and Keithley 2000 multimeter. The magnetite film of a thickness of 42 nm was formed on the chemically oxidized silicon substrate of 7.5 Ω-cm resistivity. Details of the preparation and characterization of magnetite film are described in Ref. [18]. Aluminum electrodes for LPV measurements were formed on the Fe₃O₄ film surface by thermal vacuum deposition through a metal mask. The response time of the structure at pulsed illumination was observed by combining optical bench, a chopper and a digital oscilloscope (AKIP-4115) of 150 MHz.

It is found that at 300 K LPE exhibits the high sensitivity of 112 mV/mm and the weak nonlinearity of 4.7%, whereas a decrease in temperature up to 122 K results in the appearance of strong nonlinearity of 28%, which extends for 500 μm from the contact, meanwhile the central portion remains linear, and its sensitivity is 65 mV/mm.

Based on the analysis of the time dependences of LPV response at pulsed illumination, it was found that at 300 K the rise time and fall time are equal 8.3 and 25 μs, respectively. In addition, the peak is observed on the rising

edge of LPV. Decreasing the temperature up to 122 K results in the disappearance of this peak and the increase of the time characteristics of LPV response by ~15 times.

So, it is shown that a decrease of temperature results in a change of basic parameters LPE, such as the sensitivity, as well as a rise time and a fall time at pulsed illumination. It is assumed that the observed effects are due to a decrease in the built-in barrier height, leading to a decrease in the concentration of photogenerated carriers, as well as due to the temperature dependence of magnetite resistivity.

References

- [1] J.T. Wallmark. Proc. IRE. **45** (1957) 474.
- [2] G. Lucovsky. J. Appl. Phys. **31** (1960) 1088.
- [3] J. Henry, J. Livingstone. J. Phys. D. Appl. Phys. **41** (2008) 165106.
- [4] C.Q. Yu, H. Wang, S.Q. Xiao, Y.X. Xia. Opt. Express. **17**(24) (2009) 21712.
- [5] S.H. Wang, W.X. Wang, L.K. Zou, X. Zhang, J.W. Cai, Z.G. Sun, B.G. Shen, J.R. Sun. Adv. Mater. **26** (2014) 8059.
- [6] S.H. Wang, X. Zhang, L.K. Zou, J. Zhao, W.X. Wang, J.R. Sun. Chin. Phys. B **24** (2015) 107307.
- [7] C. Yu, H. Wang. Sensors. **10** (2010) 10155.
- [8] H. Wang, S.Q. Xiao, C.Q. Yu, Y.X. Xia, Q.Y. Jin, Z.H. Wang. New J. Phys. **10** (2008) 093006.
- [9] S.Q. Xiao, H. Wang, Z.C. Zhao, Y.Z. Gu, Y.X. Xia, Z.H. Wang. Opt. Express. **16**(6) (2008) 3798.
- [10] J.P. Cascales, I. Martinez, D. Diaz, J.A. Rodrigo, F.G. Aliev. Appl. Phys. Lett. **104** (2014) 231118.
- [11] L. Chi, P. Zhu, H. Wang, X. Huang, X. Li. J. Opt. **13** (2011) 015601.
- [12] S. Liu, X. Xie, H. Wang. Opt. Express. **22**(10) (2014) 11627.
- [13] X. Huang, C. Mei, J. Hu, D. Zheng, Z. Gan, P. Zhou, and H. Wang. IEEE Electron Device Lett. **37** (2016) 1018.
- [14] M. Fonin, R. Pentcheva, Yu.S. Dedkov, M. Sperlich, D.V. Vyalikh, M. Scheffler, U. Rüdiger, G. Güntherodt. Phys. Rev. B **72** (2005) 104436.
- [15] V.A. Vikulov, A.A. Dimitriev, V.V. Balashev, T.A. Pisarenko, V.V. Korobtsov. Mater. Sci. Eng. B **211** (2016) 33.
- [16] X. Wang, B. Song, M. Huo, Y. Song, Z. Lv, Y. Zhang, Y. Wang, Y. Song, J. Wen, Y. Sui, J. Tang. RSC Adv. **5** (2015) 65048.
- [17] T.A. Pisarenko, V.V. Balashev, V.A. Vikulov, A.A. Dimitriev, V.V. Korobtsov. Phys. Solid State. **60** (2018) 1316.
- [18] V.V. Balashev, V.A. Vikulov, T.A. Pisarenko, V.V. Korobtsov. Phys. Solid State. **57**(12) (2015) 2532.

**VI. Nanostructured coverages, nanocomposites,
functional hybrid materials: formation,
structure and properties**

Effect of electrolyte temperature on the kinetic of germanium nanowire growth by the electrochemical liquid-liquid-solid mechanism

I.M. Gavrilin^{*,1,2}

¹ Frumkin Institute of Physical Chemistry and Electrochemistry, RAS, Bld. 4, 31, Leninsky prospect, Moscow, Russia

² National Research University of Electronic Technology – MIET, Bld. 1, Shokin Square, Zelenograd, Moscow, Russia

*e-mail: gavrilin.ilya@gmail.com

Germanium nanowires fabricated by electrochemical liquid-liquid-solid (ec-LLS) deposition from water solutions at nearly room temperature without the use of templates and toxic precursors are under intense investigation during recent years [1, 2]. Due to its high theoretical capacity, excellent electrical conductivity, rapid Li^+ and Na^+ mobility and remarkable mechanical strength this material has an increasing prominence as an anode material in Li-ion and Na-ion batteries [3, 4]. ec-LLS method based on electrochemical deposition of Ge from aqueous solutions. In this case liquid metal nanodroplets that have low melting points are used as an electrode for reduction of Ge-containing ions at the electrode surface, followed by dissolving and crystallizing the melt at the substrate interface.

This work presents results of electrolyte temperature on the obtained Ge structures morphology and kinetic growth.

As substrates for electrochemical deposition, Ti foil and In nanoparticle arrays, that were deposited onto the Ti film surface by vacuum-thermal evaporation, were used [5]. Electrochemical deposition was performed in a three-electrode cell. A platinum plate was used as a counter electrode. A calomel electrode ($\text{Pt}|\text{Ag}|\text{AgCl}|\text{KCl}^-$) was used as the reference electrode. Deposition was performed in an electrolyte solution contained 0.05 M of germanium oxide (IV) GeO_2 , 0.5 M of potassium sulfate K_2SO_4 and 0.5 M of succinic acid.

The morphology and composition of the samples were investigated by scanning electron microscopy (SEM), transmission electron microscopy (TEM) with an energy dispersive X-ray (EDS) detector and Raman spectroscopy.

From chronoamperometry curves analysis three specific curve sections were identified. The length of each section depends on the electrolyte solution temperature. Obtained results show that using different temperatures

allows controlling Ge growth kinetics and expanding the Ge nanowire growth mechanisms understanding during liquid metal-assisted electrochemical deposition processes.

The results also show that at a higher electrolyte-solution temperature (90°C) the filament has a coaxial structure: the inner part is a crystalline phase of germanium, which also contains In atoms, and the outer one is an amorphous phase of germanium oxides. The formation of germanium oxides (hydroxides) is most likely due to the presence of side chemical reactions that occur during the formation of filaments and are caused by a local change in pH near electrode surface.

Acknowledgements

The reported study was funded by RFBR, project number 19-38-60058

References

- [1] E. Fahrenkrug, S. Maldonado. *Accounts of Chemical Research* **48** (2015) 1881.
- [2] I. M. Gavrilin, D. G. Gromov, A. A. Dronov, S. V. Dubkov, R. L. Volkov, A. Yu. Trifonov, N. I. Borgardt, and S. A. Gavrilov. *Semiconductors* **51** (2017) 1067.
- [3] I. M. Gavrilin, V. A. Smolyaninov, A. A. Dronov, S. A. Gavrilov, A. Yu. Trifonov, T. L. Kulova, A. A. Kuz'mina, and A. M. Skundin. *Russian Journal of Electrochemistry* **54** (2018) 1111.
- [4] I. M. Gavrilin, V. A. Smolyaninov, A. A. Dronov, S. A. Gavrilov, A. Yu. Trifonov, T. L. Kulova, A. A. Kuz'mina, and A. M. Skundin. *Mendeleev Communications* **28** (2018) 659.
- [5] D. G. Gromov, L. M. Pavlova, A. I. Savitskii, A. Yu. Trifonov. *Phys. Solid State* **57** (2015) 173.
- [6] S. A. Gavrilov, A. A. Dronov, I. M. Gavrilin, R. L. Volkov, N. I. Borgardt, A. Y. Trifonov, A. V. Pavlikov, P. A. Forsh, and P. K. Kashkarov. *Journal of Raman Spectroscopy* **49** (2018) 810.

CNT formation at the edge of a Co-Zr-N- (O) alloy film with a low content of catalytic metal for using in VLSI technology

G.S. Eritsyun^{*1,2}, E.P. Kitsyuk², A.A. Shamanaev², D.G. Gromov¹

¹ National Research University of Electronic Technology (MIET), Moscow, Zelenograd, Russia

² Scientific-Manufacturing Complex "Technological Centre", Moscow, Zelenograd, Russia

*e-mail: gosha22_07@mail.ru

As further scaling down size of the silicon field-effect transistor (FET) becomes weakly efficient and increasingly costly, there is growing interest in FETs based on nanomaterials and technologies. Carbon nanotubes are outstanding among many nanomaterials that are considered for next-generation energy-efficient electronic systems. It is expected that due to the nanoscale and simultaneously CNT high carrier mobility digital systems built by FET, the channel of which is made on the basis of CNTs, will improve the energy efficiency of modern silicon-based technologies by an order of magnitude.

A working 16-bit microprocessor was demonstrated, last year, which is completely built on CNTs-based FET [1]. However, the technique of forming the FET channel from CNTs, which was used in this work, is difficult to consider as perfect and technological. Therefore, we need to look for other more technologically advanced techniques that integrate well with existing VLSI technology.

It has recently been shown that a CNT array can be grown by CVD on alloy films with a low content of catalytic metal, the nanoparticles of which are necessary for the CNTs growth [2,3]. The attractiveness of using such alloys is that the initial film of the alloy is amorphous, and the catalyst nanoparticles which are necessary for the CNTs growth can be formed locally in the required places immediately before the synthesis of CNTs. Moreover, the necessary topology can be obtained before the alloy film. Then catalyst particles can be formed. In particular, the possibility of CNTs local growth at the films edges [4] has been shown. This makes described technique attractive for embedding in VLSI technology.

The features of the CNT array formation were investigated in this work. They formed at the edges of a thin

film Co-Zr-N-(O) alloy with a low content of catalytic metal for the channel formation of the FET based on CNTs.

Co-Zr-N-(O) alloy films were deposited by magnetron sputtering on Si substrates coated with SiO₂. For topology creating the Co-Zr-N-(O) film was etched using the DRIE method. Next step is the CNTs growth from a C₂H₂ + NH₃ + Ar gas mixture using the CVD method in Oxford Plasma Lab 100. It is instrumentally shown that heating an amorphous alloy causes its crystallization and extrusion of the catalytic metal to the surface. As a result, small catalyst particles formed on the surface. CNT growth occurs after the appearance of these particles. The results are analyzed and discussed.

Acknowledgements

The work was financially supported by RFBR (project № 19-38-90206)

References

- [1] G. Hills, C. Lau, A. Wright, S. Fuller, M. Bishop, T. Srimani, P. Kanhaiya, R. Ho, A. Amer, Y. Stein, D. Murphy, A. Chandrakasan, M. Shulaker. *Nature* **572** (2019) 595.
- [2] P. Mierczynski, S. Dubkov, S. Bulyarskii, A. Pavlov, S. Skorik, A. Trifonov, A. Mierczynska, E. Kitsyuk, S. Gavrilov, T. Maniecki, D. Gromov. *Journal of Materials Science & Technology* **34** (2018) 472.
- [3] D. Gromov, S. Bulyarskii, A. Pavlov, S. Scorik, A. Shulyat'ev, A. Trifonov. *Diamond and Related Materials* **64** (2016) 97.
- [4] S. Dubkov, S. Bulyarskii, A. Pavlov, A. Trifonov, E. Kitsyuk, P. Mierczynski, T. Maniecki, R. Ciesielski, S. Gavrilov, D. Gromov. SPIE 10224, International Conference on Micro- and Nano-Electronics (2016)

Study of plasmons and thermoelectric properties of nanoparticles connected by thin conductive bridges

A.S. Fedorov^{*,1,2}, P.O. Krasnov², M. A. Visotin¹, H. Ågren³

¹ Kirensky Institute of Physics, Federal Research Center KSC SB RAS, 660036 Krasnoyarsk, Russia

² Siberian Federal University, 660041 Krasnoyarsk, Russia

³ Division of Theoretical Chemistry and Biology, Royal Institute of Technology, SE-100 44 Stockholm, Sweden

*e-mail: alex99@iph.krasn.ru

Plasmonics, a subfield of nanophotonics, is mainly concerned with control and manipulation of electromagnetic fields with noble metal nanoparticles which possess free electron gas that can strongly interact with the electromagnetic radiation to produce an interesting phenomenon called surface plasmon resonance [1,2]. Recently, a number of theoretical and experimental reports have been emerging on the conductive coupling and plasmon of metallic nanoparticles (charge transfer plasmon- CTP) owing to its promises in sensing, waveguiding, molecular electronics and even building artificial molecules [3-6]. Unfortunately, in all these works systems were studied where particles were connected by a thick conductive bridge having thickness more than 5 nm.

So, here it is proposed and investigated the possibility of CTP existing in systems consist of metal nanoparticles interconnected by thin conductive molecules. An original quantum hybrid model of oscillator type is developed for describing of these plasmons [7]. The model takes into account the kinetic energy of conductive electrons composing ballistic current through the conductive bridge and electrostatic potential energy of charged nanoparticles. The model used parameters which were calculated by DFT simulations.

The CTP are investigated for some test system, consisting of 2,3,4 and more small gold nanoparticles having some hundreds atoms and bridged by the conjugated polyacetylene molecule C_nH_n terminated by sulfur atoms. For simple systems consisting of a pair of nanoparticles connected by a conducting bridge, using this approach, a formula is derived that determines the effective

plasma frequency $\tilde{\omega}_{pl}$, see (1).

$$\tilde{\omega}_{pl}^2 \approx \frac{2ne^2}{m^* L^2 R} \quad (1)$$

Here, n is the concentration of conduction electrons in the conducting bridge, m^* is the effective mass of these

electrons, R is the radius of the nanoparticles, and L is the length of the conducting bridge.

Using this formula, we can verify that the plasmon frequencies in the proposed systems lie in the infrared (IR) region. Strong dependence of plasmon frequency on the system conductivity makes possible to use systems consist of metal nanoparticles bridged by conductive molecules to build chemical gas sensors based on a change in the conductivity of the conducting molecule during its chemical interaction with gas molecules. The interaction can significantly change the conjugated character of the π -bonding in the molecule and its conductivity.

Thermoelectric properties of periodic systems consisting of gold metal nanoparticles connected by conducting bridges C_nH_n are also considered. It is shown these properties strongly depend on the bridge electrical conductivity and its thermal conductivity. The perspectives of these systems as novel thermoelectric materials are discussed.

Acknowledgements

This study was supported by the Russian Science Foundation, project no. 16-13-00060.

References

- [1] S. A. Maier, Plasmonics: Fundamentals and Applications (Springer, 2007).
- [2] M. I. Stockman, Opt. Express **19** (2011) 22029.
- [3] O. Perez-Gonzalez, N. Zabala, A. G. Borisov, N. J. Halas, P. Nordlander, and J. Aizpurua, Nano Lett. **10** (2010) 3090.
- [4] L. Liu, Y. Wang, Z. Fang, and K. Zhao, J. Chem. Phys. **139** (2013) 064310.
- [5] Y. Huang, L. Ma, M. Hou, Z. Xie, and Z. Zhang, Phys. Chem. Chem. Phys. **18** (2016) 2319.
- [6] N. Koya and J. Lin, J. Appl. Phys. **120** (2016) 093105.
- [7] A. Fedorov, P. Krasnov, M. Visotin, F. Tomilin, S. Polyutov and H. Ågren. J. Chem. Phys. **151** (2019) 244125.

Heat treatment of nanostructured powders obtained by spark erosion of WC-8Co cemented carbide in oil

M.I. Dvornik, E.A. Mikhailenko*

Institute of Material science of FEB RAS, 153 Tikhoookanskaya St., Khabarovsk 680045, Russia

*e-mail: Mea80@list.ru

Introduction

Cemented carbides have remained the most common tool material used for metall cutting for almost 100 years [1]. Modern researchers have developed ultrafine-grained (UFG) cemented carbides that are significantly superior to other types of cemented carbides in terms of wear resistance due to high hardness [1-2].

A promising economical method for producing UFG powders from cemented carbides waste is spark erosion (SE) in oil [3-4]. The SE is based on the action of discharges between the anode and cathode in liquid. The surface layers of electrodes changed under the influence of spark discharges erode in the liquid, vapor, and solid phases. One of the main problems of SA is an uncontrolled change in chemical composition [3-4]. During SA in oil an excess of carbon is formed, which makes the resulting powder unsuitable for further use in the production of cemented carbides. The aim of this work is to obtain a WC-Co stoichiometric powder by SE in oil and heat treatment in a CO₂ atmosphere.

Results and discussion

The average WC grain diameter in the initial alloy WC-Co is 1.6 μm (fig. 1a). Microstructure of the particles obtained by SE in oil consists of rounded WC grains and cobalt layers (fig. 1b). The measurements showed that the average diameter of the formed WC grains is approximately 0.18 μm. The total carbon content of the powder increased from 5.6% to 9.0%. This means that the powder contains 3.4% free carbon.

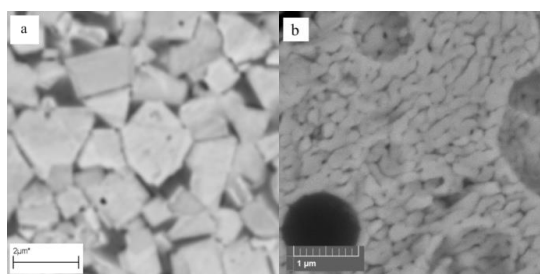


Figure 1. The microstructure of the initial alloy WC-8Co (a) and the microstructure of the particle obtained by SE (b).

The carbon excess was removed by heat treatment in a CO₂ atmosphere:



At the selected temperature (1000 °C), the equilibrium of reaction (1) is shifted toward CO, which accelerates the process. The amount of CO₂ supplied was calculated based on the value of the free carbon mass ($\Delta m = 0.44$ g), which must be removed:

$$V_{CO_2} = \frac{\Delta m \cdot V_m}{Ar_C} \quad (2)$$

Where $Ar_C = 12$ g / mol - atomic mass of carbon, $V_m = 22.4$ l / mol - the molar volume of ideal gas. The pressure ($P(t)$) in the furnace was continuously measured, based on which the current amount of removed carbon was calculated:

$$\Delta m_C(t) = \left(\frac{V_{\text{furn}} \cdot P(t) / P_{\text{atm}} - V_{CO_2}}{V_m} \right) \cdot Ar_C \quad (3)$$

Where $P_{\text{atm}} = 1000$ mbar - atmospheric pressure, $V_{\text{furn}} = 2.8$ l - the volume of gas that is placed in a furnace heated to 1000 °C.

As can be seen in fig. 2, the pressure increase slows down when the mass fraction of carbon approaches the target value (5.6%). After 120 minutes, the calculated value of the excess carbon did not exceed 0.1%. A phase analysis of the obtained powder confirmed that it consists only of the WC and Co phases. Analysis for carbon showed that the carbon content in the powder (5.5%) decreased to the target value (5.6%). The average grain diameter increased to 0.43 microns.

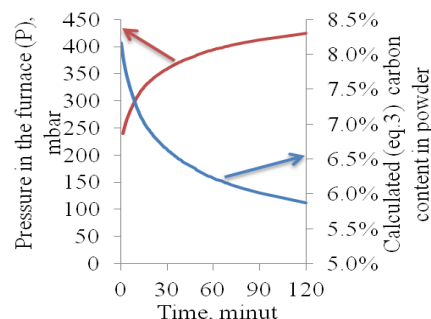


Figure 2. The dependence of the pressure in the furnace on the treatment time ($P(t)$) and the carbon content in the powder calculated by eq. (3).

Summary

As a result of spark erosion (SE) of medium-grained WC-8Co cemented carbide in oil, a nanostructured powder was obtained. As a result of heat treatment at a temperature of 1000 °C for 120 minutes in CO₂ the excess of carbon was removed. Obtained powder is suitable for the production of UFG cemented carbide.

References

- [1] Fang Z.Z., Wang X., Ryu T., Hwang K.S., Sohn H.Y. *IJRMHM* **27** (2009) 288.
- [2] H.Saito, A. Iwabuchi, T.Shimizu. *Wear.* №261(2006), 126
- [3] R. A. Latypov, E. V. Ageev, G. R. Latypova, A. Yu. Altukhov, E. V. Ageeva. *Russian Metallurgy (Metally)* **6** (2018) 573.
- [4] F. Kabirinia, M. Shabgard, N. S. Tabrizi. *Applied Physics A* **125** (2019) 1.

Metal and non-metal co-substituted titanium dioxide derivatives: synthesis and electrochemical performance

A.A. Sokolov^{*1,2}, D.P. Opra¹, S.V. Gnedenkov¹, S.L. Sinebryukhov¹, E.I. Voit¹, A.Y. Ustinov¹, V.Y. Mayorov¹, V.V. Zheleznov¹

¹ Institute of Chemistry of FEB RAS, 159 Pr. 100-letiya Vladivostoka, Vladivostok 690022, Russia

² Far Eastern Federal University, 8 Sukhanova St., Vladivostok 690950, Russia

*e-mail: alexsokol90@mail.ru

Titanium dioxide is positioned as a safety anode material for high power density lithium-ion batteries (LIBs), mainly due to their high Li^+ insertion potential (1.6–1.7 V). Among the titania polymorphs the TiO_2 (anatase) and TiO_2 (B) are intensively investigated as LIB anodes due to features of their crystal lattices – the accessibility of voids and channels for the incorporation of Li^+ or Na^+ ions. However, unlike TiO_2 (anatase), the use of TiO_2 (B) in LIB is limited by the complexity and high cost of its preparation. At the same time, the anatase is characterized by low Li-ion diffusivity (10^{-15} – 10^{-9} $\text{cm}^2 \text{s}^{-1}$) and poor electrical conductivity (10^{-12} – 10^{-7} S cm^{-1}) that deteriorate the reversible capacity and rate capability. A promising way for modification of TiO_2 (anatase) is a cationic (partial substitution of Ti^{4+} with metal ions) and anionic (replacement of O^{2-} with non-metals) doping.

Within the scopes of the present work, the nanostructured TiO_2 (anatase) doped with Hf^{4+} ($\text{Ti}_{0.95}\text{Hf}_{0.05}\text{O}_2$), Zr^{4+} ($\text{Ti}_{0.97}\text{Zr}_{0.03}\text{O}_2$), and $\text{Zr}^{4+}/\text{F}^-$ ($\text{Ti}_{0.97}\text{Zr}_{0.03}\text{O}_{1.98}\text{F}_{0.02}$) have been synthesized by a template sol-gel method on a carbon fiber and investigated as an anode materials for LIB.

The scanning electron microscopy and transmission electron microscopy investigations show that as-synthesized TiO_2 -based materials have the similar tubular microstructure. Samples consisted of tubes ranging in length from 5 to 300 μm . Outer diameter of tubes varies in the range 2–5 μm . Tubes have nanostructured surface, their walls composed of nanoparticles with a size of 10–25 nm.

According to Raman spectroscopy studies, the incorporation of dopants into titania crystal structure leads to increase of unit cell parameters due to the difference in the Zr^{4+} (0.72 Å), Hf^{4+} (0.71 Å) and Ti^{4+} (0.604 Å) ionic

radius values. It can play a significant role for ionic transport within TiO_2 structure. At the same time, replacement of O^{2-} with F^- contributes to Ti^{3+} generation into the crystal lattice and affects the conductivity. In particular, the conductivity of $\text{Ti}_{0.97}\text{Zr}_{0.03}\text{O}_{1.98}\text{F}_{0.02}$ reaches $1.7 \cdot 10^{-9}$ S cm^{-1} , that is at least a four order of magnitude higher as compared undoped TiO_2 ($7.36 \cdot 10^{-13}$ S cm^{-1}) sample.

The electrode from of as-synthesized TiO_2 materials was tested in half-cell with a lithium counter electrode in the voltage range of 1–3 V. After the 35th cycle of galvanostatic charge/discharge at a current density of 0.1C the reversible capacity was equal to 55.9 mA g^{-1} (undoped TiO_2), 154.2 mA g^{-1} ($\text{Ti}_{0.95}\text{Hf}_{0.05}\text{O}_2$) and 135 mA g^{-1} ($\text{Ti}_{0.97}\text{Zr}_{0.03}\text{O}_2$). Meanwhile, reversible capacity of $\text{Zr}^{4+}/\text{F}^-$ -co-doped TiO_2 still is equal to 163 mAh g^{-1} even after cycling at 1C, whereas single-doped samples gave only about 34 mAh g^{-1} .

Thus, it was established that single-doping with hafnium or zirconium and co-doping with zirconium/fluorine of anatase titanium dioxide has a beneficial effect on its performance as an anode material for LIBs. The main reasons are as follows: i) unit cell volume increases due to the incorporation of hafnium and zirconium; ii) conductivity improves after doping with fluorine.

Acknowledgements

The investigations on Zr-doped titania were carried out under the grant № 18-33-00345 from Russian Foundation for Basic Research. Russian Science Foundation (grant № 19-73-10017) supported the studies on Hf- and F-doped TiO_2 .

Enhancement the lithium storage performance of TiO₂(B) through zirconium and vanadium doping

D.P. Opra*, S.V. Gnedenkov, S.L. Sinebryukhov, A.A. Sokolov, A.B. Podgorbunsky, A.Yu. Ustinov, A.I. Neumoin, I.V. Imshinetskiy, K.V. Nadaraia, K.P. Opra, D.V. Mashtalyar

Institute of Chemistry of FEB RAS, Prospekt 100-letiya Vladivostoka 159, Vladivostok 690022, Russia

*e-mail: dp.opra@ich.dvo.ru

Recently, lithium-ion batteries (LIBs) are widely used as energy sources for different applications, e.g. portable electronics, tools, medical instruments, etc. Typical LIB is constructed of graphite anode that possesses natural abundance, low cost, and good specific capacity (372 mAh g⁻¹). However, lithiated graphite has a potential of below 0.3 V vs. Li/Li⁺ that lead to LIB electrolyte decompose to a form of solid electrolyte interphase film. The latter results in insufficient safety of commercial LIBs for moderate- and high-rate (more than 1C) applications [1,2].

Titanium dioxide polymorphs have a high Li⁺ insertion potential of more than 1.5 V that is within the electrochemical window of typical LIB electrolytes. Additionally, as opposed to graphite, the volume changes effect during lithiation/delithiation is almost absent for TiO₂ materials that results in good stability of anode during cycling. Among other polymorphs, TiO₂(bronze) has gained much attention as high-rate anode due to its crystallographic features. TiO₂(B) is a monoclinic crystal system (space group *C2/m*) composed of TiO₆ octahedra sharing by edges and connecting by corners, that possesses an open channel parallel to the *b*-axis. The open structure of TiO₂(B) shortens Li⁺ ions diffusion pathways without irreversible lattice distortions that results in its able to accommodate of 1 Li⁺ per formula unit, corresponding a capacity of 335 mAh g⁻¹. Unfortunately, TiO₂(B) has a poor electronic conductivity (10⁻¹²–10⁻⁷ S cm⁻¹ [3]), that limits its application as high power density LIB anode.

Over the last 5 years, it had been demonstrated that intrinsic electronic conductivity of TiO₂-based anode materials could be effectively improved by doping. In particular, the incorporation of ions with the oxidation number less than +4 (e.g. Co²⁺ [4]) creates an oxygen vacancies that results in increase of anatase ionic conductivity. On the other hand, partial substitution of Ti⁴⁺ into the anatase lattice by the ions with the oxidation number more than +4 (e.g. Mo⁶⁺ [5]) causes the charge redistribution due to partial reduction of Ti⁴⁺ to Ti³⁺ enhancing electronic conductivity. Additionally, anatase structure modification is achieved due to the difference in the values of Ti⁴⁺ and Mⁿ⁺ ionic radius [6]. The latter may decrease the crystal lattice stresses induced by Li⁺ ions insertion.

Herein we report a synthesis procedure, physicochemical parameters, and electrochemical performance of TiO₂(B) doped with Zr and V metals.

Zirconium-doped TiO₂(B) had been fabricated by a hydrothermal treatment of TiO₂(anatase) and ZrOCl₂·8H₂O in 10 M NaOH at 170 °C for 96 h. According to SEM, the hydrothermal reaction results in complete conversion of anatase precursor particles into belt-like structures

(thickness: 10–15 nm, width: 50–150 nm, length: some microns, surface area: 72–76 m²/g). The XRD confirmed that Zr⁴⁺ ions substitute in the Ti⁴⁺ sites, forming Ti_{1-x}Zr_xO₂(B) solid solutions up to Zr to Ti atomic ratio of 0.06, where the unit cell volume increases as the zirconium content rises. After 90 charge/discharge cycles at 33.5 mA g⁻¹, Ti_{0.94}Zr_{0.06}O₂(B) electrode had a capacity of 165 mAh g⁻¹. For undoped TiO₂(B) nanobelts, this parameter was only 135 mAh g⁻¹. However at a current load of 1675 mA g⁻¹, the Ti_{0.94}Zr_{0.06}O₂(B) retained a reversible capacity of only 107 mAh g⁻¹.

TiO₂(B) nanotubes doped by vanadium have been synthesized through an autoclave treatment of anatase nanopowder and NH₄VO₃ in 12 M NaOH aqueous solution at 150 °C during 48 h. The material shows a mesoporous structure with a specific surface area of about 180 m² g⁻¹. XPS data presume the presence of V³⁺, V⁴⁺, V⁵⁺, and Ti³⁺ in doped TiO₂(B). As found by XRD and EIS investigations, the vanadium expands bronze titania crystal structure and enhances the conductivity of material by three orders of magnitude. When tested for lithium storage, the V-modified (V/Ti = 0.04) titania nanotubes show a specific capacity of 133 mAh g⁻¹ after 100 charge/discharge cycles at the current density of 3000 mA g⁻¹ with a Coulombic efficiency of around 98.9%, resulting in its good cycleability. The material still possesses a reversible capacity of 114 mAh g⁻¹ at a very high current load of 6000 mA g⁻¹, demonstrating superior rate characteristics for secondary lithium batteries.

Acknowledgements

The studies on Zr-doped titania was supported by Russian Foundation for Basic Research (grant No. 18-33-00345). The synthesis and investigation of V-doped TiO₂(B) was carried out under the grant № 19-73-10017 from Russian Science Foundation.

References

- [1] M. Fehse, E. Ventosa. *ChemPlusChem* **80**(2015)785.
- [2] D.P. Opra, S.V. Gnedenkov, S.L. Sinebryukhov. *J. Power Sources* **442** (2019) 227225.
- [3] M. Zúcalová, M. Kalbáč, L. Kavan, I. Exnar, M. Graetzel. *Chem. Mater.* **17** (2005) 1248.
- [4] A.A. Kashale, A.S. Rasal, G.P. Kamble, V.H. Ingole, P.K. Dwivedi, S.J. Rajoba, L.D. Jadhav, Y.-C. Ling, J.-Y. Chang, A.V. Ghule. *Compos. Part B: Eng.* **167**(2019)22.
- [5] T.V. Thi, A.K. Rai, J. Gim, S. Kim, J. Kim. *J. Alloy. Compd.* **598** (2014) 16
- [6] S.V. Gnedenkov, S.L. Sinebryukhov, V.V. Zhelezov, D.P. Opra, E.I. Voit, E.B. Modin, A.A. Sokolov, A.Yu. Ustinov, V.I. Sergienko. *Roy. Soc. Open Sci.* **5** (2018) 171811.

Composite coatings formed on PEO pretreated MA8 magnesium alloy in aqueous suspension of PTFE

E.A. Belov^{*1}, K.V. Nadaraia^{1,2}, D.V. Mashtalyar^{1,2}, I.M. Imshinetsky¹, A.N. Minaev², S.L. Sinebryukhov¹, S.V. Gnedenkova¹

¹ Institute of Chemistry of FEB RAS, 159 pr. 100-letiya Vladivostoka, Vladivostok 690022, Russia

² Far Eastern Federal University, 8 Sukhanova St., Vladivostok 690950, Russia

*e-mail: belov_eal@mail.ru

Formation of composite coatings on the MA8 magnesium alloy is already a common practice [1], since magnesium has high specific strength properties, but its corrosion resistance and wear resistance are too low for a wide range of applications [2]. The formation of a protective coating on the surface of magnesium alloy by plasma electrolytic oxidation (PEO) with the further incorporation of fluoropolymer materials favorably affects its resistance to corrosion and wear [3]. The previously used in our studies alcohol suspension [3] of superdispersed polytetrafluoroethylene (SPTFE) hazardous for workers and manufacturing. Therefore, the properties of composite coatings (CC) formed using the aqueous suspension of SPTFE were investigated in this work.

As samples for research we used MA8 magnesium alloy plates of sizes 30×20×1 mm³. For standardization the samples were grinded with sand paper. Then, the samples were washed with distilled water and degreased with alcohol. Process of plasma electrolytic oxidation was carried out in NaF and Na₂SiO₃ electrolyte, in bipolar mode, in two stages. Whole time of PEO process was equal to 800 s. The formation of composite coating was carried out by immersing samples in 12.5% SPTFE aqueous suspension for 10 s. After withdrawal from the suspension, the samples were air dried. Then, the samples were subjected to heat treatment at a temperature of 315 °C for 15 min. Coatings were formed with single (CC-1x), double (CC-2x) and triple (CC-3x) polymer application. Electrochemical properties of the samples were studied by electrochemical impedance spectroscopy and

Table I. Corrosion properties (E_c is the corrosion potential, I_c is the corrosion current density, R_p is the polarization resistance) of samples with various types of surface treatment

Sample	R_p [$\Omega \times \text{cm}^2$]	I_c [A/cm ²]	E_c [V]
Bare alloy	489.5	3.3×10^{-5}	-1.56
With PEO coating	1.03×10^5	2.4×10^{-7}	-1.45
CC-1x	2.2×10^8	2.5×10^{-10}	-1.43
CC-2x	2.9×10^8	1.6×10^{-10}	-1.42
CC-3x	6.3×10^8	7.7×10^{-11}	-0.97

potentiodynamic polarization, using the VersaSTAT MC system (Princeton Applied Research, USA). The adhesion of the coatings to substrate were evaluated using a Revetest Scratch Tester (CSM Instruments, Switzerland).

From the results of electrochemical tests (Table I) a decrease in the corrosion current density by several orders of magnitude was revealed in comparison with the base PEO-layer. The scratch test data presented in the Table II allow us to talk about an increase in the loads, at which the coating is scratched to the substrate, and at which the indenter penetrates to the metal. From the analysis of the data, it can be concluded that the obtained composite coatings in their protective properties exceed the base PEO-coating. Formed composite layers decrease corrosion current density by more than 3 orders of magnitude in comparison with the base PEO-coating. Adhesion strengths of polymer-containing coatings is higher than that of PEO-layers.

Table II. Adhesive characteristics of formed coatings

Sample	L_{c2} [N]	L_{c3} [N]
PEO-coating	4.6	10.2
CC-1x	6.7	11.9
CC-2x	6.8	12.9
CC-3x	6.8	13.1

Acknowledgements

This work was supported within the frames of the State Order of the Institute of Chemistry of FEB RAS, project no. 0265-2019-0001. Adhesive characteristics have been studied within the framework of the Grant of the Russian Foundation for Basic Research (project no. 19-29-13020 mk).

References

- [1] F. Henry, F. Renaux, S. Coppée, R. Lazzaroni, N. Vandecasteele, F. Reniers, R. Snyders *Surf. Sci.* **606** (2012) 1825.
- [2] M. Esmaily, J.E. Svensson, S. Fajardo, N. Birbilis, G.S. Frankel, S. Virtanen, R. Arrabal, S. Thomas, L.G. Prog. Mater. Sci. **89** (2017) 92.
- [3] S.V. Gnedenkova, S.L. Sinebryukhov, V.S. Egorkin, D.V. Mashtalyar, I.E. Vyalyi, K.V. Nadaraia, I.M. Imshinetskiy, A.I. Nikitin, E.P. Subbotin, A.S. Gnedenkova. *J. Alloys Compd.* **808** (2019) 151629.

PEO coated porous Mg/HAp implant materials impregnated with bioactive components

A.B. Podgorbunsky*, S.L. Sinebrukhov, I.M. Imshinetsky, S.V. Gnedenkova

Institute of Chemistry of FEB RAS, 159 pr. 100-letiya Vladivostoka, Vladivostok 690022, Russia

*e-mail: pab@ich.dvo.ru

In this study, for design a scaffold for tissue engineering from magnesium porous scaffold was fabricated by means of powder metallurgical process (using cold pressing technique) followed by a protective coating application. The formed scaffolds before PEO coating were infiltrated with bioactive components. The structural characteristics, mechanical properties of the porous Mg specimens were investigated. The findings of the study indicates that developing different porosity, therefore, a different degree of biodegradability, followed by protection with sodium silicate coating are expected to have wide application in tissue engineering.

A recent years trend in the implant's design is development scaffolds and composites of magnesium with controlled porosity. The main source of magnesium in the human body is found in bone tissue. With a high strength, magnesium evinces rigidity and density comparable to these parameters for cortical bone. In addition, the carcass material is able to completely biodegrade after an appropriate period in the human body [1-3]. Since the corrosiveness of magnesium is too high and does not allow the mechanical properties of a temporary implant to be maintained for the period necessary for the bone splicing, its necessary to protect the metal base from destruction, including through forming a coating. An integrated approach to solving problems of protecting magnesium alloys from rapid dissolution and ensuring their bioactivity is already actively used by scientists working in this field recently [4, 5]. Directional synthesis of a composite material combining acceptable elastoplastic properties close to bone and bioactivity of the ceramic component (hydroxyapatite) as an osteointegration basis for the formation of new bone tissue are at the forefront of global research in the field of development of materials for implantology [1, 6].

Pure magnesium powder (purity $\geq 99.9\%$, powder size $\leq 40 \mu\text{m}$, Sigma-Aldrich), hydroxyapatite (HAp) powder and carbamide ($\text{CO}(\text{NH}_2)_2$, range of 200–400 μm , purity of 99.0%, Sigma-Aldrich) particles were used as starting materials. Urea was used as a space holder particles as elsewhere to prepare a porous structure [7]. Pure hydroxyapatite nanoparticles were obtained from calcium hydroxide and di-ammonium hydrogen phosphate in a rapid way by microwave processing. The magnesium, hydroxyapatite and the carbamide particles were thoroughly mixed. The mixed powders were uniaxially pressed at a pressure of 200 MPa into pellets with 10 mm radius and 2-3 mm thickness. The compacts were then heat

treated to burn out the spacer particles, and to sinter into the porous magnesium foams. Then the samples were impregnated in an alcoholic solution of stone oil (brashun). Formation of coatings occurred in the two-stage bipolar PEO-mode as described in [8]. After PEO process, the samples were cleaned with de-ionized water to remove the remained electrolyte and then dried in air.

The obtained hydroxyapatite powder was analyzed for phase composition, shape and particle size. Morphology of the prepared scaffolds were analyzed by Scanning Electron Microscopy which showed pore size of 100 to 200 μm . It is shown that in the case of using hydroxyapatite powder as a bioactive additive, it agglomerates into large particles. In the case of using stone oil, there are compositions of various sizes in the pores are formed.

Porous magnesium specimens impregnated with bioactive component and coated with a high adhesion protective layer have been fabricated. It has been established that the fabricated samples are characterized by a branched and an open-cellular structure. There are nanosized inclusions form on the surface and inside the pores.

Acknowledgements

Synthesis, estimation of the morphological properties of composites was supported by the Russian Science Foundation (grant № 19-73-00073). The electrochemical studies were supported by the Russian Foundation for Basic Research (grant № 19-29-13020).

References

- [1] A. Kucharczyk, K. Naplocha, J.W. Kaczmar, H. Dieringa and K.U. Kainer. *Adv. Eng. Mater.* **20** (2018) 1.
- [2] N. Sezer, Z. Evis, S.M. Kayhan, A. Tahmasebifar, M. Koç. *J. Magnesium Alloys* **6** (2018) 23.
- [3] M.A. Velasco, C.A. Narváez-Tovar, D.A. Garzón-Alvarado. *Biomed Res. Int.* (2015)1.
- [4] S.V. Gnedenkova, Y.P. Sharkeev, S.L. Sinebrukhov, O.A. Khisanfova, E.V. Legostaeva, A.G. Zavidnaya, A.V. Puz', I.A. Khlusov and D.P. Opra. *Corros. Rev.* **34** (2016) 65.
- [5] S.V. Gnedenkova, O.A. Khisanfova, A.G. Zavidnaya. *Surf. Coat. Technol.* **204** (2010) 2316.
- [6] S. Agarwal, J. Curtin, B. Duffy, S. Jaiswal. *Mater. Sci. Eng., C.* **68** (2016) 948.
- [7] H. Zhuang, Y. Han. *Ailing Feng. Mater. Sci. Eng., C.* **28** (2008) 1462.
- [8] A.B. Podgorbunsky, K.V. Nadaraia, I.M. Imshinetsky, S.L. Sinebrukhov and S.V. Gnedenkova. *J. Phys. Conf. Ser.* **1092** (2018) 1.

Formation of PEO-coatings for implant materials

K.V. Nadaraia^{*1,2}, A.I. Pleshkova², M.A. Piatkova², I.M. Imshinetskiy¹, D.V. Mashtalyar^{1,2},
N.G. Plekhova^{1,3}, S.L. Sinebryukhov¹, S.V. Gnedenkov¹

¹ Institute of Chemistry of FEB RAS, 159 pr. 100-letiya Vladivostoka, Vladivostok 690022, Russia

² Far Eastern Federal University, 8 Sukhanova St., Vladivostok 690950, Russia

³ Pacific State Medical University, 2 Ostryakova St., Vladivostok 690002, Russia

*e-mail: nadaraiakv@mail.ru

Currently, bioinert materials, in particular titanium, are used to obtain implants. Despite the undeniable advantages, the use of implants of this type is accompanied by a number of problems, mainly related to tribological properties. We propose to use biodegradable materials, in particular magnesium, as a material for implants. In this study, we investigated the biological activity of magnesium and titanium samples with protective coatings formed by the plasma electrolytic oxidation method (PEO). According to our assumptions, such a coating will solve the problem of high reactivity of magnesium, improve tribological properties of studied metals and facilitate faster restoration of the patient due to cell adhesion to the porous surface, formed by PEO.

Plasma electrolytic oxidation is one of the most promising ways of the alloys and metals surface treatment [1]. During the PEO process, the oxidation of the treated sample is performed using high values of the applied electrode potential difference in comparison with conventional anodizing. PEO-coatings are hard, dense, wear-resistant, and well-adhered for metals [2].

Bioinert and bioresorbable implants initiate an immune response when introduced into the body. This reaction is mediated by antigen-presenting cells, including dendritic. The paper presents the results of a study of immunomodulatory properties of our samples under their effects on receptor phenotype of dendritic cells (DC). In a population of hematopoietic cells in the presence of magnesium, an increase in the expression of CD80 / CD86 differentiation markers was detected, as well as the CD38 activation antigen and CD34 adhesion receptor, whereas expression of the CD14 leukocyte marker was reduced. Thus, magnesium in comparison with titanium has a more pronounced effect on the process of differentiation and maturation of hematopoietic cells into dendritic direction.

In this study, we have used commercial pure titanium VT1-0. All samples were made in the following size: 30×15×1 mm³. All specimens were mechanically ground successively to P1200 grit. We used the primary culture of undifferentiated cells of the myeloid pool obtained from the bone marrow of the femoral bone of the guinea pigs by washing the bone marrow canal with RPMI-1640 medium. The degree of cells differentiation was measured by indirect fluorescent antibody technique.

The degree of differentiation and maturity of DC can be studied by the change in the expression level of their differentiating molecular clusters CD34, CD38. The hematopoietic pool CD34 receptor relates to the intercellular adhesion ligands and plays an important role in the early stages of hematopoiesis.

As a control, cells adhered to the surface of a specialized plastic coated with lectin were used, and

Escherichia coli lipopolysaccharide (LPS) was introduced to obtain a mature DC population. It is known that the cultivation of DC in the presence of GM-CSF and IL-4 with the addition of 2.5 ng/ml LPS stimulates the maturation of DC and reduces the content of macrophages in the culture [3]. It was determined that the maximum expression of CD34 on the surface of DC was observed on the first day of joint incubation with LPS, and the cell content was 72.1±5.8%. Subsequently, their number decreased, reaching the minimum figures by the end of the observation period (1.61±0.08%). Under the influence of implants, the number of CD34 positive cells was lower compared to the control. Therefore, for samples with titanium after 1 day, the indicator was 56.1±4.8%, and for samples with magnesium 48.1±4.6%. The minimum number of these cells was noted at the end of the observation period (21 s) and amounted to 1.8±0.2% and 2.4±0.6%, respectively. Thus, our data indicate that the effect of implants on the adhesion receptor expression is the same relative to each other, and the percentage of these cells on their expressed effect as inducers of cell maturation is reduced relative to the control.

The presented data indicate that the effect of the implants on the expression of the adhesion receptor CD34 for hematopoietic cells is the same relative to each other, and the percentage of these cells on their action as maturation inducers is reduced relative to the control. The effect of magnesium on differentiation of the hematopoietic cells is predominantly more pronounced than titanium, particularly towards dendritic. Of particular interest is the property of the magnesium implant that we discovered. Biodegradable magnesium had a more pronounced effect on the process of directed differentiation and maturation of DCS compared to bioinert titanium.

Acknowledgements

This work was supported within the frames of the State Order of the Institute of Chemistry of FEB RAS, project no. 265-2019-0001. Coatings formation have been carried out within the framework of the Grant of the Russian Foundation for Basic Research (project no. 19-29-13020 mk).

References

- [1] D.V. Mashtalyar, S.L. Sinebryukhov, I.M. Imshinetskiy, A.S. Gnedenkov, K.V. Nadaraia, A.Y. Ustinov, S.V. Gnedenkov. *Appl. Surf. Sci.* **503** (2020) 144062.
- [2] S.V. Gnedenkov, S.L. Sinebryukhov, V.S. Egorokin, D.V. Mashtalyar, I.E. Vyalyi, K.V. Nadaraia, I.M. Imshinetskiy, A.I. Nikitin, E.P. Subbotin, A.S. Gnedenkov. *J. Alloys Compd.* **808** (2019) 151629.
- [3] J. Banchereau, R.M. Steinman. *Nature* **392** (1998) 245.

Synthesis of phosphate phases on polysaccharide template

V.E. Silant'ev*, V.S. Egorkin, L.A. Zemskova, S.L. Sinebryukhov, S.V. Gnedenkov
Institute of Chemistry of FEB RAS, 159 100-letiya Vladivostoka Pr., Vladivostok 690022, Russia

*e-mail: vladimir.silantyev@gmail.com

Hybrid materials based on different polymers including biopolymers with addition of metal nanoparticles and metal oxides have been developed over recent years due to the excellent properties of individual components and outstanding synergistic effects. Chitosan as biodegradable, biocompatible and nontoxic biopolymer is a perfect object for this purpose. Chitosan composites are becoming promising alternatives for conventional adsorbents of heavy metal ions, dyes and proteins in various media and may be employed to solve numerous problems in environmental engineering.

Chitosan and chitosan-based particulate systems can be used as thickening agents in food industry and as potential drug deliveries in pharmaceutical and biomedical fields. Composite materials currently are under investigation for application as biomedical implants [1, 2]. Significant interest has been generating in development of composites that contain hydroxyapatite because its chemical composition is similar to bone tissue.

Design of composite coatings for biomedical applications is inevitably related to deposition techniques. The two main routes of synthesis of polymer-loaded nanoparticles are ex-situ and in situ. Ex-situ method is realized by synthesis of inorganic nanoparticles in the first place and their dispersion in a polymer solution or three-dimensional matrix in the second. However, blending polymers and nanoparticles pose significant challenges to obtain homogenous and well dispersed inorganic material in the volume of polymer. Different in-situ processes are used to overcome these difficulties. In this case polymer phase acts as a micro-reactor and inorganic nanoparticles are generated inside the polymer phase from precursors that are transformed into desired nanoparticles by a series of appropriate reactions [3, 4].

In this work we represent method of calcium orthophosphate preparation on chitosan template. For this

purpose precursor salts (calcium nitrate and potassium dehydrate phosphate) were added to the chitosan solution to form calcium phosphate particles. Stoichiometric ratio of the salts was set as 1.67. Production of calcium phosphate and simultaneous deposition of the biopolymer were carried out in an atmosphere of ammonia vapor that contributes to alkalization of the solution. Materials obtained as films on a glass substrate were sequentially dried and warmed at 100 °C.

Composite films were characterized in terms of physicochemical properties by scanning electron microscopy and x-ray phase analysis (XRD). XRD data for calcium phosphate powders are not similar to calcium phosphate phases detected in our spectra. Problem of converting of calcium orthophosphate phases into hydroxyapatite was discussed in the report.

Acknowledgements

This research was supported by Russian National Foundation, grant № 20-73-00379.

XRD data were collected within the frames of the State Order of the Institute of Chemistry of FEB RAS, project № 0265-2019-0001.

Morphological studies were performed within the frames of the State Order of the Institute of Chemistry of FEB RAS, project № 0265-2019-0004.

References

- [1] I. Yamaguchi, K. Tokuchi, H. Fukuzaki, Y. Koyama, K. Takakuda, H. Monma, J. Tanaka *J. Biomed. Mater. Res.* **55** (2001) 20.
- [2] J. Redepening, G. Venkataraman, J. Chen, N. Stafford *J. Biomed. Mater. Res.* **66** (2003) 411.
- [3] W. Fang, H. Zhang, J. Yin, B. Yang, Y. Zhang, J. Li, F. Yao *Cryst. Growth Des.* **16** (2016) 1247.
- [4] R. Kumar, K.H. Prakash, P. Cheang, L. Gower, K.A. Khor *J. R. Soc. Inter-face* **5** (2008) 427.

Correlation between the properties of PEO-layer and coating formation current density

S.N. Suchkov^{*1,2}, M.S. Gerasimenko², K.V. Nadaraia^{1,2}, I.M. Imshinetsky¹, D. V. Mashtalyar^{1,2},
A.N. Minaev², S.L. Sinebryukhov¹, S.V. Gnedenkov¹

¹ Institute of Chemistry of FEB RAS, 159 pr. 100-letiya Vladivostoka, Vladivostok 690022, Russia

² Far Eastern Federal University, 8 Sukhanova St., Vladivostok 690950, Russia

*e-mail: snsuchkov@yandex.ru

Magnesium alloys are widely used in various industries due to their properties such as high specific strength and low density. However, high electrochemical activity and low wear resistance limit their application field [1]. One of the ways to prevent the negative effects of the environment on the metal surface is the protective coating formation. One of the most promising ways of the coatings formation is the plasma electrolytic oxidation (PEO) [1, 2]. Coating obtained by PEO have necessary functionally significant properties such as the large thickness, high porosity and resistivity to aggressive environment.

The inertness of the coating is determined by the composition, and it depends on the substances involved in the reactions during the oxidation process [2]. Thickness, porosity, corrosion resistance and wear resistance largely are depended on the formation mode and its characteristics. One of the most significant is the coating formation current density; since it determines the density of plasma discharges in which ion-exchange processes take place, resulting in a PEO-coating formed on the metal surface.

Thus, it is of interest to identify the relationship between the properties of synthesized coatings and process parameters. In this work, one of the most important parameters was investigated, namely, the current density of the coating formation.

In this research, the corrosion properties of coatings were investigated by potentiodynamic polarization and electrochemical impedance spectroscopy techniques. The structure and thickness of the coatings were examined using a scanning electron microscope.

Table I. Dependence of the coating properties on the formation current density (the table presents a selection of key points)

i [mA/mm ²]	d [μm]	R_p [kΩ×cm ²]
2.03	24	0.006
2.63	26	0.014
3.03	29	0.029
3.69	35	0.124
3.81	35	0.395

As it was shown (Table I), the coating thickness increased linearly, and the polarization resistance increased exponentially with the growth of the formation current density in the investigated range.

When the formation current density is less than 1.5 mA/mm², the anodizing process is carried out and the PEO-coating not formed. At values higher than 4.5 mA/mm², the coating was destroyed and deteriorated due to high current loads.

Thus, in the considered range of the most frequently used formation current densities there are functional dependencies between this parameter and the coating thickness (1) and the polarization resistance (2) are corresponded to the equations:

$$d = c_1 \cdot i + c_2, \quad (1)$$

$$R_p = c_3 \cdot e^{\alpha \cdot i}, \quad (2)$$

The constants in the equations are determined experimentally and do not depend on the coating thickness and polarization resistance. The calculated parameters are given in table II.

Table II. The constant of equations (1) and (2).

c_1 [mm ³ /mA]	c_2 [mm]	c_3 [kΩ×cm ²]	α [mm ² /mA]
6.96	8.11	0.01	2.03

The functional relationship between the process parameters and the properties of the resulting coatings is the result of this study.

Acknowledgements

This work was supported within the frames of the State Order of the Institute of Chemistry of FEB RAS, project no. 265-2019-0001. Electrochemical studies have been carried out within the framework of the Grant of the Russian Foundation for Basic Research (project no. 19-29-13020 mk).

References

- [1] Gh. Barati Darband, M. Aliofkhazraei, P. Hamghalam, N. Valizade, J. Magnesium Alloys **5** (2017) 74.
- [2] A.N. Minaev, S.V. Gnedenkov, S.L. Sinebryukhov, D.V. Mashtalyar, V.S. Egorkin, A.S. Gnedenkov, K.V. Nadaraia, Proc. Int. Offshore Polar Eng. Conf. 2014, 418-422.

Formation of protective coatings on AMg3 aluminum alloy using fluoropolymer nanopowder

V.S. Filonina^{*1,2}, K.V. Nadaraia^{1,2}, D.V. Mashtalyar^{1,2}, A.S. Gnedenkov¹, I.M. Imshinetsky¹, I.E. Vyaliy¹, V.S. Egorin¹, A.N. Minaev², S.L. Sinebryukhov¹, S.V. Gnedenkov¹

¹ Institute of Chemistry of FEB RAS, 159 pr. 100-letiya Vladivostoka, Vladivostok 690022,

² Far Eastern Federal University, 8 Sukhanova St., Vladivostok 690950, Russia

*e-mail: filonina.vs@gmail.com

Due to various reasons, reducing the weight of the structure without losing its functional characteristics is one of the urgent tasks of modern industry. It is well known that the structural properties of many aluminum alloys, having a lower specific weight, are comparable to the characteristics of steels [1]. However, the level of protective and mechanical properties of aluminum alloys may not be sufficient under the aggressive influence of the environment or when they work in a friction pair; this contributes to the expansion of the research area of methods for protecting the surface of aluminum and its alloys. It is revealed that morphology of surface layers, obtained by plasma electrolytic oxidation (PEO) on aluminum alloys allows modifying the formed coatings with various materials with the aim of improvement of a material protection [2].

The rectangular plates made of AMg3 aluminum alloy were used as experimental samples. After the mechanical pre-treatment of the samples with the aim of surface standardization, specimens were treated by the plasma electrolytic oxidation (PEO). PEO process was carried out in combined bipolar mode, comprising potentiodynamic and galvanodynamic stages. The formed oxide surface layer was further modified with use the superdispersed polytetrafluoroethylene (SPTFE) to form a protective polymer layer. SPTFE was applied from one to four times (CC-1x–CC-4x, respectively) using the dip-coating method in the suspension based on isopropanol, with the following heat treatment.

Further, the protective characteristics of the formed coatings were studied. Tribological tests were carried out using a Tribometer TRB-S-DE (CSM Instruments, Switzerland) in accordance with the “ball-on-disk” scheme. Wettability of the coatings was evaluated by sessile drop technique on a Drop Shape Analyzer DSA100 (KRÜSS, Germany). Adhesive characteristics were tested using scratch-tester REVETEST (CSM Instruments, Switzerland).

Results of analysis of the tribological data showed that the incorporation of a fluoropolymer component has a positive effect on wear resistance of formed coatings. A wear was decreased by two-fold as the SPTFE application treatment was increased, and a number of wear cycles was

increased in 50 times in comparison with base PEO-layer. This effect is explained by the fact that the polymer material, gradually releasing from the pores during wear, and acts as a dry lubricant, decreasing the friction coefficient.

Results of wettability investigations revealed highest hydrophobic properties of samples with CC-3x. Contact angle values of this coating was attained to 155°, that allows considering the coating as a superhydrophobic one.

Scratch-tests also allowed identifying a positive impact of SPTFE incorporation into the PEO-layer. Friction reduction contributes to an increase of the load value, at which the coating begins to peel off (L_{C2}), as well as end load required for the coating wear until metal (L_{C3}). As a result, the best adhesive characteristics observed for a sample with fourfold deposition of polymer-containing layer (CC-4x). For this coating critical loads increase by 1.5 (L_{C2}) and 2.9 (L_{C3}) times in comparison with the base PEO layer.

Summarizing all aforesaid it can be concluded that a method of the formation of PEO coatings with subsequent surface modification with a fluoropolymer material is suggested. It was established that incorporated superdispersed polytetrafluoroethylene has a positive effect on protective properties of obtained surface layers. There is an improvement in all studied properties: tribological, wettability, adhesive strength.

Acknowledgements

This work was supported within the frames of the Grant of Russian Science Foundation (project 19-73-00078). Adhesive characteristics have been studied within the framework of the Grant of the Russian Foundation for Basic Research (project no. 19-29-13020 mk).

References

- [1] J. R. Kissell, Robert L. Ferry, Aluminum structures: A Guide to Their Specifications and Design, second ed., John Wiley & Sons, Inc., New York, 2002.
- [2] A.N. Minaev, S.V. Gnedenkov, S.L. Sinebryukhov, D.V. Mashtalyar, V.S. Egorin, A.S. Gnedenkov, K.V. Nadaraia. Proc. Int. Offshore Polar Eng. Conf. **2014** (2014) 418.

Incorporation of TiO₂(B) nanoparticles into PEO coatings on MA8 magnesium alloy

I.M. Imshinetsky^{*1}, D.P. Opra¹, K.V. Nadaraia^{1,2}, V.S. Ivashina², A.A. Sokolov^{1,2},
D.V. Mashtalyar^{1,2}, S.L. Sinebryukhov¹, S.V. Gnedenkov¹

¹ Institute of Chemistry of FEB RAS, 159 pr. 100-letiya Vladivostoka, Vladivostok, 690022, Russia

² Far Eastern Federal University, 8 Sukhanova St., Vladivostok, 690950, Russia

*e-mail: igorimshin@gmail.com

Magnesium alloys, possessing low density and high specific strength, are now actively used in the automotive industry, aviation, medical equipment and electronics. The main limiting factor of their wider use is the high corrosion activity and low resistance to wear. Traditional corrosion protection methods, such as painting and anodizing, have a limited range of use due to low adhesion and hardness of the obtained layers [1–2].

Currently, the technology of coatings formation by plasma electrolytic oxidation (PEO) is being intensively developed [3-4]. This technology allows forming hard, wearproof layers with high corrosion properties.

One of the directions in the development of PEO method involves the use of nanosized dispersed materials as electrolyte component, that have certain physicochemical properties. It allows improving the performance of the surface layers and expand the field of practical use of coated materials [5-6].

Currently, there are a number of works, in which coatings modified with titanium dioxide are studied. These studies cover a wide range of different aspects that are affected by the incorporation of nanoparticles into coating.

TiO₂ (B) particles obtained by hydrothermal synthesis were used in this work to modify the coatings. The tape-like particles have a width of about 100 nm and a length of 1000 nm.

Particles TiO₂ (B) have a high chemical resistance, and therefore contribute to an increase in the electrochemical characteristics of the resulting coatings. Also, the incorporation of nanoparticles will improve the mechanical characteristics of the samples, as a result of filling the pores of the coatings.

The high photocatalytic activity of TiO₂ (B) particles can help in the creation of self-cleaning coatings, as well as coatings with antibacterial properties.

This work is aimed to study the formation conditions of coatings containing TiO₂ (B) nanoparticles and characterization of their physicochemical properties.

Formation of coatings was carried out on rectangular plates of the magnesium alloy MA8 (1.5 wt. % Mn; 0.15 wt. % Ce; Mg – balance) with dimensions of 15 mm × 20 mm × 2 mm. The electrolyte containing sodium fluoride (5 g/l) and sodium silicate (15 g/l) was selected to treat samples by PEO. Content of TiO₂(B) nanoparticles in

electrolyte was equal to 2 and 4 g/l. Since during the plasma electrolytic oxidation the coating growth on the sample proceeds, as a rule, at anodic polarization, to ensure the maximal incorporation of particles into the coating, an anionic surfactant (sodium dodecylsulfate) was used as a stabilizer of the dispersed system.

The elemental analysis of the coatings demonstrates that the presence of titanium in the composition of PEO-coating after coating formation (2 g/l – 1.6 % wt.; 4 g/l – 4.4 % wt.).

The incorporation of nanoparticles leads to an increase in the microhardness of the coating by more than 1.5 times as compared to coating without particles, from (2.1 ± 0.3) GPa to (3.5 ± 0.5) GPa.

The increase of the nanoparticles concentration up to 4 g/l results in a monotonous increase of the load ($L_{C2}(\text{PEO}) = (12.2 \pm 1.2) \text{ N}$, $L_{C2}(\text{PEO}+\text{TiO}_2(\text{B})) = (17.4 \pm 1.4) \text{ N}$), at which the disruption of the coating adhesion is observed, as well as in the increase of the load ($L_{C3}(\text{PEO}) = (7.3 \pm 0.3) \text{ N}$, $L_{C3}(\text{PEO}+\text{TiO}_2(\text{B})) = (10.2 \pm 1.1) \text{ N}$), at which scratching proceeds down to the substrate (plastic film abrasion until the metal).

Acknowledgements

The studies were carried out with the support of the Russian Science Foundation (project No. 19-73-10017). Adhesive characteristics have been studied within the framework of the Grant of the Russian Foundation for Basic Research (project no. 19-29-13020 mk).

References

- [1] G. Barati Darband, M. Aliofkhaezrai, P. Hamghalam, N. Valizade, *J. Magnes. Alloy.* **5** (2017) 74.
- [2] R. Arrabal, E. Matykina, T. Hashimoto, P. Skeldon, G.E. Thompson, *Surf. Coat. Technol.* **203** (2009) 2207.
- [3] S.V. Gnedenkov, S.L. Sinebryukhov, D.V. Mashtalyar, I.M. Imshinetskiy, A.S. Gnedenkov, A.V. Samokhin, Y.V. Tsvetkov, *Vacuum* **120** (2015) 107.
- [4] R.O. Hussein, X. Nie, D.O. Northwood, *Electrochimica Acta* **112** (2013) 111.
- [5] D. V. Mashtalyar, S.L. Sinebryukhov, I.M. Imshinetskiy, A.S. Gnedenkov, K. V. Nadaraia, A. Yu. Ustinov, S. V. Gnedenkov, *Appl. Surf. Sci.* **503** (2020) 144062.
- [6] D.V. Mashtalyar, S.V. Gnedenkov, S.L. Sinebryukhov, I.M. Imshinetskiy, A.S. Gnedenkov, V.M. Bouznic, *J. Alloys Compd.* **767** (2018) 353.

Mesoporous materials based on CeO₂ and Sn with a core-shell hollow structure for electrochemical energy storage and conversion

A.B. Podgorbunsky*, D.P. Opra, A.A. Sokolov, A.I. Neumoin, S.L. Sinebryukhov, S.V. Gnedenkov
Institute of Chemistry of FEB RAS, 159 pr. 100-letiya Vladivostoka, Vladivostok 690022, Russia

*e-mail: pab@ich.dvo.ru

Using the hydrothermal method, compounds based on cerium oxide in the form of hollow nanospheres were synthesized. The effect of SnO₂ in the CeO₂-SnO₂ system on the morphology and electrochemical behavior of the material using ones as an anode for a lithium-ion battery was determined. The reversible capacity realized during the first charging half cycle (delithiation) exceeded 800 mA•h/g.

The trends in the development of power sources in recent years are regarded to the improvement of their characteristics, such as high specific power, cycling capacity and safety. Particular attention is paid to the development of new anode materials for lithium batteries, since graphite, which is currently used for the manufacture of anodes for industrial lithium-ion batteries (LIB), does not provide modern capacity requirements (372 mAh / g). A promising replacement of graphite today is Sn-containing compounds due to the large gravimetric and bulk capacity (990 mA • h / g) [1-3]. A significant barrier for using tin in LIB is the significant volumetric deformations (up to 300%) that accompany the lithiation and delithiation [3]. The solution to this problem is the synthesis of tin-containing materials formed in the form of composites, various core-shell structures, etc. [4, 5]. Due to significant structural stability and high theoretical capacity (623 mAh / g) Ce based compounds could be considered as favorable candidates for anode material.

In the present work, cerium dioxide in the form of hollow micro / nanospheres (CeO₂) was obtained by hydrothermal synthesis in a mixture of ethyl alcohol, deionized water, cerium (III) hexahydrate nitrate, urea, and citric acid. The homogenized solution was heated in an autoclave at a temperature of 90 ° C for 12 hours. The resulting precipitate was separated from the solution by centrifugation, washed with distilled water, alcohol and acetone, and dried for 6 hours at 80 ° C. Annealing was carried out in an atmosphere of air at 500 ° C for 3 h. To obtain samples with tin oxide (CeO₂-Sn), tin (II) chloride

dihydrate was added to the solution.

According abovementioned, cerium dioxide in the form of hollow micro / nanospheres and CeO₂-Sn compounds were obtained by hydrothermal synthesis. Studies of the phase, elemental analysis of the obtained compounds were held. According to X-ray phase analysis, the addition of 0.01 and 0.005 M of SnCl₂ significantly changes the diffraction pattern, leading to the appearance of peaks of SnO, SnO₂ and the X-ray amorphous phase. Micro / nanospheres formed during the synthesis of the initial cerium dioxide are “split” when tin chloride is added, forming nanostructured flakes. According to the data of elemental analysis, the formation on the walls of the spheres consists of the elements Sn and O.

Tin addition improves the electronic conductivity of CeO₂ that is promising in terms of rate capability of the battery. An analysis of the results allows us to conclude the prospects of the proposed approach for the production of anode material for highly energy-intensive LIB based on the formation of a core / shell structure.

Acknowledgements

The work was performed as part of the State order of the Federal State Institute of Chemistry, Far Eastern Branch of the Russian Academy of Sciences No. 265-2019-003. The electrochemical studies were supported by the Russian Foundation for Basic Research (grant № 19-29-13020).

References

- [1] Kulova T.L. Russ. J. Electrochem. **49** (2013) 1.
- [2] Marom R., Amalraj S.F., Leifer N. et al. J. Mater. Chem. **21** (2011) 9938.
- [3] Hassoun J., Reale P., Panero S. J. Power Sources **174** (2007) 321.
- [4] Jung Y. S. et al. J. Electrochem. Soc. **152** (2005) A1452.
- [5] Huang H. et al. Solid State Ionics **120** (1999) 205.

Influence of formation conditions on corrosion behavior of PEO-coatings during salt-spray test

V.S. Egorkin^{1,2}, I.E. Vyaliy^{*1}, A.S. Gnedenkov¹, N.V. Izotov^{1,2}, D.K. Tolkanov¹, A.K. Runov¹, A.N. Minaev², S.L. Sinebryukhov¹, S.V. Gnedenkov^{1,2}

¹ Institute of Chemistry of FEB RAS, 159 pr. 100-letiya Vladivostoka, Vladivostok 690022, Russia

² Far Eastern Federal University, 8 Sukhanova St., Vladivostok 690950, Russia

*e-mail: igorvyal@gmail.com

Currently, in order to reduce energy costs and greenhouse gas emissions, there is a tendency to replace steel structures with aluminum, which is lighter. In this regard, aluminum alloys (AMg3, D16) are popular materials in the automotive and aerospace industries, where operating conditions require high anti-corrosion properties.

Anodizing or various methods of applying paint are often used to process aluminum parts in order to improve protection against long-term corrosion. However, the resulting coatings possess lower adhesion, in comparison with the layers formed by plasma electrolytic oxidation (PEO) [1]. The non-porous sublayer of PEO-coatings provides an advantage in reducing the corrosion of the metal substrate in comparison with other protective coatings. However, microdischarges inevitably form a porous outer layer, the barrier properties of which degrade upon prolonged contact with a corrosive environment, which in turn, does not fully reveal the protection potential of PEO layers. In early work [1], the main part of the pores in the coatings was healed by increasing the duty cycle (D) of the short-pulse signal ($t_{\text{pulse}}=5 \mu\text{s}$). As a result of the study by potentiodynamic polarization and impedance spectroscopy, high barrier properties of PEO-coatings were determined, which reduce the corrosion current by nearly 3 orders of magnitude, in comparison with the unprotected aluminum alloy AMg3. However, the conditions for industrial operation and electrochemical testing may vary significantly.

Consequently, in this work, jointly with electrochemical studies of PEO-coatings, tests in salt mist environment were carried out according to GOST 52763-2007 to assess the protective properties of PEO-coatings under identical operating conditions (GOST 51801-2001). Spraying of the 5% NaCl solution and repeating it were performed with a duration of 15 minutes and every 45 min respectively. The temperature in the salt fog chamber was set in the range of 27–29 °C. The test duration is 7 days. Comparative analysis of the morphology of the starting and after the corrosion test of PEO-coating was conducted on Evex Mini-SEM (Evex Analytical Instruments, USA). The porosity of the coatings was determined using the ImageJ 1.50v software.

The formation of PEO-coatings was carried out on aluminum alloys AMg3 and D16 in bipolar 30 and 60 min modes using a transistor power supply [1]. During the anode phase, the voltage was increased in two stages: during the first 5 minutes from 30 to 360 V and from 360 to 420 V for the remaining 25 and 55 minutes, respectively.

In both cases, in the cathode phase, the PEO-treatment was performed at a constant current density of 0.1 A/cm².

In order to establish the necessary values of D , the frequency of the pulse signal was changed, which was: 20.8 kHz ($D = 0.21$), 11.9 kHz ($D = 0.12$) and 6.0 kHz ($D = 0.06$). A multicomponent electrolyte is an aqueous solution of the following composition: 0.6 g/l NaF, 5 g/l C₄H₄O₆K₂·0,5H₂O, 10 g/l Na₂MoO₄·2H₂O, 10 g/l Na₂B₄O₇·10H₂O, 10 g/l Na₃PO₄·12H₂O.

The analysis of SEM-images of the cross-sections of the PEO-layers showed the highest coatings porosity were obtained at $D = 0.06$ and time of 30 minutes for the AMg3 alloy – 11.1% and 14.1% for the D16 alloy. Therefore, the barrier properties of these coatings below the rest ($9.0 \cdot 10^{-10}$ A/cm² and $9.9 \cdot 10^{-9}$ A/cm², however, more than 2 orders outperform unprotected aluminum alloys AMg3 ($1.8 \cdot 10^{-7}$ A/cm²) and D16 ($4.5 \cdot 10^{-6}$ A/cm²). An increase in the oxidation time to 60 min and D to 0.21 made it possible to reduce the defectiveness of the coatings to 6.1% and 8.8% for AMg3 and D16 alloys, respectively. Therefore, the main part of defects in PEO-layers closes when the duty cycle increases to 0.21, due to the higher energy of microdischarges than at $D = 0.05$ and 0.12. At the same time, these coatings have a large thickness ($11.6 \pm 1.9 \mu\text{m}$ and $9.1 \pm 0.9 \mu\text{m}$), which provided even higher barrier properties. Analysis of the polarization curves showed a decrease in the corrosion current density for AMg3 alloys to $2.4 \cdot 10^{-10}$ A/cm² and to $2.9 \cdot 10^{-10}$ A/cm² for D16 alloy.

These PEO-layers after 7 days salt-spray test have not changed, determined both by inspection of the appearance and analysis of surface images obtained using an electron scanning microscope. All coated samples after corrosion testing exhibited a mass loss less than 1% with no signs of pittings and defects. Thereby, protective PEO-layers can be characterized as satisfying the required level of anticorrosion properties for long-term operation in a corrosive environment.

Acknowledgements

Morphological and adhesion studies were funded by RFBR, project number 19-29-13020.

Corrosion testing was performed under financial support of President Grant (SP-3958.2019.1).

References

- [1] V. S. Egorkin, S. V. Gnedenkov, S. L. Sinebryukhov, I. E. Vyaliy, A. S. Gnedenkov, R. G. Chizhikov. Surf. Coat. Technol. **334** (2018) 29.

Morphology and chemical composition of organic coatings formed atop PEO-layers

V.S. Egorkin^{1,2}, U.V. Kharchenko¹, N.V. Izotov^{*1,2}, I.E. Vyaliy¹, A.S. Gnedenkov¹, D.K. Tolkanov¹, A.K. Runov¹, A. N. Minaev^{1,2}, S.L. Sinebryukhov¹, S.V. Gnedenkov^{1,2}

¹ Institute of Chemistry of FEB RAS, 159 100-letiya Vladivostoka Pr., Vladivostok 690022, Russia

² Far Eastern Federal University, 8 Sukhanova St., Vladivostok 690950, Russia

*e-mail: izotovnv@ich.dvo.ru

To protect aluminum and its alloys from corrosion, organic coatings are used often. Moreover, the adhesion of the layers to the metal in some cases does not meet the requirements of the operating conditions of the processed materials. In this regard, when painting metal parts, a primer is applied to ensure good adhesion. Oxide coatings could also be used as an adhesive sublayer, which could be formed by plasma electrolytic oxidation (PEO).

Currently, to increase the adhesion strength of organic coatings to the surface of aluminum and its alloys, several works were devoted to the formation and study of two-layered PEO coatings [1, 2]. The first sublayer is formed by anodizing aluminum alloys in an acid electrolyte, and the second layer is obtained by the next stage of PEO. As a result of the two-stage formation, denser coatings are formed, which, in turn, reduce energy consumption and increase anticorrosion properties. On the other hand, the formation of PEO coatings in several stages complicates the process, and the use of acidic electrolytes is unsafe for the environment. In this regard, in a previous work, a method was proposed for the formation of similar layers in a single-stage PEO on an aluminum alloy AMg3 in tartrate and silicate-containing electrolytes [3]. At the same time, an increase in the concentration of sodium metasilicate in the tartrate electrolyte structured the oxide layers in different ways, and as a result increased their roughness, porosity, and thickness. Therefore, for high-quality deposition of organic coatings on PEO layers, it is necessary to study the effect of PEO conditions and the concentration of sodium metasilicate on the morphology and structure of the coatings formed.

To carry out oxidation, 0.6 g l⁻¹ sodium fluoride (NaF), 10 g l⁻¹ sodium tetraborate (Na₂B₄O₇ · 10 H₂O), 25 g l⁻¹ potassium tartrate (C₄H₄O₆K₂ · 0.5H₂O) were diluted in 2 l of deionized water and 0 g l⁻¹, 5 g l⁻¹ sodium metasilicate (Na₂SiO₃ · 5H₂O). The formation of protective layers was carried out in bipolar mode. During the anode phase, a potentiodynamic mode was implemented and in the cathode phase, the galvanodynamic mode was realized. For a detailed analysis of the transition of the structure of oxide layers, the oxidation time was: 5 min, 25 min, and 45 min, after which the surface and cross sections of the formed coatings were examined using a Zeiss EVO 40 scanning electron microscope.

At the first control time, the formation of coatings similar to the anode layers was observed in both electrolytes. At the end of the second duration in an electrolyte with no Na₂SiO₃, this anode-like layer was transformed by 50–60% in thickness into a traditional PEO layer. With the addition of 5 g l⁻¹ Na₂SiO₃ to the electrolyte, the transformation of the oxide layer was significantly

accelerated. Since, in the cross section, a traditional PEO coating was observed with rare inclusions of the anode layer located near the aluminum substrate. However, the third control stage ensured the complete transformation of oxide layers formed in electrolytes with the absence and addition of sodium metasilicate.

At the same time, analysis using the MetekSurtronic 25 profilometer of the surface of PEO coatings showed that the addition of 5 g l⁻¹ sodium metasilicate leads to a 1.7-fold increase in the roughness parameter Ra, compared to layers obtained without addition of Na₂SiO₃ to the electrolyte (Ra = 1.6 ± 0.2 μm). The study of the morphology and structure of PEO layers after applying an organic coating to their surface showed that the first composite coatings (KP) exhibit a sharper transition at the oxide layer / paint interface, and the organic layer is 50–60 microns thick. For PEO coatings formed with 5 g l⁻¹ sodium metasilicate, due to the greater roughness, the paint layer reached 90–100 μm. Therefore, paint consumption increased by 40%, which provided a more even and glossy surface and high anticorrosion properties, in comparison with oxide coatings obtained in an electrolyte with no Na₂SiO₃. Further analysis of the second KP showed that due to the more developed porous part, the interface between the coating and the organic layer expanded significantly, and its high filling density with paint was provided by the spray gun.

Acknowledgements

Far Eastern Center for Electron Microscopy, A.V. Zhirmunsky Institute of Marine Biology FEB RAS (Vladivostok, Russia)

Morphological and adhesion studies were funded by RFBR, project number 19-29-13020.

XRD data were collected under financial support of President Grant (SP-3958.2019.1).

References

- [1] Hongjian Huang, Jianhui Qiu, Manxi Sun, Wendi Liua, Xiaowei Wei, Eiichi Sakai, Kazushi Ito. *Surf. Coat. Technol.* **360** (2019) 307.
- [2] E. Matykina, R. Arrabal, M. Mohedano, B. Mingo, J. Gonzalez, A. Pardo, M.C. merino. *Transactions of Nonferrous Metals Society of China* **27** (2017) 1439.
- [3] V.S. Egorkin, I.E. Vyaliy, N.V. Izotov, S.L. Sinebryukhov, S.V. Gnedenkov. *Defect and Diffusion Forum*, **386** (2018) 309.
- [4] S.V. Gnedenkov, S. L. Sinebryukhov, A. V. Puz', A. S. Gnedenkov, I. E. Vyaliy, D. V. Mashtalyar, V. S. Egorkin. *Solid State Phenomena* **213** (2014) 149.

Structural heterogeneity of an amorphous nanocrystalline alloy in the nanometer range

A.M. Frolov*, S.V. Dolzhikov, V.I. Belokon

Far Eastern Federal University, 8 Sukhanova St., Vladivostok, 690950, Russian Federation

*e-mail: froloff5@yandex.ru

The structure of amorphous rapidly quenched alloys is quite complex for description and interpretation in various approaches. The theoretical task of describing the structure of such objects did not find a reliable solution. The image has a fairly recognizable salt-pepper structure for objects of this kind. The size of the inhomogeneities is ~ 0.2 nm [1]. In terms of transmission electron microscopy, darker areas have a higher density, light areas have a lower density. The differences in the density of the material can be identified even for samples that are X-ray amorphous.

Landau's theory of phase transitions [2] is based on the assumption of a one-parameter description of the system. Thus, the thermodynamic potential of the system becomes a function defined parametrically. The parameter is considered further as an order parameter and assigned by a physical meaning, based on the physical conditions of the problem under consideration. So, in the original work, it was a scalar degree of ordering with a range of admissible values $0 \leq \varphi \leq 1$.

The validity of series expansion is obvious to the class of objects under consideration, which are amorphous metal alloys and which are far from thermodynamic equilibrium. For complete indisputability, we will use a standard method: replacing φ by $\Delta\varphi$ and expanding in a change series the of φ , that is in a typical series

$$F(x) = F_0 + V \left(\frac{1}{2} a \varphi^2 + \frac{1}{4} b \varphi^4 + \frac{1}{6} d \varphi^6 \right), \quad (1)$$

where V - system volume. Coefficients a, b, d and others are functions of temperature and pressure

An expansion of type (1) implies the invariance of the energy relatively to the change of sign φ ($\varphi \rightarrow -\varphi$), that is why there are no odd degrees in the expansion.

If the rate of change in the state of the system is finite, then the thermodynamic degrees of freedom do not necessarily have time to come into equilibrium. Degrees of freedom, whose relaxation times are large enough, are frozen. In particular, we can talk about fields $\varphi(x,t)$ of the order parameter that satisfy the conservation law $\varphi(x,t)$

$$\frac{\partial \varphi}{\partial t} + \text{div} j = 0. \quad (2)$$

For the thermodynamic potential F, taking into consideration the replacement of φ by $\Delta\varphi$ and $\varphi(x,t)$ the field of the density order parameter ρ in (1), we have the following equation

$$F = \frac{1}{2} \int \left\{ c (\nabla \varphi)^2 + \alpha \tau \varphi^2 + \frac{1}{2} \beta \varphi^4 + \frac{1}{6} \varphi^6 \right\} d\varphi \quad (3)$$

Contrary to (1), expansion (3) takes into consideration the sign-invariant form of the gradient of the order parameter, since we study the inhomogeneous state of the system.

For equation (2) we get

$$\frac{\partial \rho}{\partial t} = \Delta \left\{ -\Delta \rho + \tau \rho^3 + \rho^5 \right\} \quad (4)$$

In case of complete equilibrium $j = 0$, that means

$$\tau_0 \rho_0 + \rho_0^3 + \rho_0^5 = h, \quad (5)$$

where τ_0 and ρ_0 the values of τ and ρ at the point A_0 , $h \sim \mu_0$ (μ_0 - is the chemical potential at the point A_0). The immediate change of τ value from $\tau_0 > 0$ to $\tau_1 < 0$ makes the value $\rho = \rho_0$ non-equilibrium. For the initial stage, relaxation is determined by the equation

$$\frac{\partial \rho}{\partial t} = \Delta \left\{ -\Delta \rho + \tau \rho + 3\rho_0^2 + 5\rho_0^4 \rho \right\} = D \Delta \rho - \Delta^2 \rho, \quad (6)$$

where $D = \tau + 3\rho_0^2 + 5\rho_0^4$ (7) value, that has the

meaning of a dynamic diffusion coefficient in a nonequilibrium state. In the phase separation area, the coefficient D is negative. It should be noted that we are talking about a thermodynamically unstable state. The possibility of describing this state in thermodynamic terms is due to the fact, that the state is close to equilibrium near the separation point. As in the Landau theory, this allows us to use expansion (3), where we hold the terms of the sixth order in ρ and the second order in $\nabla \rho$. The presence of a gradient term determines the wave solutions of this equation. Negative values of the dynamic diffusion coefficient in the unstable state of the system mean that the inhomogeneity during the relaxation of the system grows to values of density (concentration) corresponding to the equilibrium values with the formation of the bound between cells.

This result means that in time $t \sim \theta$ the system is divided into cells with dimensions $\lambda \sim k^{-1}$.

$$\lambda^2 \sim |D|^{-1}$$

Cells of size λ arising in the system in the case of a rapid transition from state A_0 to state A_1 can be interpreted as the structure of an amorphous "salt-pepper" alloy, which is formed upon rapid quenching from the melt. The characteristic cell size depends on the temperature of the melt and the temperature of the formation of an amorphous state, which is quenching temperature

References

- [1] Fedorets A.N., Pustovalov E.V., Plotnikov V.S., Modin E.B., Kraynova G.S., Frolov A.M., Tkachev V.V., Tsesarskaya A.K. AIP Conf. Proc. Vol. 1874 (2017), P. 040008-1–040008-4.T.
- [2] Landau L.D., Lifshits E.M. Statistical Physics. M.: "Science". 1964.

The growth of microcrystals on the surface of oxide coatings

V.S. Rudnev^{1,2}, K.N. Kilin¹, I.V. Lukiyanchuk^{*1}, M.S. Vasilyeva^{1,2}

¹ Institute of Chemistry of FEB RAS, 159 Pr. 100-letiya, Vladivostok 690022, Russia

² Far Eastern Federal University, 8 Sukhanova St., Vladivostok 690950, Russia

*e-mail: lukiyanchuk@ich.dvo.ru

This work demonstrates how the application of certain approaches can affect the surface morphology of PEO coatings, the growth of micro- and nanocrystals on their surfaces, and functional properties of PEO layers.

One of these approaches is the introduction of various additives into electrolytes for creating conditions for precipitating dispersed particles of a disarable composition. Such an approach was used to obtain $WO_3 - MWO_4$ oxide structures ($M = Fe, Cu, Ni, Mn, Zn$) on titanium. PEO treatment of titanium samples was carried out in acidified aqueous solutions of sodium tungstate (0.1 mol/L Na_2WO_4) with the addition of transition metal salts (0.05 mol/L of $Cu(CH_3COO)_2$, FeC_2O_4 , $Ni(CH_3COO)_2$, $Zn(CH_3COO)_2$, or $Mn(CH_3COO)_2$). In most cases, the coatings obtained include tungsten oxide and transition metal tungstate - $WO_3 + MWO_4$ (Table I). Micro- and nanocrystals were found on the surface of a number of coatings obtained. The bandgaps E_g for oxide layers have been determined from diffuse reflectance spectra recorded in the range of 200-800 nm using a Cary Varian 5000 spectrophotometer with a spectral resolution of 1 nm, similarly to that in [1]. These E_g values indicate that the absorption of photons by these structures is possible in UV and visible radiation range.

Table I. The E_g values of a number of $WO_3 + MO_x$ PEO coatings obtained for 5 min at $i = 0.2 A/cm^2$.

PEO coating	Element composition of crystallites, (at. %)	Phase composition of coatings	E_g , (eV)
$WO_3 + CuO_x$	Rectangular: 19.4 C; 57.6 O; 5.6 Cu; 17.4 W	$WO_3 + CuWO_4$	2.8
$WO_3 + FeO_x$	-	$WO_3 + FeO(OH)$	2.36 and 2.73
$WO_3 + MnO_x$	Lamellar: 76.3 O; 1.9 Ti; 5.2 Mn; 16.5 W	$WO_3 + MnWO_4$	-
$WO_3 + ZnO_x$	Star: 15.7 C; 56.5 O; 2.4 Ti; 11.1 Zn	TiO_2 (rutile) + $WO_3 + ZnWO_4$	2.78
$WO_3 + NiO_x$	Granular: 18.9 C; 56.0 O; 13.7 Ni; 11.3 W	$WO_3 + ?NiWO_4$	2.08, 2.47 and 3.08

The properties of the coatings have depended on the composition and microcrystals on their surface. The composites are promising for use as photocatalysts operating in the visible radiation range.

Another approach is the use of complexing agents or substances that change the mechanism of incorporation of electrolyte components into PEO coating compositions [2]. The introduction of acetonitrile into $Na_2B_4O_7 + Mn(CH_3COO)_2$ electrolyte results in PEO layers having increased adhesion to the substrate metal, but differing in surface morphology and composition. Instead of granules, "leaf-like" structures with a high manganese content (~ 11 at.%) are formed on the coating surface. However, average manganese concentration decreases from 30 to 6 at. %, leading to a loss of their catalytic activity in the oxidation of CO in CO_2 .

Post-treatment of PEO-coated metals, in particular impregnation and/or annealing, also affects the formation and growth of crystallites on their surface. Annealing of W-containing PEO coatings on titanium at a temperature of 700°C and above leads to regular WO_3 microcrystals on their surface [3]. The results of work [4] have shown that, depending on the annealing temperature, crystals of various shapes and compositions are formed on the surface of Mn-, W-containing PEO coatings on titanium. The crystals formed after air annealing at 700 °C are tetrahedral prisms of the assumed composition of $MnWO_4$. The crystals formed after annealing at 850 °C are hexagonal prisms of the assumed composition of $Na_2Mn_2Ti_6O_{16}$.

The composition of crystals growing on the surface of $NiO + CuO/TiO_2/Ti$ composites formed by a combination of PEO and impregnation strongly depends on the annealing temperature [5]. CuO crystals are formed on the surface after annealing at 500–700°C, $NiWO_4$ crystals are present at 750–850°C, and $Ni_{2.62}Ti_{0.69}O_4$ whiskers at $T \geq 900^\circ C$. The data obtained indicate that the electrolyte residues and the impregnating solution accumulated on the surface and in the pores of the coatings, as well as the diffusion of titanium from the depth of the coating to the surface play an important role in the formation of micro- and nanocrystals.

Acknowledgements

The work was partially supported by grant of RFBR No. 18-03-00418.

References

- [1] M.S. Vasilyeva, V.S. Rudnev, A.P. Parkhomchuk, I.V. Lukiyanchuk, K.A. Sergeeva, A.A. Sergeev. Key Eng. Mater. **806** (2019) 51.
- [2] M.S. Vasilyeva, V.S. Rudnev, V.G. Kuryavyi. Prot. Met. Phys. Chem. Surf. **55** (2019) 473.
- [3] V.S. Rudnev, et.al. Inorg. Mater. **55** (2019) 681.
- [4] K.N. Kilin, V.S. Rudnev, I.V. Lukiyanchuk, et.al. Russ. J. Appl. Chem. **92** (2019) 1674.
- [5] V.S. Rudnev, I.V. Lukiyanchuk, M.S. Vasilyeva, T.A. Kaidalova. Vacuum **167** (2019) 397.

Comparison of ordering characteristics of anodic formed nanostructured aluminum and titanium oxides coatings

N.B. Kondrikov¹, P.L. Titov¹, S.A. Shchegoleva^{*1}, V.B. Cherepanov¹, M.S. Vasileva^{1,2}

¹ Far Eastern Federal University, 8 Sukhanova St., Vladivostok 690950, Russia

² Institute of Chemistry of FEB RAS, 159, pr. 100-letiy Vladivostoka, Vladivostok 690022, Russia

*e-mail:sveta170@bk.ru

This study is devoted to an analysis of the ordering of the TiO_2 [1] and Al_2O_3 [2] nanotubes' arrays using the correlation-spectral methods. As the tools, the spatial Fourier spectrum and one-dimensional autocorrelation function (ACF) of the SEM image have served.

The test specimens of the TiO_2 nanotubes were obtained in the aqueous-non-aqueous and aqueous electrolytes by anodizing method using the stabilized constant voltage source. Preliminarily, the titanium foil specimens were chemically polished in the $\text{HF}/\text{HNO}_3/\text{H}_2\text{O}$ (1:4:5) mixture (Table 1).

Table 1. Modes of oxydation

Sample	Time of experiment, h	Potential, V	Current, mA	Electrolyte
No.1	1.5	20	35	(Glycerin+ SAW + 0.5% NH_4F) 1:1
No.2	4	30	40	H_2SO_4 +0,15% HF

In obtaining the anodic Al_2O_3 (specimens No. 3, 4), the surfaces were preliminarily prepared. Primarily, the mechanical polishing was performed, further some specimens (No. 4) were annealed and after all that all specimens were exposed to chemical etching and electrochemical mirror polishing. At that, the commercial-purity aluminum was used for the specimen No. 3 while very-high-purity one for specimen No. 4.

The nanostructured Al_2O_3 was obtained using the technique of two-stage anodizing in the potentiostatic mode. After the first stage, the removal of the oxide layer was carried out and, further, the repeated anodizing was conducted in the same electrolyte. As electrolyte, the 0.3-molar solution of the ethanedioic acid at temperature of $\sim 5^\circ\text{C}$ and potential of 40V was used. The time of each stage was 3 hours. The morphological characteristics of specimens were obtained using the SEM "Hitachi S-5500" (Japan).

The TiO_2 nanotubes are characterized by distinct structures and each nanotube has its own wall, boundary, which does not unite with the walls of other nanotubes into the continuous array. Upon a small scale, one can identify both tetragonal (specimen No. 1) and hexagonal (specimen No. 2) ordering. On the contrary, the Al_2O_3 nanotubes are combined through the common walls into the single structure. The main part of pores can be outlined by the cell corresponding to the hexagonal ordering [3].

The local, short-range order is visible in all SEM-images of the specimens No. 1-4. In the arrays of the Al_2O_3 nanotubes, especially in the specimen No. 4, one can identify the areas of almost strict periodicity [2]. Usually,

both TiO_2 and Al_2O_3 nanotubes are tightly packed at the surface.

The Fourier spectra of TiO_2 images have a characteristic ring (halo) corresponding to the short-range coordination order within the limits of the first coordination sphere of nanotubes. Any pronounced secondary rings are absent and spectra decay smoothly. In the spectrum of specimen No. 2, a halo begins to take on a form of a hexagon.

The spatial spectra of the Al_2O_3 nanotubes images have three rings, the last of which is feeble marked. The first (inner) ring answering for the significant period of structure for specimen No. 3 has the shape of circle. In the spectrum of the specimen No. 4, the first ring separates into 6 maxima. Their number is confirmed by the presence of almost strict hexagonal ordering on the sufficiently great areas. Generally, one can deduce according to type of the Fourier spectra that the arrays of Al_2O_3 nanotubes in the case under consideration are more ordered and have a more well-defined structure than the TiO_2 nanotubes. All of obtained ACFs can be divided into two groups. According to the degree of order, the first group is presented by ACFs of specimens Nos. 1, 2. The first maxima and minima are manifested quite clearly and have the significant amplitudes.

Within the group of more distinct, structured ACFs, the specimens Nos. 3, 4 fall. The first and second maxima in both ACFs are clearly visible, and the second maximum in the ACF of specimen No. 4 has nearly the same relative amplitude as the first one. In addition, the periodicity in these ACFs after two maxima is not lost, it is further evident if not so clearly. According to the type of ACFs, the specimen No. 4 is most ordered while, in this context, the specimen No. 1 is the most ordered of the TiO_2 specimens.

The further all-round analysis of ordering can be carried out using the configuration geometric entropy, fractal and multi-fractal techniques as well as formalism of the coordination tree graphs [4].

Acknowledgements

This research was done with support of grant of the Russian Foundation for Basic Research RFBR (project no. 18-03-00418).

References

- [1] J.M. Macak, H. Tsuchiya. Current opinion in Solid State & Materials Sci **11** (2007) 3.
- [2] K. Nielsch, J. Choi, K. Schwirn, R. Wehrspohn, U. Gösele. Nanoletters. **2**(7) (2002) 676.
- [3] L. Zaraska, G.D. Sulka, M. Jaskuła/ Journal of Solid State Electrochem. **15** (2011) 2427.
- [4] V.V. Yudin, P.L. Titov, A.N. Mikhalyuk. Theoretical and Mathematical Physics. **164** (2010) 905.

Explosive pressing of organic and inorganic compounds

G.A. Zverev¹, L.N. Ignatieva¹, N.A. Adamenko²

¹ Institute of Chemistry of FEB RAS, 159 Prosp. 100-letya Vladivostoka, Vladivostok 690022, Russia

² Volgograd State Technical University, 28 Lenin avenue, Volgograd 400005, Russia

*e-mail: bronatin@mail.ru

Polytetrafluoroethylene (PTFE) and Polyvinylidene fluoride (PVDF) are two of the well-known basic fluoropolymers [1]. Although PTFE and PVDF are widely applied in different areas of industry, household, in medicine, the requirements of advanced technologies stipulate for the necessity of improvement of the materials functioning parameters, which is implemented through modification of available materials or fabrication of novel ones. Modified forms of the materials having promising properties are fabricated using different methods of their treatment. An effective way to modify fluoropolymers is to fill them with metal powders. Filling polymers with dispersed substances, especially metals, makes it possible to obtain composites with higher physicomechanical and operational properties compared with traditionally used materials [2]. This type of method includes explosive pressing. The explosion treatment (explosive pressing, EP) is a promising method of fluoropolymers modification and creation of composite materials [3]. The method is based on the formation of shock waves in the solid body which offers the possibility to realize the specific type of the mechanochemical impacts for a short period at pressure from dozens of MPa to a few hundreds of GPa and a broad range of temperatures from dozens to a thousand of centigrade's. Such impact results in structural transformations and rise in the adhesive interaction between components. The possibility for the creation of the composite metalopolymer materials with the use of explosive pressing of the metal- fluoropolymer mixture was shown in a number of studies [4].

This paper illustrates the results of investigating the composites of the PTFE+Cu, PTFE+Ni, PTFE+Al, PVDF+Al₂O₃ obtained by the method of explosive pressing. The main attention is paid to results revealing of the composite morphology, molecular structure, phase composition, and thermal properties.

Studies of PTFE + M composites (M - Al, Cu, Ni) by SEM method revealed the conditions for the preparation of composites of various morphologies.

For Al add Cu composites, we see a heterogeneous structure: it is composed of a monolith mass with embedded particles. In the course of fabrication of a composite with nickel, a loose nickel monolith is formed: its pores and interfacial layer are filled with formations from polytetrafluoroethylene particles. It has been revealed that in all cases during explosive pressing, an intermediate layer is formed consisting of nanofibrils, which enhance the adhesion of the metal to the polymer, thereby contributing to the formation of a durable composite.

The effect of pressure on the morphology of the obtained material was studied for a sample formed from a mixture of PVDF polymer and metal oxide. A sample of 80% PVDF + 20% Al₂O₃ was studied. By SEM study at using of EP=1GPa for the sample, the two types of areas

were revealed: lamellar structures 400 nm in size, on the surface of which particles of microns are visible. With a higher magnification fibers are visible.

The element composition of the PVDF + Al₂O₃ (EP=1GPa) are shown in the table I.

Table I. Element analysis of the PVDF + Al₂O₃ sample performed using the SEM method (EP = 1 GPa)

Sample \ element	C, at%	F, at%	Al, at%	O, at%
lamellar structures	67	33	-	-
particles	52	27	8	13

As it is seen from table the sample includes carbon, fluorine, aluminum oxygen. The ratio of Al / O is 2/3 corresponds to Al₂O₃. Monolith consists from lamellas formed with fibrils.

Table II. Element analysis of the PVDF + Al₂O₃ sample performed using the SEM method at various points (EP = 3 GPa)

Sample \ element	C, at%	F, at%	Al, at%	O, at%	Si, at%
(1)	48	13	26	12	1
(2)	54	19	-	19	8
(3)	55	20	2	23	-
(4)	41	23	28	7	1

At EP with a pressure of 3 GPa PVDF+Al₂O₃, the morphology of the sample varies greatly, moreover the sample becomes brittle. According to SEM studies, it is composed of particles with sizes from 50 nm to 10 μm, which are compressed into agglomerate. As can be seen from table II, The distribution of elements in the sample also changes. The ratio of Al / O does not correspond to Al₂O₃, the C / F ratio also changes. Therefore, we suggested the destruction of the components of the composite.

The undertaken studies of the samples by XRD, IR spectroscopy, and DSC confirmed the assumption made.

Acknowledgements

The work was supported by the "Far East" Program of Basic Research of FEB RAS (project no. 18-3-014)

References

- [1] V. M. Bouznik. Fluoropolymer materials (2017) 600.
- [2] N.A. Adamenko, A.V. Kazurov, A.V. Fetisov, G.V. Agafonova, Russian nanotechnology **2** (2009) 137.
- [3] N.A. Adamenko, A.V. Fetisov, A.V. Kazurov, The explosive processing of metal compositions (2007) 240.
- [4] N.A. Adamenko, A.V. Kazurov, A.V. Fetisov, G.V. Agafonova, Nanotechnologies in Russia **4** (2009) 85.

Magnetically active sorption material SiO₂ – CoFe₂O₄

I.A. Tkachenko¹, A.E. Panasenko^{1,2}, M.M. Odinokov^{*,1,2}

¹ Institute of Chemistry of FEB RAS, 159 pr. 100-letya Vladivostoka, Vladivostok 690022, Russia

² Far Eastern Federal University, 8 Sukhanova St., Vladivostok 690950, Russia

*e-mail: odinokov.mm@students.dvfu.ru

The work presents a study of the magnetic and sorption properties of nanocomposites CoFe₂O₄-SiO₂. Samples were obtained by precipitation and impregnation using silica of plant and mineral origin. The sorption capacity studied by methylene blue is from 8.8 to 26.7 mg/g, which is higher than the sorption capacity of the initial SiO₂. It was established that all the studied composite materials are ferromagnetic at room temperature, and the saturation magnetization increase from 1.2 to 29.0 e.m.u/g with increasing cobalt ferrite content.

Pollutants is an important issue and are harmful to our daily life. Among different sources of pollutants, organic dyes in effluents from printing, dyeing, textile manufacture, paper industries, and many other industrial processes have caused serious environmental problems. Adsorption is typical method used to treat dyeing materials before they are discharged into natural water systems. Furthermore, adsorption could avoid the problem of secondary pollution by adsorption agents. To collect the adsorption agents, we adopted a magnetic approach in which spinel cobalt ferrite (CoFe₂O₄) was used as the magnetic medium. Therefore, we synthesized a new material, which comprises a CoFe₂O₄ core and a silica shell to adsorb methylene blue (MB) [1].

CoFe₂O₄-SiO₂ particles were prepared by the method I (precipitation) and method II (impregnation) [2]. Precipitation method was the precipitation of CoFe₂O₄ from an acidic solution of iron and cobalt chlorides. After that, sodium silicate was controllably hydrolyzed in the suspension to form a silica shell. The impregnation method consisted in the impregnation of porous silica of plant

origin with a solution of Fe(acac)₃ and Co(acac)₂ followed by calcination.

The morphology of the samples was confirmed using electron microscope. The size of CoFe₂O₄ core particles is approximately 20 nm.

The sorption properties of materials were investigated by adsorption of MB. MB was sorbed from aqueous solutions in static conditions. The concentration was determined by the photocolometric method. Sorption capacity of materials is presented in table I.

The magnetic properties of the obtained materials were investigated. The magnetic characteristics of materials depend on the method of their preparation, structure, and content of cobalt ferrite in them. Table II shows the saturation magnetization (Ms) and the coercive force (Hc) of the samples at 300 and 3 K.

Table II. Magnetic characteristics of composite materials

Sample	Methods	SiO ₂ , (%)	Fe ₂ O ₃ , (%)	CoO, (%)	Sorption capacity mg/g
1	precipitation	40.9	39.5	19.7	25.9
2	precipitation	69.1	20.4	10.5	8.8
3	precipitation	70.4	19.6	10.1	16.9
4	precipitation	78.9	14.0	7.1	15.4
5	impregnation	94.4	4.5	1.1	18.1
6	impregnation	94.6	3.9	1.4	16.7

Depending on the CoFe₂O₄ content in the samples, the saturation magnetization (300 K) varies from 1.2 to 29.0 e.m.u/g (Table II). These values of Ms are sufficient to extract the material from an aqueous suspension under the external magnetic field of a permanent magnet and to use these materials as magnetic sorbents.

References

- [1] Z. Li, J. Wang, M. Liu, T. Chen, J. Chen, W. Ge, Z. Fu, R. Peng, X. Zhai, Y. Lu. Core-shelled mesoporous CoFe₂O₄-SiO₂ material with good adsorption and high-temperature magnetic recycling capabilities **115** (2018) 300.
- [2] F. Hoffmann, M. Cornelius, J. Morell, M. Froba. Silica-based mesoporous organic-inorganic hybrid materials **45** (2006) 3216.

Table I. Sorption capacity and consist of samples

Sample	M _s , (e.m.u./g)		H _c , (Oe)	
	300 K	3 K	300 K	3 K
1	29.0	41.0	163	9390
2	13.0	21.0	155	8813
3	17.0	25.0	166	9506
4	11.0	17.0	150	9400
5	1.2	5.0	425	6400
6	1.2	6.1	360	5400

The influence of washing step conditions as-prepared anodic TiO₂-NTs structures on their photoactivity

T.P. Savchuk*, I.M. Gavrilin, A.A. Dronov, S.A. Gavrilov

National Research University of Electronic Technology, Shokin Square, Bld 1, 124498, Moscow, Russia.

*e-mail: wewillbe01@gmail.com

Anodic titania nanotubes (TiO₂-NTs) structures are widely known as chemical stable photoelectrodes with a large surface area. The material is being intensively investigated for photovoltaic and photocatalytic applications.

Well known that anodic oxidation method for obtaining vertical oriented TiO₂-NTs typically includes next steps: first anodic oxidation, removing of the prepared sacrificial layer, second anodic oxidation, and washing step of the obtained sample from electrolyte and reaction products. Such solutions often used for the washing step: water and ethanol. Also, the washing step provides in the ultrasonication bath step by step in acetone, ethanol and water for removal of the initiation layer. Already known that long soaking as-prepared amorphous anodic TiO₂ nanotubes in water lead to the crystallization of the oxide layer and growth of nanoparticles on the surface and walls of the structure.

However, the comparing of various washing methods and solutions influences on the photoactivity of the TiO₂ nanotubes structures isn't described.

In this work, the TiO₂-NTs structures were obtained by electrochemical anodization in fluorine-containing an electrolyte based on ethylene glycol. The photoactivity of prepared TiO₂ nanotubes structures washed in solutions such as water, ethanol and unwashed was studied by photoelectrochemical techniques (photocurrent, photopotential, IPCE). The morphology and geometry of obtained samples were investigated by scanning electron microscopy method. The structure and composition of the material were investigated by XRD and EDX methods respectively.

Acknowledgement

This work was supported by RFBR grant № 18-29-23038 mk.

Influence of a magnetic field on the scattering of γ -quanta on F_3O_4/Au particles

K.S. Lukyanenko, L.L. Afremov, Y.M. Borodaenko, A.V. Ognev, I.G. Iliushin*, V.O. Trukhin
Far Eastern Federal University, 8 Sukhanova St., Vladivostok 690950, Russia

*e-mail: iliushin.ig@dvfu.ru

It is known that in the treatment of malignant neoplasms, the greatest therapeutic effect is achieved by irradiating the tumor with photons having energies from 20 keV to 200 keV [1]. However, the prone ability of photons with such energy is small, so they are used for radiation therapy of superficial tumors. For the treatment of malignant neoplasms located deep in the human body, higher-energy γ -quanta are used, for example, photons emitted by the ^{60}Co isotope with energies of 1173.2 keV and 1332.5 keV. The disadvantage of such radiation is their weak interaction with cancer cells, which, in order to achieve the desired therapeutic effect, they usually try to level by increasing the intensity of radiation. On the other hand, an increase in radiation intensity can lead to significant damage to healthy tissues surrounding the tumor. One way to resolve the above “therapeutic paradox” is the conversion of high-energy γ -quanta ($E_\gamma \sim 1 \div 5$ MeV) into quanta with $E_\gamma \sim (20 \div 200)$ KeV, due to the scattering of high-energy photons by nanoparticles introduced into the tumor containing atoms of elements with a large atomic number [2].

In order to increase the efficiency of radiation therapy by delivering particles to the tumor area, magnetic particles coated with a substance with a high charge number Z can be used. For example, the core/shell of gold-coated magnetite nanoparticles (F_3O_4/Au) can serve as a source of secondary photons.

In this work, we conducted an experimental study and modeling of the effect of the concentration of core-shell F_3O_4/Au nanoparticles on the intensity of secondary radiation of gamma rays in the energy range 20-200 keV.

The energy spectrum of scattered radiation from a radionuclide source was measured (a gamma radiation source (OSGI type) with an activity of 10 kBq was used) when gamma radiation passed through solutions of particles containing core-shell F_3O_4/Au nanoparticles. The measurement results were recorded in the form of emission spectra on a gamma spectrometer. The ionizing radiation source was located at an angle of 45 degrees to the spectrometer detector. Nanoparticle solutions were investigated: Au (20nm); F_3O_4 (224nm)/ Au (14nm); F_3O_4 (227nm)/ Au (16nm) with different concentrations in solution.

In addition, the effect of an inhomogeneous magnetic

field H on the concentration of F_3O_4/Au nanoparticles was studied. It was shown that the growth of H leads to an increase in the concentration of nanoparticles in the region of maximum inhomogeneity.

For modeling, we used the Geant4 toolkit version 10.05. Geant4 is a C++ Monte Carlo simulation tool originally developed for high-energy physics applications, and has found widespread use in radiation therapy, medical imaging, and radiation protection. In our program, Geant4 imitates a beam of quanta emitted by a ^{60}Co source and is responsible for the process of primary particle generation and for the production of secondary particles after radiation hits the target. The process of interaction of radiation with matter was calculated using the library for the description of electromagnetic interactions G4EMLOW7.9 and the subsequent Monte Carlo simulation. Based on the information about the experiment, a geometric model was constructed consisting of a source with a cascade β -decay of ^{60}Co with an activity of 2 kBq and an emitted radiation energy of 1.33 MeV and 1.17 MeV in the lead collimator, radiation directed at an angle of 45 degrees to the aluminum substrate, on the surface of which there is an aqueous solution of Fe/Au nanoparticles with a core/shell structure, all objects are located in the bulk filled with air. Scattered radiation is collected by a detecting volume that corresponds to the passport specifications of the high purity germanium detector used in the experiment. During the simulation, an aqueous solution of F_3O_4/Au nanoparticles was set using a volume with a random density distribution.

Acknowledgements

This work was financially supported by the state task of the Ministry of Science and Higher Education (Russia) # 3.7383.2017/8.9.

References

- [1] Kimlin, K., J. Mitchell, and R. T. Knight. Radiographer, **53**(2) (2006) 30.
- [2] K.S. Lukyanenko, V.I. Apanasevich, S. A.V. Lagureva, O.S. Plotnikova, I.V. Pankratov, V.P. Rudyuk, L.S. Stebunov, A.A. Chernobaev, P.A. Lykanov, N. Davydova, M.A. Medkov, V.N. Kustov, V.V. Temchenko. Pacific Medical Journal **4** (2016) 38.

Photocatalytic reduction of CO₂ over metal/BaTiO₃ catalysts

A.I. Savitskiy^{*,1,2}, R.M. Ryazanov², D.G. Gromov¹, V.I. Shatilo³, A.A. Shkal¹, E.P. Kitsyuk²,
A. Shtyka³, R. Ciesielski³, S.V. Dubkov¹

¹ National Research University of Electronic Technology, Bld. 1, Shokin Square, Zelenograd, Moscow 124498, Russia

² Scientific-Manufacturing Complex "Technological Centre", 1, Bld. 7, Shokin Square, Zelenograd, Moscow 124498, Russia

³ Institute of General and Ecological Chemistry, Lodz University of Technology, Zeromskiego 116, Lodz 90-924, Poland

*e-mail: andr.savitskiy@gmail.com

One-dimensional (1D) structured materials, such as nanotubes, nanorods, nanofibres, etc., attract a lot of attention because of their potential applications in the automotive, aerospace, microelectronic industry and medicine [1]. It is worth noting perovskite phase metal oxides that exhibit various physical properties including ferroelectric, dielectric, pyroelectric and piezoelectric. Among the class of these materials, BaTiO₃ can be distinguished, which is widely used in photocatalysis [2], multilayer ceramic capacitors [3], chemical sensors [4], due to its attractive dielectric and ferroelectric characteristics.

For the synthesis of low-dimensional nanostructures, a number of methods have been developed over the past decades. All these methods can be roughly divided into two groups. The first and simplest process for the synthesis of molten salt (MSS) [5]. The second process is a wet chemical process with or without a template. Wet chemical methods, as a rule, have some disadvantages, such as complex synthesis routes and the high cost of the process. The synthesis of one-dimensional structures can be carried out by different methods: MSS, sol-gel, hydrothermal, direct oxidation, using microwaves, etc. [6]. It is worth noting that among the presented methods, the CPC method stands out, which is a relatively simple synthesis method in which the molten salt is used as a reaction medium for dissolving the reagent and precipitation. Thus, MSS is widely used for the synthesis of functional 1D structured oxide ceramics.

In this work, a simple approach to the synthesis of barium titanate nanowires based on the reaction of molten salt was demonstrated. The starting materials used in this experiment were analytical grade reagents. Barium nitrate (Ba(NO₃)₂) was mixed with titanium dioxide (TiO₂) P25 at a molar ratio of 1: 1. Then the mixture was mixed with KCl salt at a mass ratio of 1:10. After this, the solution underwent ultrasonic treatment for 30 minutes and mechanically milled for 1 hour. Then the resulting mixture was placed in a corundum crucible. The synthesis took place in an air atmosphere at 1000 ° C for 5 hours. The synthesized nanowires had an average diameter of about

80 nm and a length of up to several tens of micrometers. On the samples deposited metallic nanoparticles of gold, silver and platinum impregnation method. The size of the metal particles was about 30-60 nm.

Arrays of nanoparticles were studied using FEI Technai G2 20 S-Twin transmission electron microscope equipped with EDAX attachment for X-ray energy dispersive spectroscopy. The study of the obtained samples of barium titanate nanowires was carried out using a two-beam scanning electron microscope Helios NanoLab 650i.

The obtained Me\BaTiO₃ samples were analyzed using gas analysis was performed on a Hewlett Packard 5890 Series II 2-FID equipped with a flame ionization detector. The carrier gas is helium; the velocity of the carrier gas in the column is 10 ml/min. A special stand, which includes 2 UV lamps, a reactor, and a heating element was developed and manufactured to study the photocatalytic activity CO₂ recovery. The specific surface area and porosity of the catalysts and their supports were determined with automatic sorptometer Sorptomatic 1900.

The molten salt method is simple and cheap, therefore, it is of interest for the formation of photoactive catalytic structures based on BaTiO₃. The formed Me (Au, Ag, Pt) / BaTiO₃ heterostructures have demonstrated the promise of using barium titanate as a carrier for photocatalytic applications.

Acknowledgements

This work was supported by the Russian Science Foundation (project No. 19-19-00595)

References

- [1] M. Acosta, N. Novak, V. Rojas, S. Patel, *Applied Physics Reviews* **4** (2017).
- [2] B. Zhang, Sh. Cao, M. Du, X. Ye, *Catalysts* **91** (2019).
- [3] K. Hong, T. Hyung lee, J. M. Suh, *J.Mater.Chem.* **7** (2019).
- [4] Z. Meng, R. M. Stolz. *Chem. Rev.* **119** (2019).
- [5] Bao-rang Lin, W. Shang, Z.-l. Hu, N. Zhang. *Ceramics International* **40** (2014).
- [6] X. Chen, S. S. Mao. *Chem. Rev.* **107** (2007).

Nanocomposite of tin and lead oxides prepared in plasma of pulsed high-voltage discharge process: synthesis and electrochemical characteristics

A.I. Neumoin^{*1,2}, D.P. Opra¹, S.V. Gnedenkov¹, S.L. Sinebryukhov¹, A.A. Sokolov^{1,2},
V.G. Kuryavyi¹, V.I. Sergienko¹

¹ Institute of Chemistry of FEB RAS, 159 pr. 100-letiya Vladivostoka, Vladivostok 690022, Russia

² Far Eastern Federal University, 8 Sukhanova st., Vladivostok 690950, Russia

*e-mail: anton_neumoin@ich.dvo.ru

The technologies of energy storage and conversion based on Li⁺ charge transfer process have been widely used for portable devices. At the same time, usage of lithium-ion batteries (LIBs) for hybrid and electric vehicles, autonomous underwater unmanned complexes, etc. is limited by a number of problems, e.g. low specific capacity of traditional electrode materials. Indeed, the most part of commercial LIBs are involved carbonaceous anode material. However, such anodes can uptake no more than one lithium ion per six atoms forming LiC₆, which limits its capacity to a value of 372 mA·h/g. Thus, the design of new electrode-active materials is an urgent task for scientists and battery engineers. Tin can interact with lithium to a form of Li_{4.4}Sn intermetallic compound providing a capacity of approximately 991 mA·h/g. The main shortcoming to commercialize the tin-based electrode is huge volume changes during the alloying/dealloying process. Such lithiation-induced changes can achieve to 257% of the original Sn volume and cause the mechanical destruction (pulverization) of electrode with a rapid degradation of storage capacity. Lead, which is in the same group of the periodic table as tin, forms the compounds with a similar stoichiometry and according to similar principles. On the other hand as compared to tin, lead has a larger unit cell volume resulting in lower volume variations upon alloying/dealloying. However, lead is noticeably heavier than tin (almost twice), and, hence, its specific capacity is much lesser (582 mA·h/g).

It is well-known that creation of hybrids and nanocomposites, having properties that are not typical for microscale materials, is a promising way to design an advanced electrodes for LIBs. The usage of Sn or Pb in a form of oxides, chlorides, fluorides, sulfides, etc. facilitate the volume stresses due to the formation of damping matrices during initial alloying process. In this case only tin/lead particles are involved in further charge/discharge cycles.

In this work, a nanostructured composite based on tin and lead oxides was synthesized by the one-step method of pulsed high-voltage discharge, which is low cost, safety, and facile.

As found by SEM the prepared material has a rough microstructure and consists of particles with a size of 350 nm. On their surface one-dimensional filamentous crystals (nanowhiskers) with a diameter of up to 100 nm and a length of several microns are observed. The X-ray microanalysis represents a uniform distribution of tin and lead in the material.

According to XRD, the material contains tin dioxide SnO₂, lead oxide PbO, and mixed oxide SnPb₂O₄. The

analysis of experimental data allows us to assume that the particles is SnO₂ and PbO, while the nanowhiskers growing from their surface consist of SnPb₂O₄ mixed oxide.

Figure shows cyclic voltammograms of the first and second cycles for SnO₂/PbO/SnPb₂O₄ electrode. The cathode region of the initial curve includes a series of peaks in the range from 0.15 to 1.65 V associated with the reduction of metal oxides (Eq. 1–3) and the formation of Pb and Sn particles, as well as their subsequent alloying with lithium (Eq. 4, 5). The anode peaks near 0.61 and 0.73 V of the first cycle curve correspond to the decomposition of Li_{4.4}Sn and Li_{4.4}Pb intermetallides. The second voltammogram differs significantly from the first ones in the cathode region, while their anode regions are similar. This confirms the irreversibility of the processes associated with the formation of lithium oxide and demonstrates the reversible nature of interactions between Li⁺ ions and Sn and Pb.

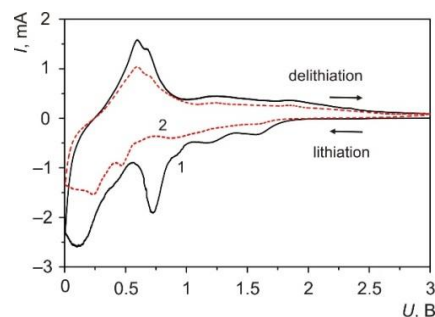
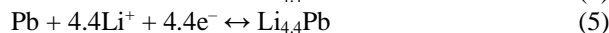
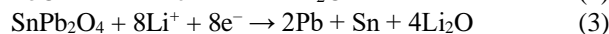
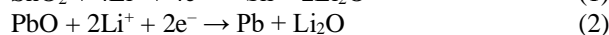


Figure. Cyclic voltammograms of the first (1) and second (2) cycles for nanocomposite of mixed tin and lead oxides

Acknowledgements

This work was supported by «Far East» FEB RAS Program (grant No. 18-3-006) and RFBR (grant No. 18-33-00345). The XRD data were collected under encouragement of the Ministry of Science and Higher Education of the Russian Federation (theme № 0265-2018-0003) using equipment of Core Faculty «Far Eastern Center of Structural Investigations» (Institute of Chemistry of FEB RAS).

Composite cryogel for Hg(II) ions recovery

I.A. Malakhova, Yu.O. Privar, Yu.A. Azarova, A.Yu. Mironenko, S.Yu. Bratskaya*
Institute of Chemistry, 159 Pr. 100-letiya Vladivostoka, Vladivostok 690022, Russia

*e-mail: sbratska@ich.dvo.ru

Drinking water quality and safety is highly sensitive issue for the population even in developed countries with high standards of water treatment technologies. As a result of industrial activities continually increasing flow of wastewaters containing toxic heavy metals, among which Hg(II), As(III)/As(V), Pb(II), and Cd(II) ions are the most harmful to human health already at ppb level, is released into the environment.

Currently, numerous organic and inorganic sorption materials are available for removal of toxic metal ions; however, in case of most toxic pollutants, they often fail to provide the efficiency of water treatment to the level required by Guidelines for Drinking-water Quality, published by the World Health Organization. This value for Hg(II) ions is just 0.0005 mg/L that is lower than the detection limit of atomic absorption spectroscopy widely used for water quality control. Since chronic exposure even to the low-level concentrations of mercury can result in many serious health damages [1], simple and efficient water treatment technologies, especially those applicable in point of use, e.g., regions with artisanal and small-scale gold-mining, are of high importance.

Recently, cryogels have been considered as promising materials for water treatment [2–5], point-of-use disinfection [6] and removal of metal ions [4]. Designing composite materials using chelating cryogels, e.g., based on polyethyleneimine, and inorganic nanomaterials can significantly improve efficiency of water treatment due to synergetic sorption mechanisms.

Here we report on fabrication of monolith composite sorbents (cryogels) based on polyethyleneimine (PEI) cross-linked with diglycidyl ether of 1,4-butanediol and zinc sulfide nanoparticles formed *in situ* by successive adsorption of Zn²⁺ and S²⁻ ions on PEI cryogel. The sorption of Hg(II) ions on PEI/ZnS cryogel was studied from solution of HgCl₂ in 0.0005M NaCl in batch and fixed bed. Sorption of Hg(II) ions in fixed-bed on monolith PEI and PEI/ZnS cryogels was investigated as follows: solution containing 200 mg/L of Hg(II) was fed through a syringe with 1 ml of the swollen cryogel (inner diameter – 4.8 mm, bed length – 6 cm) at a flow rate of 40 b.v.(bed volumes)/h, the samples were collected for analysis every 5 mL, the mercury concentration was determined using a HVG-1 Hydride Vapor Generator and an AA-6200 atomic absorption spectrometer (Shimadzu, Japan).

Although we have earlier shown [7] that PEI cryogels

were efficient sorbents for Hg(II) ions in batch, recommended by WHO level was not reached for the sorption from solutions containing 50 mg(Hg)/L. Due to the significant improvement of transport properties of cryogels under dynamic conditions, fixed-bed application of monolith PEI cryogel allowed Hg(II) removal from solution containing 200 mg/L down to the concentration <0,005 mg/L. Modification of PEI cryogel with ZnS nanocrystals resulted in increased affinity and sorption capacity of the material. The isotherms of Hg(II) ions sorption on PEI and PEI/ZnS cryogels fitted with the Langmuir equation showed that affinity of the sorbent to Hg(II) ions (Langmuir constant) and maximal sorption capacity were 4.5-folds and 1.5-folds higher for the composite sorbent. The fixed-bed application of the PEI/ZnS composite allowed to decrease the Hg(II) concentration to the level 10-fold lower than the WHO guideline value. Sorption of Hg(II) was preferential in the solutions containing equimolar concentrations of Hg(II) and Fe(III), Cu(II), Cd(II), although these transition metals were also recovered by the composite. The PEI/ZnS composite application in fixed-bed did not result in release of Zn(II) ions until the breakthrough point, which makes it applicable as highly efficient material for Hg(II) removal.

Acknowledgements

This work was supported by the Russian Foundation of Basic Research (project # 19-33-90143).

References

- [1] Environmental and occupational health hazards associated with artisanal and small-scale gold mining. World Health Organization. Technical paper #1: Environmental and occupational health hazards associated with artisanal and small-scale gold mining. ISBN 978 92 4 151027 1.
- [2] A. Baimenov, D.A. Berillo, S.G. Pouloupoulos, V.J. Inglezakis. Adv. Colloid Interface Sci. **276** (2020) 102088.
- [3] E.S. Dragan, D. Humelnicu, M.V. Dinu. Carbohydr. Polym. **210** (2019) 17.
- [4] E.S. Dragan, D.F.A. Loghin. Int. J. Biol. Macromol. **120** (2018) 1872.
- [5] L. Önnby. Biomed. Biotechnol. Appl. (2016) 333–361.
- [6] D.C. Wang, H.Y. Yu, M.L. Song, R.T. Yang, J.M. Yao. ACS Sustain. Chem. Eng. **5** (2017) 6776.
- [7] Y. Privar, I. Malakhova, A. Pestov, A. Fedorets, Y. Azarova, S. Bratskaya. Chem. Eng. J. **334** (2018) 1392.

VII. Biomaterials and sensors on their base

Conformational changes in DNA aptamers upon binding to Pb ions

R.V. Moryachkov^{*,1,2}, A.N. Berlina^{1,2}, P.V. Artyushenko², V.N. Zabluda¹, G.S. Peters⁴,
A.E. Sokolov^{1,5}

¹ Kirensky Institute of Physics, Akademgorodok 50, Krasnoyarsk 660012, Russia

² Federal Research Center "Krasnoyarsk Science Center SB RAS", Akademgorodok 50, Krasnoyarsk 660012, Russia

³ Federal Research Centre "Fundamentals of Biotechnology", Leninsky pr. 33, Moscow 119071, Russia

⁴ National Research Center "Kurchatov Institute", Akademika Kurchatova pl. 1, Moscow 123182, Russia

⁵ Siberian Federal University, Svobodny pr. 79, Krasnoyarsk 660041, Russia

*e-mail: mrv@iph.krasn.ru

To provide the extensive monitoring of environmental pollution the highly sensitive analytical methods are required. For the heavy metal detecting and control a few methods were proposed [1]. One of the directions is the development of the specific molecules to heavy metal ions, such as Mg^{2+} , Pb^{2+} and Hg^{2+} . These molecules are able to detect and recognize certain metals due to their structure and surface charge distribution. One of the most promising molecules for this aim are aptamers - single stranded DNA or RNA short chains which have a high selectivity and activity to their target - other biomolecules, viruses or even whole cells and also to heavy metal atoms [2,3].

A short aptamer (13 nucleotides) GT_obog was observed to specifically bind to the Pb^{2+} ions. The primary sequence of the thiolated aptamer is (SH-C6)-5'-GGGTG GGTGG GTG-3'.

Knowledge of the spatial three-dimensional structure of aptamer molecule is crucial for understanding the functions of specific aptamers and for determination of quantitative parameters of its specific binding. For this purpose the small-angle X-ray scattering (SAXS) method coupled with molecular simulations was applied [4].

The questions arised are: a) what is the nature of the specific binding the aptamers to the heavy metal; b) what the structure changes would occur during the binding; c) how much heavy atoms would able to be absorbed by the aptamer. A part of the answers may provide the SAXS method.

The measurements of scattering the X-rays on the DNA aptamers GT_obog in water solution were carried out on the BioSAXS beamline at the Kurchatov Institute, Moscow. The wavelength of the X-rays was 0.145 nm, sample-to-detector distance - 30 cm. Initially the structure analysis for the aptamer before Pb addition was performed. Then the SAXS patterns for GT_obog were collected at different concentrations of the Pb in solution from half-molar to many-fold increasing presence of the lead atoms.

The structure analysis was performed by standard procedure according the SAXS method pipeline [5]. The

SAXS data was treated in the program suite ATSAS [6], structure parameters such as maximal dimension of the molecule D_{max} , radius of gyration R_g , molecule volume converted to the molecular weight were derived. The SAXS curve analysis provided the observation of the conformational changes occurred with lead ion addition to the aptamer solution. These changes appeared to be no single direction. The form of the molecule shifts from the possibly aggregated state to the monodisperse solution, and from open structure to more compact conformation including peak at the definite Pb^{2+} concentration with the transfer to the open structure again during further increasing the heavy metal concentration. This behavior of the molecule structure requires the detailed and comprehensive interpretation utilizing molecular modeling approach.

This study gives a key information to the understanding the specific binding the aptamers with the targets and to the explanation of the chemical bonding between DNA aptamers and heavy metals.

Acknowledgements

The reported study was funded by RFBR, project number 19-32-90266.

References

- [1] M. Li, H. Gou, I. Al-Ogaidi, N. Wu. ACS Sustainable Chem. Eng. **1** (2013)713.
- [2] W. Zhou, R. Saran, J. Liu. Chemical reviews. **117** (2017) 8272.
- [3] N. K. Navani, Y. Li. Current opinion in chemical biology, **10** (2006) 272.
- [4] H. D. T. Mertens, D. I. Svergun. Journal of Structural Biology. **172** (2010) 128.
- [5] C. M. Jeffries, M. A. Graewert, C. E. Blanchet, D. B. Langley, A. E. Whitten, D. I. Svergun. Nature Protocols. **11** (2016) 2122.
- [6] D. Franke, M. V. Petoukhov, P. V. Konarev, A. Panjkovich, A. Tuukkanen, H. D. T. Mertens, A. G. Kikhney, N. R. Hajizadeh, J. M. Franklin, C. M. Jeffries, D. I. Svergun. J. of Appl. Cryst. (2017) 1212.

The Fe-Si-Au magnetic Janus particles for biomedical applications

S.A. Lyaschenko^{*1}, I.A. Yakovlev¹, I.A. Tarasov¹, D.A. Velikanov¹, Y.L. Mihlin², A.E. Sokolov¹, S.M. Jarkov³, I.V. Nemtcev⁴, M.N. Volochaev⁴, S.N. Varnakov¹, S.G. Ovchinnikov^{1,3}

¹ Kirensky Institute of Physics of SB RAS, Akademgorodok 50 bld. 38, Krasnoyarsk 660036, Russia

² Institute of Chemistry and Chemical Technology of SB RAS, Akademgorodok 50 bld. 24, Krasnoyarsk 660036, Russia

³ Siberian Federal University, 79 Svobodny pr., Krasnoyarsk 660041, Russia

⁴ Federal Research Center KSC Siberian Branch Russian Academy of Sciences, Akademgorodok 50, Krasnoyarsk 660036, Russia

*e-mail: lsa@iph.krasn.ru

In last time, there is an active introduction of nanotechnology and magnetic materials in biomedicine. In particular, magnetic nanoparticles are used for physico-chemical labeling of cancer cells and targeted drug delivery systems. Depending on the type of magnetic nanoparticles, abnormal cells can be visualized in vivo using magnetic resonance imaging (MRI), to extract cancer cells from saline by magnetic separation for in vitro analysis, to causing hyperthermia of cells in a high-frequency magnetic field and to exerting a magnetomechanical effect to initiate cancer cell apoptosis in low-frequency low intensity magnetic field.

MRI, as a safe and common medical diagnosis method, lets the use of superparamagnetic nanoparticles as a contrasting agent [1]. For MRI, it is advisable to use superparamagnetic nanoparticles with sizes less than 50 nm, since they easily penetrate cell membranes and do not exhibit ferromagnetic properties at room temperature. Magnetic nanoparticles with sizes from 50 to 150 nm showed high efficiency in magnetomechanical activation of apoptosis and suppression of proliferation of tumor cells marked by them in low-frequency non-heating magnetic fields [2]. Such nanoparticles weakly penetrate the cell, but freely overcome the extracellular space and are distributed throughout the body.

The optimal solution is the use of superparamagnetic nanoparticles of non-toxic elements with a size less than 150 nm with a high specific magnetic moment, a bioinert shell and anisotropy of shape. This work presents results of the synthesis of the Janus magnetic nanoparticles [3] with iron-silicon core, gold shell on up side and bioinert silicon oxides shell on down side (MNPFSAs). MNPFSAs are obtained by the method of solid-phase synthesis in ultrahigh vacuum and have both a rounded and an elongated shape depending on the density of the vicinal faces of the single-crystal substrate NaCl.

For MNPFSAs, structural, morphological, magnetic, and optical properties were investigated. According to electron diffraction data the structure of the Fe₃Si nucleus is revealed, which oxidizes in the presence of oxygen to form a bioinert shell of silicon dioxide on the surface. From the transmission electron microscopy data (TEM) the MNPFSAs sizes is 10-30 nm for round shape (Fig. 1). Chains can reach a length of 100 nm. The specific magnetic moment of the MNPFSAs nucleus were measured by vibrational magnetometry at 300 K and it is comparable

that of superparamagnetic magnetite nanoparticles (60 emu/g). However, magnetic moment can be increased by varying the stoichiometric composition of the nucleus.

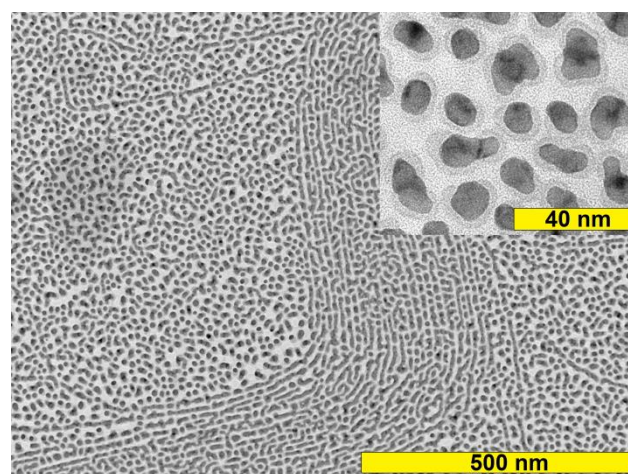


Figure 1. TEM of MNPFSAs after washing in water.

Samples were studied by X-ray photoelectron spectroscopy (XPS) to determine the chemical composition of the nanoparticle shell. The energy peaks from Fe, Si, and O were analyzed using the CasaXPS software. It was found that the surface layer of nanoparticles up to 3 nm thick contains iron, 96.7 at. % of which is associated with oxygen and silicon, but only 3.3 at. % has Fe-Fe bonds. Analysis of the peaks for oxygen showed that 63.8 at. % of it is associated with silicon and 36.2 at. % is associated with iron. Data for silicon showed 90.8 at. % bonds with oxygen and only 9.2 at. % bonds with iron. The nanoparticle shell consists mainly of silicon oxides and contains up to one third (atomically oxygen) of iron oxides.

The TEM and XPS results were obtained by a Hitachi HT7700 transmission electron microscope and a SPECS UNI-SPECS photoelectron spectrometer in the Krasnoyarsk Regional Center of Research Equipment of Federal Research Center «Krasnoyarsk Science Center SB RAS».

References

- [1] M. Shinkai, J. Biosci. Bioeng. **94** (2002) 606.
- [2] I.V. Belyanina, T.N. Zamay, G.S. Zamay et al. Theranostics, **7** (2017) 3326.
- [3] Y.I. Golovin, S.L. Gribanovsky, D.Y. Golovin et al. Journal of Nanoparticle Research, **19** (2017) 59.

Protein biosensor based on nanowire field effect transistor

T.E. Smolyarova^{*1,4}, A.V. Lukyanenko^{2,4}, L.V. Shanidze¹, V.V. Krasitskaya³, A.S. Tarasov^{2,4}, N.V. Volkov²

¹ Krasnoyarsk Science Center of SB RAS, 50 Academgorodok St., Krasnoyarsk, 660036, Russia

² Kirensky Institute of Physics KSC SB RAS, 50/38 Academgorodok St., Krasnoyarsk, 660036, Russia

³ Institute of Biophysics KSC SB RAS, 50/50 Academgorodok St., Krasnoyarsk, 660036, Russia

⁴ Siberian Federal University, 76 Svobodny Av., Krasnoyarsk, 660041, Russia

*e-mail: smol_nano@iph.krasn.ru

Silicon nanowires (NW) attracted considerable attention during the last years because of their possible application as sensors [1, 2]. In this paper we describe the application of SiNW sensors as typical FET-based devices with Schottky contacts for green fluorescent protein (GFP) detection.

Silicon nanowires were fabricated from SOI (100) wafers using thermal evaporation in ultra-high vacuum was used to obtain the thin film of Fe and then the electron beam lithography (EBL) process was used to obtain Fe contact pads to allow the carrying out of the investigations of the electric properties. EBL exposure process and reactive ion etching (RIE) were used to obtain the array of silicon nanowires. Besides of the metal pads in the fabricated structure a back gate was obtained on the backside of the SOI substrate using doping with indium (In). AFM images show the width of the silicon nanowires are correspondingly 0.8, 1, 3 μm Fig 1(a, b, c).

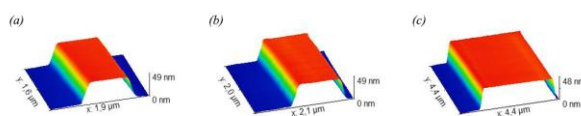


Figure 1. AFM images of fabricated 0.8 μm , 1 μm and 3 μm NWs correspondingly

SiNWs surface was functionalized with APTES molecules by the probe of atomic force microscope in contact mode [3, 4]. These molecules give amino groups ($-\text{NH}_2$) on the surface that react to amino groups in proteins. Here we present the results of GFP detection by SiNW FETs with different widths of NWs (Fig. 2).

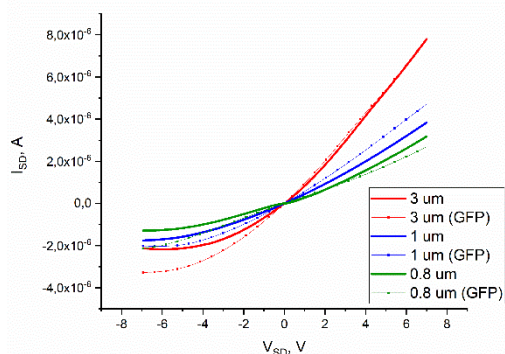


Figure 2. I_{SD} - V_{SD} dependences of fabricated SiNW FETs

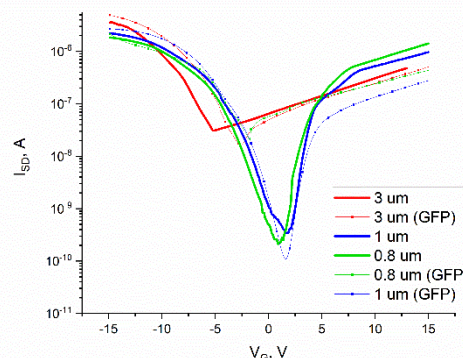


Figure 3. Transfer dependences of fabricated SiNW FETs

According to the carried out investigations it is possible to conclude that the fabricated nanowire biosensors have great potential for protein diagnostic applications.

Acknowledgements

The work is carried out with the assistance of Krasnoyarsk Regional Center of Research Equipment of Federal Research Center «Krasnoyarsk Science Center SB RAS» and Russian Foundation for Basic Research, Government of Krasnoyarsk Territory, Krasnoyarsk Regional Fund of Science to the research project № 18-42-243013.

References

- [1] Zhang, Guo-Jun, and Yong Ning. *Analytica chimica acta* **749** (2012) 1.
- [2] Mikolajick, Thomas, and Walter M. Weber. *Anisotropic nanomaterials*. Springer, Cham, 2015. 1-25.
- [3] Mohammed, Ahmed Mishaal, et al. *Journal of Nanomaterials* 2014 (2014).
- [4] Liang, Yuchen, et al. *Applied surface science* **322** (2014) 202.

Tomato (cv. Bonsai) plant development under different light spectra

O.V. Nakonechnaya^{*1}, A.S. Kholin², E.P. Subbotin², O.V. Grishchenko¹, E.V. Burkovskaya¹, Yu.A. Khrolenko¹, M.L. Burdukovskii¹, A.V. Mischeeva¹, I.V. Gafitskaya¹, I.Yu. Orlovskaya¹, Yu.N. Kulchin²

¹ Federal Scientific Center of the East Asia Terrestrial Biodiversity, 159 Stoletiya Street, Vladivostok 690022, Russia

² Institute of Automation and Control Processes of FEB RAS, 5 Radio St., Vladivostok 690041, Russia

*e-mail: markelova@biosoil.ru

Tomatoes are among the top ten crops most consumed by the population [1,2]. Tomato plants synthesize bioactive carotenoid pigments (lycopene and β -carotene), glycoalkaloids (dehydrotomatine, α -Tomatine and esculoside A), phenolic compounds, and vitamin C [1,3]. These compounds provide antioxidant properties and reduce the risk of cancer developing [4,5]. Growing of tomato plants in controlled conditions of greenhouses gains popularity nowadays, as it allows to get a crop all year round. The light spectrum is an important component that determines plant growth. Therefore the aim of the study was to study the effect of different polychromatic LED light varieties on the growth and development of tomato plants (*Solanum lycopersicum* L. cv. 'Bonsai').

Experiments were carried out in the Federal Scientific Center of the East Asia Terrestrial Biodiversity (FSCATB), Far Eastern Branch of the Russian Academy of Sciences (Vladivostok) in 2019. For the experiment, a different LED light sources were designed and manufactured in the Center of Laser Technologies of the Institute of Automation and Control Processes of the Far Eastern Branch of the Russian Academy of Sciences (IALS RAS, the Far Eastern Branch of the Russian Academy of Sciences). Experimental setup consisted of 4 isolated boxes equipped with LED light sources with different spectral characteristics: full spectrum (FS) - blue+red; RGB - blue+red+green; SunBox (SB) simulating the solar spectrum in the wavelength range of 440–660 nm, and warm white light (WW) used as a control.

The results showed that tomato plants cv Bonsai passed through age-related stages of the seedling and juvenile plant during the first 2 weeks of the experiment. The highest hypocotyl height and cotyledon sizes (length and width) were observed in the seedlings under FS. The maximum length and width of the first leaf of the juvenile plants were also noted in the group of FS box. The minimum sizes of cotyledon leaves and the first leaf were observed in control plants under WW light.

Over the next 1.5 months of development, the plants increased in height by almost 2 times. The maximum height values were typical for plants under FS. Tomatoes grown under RGB light were the leaders in the number of leaves. Values of the leaf size (length and width) and fresh mass of aerial parts were the highest in SB plants. Root fresh mass was identical in plants of all experimental groups, except for the FS plants with the lowest meanings. The maximum ash percentage was observed in FS plants, which was consistent with the data on the amount of water in plants.

When studying stomatal apparatus of leaves, it was shown that the WW light stimulated the stomata formation. The FS light caused the increase in the size of stomata guard cells. The tendency of the inverse relationship between the values of the studied stomata indices remained in all variants of experiment, except the plants under SB, in which the average values of both indices were observed. This combination of stomatal apparatus parameters turned out to be optimal, since SB plants with the largest leaves had the maximum weight of the aerial part.

Thus, the results showed that the spectrum of the FS LED light source provided plant extension, probably due to the greater proportion of red in the spectrum. A 10% decrease in the portion of red light and 10% increase in the portion of green light (RGB light source) led to a development of a larger leaves number and size on tomato plants in comparison with other experimental groups. At the same time, a large portion of green light in the spectrum (40%) contributed to the accumulation of a larger amount of water, which caused the maximum values of fresh aerial and root mass. Meanwhile, the combination of blue, green, and red in SB in proportion of 26%, 41%, 33%, respectively, led to the specific adaptive reaction of the stomatal apparatus in the experiment, which ensured sufficient leaf gas exchange. At the same time, a decrease in blue or green irradiation by 2 times in plants under FS and WW lights caused the formation of a potentially higher stomatal conductivity.

Acknowledgements

The work was supported by the Ministry of Science and Higher Education of the Russian Federation (Agreement No. 075-15-2019-1696, from 02.12.2019. Unique project identifier - RFMEFI60419X0229).

References

- [1] M. Friedman. J. Agric. Food Chem. **61**(2013) 9534.
- [2] K.-H Son, E.-Y. Kim, M.-M. Oh. Protected Horticulture and Plant Factory **27** (2018) 54.
- [3] R. Garcia-Closas, A. Berenguer, M.J. Tormo, M.J. Sanchez, J.R. Quiros, C. Navarro, R. Amaud, M. Dorronsoro, M.D. Chirlaque, A. Barricarte, E. Ardanaz, P. Amiano, C. Martinez, A. Agudo, C.A. Gonzalez. Brit. J. Nutr. **91** (2004) 1005.
- [4] M. Etminan, B. Takkouche, F. Caamano-Isorna. Cancer Epidemiol. Biomarkers Prev. **13** (2004) 340.
- [5] N. Khan, F. Afaq, H. Mukhtar. Antioxid. Redox Signal. **10** (2008) 475.

Soybean plant growth under different light conditions

A.V. Micheeva¹, O.V. Nakonechnaya^{*1}, E.P. Subbotin², O.V. Grishchenko¹, I.V. Gafitskaya¹, Yu.N. Kulchin²

¹ Federal Scientific Center of the East Asia Terrestrial Biodiversity, 159 pr. 100 let Vladivostoku, Vladivostok 690022, Russia

² Institute of Automation and Control Processes of FEB RAS, 5 Radio St., Vladivostok 690041, Russia

*e-mail: markelova@biosoil.ru

The soybean (*Glycine max* (L.) Merr.) is one of the major food crops and an alternative protein source. It is a self-pollinated species with low genetic variation. To expand the range of genetic variation, biotechnological method of inducing somatic embryogenesis, i.e. the formation of embryoid structures (embryoids) in the cell culture without any additional mutagens influence on the plant can be used. Somatic embryogenesis is a process in which a plant is derived from a single haploid or diploid somatic cell through characteristic embryological stages without gamete fusion [1]. Regenerated plants are considered to be clones, varying at the same time from the parent plants by one or a few characters [2]. An influence of light of different spectra and intensities on embryogenesis of soybean plants was studied previously in connection with hormone regulation [3].

Investigation of somatic embryogenesis induction in soybean *in vitro* by mono- and polychromatic radiation using the light-emitting diodes (LEDs) with a wavelength range from 440 to 660 nm and subsequent selection the optimal spectrum for developing the fully formed plants were the aim of our research.

To induce somatic embryogenesis, immature cotyledons without the embryonic axis, isolated from unripe beans were used. The cotyledons were placed onto nutrient medium MS [4] with phytohormones. Test-tubes with embryoids under the cotyledonary development stage were placed in boxes with different LEDs. Light irradiation with intensity of 48 mmol/(m²*s) was generated by different types of LEDs with various spectra: cold white (CW), white (W), warm white (WW), full spectrum (FS, 450 nm and 660 nm), red (630 nm), and royal blue (RB, 440 nm). Three variants of white light sources had the first emission maximum at approximately 440 nm corresponding to blue light, with different intensity for each type of white light. The second maximum corresponded to red-to-green spectrum within the wavelength range of 540–660 nm. Fluorescent lamps OSRAM L 36W/765 were used as control illumination (K) in the same climate conditions and photoperiod (16/8 h). An innovative LED light source sunbox (SB) simulating the solar spectrum in the wavelength range of 440–660 nm [detailed description in: 5] was also used.

The results showed that embryoids had different growth rates during two months of cultivation, depending on the light spectrum. For the first month of cultivation the maximum growth rate was observed in boxes with the FS and SB spectra, and an increase coefficient in embryoid

height was 2.1 and 1.8, respectively, against the data on the intact embryoid height. The rapid growth was probably determined by the proportion of red LEDs (more than 30%), since red light is known to promote plant extension. The lower growth rate was registered in boxes with R and RB spectra – 1.62 and 1.59, respectively. Formation of one, sometimes two and three roots and the first true leaf was noted by the end of the first month of cultivation for plants under mentioned spectra, as well as under FS spectrum. The lowest growth rate was observed for embryoids cultured under the polychromatic spectra CW, W, WW and K. The increase coefficients of embryoid height were 1.49, 1.41, 1.19, and 1.21, respectively. A decrease in the growth rate can probably be explained by the difference in spectral composition.

During the second month of cultivation the growth rate remained the same for embryoids under CW, W, WW spectra. Growth intensity for embryoids under other light variants slowed down, in comparison with that during the first month of cultivation. Despite that, plants under FS spectrum had the maximum height at the end of the experiment. Size of the roots and true leaves increased during the second month of culturing in plants grown under R and FS light. All soybean plants obtained during the experiments have been adapted to growth in soil. Thus, according to the results, application of FS, R, RB seems to be preferable for obtaining soybean fully formed plants from embryoids *in vitro*.

The experiments showed that light spectrum is an effective non-chemical agent promoting the survival of soybean embryoids and their development into viable plants.

Acknowledgements

The work was supported by the Ministry of Science and Higher Education of the Russian Federation (Agreement No. 075-15-2019-1696, from 02.12.2019. Unique project identifier - RFMEFI60419X0229).

References

- [1] E.G. Williams, G. Maheswaran. *Annals of Botany* **57** (1986) 443.
- [2] P.J. Larkin, W.R. Scowcroft. *Theor. Appl. Genet.* **60** (1981) 197.
- [3] G. A. Bonacin, A. O. Mauro, R. C. Oliveira, D. Percin. *Genet. and Mol. Biol.* **23**(4) (2000) 865.
- [4] T. Murashige, F. Skoog. *Physiol. Plant.* **15** (1962) 473.
- [5] E.P. Subbotin, I.V. Gafitskaya, O.V. Nakonechnaya, Yu.N. Zhuravlev, Yu.N. Kulchin. *Turczaninowia.* **21**(2) (2018) 32.

Increased antibacterial activity by photoactivation of composites based on ZnO nanoparticles

D.A. Goncharova^{*1}, S.A. Kulinich², A.L. Nemoynkina¹, V.A. Svetlichnyi¹

¹ Tomsk State University, 36 Lenin Ave., Tomsk 634050, Russia

² Tokai University, 4-1-1 Kitakaname, Hiratsuka-shi Kanagawa 2591292, Japan

*e-mail: dg_va@list.ru

The development of functional textile materials today is of a great demand. Modification of cellulose fibers' surfaces by ZnO nanostructures allows creating many applications, such as UV protection, hydrophobicity/self-cleaning and antibacterial effect [1, 2]. ZnO NPs are biologically safe and biocompatible with unique structural, electrical, and thermal properties that depend on the size, shape, morphology and localization of the particles [3]. ZnO NPs are capable of generating reactive oxygen species (ROS) possessing photo-oxidizing and photocatalysis impacts on chemical and biological species. These NPs highly absorb UV light increasing their conductivity. Accordingly, UV irradiation can be used as an additional activator that increases the effectiveness of the antibacterial action of ZnO NPs [4].

The present study included the preparation of antibacterial composites based on linen and NPs obtained by PLA of a zinc target in air at atmospheric pressure. The experimental setup, synthesis conditions of the PLA and a detailed characterization of the obtained NPs are described in [5]. NPs were dispersed in water and applied onto linen surface by a pipette, and then was dried via airflow at room temperature. The operation was repeated several times in order to ZnO concentration on the surface was 0.1 and of 0.25 mg/cm².

The optical properties of antibacterial composites were analyzed by the spectrophotometer Cary100 (Varian, Australia). SEM analysis of Zn/linen composites' morphology was carried out using a scanning electron microscope VEGA 3 SBH (Tescan, Czech Republic). The antibacterial activity of the ZnO/linen composites was tested on *S.aureus* in accordance with ISO 20743:2013. The effect of irradiation by LEDs ($\lambda=365$ nm for 10 min) on the antibacterial activity of composites was also tested in accordance with adapted ISO20743:2013. Testing methodology and an installation for photoactivation is described in [6].

SEM analysis of pure linen fibers and ZnO/linen composites at various concentrations of ZnO NPs shown that the linen fibers have an average diameter of 5 to 80 μm and a smooth surface. NPs are presented on the surface of the ZnO/linen composites mainly on fibers defects. The fiber coating thickness increases with ZnO concentration increasing from 0.1 to 0.25 mg/cm². A study of optical properties showed that pure linen does not absorb the radiation of the LEDs used. The absorption band edge at 360 nm is observed for ZnO/linen composites. This band is caused by the presence of ZnO NPs, which are effectively excited by radiation of the LEDs used.

The investigation of the composites antibacterial activity (AA) shown that a bacteriostatic effect was at a

concentration of the active component (ZnO NPs) of 0.1 mg/cm² (AA = 1.83). And the concentration increasing up to 0.25 mg/cm² led to the antibacterial activity appearance (AA = 3.58). Additional irradiation of the ZnO/linen composites with LEDs light ($\lambda=365$ nm) for 10 min led to the total death of bacteria (AA = 7.09) even at the minimum concentration of the antibacterial component (0.1 mg/cm²) used. The irradiation of the control samples of pure linen fabric did not affect the growth of bacteria. The irradiation of the ZnO/linen composite with a wavelength of 365 nm stimulates additional mechanisms of pathogenic bacterium *S.aureus* destruction. The photo-irradiation of ZnO semiconductor particles promotes the formation of holes (h^+) in the valence band and electrons (e^-) in the conduction band. These electron-hole pairs cause a series of photochemical reactions with the formation of reactive oxygen species (ROS). The resulting ROS can penetrate the cell membrane, causing fatal damage to the bacteria [4].

Thus, it was found that the concentration of the antibacterial component of 0.1 mg/cm² and irradiation of 365 nm for 10 minutes are sufficient for the complete death of *S.aureus* bacteria in accordance with ISO 20743:2013. Further research will be focused on: (a) the minimizing the concentration of ZnO NPs in antibacterial coatings, (b) optimizing the radiation dose and exposure time, (c) testing antibacterial activity against bacteria with a more complex cell wall (*E.coil*).

Acknowledgements

The work was supported by the scholarship program of the President of the Russian Federation for young scientists and post-graduate students (SP-1772.2018.4)

References

- [1] R. Pandimurugan, S. Thambidurai. Int. J. Biol. Macromol. **105** (2017) 788.
- [2] M. Shaban, F. Mohamed, S. Abdallah. Sci. Rep. **8** (2018) 3925.
- [3] G. Sangeetha, S. Rajeshwari, R. Venkatesh. Mater. Res. Bull. **46** (2011) 2560.
- [4] A. Sirelkhatim, S. Mahmud, A. Seeni, N.H.M. Kaus, L.C. Ann, S.K.M. Bakhori, H. Hasan, D. Mohamad. Nano-Micro Lett. **7**(3) (2015) 219.
- [5] E.A. Gavrilenko, D.A. Goncharova, I.N. Lapin, A.L. Nemoynkina, V.A. Svetlichnyi, A.A. Aljulaih, N. Mintcheva, S.A. Kulinich. Materials **12** (2019) 186.
- [6] D.A. Goncharova, E.S. Savelev, I.N. Lapin, V.O. Trufanov, V.A. Svetlichnyi. 20th Int. Conf. of Young Special. on Micro/Nanotechnol. and Electron Devices, (EDM 2019) IEEE (2019) 601.

СБОРНИК ТРУДОВ

(на англ. яз.)

Научное издание

Пятая азиатская школа-конференция по физике и технологии наноструктурированных материалов

Международная школа-конференция
Владивосток, Россия, 30 июля – 03 августа 2020

Proceedings

Scientific publication

Fifth Asian School-Conference on Physics and Technology of Nanostructured Materials

International School-Conference
Vladivostok, Russia, July 30 – August 03, 2020

In charge of publication *N.G. Galkin*
Design and layout *S.V. Chusovitina and E.A. Chusovitin*

Отпечатано с оригинал-макета,
подготовленного в Институте автоматизации и процессов управления ДВО РАН,
минуя редподготовку в издательстве «Дальнаука»

Printed from the original layout,
prepared at the Institute of Automation and Control Processes, FEB RAS,
bypassing the preparation in the Dalnauka Publishing

Signed into print 27.07.2020.
Format 60x84/8. Printed sheets 23,33.

Dalnauka Publishing, Vladivostok